

# AGARD

ADVISORY GROUP FOR AEROSPACE RESEARCH & DEVELOPMENT

7 RUE ANCELLE, 92200 NEUILLY-SUR-SEINE, FRANCE

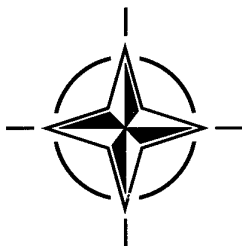
## AGARD CONFERENCE PROCEEDINGS 558

### Erosion, Corrosion and Foreign Object Damage Effects in Gas Turbines

(Les conséquences de l'endommagement des turbines  
à gaz par érosion, corrosion et objets étrangers)

*Papers presented at the Propulsion and Energetics Panel (PEP) Symposium held in Rotterdam,  
The Netherlands, 25-28 April 1994.*

DTIC  
ELECTE  
JAN 23 1995  
S G D



**NORTH ATLANTIC TREATY ORGANIZATION**

DISTRIBUTION STATEMENT A

Approved for public release;  
Distribution Unlimited

Published November 1994

*Distribution and Availability on Back Cover*

19950118020

# AGARD

ADVISORY GROUP FOR AEROSPACE RESEARCH & DEVELOPMENT

7 RUE ANCELLE, 92200 NEUILLY-SUR-SEINE, FRANCE

DTIC  
ELECTE  
JAN 23 1995  
S G D

AGARD CONFERENCE PROCEEDINGS 558

## Erosion, Corrosion and Foreign Object Damage Effects in Gas Turbines

(Les conséquences de l'endommagement des turbines  
à gaz par érosion, corrosion et objets étrangers)

Papers presented at the Propulsion and Energetics Panel (PEP) Symposium held in Rotterdam,  
The Netherlands, 25-28 April 1994.

Accession For	
NTIS CRA&I	<input checked="" type="checkbox"/>
DTIC TAB	<input type="checkbox"/>
Unannounced	<input type="checkbox"/>
Justification	
By	
Distribution /	
Availability Codes	
Dist	Avail and/or Special
A-1	



North Atlantic Treaty Organization  
Organisation du traité de l'Atlantique Nord

DATE QUALITY INSPECTED 3

DISTRIBUTION STATEMENT A

Approved for public release;  
Distribution Unlimited

19950118 020

# The Mission of AGARD

According to its Charter, the mission of AGARD is to bring together the leading personalities of the NATO nations in the fields of science and technology relating to aerospace for the following purposes:

- Recommending effective ways for the member nations to use their research and development capabilities for the common benefit of the NATO community;
- Providing scientific and technical advice and assistance to the Military Committee in the field of aerospace research and development (with particular regard to its military application);
- Continuously stimulating advances in the aerospace sciences relevant to strengthening the common defence posture;
- Improving the co-operation among member nations in aerospace research and development;
- Exchange of scientific and technical information;
- Providing assistance to member nations for the purpose of increasing their scientific and technical potential;
- Rendering scientific and technical assistance, as requested, to other NATO bodies and to member nations in connection with research and development problems in the aerospace field.

The highest authority within AGARD is the National Delegates Board consisting of officially appointed senior representatives from each member nation. The mission of AGARD is carried out through the Panels which are composed of experts appointed by the National Delegates, the Consultant and Exchange Programme and the Aerospace Applications Studies Programme. The results of AGARD work are reported to the member nations and the NATO Authorities through the AGARD series of publications of which this is one.

Participation in AGARD activities is by invitation only and is normally limited to citizens of the NATO nations.

The content of this publication has been reproduced  
directly from material supplied by AGARD or the authors.

Published November 1994

Copyright © AGARD 1994  
All Rights Reserved

ISBN 92-836-0005-3



*Printed by Canada Communication Group  
45 Sacré-Cœur Blvd., Hull (Québec), Canada K1A 0S7*

# **Recent Publications of the Propulsion and Energetics Panel**

## **CONFERENCE PROCEEDINGS (CP)**

### **Interior Ballistics of Guns**

AGARD CP 392, January 1986

### **Advanced Instrumentation for Aero Engine Components**

AGARD CP 399, November 1986

### **Engine Response to Distorted Inflow Conditions**

AGARD CP 400, March 1987

### **Transonic and Supersonic Phenomena in Turbomachines**

AGARD CP 401, March 1987

### **Advanced Technology for Aero Engine Components**

AGARD CP 421, September 1987

### **Combustion and Fuels in Gas Turbine Engines**

AGARD CP 422, June 1988

### **Engine Condition Monitoring – Technology and Experience**

AGARD CP 448, October 1988

### **Application of Advanced Material for Turbomachinery and Rocket Propulsion**

AGARD CP 449, March 1989

### **Combustion Instabilities in Liquid-Fuelled Propulsion Systems**

AGARD CP 450, April 1989

### **Aircraft Fire Safety**

AGARD CP 467, October 1989

### **Unsteady Aerodynamic Phenomena in Turbomachines**

AGARD CP 468, February 1990

### **Secondary Flows in Turbomachines**

AGARD CP 469, February 1990

### **Hypersonic Combined Cycle Propulsion**

AGARD CP 479, December 1990

### **Low Temperature Environment Operations of Turboengines (Design and User's Problems)**

AGARD CP 480, May 1991

### **CFD Techniques for Propulsion Applications**

AGARD CP 510, February 1992

### **Insensitive Munitions**

AGARD CP 511, July 1992

### **Combat Aircraft Noise**

AGARD CP 512, April 1992

### **Airbreathing Propulsion for Missiles and Projectiles**

AGARD CP 526, September 1992

### **Heat Transfer and Cooling in Gas Turbines**

AGARD CP 527, February 1993

### **Fuels and Combustion Technology for Advanced Aircraft Engines**

AGARD CP 536, September 1993

### **Technology Requirements for Small Gas Turbines**

AGARD CP 537, March 1994



## **AGARDOGRAPHS (AG)**

**Measurement Uncertainty within the Uniform Engine Test Programme**  
AGARD AG 307, May 1989

**Hazard Studies for Solid Propellant Rocket Motors**  
AGARD AG 316, September 1990

**Advanced Methods for Cascade Testing**  
AGARD AG 328, August 1993

## **REPORTS (R)**

**Application of Modified Loss and Deviation Correlations to Transonic Axial Compressors**  
AGARD R 745, November 1987

**Rotorcraft Drivetrain Life Safety and Reliability**  
AGARD R 775, June 1990

## **ADVISORY REPORTS (AR)**

**Performance of Rocket Motors with Metallized Propellants** (*Results of Working Group 17*)  
AGARD AR 230, September 1986

**Recommended Practices for Measurement of Gas Path Pressures and Temperatures for Performance Assessment of Aircraft Turbine Engines and Components** (*Results of Working Group 19*)  
AGARD AR 245, June 1990

**The Uniform Engine Test Programme** (*Results of Working Group 15*)  
AGARD AR 248, February 1990

**Test Cases for Computation of Internal Flows in Aero Engine Components** (*Results of Working Group 18*)  
AGARD AR 275, July 1990

**Test Cases for Engine Life Assessment Technology** (*Results of Working Group 20*)  
AGARD AR 308, September 1992

**Terminology and Assessment Methods of Solid Propellant Rocket Exhaust Signatures** (*Results of Working Group 21*)  
AGARD AR 287, February 1993

**Guide to the Measurement of the Transient Performance of Aircraft Turbine Engines and Components** (*Results of Working Group 23*)  
AGARD AR 320, March 1994

**Experimental and Analytical Methods for the Determination of Connected Pipe Ramjet and Ducked Rocket Internal Performance** (*Results of Working Group 22*)  
AGARD AR 323, July 1994

## **LECTURE SERIES (LS)**

**Engine Airframe Integration for Rotorcraft**  
AGARD LS 148, June 1986

**Design Methods Used in Solid Rocket Motors**  
AGARD LS 150, April 1987  
AGARD LS 150 (Revised), April 1988

**Blading Design for Axial Turbomachines**  
AGARD LS 167, June 1989

**Comparative Engine Performance Measurements**  
AGARD LS 169, May 1990

**Combustion of Solid Propellants**  
AGARD LS 180, July 1991

**Steady and Transient Performance Prediction of Gas Turbine Engines**  
AGARD LS 183, May 1992

**Rocket Motor Plume Technology**  
AGARD LS 188, June 1993

**Research and Development of Ram/Scramjets and Turboramjets in Russia**  
AGARD LS 194, December 1993

**Turbomachinery Design Using CFD**  
AGARD LS 195, May 1994

## Theme

The operation of gas turbine engines can be degraded severely by the effects of erosion, corrosion, ice ingestion and foreign object damage (FOD). The Gulf War conflict highlighted the problems that sand can cause. This Symposium acts as a focus for the discussion of relevant research and engineering solutions to these difficult problems, and allows lessons and experience to be shared amongst the NATO research community.

Experience from both military and civil operations is included. The impact on component design and repair is addressed, and techniques discussed to reduce erosion, including materials coatings and inlet particle separators. Testing procedures to investigate erosion, corrosion and FOD are included.

## Thème

Le fonctionnement des turbomoteurs peut être fortement dégradé par les effets de l'érosion, de la corrosion, de l'ingestion de glace et de corps étrangers (FOD). La guerre du golf a mis au premier plan les problèmes que peuvent présenter le sable. Ce symposium sert de forum pour une discussion sur les travaux de recherche en cours, ainsi que sur les éventuelles solutions technogéniques à ces problèmes difficiles. Il permet à la communauté de recherche scientifique de l'OTAN de partager l'expérience acquise et les enseignements tirés des travaux réalisés dans ce domaine.

Le symposium couvre l'expérience acquise lors d'opérations civiles et militaires. L'impact sur la conception et la remise en état est examiné et les techniques permettant de réduire l'érosion, y compris le revêtement des matériaux et les séparateurs de particules des entrées d'air, sont discutés. Les procédures d'essais pour l'étude de l'érosion, de la corrosion et du FOD y sont incluses.

# Propulsion and Energetics Panel

**Chairman:** Mr. R.E. Henderson  
Chief Advanced Propulsion Division  
Wright Laboratory  
WL/POP  
Wright Patterson AFB, OH 45433-7166  
United States

**Deputy Chairman:** Professor Dr. D.K. Hennecke  
Fachgebiet Gasturbinen und Flugantriebe  
Technische Hochschule Darmstadt  
Petersenstrasse 30  
64287 Darmstadt  
Germany

## Programme Committee

Mr. D.J. Way (Chairman)  
Manager, Propulsion Technology Department  
Aerodynamics and Propulsion Dept.  
Defence Research Agency  
Pyestock, Farnborough, Hants GU14 0LS, UK

Prof. Dr. Ing. K. Broichhausen  
Motoren- und Turbinen Union München GmbH  
Hauptabteilungsleiter Stromungsmaschinen, Berechnung  
80976 München, Germany

Lt. Col. Ing. M. de Matos G. Chambel  
CLAFA/DMA  
Av. Vasconcelos  
Alfragide-2700 Amadora, Portugal

IPA P. Fayol  
DCAe/Service Technique des  
Programmes Aéronautiques  
Département Moteurs  
4 avenue de la Porte d'Issy  
00460 Armées, France

Capt. E. Gunes  
1 nci Hava İkmal Bakim Merkezi  
26030 Eskisehir, Turkey

Prof. Dr. P. Kotsiopoulos  
Hellenic Air Force Academy  
Chair of Propulsion Systems  
Dekelia, Attiki, Greece

Mr. M. Mulero Valenzuela  
Adjunto al subdirector de Programas y  
Sistemas Aeronauticos  
INTA, Crta. Torrejón a Ajalvir, Km 4  
28850 Torrejón de Ardoz, Madrid, Spain

Prof. G. Torella  
Accademia Aeronautica  
Direzioe Studi  
80078 Pozzuoli (Napoli), Italy

Mr. W.W. Wagner  
Technical Director (Code 07)  
Naval Air Warfare Center  
Aircraft Division, P.O. Box 7176  
Trenton, New Jersey 08628-0176, USA

Prof. Ir. W.B. de Wolf  
National Aerospace Laboratory  
P.O. Box 153  
8300 AD Emmeloord, The Netherlands

Mr. J. A. Ziemianski  
Chief, Propulsion Systems Division  
Aeronautics Directorate, Mail Stop 86-1  
NASA Lewis Research Center, Cleveland, OH 44135  
USA

### HOST NATION COORDINATOR

Captain (Rtd) Ir. L. Sombroek

### PANEL EXECUTIVE OFFICE

Dr. Peter Tonn

Mail from Europe:  
PEP, AGARD-OTAN  
7, rue Ancelle  
92200 Neuilly sur Seine, France

From US & CANADA  
PEP, AGARD-NATO  
PSC 116  
APO AE 09777

Tel: 33 (1) 47 38 57 85 — Telex: 610176 (France)  
Fax: 33 (1) 47 38 57 99/ 47 38 67 20

# Contents

	Page
<b>Recent Publications of PEP</b>	iii
<b>Theme/Thème</b>	vi
<b>Propulsion and Energetics Panel</b>	vii
	<b>Reference</b>
<b>Technical Evaluation Report</b> by H.I.H. Saravanamuttoo	T
<b>Keynote Address</b> Understanding and Preventing Failure Causes and their Effects in Gas Turbine Engines by F. Aydinmakine	K
<b>SESSION I — OPERATIONAL EXPERIENCE AND REQUIREMENTS</b>	
<b>Out of Area Experiences with the RB199 in Tornado</b> by M.G. Down and M.J. Williams	1
<b>The Operation of Gas Turbine Engines in Hot and Sandy Conditions</b> by R.C. Sirs	2
<b>US Army Rotorcraft Turboshaft Engines Sand and Dust Erosion Considerations</b> by V.R. Edwards and P.L. Rouse	3
<b>Future Directions in Helicopter Engine Protection System Configuration</b> by D.L. Mann and G.D. Warnes	4
<b>Paper 5 withdrawn</b>	—
<b>Navy Foreign Object Damage and its Impact on Future Gas Turbine Engine Low Pressure Compression Systems</b> by P.C. DiMarco	6
<b>Scandinavian Airlines Systems Experience on Erosion, Corrosion and Foreign Object Damage Effects on Gas Turbines</b> by P. Stokke	7
<b>Paper 8 withdrawn</b>	—
<b>Modern Transport Engine Experience with Environmental Ingestion Effects</b> by T.L. Alge and J.T. Moehring	9
<b>SESSION II — DEPOSITION AND EROSION</b>	
<b>Particle Deposition in Gas Turbine Blade Film Cooling Holes</b> by V.H.M. Kuk, P.T. Ireland, T.V. Jones and M.G. Rose	10
<b>Experimental and Numerical Simulations of the Effects of Ingested Particles in Gas Turbine Engines</b> by A. Hamed and W. Tabakoff	11

<b>Paper 12 withdrawn</b>	—
<b>Paper 13 withdrawn</b>	—
<b>Particle Trajectories in Gas Turbine Engines</b> by S.C. Tan, R.L. Elder and P.K. Harris	14
<b>The Calculation of Erosion in a Gas Turbine Compressor Rotor</b> by G.C. Horton, H. Vignau and G. Leroy	15
<b>Performance Deterioration of Axial Compressors Due to Blade Defects</b> by J. Schmücker and A. Schäffler	16
<b>Erosion of T56 5th Stage Rotor Blades due to Bleed Hole Overtip Flow</b> by B.C. Barry and T.C. Currie	17
<b>Investigation of Mechanical Erosion in Fuel Pipelines</b> by M. Founti and A. Klipfel	18
 <b>SESSION III — FOREIGN OBJECT DAMAGE</b>	
<b>An Airborne Monitoring System for FOD and Erosion Faults</b> by G. Lombardo and G. Torella	19
<b>Conception des aubes fan soumises à l'impact d'oiseaux</b> (Fan Blades Design Under Bird Impact) by P. Vignolles, P.X. Bussonnet and J. Talbotec	20
<b>Impact Loading of Compressor Stator Vanes by Hailstone Ingestion</b> by J. Frischbier	21
<b>Soft Body Impact on Titanium Fan Blades</b> by D.A. Hughes, I. Martindale and C. Ruiz	22
<b>Ice-Impact Analysis of Blades</b> by C.C. Chamis, P.L.N. Murthy, S.N. Singhal and E.S. Reddy	23
 <b>SESSION IV — COATINGS, REPAIR AND MATERIALS ASPECTS — 1</b>	
<b>Paper 24 withdrawn</b>	—
<b>Damage of High Temperature Components by Dust-Laden Air</b> by P. König, T. Miller and A. Rossmann	25
<b>Analyse de l'érosion de matériaux métalliques de structures cubiques centrée et face centrée</b> (Generalized Law of Erosion: Application to Various Alloys and Intermetallics) by A. Magnée	26
<b>Protective Coatings for Compressor Gas Path Components</b> by D.R. Nagy, V.R. Parameswaran, J.D. MacLeod and J.P. Immarigeon	27
<b>New Trends in Coatings Developments for Turbine Blades: Materials Processing and Repair</b> by S. Alperine, R. Martinou, R. Mévrel and J.P. Huchin	28

## SESSION V — COATINGS, REPAIR AND MATERIAL ASPECTS — 2

<b>Braze Repair Possibilities for Hot Section Gas Turbine Parts</b>	<b>29</b>
by G. Marijnissen and R. van Gestel	
<b>Gas Turbine Compressor Corrosion and Erosion in Western Europe</b>	<b>30</b>
by H.J. Kolkman	
<b>Revêtements anti-érosion multicouches</b>	<b>31</b>
by P. Monge-Cadet, F. Pellerin, C. Farges, D. Rickerby and E. Quesnel	
<b>High Velocity Oxygen Fuel Spraying of Erosion and Wear Resistant Coatings on Jet Engine Parts</b>	<b>32</b>
by A.T.J. Verbeek	
<b>Thermal Testing of High Performance — Thermal Barrier Coatings for Turbine Blades</b>	<b>33</b>
by L. Bertamini and A. Di Gianfrancesco	
<b>Paper 34 withdrawn</b>	<b>—</b>
<b>X-Ray Absorption Spectroscopy in High Temperature Oxidation of Metals and Alloys</b>	<b>35</b>
by D. Gozzi and M. Tomellini	
<b>Resistance of Silicon Nitride Turbine Components to Erosion and Hot Corrosion/Oxidation Attack</b>	
by T.E. Strangman and D.S. Fox	

## SESSION VI — TESTING AND CERTIFICATION PROCEDURES

<b>Testing Considerations for Military Aircraft Engines in Corrosive Environments (A Navy Perspective)</b>	<b>37</b>
by F.T. Carroll and D.R. Parish	
<b>Paper 38 withdrawn</b>	<b>—</b>

## Technical Evaluator's Report

H.I.H. Saravanamuttoo  
 Carleton University, Dept. of Mechanical and Aerospace Engineering  
 3135 Mackenzie Building  
 1125 Colonel By Drive  
 Ottawa, Ontario, Canada  
 K1S 5B6

### Erosion, Corrosion and Foreign Object Damage in Gas Turbines

In 1990, PEP held a very successful meeting on cold weather operational problems in gas turbines (AGARD CP 480).

Following the Gulf War, it was obvious that climatic and environmental considerations had played a major role in aircraft operations, coupled with the problems of operating in high ambient temperatures. It was for these reasons that this meeting was organized.

The program was divided into the following sessions:

- I. Operational Experiences and Requirements
- II. Deposition and Erosion
- III. Foreign Object Damage
- IV. Coatings, Repair and Materials Aspects — 1
- V. Coatings, Repair and Materials Aspects — 2
- VI. Testing and Certification Procedures

Gas turbine operational and design problems cover many specialist areas, and the Structures and Materials Panel (SMP) was invited to contribute a session on coatings, repairs and material aspects, while the host Propulsion and Energetics Panel (PEP) supplied a similar session. It is one of the strengths of the AGARD organization that cross fertilization of ideas between technical panels is encouraged.

Another important aspect of AGARD meetings is the sharing of lessons and experience amongst the NATO research community. The Program Committee did an excellent job of gathering papers from across the membership spectrum. The final distribution of papers presented is given below.

Belgium	1
Canada	2
France	3.5
Germany	3
Greece	2

Italy	2
Netherlands	3
Norway	1
UK	6.5
US	7

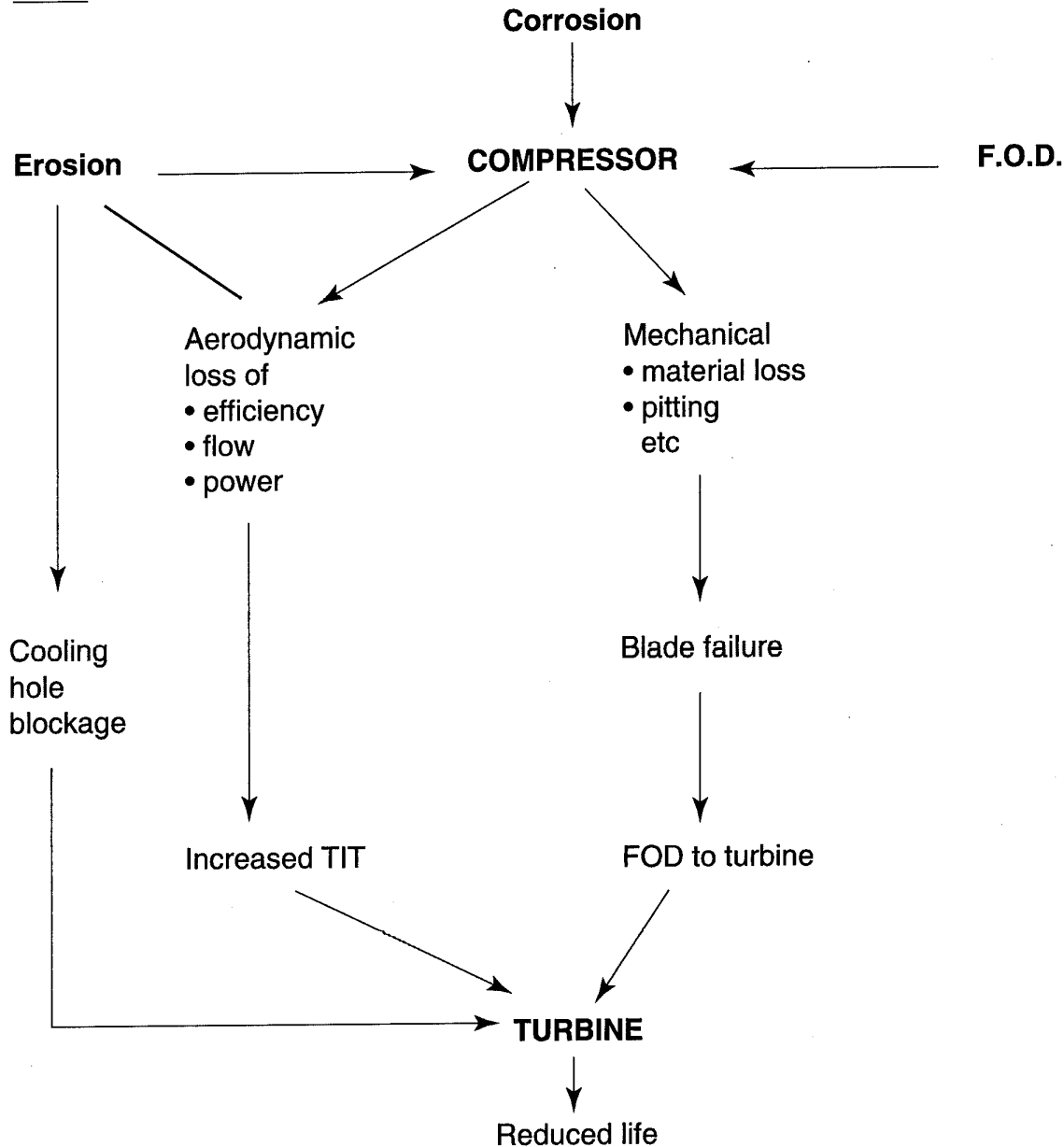
(One paper was a joint UK/France submission.)

#### OVERVIEW

Erosion, Corrosion and Foreign Object Damage (FOD) are often treated separately, but they all impinge on engine operability. It is useful to consider the broad picture of how these differing phenomena interact, as shown in Fig. 1.

**Erosion** is going to have its primary effect on the compressor, where frequent impact of hard particles will lead to abrasive removal of material from the rotor blades. The leading edge shape may be blunted, leading to a loss of aerodynamic efficiency. Vlegghert<sup>1</sup> showed that the effect of repeated abrasive cleaning on the J79 engine used in the F104 aircraft of the Netherlands Airforce resulted in a considerable loss of thrust, which was only detectable from aircraft performance deterioration at high speeds; it was thought that corrosion resulting from industrial pollution and sea air played a significant role, requiring frequent cleaning. Erosion is a major problem in helicopters operating in desert conditions, especially during take-off, landing or hover; the helicopter, of course, normally cruises at a height above that of the dust cloud formed. Two applications where this problem becomes even more critical are tanks and air cushion vehicles (ACV), which create a dust storm and then carry it with them; it is unfortunate that neither application was dealt with in this meeting. The effect of erosion will be to reduce both compressor efficiency and mass flow, resulting in either a loss of power at a fixed turbine inlet temperature (TIT) or an increased TIT for a

<sup>1</sup>Vlegghert, J.P.K., 'Handling Problems Through Compressor Deterioration', AGARD Conference Proceedings, 1978

**FIG. 1**

### **ECONOMIC AND SAFETY ISSUE**

given power. Erosion may also increase the flow areas in turbines, which will tend to reduce pressure ratio across the compressor with a further loss in power. With modern engines, however, using highly sophisticated turbine blades with very small cooling passages, sand and dust may plug the cooling holes; the resulting loss in cooling can rapidly cause local overheating and turbine blade failure.

**Corrosion** will result in roughening and pitting of blade surfaces, which will again cause a loss of aerodynamic efficiency. A more serious effect is the likely loss of blade material and the initiation of cracks eventually leading to blade failure. Corrosion can be a serious problem at high turbine inlet temperatures, and efficient filtration of airborne salt is very important in operations in a maritime environment. Blade failures in the front of the engine may result in FOD (more correctly



DOD, or Domestic Object Damage) in downstream components.

**FOD** will affect the compressor first, and may be caused by problems as diverse as bird strikes, ice ingestion or tools left in the intake ducting. FOD may result in serious out of balance or vibration problems, or engine flame out, leading to the loss of a single engined aircraft. Bird strike resistance is a prime feature of civil engine certification programs and civil transport aircraft often encounter bird strikes, which can cause major engine damage but seldom result in loss of the aircraft. The effect of FOD in the compressor will also reduce efficiency and flow, once again driving the engine to higher TIT. It should be noted that small scale FOD is common due to debris on runways, and this usually appears as nicks and dents in fan and compressor blades. Large scale FOD resulting from bird strikes may require the replacement of several fan blades; current fan designs, however, are moving towards wide chord blades which are more resistant to bird strikes.

#### SCOPE OF MEETING

The papers presented could be usefully classified in four basic areas.

1. Operations	6 papers
2. Research	11
3. Support of Operations	8
4. Design aspects	6

These classifications, of course, are somewhat arbitrary. It is also interesting to classify papers under the three main topics of the meeting.

Erosion	18
Corrosion	4
FOD	8

Some papers, of course, deal with more than one of these. Nevertheless, it is interesting to observe the heavy domination of erosion based papers; this is perhaps not surprising considering the problems of desert operations in the Gulf War.

It is not the intention of the Technical Evaluator to offer comments on each paper; rather a summation of interesting points from the areas described above will be presented.

#### Operations

Three papers were directly related to operations in desert conditions (Papers 1, 2 and 3). Paper 1, by

Rolls-Royce, discussed the problems arising from Tornado operations in hot, sandy conditions. Initially, it was found that plugging of the blade cooling holes was a major problem, but ingenious development of high pressure water blade cleaning systems proved highly successful in dealing with this problem. It was found that different standards of blades designed for the Royal Saudi Air Force (RSAF) and the RAF had different trailing edge blockage characteristics. Overall, engine reliability was good and no operational missions were lost due to engine related problems. Paper 2, by the RAF, concentrated on operations by Jaguar, Buccaneer and helicopters. The Adour engines in the Jaguar were primarily affected by loss of thrust at high ambient temperatures, requiring the use of increased turbine temperatures (25°C) which caused hot-end damage. Buccaneers operated at higher altitudes and the Spey engines encountered few problems. Considerable effort was expended in removing airborne sand from the intakes of helicopter engines. Engine Air Particle Separators (EAPS) were used quite successfully in both Puma Turbo III C4) and Chinook (T55-712E). The EAPS in Chinook resulted in an 'all-causes' engine rejection rate that was similar (actually slightly better) to the peace time rate, with a best achieved life of 240 hours. Paper 3, by the US Army, traced the introduction of Inertial Particle Separators (IPS) with the GE T-700 and showed that the IPS protected T-700 fared much better than older engine designs during a major exercise in Egypt. It appeared, however, that actual operating conditions in the Gulf War were significantly worse than anticipated and operating limits had to be relaxed. Paper 3, unfortunately, did not give any data on Gulf operations.

Papers 7 and 9 dealt with commercial airline experience. Paper 7 (by SAS) was primarily concerned with ice FOD on MD-80 aircraft; the MD-80 configuration appeared to be susceptible to both ice shedding from the wings and slush from the undercarriage. Paper 9 (by GE) stated that 90% of FOD occurrences were due to bird strikes, with 98% of these occurring close to airports; the location of garbage dumps close to airports was a major concern. This paper also dealt with problems of flame-out due to massive water or hail ingestion.

Paper 30 (NLR, Netherlands) discussed corrosion and erosion in compressors in Western Europe, where it was shown that the atmosphere was quite hostile. A major source of corrosion was the large quantities of manure associated with pig-breeding; a similar problem with fertilizers was described in

a German paper. It is clear that a rural atmosphere is not necessarily clean.

### Research

Research papers covered a wide variety of topics. Several dealt with FOD due to soft body (bird) impact and ice/hail impact (Papers 20, 21, 22, 23), while one paper (38 — not presented) dealt with bird impacts on propellers. Paper 26 presented generalized laws of erosion, with particular emphasis on various alloys and intermetallics. A joint NASA/Allied Signal paper (36) presented some interesting results on resistance of silicon nitride turbine components to hot corrosion/oxidation attack. Paper 19 (Italy) described a system for monitoring FOD and erosion faults; the proposal to use actual engine data to provide baselines is interesting, but it is not clear that this can be done without an improvement in on-board instrumentation fit. The results presented in Paper 19 are clearly incorrect; Table 1 shows turbine corrected flow functions apparently increasing without limit. These, of course, are limited at their choking values and the method proposed does not appear to account for compressor-turbine matching requirements. Several papers (10, 11, 12, 14) dealt with both theoretical and experimental prediction of particle trajectories and deposition on blade surfaces.

### Support of Operations

Some of the work in this area could certainly be described as research, but the prime aim is support of actual engine operation. Two papers from Canada (17, 27) dealt with operational problems on the T56; one dealt with a specific blade erosion problem, while the other covered the development of compressor coatings. MTU presented papers on performance deterioration in axial compressors, impact loading of stators due to hailstones and gas path degradation due to particles (16, 21 and 25). Paper 16 presented some very useful quantitative data on tip clearance and other damage on compressor efficiency, flow and surge margin. Both SNECMA and Turbomeca presented papers on coatings (28, 31) while the Dutch and Italian communities gave papers on both repair methods and thermal barrier coatings (29, 32, 33). The US

Navy gave a review paper discussing the evolution of design and test conditions for military aircraft engines in corrosive environments (37).

### Design

It is clear that considerable progress has been made in using research methods for prediction of particle trajectories in the design of Inertial Particle Separators. Both Rolls-Royce and SNECMA (with DRA) presented interesting papers (4, 15). The SNECMA paper showed severe erosion at the root section of a first stage axial compressor, while another showed erosion at the tip section. Clearly parameters such as blade Mach number and material properties are important variables. The design of fan blades to resist bird strike was described by SNECMA (20), this paper particularly emphasized the inter-relationship between aerodynamic design and structural integrity. The US Navy (6) gave a paper describing the effect on fan design of imposing a requirement for being able to change out damaged fans on-board an aircraft carrier; this shows the importance of considering operational restrictions right at the design stage.

### CONCLUSIONS

The Program Committee are to be congratulated on organizing a meeting which provided much valuable information on the effects of erosion, corrosion and FOD in gas turbines. The NATO research community owes a debt of gratitude to those companies that provided frank and honest discussions of problems encountered in hostile operating environments. This information will be extremely valuable in both new designs and specification of operating procedures.

It is clear that much has been learned about these critical problems. A great deal of on-going research is being carried out and the results incorporated into new designs. Erosion, corrosion and FOD will always affect gas turbine operations, influencing both safety and operating economics, and every effort must be made to minimize these problems at the design stage. This meeting has added considerably to the required body of knowledge.

H.I.H. Saravanamuttoo,  
Ottawa, May 1994

# **UNDERSTANDING AND PREVENTING FAILURE CAUSES AND THEIR EFFECTS IN GAS TURBINE ENGINES**

by

**Maj. Gen. Fazil Aydinmakine  
2nd Supply and Maintenance Center  
38095 Kayseri  
Turkey**

## **1. ABSTRACT**

The operation of gas turbine engines can be degraded severely by the effects of erosion, sand, corrosion, ice ingestion and foreign object damage. Due to geographical and environmental conditions, the effects of the erosion, corrosion and ice ingestion are in very limited amounts for TUAF's engines. However Foreign Object Damage is a major issue. In this presentation FOD of TUAF gas turbine engines, the current precautions taken, the FOD elimination program and the probable suggestions will be considered.

## **2. INTRODUCTION**

### **2.1. FOD as a Main Concern**

Ever since aircraft were powered by gas turbine engines, Foreign Object Damage (FOD) has been a main concern. FOD could be defined as any damage attributed to a foreign object that can be expressed in physical or economical terms which may or may not degrade the product's required safety and/or performance characteristics. Here are some examples of potential FOD;

- a. Tools, manufacturing and inspection hardware and other objects left in the vicinity of, or in a migratory path of engine inlets.
- b. Metal or wire clippings, solder balls and debris lying in the vicinity of electrical terminals circuitry, connectors, components, etc.
- c. Tools, hardware or debris left in the vicinity or in a migratory path of a vehicle's control system.
- d. Debris lying on runways ramps and taxiways.
- e. Nature creatures such as birds, insects, etc.

### **2.2. Acquaintance of TUAF with Gas Turbine Engines and FOD**

TUAF was first acquainted with gas turbine powered aircraft early in the 1950's. F-84's, F-86's and F-100's became the main aircraft of TUAF during that time. Gas turbines repair and overhaul business started in mid 60's. The early capabilities were limited to disassembly of major components, cleaning, inspecting, parts replacement, various levels

components tests and adjustments, final assembly and performance testing. Early in 1970's Pratt and Whitney's J57-21 engines of F-100 Super Sabres, General Electric J79-11 engines of F-104 Starfighters and J85-13 engines of F-5 Tigers had been handled. Within the same period the gas turbines such as J33-A35, J69-T25, NENE-10 and some others belonging to training aircraft had been repaired and overhauled.

Due to the limited repair, testing and overhaul capability various engine components such as controls and accessories had been shipped to USAF or foreign contractors to be tested and repaired.

Mid 1970's, TUAF received General Electric J79-17 engines of F-4 Phantoms, J79-19 engines of Italian F-104S aircraft and Rollce Royce Tyne-Mk-22 engines of German C-160 Transall aircraft.

Late in 1970's the TUAF focused on high degree of component repairs, controls and accessories testing and overhauling business. Considerable investments had been made in the machining, welding, electroplating, metal spraying, heat treatment, corrosion prevention areas and so on. A completely new facility had been constructed to test and overhaul main fuel controls, after/burner fuel controls, pumps, filters, valves, actuators etc.

As of today, this facility has more than one hundred state of art test benches. The second half of the 1980's became the years of investment for the new generation General Electric's high trust F 110 engines of F-16 Fighting Falcons. Today, near by the 1st Air Supply and Maintenance Center (1st ASMC), TUSAŞ Engine Industries (TEI) which manufactures F 110 engines under a joint-venture agreement, TUAF's engines repair and overhaul facilities are completely capable of repairing, testing and overhauling gas turbine engines including controls and accessories.

TUAF engine facilities has repaired and overhauled more than 5000 engines to date. Within this accomplishment Foreign Object Damage always became a major concern creating a heavy work load for the TUAF's engine facilities. Out of 5000 engines repaired since 1970's approximately 10 % of this figure was directly related to Foreign Object Damage repairs.

### 2.3. The Mission Requirements of TUAf's Engine Maintenance Facilities

To support operational bases with gas turbine engines being repaired and overhauled;

- At highest quality to assure and sustain flight safety.
- With maximum speed and effectivity to enhance combat readiness.
- With great savings to lower maintenance costs.

These mission requirements sometimes are in conflict due to the design characteristics and repair procedures of the current gas turbines.

### 2.4. The Effect of Design Characteristics and Repair Procedures on TUAf's Maintenance Mission Requirements

In achieving these requirements namely to maintain engines at highest quality with minimum time and cost;

- Early detection of internal engine problems by built in engine health monitoring systems,
- Quick disassembly and assembly, parts removal and replacement features,
- Highest durability of parts and components against erosion, corrosion, thermal stresses and cyclic loads.
- Longer service life limits for critical items.
- Unlimited service life for the majority of items.
- Extensive repair receiving nature of parts and components.
- Quick and easy component repair procedures and
- Built in self protection systems against FOD and severe environmental conditions.

are considered extremely important design characteristics for the gas turbines

## 3. EXPERIENCE ON FOD WITHIN TUAf

### 3.1. Operation Needs and Requirements

With the understanding that all systems are bound to fail, we all need to understand the cause of failures to correct and prevent them, for better performance.

During operation, failure identification are made by aircraft mechanics or the pilots. Here I would like to present real data of failure statistics based upon the last five years of operations and analyse them. Taking as reference 100.000 flight hours we note the following;

- 60-65 % of the aircraft are twin engines

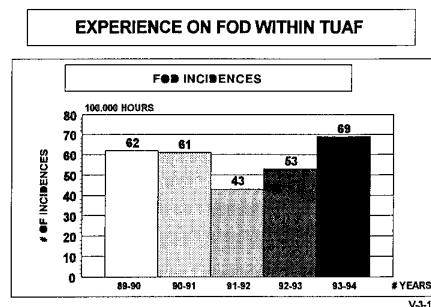


Fig. 1

- 1/4 to 1/5 th of the failures are reported by the pilots, (mostly bird strikes) and the rest by aircraft mechanics and/or overhaul engine receiving technicians.
- The periods corresponds to annual training schedules.

With the above clarifications the failure statistics in the first two years indicated roughly sixty incidents (Fig.1). The following 3 rd, 4 th and the fifth years showed an increase from roughly forty to seventy incidences.

Investigating further, bird strikes contribution to the above statistics, was identified to be the main cause of the high failure rates (Fig. 2).

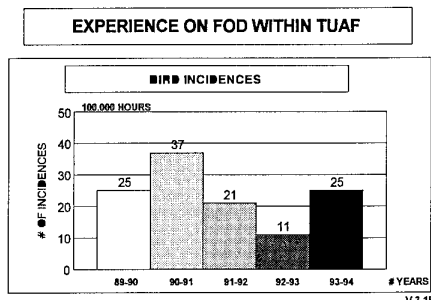


Fig. 2

Furthermore, discriminating between the fractions of a standard flight, namely the take of, cruise, final approach and the landing and applying the Montecarlo Techniques, we could identify that the bird strikes were concentrated on the cruise time, because of ground precautions were already taken (Fig.3).

As a consequence of those finding, an effort to draw bird concentration maps was initiated to be included in pre-flight briefings.

Having eliminated the less important bird strike incidences, which only increased the unscheduled maintenance requirements, we focused on the more serious remaining inorganic cause of failures.

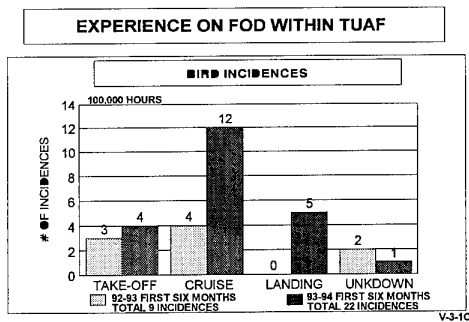


Fig.3

In general easily identifiable (e.g. large in size) objects, can be controlled as FOD agents. However in most of the cases the severe damages caused by small objects are much more difficult to identify and also to prevent them. This was the main reason for us to look for "microscopic" methods in assessing the damage and search for debris or trace of these types of foreign objects.

### 3.2. The Potential FOD Hazards Areas

The potential FOD hazards areas are mainly grouped as;

- a. Engineering design.
- b. Maintenance and manufacturing operations.
- c. Test cell activities.
- d. Flight line maintenance.

### 3.3. Identification and Elimination of Potential FOD Hazards Based on Engineering Design

Design engineering procedures and requirements shall emphasize the reduction of risk and the potential for elimination of FOD hazards as basic design criteria. The contractor shall establish adequate procedures to meet these requirements and shall assure that the product design reflect adequate consideration for FOD prevention. Some of these considerations are as follows.

- a. Identification and elimination of foreign object entrapment areas.
- b. Identification and sealing of areas through which foreign object can migrate.
- c. Use of adequate connectors, filtering devices and protective covers over critical mechanical, hydraulic and pneumatic components to prevent foreign object entry.
- d. Use of screens over exposed openings when appropriate; e.g.intakes, exhausts, etc.
- e. Installation of special access panels, ports, etc. for inspection and cleanout of foreign object that could potentially cause damage.

- f. Installation of devices to divert migrating foreign object from critical mechanisms or components to special access areas for removal.
- g. Use of fasteners with positive locking mechanism in areas where high vibration levels are expected or where separation of the fastened item could result in potential damage.
- h. Use of blind fasteners in critical areas, e.g. fuel cells, that are not prone to leaving debris upon extraction.
- i. Use of fasteners with self-retaining features capable of withstanding flight loads to secure high usage access panels.
- j. Elimination of potential foreign object built into equipment such as nameplates that can separate under dynamic loads anticipated.
- k. Locating service points, grounding points, build-in test equipment, etc. in areas which are least FOD sensitive.
- l. Use of competent metals and seals to prevent accelerated deterioration and subsequent spalling of the seal material.
- m. Use of conformal coating as a positive seal against entry of minute foreign object including dust and water vapor.
- n. Procedures shall include provisions for FOD incident feedback to manufacturing engineering and quality assurance for review and appropriate corrective action.
- o. Consideration should be given to airfoil design which can ingest foreign object without sustaining damage requiring replacement and rotor designs which allow replacement of individual damaged airfoils.
- p. Aircraft inlets should be designed to minimize traps where water can collect and freeze.

### 3.4. Control of Debris During Maintenance/Manufacturing

To establish an effective program for FOD prevention shall include a disciplined approach to manufacturing processes for the control of contamination and debris. As a minimum, the program shall address storage and handling of materials work instructions, tool control, parts control and good housekeeping practices. Procedures for storage and handling of materials and hardware components used in fabrication, assembly and test processes shall include measures for protection against contamination or damage from time of receipt until the finished product is delivered. Some of these measures are the following.

- a. Upon initial receipt of materials and components inspect the items for contamination, damage and assure that they are clearly and properly identified.

- b. Assure that corrosion control measures are implemented as required.
- c. Assure that open fittings or open ends of tubes, valves, pumps, air ducts and fluid-carrying items are protected with approved closures.
- d. Protect equipment items from exposure to physical, chemical or environmental damage.
- e. Assure that approved protective devices for materials and components are properly installed before storage and prior to shipment.
- f. Assure that material, equipment items, assemblies, etc. are moved with proper transportation and handling equipment and that this equipment is clean and free from extraneous debris.
- g. Install protective covers on components, major assemblies and equipment sensitive to damage or foreign object contamination during follow-on maintenance/manufacturing operations.
- h. Prior to movement of the assembly or subassembly conduct a through inspection for damage and debris and correct deficiencies.
- i. Provide covered foreign object containers in strategic locations in maintenance areas. These containers shall be emptied at regular intervals to prevent overfilling.

### 3.5. Prevention of FOD During Engine Test Cell Activities.

Prevention of FOD in a test cell environment can be broken into four main areas, as follows;

- General Precautions
- Pre Operation Precautions
- Operation Precautions
- Post Operation Precautions

Each one is detailed below;

#### a. General Precautions:

- (1) Insure personnel are aware of local FOD prevention program.
- (2) Insure that equipment is serviceable by performing scheduled preventive maintenance (i.e. inlet screen, thrust stand)
- (3) Inspect facility for any items which may be loose or damaged (i.e. broken concrete, loose acoustical panels).
- (4) Visually inspect test area daily for foreign objects/debris.
- (5) Insure hand tools/test equipment are inventoried and accounted for.

#### b. Pre Operation precautions:

- (1) Inspect test item (engine) for loose/missing/damaged conditions.
- (2) Visually inspect engine compressor/exhaust for damage and foreign objects.
- (3) Install engine on thrust stand, make engine to test cell connections insuring that leads/hoses/connectors are restrained/positioned so that they don't pose a potential for FOD.
- (4) Insure clean sources of air/oil/fuel and connect to the engine properly.
- (5) Insure weather conditions (dew-point) permit engine running without the possibility of engine icing.
- (6) High pressure water wash floor to insure no foreign objects were introduced during pre operation maintenance.
- (7) Insure test personnel do not have loose articles in their pockets (i.e. pens, ID badges, loose buttons).

#### c. Operation precaution:

Constant visual inspection of engine/facility/ equipment for any potential FOD conditions.

#### d. Post operation precaution:

- (1) Visually inspect engine compressor/exhaust for damage and foreign objects.
- (2) Disconnect test cell to engine connections and cap/plug all openings.
- (3) High pressure water wash floor to insure no foreign objects were introduced during operation.
- (4) Inspect facility and test equipment for serviceability.

### 3.6. Prevention of FOD During Flight Line Maintenance

FOD prevention procedures observed during flight line maintenance and launch activities are as follows;

- a. Insure personell are aware of local FOD prevention program:
- b. Assure personnel are aware of a need to keep flight lines/hangar areas clean.
- c. Any potential FOD conditions are reported to local FOD prevention contact point and corrected on the spot.
- d. Insure that equipment is serviceable by performing scheduled preventive maintenance (i.e. Hydraulic cart, Air start cart).

- e. Before performing Aircraft maintenance, insure that;
  - (1) Maintenance personnel do not have loose articles (i.e. pens, ID badges)
  - (2) Hand tools/test equipment are inventoried and accounted for.
- a. Visually inspect Aircraft and it's openings for loose/damaged parts/hardware or foreign objects.
- b. Inspect engine compressor/exhaust for damage and foreign objects.
  - c. Clean and inspect inlet screens and install properly.
  - d. Insure a clean source of starting air and connect to the aircraft properly.
  - e. Make sure all protective covers and caps/plugs are removed prior to operation.
  - f. Inspect immediate area for foreign objects immediately prior to operation.
  - g. Make sure that people/equipment/tools etc. are away from danger areas.
  - h. While operating, perform constant visual inspection of aircraft/surrounding area for any potential FOD conditions.
  - i. Same steps explained above should be followed in reverse order after completion of operation.

### 3.7. FOD Prevention Activities Within TUAF

- a. The concept: In order to prevent FOD or at least keep it at absolute minimum; the design, development, safety, test, quality assurance, maintenance and manufacturing functions should be properly planned, integrated and developed (Fig.4).

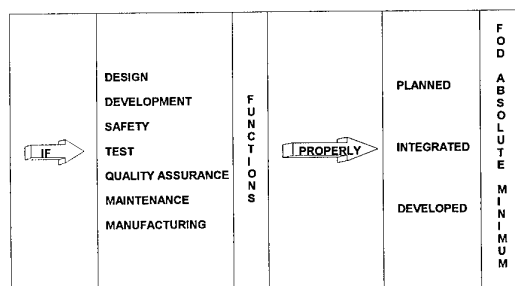


Fig.4

- b. Program: FOD Prevention Program is a formal, documented, disciplined, program designed to prevent FOD causes by events or conditions of various activities and operations. TUAF has such a FOD Prevention Program. In this program all potential FOD threats and hazard possibilities are included and for each threat a proper prevention action or actions are listed in priority sequence.

Each year FOD Prevention Program is being reviewed and the effectivity of actions taken against each threat area is reevaluated. If any weakness is detected the actions are either changed or more appropriate actions are included in the program. The FOD Prevention Program is a dynamic program which is changed and enhanced based upon FOD analysis periodically.

### 3.8. A Case Study.

In this section, we shall present a typical problem, TUAF was exposed to and the method we developed, in overcoming it.

Having appointed a staff for FOD control on incoming engines, we noticed the need for extensive analysis of the unreported damages.

First concentrating upon flight personnel reports of bird ingestion, we started to apply organic chemistry in order to investigate organic debris existence in damaged areas.

Then, also noticing inorganic foreign objects in damaged locations, we needed more elaborate methods to identify them.

After several trials, we decided to apply Scanning Electron Microscopy and Energy Dispersive X-Ray Spectroscopy (SEM/EDS) methods. Thus we initiated a project accordingly. During the investigation the first, impact point of the damaging foreign particles was located. Isolating it from others, the foreign particles left at damaged section were carefully studied by SEM/EDS methods. Even the residues were very little at the first impact point it has given satisfactory input to verify the source of the damage.

Damaged regions, were first examined, under a stereo optical microscope. Following that, damaged sections were carefully cut out and prepared for examination in a SEM.

Each specimen was examined in a scanning electron microscope (Jeol SEM 6400). The damaged surfaces were carefully scanned for particles left over from the foreign object that caused the damage. To identify each particle, micrographs were taken and EDS point or area analysis were carried out which were also compared with those of the alloy of the blade and of the coating. Where necessary elemental X-ray mapping were also produced.

Any particle that was found to be foreign to the blade was noted.

The shape and the size of the damage as well as the foreign objects that were identified were then evaluated on a comparative basis with others from different stages of the each engine.

As an immediate result of this project, we identified particles of sand, bolts, nuts, aircraft parts bullet noses etc. in different damage cases. In addition, in a fatal instance a bullet nose fracture was identified, and preventive measures were taken accordingly.

### 3.9. Internal FOD Cases

Internal FODs caused by the fractions of the deteriorated engine parts such as combustion chambers, rotor blades, turbine nozzle segments, vanes and fuel nozzles etc. are the main causes of internal object damages. These should also be clearly studied. If the real causes of these incidences are not clearly identified, severe engine failures are unavoidable. Since TUAF does not have healthy statistical data due to the low number of incidences based on the previous years. I will not focus on these types of failures deeply.

FOD DISTRIBUTION BY CAUSES "1992-1993 TRAINING PERIOD"											
INCIDENCES	OPERATION BASES										TOTAL
	USER #1	USER #2	USER #3	USER #4	USER #5	USER #6	USER #7	USER #8	USER #9	USER #10	
EXTERNAL	METALS, STONE ETC.	2	-	8	2	10	5	-	2	-	31
	BULLETS	-	-	-	-	-	2	-	-	-	2
	BIRD STRIKE	1	1	1	2	1	2	-	1	1	10
INTERNAL	BLADE FRACTURE	5	-	1	-	8	-	-	1	-	15
	PARTS FRACTURE	-	5	4	4	1	3	1	-	-	18
	UNDER INVESTIGATION	-	1	2	-	-	-	-	-	-	3
TOTAL											79

Fig.5

However last year, out of 79 FOD incidences 33 were directly related to internal FOD's (Fig.5). Out of that number, 15 incidences were directly related to the cracking and fracturing of rotor blades due to the fatigue fracture based on stress corrosion and 18 incidences were directly related to the cracking and fracturing of various engine parts which were highly effected by the thermal stresses, erosion and corrosion.

### 4. CONCLUDING REMARKS

Engine performances are deeply affected by external environmental conditions. Chronic effects of erosion, corrosion and acute effects of FOD should be carefully investigated.

One should always remember that, after all, these are local problems. The depth of our isolated knowledge is therefore very much limited by our experience.

Since our aim is to provide better performance in all possible conditions exchange of our experience and the information base we developed from them is vital to our flying personnel.

We shall have plenty of time, with this audience to focus on very specific problems. Here I would like to broadly stress, the need for a systematical approach.

That is a process which starts with monitoring and observing the agents of performance degradations. From visual inspection methods where we used to look for (e.g.) the damaging object, we have come a long way to analyze the impact in deriving the cause. This process starts from the design and is valid throughout the service life of the engines.

The third stage in this chain of the process, is the correction (repair and maintenance activities) and prevention of such effects by the initiation of relevant procedures as necessary.

An important aspect of the process is the impacted analysis of the new procedures introduced. Random and systematical causes are also to be discriminated.

We all need the contribution of very sophisticated techniques available on analytical stand vis a vis the problems. One thing for sure also a lot of efforts to share the result are required.

I wish this platform, as a vehicle for much better performances in all allied countries, be fruitful for all.

### ACKNOWLEDGMENTS

Special thanks are due to Dr. E.Tekin from the Middle East Technical University and Mr. U.Iplikci and Mr.M. Bulbul from the Turkish Petroleum Inc. RSL Laboratories. It is also a pleasure to mention the importance of the contribution from Dr. F.Yarman, Colonel B.Caglar; MS.Mechanical Engineer and Mrs. Ş.Akbacak; Metallurgical Engineer.

### REFERENCES

1. Goldstein J.I., Newbury, D.E., Echlin P., Joly D.C., Fiori C., Liftshin E., "Scanning Electron Microscopy and X-Ray Microanalysis", 1981.
2. "Foreign Object Damage Prevention in Aerospace Products", MIL-STD-980, May 1988.
3. Goodhew P.J. and Humphreys, F.J., "Electron Microscopy and Analysis, 1988.
4. Tekin E., "1st ASMC Foreign Object Damage Report", METU-Metallurgical Eng. Div., Ankara, Feb. 1991.
5. Furler R., Aydınmakine F., "Metallographic Inspection of Foreign Object Damage in Jet Engines", Univ. of Pamukkale 5 th Material Srupasium Proceedings, April 1993.
6. Tekin E., "1st ASMC Foreign Object Damage Reports", METU-Metallurgical Eng. Div., Ankara, April, July, Sept. 1993.
7. Annual Evaluation Report of Quality Activities of 1st ASMC., Feb.1994.
8. TUAF Semi-Annual Flight Safety Evaluation Report, March 1994.



## Out of Area Experiences with the RB199 in Tornado M G Down & M J Williams

Rolls-Royce plc  
PO Box 3  
Filton  
Bristol  
BS12 7QE  
England

### Summary

The Turbo Union RB199 engine was developed during the late 1960's / early 1970's to meet a specification requirement aimed at defence of the Western European NATO alliance countries against the (then) perceived threat.

During the latter part of the 1980's Tornado aircraft were delivered to the Royal Saudi Air Force and, supplemented by deployed units from the Royal Air Force, were engaged in an operational role during 1990 / 1991.

Aircraft operations in the Saudi Arabia climates and natural environment created problems with engine life, hitherto not encountered in the European area of operation, nor during many RAF overseas deployments, including North America.

These problems, mainly concerned with turbine blade contamination from airborne sand, were alleviated by the introduction of unique engine maintenance management techniques and eliminated by design changes.

### 1. Engine Description

The basic engine layout comprises a compact 3 spool configuration which combines high compression and bypass ratios with a fully modulating reheat system and integrated thrust reverse (see fig 1). This configuration not only obviates the need for variable geometry blading but gives exceptional tolerance to Foreign Object Damage (FOD) and bird strikes.

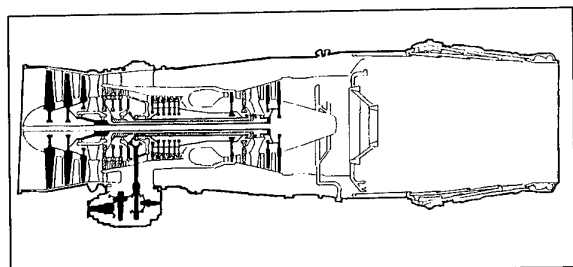


Figure 1 - RB199 General Arrangement

The fully modular construction and "On Condition" maintenance policy allows the operator optimum operational readiness and flexibility while minimising cost of ownership.

The Low and Intermediate Pressure Compressors incorporate corrosion resistant Titanium components, with the High Pressure Compressor (HPC) in a combination of Titanium and Nimonic alloys.

The Combustor and Turbines are manufactured from high temperature nickel based alloys.

The design criteria include resistance to icing, atmospheric liquid water, salt water corrosion, ice, bird and sand ingestion.

As part of the qualification evidence, the specification required that the engine continued satisfactory operation in environmental conditions containing sand dust in concentrations up to  $4.4 \times 10^{-5}$  sand / air ratio by mass.

The sand contaminant was defined as crushed quartz with particle size distribution from 1000 down to 75 microns or less, but predominantly within the range 125 to 400 microns.

The capability to operate in these conditions was satisfactorily demonstrated in 1978 and considered acceptable for qualification.

Subsequent strip examination of the qualification engine revealed some erosion damage to the compressor blade leading edges. The HP Turbine nozzle guide vanes and blades suffered minor restriction of some leading edge cooling holes with evidence of fused silica on the leading edge and concave aerofoil surfaces.

As a result of these findings, no modification action was considered necessary.

### 2. Initial Service Experience

Tornado Interdictor Strike (IDS) aircraft entered service with the Royal Air Force in early 1980, followed closely by the German Navy and German and Italian Air Forces. The majority of missions took place at high speed and low level in the European theatre.

In 1984, the Royal Air Force introduced the Tornado Air Defence Variant (ADV) into service. The engines were basically the same as those in the IDS, apart from increased engine operating temperatures and enhanced reheat capability. ADV flying was mainly carried out at medium to high level including Combat Air Patrol and Air Interceptions.

During this period detachments out of Europe took place and included North American desert environments.

Throughout these operations there was no indication of any adverse engine effects associated with erosion or corrosion of turbo machinery components or accessories.

However, problems were already being experienced with the HP and IP Turbine blades, both being of cast equiaxed IN100 material.

The HPT blade was suffering shroud loss and aerofoil failures due to thermal fatigue and creep. Regular borescope inspections were carried out to reduce the instances of blade failures.

The IP turbine blade was suffering failures due to High Cycle Fatigue (HCF), Thermal Fatigue and in some cases aerofoil creep.

Although minor modifications to both stages of turbine blades were carried out and reliability improved, these basic failure modes persisted.

### 3. Early Saudi Arabian Experience

In March 1986, 6 weeks after the signing of a Memorandum of Understanding (MOU) between the British Government and the Kingdom of Saudi Arabia, Tornado aircraft originally ordered for the RAF were delivered to the Royal Saudi Air Force (RSAF). By late 1990 a total of 72 aircraft (48 IDS and 24 ADV) had been delivered.

Due to the short delivery timescales, only very minor modifications were carried out to both the aircraft and engines. These changes included fitment of the latest standard of HP Turbine blade and air / oil system modifications already adopted by the NATO airforces. Furthermore, these engines were operated at maximum cleared temperature levels compared with the slightly lower thrust and temperature levels that had been implemented by the RAF.

Operations commenced immediately from the King Abdul Aziz Base (KAAB) at Dhahran (see Fig 2).

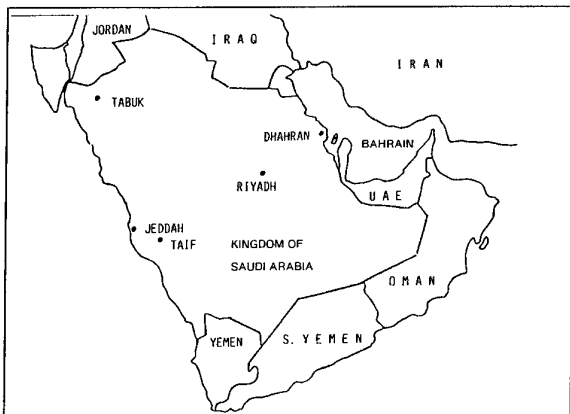


Figure 2

The first engine rejection occurred at unexpectedly low life due to High Pressure Turbine (HPT) blade Leading Edge (L/E) burning and, by the end of 1986, a significant number of engines had been rejected due to similar problems.

Laboratory examination of failed RSAF HPT blades showed that both the external leading edge (see Fig 3) and internal film cooling holes were being restricted. Measurements of L/E cooling hole **outlet** diameters revealed varying degrees of restriction from the nominal size of 0.3 mm with, in some cases, total blockage (see Fig 4).

Sectioned blades showed that the **inlet** diameters of the L/E film cooling holes could be restricted to as little as 30% of nominal diameter.

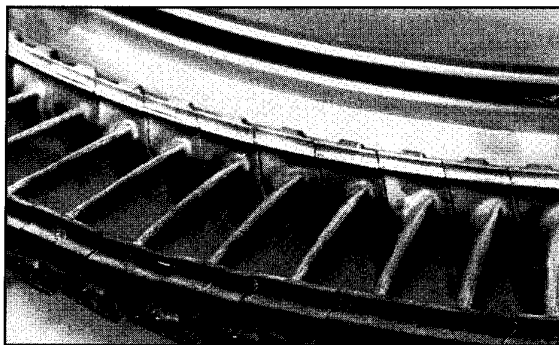


Figure 3

Restriction, predominantly at 2/3 blade height, was found to be time related (see Fig 5). Total blockage was also found at the inlet of trailing edge cooling holes. These restrictions resulted in overheating and less of aerofoil creep life. Metal temperatures of between 1100 - 1150°C were being experienced. This compared with a design value of 950 - 1000°C and was similar to that normally seen in European operation.

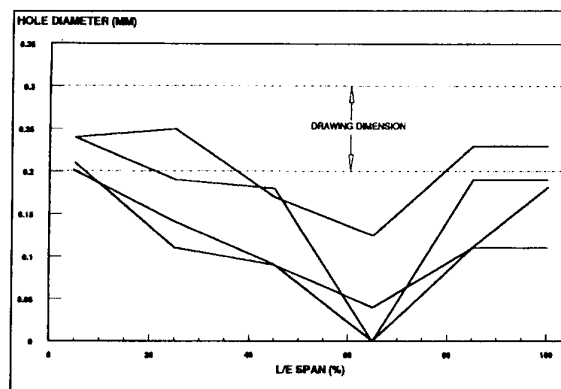


Figure 4 - External pressure side leading edge cooling hole diameters in RSAF

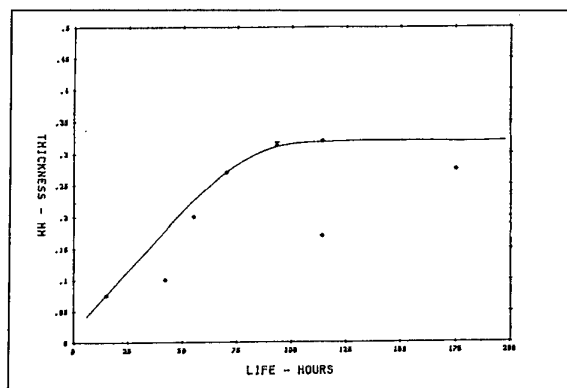
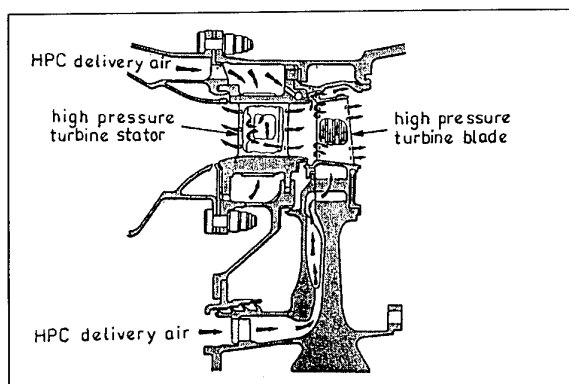


Figure 5 - Deposit thickness on the concave aerofoil of equiaxed Saudi HP turbine blades

Examination of particles taken from the HP turbine blade cooling system showed that 90% of them were less than 20 microns in size with 30% being less than 4 microns. It is considered that the extremely fine particle size was due to grading caused by venturi and centrifugal effects, turbine blade cooling air being fed from the HP compressor inner annulus. (see Fig 6)



**Figure 6 - High pressure turbine cooling**

In contrast, 50% of sand from the runway at Dhahran is greater than 200 microns and 55% of windblown sand is more than 100 microns. It was therefore concluded that the majority of the dust was being ingested during flight.

The prevailing winds in the Middle East are such that airborne sand is blown across Saudi Arabia from Iraq and Iran. It was also established that the concentration of atmospheric sand is seasonal with the highest concentration during the summer months (see Fig 7).

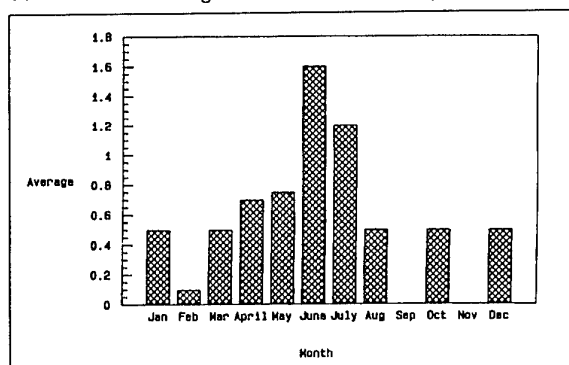


**Figure 7 - Average No of dust storm days per month**

The Laboratory analysis of the deposits taken from the turbines of several engines showed them to vary according to whether they had passed through the combustor or had been carried with the cooling air.

- HP turbine blade external deposits were a mixture of amorphous silicate material and calcium magnesium silicate.
- HP turbine blade cooling hole deposits were a mixture of silica (quartz) and calcium sulphate (anhydrite).
- HP nozzle guide vane surface deposits were a mixture of calcium magnesium silicate and calcium sulphate (anhydrite).

Following the formation of silicate in the combustion chamber, the compound may exist in a molten or semi molten state. Adhesion of these compounds may occur at metal temperatures of approximately 950°C. As a result, the HP is the only turbine stage in the engine to suffer from build up of fused silicate deposits. Further, the HP turbine is the only stage which has leading edge film cooling and trailing edge cooling.

#### 4. Maintenance Actions

As a result of the above, development of a practical cleaning process to remove external contamination from the HPT blade was deemed necessary. In considering such a process, the following constraints were defined:

- applicable on aircraft
- minimal aircraft downtime
- no adverse affect on other parts of the engine

The method introduced was abrasive cleaning, which was already being used "off aircraft" primarily to clean the HP nozzle guide vanes. The abrasive used was 27 micron aluminium oxide blasted onto the vane by high pressure air.

Initial trials showed this to be an effective method of removing fused deposits from rejected HP turbine blades.

On aircraft cleaning equipment was developed, tested and supplied to the RSAF towards the end of 1986 four months after problem identification. A schematic of the equipment is shown in Fig 8, and includes motorised indexing of the HP turbine coupled with automatic traversing of the cleaning nozzle. This process is viewed via a television monitor linked to a borescope inserted into the combustion chamber. Figure 9 shows the method introduced to prevent accumulation of abrasive medium in the radial passage.

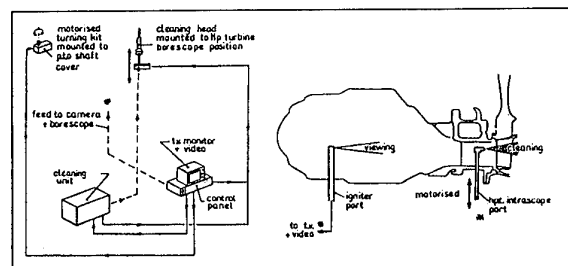


**Figure 8 - HP turbine blade cleaning equipment - schematic**

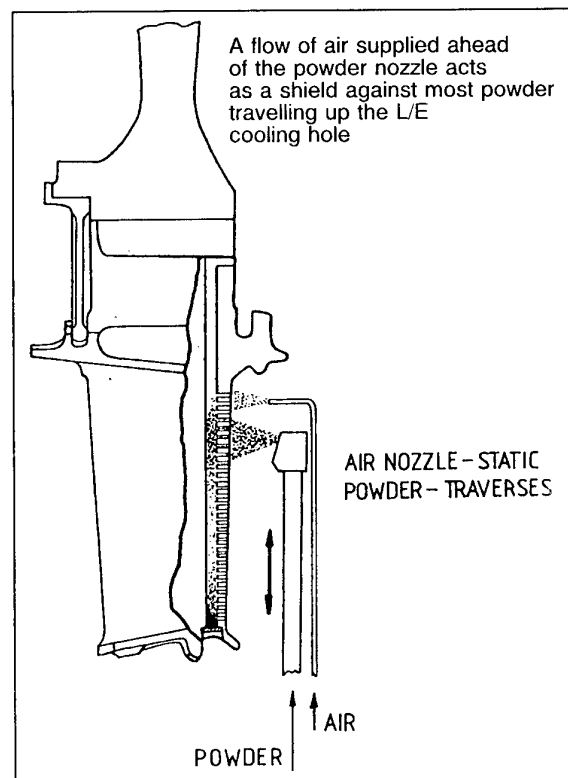


**Figure 9 - Close up showing blade L/E and nozzle configuration**

External cleaning was carried out every 40 engine flying hours during the hot sandy summer months. Outside this period, cleaning was carried out on an 'on-condition' basis. As a result a two-fold improvement in blade life was evident.

However, the maintenance penalty involved was considered to be excessive and therefore work continued to develop an alternative method that was quicker and more effective.

By mid 1987, a high pressure water cleaning system had been produced. Contamination was removed by water blasted onto the blade L/E at 9,000 psi (62 MPa). Trials showed this method to be more effective than abrasive cleaning, with the time taken reduced by some 90%. However, as the single crystal HPT blade was about to be introduced into service with the RSAF, it was decided to assess the performance of this blade before making a decision on supplying water cleaning equipment. (see Fig 10)

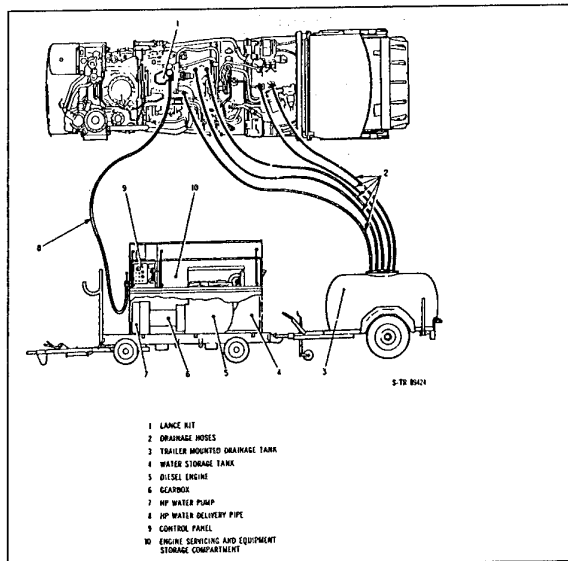


Figure 10 - High pressure water blade cleaning kit

## 5. Design Actions

### a) Equiaxed blade with slotted L/E

In order to reduce the effects of L/E film cooling hole restriction, a slot was introduced at the blade L/E to provide a larger total exit area than that of the individual cooling holes. (see Fig 11) In addition the sharp edges of the slot make it more difficult for the fused sand to build up and restrict the holes.

Blades to this standard were delivered to the RSAF from January 1987. The benefit of this blade variant was that it gave the life of the non-slotted blade, but obviated the need for scheduled cleaning.

### b) Single crystal blade

Whilst the combination of maintenance actions and blade modification had resulted in improved reliability, these were only seen as the first in a series of improvements. The final solution to the sand problem lay with the introduction of the single crystal HPT blade.

This blade was already being developed for the NATO operators. This casting technology results in a significant improvement in creep life, and the change also offered further development opportunities including:-

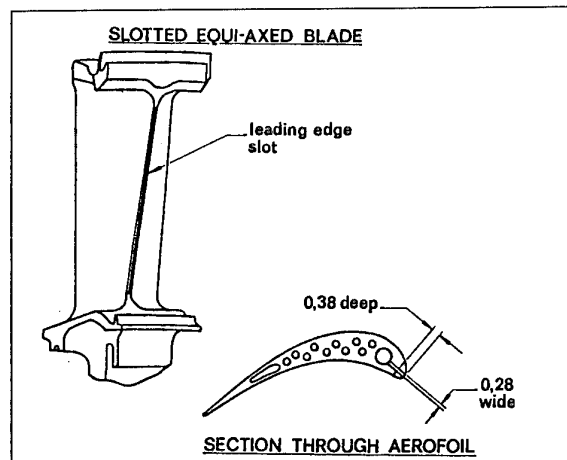


Figure 11

- Better aerodynamics - through a 3D aerofoil shape
- Improved cooling system
- Incorporation of sand tolerant features

For the RSAF, emphasis was given to the latter two design features.

The single row of film cooling holes at the L/E were replaced with 2 rows of cooling holes, each side of the stagnation point. Both rows have holes drilled at 45° to the L/E instead of at 90° as on the equiaxed blade. This improves cooling efficiency by increased hole length over diameter (L/D) ratios and reduced wall thickness between adjacent holes, thus enhancing convection cooling effectiveness.

In addition the reduction in film cooling hole 'entry' angle has the effect of maintaining a higher air flow velocity at this point and hence reduces the propensity of internal sand deposition.

The design solution included retention of the slot geometry at the exit of the pressure surface film cooling holes (see Fig 12).

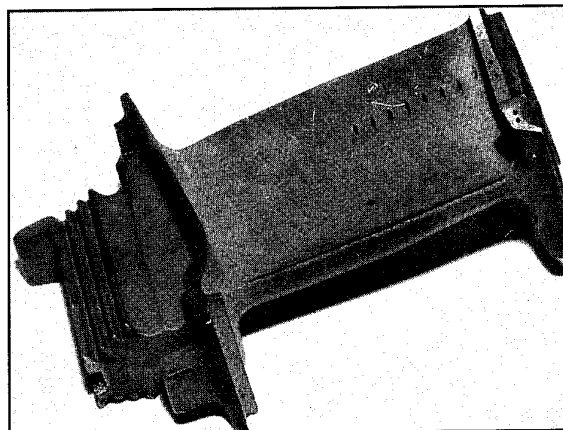


Figure 12 - Single crystal blade

The T/E cooling design was also changed to include 45° drilled holes, as testing had shown this configuration greatly to reduce internal cooling hole restriction.

## 6. RAF Tornado Experience in the Gulf

In August 1990 the RAF deployed 12 ADV aircraft to Dhahran in response to a Saudi Arabian request for assistance.

This initial batch of aircraft came from squadrons which were engaged in routine training exercises in Cyprus. Within two hours of arrival the ADVs were carrying out Combat Air Patrol (CAP) along the Saudi Arabian border. As the aircraft had been re-deployed from the European field of operation, the engines did not have any of the changes previously discussed, but did incorporate the NATO standard of single crystal blade (Non-slotted L/E and 90° T/E cooling holes).

By November the number of Tornado ADV in Kingdom had increased to 18. CAPs were being carried out utilising 4 aircraft per mission, typically, of, 4½ hours duration at medium altitude.

Towards the end of August, 12 Tornado GR1 aircraft (IDS) were detached from RAF Germany to Bahrain. These were supplemented over the next few months by a further 12 GR1s to Dhahran, 18 GR1s to Tabuk and finally early in January 1991, 6 GR1A (reconnaissance) aircraft to Dhahran.

The early detachments of IDS aircraft used Mk103 engines with NATO standard equiax HP turbine blades, and it rapidly became clear that these blades suffered from sand contamination, similar to that seen on the original RSAF blades.

Embodiment of single crystal HP turbine blades into the RAF Mk104 engines for ADV began in early 1989 and by the onset of the Gulf crisis, much of the fleet had been converted. It was then decided to accelerate embodiment of single crystal into Mk103 engines. This campaign was undertaken using the extensive engine repair facilities at the RAF's European bases. As IDS aircraft were rotated for servicing through September and October, they were replaced by aircraft fitted with modified engines. By the end of 1990 all deployed aircraft and spare engines had been modified to the single crystal blade standard.

As the NATO standard of single crystal blade does not embody any of the sand tolerant features previously described, the effects of sand deposits were controlled by the introduction of borescope inspections, initially at 128 hours, then every 32 hours thereafter.

During operation "Desert Storm", Tornado aircraft, operating in all weather conditions, flew some of the most arduous missions undertaken by Allied aircraft.

No operational missions were lost due to engine related problems and engine reliability was no worse than in peacetime. There were no engine rejections due to HPT blade defects, although sand contamination was often quite extensive. (see Fig 13)

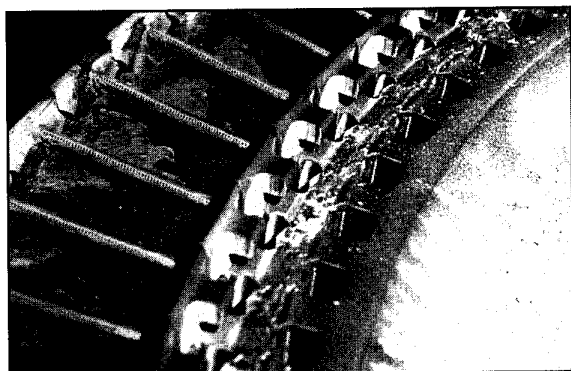


Figure 13

## 7. Post Gulf Conflict Actions

Following cessation of hostilities, the majority of RAF aircraft returned to Europe, but a number of Tornado IDS aircraft remained in the Gulf as part of a long term RAF commitment. Single crystal HPT blade reliability had been exceptionally good. However, it was decided to examine blades from the RAF to determine long term environmental effects of Gulf operation.

Samples of blades were taken from both Mk103 and 104 engines which had accumulated in excess of 200 hours in the Gulf. These showed that external sand build up was dependent upon:

- Mission flown
- Time in theatre
- Base of operation

In general, IDS low level missions resulted in heavier build up than ADV missions. IDS aircraft were flown from Dhahran, Bahrain, and Tabuk, while ADV's flew from Dhahran only. Sand accretion was similar for operations flown from Dhahran and Bahrain, while engines flying further north, from Tabuk experienced only light accumulation.

Typical RAF HPT blade condition at 200 hours is shown in figure 14 and includes:

- |               |                  |                          |
|---------------|------------------|--------------------------|
| Leading edge  | - Corrosion      | - heavy at 2/3 height    |
|               | - Internal holes | - 10% restriction        |
|               | - external holes | - over 75% restriction   |
| Trailing edge | - Internal holes | - up to 100% restriction |

### Corrosion

Analysis of RSAF blades had already shown that the Pack Aluminide Coating (mean thickness 0.025 mm) was progressively lost, followed by oxidation and sulphidation of the base material. This was occurring at lower life than expected and was believed to be the result of accelerated degradation of the coating due to depletion of the aluminium into the calcium rich sand deposit, exacerbated by the higher metal operating temperatures. Trials had taken place on alternative coatings for the RSAF. However, in view of the level of reliability being achieved by the single crystal blade, no change of coating was considered necessary.

### Trailing edge hole blockage

RAF blades incorporated holes drilled at 90° compared with 45° for the RSAF. Blockage of the RAF blade T/E holes was causing excessive metal temperatures and burning. In contrast, the RSAF T/E holes remained clear.

### Chemical cleaning process

As the Single crystal HPT blade life expectancy was in excess of 1000 hours (under "normal" operating conditions), RAF blades which had flown for typically 200 hours in the Gulf needed to be cleaned to restore both cooling system efficiency and life potential.

A process was developed which cleaned the blades after removal from the engine, using a combination of chemical and ultrasonic processes. Following cleaning, airflow checks showed that cooling flow was restored to within new manufacturing tolerances. Sectioning of cleaned blades confirmed the cooling holes to be clear of sand deposits.

The majority of blades have now been successfully cleaned and returned for service use. (Figures 14 and 15 show typical before and after conditions)

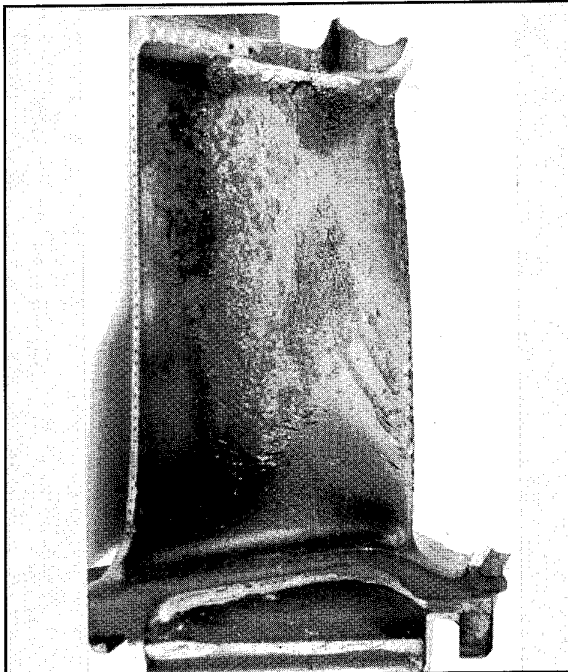


Figure 14



Figure 15

#### Water Cleaning

The high pressure water cleaning technique (initially developed for the RSAF) is now being utilised by the RAF during current peacekeeping operations. Blades are being cleaned every 32 hours or, as sand accumulation exceeds acceptable limits. Furthermore, equipment has also been supplied to the RSAF. This will be used on aircraft when HPT blade cooling hole blockage limits are exceeded.

#### 8. Conclusions

The technical difficulties experienced when the engine was operated in "adverse" climatic and environmental conditions resulted in:

- Introduction of "radical" processes to effect successful on-aircraft cleaning techniques with minimum downtime, thus increasing turbine life and engine reliability.
- Identification of "sand tolerant" turbine blade design features with demonstrable improvements in turbine blade service life.

Lessons drawn from the foregoing experience will clearly be applicable in the design and operation of future NATO military aircraft engines. However, it should be noted that consideration of these factors are of the highest benefit when considered within the initial component design phase, and validated prior to entry into service. Therefore, for future generations of engine, a broader view of the possible operational environments needs to be taken and considered during the engine specification definition phase.

## QUESTIONS

### **R.E. SMITH (US)**

- Q. What is the physical interpretation as to why the deposition was dominant on the rotor blades and was substantially less on the first turbine vanes?
- A. a) Metal temperatures of stators are generally higher and therefore the silica tends not to adhere readily to the surface.  
b) Fused deposits were found on areas of the stator vane surfaces but did not restrict cooling holes; therefore, no life penalties resulted.

### **D. NAGY (CA)**

- Q. Were there any secondary effects, such as erosion or hot corrosion, attributed to the presence of sand deposits on the HP blades and vanes? If so, did they contribute to the limiting of service life?
- A. HPT rotor blades include a PACK ALUMINIDE aerofoil coating. Degradation of the coating due to Al depletion into the calcium rich deposit resulted, in the medium term, in loss of blade life due to base material oxidation and sulphidation attack.

## THE OPERATION OF GAS TURBINE ENGINES IN HOT AND SANDY CONDITIONS

### ROYAL AIR FORCE EXPERIENCES IN THE GULF CONFLICT

Sqn Ldr R C Sirs RAF  
Defence Research Agency  
Air Vehicle Performance Department  
Pyestock, Farnborough,  
Hampshire. GU14 0LS  
United Kingdom

#### ABSTRACT

During the initial phase of the Gulf Crisis, the principal instrument at the disposal of the British Government which could respond in time was air power. This situation continued, and throughout the period of military build up and subsequent conflict air power remained a dominant factor.

During the period, many equipment modifications were incorporated to increase both performance and reliability, and the gas turbine engines which powered the RAF's aircraft were no exception. However in some cases, engines were operated at a much increased flying rate in harsh operating conditions in standard configuration.

This paper reviews the operating experiences and some of the modifications incorporated, including the subsequent effect on aero-engine reliability trends.

#### 1. INTRODUCTION

For the Royal Air Force, Gulf operations, began in August 1990 with the decision to deploy large scale forces to the region. Within 48 hours a squadron of RAF Tornado F3's arrived in Saudi Arabia, and two hours later flew their first operational Combat Air Patrol. This rapid deployment was the start of a military operation (details of which are contained in ref 1 and 2), in which air power was to play the dominant part and one from which many lessons can be learnt.

By the start of the conflict in Jan 91, the in-theatre RAF strength stood at 76 strike/attack and reconnaissance aircraft, 17 tankers, 3 Maritime Patrol aircraft, 36 Support Helicopters and 7 transport aircraft. The Army Air Corps had

deployed in the region of 50 helicopters and the RN had assigned 12 of its helicopters for land based operations.

The total UK aircraft deployed or allocated to Gulf operations accounted for 10% of the total allied air power available. The deployed RAF aircraft flew a total of over 14,000 sorties, of which 6000 were during the 49 days of the military conflict. This sortie rate was around twice that normally flown, and on some aircraft the peak rate was in the order of three to four times. The RAF's Air Transport Force, although not permanently in-theatre, was also heavily committed to all aspects of Gulf operations. By the end of the conflict it alone had accumulated 50,000 hours and carried 26,000 personnel and 54,000 tonnes of freight.

Much of the RAF's equipment, planning and training was aimed at fighting a European War and was not therefore best suited to operations in the Middle East. The level of output at all Repair and Overhaul locations was increased in an effort to maximise stocks and over 300 individual modifications to some 12 different aircraft types were incorporated at a cost of over 300,000 manhours and £66M. Most of the modifications to aero-engines were incorporated to increase performance and reliability, both of which were expected to be degraded due to the high ambient temperatures and harsh environmental conditions.

The purpose of this paper is to review and examine the operational experiences and type of faults encountered as a result of sustained aero-engine operations in harsh operating conditions. Some of the modifications incorporated during the Gulf conflict and the effects they had on subsequent operations are also examined.



The paper does not cover the RB199 engine in the Tornado aircraft, which is the subject of a separate paper.

## 2. COMBAT AIRCRAFT

Both the Jaguar and Buccaneer aircraft were employed on air-to-surface operations, although the Buccaneer was only deployed in the later stages and was operational for only about 30 days. Jaguar operations consisted of day-time attacks, firstly at low level, but progressing to medium altitudes later in the campaign. The Buccaneer aircraft were operated only at medium level and were predominantly utilised for laser target designation.

### a. Jaguar - RR/Turbomeca Adour Mk 104 Engine.

The thrust loss experienced due to the high ambient temperatures (15% at ISA+25 C conditions) was a primary problem facing Jaguar air-to-surface operations in the low level environment. The Jaguar aircraft is particularly performance critical at high all up weights and furthermore, high airspeeds were necessary for survivability and mission effectiveness.

An in-service maintenance instruction was devised with Rolls-Royce (RR) assistance which involved adjustment of the TGT Control Amplifiers and could be quickly and easily carried out on the flight line. By allowing the engine to run up to 25 C hotter, this measure recovered approximately half of the thrust lost.

The up-rating of the engine increased the possibility of occurrences of a phenomenon known as reheat screech, which is a high frequency instability of the gas stream and can result in mechanical failure of the jet pipe liner in a matter of seconds. An improved jet-pipe screech damper was provided by RR with additional cooling holes to damp out any such frequencies.

Introduction of these instructions caused no lifing penalties in Group A parts; however, it was predicted that the useful lives of hot-end, non-group A parts, which includes blades could be reduced by as much as 50%. As most blades are lifed 'on condition', a routine intra-scope inspection was introduced at 35 hour intervals. To avoid possible lifing penalties an improved standard of directionally-solidified HP turbine blade was also used on all deployed engines.

Few engines were rejected specifically for visible hot-end damage (figure 1), but it is

probable that the large proportion of FOD (believed to be caused by missile debris) and power related rejections were engines which would soon have been rejected for hot-end damage. The overall engine rejection rate for the deployment was lower than that normally experienced, but this was to be expected, due to relaxed condition acceptance levels and the fact that engines for deployment to the Gulf were specially selected and prepared to the highest modification standards.

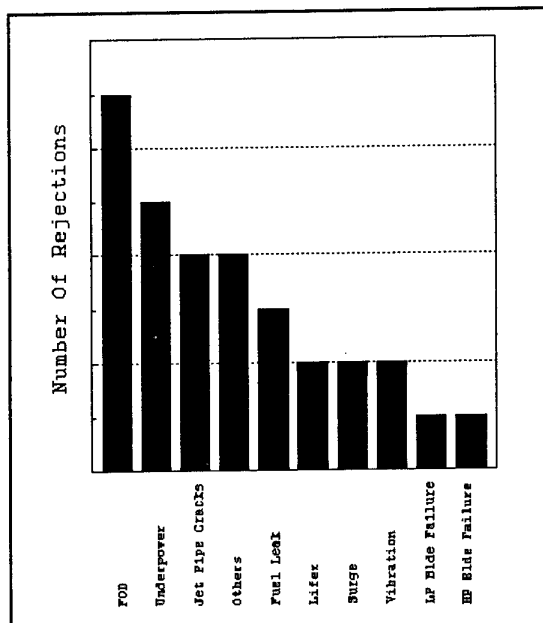


Figure 1. Gulf Adour Engine Rejections.

While the engine rejection rates did not increase, the eventual level of work required and subsequent module replacement rates did increase considerably. The defects discovered were considered to be of the level expected and acceptable. Most engines revealed evidence of high temperature operation and the type of hot-end damage encountered was as follows:

- Slight bulging of the combustion section, but no problems with fretting or cracking.
- Sand contamination of the HP NGV, but no cooling hole blockage.
- Aerofoil cracking and burning of the HP NGV.
- Leading edge erosion and shroud tip curl of HP Turbine rotor blades.
- Detwisting of LP Turbine rotor blades.

In an effort to further improve thrust in high ambient temperatures, consideration was given to upgrading a number of engines to the MK811 standard (the export variant), but sufficient parts were not available within the timescales required. A further thrust enhancement measure was however investigated which would have enabled the engine to run both faster and hotter. This involved re-worked TGT amplifiers and adjustments to the fuel control system. This enhancement would have recovered most of the thrust lost, but would have necessitated revision of cyclic exchange rates and could have reduced Group A parts life by a factor of 4. This measure was never authorised for embodiment due to the shift to medium level attacks and the conflict being restricted to the colder months of the year.

#### b. Buccaneer - RR Spey Mk 101

The Buccaneer arrived in theatre after the initial phase of the conflict when air-to-surface operations were then being carried out at medium-level. At such altitudes, engine performance loss was less critical than it had been during low level operations. The Spey Mk 101 engines were therefore unmodified and normal operating limitations were not exceeded. The medium-level environment presented a less arduous operating regime than that normally encountered in the UK, where operations are predominantly carried out at low level over the sea. Despite a much increased flying rate, the engine rejection trend reduced before returning to normal levels, post Gulf operations (see Fig 2).

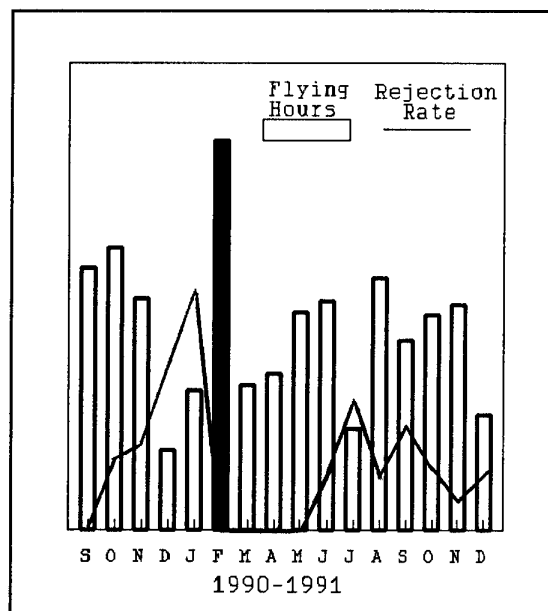


Figure 2. RAF Buccaneer Operations.

The absence of a post conflict increase in rejections would suggest that the low rejection rate was not due to relaxed acceptance standards. Engines which were investigated post conflict showed no problem areas or abnormal internal damage.

### 3. HELICOPTERS

The effect of dust erosion on helicopter engines was well known in the UK prior to the Gulf crisis and urgent dialogue was taking place between industry and MOD departments, as soon as deployments were envisaged. These concerns were supported, when initial deployments of US Army helicopter units, experienced a poor level of engine reliability. It was reported that sand ingestion was causing erosion of the compressor blades, and hence loss of power and surge margins, with some engines being removed after less than 20 hours flying.

A level of erosion was to be expected as in the desert, sand, dust and other loose debris are plentiful and the nature of helicopter operations leads to large amounts of surface material being disturbed by the rotor downwash and ingested by the main engines. The ingestion problem was found to be worst in the hover and during landing and take-off, although avoiding certain manoeuvres was found to have advantageous effects. The typical engine dust ingestion rates for different UK military helicopter types in 'zero visibility' conditions are shown in Fig 3, and help to demonstrate the magnitude of the problem.

Gazelle	15.2 kg/hr
Lynx	15.2 kg/hr
Puma	23.5 kg/hr
Chinook	56.5 kg/hr

Figure 3. Helicopter Dust Ingestion Rates.

The decision was made that the problems of sand erosion should not be underestimated, and that the RAF Support Helicopter force, which consisted of the Puma and Chinook should not be deployed without environmental protection.

**Helicopter Intake Filters.** There are several types of system which can be fitted for helicopter engine environmental protection. Barrier filters, inertial separators and multi-tube vortex separators. Multi-tube vortex separators, often referred to as Engine Air Particle Separators (EAPS) were used on all UK helicopters during Gulf operations. Such systems are designed specifically to helicopter type and are procurable assets. Whilst occasionally they have all-weather clearance, they are often classified as role equipment. These equipments can be produced to provide a high degree of performance efficiency, and minimal power plant loss penalty. They all require only limited in-service maintenance, and this to 'on-condition' principles.

**Engine Air Particle Separators.** An EAPS (Ref 3) consists of a number of inertial separator tubes, known as 'Vortex Tubes', the operating principle of which is shown in Fig 4. Air is drawn through the tube by the engine suction and is caused to swirl by a fixed vortex generator. The swirling flow imparts a centrifugal force on the dust particles which causes them to migrate towards the outer wall of the tube. An annular gap exists between the vortex body and outlet tube through which the dust laden air is extracted.

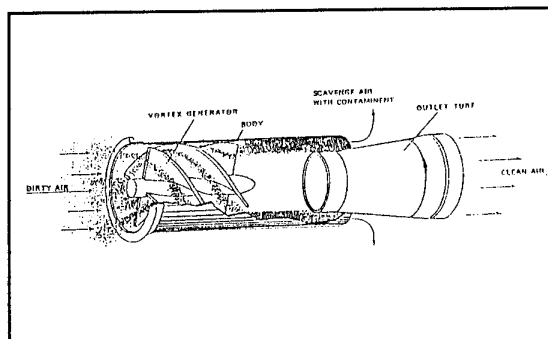


Figure 4.

A complete EAPS unit consists of numerous Vortex Tubes mounted as shown in fig 5 and a scavenge system to continually remove separated debris. The EAPS unit for the Chinook engine consists of approximately 3200 individual tubes.

The scavenge system employed is dependant on installation type but generally scavenge flow can be induced by either mechanical scavenge fans or engine bleed air ejectors.

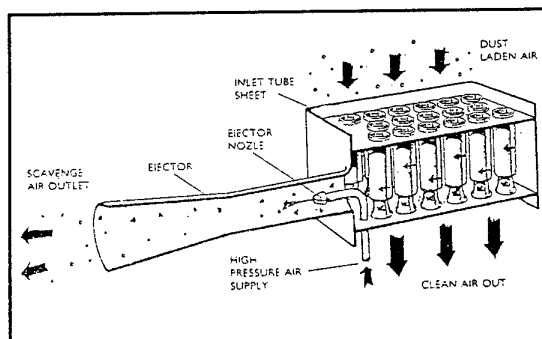


Figure 5.

Separation efficiency can vary with installation type and design, but between 93% and 98.5% can be achieved with some of the latest EAPS units. Efficiency can be related to erosion levels and hence engine life and fig 6 shows a comparison of dust separation efficiency against engine life improvement (Ref 4).

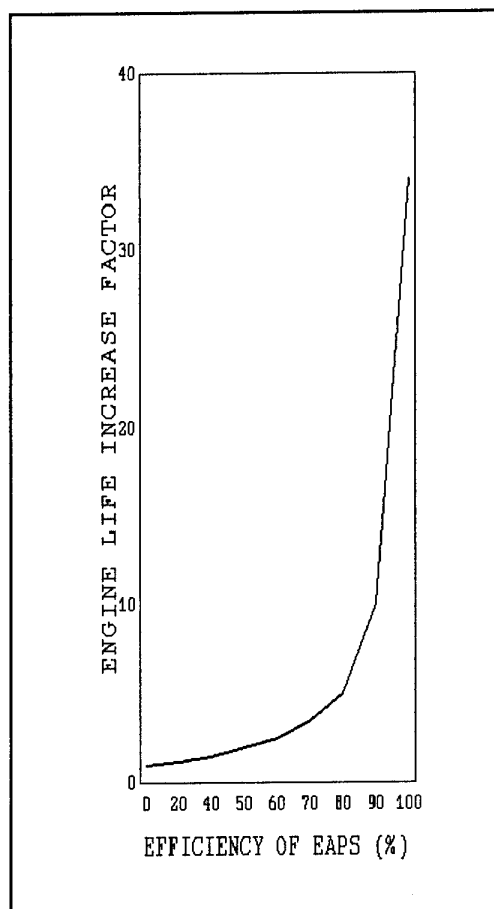


Figure 6. EFFECT OF CENTRISEP EAPS ON GAS TURBINE LIFE

The decision to install EAPS was reinforced when the Army Air Corps deployed the Lynx helicopter without environmental protection, and in the

worst case rejected both engines from one aircraft after only 6.5 hours running. The Gazelle helicopter accompanied the Lynx to the Gulf but had EAPS fitted, and as a result its engines fared better, but reliability was still below that experienced in European operations.

The Lynx helicopter was retro-fitted in-theatre with an EAPS and therefore provides an approximate performance comparison of helicopter engine reliability with and without environmental protection. The average life of an un-protected Lynx engine was 22 hours compared to an average attained life of 58 hours with EAPS, a life improvement in the order of 2.6. The design efficiency of the Lynx EAPS which is the order of 85% would suggest a theoretical life improvement factor of 4 to 5. The Lynx EAPS units however were very old (1978 design standard) at time of fit and problems were reported with sealing of the unit to the intake surfaces. This may account for the relatively poor performance.

The RAF Puma helicopter has a permanent EAPS fitted and was therefore available for immediate deployment.

The main RAF concern was the Chinook. The RAF did not have sufficient spare engine assets to support operations if engine attrition rates to the levels previously indicated were confirmed. The UK MOD therefore initiated a design, development and build programme in August 1990 in anticipation of such a potential operational logistic and cost penalty. An EAPS system was purchased, fitted and tested on every RAF Chinook before deployment in Dec 90.

#### **RAF Gulf Helicopter Operating Experiences.**

##### **a. Puma HC MK1 - Turmo IIIC4**

The EAPS units installed on the RAF Puma had been fitted by a modification in the 70s. It is a permanent fit and is selected for operation from the cockpit. Selection introduces a blank to obstruct the normal intake and diverts all incoming air via the EAPS units, while an electrical air bleed valve opens an engine bleed to supply scavenge air.

Despite the existence of this system compressor blade erosion was still apparent with an occasional engine/EAPS module mix exposing an excessive, unpredictable and unacceptable wear rate which justified further investigation. On some occasions affecting only one engine in a particular aircraft. Some Puma EAPS modules were

however of various design standards producing dust separation efficiencies between 73% to 80%, depending on the standard concerned.

Following investigations by RAF engineering staff, Rolls-Royce and the EAPS unit manufacturer, it was discovered that some scavenge systems were not operating correctly due to system faults. With incorrect or non existent scavenge supply the separator cannot function and sand collects in the units and eventually enters the engine. In many cases no scavenge air was available due to failure of the engine mounted selection valves, although all cockpit indications were normal. It had not been previously appreciated that the indicator light which confirmed scavenge air selection, was in fact only connected to the electrical supply. Therefore it confirmed only a supply was present, not that the valve had opened.

Once the EAPS scavenge systems had been fully serviced and all faults eliminated, engine reliability improved to an acceptable level. Operations were ultimately limited by a routine MDT inspection which was required to the engine turbine case, one of which had fractured due to thinning of the case wall. This fault was not a consequence of Gulf operations as instances of case wear had occurred previously, but it was thought that the level of abrasion may have exacerbated them.

Following the above work the manufacturer was tasked by the MOD to develop the Puma EAPS module design still further. This was done and a dust separation efficiency of 92.5% was achieved. A total of 20 aircraft sets of these new standard were subsequently supplied to the RAF for operational use in theatre.

Blade erosion limits were extended by the engine Design Authority for the period of the conflict with no adverse effects, however on the return to peace time operations a large number of engines were rejected. No specific statistics are readily available to quantify engine reliability levels, but other than the faults noted there were no other areas of concern.

##### **b. Chinook MK1 - Textron Lycoming T55-712E**

The trial installation for the Chinook EAPS modification was begun in Oct 90 and by Dec 90 all 17 aircraft were completed and deployed to the Gulf region (Ref 5&6). The modification involved an airframe modification to accept the two EAPS units and some electrical system

modifications, including provision of a supply for the scavenge fans which were rated at 20 amps each running circuit.

The RAF Chinooks were operated during the Gulf as troop carriers and supplies transports. The deployed aircraft operated in the desert, with typical sorties being of around 600 mile round trips and were flown at 30/60m. It was estimated that about 10% of flying time was spent in 'zero visibility' conditions and that on landing the dust cloud spread was around 100m fore and aft. When flying above around 30m the Chinook did not stir the desert surface.

The 'all-causes' engine rejection rate experienced during the 3 months of the Chinook Gulf operations was 4.46 per 1000 aircraft flying hours, compared with a normal peace time rate over the proceeding 12 months of 6.09. It has been reported that the US Army Gulf engine rejection rate may have been as low as 40 per 1000 engine hours. The UK rejection rate would suggest an engine installation life or Mean Time Between Removals (MTBR) of about 450 hours. The reported US Army rate would suggest a life of 25 hours, which is in line with that published at the time. The Chinook EAPS unit is 90.5% efficient and the estimated life improvement factor of 10 suggested by figure 6 would appear to be supported.

The T55 engines were examined every 25 hours for erosion, but no engine was rejected for such faults. Some first stage compressor blades experienced minor FOD probably caused by objects of higher mass entering the EAPS units. These particles would have had sufficient mass to follow a ballistic trajectory rather than being centrifuged by the air flow. As with the Puma, damage limits were extended for the duration of the conflict and therefore the majority of this damage was acceptable. It did however lead to numerous rejections when normal acceptance limits were restored.

A large amount of dust was found to collect in the engine bays and other concealed areas but this did not cause any problems. Salt spray was experienced when flying in the Wadis, but the effects were minimised by the secondary EAPS contribution of water droplet separation. Operators occasionally saw the accumulation of a thin black deposit film upon the compressor blades. The film would have been deterred from unprotected engines by the intake sand abrading process. The deposit was easily removed by compressor washing and the frequency of this

action was increased accordingly.

Several engines which had seen in theatre use, were found during subsequent repair to have severe trapped dust deposits in the blade root areas of the Stage 2 turbine disc. A build up had occurred on the face of the disc against a lip protrusion and dust migration had then followed adjacent cooling holes to the blade roots. Several blades were flow tested and showed no blockage of internal passages and hardness tests proved that no material degradation had resulted from localised overheating. It is not known what possible effects this apparently benign build-up could have had if operations had been continued for a longer period.

#### 4. RAF AIR TRANSPORT OPERATIONS

The RAF Air Transport Force was operated from the outset of the crisis to the conclusion of the conflict, predominantly on the UK/Cyprus/Gulf supply route. The resulting sorties were longer than those normally experienced in routine operations and therefore despite an increase in monthly flying hours, up to three times on some aircraft, a reduced number of operating cycles was accumulated. The result was a general reduction in engine rejection rates.

The Airborne Air Refuelling and Maritime Patrol aircraft were also operated at increased utilisation rates, but on sorties of normal duration with normal operating limitations. The rejection rates experienced on these engines remained at peace time levels, with the number of engines rejected generally being in line with increased flying rates.

There were no abnormal reliability trends or faults encountered during any of these operations. After the conflict no evidence of internal distress was reported.

#### 5. CONCLUSION

The UK deployment to the Gulf region involved over 200 aircraft and contributed about 10% of the available air power. The utilisation of most RAF aircraft was in the order of 2 to 3 times the level normally experienced, but the ratio of engine removals to flying hours predominantly remained steady and for some engine types actually reduced.

The engines operated from normal airfield surfaces, at medium to high level and within

normal operating limitations, experienced normal engine reliability levels. These were attained without the need for modifications and few technical faults were encountered on such engines as a direct result of the climatic conditions. Analysis of engine removal statistics shows no post-conflict increase in engine removals and therefore it is thought that engines were generally more reliable rather than because maintenance standards were relaxed.

The engines of Jaguar aircraft operating at low level were modified to compensate for some of the performance loss caused by the high ambient temperatures. However as a result of hostilities being concluded ahead of the hotter summer months only a minor change to the TGT limit sufficed in obtaining a sufficient performance improvement. The decision to deploy only engines to the latest modification standards helped maintain similar engine removal rates to those experienced during European type operations. However the level of internal damage noted was much higher, suggesting that the engine was operating very close to its material limits.

The RAF was most at risk from engine - related operational failures in the helicopter fleet. The reports received following initial US Gulf helicopter operations confirmed the thoughts that unless action was taken the problem of sand erosion would be a major limiting factor to UK helicopter forces. On the Chinook, the expenditure on a modification to install an EAPS was fully justified when the merits of the system were evaluated. The RAF did not reject an engine in the Gulf from its Chinook helicopters for power degradation, the main consequence of extreme sand erosion. The attained engine removal rate was better than that recorded over the previous 12 months.

Following the conclusion of RAF Gulf operations, the service was more than satisfied with the levels of overall performance and reliability which had been attained by its aircraft gas turbine engines.

#### ACKNOWLEDGEMENTS

The author would like to thank the many colleagues in the Royal Air Force and Ministry of Defence, for their advice and assistance in the preparation of this paper.

The author would further like to thank the staff of 'Aircraft Porous Media Europe Limited' for their advice and assistance.

The views expressed are those of the author, and do not necessarily represent the policy of the Ministry of Defence.

#### REFERENCES

1. Air Marshal Sir Michael Alcock, Chief of Logistic Support and Chief Engineer, Royal Air Force. 'Supporting the Royal Air Force', Aeronautical Journal, Vol 7 No 967, August/September 1993.
2. J. Stamp. 'Engine Air Particle Separator Panels for Helicopter Engine Protection', Aircraft Porous Media Ltd. 16th European Rotorcraft Forum, Glasgow, Sep 1990.
3. Curve based on Detroit diesel Allison 570-k gas turbine installation manual and applied technology laboratory, FT. Eustis, V.A. data.
4. P. Stallard. The Development of an Engine Air Particle Separator System for the CH-47 Helicopter. Aircraft Porous Media Ltd. 16th European Rotorcraft Forum, Glasgow, Sep 1990.
5. P. Stallard. Chinook HC.MK1 Centrisep EAPS Gulf War De-Brief. Aircraft Porous Media Ltd. PS.679 - 28 Nov 1991.

© British Crown Copyright 1994/DRA.

Published with the permission of the Controller of Her Britannic Majesty's Stationery Office.

## QUESTIONS

### F. AYDINMAKINE (Tu)

- Q. Do we have to use external or aircraft power to get EAPS running? Where is the power obtained from and what is the resulting power loss?
- A. The EAPS units require no power to operate other than required by the scavenge system; on the CH47 Chinook, the scavenge system uses 2 electric fans rated at 20 Amps each. The scavenge system losses, therefore, are low, but the system does cause an inlet pressure loss resulting in a power loss of about 2% in the hover and 6% in the maximum speed region.

### G. LAZALIER (US)

- Q. What were the upper and lower particle size limits associated with the EAPS removal efficiencies quoted for the units cited?
- a. The efficiencies quoted were measured using A.C. Coarse test duct.

### A.R. OSBORNE (UK)

- Q. A performance degradation of 1.3% was quoted for the Chinook. What does this translate to in terms of payload when EAPS are fitted? If payload loss is low, why do we not fit protection to all helicopters as a matter of course?
- A. The quoted 1.3% was a fuel flow/range penalty, the payload penalty is about 900 lb. The advantage of the system from an engineer's viewpoint would be greater than the penalties, but we are not the only parties involved.

### K. BROICHHAUSEN (Ge)

- Q. I have the impression that UK experience shows no major influence of erosion, but US experience indicates it can be significant. Would you comment?
- A. Erosion is a major cause of engine degradation; however, all UK helicopters used in the Gulf Conflict had EAPS systems fitted and, as a result, our erosion experiences were minor. These systems were installed at considerable expense because of concern about the effects of erosion on engine reliability.

### M. LEWIS (UK)

- Q. Were there any deposition problems with the T55?
- A. I am not aware of any major deposition problems on RAF T55 engines.

# U.S. ARMY ROTORCRAFT TURBOSHAFT ENGINES

## SAND & DUST EROSION CONSIDERATIONS

Vernon R. Edwards

Peter L. Rouse

U.S. Army Aviation & Troop Command

Directorate for Engineering

4300 Goodfellow Boulevard

St. Louis, Missouri 63120-1798

United States of America

### SUMMARY:

The impact of operating in a sand and dust environment on U.S. Army rotorcraft turbine engines has been a major concern since the first turbine powered UH-1 Iroquois (Huey) helicopter was fielded in the early 1960s. The implication on turbine engine performance and durability had not sufficiently been recognized, or addressed, in early engine designs. Early engine military specifications had been primarily concerned with U.S. Air Force "jet" engines for fixed wing aircraft. Although these early specifications included sand and dust requirements relative to ingestion capability and test substantiation, actual rotorcraft field experience was not considered, nor, in fact, was actual data available. This paper provides a brief history of the impact of operation in sand and dust and operational considerations on U.S. Army rotorcraft turbine engines. The general effects of sand and dust erosion, compaction, deformation, glassing, etc., on engine turbo machinery will be discussed. Finally, the results of operation in Southeast Asia, and during Desert Shield/Desert Storm, possibly the worst case operational environment encountered to date, will be presented.

### LIST OF SYMBOLS:

$\partial$	partial derivative
$\mu$	viscosity
$\eta$	efficiency
$\delta$	ambient pressure/29.92 mm hg
$\theta$	ambient temperature/519°R
ft	feet
N	rotational speed
NDOT	$dN_{GGT}/dt$
P	pressure
PRc	compressor pressure ratio
SFC	specific fuel consumption

SHP	shaft horsepower
t	time
T	temperature
u	local velocity
U	freestream velocity
W	massflow

### Subscripts

3	compressor discharge station
a	airflow
Comp	compressor
F	fuel
GGT	gas generator turbine
PT	power turbine

### INTRODUCTION:

The detrimental effects of operating military equipment in desert sand, dust, and extreme temperatures, have been known, in a general way, for many years. Specifically, however, the impact of operating in sand and dust on U.S. Army rotorcraft/helicopter turbine engines began to become a major concern with the first turbine powered UH-1 Iroquois (Huey) initial operational trials in the late 1950s.

In the preceding years, the Army has studied the effects of erosion on rotorcraft turbine engines based on both engine contractor testing and actual fielded engine operations. New technologies such as improved materials and erosion resistant coatings have been evaluated. Special specification requirements and innovative component designs were incorporated into new engine models to improve durability. However, the experience gained from extended operation in an extremely erosive environment during Desert Shield/Storm demonstrated the need to pursue additional improvements in turbine engine durability.



### EARLY BACKGROUND:

Helicopter tail and main rotor downwash effects churned up terrain wherever U.S. Army helicopters were being flown, particularly if operating in a desert environment. Sand and dust, small rocks, and other loose debris were propelled into the atmosphere surrounding the helicopter. Figure 1 is one of the first photographs of early UH-1 desert trials.

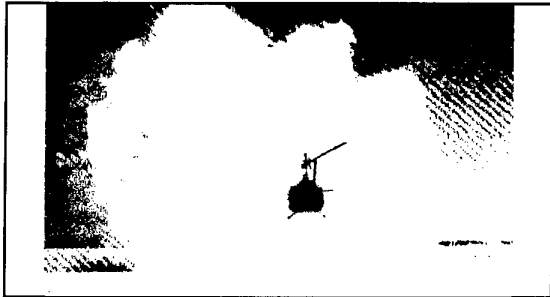


Figure 1

Obviously, helicopter altitude plays a major role in the severity of this environment. But, from day one, military helicopter operations called for many take-offs, landings, hover, and Nap-of-the Earth (NOE) operations, from typical U.S. Army "unimproved" areas. Rotor downwash created dust clouds of such intensity that pilot visibility virtually becomes zero; this condition is known as "brown-out". These airborne particles may then be ingested at high speed into the engine inlet. The U.S. Army became extremely anxious to evaluate the effects of this sand and dust ingestion upon helicopter turbine engines.

It had been generally expected that severe damage, due to sand and dust ingestion, would occur on the close tolerance, rapidly rotating turbo-machinery parts. Earlier operational experience with piston engine helicopters in similar environmental conditions had demonstrated the necessity for cumbersome, power robbing filtration of inlet air to keep these conventional engines operational for just a fraction of their normal service life. Since gas turbine engines utilize many times the volume of air that conventional piston engines use, the consideration of sand and dust effects became increasingly critical for continued successful development and operation of gas turbine powered rotorcraft by the U.S. Army.

As expected, early trials began to identify the severity of material erosion and dust compaction in helicopter

engines. The result of these conditions was exhibited, initially, through engine performance losses, compressor surge encounters, and a general deterioration of all engine mechanical components. Early Light Observation Helicopter (LOH) desert tests in the mid 1960s lasted as short as 30 minutes in severe desert conditions. Rapid deterioration was due, in this case, to a compressor configuration utilizing a plastic lining, and a pneumatic fuel control which rapidly accumulated dust and plugged.

As the U.S. Army began to analyze the results of sand and dust ingestion through engine hardware inspection, and technical and metallurgical analyses, the general conclusion was that the deterioration manifested itself in similar phenomena for all engine models studied. Much of the performance deterioration was due to the degraded compressor efficiency and loss of pumping capacity resulting from compressor blade, stator, and shroud erosion. Hot section deterioration was due to "glassed" over cooling air exit holes, and impaction of fine material in internal passageways and turbine nozzles. In addition, gas generator turbine efficiency deteriorated due to turbine blades and nozzles erosion, although not to the extent of compressor hardware. Hot section abrasion coatings for enhanced blade tip control were particularly susceptible. Glassing in the engine combustor and impaction on turbine disks and sealing plates also resulted in turbine efficiency reductions. The following section describes the mechanisms involved in rotorcraft turbine engine deterioration due to sand and dust ingestion.

### TECHNICAL DISCUSSION:

The results of sand erosion on turbine engines are decreased power, increased fuel consumption, decreased surge margin, increased transient acceleration times, and reduced transient stability. All of these impact the operation of turbine engines in Army rotorcraft.

Compressor erosion patterns are unique to each engine, depending on compressor design. Axial flow compressors of varying stages and axial/centrifugal designs exhibit repeatable and predictable deterioration patterns. However, compressor erosion is unique to each turbine engine model, individual compressor blade and vane design, and depending upon their location in the engine. Further, the inlet flow path contributes to the erosion pattern in the initial stages. In general, within a given engine compressor, some blade stages revealed only chordal width erosion, other

stages revealed only tip erosion and other stages could sustain both tip and chordal erosion. First stage leading edges tended to "roll-over" on the lower 1/3 leading edge. Subsequent stages exhibited blade tip rounding of more severity in the succeeding stages.

As the sand enters the engine inlet, it has kinetic energy proportional to a particular particle size and velocity. The turbine engine may impart radial and axial velocity to the sand particles. Each particle has finite kinetic energy that may remove a small portion of the hardware that it impacts: i.e., compressor blades, stator, etc.. In severe cases, this impaction and resulting erosion results in localized stress which in some cases reaches critical value. The extent of erosion depends on several parameters: kinetic energy of the particle, material make up of the particle, material of the engine hardware, geometric form of both the particle and hardware, and incident angle of particle impact.

The extent of glassing in the engine hot section, including the combustor, is dependent on several parameters. These parameters are: pressure ratio, turbine inlet temperature, blade and nozzle surface temperature, sand particle size, and sand composition make-up. Depending on these variables, some material may only stratify on nozzle vanes, or blades, forming a semi-solid mass which may be easily removed by mechanical means. However, under conditions typical of our more modern high performance turbine engines, sand particles can reach glassing temperatures and cool to a solid state that is extremely difficult to remove. This glassing, as discussed earlier, plugs cooling holes and slots, denying cooling air to hot section components, consequently impacting structural integrity.

From an overall performance standpoint, sand ingestion is one of the most detrimental events that occur in a gas turbine engine's life. The effects of sand ingestion cover both the micro and macroscopic aspects of gas turbine engine performance.

The macroscopic effects of sand ingestion on gas turbine engine performance are:

- ◆ Decrease in the engine shaft horsepower (SHP) at constant turbine inlet temperature.
- ◆ Increase in the specific fuel consumption (SFC) at constant power.
- ◆ Decrease in the engine surge margin.

- ◆ Slower engine transients and or reduced transient stability.

All of the macroscopic effects listed above are a result of sand ingestion reducing component efficiency.

#### ENGINE PERFORMANCE SENSITIVITY TO COMPONENT EFFICIENCY LOSS:

Compressor efficiency is one of the most important aspects of turbine engine design and performance. Gas turbine engines did not become practical to use as a means of propulsion until the 1940's. Early compressors were so inefficient that they required essentially all the power than the turbine was able to supply; the net effect was little or negative work output.

The effect of a 1% reduction in compressor efficiency at constant turbine temperature results in a decrease of approximately 3% power; gas generator turbine efficiency has a similar relationship. Power turbine efficiency effects on power are approximately 1 to 1 at constant turbine temperature.

$$\frac{\partial \text{SHP}}{\text{SHP}} = 3 \left( \frac{\partial \eta_{\text{Comp}}}{\eta_{\text{Comp}}} \right)_{T=\text{const}}$$

$$\frac{\partial \text{SHP}}{\text{SHP}} = 3 \left( \frac{\partial \eta_{\text{GGT}}}{\eta_{\text{GGT}}} \right)_{T=\text{const}}$$

$$\frac{\partial \text{SHP}}{\text{SHP}} = \left( \frac{\partial \eta_{\text{PT}}}{\eta_{\text{PT}}} \right)_{T=\text{const}}$$

The effect of a 1% reduction in compressor efficiency at constant power is an increase of approximately 1% in turbine temperature. Gas generator turbine efficiency has a similar relationship. The decrease in power or the increase in turbine temperature becomes very important when the rotorcraft is operated in hot and high conditions where the engine is temperature limited. The most likely scenario of the reduced compressor efficiency would be a reduction in payload capability. If the reduction occurred during the mission, then a rotor droop could be encountered as the power available, at the temperature limit, would be reduced.

The reduced component efficiency due to sand erosion also results in increased specific fuel consumption. A 1% reduction in compressor efficiency at constant SHP results in an increase of approximately 1% in SFC.

Gas generator turbine efficiency and power turbine efficiency have a similar relationship. This means that the engine uses more fuel to produce the required power. The increase in SFC can impact the capability of the rotorcraft to accomplish the mission due to range reduction.

$$\frac{\partial \text{SFC}}{\text{SFC}} = - \left( \frac{\partial \eta_{\text{Comp}}}{\eta_{\text{Comp}}} \right)_{\text{SHP=const}}$$

$$\frac{\partial \text{SFC}}{\text{SFC}} = - \left( \frac{\partial \eta_{\text{GGT}}}{\eta_{\text{GGT}}} \right)_{\text{SHP=const}}$$

$$\frac{\partial \text{SFC}}{\text{SFC}} = - \left( \frac{\partial \eta_{\text{PT}}}{\eta_{\text{PT}}} \right)_{\text{SHP=const}}$$

The decrease in the engine surge margin is a very serious problem in rotorcraft operation. The prime concern of rotorcraft operators is the stable delivery of power on demand. There are three manifestations of sand ingestion that can reduce engine stability:

The first of these is reduced compressor efficiency due to erosion of the blades and stators/diffusers. As noted above, this requires an increased turbine temperature to produce constant power. This means increased compressor loading at a fixed speed to achieve constant power. The resulting operating line is higher, closer to the surge line, than a nominal operating line. In addition, the compressor surge line will tend to drop below the nominal surge line as a result of erosion. This will be explained in the microscopic effects section.

The second factor to influence engine stability is reduced gas generator efficiency due to erosion of the turbine nozzles and blades. As was the case for compressor erosion, maintaining constant power with a reduced gas generator turbine efficiency requires operation at increased turbine temperature. Thus, using an argument similar to that for compressor erosion, the gas generator turbine efficiency reduction will cause the operating line to rise above the nominal operating line.

The third factor to influence the engine stability is reduced gas generator turbine nozzle throat area due to "glassing" of the nozzle. The "glassing" is due to melted sand sticking to the nozzle and reducing the throat area. The undesired reduction of the nozzle throat area has an effect on compressor performance analogous to closing a variable area turbine nozzle.

Again, compressor loading must increase, and likewise, the operating line will tend to rise above the nominal operating line.

As a result of all three of these effects, there is less compressor surge margin available. The engine then is

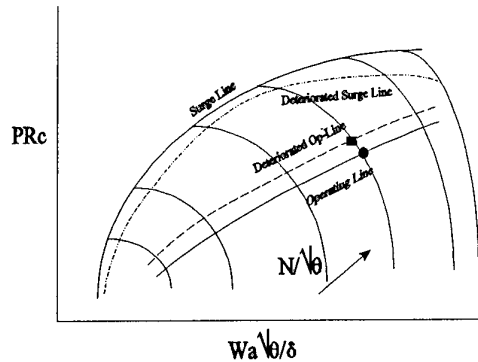


Figure 2

more susceptible to stall/surge inception during transients or as a result of a disturbance such as inlet distortion.

The effects of erosion on the surge line and operating line can be seen in Figure 2.

The engine transient capability will be affected by sand erosion due to the changes in compressor and gas generator turbine efficiency, and/or the reduction of gas generator turbine nozzle throat area due to glassing.

If the engine has a ratio unit control,  $W_F/P_3$  versus  $N_{\text{GGT}}$ , then a specific amount of fuel will be scheduled for a given  $N_{\text{GGT}}$  speed and  $P_3$ . This amount of fuel produces a certain unbalanced torque available to accelerate the engine. The reduced efficiency of the compressor/gas generator will require production of a larger unbalanced torque to accelerate the engine at the same rate as a healthy engine than is available with the existing transient schedule, thus the acceleration will be slower. Another issue with the transient schedule is the possibility of surging during the transient. Surging during a transient is a result of excessive compressor loading. If the compressor surge line has deteriorated below the nominal surge line, then incursions into the surge region could result during transients.

If the engine has an NDOT control, it may be able to schedule the necessarily increased fuel into a deteriorated engine in order to accelerate at the same rate as a healthy engine; an NDOT control uses the engine's  $dN_{GT}/dt$  as the controlling variable for fuel input. The increased fuel flow results in increased compressor loading, thus incursions into the surge region could occur as a result of the increased compressor loading during transients.

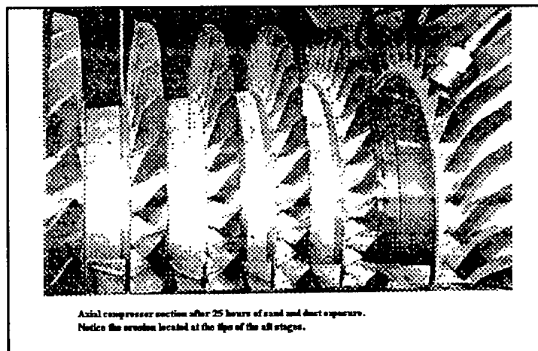


Figure 3

The microscopic effects of sand erosion on engine performance are a result of the changes in the flowpath aerodynamics. Figure 3 is an example of an eroded axial compressor.

Erosion affects the profiles of the airfoils reducing the airfoils aerodynamic efficiency. The airfoil loadings will change due to the eroded profiles. The airfoil's eroded profile will be dependent upon the incidence angle of the sand impact. Figure 4 illustrates an eroded compressor blade profile with leading edge "rollover". If the sand impact is tangential to the airfoil, then the energy transferred to the airfoil will be less than for a normal impact. The difference in the impact angle of the sand can result in the airfoils being polished instead of eroded.

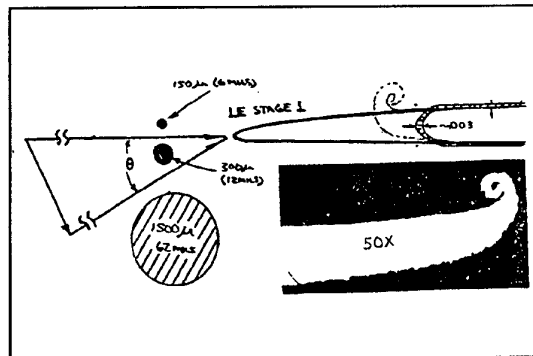


Figure 4

Erosion can also increase the surface roughness of the airfoils near the leading and trailing edges. Increasing surface roughness increases the drag of the airfoils.

Reduced aerodynamic efficiency and increased airfoil drag result in more power required to operate the compressor and less work available from the turbine. It should be noted that when the airfoil surface is parallel to the flow a polishing can occur on those surfaces; however, the polishing effect of the airfoils does not compensate for the detrimental effects of erosion and increased surface roughness elsewhere on the airfoil.

Erosion effects the stability of the compressor due to the disruption of the boundary layer. The boundary layer is very sensitive due to the adverse pressure gradient in the compressor; the momentum of the fluid in the boundary layer is trying to "push" against the pressure rise in the compressor. If the momentum of the fluid in the boundary layer is not sufficient, the flow in the boundary layer reverses and the flow separates. If the separation is great enough, then a compressor surge could occur. Profile changes due to erosion can aggravate the tendency of the boundary layer to separate. "Trips" in the surface could also cause the boundary layer to separate.

The effects of adverse pressure gradients on the boundary layer can be seen in Figure 5.

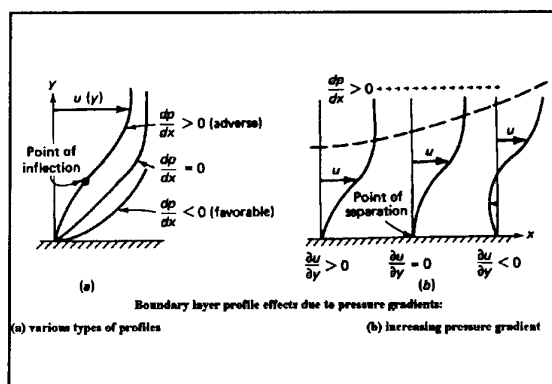


Figure 5

The cumulative effects of the blade profile changes and increased surface roughness is a decrease in the amount of allowable compressor blade loading. The reduced allowable compressor blade loading results in a lower compressor surge line as seen in Figure 2. The maximum angle of attack the compressor blades can sustain before separation is thus reduced due to the blade profile changes and the increased surface roughness. The lower compressor surge line results in a decrease in the available compressor surge margin of the engine.

#### REFINING TECHNICAL REQUIREMENTS

With the understanding that U.S. Army helicopters would always be utilized in field operations, potentially exposing them to extreme sand and dust environments, a refinement of engine technical requirements was needed. In addition, the understanding of how turbomachinery deteriorated due to sand and dust ingestion highlighted the need to address specific areas of concern. As previously mentioned, early U.S. Army turbine engines had been developed based on Air Force jet engine specifications dating from the early 1950s. Initial sand and dust requirements in the early 1960s had been addressed by the U.S. Army via MIL-E-8593, Turboprop/Turboshaft engine specification. Mil-spec testing included 10 hours of engine operation with a sand distribution of 0-200 microns at a concentration level of 53 mg/m<sup>3</sup>, and allowed a 5% shaft horsepower (SHP) loss and 5% specific fuel consumption (SFC) increase at the conclusion of the test. By the mid 1960s, the Air Force's MIL-E-5007 (revision C) increased the particle distribution to 0-1000 microns. The sand defined in the MIL-E-5007 (revision C) specification became known as "C-spec" sand. The condition of U.S. Army turbine engines bench tested

with military specified sand was compared to that of actual field operated engines throughout the 1960s. Studies were accomplished relative to actual sand particle sizes and distributions through collection exercises. Sand was sampled from various desert locations within the United States, the Far East, and Saudi Arabia. The U.S. engine industry was also defining additional test sands covering particle size ranges, such as Arizona road dust, "AC-Fine" and "AC-Coarse". Figure 6 illustrates the particle size distribution for various types of sand.

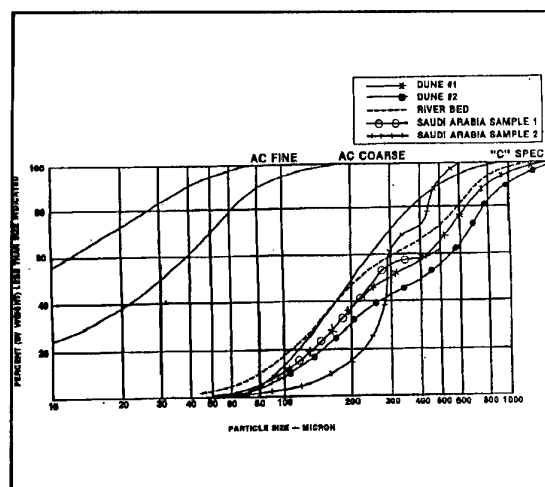


Figure 6

In operations up to an approximate 75 ft altitude, the particle size of sand collected generally fell between the C-spec and AC-Fine sands. Sand sampling from the Saudi Arabian desert also revealed that composition of particle sizes closely approximated C-spec sand distribution. The rigorous flight test sand collection and sampling at Yuma, Arizona, U.S. Army test site revealed that as altitude increases, the composition of sand and dust becomes much finer.

With the experience gained from actual field operations, engine bench testing, sand sampling and analysis, and engine hardware inspection, the U.S. Army began to refine the sand and dust requirements for future U.S. Army turbine engines in their AV-E-8593 series Turboprop/Turboshaft engine specifications. In the early 1970s, the U.S. Army began to prepare a Request For Proposal (RFP) for a 1500 SHP demonstrator engine. A new and significant requirement was decided to be applied to this engine. That requirement was for the engine to be designed with an integral inlet particle separator (IPS). The intent was to improve the engine's capability to operate

for extended periods of time in a sand and dust environment. Industry responded with several unique design concepts that addressed the new requirement. Following a competition, the General Electric Aircraft Engine Company was selected as the winner. A development and qualification program followed which eventually lead to the T700-GE-700 series engine utilized first in the UH-60 Black Hawk helicopter, and later in the AH-64 Apache helicopter. Figure 7 shows a cross-section of the T700 engine and Figure 8 shows a cutaway of the IPS.

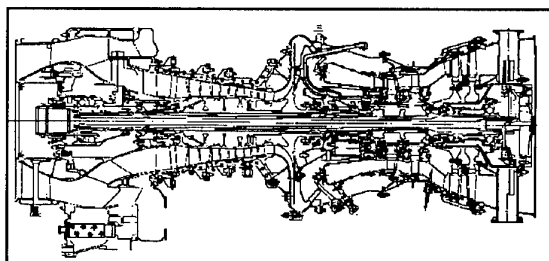


Figure 7

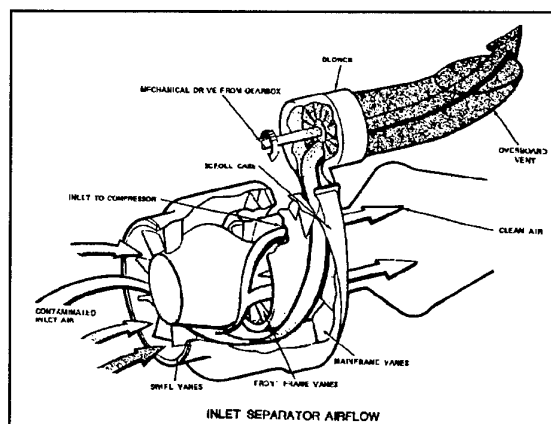


Figure 8

Revised specification requirements identified an increase in the sand testing time from a 10 hour block test to a 50 hour block test using the C-spec sand distribution at a concentration of 53 mg/m<sup>3</sup>. The 50 hour test resulted in approximately 80 pounds of sand being ingested through the engine. The amount of sand ingested is based on the engine inlet airflow, the sand concentration, and the duration of the test. The post-test requirements specified that the engine should not lose more than 10% SHP, and that the SFC would not increase more than 15%. The engine would also have to demonstrate acceptable starting and transient performance (free of stalls, and within required time

limits) at the completion of the sand ingestion test.

Through design refinements during the development and qualification program, the final engine configuration, including the integral inlet particle separator and its associated scavenge blower, demonstrated significantly improved capabilities of engine operation in an erosive environment. The qualification test was successfully completed, although the power deterioration limit was exceeded slightly. Final hardware inspection revealed the familiar mechanism causing power loss; hardware erosion with the resulting component efficiency deterioration.

### U.S. ARMY OPERATIONAL EXPERIENCE

The U. S. Army began fielding and operating the UH-60A Black Hawk in the late 1970s, and had accumulated close to 200,000 engine flight hours by mid 1982. Black Hawk operations included normal U.S. Army missions, calling for multiple take-offs and landings, near ground or Nap-of-the-earth flight, and multi-helicopter operations in severe environmental conditions. As field time increased, usage data began to reveal significant improvements; data such as Mean Time Between Engine Removals increase 2 to 4 times, compared with the older engine designs. Engines being removed for Foreign Object Damage (FOD) were also significantly reduced. These outstanding results were primarily attributed to the decision to require the integral inlet particle separator and the amount of attention that had been applied to understanding sand and dust erosion in rotorcraft turbine engines. With the fielding of the AH-64 Apache helicopter with a growth version of the T700 engine, the U.S. Army continued to assess the impact of operations of helicopters in adverse sand and dust conditions, and the level of protection afforded the basic turbine engine core by the integral inlet particle separator. It was demonstrated that significant improvements in turbine engine capabilities to operate in a desert environment was afforded by an IPS. However, extended operations in sandy desert environments increased the severity of engine component erosion significantly.

U.S. Army units were deployed to Egypt, in 1980 and again in 1981, in operations identified as Bright Star I and Bright Star II. A fleet of UH-60A Black Hawks, AH-1S Cobras, and CH-47 Chinooks were used for the distinct purpose of evaluating desert operation, and evaluating potential problems. The IPS protected T700 engine fared much better than the older engine

designs. In fact, during these two exercises, there were no T700 engine removals due to loss of performance. Following the completion of Bright Star II, the UH-60 Black Hawk engines were returned to a U.S. Army depot for a full analytical inspection in an attempt to quantify the extent of damage incurred. Compressor hardware exhibited the same trend of first stage leading edge peening, slight roll-over, subsequent stage tip rounding, axial clearance increases, air seal clearance increases, and the accumulation of extremely small sand particles plugging some of the combustor and turbine cooling air passages.

The Bright Star operations demonstrated what the U.S. Army felt were significant improvements in engine reliability and durability while operating in an adverse environment. Yet, it was believed that for extended operations in severe sand environments, additional engine improvements were desirable. The U.S. Army directed and funded additional factory engine tests utilizing the finer AC-Fine sand. The intent of the testing was to address the fine sand accumulation in the combustor and turbine cooling air passages. Results of this testing confirmed significant plugging of the cooling air supply passages and some glassing in the combustor and turbine nozzles. It was concluded that significant improvements in performance retention could be realized through the proper selection of a location for the combustor and turbine cooling air supply inlet.

The flow field which exists at the discharge of a centrifugal compressor provided an inherent sand separation action. This phenomena created within the engine was carefully studied relative to a selection of an inlet for air entering the combustor and turbine cooling air circuit. It was further decided that some gains in erosion protection could be made through the use of "coatings" in appropriate locations within the engine. Several coating programs were conducted by the U. S. engine industry with each yielding unique outcomes; the programs indicated that when properly selected and tested significant erosion protection could be provided.

In 1984 the U.S. Army issued a Request For Proposal (RFP) for a new turboshaft engine to power it's future LHX helicopter; the helicopter would later be named the RAH-66 Comanche. This engine would be known as the T800 series and there was a competition. The competition included the design and testing through the Preliminary Flight Rating (PFR) phase: i.e., actual engine hardware was evaluated prior to a final selection and subsequent Full Scale Development (FSD). The

resulting contract Statement of Work (SOW) and Prime Item Development Specification (PIDS) (derived from the latest updated version of AV-E-8593, U.S. Army Turboprop/Turboshaft specification) incorporated the most recent lessons learned and technology improvements. One lesson learned from the prior T700 experience was that, although the "integral" inlet particle separator had made a significant improvement in an engine's ability to successfully operate in a sand and dust environment, it did cause some compromise relative to basic engine design, such as anti-icing requirements. It also hampered any significant design change relative to a growth engine. Therefore, the T800 requirement was defined to include an "integral", but removable, IPS. The contract included special development test requirements during both the PFR and the full military qualification phases. The PFR special tests involved detailed evaluation and assessment of the combustor and turbine cooling air circuit inlet location. During the official qualification phase, a 50 hour test was required on AC-Fine test sand. The AC-Fine test was intended to evaluate the final design relative to the plugging of the combustor and turbine cooling air passages. There was also a requirement to complete a five hour AC-Coarse test to assess the compressor durability on the heavier sand. The Official 50 hour qualification test was conducted with C-spec sand at a concentration of 53 mg/m<sup>3</sup> with a 10% SHP loss and 15% SFC increase pass/fail criteria. Since this engine has not yet gone into production, and a growth engine is under development, actual field experience is not available. However, the following are generalized results for the engine which underwent the official C-spec sand test. The T800 test engine verified that 50 hours of C-spec sand ingestion resulted in no detrimental blockage occurring in the combustor and turbine cooling air circuit. The deteriorated engine demonstrated the performance within the allowable loss limits and without adversely affecting the engine's transient capability. The allowable overall SFC increase of 15% was easily met, with an actual maximum SFC increase of less than 5%. It had been hoped that the horsepower loss would be linear across the 50 hours, thus a requirement for no more than 5% SHP loss at 25 hours. This was slightly exceeded; however, the engine successfully completed the 50 hours with a power margin of approximately 2%. The final success of the growth T800 engine may be reported in some future presentation.

Table 1 illustrates the U.S. Army sand testing requirements from the original MIL-E-8593 through the 1984 engine RFP.

Document	Test Time (hrs)	Test Sand (microns)	Concentration (mg/m <sup>3</sup> )	Allowable Loss (%SHP) (%SFC)
MIL-E-8593 Revision April 1963	10	0-200 AC-Coarse	53	5 5
MIL-E-5000 Revision C December 1963	10	0-1000 C-Spec	53	5 5
Engine RFP July 1970	50	0-1000 C-Spec	53	10 15
Engine RFP December 1984	50	0-1000 C-Spec	53	10 15

Table 1

### OPERATION DESERT SHIELD/STORM

When this operation first began in August 1990, the U.S. Army had great confidence that the UH-60 Black Hawk and AH-64 Apache could successfully operate in the Saudi Arabian desert environment due to the durability of the T700 series turbine engine. As discussed above, this was based on previous U.S. Army helicopter operational experience world-wide, but in particular, the Bright Star exercises in Egypt.

The Bright Star exercises had verified that the T700 engine integral inlet particle separator provided good protection from sand erosion. In addition, previous commercial operations in the actual conflict area (Iraq and Saudi Arabia) had provided experience and maintenance procedures to address operation in the sand and dust environment. However, during the initial conflict, information began to trickle back, indicating that engines were losing performance at a rapid rate. The cause of the rapid performance loss was unsubstantiated, and substantiating data was unavailable. As the conflict escalated it became evident that indeed the U.S. Army's fleet of helicopter turbine engines were experiencing severe distress. Older engines without inlet particle separators experienced rapid performance loss, loss of high speed surge margin, and in some cases, loss of low speed surge margin; i.e., starting, including hot and hung starts. After the establishment of in-country mini depot and maintenance activities, the symptoms and results of desert operation were easy to recognize. It became

immediately evident that the previous desert exercises and commercial operations had failed to predict the severity of Desert Shield/Storm conditions. The Bright Star exercises had been too brief, and the commercial operations were significantly less severe. Inspection of engine hardware from Desert Shield/Storm operations showed that the hardware exhibited all of the previous conditions discussed in this paper, possibly to an even greater degree. The only possible way to maintain operational readiness was to establish "new" desert operating procedures and techniques, and to expand existing engine operating and hardware deterioration limits. The U.S. Army created several Desert Combat Operation Technical Bulletins (TBs) for each engine which were all inclusive as to 1) special inspections and maintenance procedures, 2) special operating procedures/limits, and 3) combat and battle limits and repairs. Special engine health tests were instituted. The Health Indicator Test (HIT) checks were to be performed at altitude in as clean an atmosphere as possible in-flight in lieu of performing the procedure on the ground. The U.S. Army established an in-country performance recovery plan. At the mini depot level in or near the theater of operation, the following list of typical measures were taken in an attempt to maintain readiness:

- ♦ Engine temperature and speed limits expanded
- ♦ Allowable fuel and oil leakage from drains limits increased
- ♦ Time limits for light off and idle increased
- ♦ Allowable oil consumption limits increased
- ♦ Maximum oil pressure fluctuation limits increased
- ♦ Nicks, dings, dents, cracks - expanded limits
- ♦ Burns in turbine nozzles - expanded limits
- ♦ Coating loss - expanded limits
- ♦ RTV rubber allowed on some cold section air leaks and electrical harness connections

In addition, special cleaning procedures were identified and implemented. Overnight soaking of hot section hardware and use of brass rifle bore cleaning brushes were implemented to remove hot section deposits. Grit blasting of nozzle segments was allowed to clean solidified/glass deposits from turbine nozzle segments.



Stoning or blending of compressor blades was implemented and allowed to new so called "battlefield" limits in place of normal wear limits. Technical information, relative to the results of these activities, was reported back to U.S. Army personnel via contractor technical representatives and U.S. Army engineering personnel operating in-country. The U.S. Army's Component Improvement Program was invaluable, allowing for quick engineering tear down and analyses of returned engines and components. In many cases, testing was accomplished to verify expanded limits in order to maintain airworthiness.

Engine inlet barrier filters were tested in order to determine the viability as means to provide additional protection from sand ingestion. Several designs were tested and then put to use in the Desert Shield/Storm conflict. The results of using barrier filters as means to provide protection from sand ingestion is mixed. The main problem with using a barrier filter in a desert environment is that the filtration media requires frequent cleaning. If the filtration media is not frequently cleaned, inlet pressure losses increase with resulting losses in performance. There was one case where a helicopter equipped with a barrier filter lost approximately 30% SHP in the period of less than an hour.

## CONCLUSIONS

The main conclusion, relative to information gained from operation Desert Shield/Storm, is that the requirement to operate turbine engines in an environment like that of Southwest Asia, in typical helicopter missions, demands a comprehensive review of turbine engine design requirements and projected life cycle. If extended operation in a Southwest Asia environment is required, further improvements will be necessary in U.S. Army rotorcraft turbine engines. Technology and material improvements (to include coatings), and improved erosion resistance of critical turbomachinery components will be necessary. In addition, an overall reduction of the quantity of sand that is allowed to enter the engine must be considered. Significant reduction of sand quantities entering the engine may not be achievable by improving the separation efficiency of current integral particle separator concepts; however, some efficiency improvements should be attainable. Design trade offs made during development and qualification, relative to life cycle usage, must be recognized as having a significant effect in defining boundaries of operational

options. The U.S. Army engineering community has become convinced that for prolonged desert operation a "Kit" approach should be utilized. An airframe mounted engine air inlet particle separator should be developed and tailored to each rotorcraft configuration. It has not been universally agreed as to the type: i.e., barrier filter, or inertial designs. However, definitive design requirements to include easy removal, easy cleaning, and low performance impact (inlet pressure loss) can be defined. This approach would allow, as an example, an engine with an integral particle separator (IPS) to operate quite successfully in the majority of the world's environments. If another Desert Shield/Storm type scenario arose, the airframe mounted filter system could easily be installed. This is our best approach to successfully addressing the life cycle usage of a rotorcraft turbine engine.

## REFERENCES

- (1) Fonck, A.T. (July 1993)  
*Gas Turbine Engine Performance*, Performance Seminar, U.S. Army Aviation and Troop Command, St. Louis, MO
- (2) Przedpelski, Z.J. (November 1982)  
*The T700-GE-700 Engine Experience in Sand Environment*, American Helicopter Society, Washington, D.C.

## BIBLIOGRAPHY

- a. White, F.M., (1991)  
*Viscous Fluid Flow*, 2nd Ed., McGraw-Hill, NY
- b. Schlichting, H., (1979)  
*Boundary-Layer Theory*, 7th Ed., McGraw-Hill, NY
- c. Currie, I.G. (1974)  
*Fundamental Mechanics Of Fluids*, McGraw-Hill, NY

## FUTURE DIRECTIONS IN HELICOPTER ENGINE PROTECTION SYSTEM CONFIGURATION

Darrell L Mann  
Gordon D Wames  
Rolls-Royce plc  
POB3 Filton, Bristol, B512 7QE  
United Kingdom

### ABSTRACT

Recent events have highlighted the fact that none of the currently available turboshaft intake protection systems, whether they be the permanent fit IPS or mission specific vortex pack types, have an adequate sand/dust separation capability. Evidence has been amply provided by low engine lives, consequent support logistics problems and the necessity for development of short term emergency measures. The paper seeks to quantify the extent of the problem and define the solutions which will be required if a repeat of past experiences is to be avoided.

The paper describes the directions which particles separator technology must take in order to meet future requirements. A further important aspect of future directions is the drive for an increase in an engines ability to resist damage; the paper identifies those areas of the engine which are most prone to damage, comments on the need to strike the right balance between resistance and removal, and discusses the increasing value of sophisticated computer based design methodologies.

### INTRODUCTION

Recent operations by Western forces in the Middle East have done much to focus attention on the difficulties of operating high technology equipment in adverse environments. The US Army (Reference 1) and UK MoD (Reference 2) have both published information relating to the particular problems associated with the use of gas turbines.

The large majority of helicopters operating over the mainland had some form of engine protection equipment fitted - either as engine permanent fit or bolt-on, mission specific systems. Nearly all of these engine/protection system combinations offered the possibility of passing, or had already passed, one of the standard dust certification tests. Unfortunately these design-driving tests were shown to be a poor model of actual desert operations and stories of low engine life and logistic support problems came in floods during Desert Shield/Storm. A revised 'Desert operation' certification test has yet to emerge but several programmes to tackle the engine life issue have already been instigated on both sides of the Atlantic.

Despite the obvious dangers, operators have attempted to quantify the levels of improvement in performance to which designers should aspire. In the US the burden of improvement appears to have been placed firmly in the court of the engine protection equipment manufacturer. Target separation efficiency improvements of around an order of magnitude relative to today's best equipment give a broad indication of the seriousness of the problem. Within the UK, targets are more loosely defined but if we take Reference 2 data and assume that there is an aim to achieve desert engine lives comparable with normal operation levels, we should be looking to improvement factors of between 10 and 20 times. Broadly speaking then, an overall target for a 10x improvement in engine life/protection system capability relative to today's best practice would appear to have some credence. This paper will concentrate on means by which the 10x improvement may most prudently be achieved.

In the first instance the problem needs to be recognised as one which has two distinct solution routes; firstly keeping contaminants out of an engine and secondly increasing the engines ability to resist damage once those contaminants are allowed to enter. Factors affecting the pros and cons of each of the two routes are illustrated in Figure 1. Achieving the most appropriate mix of REMOVAL and RESISTANCE technologies is an often precarious balancing act.

The paper is split into five main sections. The first two sections examine each of the two strategies independently. In the case of REMOVAL systems, where the technology is relatively well understood, the way forward is seen to be comparatively straight forward to project. Apart from occasional component-specific improvement issues, the science of engine RESISTANCE is seen to be much less well understood - particularly in terms of overall engine considerations - and the paper is able to do little more than describe where we are and be rather more speculative about the future.

The third section presents an example of how we may combine current technologies most effectively to achieve a balanced solution to the 10x improvement problem. Section four describes some of the design methodologies which will help us to achieve our goals and the last

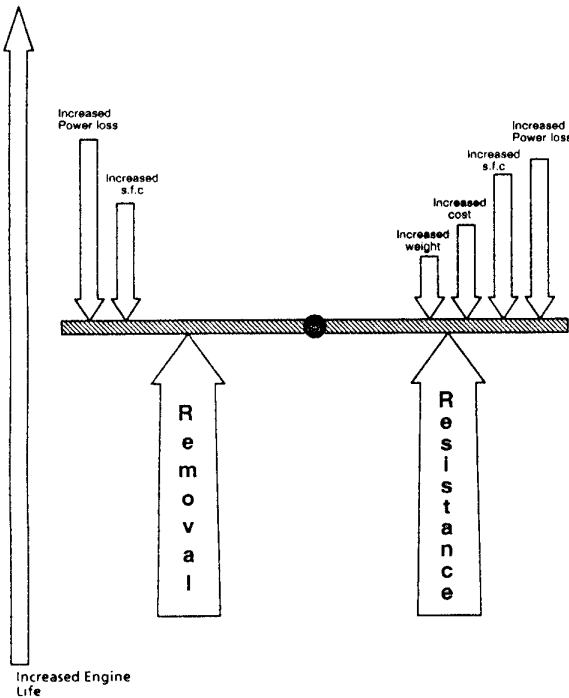


Figure 1 Removal v resistance

section looks to where the removal/resistance science should be heading in the longer term future.

#### REMOVAL

Attempts to comprehensively review the particle separator scene were presented in Reference 3. This section looks only at those separator types which are most likely to play a role in future air vehicles.

#### IPS DIRECTIONS & TRADE-OFFS

An integral engine mounted axisymmetric IPS (such as that fitted on the RTM322) offers a compact, light weight, low cost, virtually fit-and-forget solution to the requirement for a permanent fit engine inlet protection system.

The separation mechanism makes use of the inertia of the ingested contaminants, and is thus particularly effective against larger ( $>40\mu\text{m}$ ) particles. Smaller particles are inherently less susceptible to inertial separation, and hence current IPS designs are fundamentally unable to achieve the separation efficiencies consistent with a 10x increase in capability.

Improvements in separation efficiency may be achieved by intelligent management of the flowfield, so as to either increase the inertia of the smaller particles, or to make better use of the inertia they have (Figure 2). In addition other separation techniques applicable to smaller particles (for example aerodynamic centrifuging by means of swirl vanes) may be incorporated into the design.

Increasing small particle inertia may be achieved by increasing the gas velocity within the IPS. However, this implies a trade-off in terms of increased inlet total pressure loss. In order to minimise the impact on engine performance, it is envisaged that the scavenge system be powered by a variable speed fan offering a degree of controllability, with high (30%) scavenge rates being utilised only when required. Large particle bounce back problems associated with increased velocities may be controlled by the use of low restitution materials at judicious positions on the swept surfaces of the IPS.

Separation of smaller particles may also be achieved within the constraints of current IPS velocities by increasing flow curvature, for instance by reducing the radius of curvature of the hub surface. Such geometrical changes will tend to increase the propensity for air separation and hence cause dramatic increases in pressure loss. However, it is suggested that by use of carefully controlled passage area distributions - in particular seeking to resolve the almost inherent problem of separation on the IPS outer casing due to flow/area mismatches (Figure 2) - an affordable (ie low pressure loss) 'high work' device is feasible. The degree of curvature permissible will be derived from a judicious balance between particle separation benefits and increasing pressure loss.

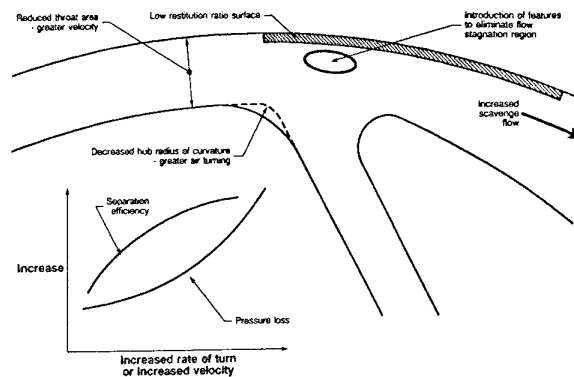


Figure 2 IPS directions

The possible use of active means of achieving high rates of air turning (for example boundary layer suction or blowing) is something which has been evaluated both experimentally and theoretically in the past. It has been concluded that the increased complexity, sensitivity to off-design conditions and maintainability issues will rule out the viable use of such features. In a similar vein, studies on the use of 'secondary scavenging' - locally scavenging areas of known particle concentration - offer little potential for contaminant removal enhancement and certainly not sufficiently to justify the additional cost, weight and complexity which result.

### VORTEX PACK DIRECTIONS & TRADE-OFFS

The vortex pack concept (Figure 3) has been extensively used as a sand/dust removal device in both the permanent fit and mission specific roles. Current packs are typically capable of around 90% installed efficiency (AC Coarse dust), while incurring a total pressure loss penalty of around 1-1.5%. Trends towards greater engine protection (higher separation efficiency), while at the same time reducing pack weight and volume, require improvements in both isolated tube, and installed pack performance.

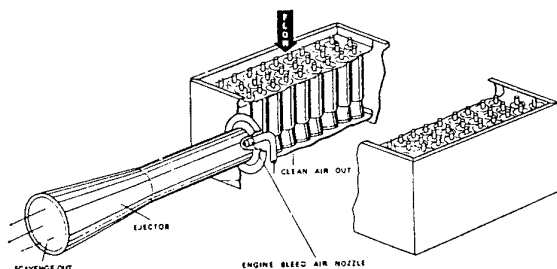


Figure 3 Typical Vortex Pack

Future vortex tube designs will feature both greater flow capacity and increased separation efficiency, while simultaneously maintaining scavenge flows and total pressure loss at current values.

Greater flow capacity at the current levels of total pressure loss is possible by improvements to the aerodynamic design of internal components (swirl vane design, splitter leading edge profile). Such designs are possible due to recent advances in CFD methods which allow the flowfield within existing tubes to be analysed in detail both on- and off-design, leading to the optimisation of internal geometry. Manufacturing advances such as stereolithography will allow rapid prototyping of candidate designs, enabling validation of both the design itself and the CFD methods.

CFD studies of vortex tube designs which include particle trajectory analysis have greatly increased our understanding of the mechanisms by which these devices perform their function. Previous analytical studies (Reference 4) have suggested that the primary mechanism of particle separation within a vortex tube is aerodynamic. The function of the swirl vanes was seen to be to introduce a swirling motion into the flow, hence generating a radial static pressure gradient which drives the particles outward. Detail design of the tube then centred around selecting a swirl vane to splitter gap and a splitter radius such that the majority of the particles passed into the scavenge flow.

However, CFD studies suggest that the primary means of separation for all but very small particles is in fact ballistic, and arises due to impacts of particles on the concave surfaces of the swirl vanes which impart both radial and circumferential accelerations on the particles. Particles rapidly reach the tube casing wall, and remain in the vicinity as a result of a series of oblique impacts (Figure 4). Separation efficiencies may therefore be improved by controlling the swirl vane shaping so as to optimise this process. Casing inner wall treatment (grooving, low restitution ratio materials) may also improve efficiency by reducing the threat of "bounce-back", particularly for particles with a significant circumferential or radial component to their entry velocities.

Installed pack efficiencies are typically several percentage points less than those obtained from an isolated tube test. This may be due to the idealised conditions used to test isolated tubes (axial flow etc), but is also in no small part due to the variation in scavenge flows which exist in tubes in differing parts of the pack. Empirical design rules have been developed to minimise these effects, but at the expense of increased volume and hence weight. A novel method of overcoming this problem might be to introduce several different grades of tube into each pack, each with a scavenge flow orifice sized to achieve the design tube scavenge flow given the prevalent local flow conditions. Designs of this form may be assisted by CFD calculations encompassing the tube layout within the pack. Studies suggest that packs comprising graded high flow capacity tubes might achieve significant volume and weight savings at only a small additional cost.

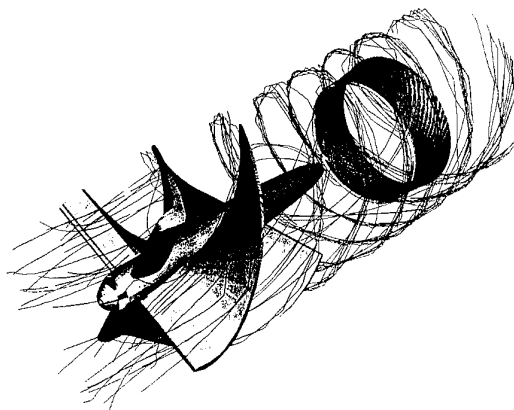


Figure 4 Example particle trajectories within a vortex tube

### BARRIER FILTER POSSIBILITIES

Barrier filters are well established within the air conditioning, industrial, and petrol/diesel engine fields as a means of achieving very high separation efficiencies for both large and small particles. However, applications to high airflow gas turbines have tended to demand difficult compromises in either bulk, installation loss, or separation efficiency, since increasing installation losses caused by progressive filter clogging lead to an unacceptable filter life for single stage filters of a realistic size. Typical of previous helicopter applications which experienced this problem are the UH-1D (low separation efficiency), and the Desert Storm Blackhawk (high installation loss).

Two generic solutions to this problem are being actively studied which may yield viable barrier filter designs for helicopter installations in the future.

The first method is to continuously clean the filter in order to extend operation life. This is particularly suited to pleated type filters which store particles on their surfaces, and are thus susceptible to cleaning by periodic reversals of the flow. Such systems are already in service in heavy automobile applications (M1A1 Tank), and trade-off studies suggest that permanent fit devices are a possibility for helicopter devices which will offer adequate protection, even in highly adverse environments.

The second design philosophy seeks to extend filter life by introducing some form of pre-cleaning device upstream of the filter. The barrier filter installation is constructed to allow removal, disposal, and replacement of the filter between missions. Judicious selection of the pre-cleaning device (for example vortex pack or offset inertial separator) can then provide adequate clean environment protection with the filter removed. The combination of offset inertial separator and removable barrier filter is particularly attractive in that the components are complementary with respect to their effectiveness against large and small particles, while at the same time allowing a simple and compact installation.

### DYNERTIAL SYSTEMS

Previous attempts at developing separator systems using rotating components to enhance separation efficiency have included work by MDI on a scale model of an axial flow device in the late 60's (Reference 5) and Pratt and Whitney adapted an impeller into a mixed flow configuration (Reference 6). Both devices produced poor separation performance (64 and 59% on AC Coarse dust respectively).

RR have investigated the physics of

sand/dust removal of this type of device using CFD including particle trajectory calculations. A single stage, self scavenging axial configuration was chosen featuring a stator positioned upstream of the rotor. This has the advantage of offering some FOD protection to the rotating machinery. It is noted that both earlier designs featured inlet guide vanes.

Results showed poor sand/dust separation. Little aerodynamic separation was achieved because the zero exit swirl design implied greater work at the tip of the blade compared to the root, and hence an adverse static pressure gradient. Ballistic separation was impaired by the small number of particle/surface collision incidents due to the guiding of the particles through the rotor blade passages by the pre-swirl vanes at velocities of the order of the blade speed.

From this study it is seen that it is not surprising that the earlier designs mentioned above yielded disappointing separation efficiency results. Improvements to aerodynamic separation could be improved by moving to a rotor/stator design.

With a downstream stator available to remove swirl, the rotor design could be optimised to generate a advantageous static pressure gradient. The rotor/stator gap would be controlled so as to allow sufficient time for centrifuged particles to be expelled into the scavenge stream. However, ballistic separation is the major effect on separation, and hence separation efficiencies may be most readily improved by increasing the particle/blade surface collision rate.

One way of achieving this is by increasing the free-path relative residence time of the particle within the blade passage. This implies a long chord blade with large numbers of blades moving at high speed, together with low axial flow velocity. Increased blade speed and reduced axial flow velocity have the additional advantage of directing the particles at the surface. This may also be achieved by decreasing blade stagger and/or increasing hade angle. Both of these features will impact on the aerodynamic design of the fan, which must operate under the constraints of providing sufficient pressure rise so as to be self scavenging, while providing an advantageous static pressure gradient. With the availability of CFD and particle tracking methods, it would appear that the dynertial system could be made into a potent separator whilst maintaining inherent qualities of compactness, low installation penalty and self-scavenging capability.

### RESISTANCE

Beyond a broad awareness that gas-turbines are vulnerable to damage from environmental contaminants, there has

been very little published work covering the scientific study of overall engine degradation effects. At least part of the reason for this is the considerable expense involved in destroying engines by passing controlled quantities of sand or dust into them. Usually the only data acquired in this field comes from one or two engine tests carried out as part of possible Mil Spec, or equivalent, certification testing.

Figure 5 collates data obtained for a variety of different helicopter gas turbine engines, either tested without intake protection equipment or corrected to remove the effects of permanently fitted equipment, to show power degradation rates following Mil C Spec sand ingestion testing. The picture highlights the significant fact that degradation appears to be independent of engine differences. Bearing in mind that the engines vary in power rating between 300 and 3000 shp and in vintage between 1955 - 1975, the trend seems even more remarkable.

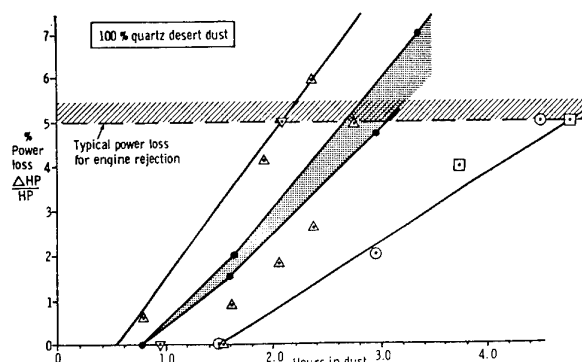


Figure 5 Different engine degradation performance

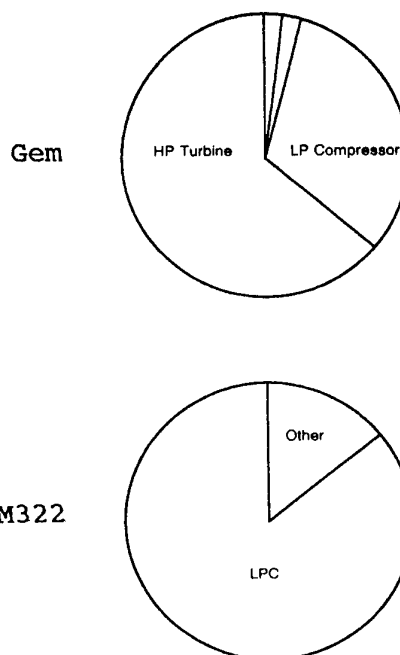
Probably the most comprehensive series of controlled engine degradation tests ever conducted were those carried out by Rolls-Royce with UK MoD support over a six year period between 1983 and 1989. During these tests, eight Gem engines were progressively destroyed by a number of different contaminants either as a bare engine or behind one of two standards of intake protection equipment. In each case, the engines were sufficiently instrumented to permit measurement of component efficiency changes and to acquire key contaminant diagnostic data.

Of the copious quantities of results obtained, three aspects in particular are of potent relevance to the determination of future directions in containment-resistant engine design:-

#### 1) SOURCES OF DEGRADATION

The Gem tests carried out under Mil Spec conditions were terminated after 25% of the maximum continuous power at a given power turbine entry temperature had been lost.

Taking data at the 15% power loss point, comparing it with later acquired RTM322 (no-IPS equivalent) results and examining the relative contributions from different components to the overall loss, the charts shown in Figure 6 were produced.



Both engines run at constant power turbine entry temperature max continuous power. AC Coarse dust ingested at 100mg/m<sup>3</sup> Figures show relative component contributions to overall 15% power loss

Figure 6 Gem v RTM322 power loss contributors

The two charts vividly highlight the fact that the two engines degrade in very different ways - an LP compressor contribution of over 80% on the RTM322 is far away from the Gem result, where LP compressor degradation was only a distant second largest source of loss.

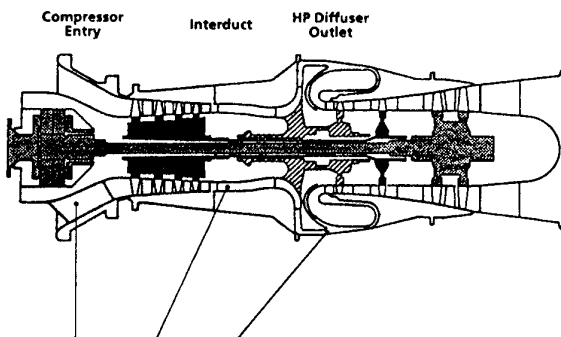
Other results further demonstrated that the equivalent chart for Gems with different standards of intake protection were again markedly different from one another. It may also be a surprise to learn that the HP turbine degradation was due primarily to erosion rather than the more obvious deposition effects often observed on other engines.

All in all, the results firmly indicate that to understand the engine degradation, or more specifically the design for increased resistance, problem is no simple task and that it will require a considerable understanding of the problem on a component by component as well as 'whole engine' basis.

## 2) PARTICLE SIZE EFFECTS

The above confirmation of the complexity of the engine resistance problem is further compounded by demonstrated particle size effects.

The Gem tests showed that the unprotected engine was as resistant to AC Coarse dust as it was Mil C Spec sand. Bearing in mind the relative size difference of the two contaminants and a knowledge that this trend is not consistent with either controlled sample plate erosion tests (Reference 7) which indicate that Mil Spec is several times more erosive or other engine experience, the result was a definite surprise. Diagnostic measurements to examine how the particles behaved within the engine helped to explain the phenomenon but in so doing raised a number of other issues.



230	5.5	5.5	Mil C Spec upstream IPS
114	39	8.8	Mil C Spec Upstream vortex pack
30	17	6.7	AC Coarse Upstream vortex pack

Mean particle sizes (microns)

Engine operating at maximum continuous power

Figure 7 Particle fragmentation through Gem

Figure 7 indicates mean particle size, as recorded by iso-kinetic sampling across the gas paths, at positions through the engine compression system. The most important point to note is that once the contaminant has passed through the LP compression system, its size is almost independent of the ingested size. By the time it has reached the HP exit, it is independent.

Coupled with the apparent relative vulnerability of the further downstream HP turbine system, this data helps to explain the apparent Mil C Spec/AC Coarse inconsistency. On the other hand it exacerbates the problem of how to design

resistance into the (cold section) of the engine in that each stage would appear to be subjected to a different array of particles, none of which is the one we started with at the inlet.

When it is further noted that the global database on these effects would appear to consist of no more than a handful of test points (Reference 7 again), it is easy to conclude that we are a long way from being able to scientifically address this problem.

## 3) HEALTH AND USAGE MONITORING

Except for the fact that it did rather more damage to the engine than a gradual decline to 25% power loss, what was initially seen as a rather inconvenient minor result has latterly taken on much more profound significance.

The concern centres around a desire, in parallel with the desire to increase engine lives when operating in adverse environments, to also be able to predict the future performance of the power-plant.

One of the Gem tests utilising AC Coarse dust suffered an unexpected sudden power loss of over 15% following mechanical failure of a number of impeller vanes - Figure 8.

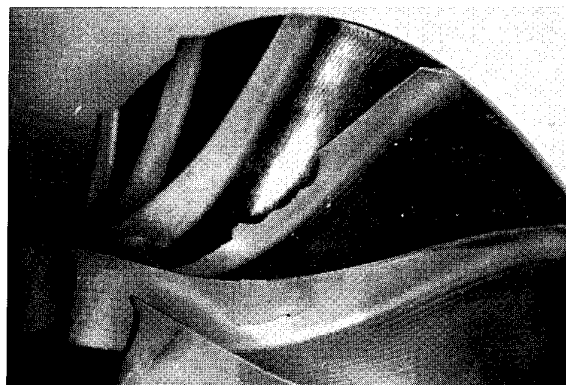


Figure 8 Gem Impeller following AC Coarse Dust Ingestion

This is of concern principally because up until the point of failure there had been virtually no (the HP compression system was contributing around a twentieth of the overall power loss) indication of imminent failure. As if to further complicate matters, this was the only one out of eight tests on which the failure occurred.

This phenomenon, if replicated elsewhere, presents a serious problem in terms of determining

whether an engine is safe to embark on another mission. Ensuring safe operation in such a case would necessitate the use of very generous safety margins.

In terms of HUMS systems it would suggest that we will have to be a deal cleverer than has thus far been the case in terms of being able to sense possibly very subtle changes in characteristics. With an increasing trend towards use of impellers in helicopter gas turbines, to not investigate the problem further could turn out to be very expensive.

The above discussions lead primarily to conclusions which state that the engine resistance problem is a very difficult one to solve. This is not to say that the problem is impossible and that we shouldn't be spending time and money to try and gain a scientific understanding of the subject - Rolls-Royce and others - including most latterly a UK MoD competitively bid Engine Environmental Protection programme - continue to address these longer term issues. The need to provide customers with solutions to current problems is also well recognised and, on a component level, much work has been done to realise reasonably effective erosion and deposition countermeasures for today's engines. The next section investigates a possible array of features which may be pragmatically brought together to provide a balance of removal and resistance to best suit operations in today's understanding of an adverse environment.

#### GETTING THE BALANCE RIGHT

Broadly speaking, the options available when considering means of improving an engine's ability to resist damage from contaminants today are:-

- 1) erosion resistant coatings
- 2) introduction of design features on hot components to reduce deposition tendencies.

In the case of 1), much research and demonstration work has been carried out and an array of scientifically understood coating systems have been derived. In the second case, although a number of design specific solutions have been developed, the scientific understanding of the problem is still in the realms of the dark ages.

Looking to the question of how a 10x improvement in life of a current state of the art turboshaft might be achieved, we first need to define the problem and a datum. Firstly, the type of operation and geography of the engine can have a profound influence on the methods which may be applied (for example fine versus coarse sands, hot and high versus icing,

and so on). For the purpose of this worked example, we will use a scenario which is now understood relatively well; that of operation in a coarse sand (Mil C Spec) desert. Definition of a datum engine is a little easier and the RTM322 with IPS fitted will be used.

Figure 6 illustrates that the LP compressor on the engine is most vulnerable to contaminant effects. This is not surprising when it is recognised that the compressor is designed with thin aerofoil sections and rotates with a high tip speed to achieve maximum aerodynamic efficiency. As a result of the high blade speeds it has been observed that the first rotor stage is an excellent particle fragmenter and that as a consequence damage to later stages is much reduced. Consequently, because incorporation of a finite thickness erosion coating degrades efficiency, only the first stage rotor need be coated. Much work has been done in this area and sophisticated hard/soft multi-layer coatings have been developed which offer appreciable protection against smaller (<100µm) particles. No coatings have been discovered which offer any significant benefit against large particles at high impact velocities. Specification of a 2µm titanium/titanium-nitride coating on the LP1 compressor stage might be estimated to offer a 5X life improvement to the overall LP compression system for smaller particles at a net cost of around ½ power loss.

Moving upstream of the compressor we now require a separator system which is a highly effective separator of large particles. Current IPS Mil C Spec efficiency is around 96% on RTM322. Observation of the Mil C Spec particle size spectrum suggests that 99% of the contaminant behaves ballistically. Modification of the IPS system towards a

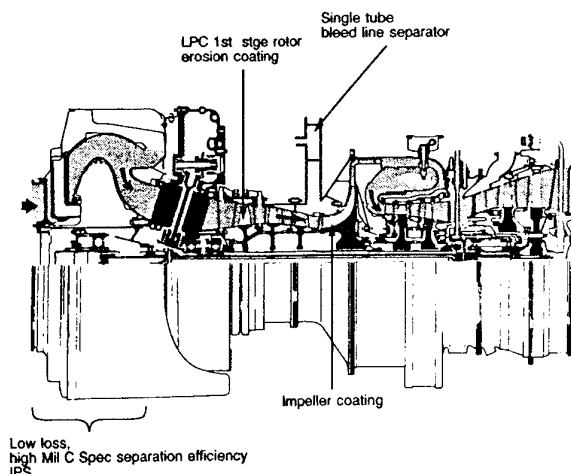


Figure 9 Pragmatic balance between removal and resistance



'one-bounce-and-out' wall profile philosophy and use of low restitution coatings should permit an efficiency of over 98% to be achieved at the same time as a small reduction in pressure loss to offset the LPC penalty.

Thus, these two mechanisms may be seen to have presented a potential 10x life improvement for net zero installation penalty.

Unfortunately the problem is not that simple because we do not understand the downstream effects of the resulting longer operation in the sand ingesting conditions. The uncertainties may cause us to erosion protect the impeller and employ means of keeping dust away from the engine hot components - primarily turbine cooling passages (although some non Rolls-Royce engines have also suffered turbine fir tree root contamination affecting dynamics) - for example by use of bleed off-take positions which are a known particle focus and then employing a single-tube vortex separator in the bleed-line.

The combined 'solutions' are illustrated in Figure 9.

It should finally be noted that whilst it has been hypothetically projected that a 10x life improvement may be obtained at zero performance penalty there will be a small mass and somewhat larger cost implication. Inclusion of these elements plus interaction effects into the example has been beyond the scope of both this paper and the overall knowledge base.

## TOOLS AND METHODS

### CFD & TRAJECTORY TOOLS & METHODS

Recent advances in the fields of computation fluid dynamics and particle trajectory tracking have provided RR with a design tool capable of assessing candidate particle separator designs both for installation loss and particle separation efficiency. This analytical method has the potential to save both time and cost in identifying the optimum separator design for a given operational requirement. Perhaps even more useful however, is the physical insight the model provides as to the physical mechanisms by which a whole spectrum of separation devices operate.

The method rests on three complementary developments in computation fluid dynamics, particle tracking physics, and flow visualisation techniques. For a particular separator geometry, a complete CFD solution (2D or 3D) of the flowfield is first generated for the prescribed operating conditions. This flowfield is then visualised via the RR Graffiti 3D CFD post-processor, which also provides the ideal framework for particle trajectory calculations. Figure 10 describes this process.

Several codes are available within the RR computational fluid dynamics system which solve the Reynolds averaged Navier Stokes equations in three dimensions, all of which are compatible with the trajectory calculations. Choice of code depends upon the flowfield to be modelled. In general, the flowfields

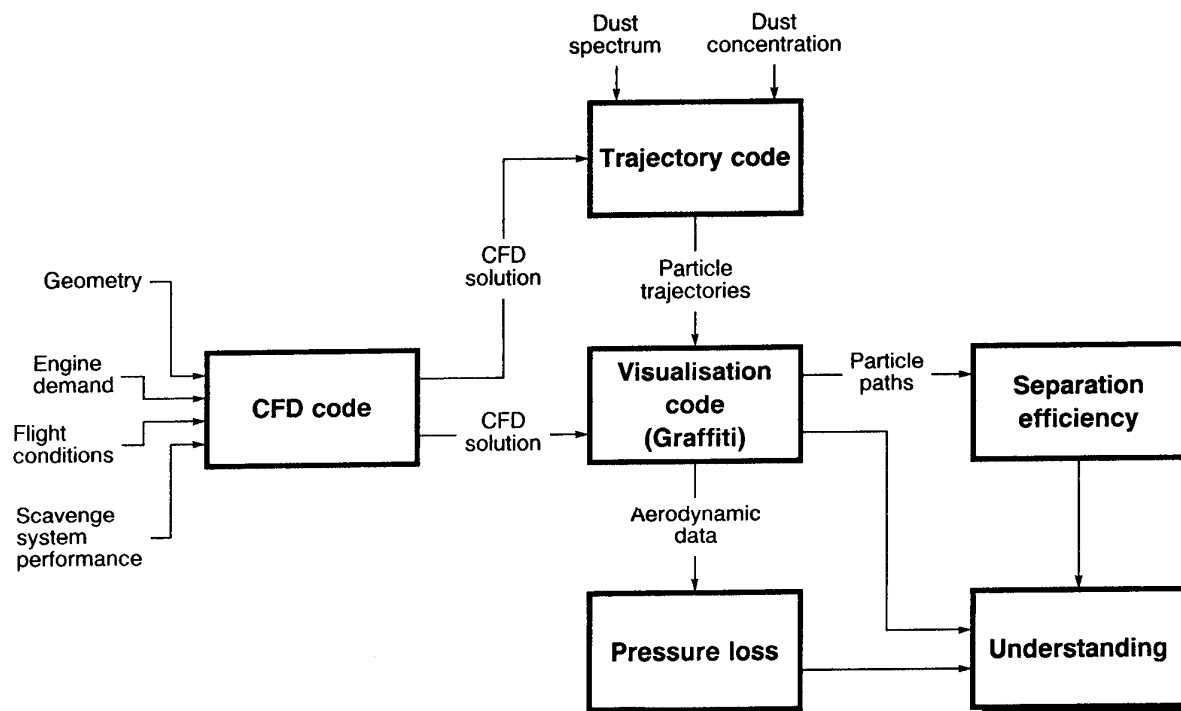


Figure 10 CFD & Trajectory Tools and Methods

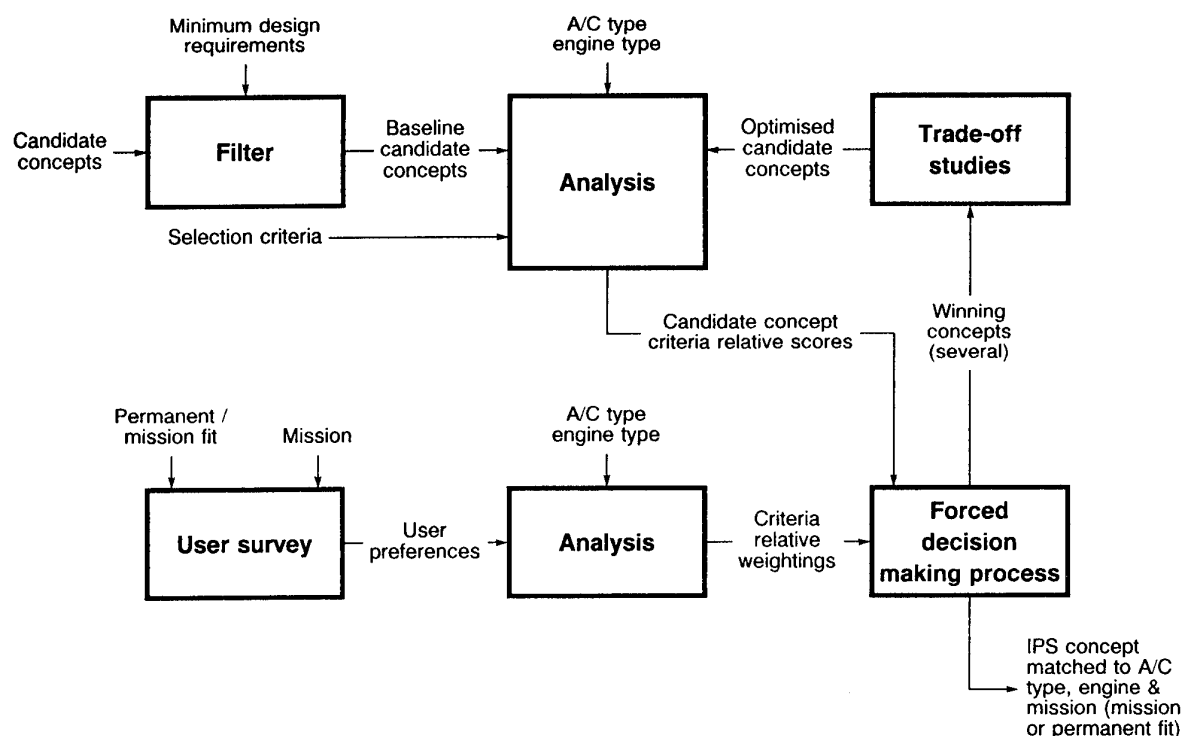


Figure 11 Formal Component Selection Methods

within particle separators are characterised by subsonic flow within a complex geometry. The RR MEFP code is well suited to this type of flow. The solution algorithm uses a two stage pressure correction iterative scheme to solve the system of equations. A structured rectangular grid is typically used although an embedded mesh capability is now available. Multiple inlets and exits are allowed, which is of particular advantage given the complex geometries involved. Turbulence modelling depends on the sophistication required; simple mixing length and k-ε models tend to be used.

The geometry of the candidate separator is simplified as a compromise between completeness and computational grid size. Grid density depends upon the use to which the solution is put. Pressure loss calculations require a body fitted mesh with extensive boundary layer coverage, while trajectory calculations typically require only a relatively coarse grid. An exception to this rule is the case of geometries which may exhibit separations leading to particle entraining recirculations.

The particle trajectory code calculates the motion of individual particles within a prescribed flowfield including the results of collisions with solid surfaces. The motion of the particle in free space is governed by an aerodynamic drag calculation under the assumption that individual particles do not influence the flowfield or the tracks of other particles. Particle bounce from

solid surfaces is calculated based on an extensive empirical database encompassing coefficient of restitution data for several materials.

It is important to realise at this point that the motion of particles within a separator device is essentially a stochastic process. For an individual particle, its exact point of entry into the device, initial velocity vector, size, and shape are all subject to statistical variation. In order to model the particle separation efficiency of a real device operating in a real environment, it is essential to model these features. Random particle bounce associated with real (non-spherical) particles has been investigated experimentally, and an empirical database developed.

#### FORMAL COMPONENT SELECTION METHODS

As discussed in Reference 3, there is no unique design which offers an optimum solution to all particle separation problems. Recognising this, and the multiplicity of concepts available, RR have developed a formalised procedure aimed at ranking candidate designs. This forced decision process is used as a framework for developing the optimum separator for a given installation/mission combination. The process is described schematically in Figure 11.

The initial process is the generation of baseline candidate concepts including radical alternative separation methods. Particular emphasis is paid to the

generation of multistage devices. A filtering process then removes those candidate designs which fail to meet any of a series of minimum design requirements.

The candidate designs are assessed against an extensive list of selection criteria including items which impact on cost, engine life improvement, performance, and maintainability. The relative weighting given to each criteria is based on in depth surveying of customer requirements. An expert panel is then used to score each of the candidate designs against the selection criteria for the aircraft and engine type in question.

The forced decision process then sums the scores for each weighted selection criterion for each candidate design in order assign a rank to each. The top ranking design is not immediately identified as the winner, rather a series of trade-off studies between key selection criteria are performed for several high ranking designs, the data from which is fed back into the assessment procedure. An iterative procedure is then used to identify a refined design, while minimising analysis effort on non-optimum solutions.

#### MISSION PROFILE V SAND CONCENTRATION DATA

In order to identify a particle separator best suited to a particular installation, it is necessary to accurately identify the environment in which it must operate. The air-borne contaminants to which an aircraft may be exposed is critically mission dependent, particularly in terms of terrain overflow, dust cloud characteristics encountered at a given altitude, and manoeuvres which alter dust concentrations (HOGGE).

Terrain has a strong influence on engine life, as Desert Storm operations have demonstrably proved. Of particular interest are dust density, particle size distribution, and chemical composition. RR have gathered data on dust (particularly sand) characteristics on a world wide basis.

For aircraft operating over dusty terrain, the environmental factor of most direct importance is the dust density/size distribution dependency on altitude. Fine sand clouds generated by dust storms have been encountered at altitudes of 10,000 ft, which are quite capable of causing severe glassing of hot end components during prolonged exposure.

The downwash associated with HOGGE manoeuvres and multiple pick-ups with rotors turning may generate a severe dust cloud around the aircraft (zero visibility dust concentrations have

often been encountered). Large particles capable of causing severe compressor blade erosion may be propelled to altitudes in excess of 40ft.

In assessing the potential damage to which the engine may be exposed, it is therefore necessary to calculate the time integrated sand ingestion data as a function of mission profile.

#### ENGINE LIFE MODELLING METHODS

Current engine life modelling methods concentrate on calculating life improvement factors (LIF). Although adequate predictions have been achieved in the past, several disadvantages have been identified; they are generally highly engine type specific, they are based around the assumption of a simple damage mechanism, they cannot predict engine life in absolute terms with any degree of accuracy, and they take no account of progressive changes in engine operation.

To alleviate these problems, future engine life models will be based on an extension to existing engine performance decks. The building blocks of such a model are modules representing individual engine components, including intake, compressors, combustor, turbines, exhaust system, and the internal air system.

Each module will model the damage mechanisms specific to that component by the most suitable means - in-service data, rig test, and CFD particle trajectory calculations will form an important basis to these models. Tracking of progressive changes in component efficiencies and flow capacities due to contaminant damage will allow engine rematching to be implicit in the calculations. In addition the changes in contaminant characteristics throughout the engine will be accounted, an example of which is the fragmentation of large particles on passing through the compressor.

By this means a truly generic model will be developed, allowing the prediction of absolute engine life within a wide range of adverse environments. Such a model will do much to alleviate the engine resistance issues described earlier.

#### SUMMARY OF FUTURE DIRECTIONS

Looking to the longer term future, the number one priority has to be the development and validation of sophisticated design methods which will permit scientific optimisation of engine protection systems. Such methods will be required to take due account of individual component characteristics, component interaction effects as described above and somehow incorporate cost and life issues.

Beyond this primary aim, there are technology requirements within each of the REMOVAL and RESISTANCE sides of the equation which appear to have value which ever way the models eventually suggest is the most appropriate direction:

REMOVAL	- *	higher larger particle separation efficiency
	*	fit and forget/all weather operation
	*	reduced installation losses
	*	reduced size/weight
	*	variable systems (eg scavenge boost fans)
	*	readily attachable auxiliary separation devices for mission specific operations in highly adverse environments.
	*	intelligent sensors
RESISTANCE	- *	integrated component/coating design
	*	impeller degradation sensing
	*	low loss bleed separators
	*	deposition resistant turbine systems
	*	better understanding of air system particle transport.

- 4) Daniels, T.C., 'Investigation of a Vortex Air Cleaner', The Engineer, March 1957
- 5) Dowdel, W.E., Toa, T.C., 'The Development Of A Powered Centrifugal Separator To Provide Air Inlet Protection Of A Gas Turbine Engine', 67-ENV-3, 1967.
- 6) McAnally, W.J., 'Investigation Of Feasibility Of Integral Gas Turbine Engine Solid Particle Inlet Separators,' 10-ENV-4.
- 7) Goodwin, J.E., Sage, W., Tilly, G.P., 'Study of Erosion By Solid Particles', The Institution of Mechanical Engineers Combustion Engines Group Proceedings, Volume 184 Part 1, 1969-70.
- 8) Mann, D.L., Humpherson, D.V., 'Helicopter Engine/Airframe Integration - The Way Ahead', paper presented at the 82nd Symposium of AGARD PEP, Montreal, October 1993.

#### ACKNOWLEDGEMENTS

The authors gratefully acknowledge the permission of Rolls-Royce plc to publish this paper. The views expressed however are those of the authors and are not necessarily held by the Company.

Some of the work outlined in the paper was carried out with the support of the UK MoD.

#### REFERENCES

- 1) Ray, J.A., 'Environmental Effects of Operations During Desert Shield/Desert Storm', Royal Aeronautical Society Conference on Helicopter Operations In Severe Environments, London, 4 June 1992.
- 2) Paramour, M.D., Jennings, P.G., 'Operational Requirements For Helicopter Engines For UK Services', paper presented at the 82nd Symposium of AGARD PEP, Montreal, October 1993.
- 3) Mann, D.L., Hobbs, J.R., '200 Year of Rolls-Royce Helicopter Engine Protection Experience', paper presented at the American Helicopter Society Propulsion Specialists' Meeting, Williamsburg, Virginia, October 25-28, 1993.

## QUESTIONS

### **W.B. de WOLF (Ne)**

- Q. It was interesting to note that the particle size decreases downstream through the engine due to fragmentation. How does the particle size affect the susceptibility for glazing of the combustion chamber liner and what is the experience on Rolls Royce engines in this respect?
- A. None of the eight Gem engine tests produced any deposition of particulates in the hot end, either combustion chamber or turbine components. The known low particle size at compressor exit suggests non-ballistic behaviour. This, coupled with the cooling configuration of the reverse-flow combustion chamber, may well be a contributory factor in the lack of any deposition. More generally, there have not been any other Rolls Royce engines exhibiting combustion chamber sand deposition effects. I know of no scientific data correlating particle size to propensity to glaze on hot components.

### **D. NAGY (Ca)**

- Q. Your particle size measurements showed a degree of independence between the initial size and the post axial pre-impeller size. Thus, if the particles are now of a very specific size, they might be specifically 'focussed' going in to the impeller, which may lead to very specific airfoil 'piercing' action. Consequently, if a single stage impeller is exposed to a broad range of inlet particles it may not experience such intense 'focussing'. How does single stage impeller erosion compare to the Gem experience?
- A. If you observe the Gem impeller vane leading edge erosion profile in Fig. 8, you will see that the dust concentration at inlet to the impeller is very even across 90% of the vane height. Impeller erosion patterns and particle trajectory prediction work have both demonstrated a focussing effect of particles within the inducer and initial radial turning regions of an impeller. The potential for larger particles at the inlet to a first stage impeller may detract from the focussing effect, but I suspect that fragmentation in the inducer will tend to act to reinforce the effect such that focussing will still occur.

# NAVY FOREIGN OBJECT DAMAGE AND ITS IMPACT ON FUTURE GAS TURBINE ENGINE LOW PRESSURE COMPRESSION SYSTEMS

Peter Charles DiMarco  
Naval Air Warfare Center  
Aircraft Division  
Trenton, NJ 08628-0176  
USA

## Abstract

Foreign Object Damage (FOD), Domestic Object Damage (DOD), bird ingestion, and ice ingestion are all necessary factors to be considered in the design of reliable and maintainable fan systems for future U.S. Navy aircraft applications. The high rate of fan damage reported in U.S. Navy engines and its impact on repair and maintenance requirements such as engine down time, level of repair, and number of spares have caused the Navy in recent years to scrutinize the requirements which must be met in order to design a more reliable and rugged yet highly maintainable fan system for future aircraft.

This paper reports the results of an investigation into the occurrences of Foreign Object Damage in several U.S. Navy aircraft, the repair approaches presently used by the U.S. Navy, and investigates the implications which these considerations present to the design of more damage tolerant fan systems. It further investigates the trade-offs in future turbomachinery design which balance gas turbine engine performance payoff against supportability and maintainability onboard ship.

## Introduction

U.S. Naval operations encompass a wide range of locations, aircraft types, and mission requirements.

The Navy and Marine Corps aircraft fleet consists of 25 different aircraft. Fighter/Attack aircraft account for forty-nine percent of the fleet, Patrol/Transport account for twenty percent and the remaining thirty percent is composed of helicopter, search and rescue, and tanker forces as shown in Table 1. The F/A-18 is the largest single fleet of aircraft comprising 20 percent of the total Navy and Marine Corps forces.

A typical Navy conventional carrier airwing is composed of 86 aircraft. Total shipboard flight hours for all Naval aircraft exceeded 2 million hours from 1980 through 1990 with an annual average in excess of 350 thousand hours. Again, the F404-GE-400 engine in the F/A-18 is the most significant contributor to total EFH with 200 thousand average engine flight hours per year.

Fighter/attack and patrol/transport aircraft comprise the top seventy percent of the fleet and provide the bulk of the annual operating hours. It was therefore determined that an investigation of FOD should involve a fighter/attack aircraft, specifically the F/A-18 operating the F404-GE-400 engine and a patrol transport aircraft.

In addition to being a significant player in Navy carrier

## NAVY/MARINE CORPS FLEET

Aircraft Type	1992 Fleet %
F-14	8.34
F/A-18	20.25
A-4, F-4	1.50
A-6	8.19
AV-8A/B	5.32
EA-6B	2.98
ES-3A	.48
E-2C	2.62
S-3A/B	3.51
P-3B/C	9.23
SH-60, SH-3	1.19
SH-2F	2.68
SH-60B	3.69
CH-53D/E	3.28
CH-53, CH-46	8.34
UH-1	6.1
SPEC OPS	2.77
RESCUE	.71
OV-10	1.55
KC-130	1.73
RH-53, MH53	1.34
E-6A	.45
C-2A	1.10
CARGO	2.74

Table 1.

forces, the F/A-18 is also the next aircraft in line for replacement. In order to improve the reliability and maintainability of the new system, while improving its performance it was important to investigate the major contributors to engine down time and investigate the trade-offs in design for performance versus design for maintainability.

The S-3 aircraft operating the TF34-GE-400 engine was selected as the other aircraft for this review. The S-3 represents a high-bypass turbofan engine which executes carrier operations and land-based operations with an almost even mix. It was initially thought that this aircraft's FOD rates might be significantly different since the S-3 operates

approximately 50% of its time from land-based locations.

### FOD History

A major contributor to engine down time in the U.S. Navy fleet has been FOD. The U.S. Navy as a whole has double the FOD rate of its U.S. Air Force counterpart. This is attributed to the fleet operating conditions, carrier flight deck, and wide range of locations of operations.

<b>F404-GE-400 FOREIGN OBJECT DAMAGE OCCURRENCES</b>		
Year	Flight Hours	Total FOD
1981	1341	2
1982	9303	39
1983	24581	24
1984	49515	107
1985	69192	155
1986	105718	109
1987	129547	240
1988	148609	255
1989	182915	209
1990	212244	233
1991	227139	159
<b>Total</b>	<b>1160105</b>	<b>1532</b>

Table 2.

Carrier based operations also play a significantly greater role in Naval Aviation than do land based operations. With restrictions on working space and available storage area, the number of spares and equipment must be kept to a minimum. This impacts the level of repairs which can be accomplished on-board the ship.

Tables 2 and 3 summarize the FOD history for the F404-GE-400 and the TF34-GE-400 engines over a ten year period. The tables itemize all FOD instances which documented a maintenance action to the engine. The required duration of maintenance action was based upon the extent of the damage, whether the repair could be accomplished on-wing, on the carrier, or required a return to the engine depot. In some instances a module could not be repaired because there might not have been hardware available. This requires a return to depot of the engine or module, and replacement of the engine. In some cases, when minor FOD was reported in the fan on turnaround inspections the compressor was not inspected until the engine was returned to depot for another repair.

Simply averaging the results in Table 2 shows that the F404-GE-400 engine has a FOD incident about every 757 engine flight hours (EFH). The results of Table 3 show that TF34-GE-400 has a similar incident every 868 EFH. These numbers do show some agreement and one would expect to see some variation in the rates based upon the different aircraft missions. There is perhaps some significance to the

### **TF34-GE-400 FOREIGN OBJECT DAMAGE OCCURRENCES**

Years	Flight Hours	FOD Total
1980	27347	20
1981	27329	26
1982	30008	19
1983	33295	22
1984	36377	18
1985	30522	10
1986	30038	16
1987	23299	11
1988	28792	7
1989	23082	10
1990	27499	12
<b>Total</b>	<b>317588</b>	<b>171</b>

Table 3.

amount of carrier operations the S-3 performs which could influence this aircraft's FOD rate. The aircraft and engine configuration could also influence the FOD rate of this engine.

However, since the F404-GE-400 engine had three and a half times the flight hours and almost nine times the instances of FOD as compared to the TF-34, further investigation was concentrated on the F404.

### F404-GE-400

Tables 4, 5, 6, and 7 summarize the FOD repairs for the F404-GE-400 engine at the three maintenance levels in the Navy.

Table 4 shows all the documented on-wing repairs which were able to be made. Column 1 documents unspecified FOD damage to the engine which was capable of being repaired. Column 2 itemizes fan module repairs which includes any damage to any component of the module. A subset of this column is column 3 which represents blade repairs to the modules in column 2. These repairs would include blending and clipping of the blades. This column is significant because it shows that with the current design limits and on-wing repair capabilities, there were only 21 documented blade repairs completed on the wing in a ten year period. Column 4, "unknown," represents removal and replacement of the engine which was not significantly documented and can represent FOD of any component, including any fan damage, which cannot be repaired on-wing. This column introduces some scatter into the data since it may, or may not, include replacements for fan damage. Table 4 does show that of the total FOD instances 235 were capable of being repaired without removal of the engine (total of columns 1, and 2). This is approximately 15% of the total FOD instances for this aircraft engine.

**F404-GE-400  
ON-WING FOD  
REPAIRS**

	1	2	3	4
	Eng	Fan	Fan	Unk
Year	Rep	Mod	Blad	Eng
	Rep	Rep	Rep	Rem
1981	0	0	0	0
1982	5	7	0	2
1983	2	2	1	1
1984	14	4	0	9
1985	22	14	5	10
1986	10	7	4	3
1987	27	3	0	22
1988	26	18	2	17
1989	24	12	3	12
1990	10	17	5	19
1991	7	4	1	4
Total	147	88	21	99

Table 4.

Table 5 documents the intermediate level fan and compressor module repairs. All work accomplished in this

**F404-GE-400  
INTERMEDIATE LEVEL FOD  
REPAIRS**

	1	2	3
	Eng	Fan	Cmp
Year	Rep	Mod	Mod
	Rep	Rep	Rep
1981	0	1	0
1982	7	15	0
1983	5	11	0
1984	29	19	4
1985	54	38	1
1986	38	47	1
1987	85	84	3
1988	61	111	2
1989	42	104	2
1990	43	102	1
1991	26	93	2
Total	390	625	16

Table 5.

table required engine removal from the aircraft before the repair was initiated. The total number of intermediate level repairs of 1031 represents over 65% of the total repairs required by the engine. The fan module repairs were further broken down to investigate the maintenance action required. This was done to determine the level of damage seen in service, the repair capability of the fleet, and the ruggedness and flexibility of the current fan design.

**F404-GE-400  
INTERMEDIATE LEVEL  
FAN FOD REPAIRS**

	Fan	Fan	Fan
	Blad	Blad	Blad
Year	Rep	Repl	Set
1981	0	0	0
1982	1	1	1-0-0
1983	1	1	4-0-0
1984	1	4	7-0-0
1985	0	14	59-7-0
1986	1	11	58-0-0
1987	4	17	91-2-7
1988	1	11	48-1-7
1989	2	20	96-68-100
1990	1	18	36-12-20
1991	0	16	40-2-25
Total	12	113	

Table 6.

Table 6 shows column 2 from Table 5 broken down into blade repair, blade replacement, and stage blade sets. The significance of Table 6 is that of the documented cases of fan module repair and replacement from Table 5, only roughly 20% were documented as blade repair or replacement. Of these documented blade repairs, all required replacement of at least 1 set of first stage fan blades. The remaining 80% of the repairs may have required more significant maintenance than simple blade repair/replacement.

Table 7 documents depot level engine repairs which represent the most significant FOD events to the engine. These incidences required maintenance actions that were beyond the capabilities of the carrier maintenance personnel and equipment, and therefore, required that the engine be shipped back to the F404 engine depot.

The important piece of information to be gained from Table 7 is that there were at least 171 significant FOD events which required the engine be pulled and returned to the depot.

#### Significance of the Results

On average, over the last ten years, every 757 Engine Flight Hours (EFH) an F404-GE-400 engine has documented a FOD related maintenance action. With a present annual average of approximately 200 thousand engine flight hours the F404-400 engines acquire about 3846 EFH per week. This



F404-GE-400 DEPOT LEVEL FOD REPAIRS			
Year	Eng Rep	Fan Mod Rep	Cmp Mod Rep
1981	1	0	0
1982	3	0	0
1983	2	1	0
1984	9	18	1
1985	6	9	1
1986	1	2	1
1987	7	8	1
1988	12	8	0
1989	3	12	1
1990	19	23	0
1991	4	21	1
Total	67	102	6

Table 7.

equates to 5 documented FOD incidences requiring some level of repair or replacement per week.

Of the total FOD incidences, including the unknowns, 23% can be corrected on wing and 67% can be corrected at the Intermediate Level. This leaves 10% which require depot level maintenance.

Of the on wing FOD incidences approximately 72% are associated with the Fan Module, but only 15% are fan blade repairs. Of the intermediate level FOD repairs, 67% of the total, roughly 60% are Fan Module related. And of that 60%, 20% involve some blade replacement. Even at the depot level of maintenance almost 60% of the repairs are done to the Fan Module. 54% of all FOD is documented in association with the fan module.

If we look specifically at those incidences that are associated with the fan blade, the total number of repairs and replacements is approximately 10 % of the total occurrences. However, since it is important to determine an actual fan FOD rate which is realistic, it is important to include the unknown data. If we distribute this data amongst the various repair and replacement requirements in relation to the present distribution it yields a fan FOD rate of once every 4735 hours, or not quite once a week. All of these repairs can presently be accomplished on the carrier.

It does appear that this fan design is not very tolerant to FOD. However, the design is easily maintainable at the lowest levels of repair. It would be a poor compromise to jeopardize this flexibility to achieve improved performance. Therefore, the goal of the next generation of Navy fan systems will be FOD tolerance, improved repairability, and improved performance.

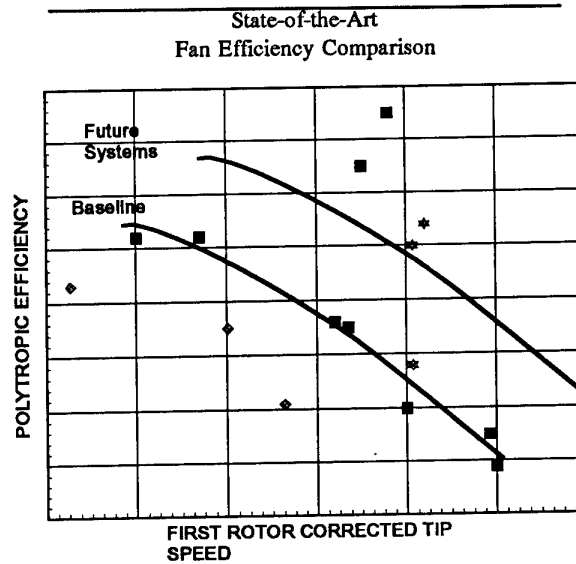


Figure 1

#### STATE-OF-OF-THE-ART PERFORMANCE

The state-of-the-art in fan system design is represented by the Low Aspect Ratio (LAR), swept, unshrouded, fan airfoil. This type of blading easily provides a 2% efficiency increase over the existing high aspect ratio, unswept, shrouded blades used presently. Figures 1 and 2 show the state-of-the-art in loading and efficiency in fan design. The polytropic efficiency increases shown are unattainable without the use of this advanced blading.

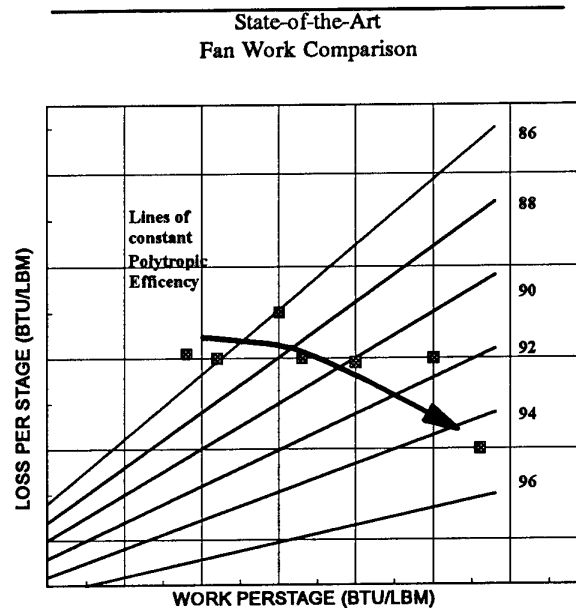


Figure 2

The loading increases shown in Figure 2 are a function of the increased chord of these blades. Figure 3 compares a highly swept LAR blade and a higher aspect ratio unswept blade. The loading and efficiency improvements associated with the LAR blade can clearly be seen as a function of the reduced separation zone on the airfoil and the weaker shock structure.

Mach Contour Comparison for  
State-of-the-Art and Existing Airfoils

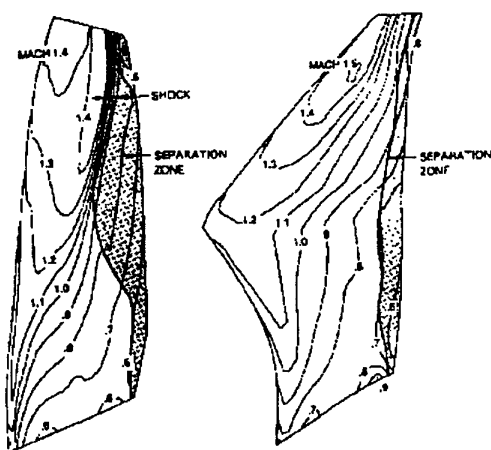


Figure 3

Blade Profiles for an Existing  
Airfoil and a FOD Tolerant Design

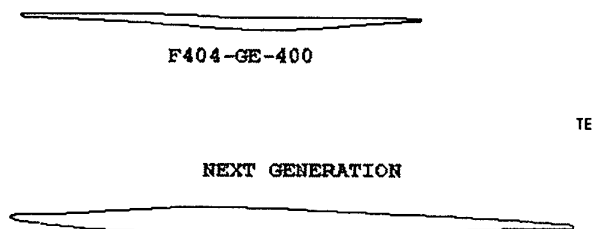


Figure 4

#### FOD TOUGHNESS

#### Blade Thickness Impacts

The U.S. Navy's next generation, fighter/attack aircraft needs to have improved birdstrike capability and FOD tolerance. Meeting these requirements has generated airfoils

with increased thickness profiles.

Figure 4 shows the blade profiles for a next generation fighter/attack fan system. The substantial increase in blade thickness to chord ratio and the 40% increase in chord length provides a significant increase in FOD tolerance. The increased leading edge thickness, increased chord and thicker profile reduce the blade stresses and allow for increased blade blending limits.

Blade Stress Profiles for a  
State-of-the-Art Fan Design

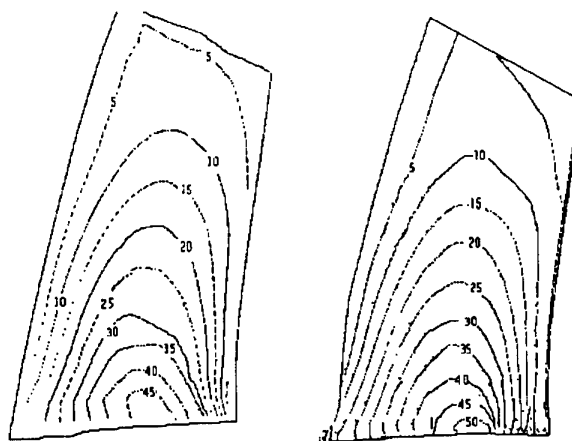


Figure 5

Figure 5 is an analysis of a LAR, moderately swept airfoil. The blade stress profiles allow for increased leading edge blendability. Even after the blending operation has been completed the stress profile has not changed appreciably and the blade may continue in service.

Figure 6 shows the increased leading edge blending limits associated with the reduced stresses in LAR blading.

Blade Blending Limits Comparison for an  
Existing Fan Design Versus a  
State-of-the-Art Fan Design

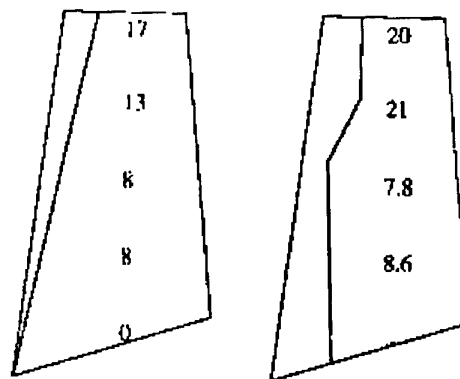


Figure 6

### Leading Edge Thickness

Leading edge thickness alone has also been shown to reduce the leading edge stresses and improve FOD tolerance. Figure 7 shows that a spanwise increases in leading edge thickness can directly improve the leading edge blending capability. A 50% increase in tip leading edge blendable depth was achieved across the span of the airfoil by non-uniformly increasing the leading edge thickness. This increase in tip leading edge blend capability will significantly reduce the blade replacement rates in service and provide increased on wing repair capability.

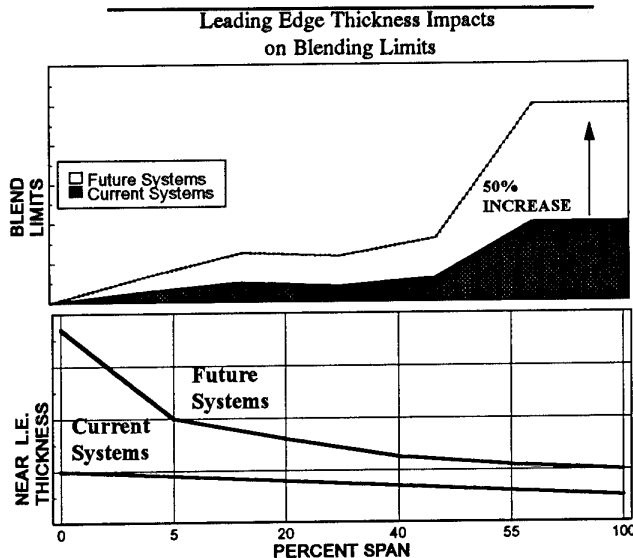


Figure 7

### PENALTIES

As expected there are penalties associated with the incorporation of these advanced airfoils into the fan. The weight and vibratory characteristics of advanced LAR airfoils have major impacts on these airfoils. Research and development programs continue to attempt to overcome these penalties in an effort to improve the overall performance of the fan component.

#### Weight

Weight is a major player in the design of an advanced fan incorporating these advanced blading concepts. The size and weight of the airfoil alone makes the design of an attachment scheme extremely difficult. One way to overcome this has been the development of the bladed disk (Blisk). By removing the blade attachment and bonding the blades directly to the disk, the amount of disk material may be reduced. The use of blisk construction in advanced systems has already been accepted by the U.S. Air Force in their next generation aircraft system. However, the implications of an attached airfoil in the first stage of the fan, and its possible impact on repair capability are still of concern to the U.S. Navy. The U.S. Navy would like to maintain the level of repair flexibility which is exhibited in the F404-GE-400. With this in mind, an investigation was begun into the design of new

types of blade attachment schemes for the first stage of the fan.

#### Advanced Attachment Study for a Next Generation Fan System

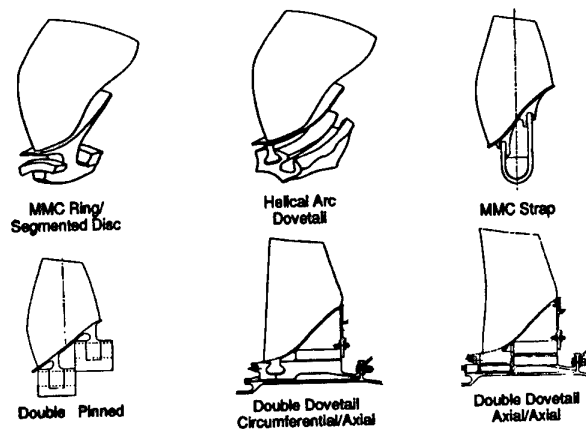


Figure 8

Figure 8 shows several of the attachment designs which were reviewed for feasibility. Most of the concepts have unacceptable stress levels in various locations of the attachment. However, the double axial dovetail did show some possibilities. This scheme was then further reviewed to determine its weight potential compared to a blisk configuration. Figure 9 shows the results of this investigation.

The analysis of the attachment showed that for a solid blade and solid bore configuration, using standard titanium materials, a replaceable scheme was so heavy as to negate the performance benefit of the LAR airfoils. The next approach was to reduce the blade weight. Hollow bladed airfoils have been manufactured with increasing success and were considered for incorporation into the first stage. The hollow design maintained substantial solid leading and trailing edge blade area to insure blendability.

The study showed that a hollow bladed airfoil could be designed with an attachment scheme with comparable weight to a blisk. Further investigation was done into weight reduction using advanced materials. The incorporation of metal matrix composites into the disk yielded even greater weight reduction and bore strength capability. More recent designs have even begun incorporating metal matrix composites into the blade skins to further reduce the blade and bore weights.

#### Vibration

The vibrational characteristics of the hollow, LAR blade also differs from the solid, high aspect ratio blade in service today. Because of its shape, the blade vibrational behavior is more like a flat plate than a beam. The bending modes experienced in the blade are characterized by complex chordwise mode shapes. These vibrational characteristics have exhibited themselves by frequent tip and corner cracking

### Weight Summary for and Advanced Military Fan Design

	Blisk	Replaceable Blades
Solid Blades with a Titanium Bore	340 lbs	
Hollow Blades with a Titanium Bore	220 lbs	290 lbs
Hollow Blades with a Titanium Metal Matrix Compopsite Bore	195 lbs	270 lbs

Figure 9

in many LAR fan system tests. Figure 10 gives an example of these mode shapes. An investigation into possible methods of damping these modes is underway.

### Low Aspect Ratio Blade Vibrational Modes

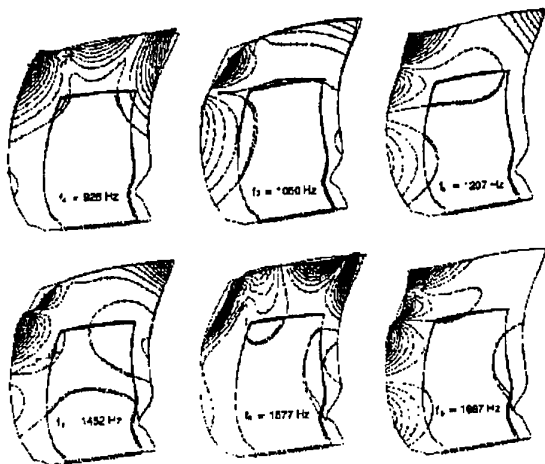


Figure 10

One possibility is the use of frictional dampers. The location of the damper, its shape, and the contact intensity are all variables which require trade-off to optimize the system for the mode shape of most importance.

Figure 11 shows that for a chordwise bending mode, the use of a vibrational damper can provide a 10-fold reduction in peak vibration response. This reduction is directly related to the blade high cycle fatigue capability, and therefore, overall blade life.

### Peak Vibrational Response for Damped and Undamped Low Aspect Ratio Hollow Fan Blades

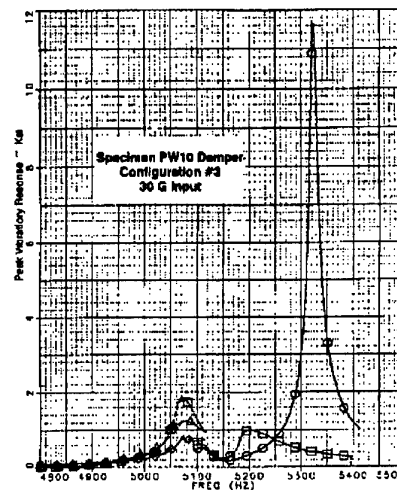


Figure 11

### TRADE-OFFS

In designing a next generation fighter/attack fan system the U.S. Navy wants to incorporate all of the best performance and maintainability aspects of these advanced airfoils. In addition, we want the repair flexibility of the F404-GE-400 and improved FOD tolerance.

The improvements in FOD tolerance associated with increases in leading edge radius do come at the expense of blade performance. Figure 12 shows that leading edge thickness penalties on efficiency can be correlated to fan operating condition. Tip relative mach number and stage pressure ratio both must be optimized with leading edge thickness to determine the efficiency impact. For a highly loaded, high-tip-speed fan, an extremely FOD tolerant design could impose to great an efficiency penalty. This would require a reconsideration of either the impact of FOD on the design or the loading level of the system.

Figure 13 outlines the optimization of a fan for sweep and leading edge radius impacts on efficiency and weight. Shifting the location of the maximum spanwise average sweep will impact the component weight by changing the blade and bore stresses. Increases in the leading edge radius, at a given design point, will impact the efficiency as seen previously. A small reduction in leading edge radius combined with a shift in spanwise sweep can yield a design with minimum weight and performance penalties.

The final design now has the performance advantages of swept, low aspect ratio blading and the FOD tolerance improvements of increased leading edge thickness.

The final trade-off to consider is the use of an attached blade or a blisk. The weight penalties associated with the attached fan may be offset by the replaceability considerations. However it is important to remember that the FOD tolerance of the LAR blade with a thicker leading edge, is significantly

### Leading Edge Thickness Effects

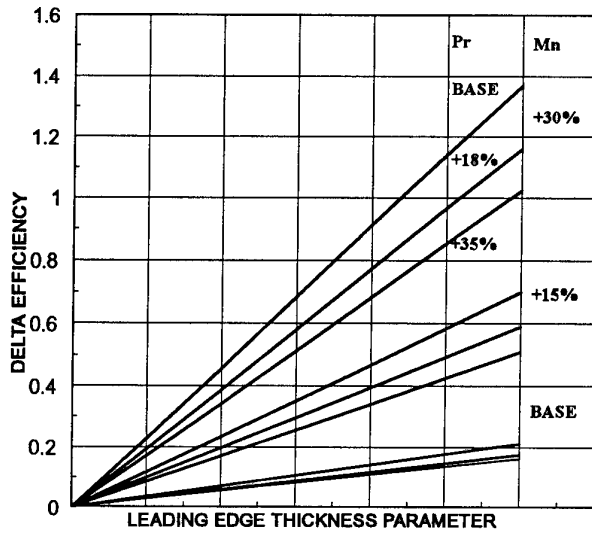


Figure 12

### CONCLUSIONS

The incidences of foreign object damage in the U.S. Navy make it clear that the next generation of aircraft must be designed with not only performance in mind, but also FOD tolerance. The unshrouded, swept, low aspect ratio blade presently represents the path to improved fan system performance. For the next generation of carrier based fighter/attack aircraft, performance requirements need to be balanced with repairability and damage tolerance. These requirements can be balanced and still provide a system with superior operating performance, FOD tolerance, and repairability.

### ACKNOWLEDGEMENTS

The author gratefully acknowledges the work of Paul Zimmerman in the acquisition of data associated with the foreign object damage encountered in the U.S. Navy fleet. Also, the efforts of General Electric and Pratt and Whitney who, under contract to the Navy and Air Force, are responsible for much of the state-of-the-art information presented.

### Sweep Optimization

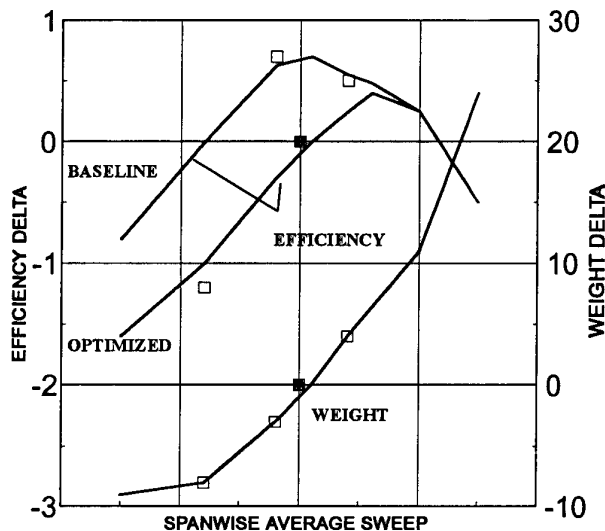


Figure 13

better than the existing blades in service.

The U.S. Air Force has decided that this improved FOD tolerance offsets the need for an attached first stage blade. The U.S. Navy has taken a more conservative approach and maintained an attached first stage design. The actual capability in military service of the blisk first stage fan remains to be validated, but with the improved FOD tolerance associated with the increased leading edge radius, it may prove itself worthy.

## QUESTIONS

### **W.B. de WOLF (Ne)**

Q. This morning we have heard about desert sand as an important source of FOD. What is the main cause of FOD for naval aircraft?

A. FOD are attributed to several causes. The varied operating conditions put the aircraft in danger of FOD from hail and ice, land based debris and, especially, birds. The carrier flight deck, which is constantly cleaned in an effort to minimize debris, is continually exposed to aircraft landings in excess of 8 gs; there is always debris created during these landings. Finally, in the confined spaces below the flight deck, there is always the possibility of FOD from lock-wire, nuts and bolts. With the many possible causes of FOD on the carrier, it is extremely difficult to determine the most significant factor. This, of course, excludes bird strikes, which are easily traced.

### **D. NAGY (Ca)**

Q. Can you comment on the relative manufacturing costs of solid, hollow, and hollow plus damper fan blades?

A. Using a large scale fan (200 - 250 lb/s flow), concentrating on a single stage, the relative manufacturing costs of a hollow airfoil vs a solid airfoil mounted on an integrally bonded rotor (blisk) are approximately 30% greater. The present machining and bonding techniques are labour intensive, requiring multiple bonds and machining operations. Advanced production techniques being investigated for hollow blades could reduce costs by reducing the number of bonding and machining processes. The addition of a blade damper does not significantly increase the cost of the aerofoil. It does, however, require that blade tolerances be relatively tight in order for the damper to be effective.

# SCANDINAVIAN AIRLINES SYSTEMS EXPERIENCE

on

## EROSION, CORROSION AND FOREIGN OBJECT

### DAMAGE EFFECTS ON GAS TURBINES

**P.Stokke**

Support Engineering Manager MD-80/DC-9

SAS

N-1330 Oslo Airport

Norway

#### 1. SUMMARY.

This article summarizes SAS' experience on engine FOD and compressor erosion.

It will mainly focus on type of damages, debris sources, modifications developed, development of maintenance and inspection methods to cope with the problem, revision of operational procedures etc.

In addition the added maintenance costs implied by FOD and erosion will be discussed, as also will be the special considerations to be used for cold winter operations.

#### 2. PREWORD.

This article is mainly prepared on SAS' experience, but much of the actions previously implemented have been addressed and more or less forced through by most of the major MD-80 operators around the world.

Accordingly, the improvements achieved so far should

be credited most of the major MD-80 operators in addition to the aircraft and engine manufacturer.

#### 3. INTRODUCTION.

Even though FOD and erosion has been known phenomena for years, the detrimental effects of FOD and erosion on gas turbine engines within the civil aviation industry had little or no attention until the early 1980's.

As a DC-9 operator since the late 1960's, it is obvious that the JT8D-engines have been subjected to blade erosion and FOD since the introduction. This has, however, never been highlighted as a major problem, mainly due to less focus on the maintenance costs within the airlines, but also due to less performance impact on older generation gas turbines. For SAS and many other operators of DC-9 and MD-80

aircraft, the interest of the FOD and erosion issue was rapidly increasing after the introduction of the MD-80 in the early to mid 1980's.

Two obvious contributors to the increased FOD-rate on the MD-80 were increased air flow and approximately 30% larger air inlet compared with the DC-9.

But this was not of course the only reasons. As a consequence of the continuous drive to performance improvements on new engines, new techniques were developed to further improve the engines gaspath flow dynamics. Optimized airfoils, seals, burners etc. combined with increasing focusing on weight reduction, lead to a optimum design that by nature will be much more vulnerable to foreign objects/debris.

What first lead us as an operator to look at the issue in the mid to late 1980's, was a chronic lack of spare engines caused by many unscheduled removals due to FOD. This was a fleetwide issue which finally brought both the aircraft and engine manufacturers attention to the problem. A joint venture between the manufacturers and some operators addressed the problem and lead to the development of some MD-80 specific modifications and JT8D-200 series in-service repairs described elsewhere in this article.

A even more serious experience, severely affecting flight safety, was the alarming increase in compressor blade fractures. In particular, blades in the fifth and seventh stage of the Low Pressure Compressor

(LPC) fractured due to fatigue, in most cases originating in impact damages (small nicks) from foreign objects. In many cases these blade fractures caused severe damage downstream the engine, thus requiring a complete engine overhaul.

What even more focused attention on the problem for the MD-80 with tail-mounted engines, was of course possible fatal consequences of uncontained blade fractures penetrating the fuselage

SAS has so far experienced three cases of fifth stage blade fracture, but all three cases has been contained and the engines operated without any complaints. The fractures were discovered during scheduled inspections of the compressor as downstream damages, and verified during the following shop teardowns.

As there's no possibility of inspecting the fifth stage blades on-wing, the only solution was to develop and install more stress-resistant blades which would preclude blade fractures. These new blades are now installed in all SAS's engines, and no blade fractures have been experienced after that. Regarding the seventh stage blade problems, this was addressed in three different directions, more detailed described elsewhere in this article:

- new compressor bleed system,
- new inspection requirements and limits, and finally
- new tooling enabling on-wing polishing of



blade nicks, cracks etc.

A rather new flight safety issue brought up as a result of FOD, is the stress-concentration nicks are causing on fan-blades. Just in the past 18 months the industry has experienced 4-5 fan-blade fractures, all originating in nicks/cracks caused by foreign objects. This has, due to the size and weight of the fan-blades, become a hot topic at the US Federal Aviation Authority (FAA). A liberated fan-blade may, if un-contained, cause considerable and fatal damages to the aircraft. Stress analysis conducted by the engine manufacturer has revealed that the stresses in the fan blades, in particular close to the blade root, has found to be in the upper region of what was predicted, thus even more pin-pointing the adverse effect of foreign object damages.

Since August 1987 all FODs on SAS MD-80 fleet has been specially coded, thus enabling later use of the data.

What easily can be seen (Fig. 1) is that despite all focusing on the problem and actions and modifications implemented, the rate of FOD is still increasing. From approx. 0,80 remarks per 1000 engine cycles in January 1989, to approx. 1,10 at date of writing. Some of the increase may however be a result of repeated highlighting the importance of proper FOD inspections, thus leading to increased detectability. If we on the other side look at engine removal rate per

1000 engine cycles, the rate is in average reduced by approx. 35% since the rates before 1990. This is mainly achieved by the new on-wing seventh stage polishing possibilities. This has dramatically helped all MD-80 operating airlines in improving the spare engine availability as fewer engines are being replaced, but the cost impact of FOD and erosion is anyway unacceptable high as described later in this article.

#### **4. MODIFICATIONS DEVELOPED/IMPLEMENTED.**

Based on above described studies and experiences, several anticipated improvements have been designed. Based on the aircraft geometry, with the main wheels located almost in line with the engine inlets' centerline, the aircraft manufacturer conducted a computer-simulated Debris Tracing Analysis mainly focusing on debris being lofted by the Main wheels. In addition real life evaluation of the air flow pattern from the thrust reversers using chalk was conducted. Furthermore, on site evaluation with a couple of the hardest affected operators, lead to the following modification releases in the 1988 to 1990 timeframe:

- repositioning (rotation) of the thrust reverser doors,
- improved main wheel water/debris deflector,
- blocking plate between flap and wing trailing edge,
- debris curtain on wing aft spar, and
- improved nose gear water deflector.

# SAS MD-80 - Foreign Object Damage

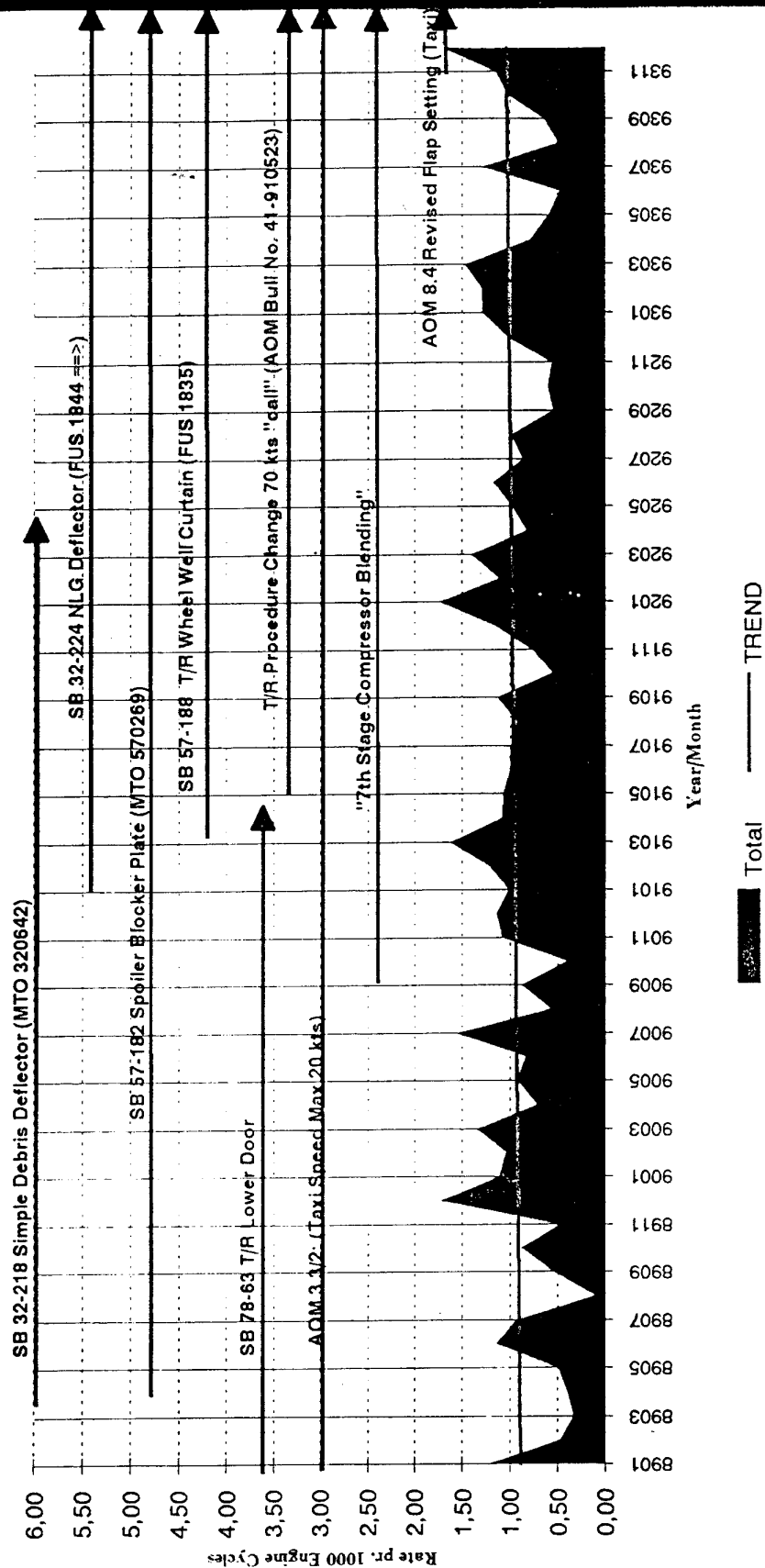


Fig.1 - MD-80 FOD Statistics

In addition the engine manufacturer as earlier mentioned introduced new improved fifth stage blades and a new sixth stage anti-flutter bleed system to reduce seventh stage blade flutter and -induced stresses.

SAS has implemented all modifications mentioned without seeing the anticipated improvements on the engine deterioration rate. The only aircraft modification that has proven to reduce the amount of debris entering the engines are the improved debris deflector on the main wheels, even though the improvement is marginal. The effect of rotating the thrust reversers a few degrees to get the blast directed away from the engine inlets, is very hard to measure. As earlier said, the FOD-rate is still increasing despite all modifications developed and incorporated.

Talking about the engine modifications, they have proven to significantly reduce the severity of the engine damages caused by FOD, as they more or less have eliminated the earlier experienced blade fractures. But despite this, the erosion effect of foreign objects still exists. And the conclusion of the fan-blade stress study is still not ready, and may give even further restrictions on in-service limitations for airliners.

## 5. INSPECTIONS.

From the introduction of the MD-80 aircraft there were no special instructions to look for FOD, it was more or less left to the airlines to

inspect based on own experience. As experience has been gathered, clearly made easier as many airlines has improved their reporting and documentation on findings, the requirements have naturally adjusted to some degree. It is however still very much up to each airline to define their own requirements.

The degree of required engine inspection of the engine after a verified FOD, in most cases triggered by a fan-blade impact, has however been adequately addressed. Both the requirements for when to inspect down-stream the compressor, and not least the allowable limits, has been adjusted to reflect the gained knowledge. This means more inspections, but as long as the problem with foreign objects entering the engines exists, there is no way but thorough inspections, and adequate actions, at intervals governed by the actual findings. Also, the requirements has been adjusted to reflect the modification status of the engine, thus giving some benefit to operators incorporating available improvements into their engines.

At all, it is better to inspect ten times without findings then permitting the chance of an airborne failure with unknown consequences.

## 6. IN-SERVICE REPAIRS.

As a result of the problems encountered in the late 1980's, with aircraft on the ground waiting for engines from the shop, there was a strong force to do something

with the engine removal rate due to FOD. Apparently there would be two solutions, eliminate foreign objects entering the engines or make the engines able to withstand the effects of foreign objects.

So far the engine manufacturer has been most successful in reaching their goals; in August of 1990, they introduced a new technique enabling continued in service operation of engines that till that time had to be removed for shop teardown and compressor refurbishment.

As a consequence of industry pressure to alleviate the problem, they developed a tool making airlines able to machining damaged seventh stage compressor blades for continued service. This tool is only possible to use on seventh stage blades through existing boroscope inspection ports. In principle this is an advanced boroscope with measuring capabilities, in addition to having the drive and control for the blade blending/polishing tool. In addition to the traditional front fan repairs using standard grinding equipment, this is the only available tools to keep the engines where they should be as long as possible.

## 7. PROCEDURAL CHANGES.

The operational procedures recommended from the manufacturer did not, and does still not, take necessary considerations to the aspect of preventing foreign objects from entering the engines. For the DC-9 and MD-80 series aircraft there are basically

two considerations to consider in this matter:

- taxi-speed, and
- thrust reverser usage limitations.

SAS did employ the following techniques at a early stage:

- taxi-speed should never exceed 20 knots, and
- thrust reversers should be fully faired (retracted) at 60 knots.

The first item is very difficult to monitor, and is by nature very much up to the crew. For an airliner depending on punctuality this may be a conflict, and the best and only way is by proper information to the flight crew. We do believe that well informed flight crews should, in combination with evaluation of existing field conditions, be able to make the necessary judgement in regard to acceptable taxi-speeds to minimize the FOD-risk.

Regarding thrust reverser usage, SAS' procedures for the approximately last four years has been to "call" for 70 knots i.e. throttles to be set at forward idle at this speed in normal operating conditions. This means that the thrust reversers will be in an faired at approx. 60 knots. This procedure is monitored through data obtained from the flight recorder, and we do know that we have met our goal in this matter; thrust reversers are only used at lower speeds when needed. The same procedure requires the captain to make a log-entry whenever reversers are used below 60 knots.

In November 1993 a new procedure was introduced on SAS' DC-9 and MD-80 aircraft

as a test in our effort to reduce FOD; all taxiing operations shall be conducted with flaps extended to landing configurations. This will narrow the "window" for objects thrown up by the main wheels possibility to reach the engine inlets. The couple of first months of this test was discouraging, but has lately started to meet our anticipation that this should help. The reason for the discouraging results in the start is most likely the early and colder than normal winter (more sanding of taxi- and runways). It is at this moment too early to draw any conclusion on the effect of this procedural change.

#### **8. SEASONAL VARIATIONS.**

From our statistics we have noticed the following seasonal variations:

- in the winter-season the FOD rate is worst up north (in Scandinavia), and
- in the summer time it seems like that the likelihood of FOD moves southward.

Talking about the winter-peaks up north, we do believe this is mainly caused by the use of sand on slippery run- and taxiways. This has to some degree been verified by debris-findings on affected airfields. The issue is regularly being addressed to the different airfield authorities, but so far with little or no success.

Regarding the FOD-rate increase on mid- and southern european airfields in the summer-period, the theory is that this is

caused by dryer environment and increased sand-transportation by the wind in this period of the year. This is however a theory which will have to be confirmed by real facts. This is one of the items we want to investigate in cooperation with one or more of the other MD-80 operators in Europe in the time to come.

#### **9. EROSION - SHOP TO SERVICE EXCHANGE.**

Based on previous years experience on blade leading edge erosion, SAS have for years operated with shorter compressor overhaul intervals than recommended by P&W. Additionally, we have had to implement a Hard Time Fan-blade replacement interval of 8000 operating hours, while the recommended interval from P&W is blade replacements to take place at shop visit for fan blades with more than 8000 hours accumulated since last overhaul.

As a consequence of the even higher attention brought up against the effects of fan-blade leading edge bluntness, SAS in cooperation with our engine overhaul partner initiated a special investigation program to survey and document the erosion effect related to operating hours and cycles. This program was initiated early in 1993, and is conducted by wax-molding of the fan blade leading edges at a predefined location. These moldings are cut in thin slices, and photographed in scale to get a uniform comparison data-package. This program is being accomplished on blades with operating hours from

1000 hours and up, and should over time give very good information about blade erosions progress on our engines.

These datas will also be used to determine if the erosion is governed by cycles rather than operating hours. To enhance this comparison, we are also collecting data from engines removed from charter-operated MD-80s as these engines in average has a cycle utilization vice operating hours at about one third of the rate for engines operating in normal SAS scheduled operations.

As it is too early to draw a firm conclusion based on the gathered data, we are unfortunately unable to present this as part of this article. However, gathered data has showed that our existing removal limits maybe are too high, as the fan blade erosion has caused blunt leading edges at as low as less than 6000 operating hours. As we all know, this adversely affects engine performance and also creates higher risks for blade failures as the stress on the blades dramatically increases when blade erosion changes the airfoils geometric data like this.

#### **10. FOD/ EROSIONS EFFECT ON MAINTENANCE COSTS.**

We have not been able to this date to clearly identify the added operational costs due to eroded engine compressors, mainly due to lack of resources. As an airline, we are naturally not staffed properly to make necessary studies like this. What we however have

documented, is the direct maintenance cost impacts related to actions necessitated by FOD. For the year of 1992, these costs related to engine FOD only accumulated additional aircraft maintenance costs at about US\$ 35 per operating hour. This meaning that engine FOD alone causes between 3 and 4% of the total aircraft maintenance costs per operating hour. Estimating a MD-80 fleet utilization of 140.000 hours per year, this adds up to just less than US\$ 5 mill. per year.

#### **11. WINTER OPERATIONS EXPERIENCE.**

Operations in rough winter climate several months a year is also a real challenge to SAS as an operator.

As earlier described, we do see an increase in the FOD-rate in Scandinavia in the winter period. Another FOD hazard is ice-formation, both on aircraft and engine inlets.

Regarding aircraft ice build-up, the industry has experienced this both as clear ice on the wings, ice build up on water & waste servicing panels due to leakage and ice build up on landing gears.

Wing clear ice build-up is a well known and thoroughly described phenomenon, and is a major threat to safe operation as ice may break loose just forward of the engines and ingested by the engines. Normally this causes soft damages (dents) on the fan-blades, and in severe cases this also may lead to engine surge(s). The only way to prevent this is by proper inspections, and

adequate deicing when needed.

Ice build-up on landing gears has been reported as a problem by many operators, and in severe cases this may also cause severe engine damage if ingested. In the same way as with wing ice, the only way to prevent this is by proper inspections and adequate de-icing.

Ice build-up around the water & waste servicing panels has been a major problem for years, and has caused many airborne ice-FOD's and following inflight shutdown. This problem is now more or less eliminated by installation of new improved ball-valves and improved caps. But as always, proper inspections and maintenance are required to verify proper valve and cap functionality. Identification of the source when an ice-FOD is experienced is very difficult, and the only possibility to preclude such events is by thorough and proper inspection and deicing when icing conditions exists.

Another hazard to safe engine operation on the MD-80 is snow ingestion. The High Power Surge(HPS) margin for the JT8D-200 series engines is decreased related to the basic JT8D-engines, and we have experienced several cases of HPS when snow has been ingested. This normally happens when snow on top of the fuselage slides down and back into the engine, and/or snow from the taxi- and runways are thrown up by the main wheels. In none of the cases this has caused any engine damage, but is an unwanted

experience with passengers onboard, and also requires thorough gas path inspections that will cease further aircraft operation for several hours.

Finally, engine inlet anti-ice capacity on the JT8D-series engines is questioned in in severe icing conditions (freezing fog). We have had several cases with ice build-up on fan-blades and inlet struts detected upon arrival in such conditions. We do believe that this happens due to extended operation at flight idle during approach. In these operating conditions we do believe that the flow and temperature of the 8th stage bleed air is insufficient to prevent ice build-up.

This issue has been discussed with both aircraft and engine manufacturer, but has been closed off as not being a flight safety issue. Engine testing has shown that that if the throttles are forwarded to get more thrust, the ice will shed off without causing engine damage, and that a momentarily engine vibration increase will be the only abnormal behaviour.

To conclude, the best and only way to prevent serious engine damage during winter operations is by proper inspections and adequate deicing/antiing.

— o —

## QUESTIONS

### **F. AYDINMAKINE (Tu)**

- Q. In your presentation you have mentioned 5th stage blade failure problem, which had considerable effect for FOD. Were these failures because of fatigue, design or material reasons?
- A. Combination of design and fatigue. The blades were not designed to take the stress-concentration caused by a foreign-object impact. This stress-concentration caused blade to fracture by HCF. The new blades have a maximum blade thickness of 0.101 inch compared with 0.056 inch on the old blades.

### **W.B. de WOLF (Ne)**

- Q. For MD-80, you mentioned a typical cost of \$30 per flight. How do the other aircraft types of your fleet compare? Also, apparently during thrust reverser operation for the MD-80, the danger of FOD occurs at a higher forward speed than the re-ingestion of the jet. Could you tell what is the cancellation speed on the MD-80 for jet flow re-ingestion?
- A. So far, we have no data available for other aircraft in the SAS fleet. Jet flow re-ingestion cancellation speed is, of course, dependent on how much reverse thrust is applied. Generally speaking, speeds above 45 - 50 knots would preclude re-ingestion.



# **MODERN TRANSPORT ENGINE EXPERIENCE WITH ENVIRONMENTAL INGESTION EFFECTS**

T.L. Alge  
J.T. Moehring

GE Aircraft Engines  
1 Neumann Way - Mail Drop J60  
Cincinnati, Ohio - USA 45215-6301

## **SUMMARY**

Modern propulsion engines have achieved a high level of reliability while manufacturers and users are always striving to further improve the safety record. The drive for safety in single-engine aircraft has resulted in safer multiple-engine applications. In modern turbofan-powered transports it is extremely unlikely that a failure intrinsic to an engine would initiate a sequence of events which could result in loss of capability for continued safe flight and landing. These rare events are limited to uncontained rotor disk fracture or uncontrolled fire.

Of greater concern today are the non-intrinsic, common-cause events which involve power loss of more than one engine. These are externally-inflicted occurrences such as ingestion events or common-cause maintenance events resulting in simultaneous loss of power on more than one engine. The most frequent are those ingestion events involving products of the flying environment - flocking birds, ice, volcanic ash and extreme inclement weather.

This environmental ingestion hazard viewed in overview is the primary subject of this paper. There is a body of knowledge on each of these subjects. Data from field operations and engine experience have provided guidelines for recognition of an occurrence and the proper action response. The primary precaution however remains - be aware, prevent, communicate and avoid.

## **1. INTRODUCTION**

Ingestion damage to aircraft turbine engines has presented a safety hazard and an economic cost problem since before the start of jet transport operations. However, with the advent of high bypass turbofan engines, with their larger intake capture area and long fan blades, the frequency of intake-ingested environmental products and foreign material has increased. It is roughly proportional to the inlet throat area.

This paper discusses, as an overview, the various threats presented by the operating environment of the modern transport powerplant. It reviews the hazards presented to the engines by the very skies in which we fly. The term environment as used here is beyond the sense of the natural environment or those hazards present in their natural form.

These include all forms of birds, volcanic ash clouds and products of weather such as natural icing and inclement conditions of extreme hail, slush and water ingestion rates. Also, although not a common-cause concern, the aircraft's self-inflicted products of frozen overboard leakage of on-board lavatory and galley drain fluids, commonly known as "blue ice", are included.

Although not generally an inflight hazard, a related area of concern involves the ingestion of man-made FOD material such as aircraft components, maintenance material, litter on runways and taxiways, as well as some land creatures. Although beyond the scope of this paper, these events are a well-known fact of life in today's operating environment of the turbine transport engine.

The hazard and repair costs posed by products occurring in the flying environment are common to air breathing turbine powerplants of all types and sizes, in varying degrees. Each of the environmental threats with each of the powerplant types and each aircraft installation could be the subject of a detailed discussion by itself. However, this paper focuses on the causes and effects of the following potential ingestion hazards:

- Birds
- Natural slab ice and lavatory blue ice
- Severe inclement weather precipitation
- Volcanic ash

## **Ingestion Threats**

The first and most important safety assessment is the likelihood of simultaneous loss of power on more than one engine. The threat of a volcanic ash encounter, severe inclement weather products and, in the case of aft fuselage mounted engines, ingestion of slab ice released from wings and fuselage can all degrade more than one engine simultaneously.

Most modern transport engines in service today were designed and certified to meet the ingestion of multiple birds (up to eight birds of 1-1/2 pounds each, per engine) at the most critical ingestion conditions of rpm and airspeed for takeoff. This requirement is intended to

represent typical flocking-bird encounters at airports. It must be recognized, however, that bird size records show there have been flocking-bird occurrences in nature that are beyond the previously certified capability of existing engine fleets.

The threat posed by flocking birds is the potential of a multiple-engine power loss caused by ingestion of an abnormally large number of birds in each engine. The ingestion of a single large bird during the period of takeoff and initial climb is also a certification requirement. Engines are designed and certified for safe-shutdown under these conditions, i.e., no uncontainment, no fire, separation from mounts, or loss of ability to shutdown. Such occurrences, although predominantly disabling only one engine on a transport aircraft, have resulted in runway departure accidents and off-airport landings of military fighter aircraft.

While engines are certified to regulatory standards which take into account severe environmental flying conditions, the possibility that an aircraft may encounter conditions posing an ingestion hazard more severe than certification standards does exist. Such exposures include extremely severe inclement weather and volcanic ash clouds as well as birds larger than the certification size and quantity.

#### Engine Example for Reference

As engines have become larger, the frequency of bird ingestion has also increased. This is primarily a result of the larger forward capture areas. High-bypass turbofan engines power today's large commercial transports because of their high thrust capabilities and low specific fuel consumption. Such engines produce over 60,000 pounds of thrust and typically have inlet capture areas of 5000 square inches or more. A schematic of the fan section of a typical high-bypass turbofan engine is shown in Figure 1.

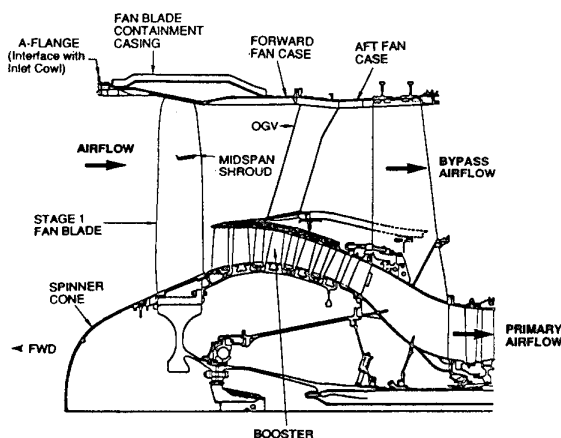


Figure 1 CF6 Fan Module Components

## 2. BIRD INGESTION

Engine birdstrikes have caused major accidents with fatalities on two large commercial transports and have resulted in at least 12 other accidents.

- The first major accident with fatalities in which bird-ingestion was a contributing factor occurred in October, 1960 when a Lockheed Electra ingested a large number of starlings and sustained partial power loss on three of its four engines. The aircraft crashed into Boston Harbor. This event led to the introduction of certification requirements for engines demonstrating flocking-bird ingestion capability.
- The second major accident with fatalities was in September of 1988 when a Boeing 737-200 ingested a large number of speckled pigeons in both engines during a takeoff at Bahar Dar, Ethiopia. During the air turnback, both engines lost power. While attempting an off-airport landing, the aircraft struck a river bank and burned.

Birds also represent a hazard to the aircraft structure. By way of historical note, a British Vickers Viscount transport crashed in the 1960's after impact by an 8-pound Whistling Swan that heavily damaged the aircraft's tail. This event led to the establishment of a design requirement to assure capability of continued safe flight and landing of an airplane after impact of an 8-pound bird on the empennage.

In the operational environment of CF6 and CFM56 commercial high-bypass engines, birdstrikes constitute 90 percent of all known ingestion events (Figure 2) and are a major ingestion concern. Atmospheric icing and ice slab ingestions accounted for 1.4 percent of all known ingestion events. Other known ingestion occurrences involved foreign objects (8.7 percent) including runway materials, ice on runways, land animals, and litter.

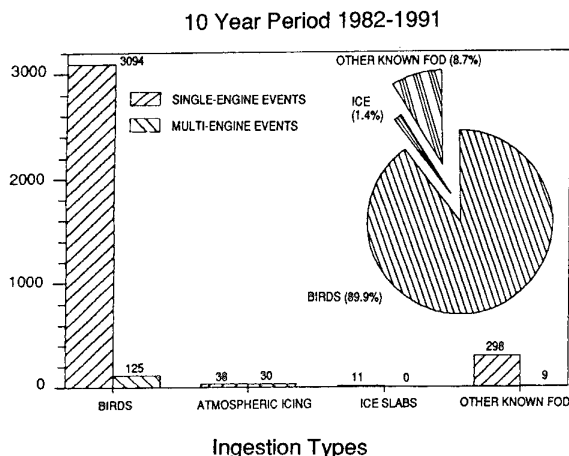


Figure 2 CF6 and CFM56 Ingestion Sources

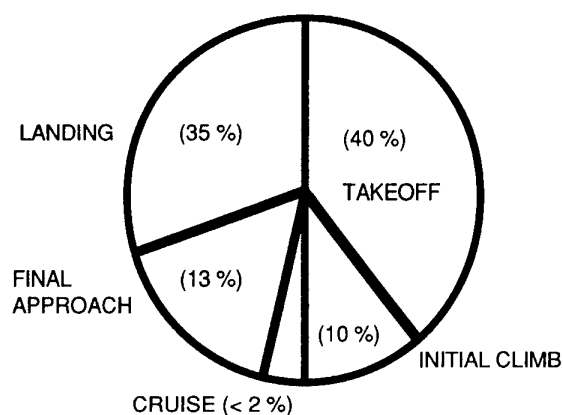


Figure 3 Percent of Birdstrikes by Flight Regime

The flight regime during which bird ingestion occurred is shown in Figure 3. Over 98 percent of all commercial CF6 and CFM engine birdstrikes occurred at or near airports during takeoff, climb, approach and landing. On or near airports is where the bird control efforts must be concentrated.

The frequency of migratory bird flock encounters in flight has been low. However, when such events occur, the results can be severe. An illustration of a Boeing 747 encounter with a flock of migrating Greater Canada Geese is shown in Figure 4. Special efforts are required to identify, warn against, and avoid these flocks during their migrations.

# Calgary Herald

WEDNESDAY, OCTOBER 28, 1992



Larry MacDougal, Calgary Herald

**REPAIRS NEEDED:** A Royal Dutch Airlines KLM 747 was grounded in Calgary Tuesday after several Canada geese were sucked into one of the engines. The flight which originated in Amsterdam, was approaching the airport around 4 p.m. Monday when it flew into the flock of geese

Figure 4 Boeing 747 Encounter with a Flock of Greater Canada Geese Just Prior to Bird Ingestion in the Outboard Left Wing Engine

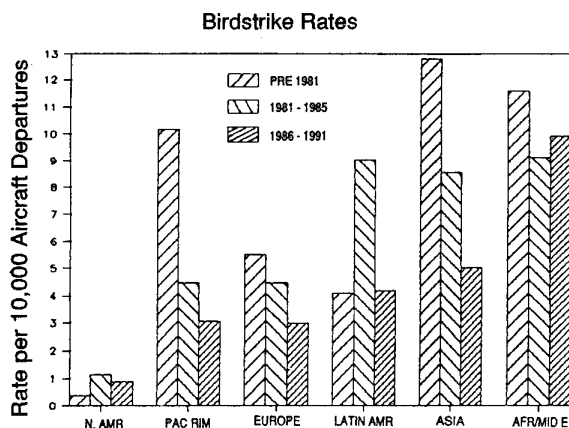


Figure 5 Birdstrike Trends by Geographic Region

Bird ingestion is a worldwide threat and some worldwide geographic regions have a higher bird threat than others. This is illustrated in Figure 5 which shows the CF6 engine birdstrike rates for six selected regions covering three time periods. This figure also shows that most geographic regions have shown some improvement since 1986. This improvement reflects greater awareness of the need for bird avoidance and reductions in the number of birds around airports.

Although the recent trend toward a lower birdstrike rate is encouraging, the frequency of occurrences is still too high. More aggressive bird control programs need to be implemented at selected worldwide airports.

The presence of a flock of birds on or near an active airport runway signals that improvements in the bird control program are required at that airport. It may also indicate that there are adverse contributing factors just beyond the premises of the airport, such as bird sanctuaries, crops, garbage landfills, abattoirs (slaughterhouses), or unsanitary local conditions. In these cases, the need for corrective actions by other regulatory agencies, working with airport authorities and local governments, is required.

The consequences of birdstrikes need to be communicated on a regular basis to airport managers and their airport bird control patrols. Through continued training and communications, flight crews and control tower personnel must be kept aware of the possible consequences of flocking bird encounters. The message is: Operations through flocking bird conditions must be avoided!

The use of posters, such as shown in Figure 6 is encouraged as a useful bird control measure. Such posters can serve as a means to remind flight crews, control tower personnel, and bird control teams of the hazards posed by birds around the airports.

Engine manufacturers generally are not involved in, and do not have directly

useful experience regarding, the control of birds and FOD at airports. The authorities at each airport must assume the responsibility to assure that their airport bird control programs are effective, remain active, and that this message is widely disseminated and applied.

The challenge is to identify bird hazards before aircraft take off or land. Identification of such hazards made after the accident come too late. Airport bird hazard control techniques alone are not adequate; they must be accompanied by diligent and effective communications between Flight Crews and Air Traffic Control.



### Airport Bird Control - An On-Going Task

Figure 6 Control Flocking Birds Through Design and Maintenance

#### 3. NATURAL ICE SLABS AND LAVATORY BLUE ICE

Loss of lift due to ice buildup upon aircraft surfaces while an aircraft is parked during a winter storm is a hazard which has been aggressively addressed. Strict disciplines governing preflight wing de-icing and operating procedures have been imposed.

For engines mounted aft on the fuselage, the hazard of multiple-engine power loss caused by the ingestion damage due to slab ice is now well known. On December 27, 1991, an MD-81 had a dual engine power loss after takeoff. This resulted in an emergency off-airport landing resulting in serious injuries and

destruction of the aircraft. Flameout of both engines was caused by ingestion of ice released from the aircraft surfaces forward of the engine intakes.

During winter storms while an aircraft is parked, ice slabs can form in the engine intakes and, if not removed, can be ingested in flight or during ground operations. Although CF6 and CFMI engine experience has involved only single-engine ingestion damage, slab ice in the inlets has the potential for causing a multiple-engine power loss.

When operating in natural icing conditions, ice can build up on, and be shed from, engine flowpath surfaces. As reported by flight crews, ice shedding is accompanied by an audible noise. Ice accretion on engine flowpath surfaces and subsequent shedding has also caused unbalance and increased engine vibration. Generally, there is little or no resultant damage or adverse consequence when prescribed operating procedures are followed during icing conditions.

Extended aircraft operations in icing conditions during a holding pattern or long descent, when the ambient temperatures and engine speeds are low, also have the potential for buildup of ice in the core engine flowpath causing local blockage, airflow distortion, and resultant thrust loss. CF6 experience includes a Boeing 747 four-engine flameout during low idle power descent after which the engines were subsequently restarted. Operation with higher descent idle rpm and prescribed operating procedures were implemented to solve this problem.

Ice can form on the inlet nacelle lip during operations in icing conditions when the anti-icing air is not turned on early enough during an icing exposure.

Aircraft-produced blue ice presents an ingestion problem of less serious but of significant cost impact in terms of engine repair and disruption to flight operations. When there is a malfunction of the overboard drain shutoff systems allowing escape of fluids from lavatory or galley drains, the formation and inflight release of large chunks of frozen waste products has resulted in damage to both wing and aft mounted engines, the horizontal stabilizer, and objects on the ground.

Because of the location of the lavatory drain ports on the aircraft and the trajectories of the liberated blue ice accumulations, blue ice is a problem which has been limited to a single engine per aircraft.

This is a maintenance inspection and system design problem which has been associated with specific aircraft models. The aircraft manufacturers have taken steps to correct the lavatory drain leakage problem through frequent FAA mandated maintenance inspection programs and the introduction of modified drain system hardware.

#### 4. SEVERE INCLEMENT WEATHER PRECIPITATION

Experience has shown that conditions of extremely severe inclement weather can result in a power loss on more than one engine. Events of partial or complete power loss have included flameouts and engine speed rollback. Rollback in engine speed occurs when the demand for heat to counteract the cooling effects of the incoming water or hail exceeds the available thermal energy from the fuel. Flameout occurs when the flowpath water-to-air ratio exceeds the level corresponding to the combustor flameout stability limit.

There has been much progress during the last several years in understanding severe inclement ingestion-caused flameout and increasing the flameout margin of turbofan engines. Investigation of operations in inclement weather has been an area of much work during the last several years and has been addressed on an industry-wide basis, with sharing of data and experience through the Inclement Weather Committee of the AIA (Aerospace Industries Association).

The AIA Inclement Weather Committee was formed in 1988 and initiated a study of world-wide weather statistics associated with power loss events. This led the AIA to develop a proposed definition for a severe inclement weather environment as shown in Figure 7. This definition of the rain and hail natural threats in terms of liquid hail or water content and altitude represents conditions more severe than the current requirements (FAR 33.77c) to which engines in service have been certified.

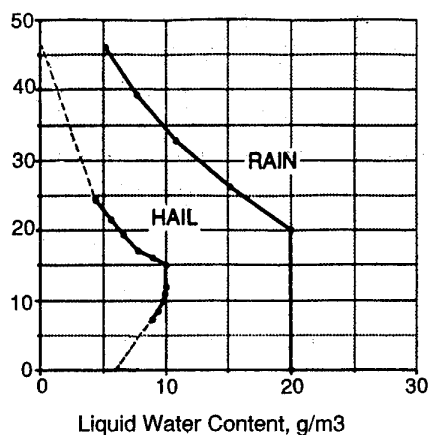


Figure 7 AIA Proposed Definition of Rain and Hail Natural Threats.  
(NOTE: Dashed lines depict extrapolation of data.)

In the ten-year period between 1980 and 1989 (Figure 8), industry experience included 48 power loss events on commercial transports. Fourteen of these involved multiple engines as shown in Figure 9. Most of these events occurred

during descent in precipitation. This is explained by the fact that during descent with the engines operating at low rpm the inlet air spillage effect results in an increased water-to-air ratio at the engine face.

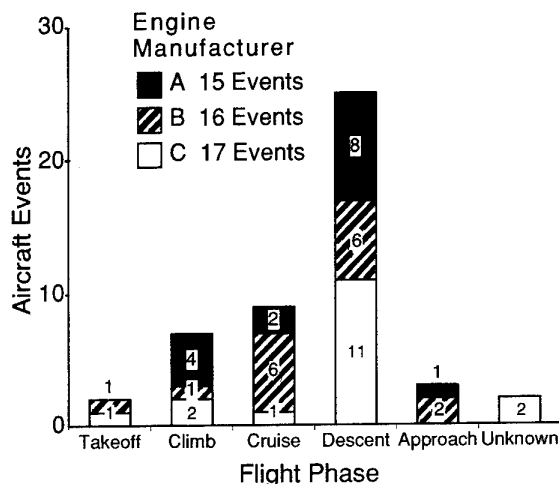


Figure 8 Inclement Weather In-Flight Shutdown Events

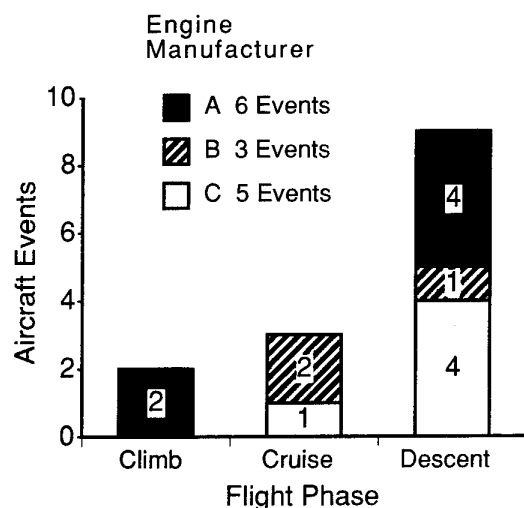


Figure 9 Multiple Engine Inclement Weather In-Flight Shutdown Events

The case histories for the following two events which occurred in 1987 and 1988 on Boeing 737-300 aircraft powered by CFM56-3 engines illustrate the potential for dual engine flameout during descent in severe inclement weather and provide an insight as to the causes and effects.

#### First Event

A Boeing 737-300 equipped with CFM56-3 engines experienced a dual engine flameout in heavy rain and hail while descending into Salonika Greece in

August 1987. The flight recorder showed that both engines had flamed out simultaneously at 8900 feet, 289 KIAS, 15°C TAT, at idle descent power. Both engines were restarted without difficulty, and the aircraft descended and landed normally.

Flight reports showed heavy rain and hail, with moderate turbulence and with lightning in the vicinity. The aircraft radar was painting red cells in the vicinity. The aircraft was operating in the yellow zone. The crew reported skirting the radar red zone but not well clear of it. Based on the crew report, the hail shower was one of the most violent ever encountered by the captain, and precipitation was heavy.

Ground inspection revealed that the airplane horizontal stabilizer had been dented from numerous large diameter hailstones. The anti-collision light was broken, and the paint had been removed from the radome. There was no damage to the wing leading edges and no damage to the engines. Engine and related system checks conducted on the ground with the airplane showed all aircraft and engine systems to be normal.

#### Second Event

A Boeing 737-300 equipped with CFM56-3 engines experienced a dual engine flameout while in descent from 35,000 feet into New Orleans in May 1988. Icing conditions were detected and cowl anti-ice was on. The crew reported severe rain and hail and lightning, with severe turbulence and high aircraft vibrations at 16,500 feet, 267 knots, -29°C TAT.

The aircraft radar was painting red cells in the vicinity. The aircraft was operating in the yellow zone. The crew reported light icing until about 30 seconds before the power loss. The crew reported a sudden encounter with heavy hail, heavy rain, with moderate turbulence and with lightning in the vicinity. The weather service reported that the storm system included level 5 and 6 activity (level 6 is the highest classification).

The crew was unable to restore power on either engine. The aircraft landed safely on a grass levee near the intercoastal waterway. There was no landing damage and no injuries.

There were hail impact dents in the leading edge of the horizontal stabilizer, and the paint had been removed from the radome. The radome was dimpled from hail stones impact, the largest being about 1.5 inches in diameter. There was no hail damage to the wing leading edges and no hail damage to the engines.

This was a new aircraft that had entered service only 11 days earlier. System checks conducted on the ground showed the engine and aircraft systems to be normal. Engine number 2 had

overtemperature damage in the turbine, from the unsuccessful in-flight start attempts in the rain and hail. Engine number 2 was replaced and the aircraft was flown to the New Orleans airport.

Engine number 1 was removed and run in a CFMI test cell, where it demonstrated normal operation and normal flameout margin.

#### **Corrective Action and Design Improvements**

Following the two dual-engine flameout events in 1987 and 1988 on Boeing 737-300 aircraft, the full resources of CFM International (GE Aircraft Engines and SNECMA) were directed to understand the phenomenon and to identify ways to improve engine capability.

This CFMI work included fundamental research into the trajectories of rain and hail particles as they pass through the engine, development of new facilities for inclement weather testing, and exhaustive ground and flight testing. Design improvements were identified and incorporated into the engine flowpath hardware and control systems of existing and new engines.

CFMI engine testing confirmed analyses that hail was the problem. The engine tolerance for hail ingestion was 14 percent of the rain ingestion capability. Rain testing demonstrated that only about 10 percent of the water captured by the engine inlet gets into the core. The rain drops break into smaller particles as they enter the engine inlet and approach the fan at gas path velocities. As these particles pass between the fan blades, they are centrifuged outward into the fan exhaust and away from the core engine primary flowpath.

On the other hand, hail particles approach the fan at aircraft velocities and, at descent idle engine rpm, pass right through the fan blade passages into the core. When hail particles strike an engine surface, they shatter into smaller particles which travel essentially tangent to the struck surface. Changing the fan spinner geometry from a conical shape to an elliptical shape to deflect some of the hail outward into the bypass stream was a big improvement.

The differences between hail and rain must be considered in the selection of engine geometry in order to design an optimum configuration to reduce the amount of moisture ingested into the engine core (compressor).

In the interest of promoting safety, CFMI has shared the results and the lessons learned with other members of the industry, through the Aerospace Industry Association (AIA) Inclement Weather Committee.

#### **5. VOLCANIC ASH CLOUD THREAT**

Volcanic ash clouds pose another multiple engine ingestion threat in the flight environment.

The first major volcanic ash cloud ingestion event involving a CF6 engine powered widebody commercial transport occurred on 15 December 1989. During descent into Anchorage near an altitude of 28,000 feet, a B747 encountered a volcanic ash cloud and all four engines flamed out. The engines were restarted successfully after several attempts. In all CFM56 and CF6 engine flight operations to date, this has been the only multiple-engine flameout event due to volcanic ash. This ash cloud was from a second eruption of Mt. Redoubt that occurred 1-1/2 hours prior to the B747 encounter. The event occurred 154 nautical miles downwind from Mt. Redoubt.

Exposures to volcanic ash clouds have resulted in major deposits of ash in turbine internal cooling passages and resultant multiple-engine flameout. When exposed to high temperature in the engine, the volcanic ash dust turns to a glass-like buildup fused upon the turbine airfoils and obstructs hot section cooling passages. Damage to the engines also included erosion of the fan rotating spinner (located ahead of the fan blades), the inlet nacelle lip, the compressor blades, and the fan blades.

Review of fleet operating data through 1993 showed that experience with GE and CFMI powered commercial transport aircraft included 17 reported multiple-engine events where the engines had been exposed to volcanic ash clouds of various "dust" densities. In most of these events, there was no effect on operations since the exposure duration and ash concentration in the cloud were relatively low.

Other than visual sighting and windscreens erosion, the entry of an aircraft into a volcanic ash cloud offers little or no advance engine warning symptoms in the cockpit prior to a flameout. Initially, engine parameters are not affected since volcanic ash, unlike icing, has little or no immediate effect on engine vibration or turbine temperature.

It is necessary to emphasize the need for better worldwide tracking and alerting of pilots of volcanic ash clouds that are present following volcanic eruptions. It must be recognized that these clouds can stay aloft for days and travel great distances.

#### **6. ROLE OF ENGINE MANUFACTURERS**

Engine manufacturers are required under regulatory requirements to design engines which will meet defined ingestion criteria. Compliance with these criteria must be demonstrated during engine certification testing.

Over the years, engine manufacturers have collected data on the extent of damage from birdstrikes and other ingestion events using the reports from flight crews, airline operators, and manufacturer's field representatives. Lessons learned during revenue service experience have led to engine design modifications which have resulted in significant improvements in engine

capability. Additional improvements will appear in the next generation of engines.

Although new engines will have increased birdstrike and inclement weather capability, there can still be ingestion encounters in nature that can exceed engine capability. It will always be necessary for flight crews, airport operators, and regulatory authorities to ensure that extreme ingestion encounters are avoided.

## 7. CONCLUSIONS

The ingestion threats in the flying environment can present a multiple-engine power loss hazard. Technology is advancing and can be expected to provide some degree of improved safety margin in the future. New engine designs, new aircraft, better aerospace systems and infrastructure advancements and improvements will appear in the form of new equipment. But for the present and immediate future, today's existing fleet of aircraft, engines, and the aerospace system, will continue in operation. Operations with the current technology must be supplemented by safety measures applied through regulations, procedures, cautions, operational alerts and good maintenance.

The ingestion events discussed in this paper pose dangers which a prudent flyer should not challenge - avoid them and stay clear of them. Manufacturers of aircraft and engines, the maintenance staff and those responsible for the aerospace system are proceeding with physical improvements and new equipment features to better the odds of success. But with the present and near term future flying machines it still all comes down to this - see, measure, communicate the hazard and avoid! Impose better control measures, warning systems and alerts; do not knowingly challenge these threats but use all available means to know where they are and avoid them.

Advances in ingestion-tolerant designs are being made in modern engines and aircraft. But these measures, on balance, are not great when compared to the overwhelming power, vastness and destructive forces which can sometimes be encountered in the operating environment.

To avoid the occurrence of environmentally caused accidents and incidents, it is necessary that the worldwide aerospace system, the government regulatory bodies, the national weather service and the air carrier operators, all together concentrate on vigorous, cooperative and coordinated programs of control:

- Control bird populations on and near the airports. Sense and communicate the presence of migrating flocks and then control aircraft operations to avoid collision with a flock which could hazard continued safe flight of an aircraft.

- Sense, track and communicate the occurrence, extent and locations of volcanic ash clouds.
- Observe maintenance and operating procedural cautions relative to wing, fuselage and engine inlet ice buildup.
- Operate the worldwide weather forecasting system so as to quickly and clearly communicate the threat areas and changing severe local conditions.
- Control airline operations in severe weather conditions with conservative procedures, good training, maintenance and advance readiness measures.

## 8. REFERENCES:

1. "Power Loss in Inclement Weather", Larry Volk, paper presented at The Joint Conference of The Flight Safety Foundation 45th International Air Safety Seminar and The International Federation of Airworthiness 22nd International Conference at Long Beach, California, November 4, 1992.
2. "Engine Ingestion Hazards - Birds, Ice Slabs and FOD", Thomas L. Alge, paper presented at The Joint Conference of The Flight Safety Foundation 45th International Air Safety Seminar and The International Federation of Airworthiness 22nd International Conference at Long Beach, California, November 4, 1992.

## AUTHORS:

Thomas L. Alge is Staff Engineer, Engine Ingestion and Birdstrike Investigations for GE Aircraft Engines. He has been in this position with GEAE at Evendale, Ohio for the last five years.

John T. Moehring is Commercial Flight Safety Director for GE Aircraft Engines at Evendale, Ohio.



## QUESTIONS

### F. AYDINMAKINE (Tu)

- Q.    i)     How do you determine that it was a bird strike?  
       ii)    How do you know how many birds were ingested?  
       iii)   What was their size?
- A.    i)     Bird-strikes are characterized by the presence of bird stains and sometimes feathers on the surface of the fan blades in the area where the bird(s) entered. Damaged blades show soft-body deformations of the airfoils. Bird stains can be detected visually for those bird ingestion events where bird material is plentiful. A black light inspection (using a FPI ultraviolet lamp) has been useful on many bird ingestion events to help identify faint areas of residual bird fluid stains.
- ii)    The number of ingested birds can be approximated by counting the number of bird-stained areas, recognizing that it takes between 2 - 7 blades to 'slice' each bird, depending on the size and orientation of the ingested bird. This requires that all blades be numbered consecutively and that both sides of all blades be examined - a 15 minute job.
- iii)   The size (weight) of the bird is based on the bird species, as determined from feather material retrieved from the engine and sent to the engine manufacturer, which are then sent to a recognized ornithologist for species identification. For a flocking encounter, feathers from dead birds on the runway or embedded in the aircraft structure have been used. Pilot reports of the bird type have also been used, but are less reliable.

### P. STALLARD (UK)

- Q.     As a result of the extensive rain and hail test program on CFM 56, was it possible to introduce changes which might improve the engine's ability to restart in flight?
- A.     Modifications introduced included a CF-6 type elliptical spinner, a cut-back booster flow splitter and scoops in the booster bleed door; the speed control schedule was also modified. These modifications were intended primarily to keep much of the hail (and rain) out of the combustor flowpath, thereby improving flame-out margin and ability to restart in flight. Levels of hail ingested successfully during the testing exceeded the requirements proposed by the Aerospace Industries Association for the most severe levels expected, based on their study of weather data. As a result, we expect no flame-outs or need to restart, consistent with CF 6-50 service experience in severe inclement weather.

**H.J. KOLKMAN (Ne)**

- Q. Why does the relocation of the splitter contribute to the solution of hail problems?
- A. Relocation of the splitter had a major impact on rain ingestion tolerance and a second-order benefit on hail ingestion capability. The additional axial space between the blades and the splitter allows more of the rain droplets, and hail, to a much lesser extent, to be deflected and centrifuged outward and away from the combustor air stream.

**D. MANN (UK)**

- Q. The physical properties of manufactured hail are profoundly different from naturally occurring hail. How did you satisfy yourselves that the hail tests carried out are representative of actual environmental conditions?
- A. Trajectory analyses and subsequent ground tests conducted on the CFM56 demonstrated that the amounts of rain and hail that can pass through the fan blades into the core engine are directly related to particle velocity levels at the fan face plane. The hail tests duplicated the particle velocity levels encountered in flight and therefore provided an accurate simulation. Although particle size levels matched the size levels that were subsequently included in the AIA hail threat descriptions, the size and shape characteristics of the simulated hail particles were considered to be of second-order importance because the trajectories are not affected unless the hail particles impact the engine surfaces.

# PARTICLE DEPOSITION IN GAS TURBINE BLADE FILM COOLING HOLES.

V. H. M. Kuk, P. T. Ireland and T. V. Jones  
Department of Engineering Science  
University of Oxford  
Parks Road  
Oxford OX1 3PJ  
United Kingdom

M. G. Rose  
Rolls-Royce PLC  
P.O. Box 31  
Derby DE2 8BJ  
United Kingdom

## 1. ABSTRACT

The aerodynamic processes leading to film cooling hole blockage have been investigated experimentally in large scale models of idealised internal cooling passages. The experimental scaling included reproducing engine cooling passage and hole Reynolds numbers together with a new dimensionless group which was matched experimentally to ensure that the measured particle trajectories were engine representative. It has been possible to achieve correct dimensional scaling with particles one thousand times larger than engine size. Simple visualisation of the particle trajectories showed concentrations of impact locations inside holes normal to and inclined to the cooling passage surface. No attempt was made to model interaction between the particles and the passage walls. A new instrument has been developed to measure the concentration of particle impacts. Use of the device provides a fast and convenient way of measuring particle impact distributions. The regions of high impact concentration are consistent with blockage structures found in engines after service. The process of internal blockage of film cooling holes has been shown to be due to inertia driven particles of the order of  $1\mu\text{m}$  in diameter. Flow conditions immune from impact concentration and hence the blockage process have been identified for the inclined film cooling hole.

## 2. NOMENCLATURE

$a$	impact meter detecting area, $\text{m}^2$	$St$	Stokes number
$A$	area, $\text{m}^2$	$t$	time, s
$c_d$	coefficient of drag	$V$	velocity vector, m/s
$d$	diameter, m	$V_{\text{slip}}$	particle slip velocity vector, m/s
$m$	mass, kg	<i>Greek</i>	
$m_{\text{rate}}$	rate of deposit, $\text{kg}/\text{m}^2\text{s}$	$\rho$	density, $\text{kg}/\text{m}^3$
$n$	number per unit volume of air, $\text{m}^{-3}$ , or number counted	$\theta$	angular position around circular cylinder
$N$	number of particles	$\mu$	viscosity, $\text{Ns}/\text{m}^2$
$r$	radial distance, m	<i>Subscript</i>	
$Re_p$	$\rho_a V_{\text{slip}} d_p / \mu_a$	$a$	air
$Re$	Reynolds number	$\text{cyl}$	cylinder
$SR$	suction ratio, hole average velocity divided by cross-flow velocity	$d$	target
		$h$	hole
		$i$	inlet
		$p$	particle
		$\infty$	free-stream

slip	slip condition
<i>Superscript</i>	
*	dimensionless

### 3. INTRODUCTION AND PREVIOUS WORK

High fuel efficiency and specific thrust are important targets for gas turbine engine designers and lead to the use of turbine entry temperatures which are unacceptable to uncooled turbine components. Modern engines use combustor exit temperatures as high as 1550°C whilst typical turbine blade materials melt at approximately 1200°C. To enable jet engines to operate with such high cycle temperatures, various cooling techniques are applied to the turbine blades. Relatively cool air is bled from the compressor and ducted through passages within the turbine vanes and rotors. Very often, this air which has been used to convectively cool the blades, is then passed to the blade surface through small holes. These film cooling holes are used to produce an insulating layer of cool air between the external blade surface and the hot combustion products.

A drawback to using film cooling can be the limited turbine blade service life. Inadequate operational blade life is frequently due to the breakdown of film cooling. One film cooling failure mode is caused by the build up of dust particles in the turbine blade cooling passages. These dust particles in the gas stream continuously strike the blade surface and, with time, build up to form a coating which can restrict the coolant flow. The build up of deposits in the film cooling holes results in a gradual reduction of the coolant flow rates and the consequent deterioration in film cooling effectiveness. The resulting excessive blade temperatures can lead to oxidation of the blade material. High temperatures are also accompanied by high creep rates and cracking due to increased thermal stresses.

The action of airborne dust on jet engines has been the subject of a great deal of research. Dunn et al. (1987) studied the performance degradation of engines subjected to severe dust loads of large (40-425 $\mu$ m) aerosols. The reduction in surge margin caused by damage to the compressor was reported in detail and erosion of the high and low pressure turbine stages was noted. Wagner et al. (1991) calculated the erosion rates of vanes and blades subject to particle loaded gas from a coal-fired combustor. They studied the effects on the

aerofoil geometries of a range of particles larger than 5 $\mu$ m representative of fly-ash after failure of a hot gas clean up process. Particles smaller than 1 $\mu$ m were considered to pose few problems. Deposition on the suction surface of hot turbine aerofoils was reported by Nomura et al. (1977) and was not thought to be due to inertial deposition. Kladas and Georgiou (1992) calculated the deposition rates in turbine cascades subjected to ash particles with different sizes. They concluded that it was not possible to avoid the inertial deposition of particles in the 1-10 $\mu$ m range.

The composition and causes of airborne particles were reviewed by Raubenheimer (1990) who concentrated on land based industrial and marine gas turbine filtration. Particles in the range 0.001-1 $\mu$ m are classified as permanent pollutants and are predominantly products of combustion (smoke). Certain pollens and other organic material are in the same diameter range. Particles classed as temporary pollutants are in the range 1-1000 $\mu$ m and are lifted from the surface of the earth by strong winds. More recently, Smialek et al. (1992) studied the composition of deposits and particles found in helicopter engines which had operated in the Persian Gulf. Samples of sand were found to be about 90% SiO<sub>2</sub> and 1-3% Al<sub>2</sub>O<sub>3</sub> and CaO with other trace materials. The composition was found to change with sand particle size. Glassy deposits on the outside of aerofoils were found to have blocked some of the film cooling hole exits and had a composition similar to fine sand. A layer with high sulphur content at the blade surface was interpreted as corrosive calcium sulphate formed by reaction between calcium carbonate in the sand and sulphur in the fuel. Analysis of powder found in the cooling passages revealed a composition similar to that of small sand particles. The powder particles sizes were in the range 1-10 $\mu$ m. The melting temperature of the deposits and of the cooling passage powder was measured as approximately 1135°C which is lower than the melting temperatures of silicon dioxide (1713°C) or calcium sulphate (1540°C). Fine sand is expected to be molten outside the aerofoils of early stages of the turbine but solid in the cooling flow.

In sections of turbine blades which are impingement cooled, small conical deposits have been found directly beneath the impinging jets, figure (1). The science of particles impacting on plates beneath normally impinging jets is well understood and has been the subject of numerous experimental and theoretical studies, e.g. Lede et

al. (1992). A review of particle impact beneath jets is given in Marple (1970) who investigated the efficiency of cascade impactors used for particle separation. He showed that particles with a Stokes number greater than about one strike a surface beneath a square jet one square dimension from the nozzle exit. For an engine size jet operating at a typical Reynolds number, this implies that sand particles greater than  $0.5\mu\text{m}$  would strike the cooling passage surface.

Film cooling hole blockage is particularly important since:-

(i) The small diameter of cooling holes leads to high local flow curvature and appreciable particle slip. It will be shown below that particles are focused into regions of high impact concentration near the entrance to the holes. The rate of deposit growth is expected to be relatively high in such regions.

(ii) The small hole area means that only a small build up of material is required to appreciably reduce the coolant flow rate.

Characteristic structures have been observed near film cooling holes entrances, figure (2), and were reported by Daubin and Defrance (1990). The structure, shown in figure (2), bisects the film cooling hole and is known as a shark's fin. Characteristic structures have also been observed at the exits to film cooling holes. One type starts from the downstream edge of the hole and is referred to in the above reference as lidding.

The objective of the present work was to investigate the aerodynamic processes responsible for film cooling hole blockage. To this end, experiments were performed at large scale to study the trajectories of engine representative particles and to determine the candidate locations for particle build up. These locations are where the particles strike the surface of the model film cooling holes. The objective was to identify cooling geometries and flow conditions which minimise the number of particle impacts in an effort to avoid deposition. The interaction between the particles and the cooling passage walls was not modelled experimentally. The results are also of value for assessing computational fluid dynamics calculations of impact distributions.

Early experiments, Kuk (1992), used optical means to track the particles, but data rates were prohibitively slow and a method of accurately measuring the concentration of particle impacts was developed. The development and commissioning of a particle impact meter is described in detail

together with measured particle concentrations. The meter is compact and easily applied to different geometries wherever it is possible to site a static pressure tapping.

#### 4. DIMENSIONAL ANALYSIS

A typical engine film cooling holes is 0.5mm in diameter and would be difficult to instrument in detail. In addition, engine coolant temperatures and pressures are approximately  $550^\circ\text{C}$  and 18bar and do not permit the use of sensitive instruments. For this reason, the experiments tested models of engine cooling passages at approximately one hundred times engine scale. The flow field was reproduced by matching the engine cooling passage Reynolds number at atmospheric pressure and ambient temperature. The experiments were performed at incompressible flow speeds since film cooling hole Mach number are often small. The coolant temperature is lower than the particle melting temperature and so the engine particles were modelled using small solid plastic and glass beads.

It would have been possible to achieve exact particle dimensional similarity by matching the ratios  $d_p/d_h$  and  $\rho_p/\rho_a$ . In the present work, dimensional analysis was used to establish that particle trajectories are similar when a single dimensionless group is matched. For simple particle motion subject to only aerodynamic forces, its equation of motion can be written as

$$m_p \frac{d\bar{V}}{dt} = c_d A_p \frac{1}{2} \rho_a |V_{slip}| \bar{V}_{slip} \quad (1)$$

Here, the assumptions have been made that:-

- (i) the fluid is incompressible;
- (ii) particle drag is independent of acceleration;
- (iii) particle interaction is negligible;
- (iv) particle motion is unaffected by an externally exposed spin;
- (v) particle number density is also assumed to be sufficiently low not to influence the coolant flow.

The coefficient of drag,  $c_d$ , is a function of the particle Reynolds number,  $Re_p$ , based on particle diameter and slip speed. At low values of  $Re_p$  (less than about unity), the drag coefficient is given by Stokes law as 24 divided by the particle Reynolds number. Substitution for  $c_d$  into the equation of motion shows that particles with the same Stokes number follow the same trajectory. The Stokes number is defined as

$$St = \frac{1}{18} \frac{\rho_p d_p^2}{\rho_a d_h^2} Re_h \quad (2)$$

Introducing dimensionless particle and slip velocities defined by  $V_p = V_p^* V_h$  and  $V_{slip} = V_{slip}^* V_h$  and dimensionless time by  $t = t^* d_h / V_h$ , equation (1) becomes

$$\frac{dV_p^*}{dt^*} = \frac{3}{2} \frac{d_h \rho_a}{d_p \rho_p} c_d |V_{slip}^*| \overline{V_{slip}^*} \quad (3)$$

where the particle has been taken to be spherical. The coefficient of drag is a function, figure (3), of  $Re_p$  which can be written as the product of dimensionless slip speed, diameter ratios and hole Reynolds number.

$$c_d = c_d(|V_{slip}^*| \frac{d_p}{d_h} Re_h) \quad (4)$$

A hole Reynolds numbers is of the order of  $10^4$  and a film cooling hole is usually about 1mm in diameter so that  $Re_p$ , for a  $1\mu\text{m}$  particle, is approximately ten times the dimensionless slip speed. The range of dimensionless slip speeds for particles travelling close to film cooling holes was calculated as 0.1 to 10. Over this range,  $Re_p$  changes from 1 to 100 which is beyond the range of validity of Stokes law. Dring et al. (1979) also noted a departure from Stokes law for particles in a turbine cascade and presented a four section fit to the standard drag curve. To enable engine particles to be experimentally modelled at large scale, a simple power law variation was fit to the standard  $c_d$  curve over the range of  $Re_p$  from 1 to 100.

$$c_d = \frac{25}{Re_p^{0.7}} \quad (5)$$

Using the expression for  $C_d$ , the equation of motion becomes

$$\frac{dV_p^*}{dt^*} = \frac{75}{2} \frac{\rho_a}{\rho_p} \left(\frac{d_h}{d_p}\right)^{1.7} |V_{slip}^*|^{0.3} Re_h^{-0.7} \overline{V_{slip}^*} \quad (6)$$

Hence particles with dimensionless slip speed in the range (0.1 to 10) have trajectories with the same dimensionless coordinates through a particular flow field when the group

$$\frac{\rho_a d_h^{1.7}}{\rho_p d_p^{1.7}}$$

is matched.

The approach used in the present work

represented the film cooling hole at large scale and then achieved engine values of the above group using the largest possible particles. The scaled particle diameter is greatest when the particle density is as small as possible. Expanded polystyrene spheres are readily available and have a density of about one seventieth of engine deposits. As a result, spheres of 1.7mm diameter can be used to represent  $2\mu\text{m}$  particles. The extent of the experimental scaling is summarised in table I. Figure (4) shows the equivalent engine size of the experimental particles used calculated using the dimensions and densities given in the table. It can be seen that both types of particle were representative of nominally the same size engine particle. The expanded polystyrene spheres were visible to the unaided eye and their trajectories were recorded during some experiments using standard domestic video equipment. By measuring streaklines produced as a result of the finite video camera exposure time (17ms) it was also possible to determine particle velocities.

The validity of equation (5) was assessed by comparison of experimental particle tracks to numerical predictions based on equation (6). Particles were dropped into the working section of a wind tunnel where the flow speed was 2.5 m/s, figure (5). In fact, the geometry illustrated is that used in the film cooling hole experiments described in section 7. The hole was at 190 mm downstream of and 170 mm below the introduction point. The particle tracks were numerically calculated using the proposed drag model. The boundary layer and initial vertical velocity were included in the calculations. It can be seen that the drag equation gives trajectories which are in good agreement with the experimental results.

## 5. DESIGN OF A PARTICLE IMPACT METER.

A device was developed to count the number of particle impacts per unit area. The objective was to use the quantitative results to assess the susceptibility of particular cooling passages to blockage caused by high impact concentrations. It would then be possible to investigate the effect of flow parameters on impact concentration and also to rank cooling hole geometries in terms of potential sensitivity to blockage. This aim was achieved using a capped sensitive pressure transducer. The experimental method yielded a

data rate significantly higher than optical means used to calculate impact concentrations.

The Particle Impact Meter, figure (6), consists of:-

- (i) a high sensitivity piezoresistive pressure transducer.
- (ii) a 2.3 mm inner diameter connecting pipe
- (iii) an instrumentation amplifier
- (iv) a digital counter.

The pressure transducer has an operating pressure range of 1000Pa, a sensitivity of 0.04 mV/Pa and the instrument has a stated response time of 500 $\mu$ s. The output from the pressure transducer is connected to an instrumentation amplifier with a gain of 1000. A metallic pipe of inner diameter 2.3 mm is fitted to pressure port one of the transducer, the other end of the metallic pipe is flush with the model surface and is sealed by a 150  $\mu$ m thick PVC membrane. The second transducer port is left open to the atmosphere. When a particle strikes the PVC membrane, it deflects and the increase in pressure inside the sealed chamber is measured by the transducer. For typical experimental conditions, the particle impact causes pressure signals which are of the order of several volts.

A digital counter was designed to identify individual particle impact signals. The signal conditioning circuit consists of a comparator, a low power bi-polar timer and a digital LCD counter. The module circuit is shown in figure (7). The pressure transducer signal is AC coupled to eliminate the effects of changes in the transducer amplifier voltage offset induced by changes in temperature. The signal is compared with a set threshold voltage at the comparator. The threshold voltage is changed by adjusting the 1 K $\Omega$  potentiometer. When the signal strength is higher than the threshold voltage the comparator output goes from low to high thus triggering the timer. The timer output then stays high for a pre-determined time typically (10 ms) which can be changed by adjusting the 250 K $\Omega$  potentiometer. Signals from the pressure transducer, comparator and the timer are shown in figure (8). The change in signal from the timer is recorded by the digital counter. During the interval for which the timer output is high, the counter can not be re-triggered by the damped oscillation typical of a single particle impact. In this way, the problem of multiple counts is avoided.

Experiments were performed to determine the area of the PVC membrane over which the

instrument produced a count. A known number of polystyrene spheres were dropped through a vertical pipe and the meter used to count the number of particles,  $n$ , at different radial distances to cover the full particle outflow, figure (9). The results are from experiments used to determine the maximum threshold voltage. Since the total number,  $N$ , of spheres released is known, the area over which particles are detected,  $a$ , was calculated from

$$N = \int_0^{\frac{a}{2}} \frac{n}{a} 2\pi r dr \quad (7)$$

The minimum impact velocity was determined by dropping particles from different heights and determining the detection area,  $a$ . This area is plotted as a function of particle velocity in figure (10) and can be seen to be sensibly constant down to the lowest velocity tested. The lowest impact velocity expected in the present experiments is 0.1m/s and hence a constant value for  $a$  of  $1.54 \times 10^{-6} \text{m}^2$  was used throughout the experiments.

## 6. VALIDATION OF THE PARTICLE IMPACT METER

A simple experiment was performed to measure the particle impact distribution on a circular cylinder. A 63.5mm diameter circular cylinder was placed in the working section of a low speed wind tunnel, figure (11). The pressure transducer was placed inside the circular pipe and connected to a short metallic pipe which extends to the cylinder surface where it was sealed by a PVC membrane. Expanded polystyrene spheres were introduced through the wind tunnel top wall 600 mm upstream of the circular cylinder. The circular cylinder was rotated to measure the impact distribution over the upstream facing  $180^\circ$  in  $7.5^\circ$  intervals. The free stream flow velocity in the tunnel was 4.3m/s and the cylinder Reynolds number was 9002. The particle speed at the cylinder location in the absence of the cylinder was 96% of the flow speed.

Analytical particle impact distributions around a circular cylinder were presented by Glauert (1940). The flow field in front of the circular cylinder was solved by potential flow theory and the drag on the particles which approach the cylinder without slip, was assumed to be governed by Stokes law. The present work results and Glauert's data are presented in terms of a filter efficiency. This is the ratio of the area at a defined inlet plane,  $A_i$ ,

through which all of the particles pass that arrive at the cylinder surface within an area  $A_d$ . The filter efficiency is plotted as a function of cylinder angular position in figure (12).

$$\text{Filter efficiency} = \frac{A_i}{A_d} \quad (8)$$

The filter efficiency can be used to evaluate the  $m_{rate}$ , at which matter accumulates at the surface from

$$m_{rate} = V_{\infty} n m_p \frac{A_i}{A_d} \quad (9)$$

where  $V_{\infty}$  is the velocity at the inlet plane. A comparison between the measurements and Glauert's calculation is shown in figure (12). The Stokes number (based on the cylinder,  $Re$  and flow approach velocity) of the experimental polystyrene spheres is between those of the two lines from Glauert. Over most of the front of the cylinder, the agreement is good. At the larger angles at which impact is predicted, the error introduced in the calculation caused by using Stokes law at  $Re_p$  greater than unity probably accounts for the over-prediction of the number of impacts.

## 7. FILM COOLING HOLE EXPERIMENTS

An idealised model of a cooling passage was used to investigate the distribution of particle impacts near to the entrance of a film cooling hole, figure (13). A 50.8mm inner diameter tube was fitted 1170mm from the plate leading edge and ran through the 100 mm thick plate. Tests were performed with the hole at 90° and at 30° to the flat plate surface. The model is fitted in the 300mm by 300mm working section of a low speed wind tunnel. This geometry simulates a single film cooling hole in a turbine blade. The position of each shutter was altered to cover a large range of suction ratios. The flow in the cooling hole was measured by an orifice plate flow meter. The instrumentation included ten particle impact meters each with its own digital output as shown in figure (14). The threshold voltage and the dead time were adjusted to be 1.0V and 10ms respectively. A spin filter was fitted downstream of the model. The filter caused a low pressure loss and permitted continuous operation. A vacuum pump was used to draw the particles from the filter for recycling.

The particle input distribution was measured using a series of particle impact meters mounted in a line

parallel to the flat plate surface and perpendicular to the flow. The diameter of the cylindrical strut into which the particle impact meters were mounted was such that all of the particles in a stream tube extending prismatically from the impact meter cap struck the PVC membrane. In other words, the average filter efficiency over the PVC cap was very close to unity. The distribution of the number of particles per unit area over a plane perpendicular to the freestream was measured in both film cooling configurations. The defined inlet plane was  $3d_h$  upstream of the hole entrance centreline. Particles were introduced through multiple holes in the top of the wind tunnel to produce as uniform a distribution of particles over the inlet plane as possible. The average number of particles per unit inlet area over a region extending  $0.5d_h$  from the plate surface and approximately  $3d_h$  above the hole centreline and  $1d_h$  below the hole centreline was used in the determination of filter efficiency as explained below.

### 7.1. 90° hole experiments

A series of tests was conducted on the 90° hole at different suction ratios and cross flows. The impact concentrations were found to be consistently on the downstream side of the cooling hole. The position of the peak concentration varied back and forth depending on the suction ratio and cross flow. The model included two rows of impact sensors and was mounted so that the instrumented section could be rotated about its own axis to determine the full impact map. The data points were taken on an irregular mesh and interpolated to give a contour map. The peak concentrations is measured from the contour map. A typical particle impact concentration map is shown in figure (15) where the measured number of impacts has been converted into filter efficiency as defined in equation (8). This ratio was calculated by dividing the number of particles striking the surface per unit surface area by the upstream number of particles per unit inlet plane area. Particle impact maps were measured at different flow conditions with different scaled particles.

At each hole Reynolds number and suction ratio tested, the impact distribution was measured using the polystyrene and the hollow glass beads. The peak impact concentration locations are shown in figure (16). The number above each marker gives the distance of the concentration peak from the hole entrance divided by hole diameter for expanded



polystyrene. The number below the marker is the non-dimensional distance for hollow glass beads. The figure shows that:-

(i) the position of the distribution peak moves further down the hole as the suction ratio is increased.

(ii) the particles strike closer to the hole entrance as the hole Reynolds number increases. This is due to higher particle inertia in the main flow direction as  $Re_h$  (at a particular suction ratio) is increased.

(iii) the particles have sensibly the same non-dimensional approach slip speed of 0.45 in all the tested conditions. However in all cases, the hollow glass beads have a consistently lower non-dimensional inlet particle slip speed than the expanded polystyrene spheres. At a lower inlet dimensionless slip speeds, and hence higher inlet particle upstream inertia, the particles strike the wall closer to the hole entrance. The dimensionless inlet particle slip speeds were calculated using equation (5) and the accuracy of the predictions was confirmed as being within 10% at selected conditions.

## 7.2 30° hole experiments

The 30° hole experiments followed the same procedure as the 90° hole experiments. Surprisingly, it was found that the particle impact points at high suction ratio were on the upstream side of the cooling hole instead of on the downstream side as was the case for the 90° hole. It is thought that, at high suction ratios, the flow separation at the downstream face is large and causes a flow distortion which forces the particles onto the upstream side of the hole. It was also found that the impact location changed from the upstream face to the downstream face as the suction decreased. At low suction ratios, the particles have sufficient inertia to strike the downstream side of the hole. This implied that there is a range of suction ratios for which particles enter the cooling hole without striking the hole surface, ie a zero blockage condition. A range of cross flow velocities was tested to determine the impact free range conditions using a powerful (100W) collimated U.V. arc light. The no-impact range of suction ratio as the hole Reynolds number increases is shown in figure (17) for the expanded polystyrene beads. The data appears to show that the suction ratio required to prevent particles striking the downstream wall decreases as the hole Reynolds number increases. This was counter to

expectation since equation (6) indicates that the aerodynamic forces decreases as  $Re_h$  increases. In other words, the particles would be expected to have more of a tendency to continue in their original direction as  $Re_h$  increased. In fact the method used to introduce the particles meant that, as  $Re_h$  increases, the particle slip speed at the inlet plane fell from 95% to 65% of the freestream velocity. The figure shows not only the existence of no impact states, but also the sensitivity of the 30° hole impact distribution to the inlet particle dimensionless slip speed.

## 8. UNCERTAINTY ANALYSIS

The largest source of potential error is expected to be the counter failing to log an impact during the insensitive period produced by the timer. This source of error can be minimised by using a slow introduction rate. For a test time of 60 seconds, the number of particles counted was, for a typical experiment, 300. Therefore the expected number of particles arriving during 10ms is 0.05. The Poisson distribution can be used to show that the probability of more than one particle arriving during the dead period is less than 4%.

## 9. CONCLUSIONS

A new means of experimentally modelling at ambient conditions the trajectories of particles within a cooling passage of order a few microns in diameter has been developed. Dimensionless analysis has been applied to determine the particle parameter that governs the trajectory at typical slip speeds. It was found that Stokes number matching is not sufficient for typical engine conditions. The experimental particles are large (of order 1mm in diameter) and can readily be visualised using domestic video equipment.

An impact counter was developed to allow quantitative comparison of cooling passage impact concentrations. The device has enabled low impact, and hence low blockage, conditions to be determined. The technique has been used to study internal cooling passage deposition and could readily be applied to the blade external flow field.

## 10. ACKNOWLEDGMENTS

The authors gratefully acknowledge the support of the Defence Research Agency (Pyestock) for part of the work and the permission of Rolls-Royce PLC. to publish the paper. The assistance of Mr. R. C. Stone who produced the impingement deposit figure is also much appreciated. The pressure transducers were supplied by Sensor Technics, Rugby.

## 11. REFERENCES

- Clift, R., Grace J.R. and Weber, M. E., 1978, "Bubbles, drops, and particles," Academic Press.
- Daubin, J. M. and Defrance, E., 1990, "Obstruction des trous de refroidissement d'aubes de turbine," Technical report, Ensica, France.
- Dring, R. P., Caspar, J. R. and Suo, M., 1979, "Particle trajectories in turbine cascades," AIAA Journal of Energy, vol. 3, no. 3, p. 161.
- Dunn, M. G., Padova, C., Moller, J. E. and Adams, R. M., 1987, "Performance deterioration of a turbofan and a turbojet engine upon exposure to a dust environment," Journal of engineering for gas turbines and power, vol. 109, pp. 336-343.
- Glauert, M., 1940, "A method of constructing the paths of raindrops of different diameters moving in the neighbourhood of (1) a circular cylinder, (2) an aerofoil placed in a uniform stream of air; and a determination of the rate of deposit of the drops on the surface and the percentage of drops caught," Rep. Dep. Sci. Industr. Res., Lond., no. 2025, pp. 46-57.
- Kladas, D. D. and Georgiou, D. P., 1992, "Turbine cascade optimization against particle deposition," ASME paper 92-GT-345.
- Kuk, V., 1992, "An investigation of dust particle trajectories and impact points in a turbine blade cooling system," MSc transition report, Department of Engineering Science, University of Oxford.
- Lede, J., Huchet, G., Marchant, S., Fayokurera, A. M. and Villermoux, J., 1992, "Depot de particules projetees par un jet gazeux sur une surface plane," Powder Technology, vol. 73, pp. 239-250.
- Marple, V. A., 1970, "A fundamental study of inertial impactors," D. Phil thesis, University of Minnesota.
- Nomura, M., Morishita, T. and Kan, S., 1977, "An experiment of deposit formation on the surface of an air-cooled gas turbine blade," Tokyo Joint Gas Turbine Congress, May 22nd to 27th, Co-

sponsors were Gas Turbine Society of Japan, Japanese Society of Mechanical Engineers, ASME., pp. 566-573.

Raubenheimer, D. S. T., 1990, "Selection and operation of gas turbine air filters," *Turbomachinery International*, vol. 31, no.1, Jan/Feb issue, pp. 26-33.

Smialek, J. L., Archer F. A. and Garlick, R. G., 1992, "The chemistry of Saudi Arabian Sand: A deposition problem on helicopter turbine airfoils," 3rd International SAMPE Metals and Metals Processing Conference, *Society for the Advancement of Material and Process Engineering*, vol. 3, pp. M63-M77.

Wagner, J. H., Johnson, B. V. and Geiling, D. W., 1991, "Effects of turbine design on particulate erosion of turbine airfoils," ASME paper 91-GT-292.

## 12. LIST OF FIGURES

- Figure (1) Deposits formed beneath impinging jets.
- Figure (2) Typical deposit near the entrance to a film cooling hole.
- Figure (3) Standard  $c_d$  curve for a sphere, after Clift (1978).
- Figure (4) Equivalent engine size for experimental particles.
- Figure (5) Numerical predictions of particle trajectories.
- Figure (6) Particle impact meter.
- Figure (7) Particle counter circuit.
- Figure (8) Counter signals.
- Figure (9) Count distribution used to calibrate the impact meter.
- Figure (10) Sensor area,  $a$ , as a function of polystyrene sphere impact velocity.
- Figure (11) Experimental arrangement for the circular cylinder experiment.
- Figure (12) Comparison of measured particle counts on the cylinder to Glauert's (1940) prediction.
- Figure (13) Experimental arrangement for the film cooling hole experiments.
- Figure (14) Particle impact meter module.
- Figure (15) Particle impact concentration map for the 90° hole.
- Figure (16) Effect of slip speed on particle impact maps.
- Figure (17) Conditions to avoid particle impact in the 30° hole.

## QUESTIONS

### DOUG NAGY (Ca)

Q. Your calculations have determined that there exists a flow condition where there will be no particle impact with the cooling hole walls. How sensitive is this solution to particle size and density? And how does that range compare with the real size and density ranges found inside turbine cooling passages?

A. The dimensionless size parameter

$$\frac{\rho_p}{\rho_a} \left( \frac{d_p}{d_h} \right)^{1.7}$$

used in our large scale experiments is such that we simulate the particle trajectories of engine dust particles in the range  $3.93 \pm 0.46 \mu\text{m}$  assuming a typical engine dust density of  $2900 \text{ kg/m}^3$ . Larger engine particles would have a larger size parameter and could easily be investigated using different plastic spheres. We anticipated that no impact range of suction for the  $30^\circ$  hole would increase with particle size and density. The no impact suction ratio ranges are achievable in engine blade cooling passages.

Parameter	Engine particle	Expanded polystyrene spheres	Hollow glass spheres
$d_p$	1 to 10 $\mu\text{m}$	1500 to 1900 $\mu\text{m}^1$	149 to 349 $\mu\text{m}$
$\rho_a$	6.3 $\text{kg}/\text{m}^3$	1.19 $\text{kg}/\text{m}^3$	1.19 $\text{kg}/\text{m}^3$
$\rho_p$	2900 $\text{kg}/\text{m}^3$	33 $\text{kg}/\text{m}^3$	1050 $\text{kg}/\text{m}^3$
$d_h$	0.5 mm	50.8 mm	50.8 mm
$V_h$	350 m/s	3 m/s	3 m/s
St	2.8 to 25.3	7.4 to 66.5	4.3 to 23.1

Table 1. Characteristics of experimental and engine cooling passage particles.

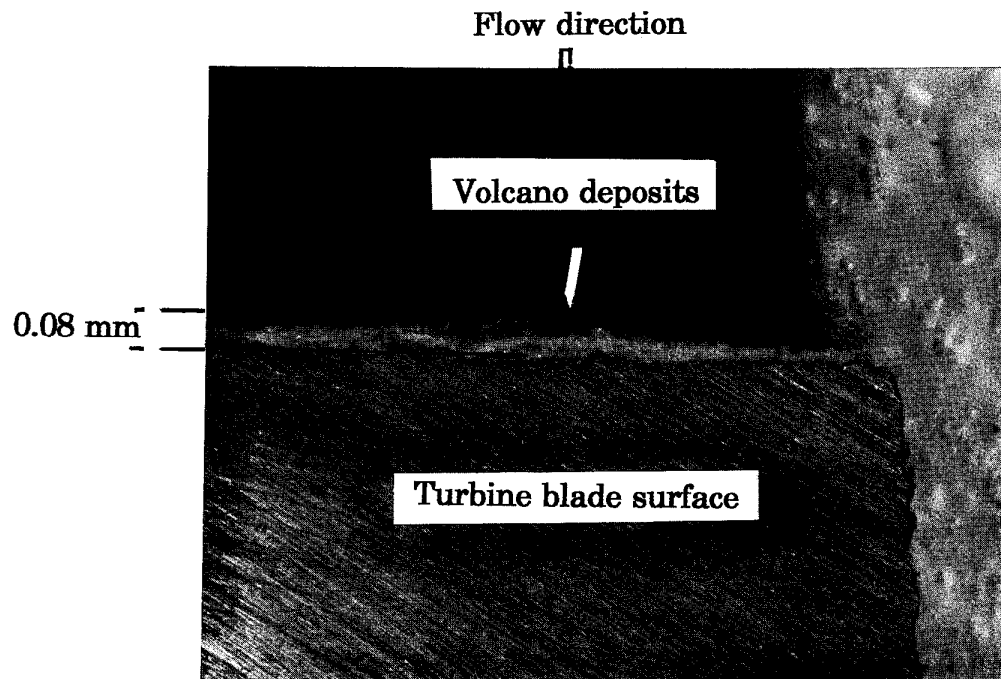


Figure (1) Deposits formed beneath impinging jets.

<sup>1</sup>Standard deviation measured as 200  $\mu\text{m}$

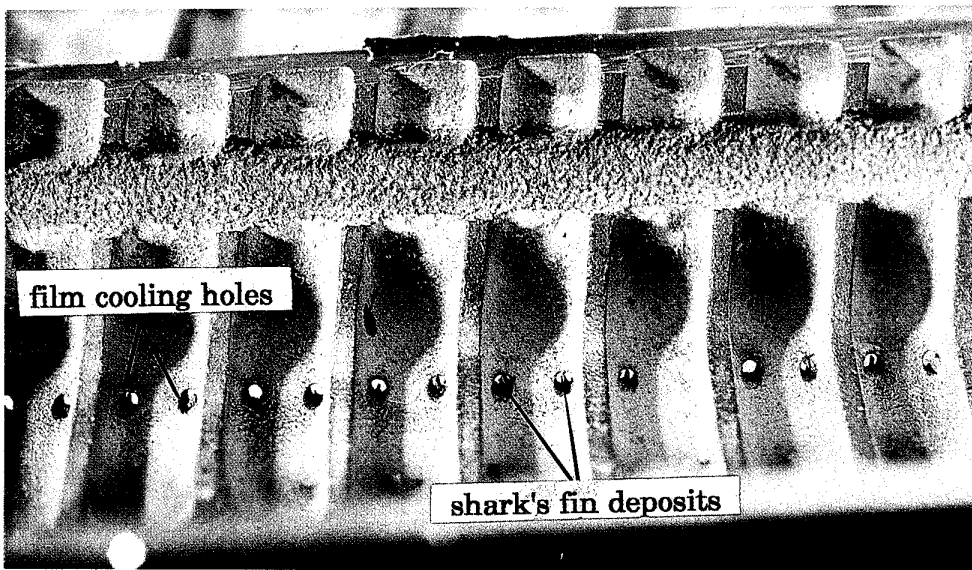


Figure (2) Typical deposit near the entrance to film cooling holes.

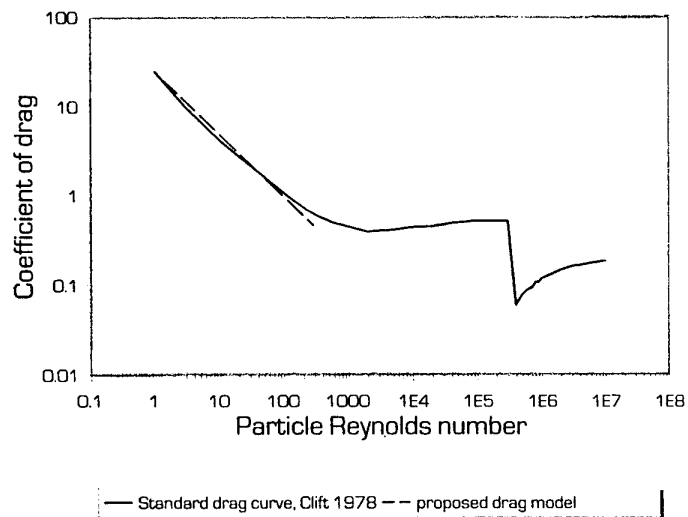


Figure (3) Standard  $c_d$  curve for a sphere, after Clift (1978).

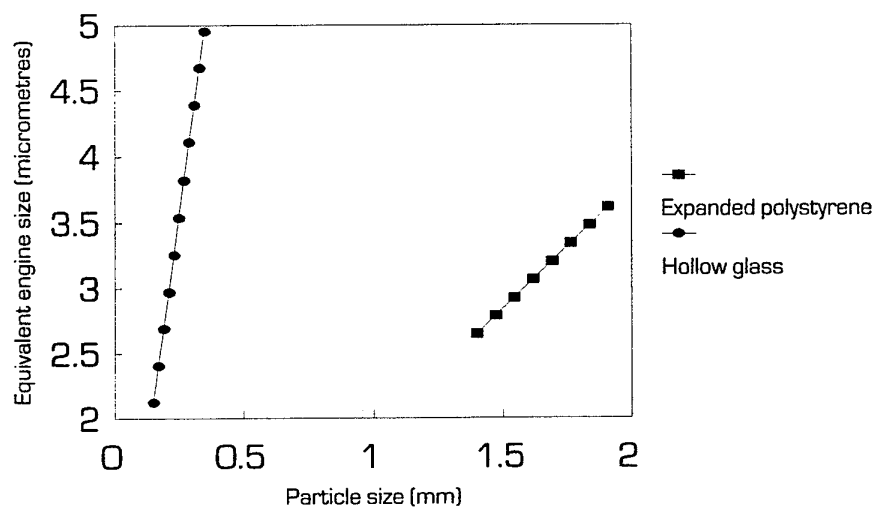


Figure (4) Equivalent engine size for experimental particles.

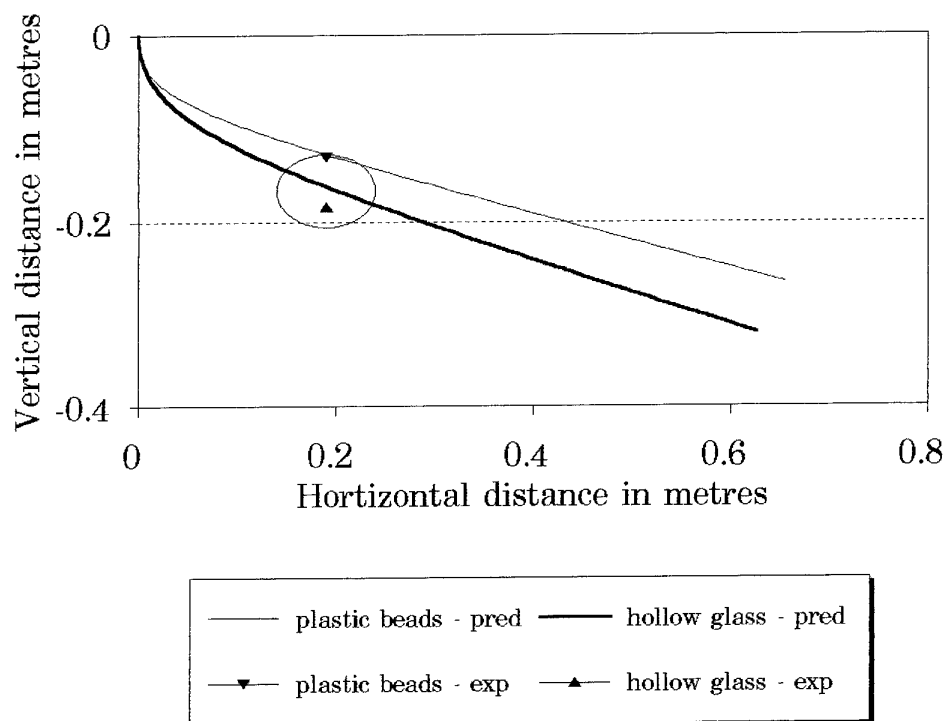


Figure (5) Numerical predictions of particle trajectories. SR = 0.

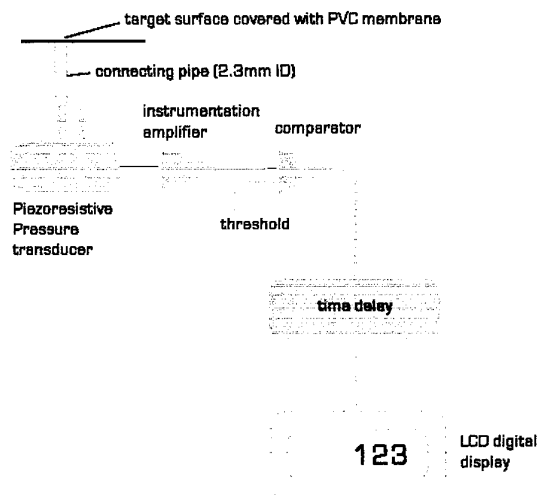


Figure (6) Particle impact meter.

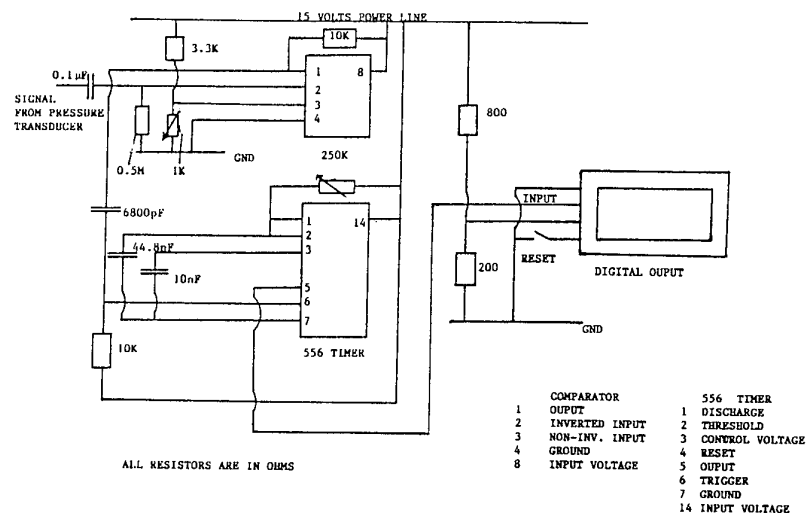


Figure (7) Particle counter circuit.

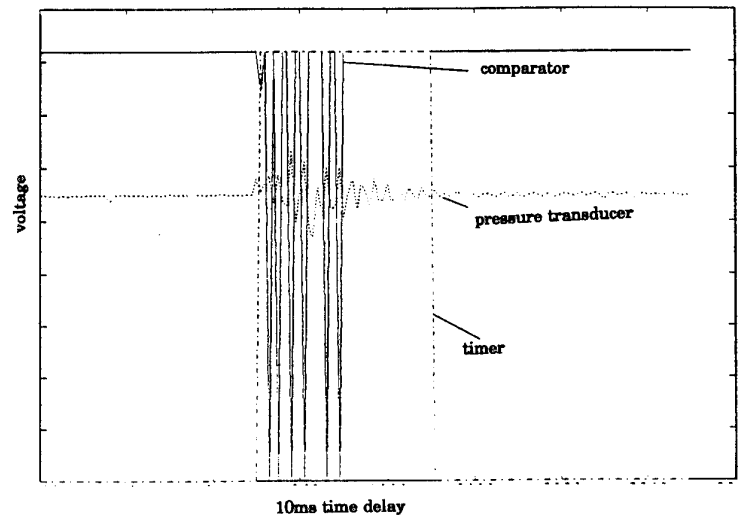


Figure (8) Counter signals.

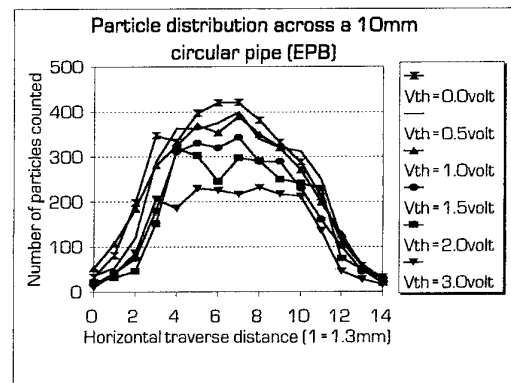


Figure (9) Count distribution used to calibrate the impact meter.



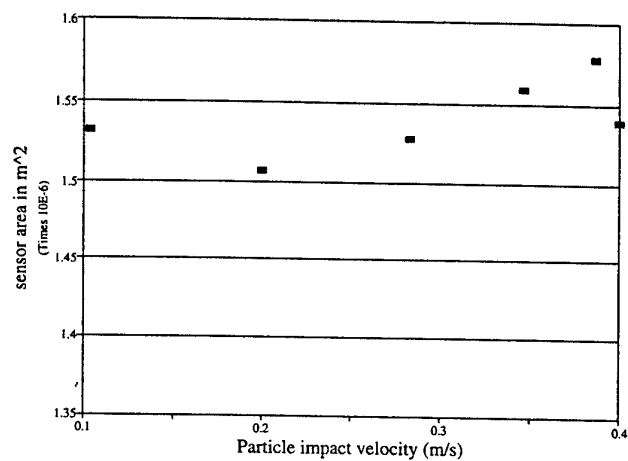


Figure (10) Sensor area,  $a$ , as a function of polystyrene sphere impact velocity.

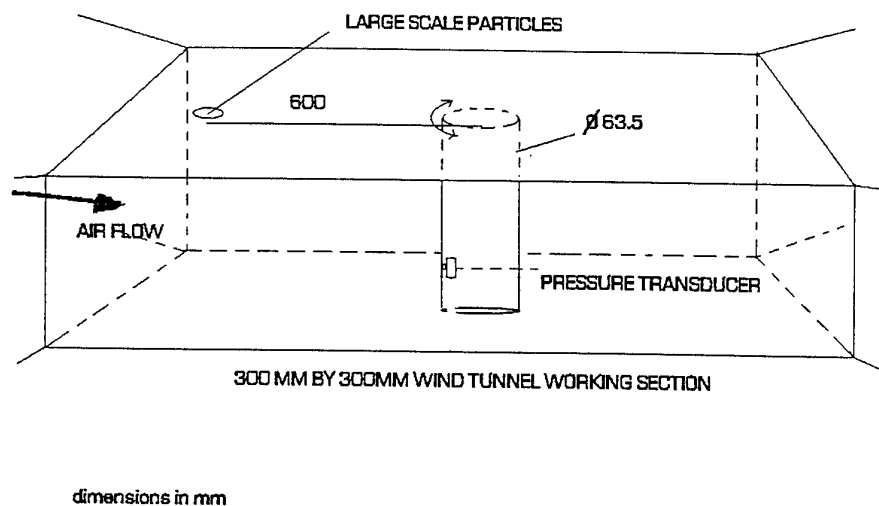


Figure (11) Experimental arrangement for the circular cylinder experiment.

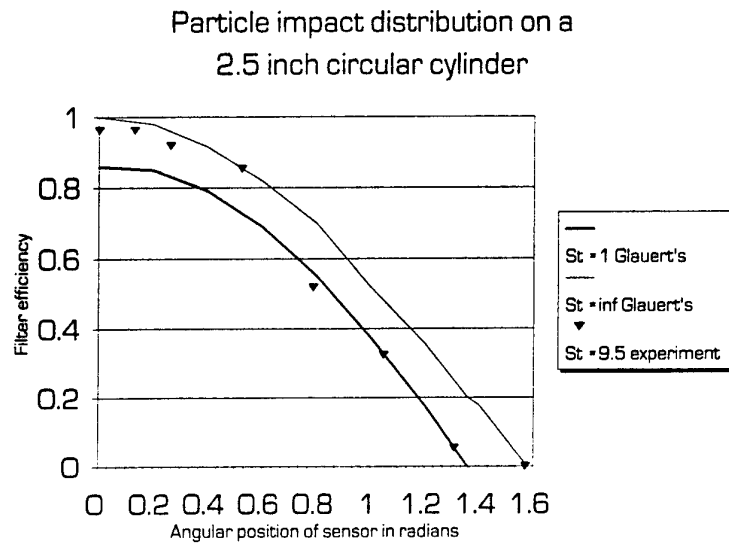


Figure (12) Comparison of measured particle counts on the cylinder to Glauert's (1940) prediction.

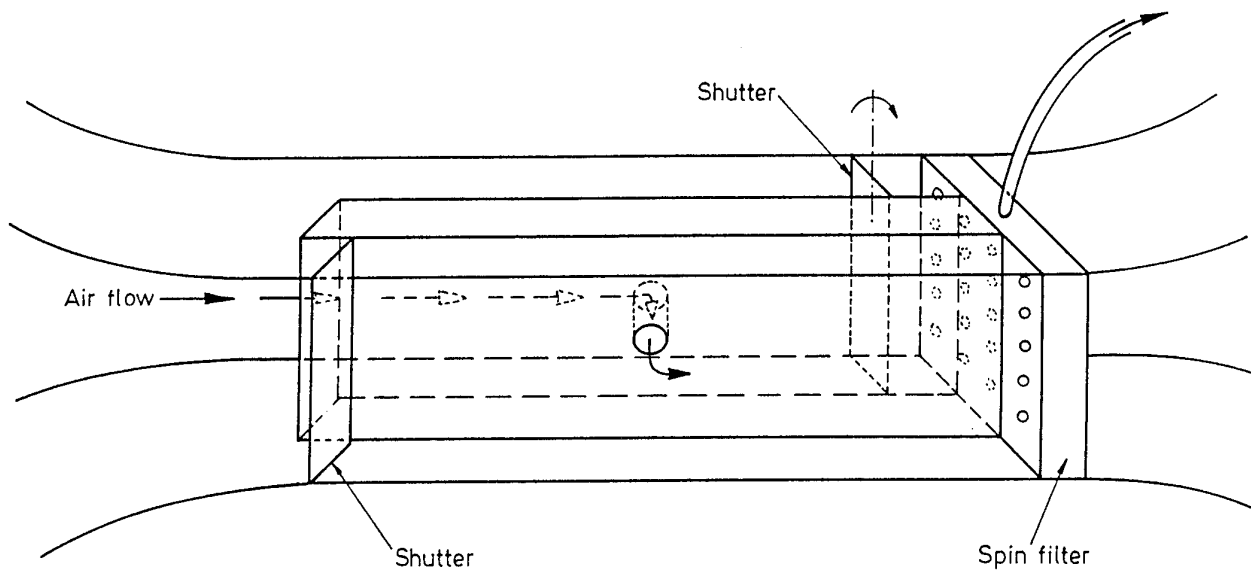


Figure (13) Experimental arrangement for the film cooling hole experiments.

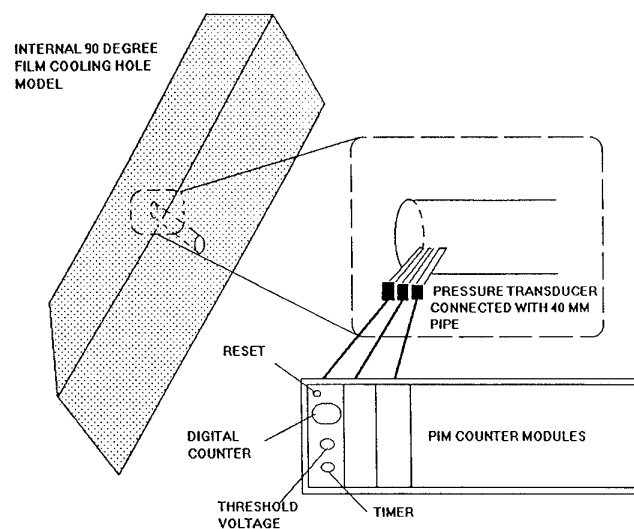


Figure (14) Particle impact meter module.

## IMNV6SR4

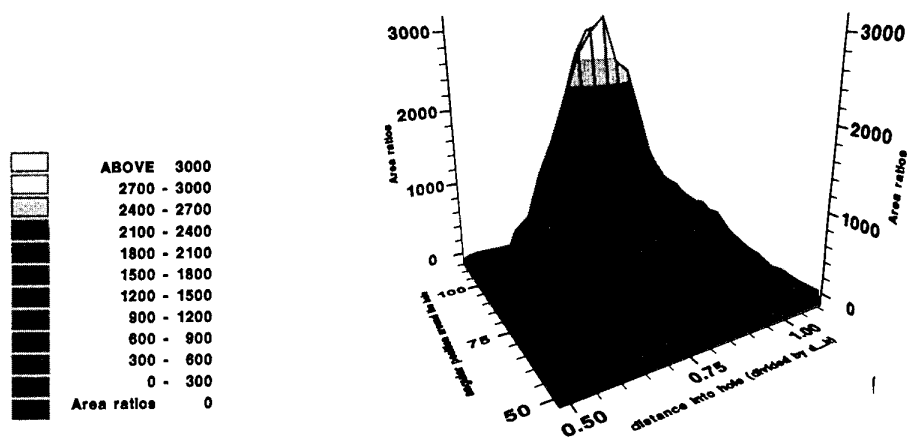


Figure (15) Particle impact concentration,  $A_i/A_d$ , map for the 90° hole.

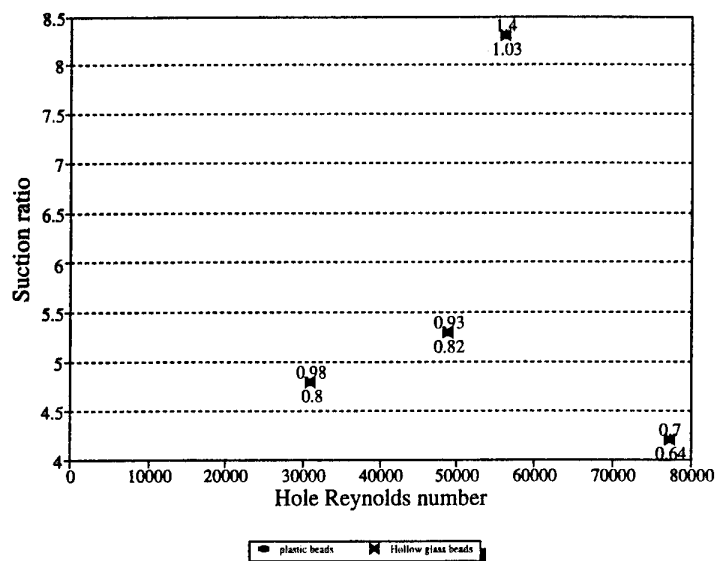


Figure (16) Experimental peak concentration locations as a function of suction ratio and hole Reynolds number for different scaled particles.

The data label is distance of the concentration peak from the hole entrance divided by hole diameter.

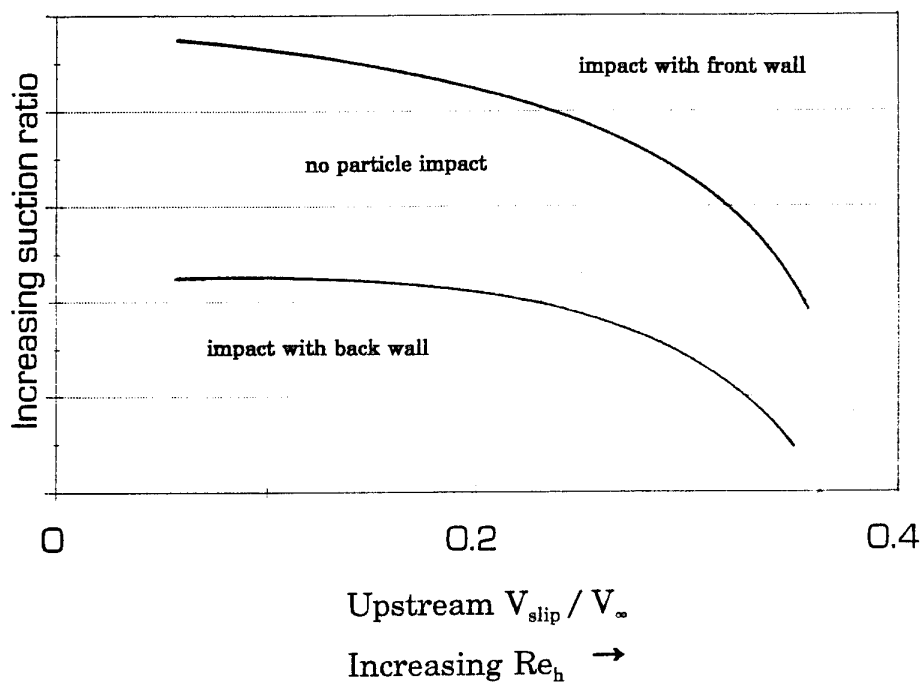


Figure (17) Conditions to avoid particle impact in the 30° hole.

## EXPERIMENTAL AND NUMERICAL SIMULATIONS OF THE EFFECTS OF INGESTED PARTICLES IN GAS TURBINE ENGINES

A. Hamed and W. Tabakoff

Department of Aerospace Engineering and Engineering Mechanics  
University of Cincinnati  
Cincinnati, Ohio 45221, USA

### SUMMARY

Particles ingested in gas turbine engines follow trajectories that generally deviate from the flow streamlines and impact the component surfaces causing erosion damage. This paper deals with the experimental and numerical simulations of particle dynamics including surface interactions and the associated blade erosion in gas turbine engines. The experimental studies of particle surface impacts include the non intrusive measurements of particle bounce conditions and the erosion testing of blade materials and blade coatings. Data obtained in the University of Cincinnati's high temperature erosion test facility at temperatures up to 1500°F for different alloys and coatings are presented. The numerical studies to simulate the particle dynamics in turbomachines are described. Results of combined experimental and computational modeling are presented for the particle dynamics, the associated turbomachinery blade erosion, and performance loss. The probabilistic modeling of the experimentally measured variance in the particle bounce conditions and the loss of performance associated with particle ingestion are discussed.

### INTRODUCTION

It is very difficult to remove the solid particles from the gas stream without taxing the performance of gas turbine engines operating in environments with suspended solid particles. Even small particles of one to thirty micron size have been known to be very damaging to the exposed components of coal burning turbines [1]. Surface erosion by particle impacts increases tip clearances and blade surface roughness and produces changes in the blade shape especially near the leading and trailing edges. All these combined effects lead to a permanent deterioration in performance and increased repair and maintenance costs.

Some of the mechanisms that cause particles' ingestion are: (a) the vortex from engine inlet-to-ground during high power setting, with the aircraft standing or moving on the runway, (b) sand storms transporting sand to several thousand feet altitude, (c) thrust reverser efflux at low airplane speed may blow sand, ice and other particles into the engine inlets. Erosive solid particles may also be produced during the combustion process, from the burning of different types of heavy oils or synthetic fuels. One of the most dangerous environments for aircraft engines is particulate clouds from the eruption of volcanoes. Tests performed at the University of Cincinnati's erosion wind tunnel show that volcanic ash is four times more erosive than quartz sand. Several incidents have been related to jet engine operation in clouds of volcanic ash.

Examples of these incidents are a British Airways 747 Boeing powered by four Rolls Royce RB211 engines on June 23, 1982, a Singapore Airline 747 Boeing powered by Pratt and Whitney engines, and a Boeing 747-400 aircraft approaching Anchorage, Alaska, on December 15, 1989 that entered a cloud of volcanic ash from Redoubt Volcano.

Under two-phase flow conditions, the gas and particles experience different degrees of turning through the blade channels. The degree of turning and acceleration or deceleration achieved by the particles depend on the ratio of the viscous forces to the inertial forces experienced by the particles. This leads to variations in particle concentration across the blade channels and causes a change in the properties of the gas flows which alters the engine performance during the period of particle ingestion [2]. If the particles are erosive, their impingement on the blade surfaces can cause severe erosion damage. This damage is manifested by pitting and cutting of the blade leading and trailing edges, and a general increase in the blade surface roughness [3].

Blade erosion in turbomachines is affected by many factors such as blade geometry, blade row location, rotational speed, flow conditions, blade material and particles' characteristics. A clear understanding of the factors affecting the particle impact conditions and the associated blade surface erosion requires basic experimental and analytical studies that simulate the erosive particle impact conditions in the engine environment. These studies which are essential to predicting blade surface erosion intensity and pattern have been conducted at the University of Cincinnati's Propulsion Laboratory over the past twenty-five years. This paper describes some of these studies, the experimental facilities in which they were performed, and the methodologies developed for the numerical simulations of particle trajectories and blade erosion in multistage turbomachines.

### EXPERIMENTAL STUDIES OF PARTICLE SURFACE IMPACTS

#### I. Experimental Determination of Surface Erosion

The erosion of metals by solid particle laden flow have been investigated experimentally under various particulate flow conditions [4]. According to these studies, the parameters that influence the surface erosion include the particles' impacting velocity and impingement angle, and the metal and gas temperatures. Empirical erosion equations [5] can be derived for a given particle target material combination from the erosion measurements. These equations have been employed

in calculating the blade erosion based on the predicted particle impact data in the particle trajectory simulations [4, 6]. The particle trajectory simulations require bounce models [4, 6, 7] to represent the particle rebound conditions after the surface impacts. Since these represent the initial conditions for the remainder of the particle trajectory, the fidelity of the rebound model in reproducing the experimentally measured particle bounce conditions [8] is critical.

### Erosion Test Facilities

The erosion testing of blade materials and their coatings require especially designed tunnels to simulate the actual particle-surface interactions in gas turbine engines. The high temperature erosion test facility at the University of Cincinnati's Propulsion Lab was designed to provide erosion in the range of operating temperatures experienced in compressors and turbines. In addition to the high temperatures, the facility properly simulates all the erosion parameters which were determined to be important from aerodynamic's point of view. Close attention was given to the flow aerodynamics to insure that important parameters, such as the angle of impact, are not masked or altered.

A schematic of the erosion test facility is shown in Fig. 1. It consists of the following components: particle feeder (A), main air supply pipe (B), combustor (C), particle preheater (D), particle injector (E), acceleration tunnel (F), test section (G), and exhaust tank (H). The equipment functions as follows: a measured amount of abrasive grit of a given mixture of constituents is placed into the particle feeder (A). The particles are fed into a secondary air source and blown up to the particle preheater (D), and then to the injector (E), where they mix with the main air supply (B), which is heated by the combustor (C). The particles are then accelerated by the high-velocity air in a constant-area steam-cooled duct (F) and impact the specimen in the test section (G). The particulate flow is then mixed with the coolant and dumped in the exhaust tank.

The particle velocity is controlled by varying the tunnel air flow, while the particle impingement angle is controlled through the target sample rotation relative to the flow. The test temperature is varied by heating the flow stream which in turn heats the erosion and sample to the desired temperature. Figure 1 shows that the tunnel geometry is uninterrupted from the acceleration tunnel into the test section. In this manner the particle laden flow is channeled over the specimen and the aerodynamics of the fluid passing over the sample are preserved. A detailed description of the erosion wind tunnel and the particle feeder is given in Ref. [9]. Numerous blade materials and coatings have been tested in the described tunnel to determine their resistance to erosion in particulate flow environments under various flow conditions [10].

### Erosion Test Conditions and Tested Materials

An extensive series of blade material erosion tests were conducted at the University of Cincinnati for the Department of Energy [11, 12 and 13]. The tested materials include

superalloys INCO-738, MAR-M246, X-40 and others, and blade coatings, 'C' (aluminized) with substrate X-40, 'N' (aluminized) with substrate M-246, 'RT-22' (platinum aluminized) with M-246 substrate, 'RT-44' (low rodium/platinum aluminized) with X-40 substrate. In addition, chemical vapor deposition coatings such as titanium carbide (TiC), titanium nitride (TiN) and alumina oxide ( $Al_2O_3$ ) were investigated under the National Science Foundation [14] sponsorship. These are widely used as thermal, wear, and corrosion barrier coatings.

The experimental measurements were obtained for fly ash particles with impact velocities ranging between 183 and 366 m s<sup>-1</sup> at temperatures ranging from ambient to 650°C. The test specimens were 25.4 mm long, 6.35 mm thick and 12.7 mm wide. Test data were accumulated by setting the particle impingement angle at 15°, 30°, 45°, 60° and 90° for each of the different test temperatures and particle velocities.

Two types of erosion tests were conducted to obtain different types of erosion data, namely the erosion rate and the cumulative erosion mass loss (cycling). The erosion rate is defined as the ratio between the change in the sample mass and the mass of the impacting particles. The erosion rate tests were carried out in one cycle using 100 gm of particles impacting the sample surface. The cumulative erosion mass loss tests on the other hand were conducted in multiple cycles. In each cycle, the specimen is impacted by a pre-weighed increment of particle mass. After each particle mass increment had impacted the sample, its surface is cleaned, the specimen weighed, and the change in specimen weight recorded. The cumulative mass erosion tests were conducted only at the impact angles corresponding to maximum erosion.

### Erosion Test Results

Sample test results for M-246 at 482°C are presented in Fig. 2 which demonstrates the effects of the particle impact velocity and impingement angle on the erosion rate. Figure 3 compares the erosion rates for 'N' and 'RT22B' coatings to the uncoated M-246 base material at a given velocity of 366 m/s and temperature of 815°C. This figure indicates that both coatings reduce the erosion rates with RT22B offering higher resistance to erosion. Figure 4 compares the maximum erosion rates of two superalloy base materials, namely M-246 and X-40 with different coatings at 815°C and 366 m/s particle velocity. One can see that the aluminide coatings ('C' and 'N') reduce the erosion rates of X-40 by 60% and M246 by 80%. However, the platinum aluminide coating (RT22 and RT44) offer the best erosion protection with nine and four-fold reduction in the erosion from that of the base materials (M246 and X-40).

The erosion mass loss (cycling) test results at 30° impingement angle are presented in Fig. 5 for RT22B coating. Figure 5b shows linear variation of mass erosion loss (constant erosion rate in Fig. 5a) up to 450 g of impacting particles. Beyond this, the coating is completely deteriorated as indicated by the sharp rise in the erosion rate. The cycling tests were

also used to determine the coating life in terms of the mass of impacting particles at which the initial penetration in the substrate is observed as indicated in Fig. 5.

## II. Experimental Determination of Particles' Bounce Conditions

The simulation of particulate flow dynamics in turbomachines requires separate models to determine the particle rebound conditions after surface impacts. These particle surface interactions occur as a consequence of the particle trajectory deviations from the flow streamlines due to their higher inertia. In addition to causing surface erosion these impacts also influence the rest of the particle trajectories including subsequent particle surface impacts and the particle redistribution through the flow field. It is particularly important to accurately model the particle surface interactions in turbomachines because of the drastic changes in the magnitude and direction of the particles' velocity after impacting the rotor blades and the effect this has on the subsequent blade rows [15].

### Experimental Set-Up

The particle rebound characteristics are determined in a tunnel similar to the erosion tunnel of Fig. 1, that is equipped with a glass window at the test section to access the measurements of the particle velocities before and after they impact the target sample. The nonintrusive velocity measurements are obtained using Laser Doppler Velocimetry (LDV). The LDV and data acquisition systems are described below.

#### a) LDV System

The LDV system used in the measurements of the particle restitution characteristics is shown schematically in Fig. 6 and described in detail in references [15, 16, 17 and 18]. It consists of the laser tube, optics, frequency shifters and photomultipliers. The light source is a five Watt argon-ion Spectra Physics, model 164-09 laser tube. The laser beam leaving the tube is separated in the dispersion prism into components with different wavelengths. Three beams with the highest intensities are used to measure the three velocity components. The beams cross at one common measuring volume producing three sets of fringes, one for each color. The scattered light from the particles in the measuring volume is collected in the off-axis backward scatter mode. Frequency shifters were used on all the three beams to sense the flow direction and reduce fringe bias errors. The analog data from the photomultipliers in the receiving optics mixed with the signals from frequency shifters are transferred to the data acquisition system.

#### b) Data Acquisition

The data acquisition system consists of three signal processors, an external circuit, and a personal computer with the associated hardware and software. While the data acquisition is software driven, the data timing is controlled by an external circuit. The LDV signals coming from the photo-

multipliers are processed in the three TSI 1990 counter type signal processors. The processed data are collected by an IBM PC/AT compatible computer for further calculations and data storage. The control of the data transfer and the synchronization of data coming from the three different channels are performed by the external circuit.

During the data collection, the external circuit is activated in order to detect the arrival of data ready signals. Whenever the external circuit receives a data ready pulse, it sends a data inhibit signal to the associated processor, preventing it from acquiring new data. When all the three data ready signals arrive within the specified coincidence limit, the circuit holds the data at the output buffers of the processors, and instructs the computer to transfer them into a file through the digital input port. The external circuit is then reset through the digital output port of CTM-05, the processors are reactivated and the procedure is repeated until a specified number of samples is collected.

### Restitution Test Results

The restitution coefficient or restitution ratio is a measure of the kinetic energy loss upon impact of two objects. Since the erosion is dependent on the erodent particle kinetic energy loss upon impacting the target, the restitution ratio will give a good indication of the type of the particle-material interaction. An erosive impact occurs when the contaminant particle is much harder than the target material. Therefore, the restitution ratio will be a measure of the distortion of the target material rather than distortion of the erosive particle.

Grant and Tabakoff [15] were the first to investigate thoroughly the rebound characteristics of high speed eroding particles. It was concluded that the restitution ratio  $V_2/V_1$ , which is directly related to the kinetic energy loss during an impact, does not give sufficient information in regard to erosion. Referring to Fig. 7, a set of two restitution ratios, are used to describe the particle bounce condition either the normal ( $V_{N2}/V_{N1}$ ) and tangential ( $V_{T2}/V_{T1}$ ) components or the velocity ( $V_2/V_1$ ) and directional ( $\beta_2/\beta_1$ ) ratios. They represent the ratio between the rebound and incoming conditions at the sample surface. Our measurements indicate that these ratios mainly depend upon the impingement angle for a given particle material combination [15].

The rebound conditions of the impacting particles exhibit variation at each of the tested conditions as shown in Fig. 8. Therefore the particle restitution ratios can be described in a statistical sense only. This can be attributed to the different geometric situations that might occur at impact. After an incubation period, the target material will become pitted with craters, and in fact after a slightly longer period, a regular ripple pattern will form on the eroded surfaces. Thus, the local impact angle between the small particles and the eroded surface may deviate considerably from the geometric average. Furthermore, the particles themselves are irregular in shape, some with sharp corners. As the particle approaches the specimen, the orientation of the particle is, for the most part,

random. Thus, some particles will impact on a flat surface and do very little work on the target material. Others will impact with a corner oriented in a manner similar to that of a cutting tool and will remove material from the surface. Figure 8 illustrates typical histogram of the restitution ratio for fly ash impacting a 2024 aluminum sample target material at  $\beta_1 = 30^\circ$ .

Figures 9 and 10 present typical rebound data for M246 alloy with and without "N" coating; in the form of tangential ( $V_{T2}/V_{T1}$ ) and normal ( $V_{N2}/V_{N1}$ ) velocity restitution ratios, as well as total velocity ( $V_2/V_1$ ) and the directional ( $\beta_2/\beta_1$ ) restitution ratios. The data points in these figures represent the mean values of the experimentally measured restitution parameter at each impact angle. The solid lines in Figures 9 and 10 represent the polynomial curve fits expressed by the following equations:

For M-246 Alloy

$$e_T = \frac{V_{T2}}{V_{T1}} = 1.00 - 0.0083224\beta_1 - 8.09523 \times 10^{-5}\beta_1^2 + 1.78601 \times 10^{-6}\beta_1^3 \quad (1)$$

$$e_N = \frac{V_{N2}}{V_{N1}} = 1.00 - 0.0080984\beta_1 - 0.0012261\beta_1^2 + 2.30864 \times 10^{-5}\beta_1^3 - 1.2922 \times 10^{-7}\beta_1^4 \quad (2)$$

$$e_V = \frac{V_2}{V_1} = 1.00 - 0.00601123\beta_1 - 0.000957896\beta_1^2 + 1.77426 \times 10^{-5}\beta_1^3 - 9.94 \times 10^{-8}\beta_1^4 \quad (3)$$

$$e_\beta = \frac{\beta_2}{\beta_1} = 1.00 + 0.0087242\beta_1 - 0.000834276\beta_1^2 + 1.63771 \times 10^{-5}\beta_1^3 - 9.75683 \times 10^{-8}\beta_1^4 \quad (4)$$

#### NUMERICAL SIMULATIONS OF THE INGESTED PARTICLE DYNAMICS AND THEIR EFFECTS

We have developed separate numerical procedures to simulate the dynamics of ingested particles in the various engine passages and to predict their erosive effects on the various components. The simulations of the particle dynamics involve the numerical integration of their equations of motion as they travel through the flow field between solid surface impacts. These simulations require accurate description of the three dimensional flow fields in the blade to blade passage, since they affect the force of interaction between the two phases. The simulations also require models for the particle rebound conditions after each of the surface impacts to constitute the initial conditions for the remainder of their trajectory. The restitution ratios for a given particle-target

material combination are used with predicted particle impact conditions relative to the impacted surface to determine the magnitude and direction of the rebounding particle velocity. The output of the trajectory computations in the form of statistical distributions of surface impact locations, and the associated impact conditions as well as the frequency of these impacts constitute the input to the blade surface erosion prediction code.

#### Particle Trajectory Simulations

In considering the particle trajectories through turbomachines, the effect of the forces due to gravity and interparticle interactions are negligible compared to those due to aerodynamic drag and centrifugal forces [19]. The general form of the equations of motion of particles immersed in a fluid are written in a rotating frame of reference using cylindrical polar coordinates as follows:

$$\frac{d^2 r_p}{d\tau^2} = F_r + r_p \left( \frac{d\theta_p}{d\tau} + \omega \right)^2 \quad (5a)$$

$$r_p \frac{d^2 \theta_p}{d\tau^2} = F_\theta - \frac{2dr_p}{d\tau} \left( \frac{d\theta_p}{d\tau} + \omega \right) \quad (5b)$$

$$\frac{d^2 z_p}{d\tau^2} = F_z \quad (5c)$$

where  $r_p$ ,  $\theta_p$ , and  $z_p$  define the particle location in cylindrical polar coordinates, and  $\omega$  is the rotor blade angular velocity. The centrifugal force and Coriolis acceleration are represented by the last term on the right-hand side of Eqs. (5a) and (5b). The first term on the right-hand side of Eqs. (5a)-(5c) represents the force of interaction between the two phases, per unit mass of particles. The force of interaction between the two phases is dominated by the drag due to the difference in velocity between the solid particles and the gas flow and is given by

$$\bar{F} = \frac{3 C_D}{4 d} \left[ \left( V_r - \frac{dr_p}{d\tau} \right)^2 + \left( V_\theta - \frac{d(r_p \theta_p)}{d\tau} \right)^2 + \left( V_z - \frac{dz_p}{d\tau} \right)^2 \right]^{1/2} \cdot (\bar{V} - \bar{V}_p) \quad (6)$$

where  $V_r$ ,  $V_\theta$ , and  $V_z$  represent the relative gas velocities in the radial, circumferential, and axial directions, respectively, and  $\rho$  and  $\rho_p$  are the gas and solid particle material densities,  $d$  the particle diameter, and  $C_D$  the particle drag coefficient. Empirical relations are used to fit the drag coefficient curve



over a wide range of Reynolds numbers [7, 20, 21].

The numerical integration of equations (5a)-(5c) are carried out in the three dimensional flow field of each blade row passage starting with the particle initial conditions. The same equations are used in both rotor and stator, with  $\omega$  set equal to zero and using the absolute gas velocities in the particle trajectory computations through stators.

### Particle Trajectory Results

A sample of the particle trajectory simulation results through a two stage axial flow turbine which was described by Roelke et al. [22] are shown in Fig. 11. The results represent the projections of 2.5 and 135 microns diameter ash particle trajectories which were simulated at 1893 rpm and 7.0171 lb/sec air flow. This figure demonstrates how the deviation of the particle trajectories from the streamlines increases with increased particle size, with many of the larger particles crossing the blade to blade passage and impacting both pressure and suction surfaces. They also tend to migrate in the radial direction as they centrifuge because of the circumferential velocities they acquire from the blade surface impacts, particularly those with the rotor.

The computed particle impact locations with the blade pressure surface of the two stage turbine are presented in Fig. 12 for the CG&E coal ash particles whose size distribution is listed in Table I. The predicted blade pressure surface impact locations as determined from the trajectory simulations of uniform size particles at the mean value of Table I are presented in Fig. 13. Comparing the two figures, one can see that the simulations representing the real ash particle sizes result in more distributed particle impacts in the radial directions since a large number of smaller particles are not centrifuged towards the tip [23].

Table I. Ash Particle Size Distribution

Diameter, $\mu\text{m}$	Percent
1-2	24
2-3	12
3-4	22.7
4-5	2.7
5-6	6.7
6-7	--
7-8	2.7
8-9	5.3
9-10	1.3
10-15	17.3
15-20	4.0
20-25	1.3

### Effect of Particle Size

In general, the trajectories of the smaller particle are more affected by the flow field, since they can accelerate quickly and approach faster the local gas velocity. Therefore, three dimensional flow phenomena such as secondary flow tend to transport the small particles in the end wall region towards

the trailing edge of the blade suction surface [24]. On the other hand, the larger particles trajectories are dominated by the surface impacts and are therefore affected by the blade to blade passage geometry and the particle initial conditions. Hamed [25] demonstrated that the magnitude and direction of the particle velocities as they enter subsequent blade rows are strongly affected by their size. The particle velocity triangles indicate that the larger particles tend to have large negative incidence angles as they enter the blade row and consequently impact the suction side of the blade leading edges in all but the first stator.

A unique phenomena occurs in the larger particle trajectories between the stator and the following rotor. A number of these large particles traverse back and forth in the space between the blade rows as they rebound from the rotor blade leading edge, reenter the preceding stator blade row, impact the stator and impact the nozzle blade trailing edge. They might repeat this cycle more than once before they finally enter and go through the rotor blade passage [24]. Figure 14 shows the trajectories of three particles of different sizes that initiate at the same location in the stator blade passage. This figure demonstrates that the larger particle trajectory exhibit this phenomena and that the three particles eventually end up in different rotor blade passages.

A similar phenomena was observed in the particle trajectories through radial inflow turbines, when some of the particles bounce back and forth in the vaneless nozzle region between the nozzle exit and the rotor tip [26]. In radial turbines, the centrifugal forces tend to push the particles back to the nozzle vanes while the aerodynamic drag act radially inward. It was determined numerically and demonstrated experimentally that particles within a given size range get trapped in the vaneless nozzle zone and do not progress through the rotor [26].

### Blade Erosion Results

The impact statistics as determined from the simulated trajectories are used together with the experimentally derived erosion equations for a given particle target combination to predict the blade surface erosion pattern. The empirical erosion equation is written in the following general format:

$$\epsilon = k_1 \left[ 1 + C_k \left\{ K_2 \sin \left( 90 \frac{\beta_1}{\beta_0} \right) \right\}^2 V_1^2 \cos \beta_1 (1 - e_t^2) + k_3 (V_1 \sin \beta_1)^4 \right] \quad (7)$$

where  $V_1$  and  $\beta_1$  are the impact velocity and impingement angle respectively.  $K_1$ ,  $K_2$ ,  $K_3$  are constants that depend on the particle target material combination.  $e_t$  is the tangential restitution ratio whose magnitude also depends on the impact angle (see equation (1)). The value of the last coefficient  $C_k$ , depends on both the impact angle  $\beta_1$  and the angle of maximum erosion, with  $C_k=1$  if  $\beta_1$  is greater than  $2\beta_0$  otherwise it is equal to zero.

Typical blade erosion results are presented in Fig. 15 using the impact statistics of 75,000 ingested particles or  $22 \times 10^{-5}$  grams of CG&E ash in the two stage turbine [22]. The blade erosion parameter is defined as the mass removal per unit area of the blade surface per unit mass of ingested particles in  $\text{mg m}^{-2} \text{gm}^{-1}$ . The figure indicates that the blade pressure surface erosion rate in the first nozzle increases in the second half of the axial chord and reaches maximum near the trailing edge. The highest erosion rate in the first rotor is seen near the leading edge where both the particle impact frequencies and impingement velocities are high. As the particles are centrifuged in the radial direction after their impacts with the first rotor, the maximum erosion rates in the subsequent blade rows are observed at the tip of the leading edge. Similar particle trajectory and blade erosion studies were carried out in axial [27] and centrifugal [28] compressors, using the same methodology.

Erosion leads to increased blade tip clearances and airfoil roughness in turbines. In addition, particulates accumulate along the cooling air path within the blade cooling passages, and blade leading edges, and tip distress due to internal cooling cavity dust accumulation and blockage. In compressors [15], rotor tip erosion causes reduced chord length and leading edge tip corner rounding and thinning, resulting in increased tip clearance. Stator erosion is mostly observed on the pressure side causing rougher vane surfaces. Inspection results of engines which have exhibited deterioration due to in-service ground particles ingestion were reported in references [29, 30]. Analysis of the engine disassembly inspections show that causes of deterioration fall into three basic categories: deposition, erosion, and rubbing wear [31-33].

#### **Probabilistic Modeling of Particle Bounce**

Experimental studies have long reported variance in particle rebounding conditions as those shown in Fig. 8. However, deterministic bounce models based on experimentally measured mean values of the particle restitution ratios continue to be used in the particle trajectory simulations. In these deterministic simulations, the experimentally measured variance in the particle restitution characteristics is not represented and the particle initial conditions uniquely determines their trajectories in the flow field and their surface impacts. Hamed et al. [34, 35] developed probabilistic methods to model the variance in the particles restitution characteristics in gas turbines and inlet separators, and their effect on the predicted particle trajectories and blade surface erosion. Results of blade erosion rate for 150 micron sand particles (Fig. 16) in the first stage of an axial flow turbine [34] indicate that the most significant differences are observed near the trailing edge of the stator suction surface and the leading edge of the rotor suction surface, where the probabilistic model predicts higher blade erosion. In the case of trajectory simulations in inlet particle separator, the trajectories with a probabilistic bounce model (Fig. 17) predicted separator efficiencies 2 to 5% less than the deterministic model for particles greater than 10 microns [35].

#### **ACKNOWLEDGEMENTS**

This work was partially supported by the National Science Foundation under Grant No. INT-9204963 and NSF Grant CTS-90123209, by the U.S. Department of Energy Contract 19X-89628C, Oak Ridge National Laboratory, Oak Ridge, Tennessee, and by the U.S. Army Research Office-Durham, under equipment Contract DAAL03-7-G-0017.

#### **REFERENCES**

1. McCay, L., "The Coal Burning Gas Turbine Project," Report of Interdepartmental Gas Turbine Steering Committee, Australian Government Publishing Service, 1973.
2. Tabakoff, W., "Review - Turbomachinery Performance Deterioration Exposed to Solid Particles Environment," ASME Journal of Fluids Engineering, Vol. 106, June 1984, pp. 125-134.
3. Tabakoff, W., "A Study of the Surface Deterioration due to Erosion," ASME Journal of Engineering for Power, October 1983, pp. 834-839.
4. Hamed, A., Tabakoff, W. and Wenglarz, R., "Lecture Series on Particulate Flows and Blade Erosion," May 24-27, 1988, von Karman Institute for Fluid Dynamics, Belgium.
5. Tabakoff, W., "Turbomachinery Alloys Affected by Solid Particles," International Journal of Turbo and Jet Engines, 7, 1991, pp. 207-215.
6. Hamed, A. and Moy, H., "Probabilistic Simulation of Fragment Dynamics and Their Surface Impacts in the SSME Turbopump," Numerical Simulations in Turbomachinery, ASME FED-Vol. 120, 1991, pp. 141-150.
7. Hamed, A. and Tabakoff, W., "The Effect of Probabilistic Restitution Characteristics of Particle Surface Interactions on the Particle Dynamics in Axial Flow Turbines," Proceedings International Symposium on Air Breathing Engines, Nottingham, U.K., 1-6 September 1991, pp. 1166-1174.
8. Hamed, A. and Tabakoff, W., "Experimental Investigation of Particle Surface Interactions for Turbomachinery Applications," Laser Anemometry Advances and Applications, 1991, Vol. 2, Dybbs, A., Editor, ASME Publication, pp. 775-780.
9. Tabakoff, W. and Wakeman, T., *Test Facility for Material Erosion at High Temperature*, ASTM Special Publication 664, 1979, p. 123.
10. Tabakoff, W., "Investigation of Coatings at High Temperature for Use in Turbomachinery," J. of Surface and Coatings Technology, 39/40, 1989, pp. 97-115.
11. Tabakoff, W., Hamed, A., Metwally, M. and Pasin, M., "High Temperature Erosion Resistance of Coatings for Gas Turbine," Journal of Engineering for Gas Turbine and

- Power, April 1992, Vol. 114, pp. 242-249.
12. Tabakoff, W., Metwally, M., "Coating Effects on Particle Trajectories and Turbine Blade Erosion," *Journal of Engineering for Gas Turbines and Power*, April 1992, Vol. 114, pp. 250-257.
  13. Tabakoff, W., "High Temperature Erosion Resistance of Coatings for Use in Gas Turbine Engines," *Journal of Surface and Coatings Technology*, April 1992, Vol. 52, pp. 65-79.
  14. Shanov, V., Tabakoff, W. and Metwally, M., "Erosive Wear of CVD Ceramic Coatings Exposed to Particulate Flow," *Surface and Coatings Technology*, 54/55 (1992) pp. 25-31.
  15. Grant, G. and Tabakoff, W., "Erosion Prediction in Turbomachinery Resulting from Environmental Solid Particles," *Journal of Aircraft*, Vol. 12, No. 5, May 1975, pp. 471-478.
  16. Tabakoff, W., Malak, M. and Hamed, A., "Laser Measurements of Solid Particles Rebound Parameters Impacting on 2024 Aluminum and 6A1-4V Titanium Alloys," *AIAA Journal of Aeronautics and Astronautics*, Vol. 25, No. 5, May 1987, pp. 721-726.
  17. Tabakoff, W., Murugan, D., and Hamed, A., "Effect of Target Materials on the Particle Restitution Characteristics for Turbomachinery Applications," *AIAA Paper 94-0143*, January 10-13, 1994.
  18. Tabakoff, W., "Measurements of Particles Rebound Characteristics on Materials Used in Gas Turbines," *AIAA Paper 89-1693*, 1989.
  19. Hamed, A., "Particle Dynamics of Inlet Flow Fields with Swirling Vanes," *AIAA Paper 81-0001*, 19th AIAA Aerospace Sciences Meeting, Jan. 1981, St. Louis, MO.
  20. Bailey, A.B. and Hiatt, J., "Sphere Drag Coefficient for Broad Range of Mach and Reynolds Numbers," *AIAA Journal*, Vol. 10, No. 11, 1972, pp. 1437-1440.
  21. Crowe, C.T., Drag Coefficient of Particles in Rocket Nozzle, *AIAA J.*, 5, (5), 1967, pp. 1021.
  22. Roelke, R.J., Stabe, R.G. and Evans, D.G. (1966), "Cold-Air Performance Evaluation of Scale Model Oxidizer Pump-Drive Turbine for the M-1 Hydrogen-Oxygen Rocket Engine-II. Overall Two-Stage Performance," *NASA TND-3368*.
  23. Tabakoff, W., Hamed, A. and Metwally, M., "Effect of Particle Size Distribution on Particle Dynamics and Blade Erosion in Axial Flow Turbines," *Journal of Engineering for Gas Turbines and Power*, Vol. 113, October 1991, pp. 607-615.
  24. Hamed, A., "Influence of Secondary Flow on Turbine Erosion," *Journal of Turbomachinery*, Vol. 111, 1989, pp. 310-314.
  25. Hamed, A., "Effect of Particle Characteristics on Trajectories and Blade Impact Patterns," *Journal of Fluids Engineering*, Vol. 110, March 1988, pp. 33-37.
  26. Clevenger, W. and Tabakoff, W., "Similarity Parameters for Comparing Erosive Particle Trajectories in Hot Air And Cold Air Radial Inflow Turbines," *Journal of Engineering for Power*, October 1974, pp. 358-364.
  27. Tabakoff, W., "Compressor Erosion and Performance Deterioration," *Journal of Fluids Engineering*, Vol. 109, September 1987, pp. 297-306.
  28. Tabakoff, W., Hamed, A., "Effect of Environmental Particles on Radial Machine," *AIAA Journal for Propulsion and Power*, December 1989, pp. 731-737.
  29. Crosby, J.K., "Factors Relating to Deterioration Based on Rolls Royce RB211 in Service Performance," *Turbomachinery Performance Deterioration*, ASME Publication, FED-Vol. 37, 1986, pp. 41-47.
  30. Sasahara, O., "JT9D Engine/Module Performance Deterioration Results from Back to Back Testing," *ASME Publication FED-Vol. 37*, 1986, pp. 25-32.
  31. Tabakoff, W., Balan, C., "A Study of the Surface Deterioration Due to Erosion," *J. of Engineering for Power*, October 1983, pp. 834-838.
  32. Tabakoff, W., "Compressor Erosion and Performance Deterioration," *J. of Fluids Engg.*, Vol. 109, September 1987, pp. 297-306.
  33. Dunn, M.G. et al., "Performance Deterioration of a Turbofan and a Turbojet Engine Upon Exposure to Dust Environment," *ASME Transactions*, Vol. 109, July 1987, pp. 336-343.
  34. Hamed, A. and Kuhn, T.P., "Effects of Variational Particle Restitution Characteristics on Turbomachinery Erosion," *ASME Paper 93-GT-124*, Int. Gas Turbine and Aeroengine Congress, Cincinnati, OH, May 1993.
  35. Hamed, A., Jun, Y.D. and Yeuan, J.J., "Particle Dynamics Simulations in Inlet Separator with an Experimentally Based Bounce Model," *AIAA Paper 93-2156*, AIAA/SAE/ASME/ASME 29th Joint Propulsion Conf., Monterey, CA, June 1993.

## QUESTIONS

### **H.J. KOLKMAN (Ne)**

- Q. Yesterday, Mr. Mann of Rolls Royce told us that the erodent particles are fragmented in the first compressor stage. Are the particle sizes used in the calculation of the trajectories realistic? What is the particle size in Figures 3 and 5?
- A. The calculations are for a turbine using fly ash; the particles are small and do not fragment. The size of the particles used in Figures 3 and 5 are 15 microns.

### **V.R. PARAMESWARAN (Ca)**

- Q. For a particular material, how sensitive is the angle at which maximum erosion occurs to the temperature of testing? Is any relationship established? How sensitive is the erosion loss to the temperature of testing, for a particular target and erodent?
- A. The erosion rate is very sensitive to high temperature. The maximum erosion angle does not change too much with increasing temperature, as is shown in several figures in the paper.

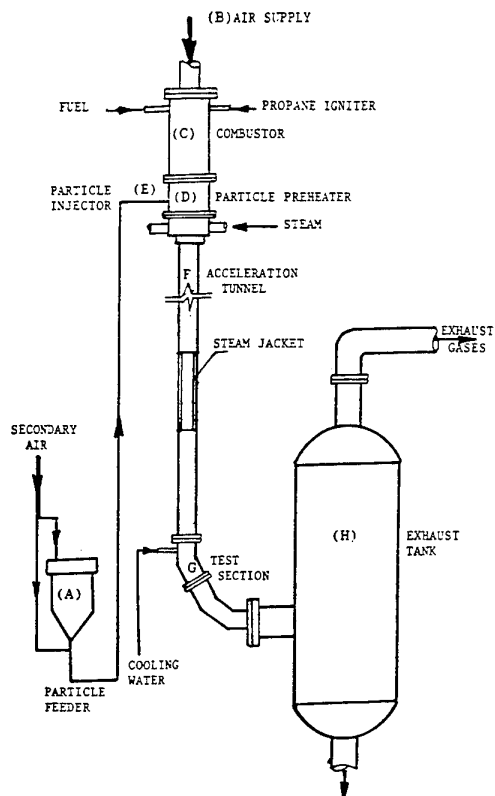


Fig. 1. Schematic of Erosion Test Facility.

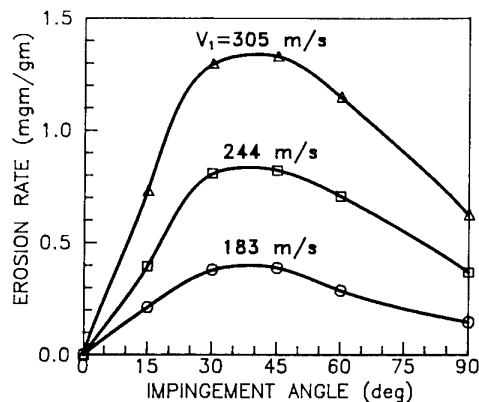
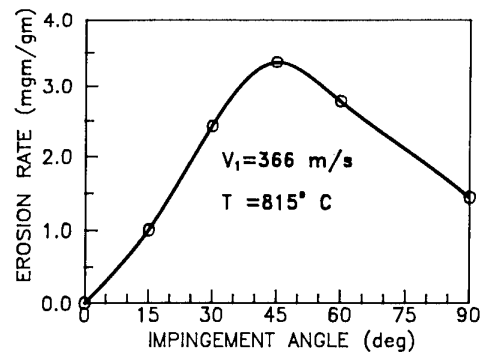
Fig. 2. M246 Erosion Rate Variation with Impingement Angle;  $T=482^{\circ}$ .

Fig. 3a. M246 Erosion Rate Variation with Impingement Angle.

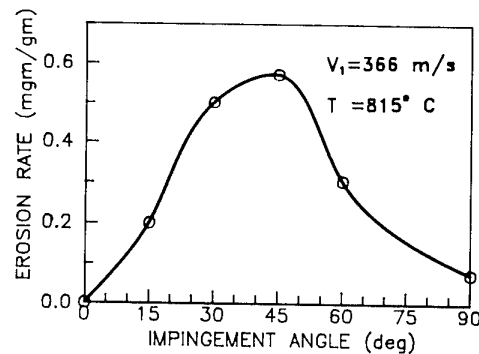


Fig. 3b. "N" Coating Erosion Rate Variation With Impingement Angle.

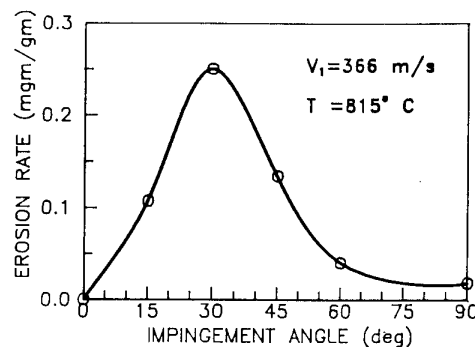
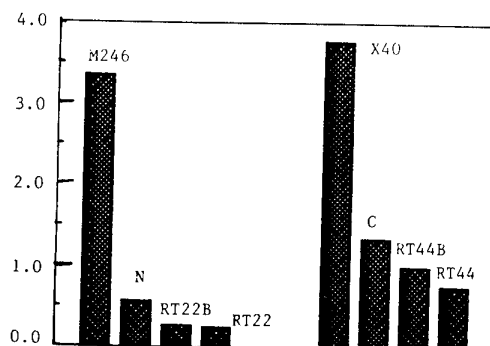


Fig. 3c. RT22B Coating Erosion Rate Variation With Impingement Angle.

Fig. 4. Comparison of Maximum Erosion Rates of Coatings and Superalloys;  $T=815^{\circ}\text{C}$ ,  $V_1=366\text{ m s}^{-1}$ .

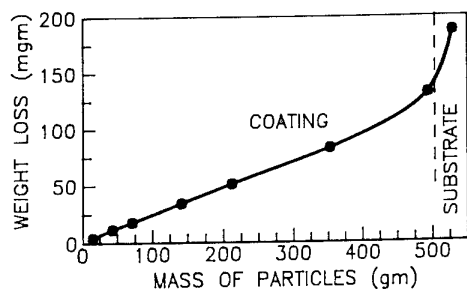


Fig. 5a. Variation of RT22B Coating Weight Loss With Particle Mass;  $T=815^{\circ}\text{C}$ ,  $V_1=366 \text{ m s}^{-1}$ .

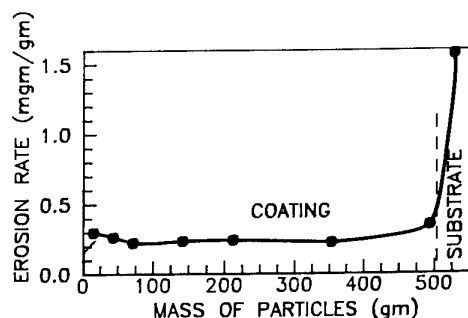


Fig. 5b. Variation of RT22B Coating Erosion Rate With Particle Mass;  $T=815^{\circ}\text{C}$ ,  $V_1=366 \text{ m s}^{-1}$ .

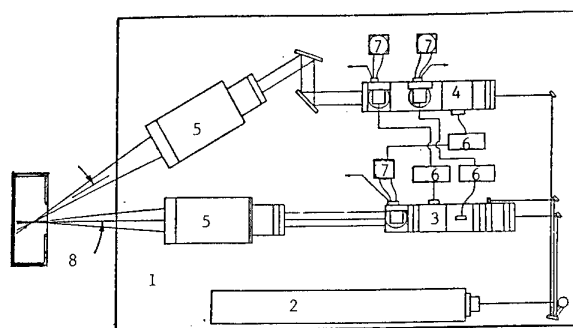


Fig. 6. Schematic of Laser Doppler Velocimeter System. (1) Optic Tube; (2) Laser Tube; (3&4) Beam Splitters and Photo Detectors; (5) Beam Expanders and Lenses; (6) Frequency Shifters; (7) Photomultipliers.

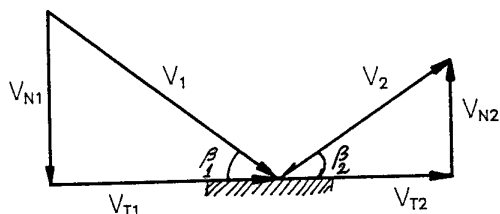


Fig. 7. Rebound Velocity and Angle Notation.

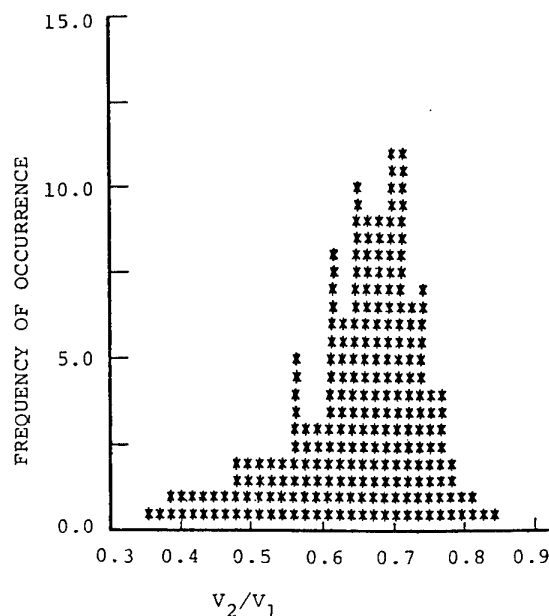


Fig. 8. Particle Velocity Restitution Ratio.

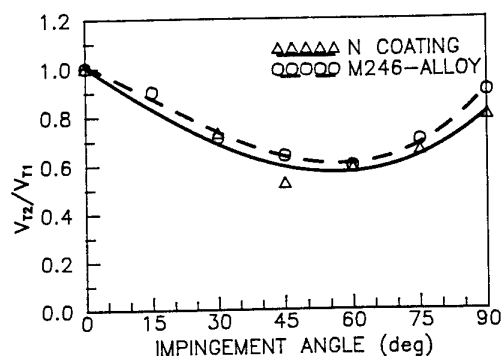


Fig. 9a. Tangential Velocity Restitution Ratio Variation with Impingement Angle  $V_1=98 \text{ m s}^{-1}$ .

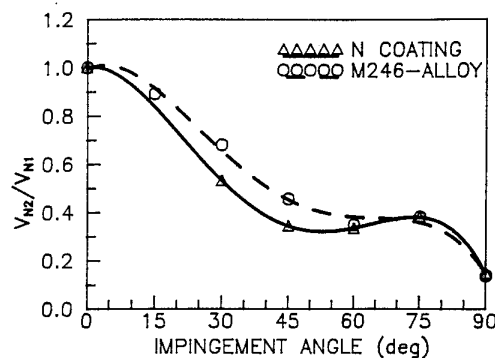


Fig. 9b. Normal Velocity Restitution Ratio Variation with Impingement Angle  $V_1=98 \text{ m s}^{-1}$ .

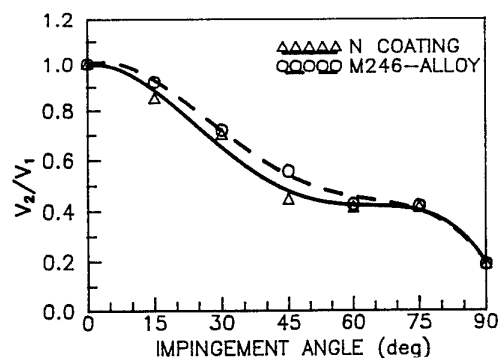


Fig. 10a. Total Velocity Restitution Ratio Variation with Impingement Angle  $V_1=98 \text{ m s}^{-1}$ .

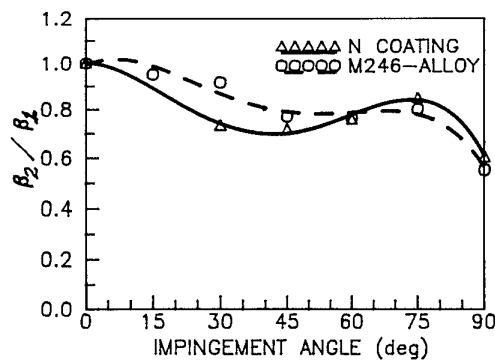


Fig. 10b. Directional Coefficient Variation with Impingement Angle  $V_1=98 \text{ m s}^{-1}$ .

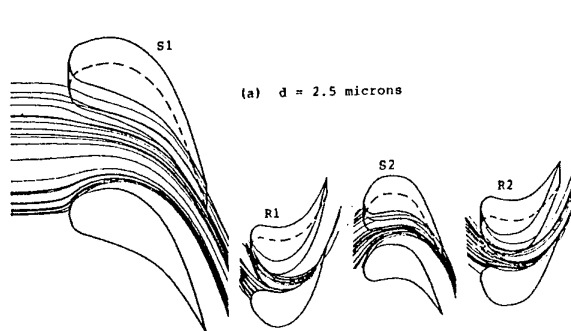


Fig. 11a. Particle Trajectory Projections in  $\theta$ -z and r-z Planes for  $d=2.5$  microns.

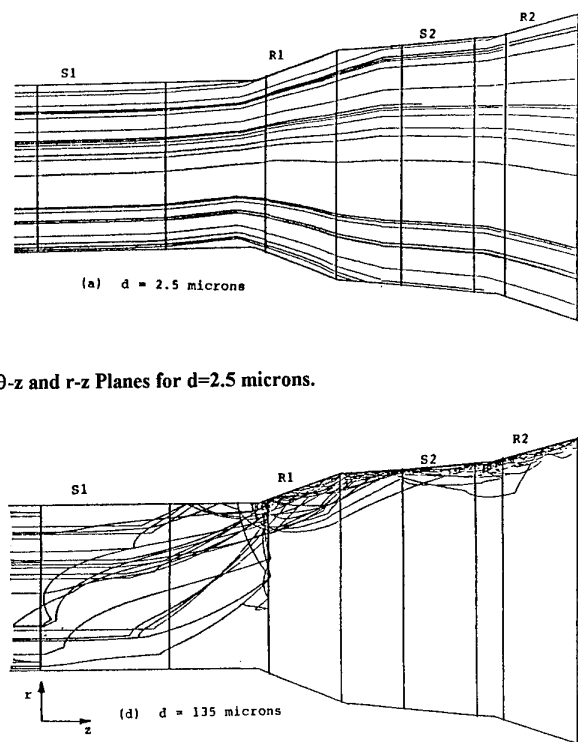


Fig. 11b. Particle Trajectory Projections in  $\theta$ -z and r-z Planes for  $d=135$  microns.

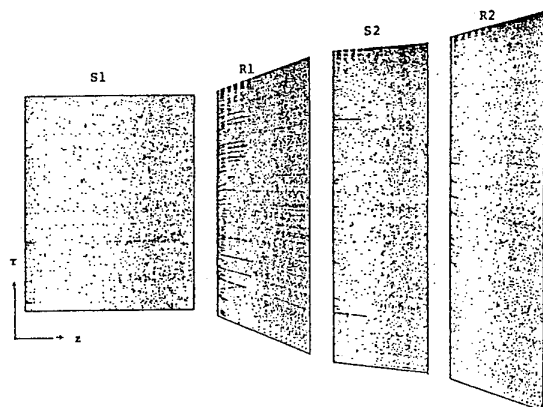


Fig. 12. Impact Locations for Nonuniform Ash Particles.

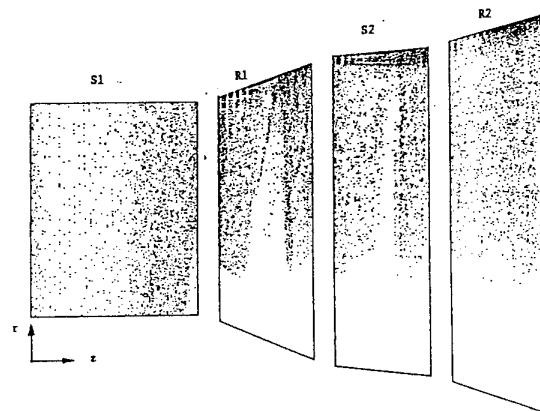


Fig. 13. Impact Locations for Uniform Ash Particles.

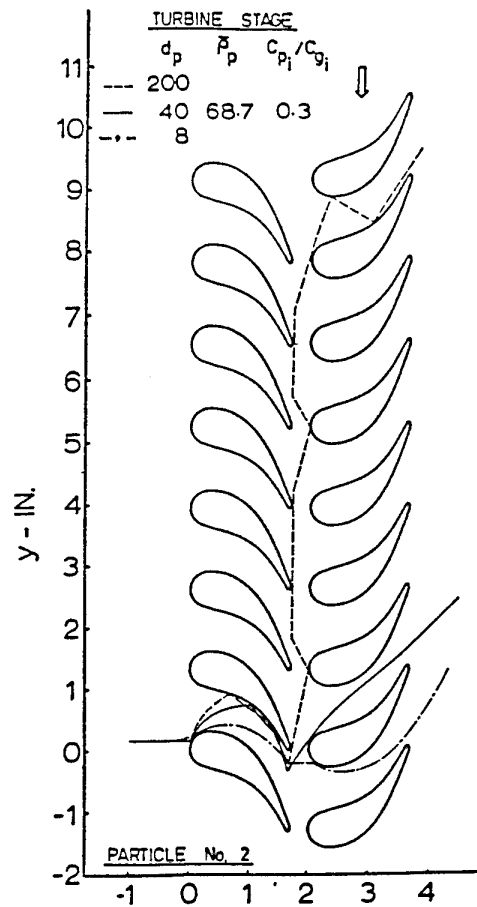


Fig. 14. Effect of Particle Size on Trajectory.

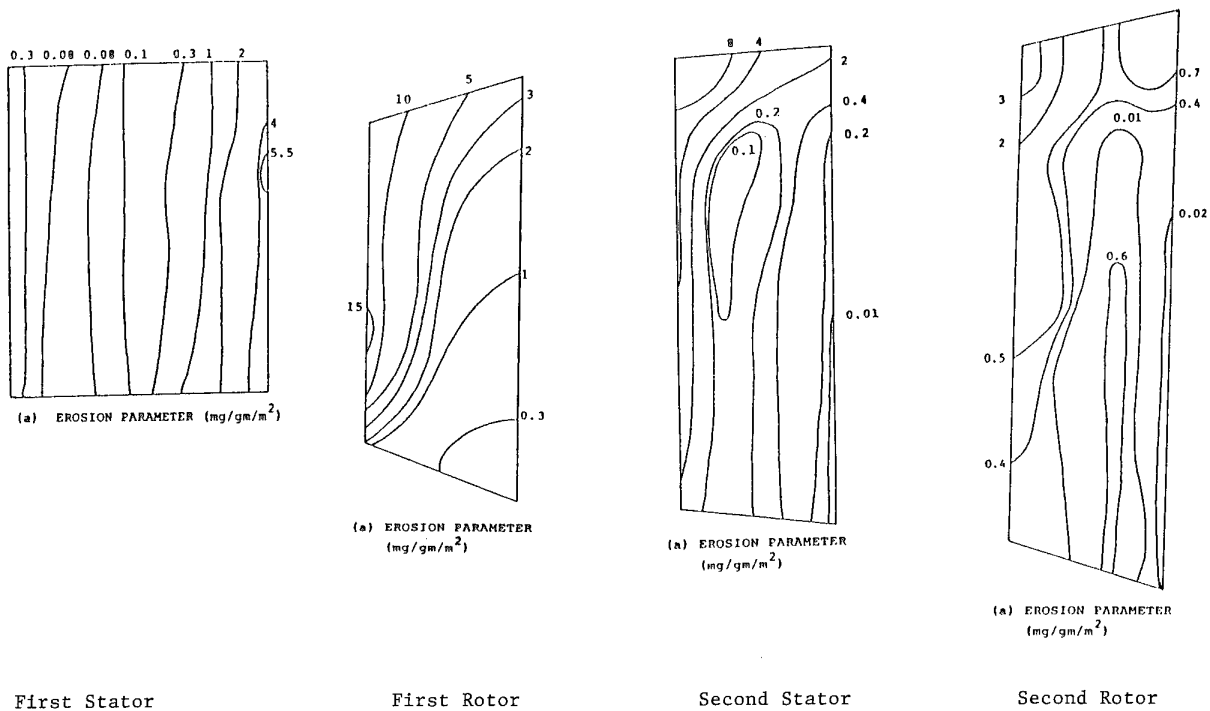


Fig. 15. Blade Pressure Surface Erosion Parameter Distribution.



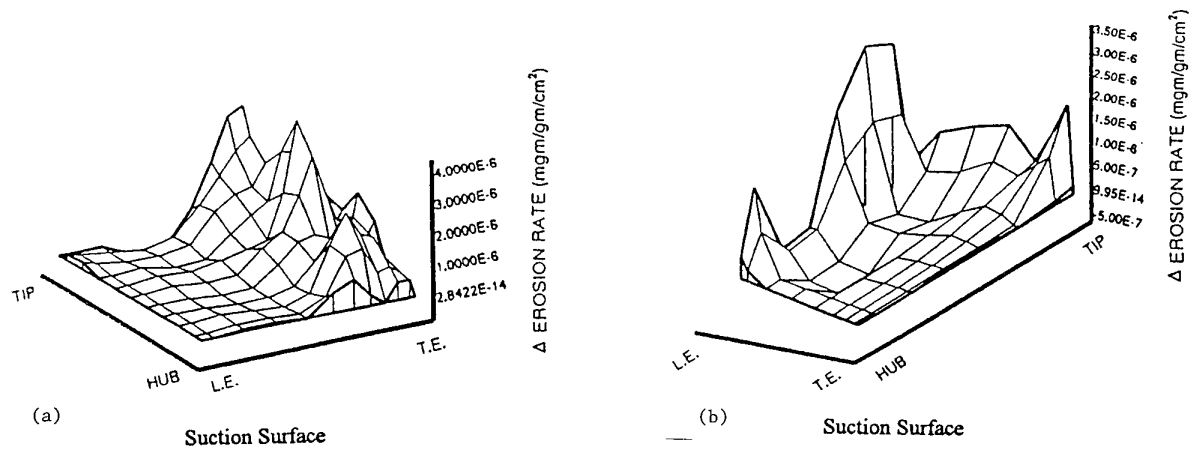


Fig. 16. Erosion Rate Difference Due to Probabilistic Sand Rebound Model  
(a) Stator Suction Surface, (b) Rotor Suction Surface.

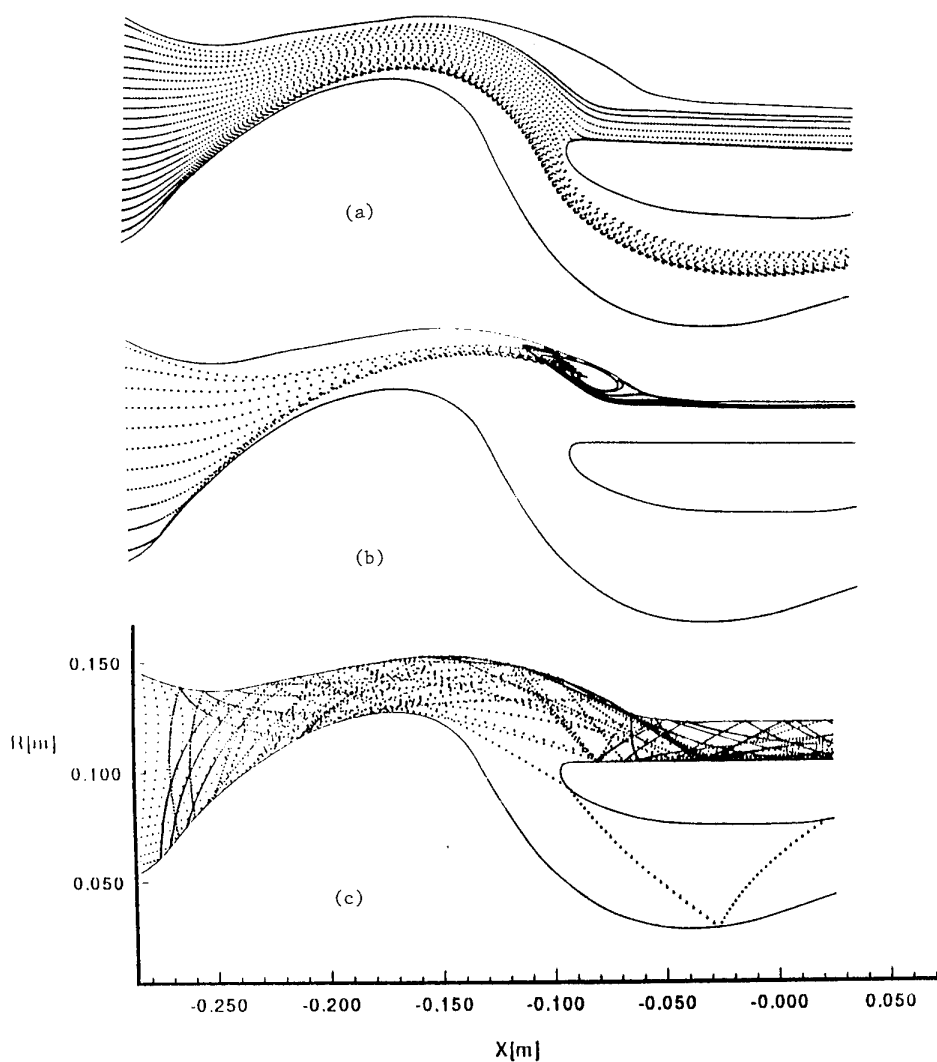


Fig. 17. Sand Particle Trajectories in Inlet Separator  
(a) 3 Micron; (b) 10 Micron; (c) 300 Micron

## PARTICLE TRAJECTORIES IN GAS TURBINE ENGINES

Dr. S.C. Tan  
Prof. R.L. Elder  
Mr. P.K. Harris  
School of Mechanical Engineering  
Cranfield University  
Cranfield  
Bedford MK43 0AL, UK

### SUMMARY

This paper describes the technique of particle trajectory modelling in gas turbine engines with applications in helicopter inertial particle separator, axial and centrifugal compressor. The model can be used with most CFD codes which utilise the finite volume (or element) techniques. Some qualitative validations were carried out using a laser transit anemometer in a particle separator and results show good comparison with predictions. The anemometer was also used to obtain restitution data for several target materials using quartz particle of different sizes at a range of impact velocities and angles.

### LIST OF SYMBOLS

$C_D$	Drag coefficient
$D_p$	Particle diameter
$m$	Mass of particle
$A_p$	Projected area of droplet on a plane normal to mean flow
$r_p, \theta_p, z_p$	Particle's cylindrical coordinates
$v_g, v_p$	Gas and particle velocity vectors
$v_f$	Relative velocity between particle and fluid
$v_{rg}, v_{\theta g}, v_{zg}$	Component gas velocities in cylindrical coordinate system
$v_{rp}, v_{\theta p}, v_{zp}$	Component particle velocities in cylindrical coordinate system
$v_1, v_2$	Impact and rebound velocities
$v_{1T}, v_{2T}$	Tangential component of impact and rebound velocities
$v_{1N}, v_{2N}$	Normal component of impact and rebound velocities
$M_{pte}, M_{wall}$	Particle and wall material
$\epsilon$	Erosion parameter (mg/g)
$K_1$	Material constant
$\rho_g, \rho_p$	Gas and particle densities
$\omega$	Rotational speed
$\beta_1, \beta_2$	Particle impact and rebound angles

### INTRODUCTION

There is a need to protect gas turbine engines operating in the desert environment where ingested

sand particles could erode engine components reducing their performance, reliability and life if left unprotected. These problems were highlighted during the Gulf conflict (Ref 1) where deficiencies in engine protection systems were discovered. The expected normal engine life cycle had been reduced drastically, curtailing its operational availability and as a result, significantly increases the cost of maintenance. Today, there is a trend towards designing engines which are inherently more resistant to the effects of sand ingestion (Ref 2) and includes the predicting of engine life cycle in a simulated sandy environment. Aerodynamic degradation of engine components due to sand erosion in a compressor, for example, can be computed and the effects of the blockage of cooling holes in turbine blades assessed.

The traditional method of assessing engine life performance is to subject a working gas turbine engine to the effects of sand particles, and record the resulting reduction in engine output power. This is usually expensive and it reveals limited information on the performance of individual components. A more cost effective way is to use computer models to simulate engine performance under the desert environment before selecting the 'best design' to be tested. Individual engine components can be subjected to the effects of sand erosion, and appropriate protection applied to improve its operational life. In this way the overall performance of a gas turbine engine can be computed by collating individual component performance.

One of the most commonly used computer models is the particle trajectory model which can predict three dimensional particle trajectories in rotating and stationary engine components. When combined with an erosion model and a CFD tool, the amount of erosion and the subsequent aerodynamic degradation can be predicted, and in the case of an inertial particle separator, its separation capability computed. Most of these trajectory codes employ the lagrangian methods of solution due to the ease of implementation because the particle equations of motion can be de-coupled from the flowfield. This is

made possible by the fundamental assumption that the presence of particles does not affect the flowfield. As a result a modular particle trajectory can be formulated which can be 'bolted' onto many of the commercial CFD tools currently residing within the aerospace industry. The trajectory model can be used to investigate the effects of the sand ingestion and predict the areas most vulnerable to erosion including the amount of material removed.

This paper will describe the technique of particle trajectory modelling including some results validating the computer predictions. A test facility for gathering information on particle rebound characteristics or restitution ratios will also be presented. In addition some examples of applications in a compressor cascade and centrifugal impeller are also provided.

### PARTICLE EQUATIONS OF MOTION

The particle equations of motion can be derived in cylindrical polar coordinates relative to a rotating frame of reference fixed in the stationary axes. The particle-particle interaction, buoyancy and basset forces have been ignored and the only forces assumed to act on a single, spherical particle are the gravitational, centrifugal, coriolis and drag forces. These assumptions simplified the formulation of the particle equations of motion which enable them to be de-coupled from the flowfield. The basic particle equations of motion are defined as follows;

$$\frac{dV_f}{dt} = g + r_p \omega^2 + \frac{V_\theta V_r}{r_p} - \frac{C_D V_f^2 \rho_g A_p}{2m}$$

The terms on the right side are due to the gravitational, centrifugal, coriolis and drag forces respectively.  $V_f$  is the particle velocity relative to the fluid and is given by;

$$V_f^2 = (V_r - V_{r0})^2 + (V_\theta - V_{\theta0})^2 + (V_z - V_{z0})^2$$

The drag coefficient,  $C_D$ , obtained from the standard drag curve defined for spherical particles, is a function of the Reynolds number based on the relative velocity between the particle and the flow.

### METHODS OF SOLUTIONS

The equations of motion were solved iteratively using the Kutta-Felberg routine in a pre-defined flowfield (Ref 3). Since the equations have been de-coupled from the flowfield, it can be calculated using any conventional CFD tools which employ the finite volume (or element) technique. The particle velocity is calculated by interpolating from the values (previously computed from the CFD code) at each

node point. The interpolation function for an 8 sided nodes element (Ref 4) is given as follows;

$$V_p = \sum_{i=1}^8 N_i(\xi_p, \eta_p, \zeta_p) V_i$$

where  $N_i$ 's are the shape functions defined for a cubic element which has been transformed from an irregular shaped tetrahedral element as shown in figure 1.  $\xi_p, \eta_p, \zeta_p$  are the local coordinates of the particle w.r.t. to the local axes system defined in the cubic element, having been transformed from its cartesian global coordinates  $x_p, y_p, z_p$  using the Jacobian transformation function and the above interpolation function defined as follows;

$$\begin{aligned} x_p &= \sum_{i=1}^8 N_i(\xi_p, \eta_p, \zeta_p) x_i \\ y_p &= \sum_{i=1}^8 N_i(\xi_p, \eta_p, \zeta_p) y_i \\ z_p &= \sum_{i=1}^8 N_i(\xi_p, \eta_p, \zeta_p) z_i \end{aligned}$$

These equations are initially solved using the Newton-Raphson method to give local coordinates,  $\xi_p, \eta_p, \zeta_p$ , before being used to interpolate for the component velocities used in the particle equations of motion. Particle tracking in a computational mesh is carried out by computing these local coordinates as the particle "crosses" from one element to the next. As the particle approaches a solid wall, the time step is reduced gradually until it just collides with the surface. At this instant, the rebound velocity (and angle) is calculated using the particle restitution ratios which relate the rebound to the impact conditions. This ratio, however, can only be obtained experimentally, therefore a test facility has been built to gather these information.

### EXPERIMENTAL VALIDATION

The validation of the trajectory code (Ref 5) was carried out in a vaneless, inertial particle separator (Fig.2) which had been designed to protect a helicopter engine. It consists of a hub, shroud and flow splitter which separates the clean from the contaminated air. The hub and shroud wall surfaces are highly contoured in order to deflect ingested dust particles into the scavenge duct. The experimental arrangement is shown in figure 3. Since the separator is axisymmetric, the study was conducted with a 30 degrees section of the intake. Particles of known sizes were (gravity) fed locally into the intake at three different radial positions, and the distribution and velocity (and angle) were measured using a two-spot laser anemometer system (Ref 7). Figures 4 and 5 show some of the measured particle distribution in the

separator obtained with the laser anemometer at several traverse stations. The mean trajectory position was calculated from each traverse station and later used as a laser measurement point for measuring particle velocity (and angle). Dust particles entering the scavenge and core flow sections were caught with a pair of filter bags located in a plenum chamber which were connected to the scavenge and core flow sections. The dust particles used include both the irregularly shaped quartz particles and spherical ballotini glass with similar densities. The tests carried out with spherical particles were used directly to validate the model since the equations of motion (and drag relations) are based on a spherical particle.

The flowfield in the separator was calculated using a viscous compressible code and the result is shown in figure 6. Particle trajectories were computed in this flowfield using the same test conditions and comparisons were made at discrete locations. In addition, comparisons were also made with irregular and spherical shaped particles as shown in figures 7 and 8.

#### PARTICLE RESTITUTION RATIOS

The continued computation of the particle trajectory after an impact with a solid wall is made possible by using a set of empirical relations known as restitution ratios. These ratios provide the particle rebound characteristics as a function of its impact conditions such as the particle impact velocity (and angle), particle diameter, and the type of particle and wall materials.

In general, the particle velocity restitution ratio,  $V_2/V_1$ , is described as the ratio of the rebound velocity to the impact velocity. Similarly, the directional restitution ratio,  $\beta_2/\beta_1$ , is defined as the ratio of the rebound angle to the impact angle as shown in figure 9.

A test facility, figure 10, had been designed to measure the rebound characteristics (or restitution ratios) at different impact velocity, angle and particle size. It consists of a dust feeder system, and accelerator and target chambers which were separated by a pinhole. Particles were injected at a target plate and the laser anemometer was used to measure the rebound velocity and angle in the target chamber. Measurements were carried out at a distance of about 1.2 mm from the plate's surface. The "spread" in the dust particles was controlled by the pinhole which ensures only a narrow stream of particles were colliding with the target plate. Both chambers were isolated from the surroundings hence measurements were carried out in a quiescent condition. The target chamber has an optical access made from perspex material for laser measurement.

The basis of the design involves the acceleration of particles of known size by an airstream and then the separation of the airstream from the particle 'stream' using the 'coanda' effect (Ref 8). This technique of accelerating particle trajectories has resulted in a simpler test facility compared to the windtunnel used by other researchers (Ref 9). This also has the advantage of measuring particle rebound in a quiescent condition where the aerodynamic effects have been minimised. The 'coanda' effect separates the particle from the airstream, and the particle then relies on its own inertia to maintain a level trajectory. Since there is no flow distribution near the target plate, the particle impact and rebound conditions very close to the plate are not affected by the boundary layer. Figures 11 and 12 show some of the results collated for quartz particles impinging on aluminium and duralumin targets.

Particle fragmentation is an important phenomenon that cannot be ignored when computing particle trajectories because it can affect the areas of erosion, and the amount of material removed. This phenomenon was observed during an experimental test where a major proportion of the initial dust sizes was found to have fragmented due to multiple impacts. An assessment of the fragmentation characteristics of particles due to impact velocity, angle and particle size was also carried out as part of the restitution study, and results are shown in figure 13 and 14.

#### EROSION MODELLING

The erosion model (Ref 10) used in the present analysis is defined as follow;

$$\varepsilon = K_1 f(\beta_1)(V_{1T}^2 - V_{2T}^2) + f(V_{1N})$$

The model assumes that erosion is due to two basic mechanisms, one predominant at low impact angle (ductile) and the other at high impact angle (non-ductile). Ductile erosion is due primarily to plastic deformation whereas non-ductile erosion is due to propagation of cracks in metal. The various aspect of erosion modelling will not be discussed because current studies have been limited to particle trajectories but it will be included in future publications.

#### RESULTS AND DISCUSSION

The predicted flowfield in figure 6 shows two regions, denoted by A and B, with recirculating flow which were later confirmed using wool tufts. The result shown in figures 4 and 5 show generally good agreement between measured and predicted particle trajectories for particle with small and large diameters. Figure 7 and 8 show the results obtained for spherical and irregularly shaped quartz particles

respectively. Good agreement in the trajectory velocities and angles at the various traverse stations were found for spherical particles (Fig. 7). In addition, further comparison was made with trajectories predicted using an inviscid flowfield which resulted in a small underprediction of the particle velocities. Figure 8 also show good agreement between measured and predicted data for irregularly shaped particles but only as a result of applying a shape factor (Ref 6) to the drag relations.

The application of this factor is a valid one because the drag relations used in the formulation of the particle equations of motion was derived for a spherical particle whereas irregularly shaped quartz particle normally experiences a greater drag. This shape factor,  $Z$ , can be expressed as the ratio of the volume of the particle to the diameter of a sphere which has the same projected area in the most stable orientation. In mathematical form, it is written as follows;

$$Z = \frac{VOL_p}{D_p^3}$$

where  $VOL_p$  is the volume of the particle. The shape factor for a spherical particle is  $\pi/6$  while irregularly shaped quartz particle is about 0.21 which was obtained by trial and error matching of the results.

#### EFFECT OF IMPACT VELOCITY AND ANGLE ON THE RESTITUTION RATIO

The restitution result for aluminium material, figure 11, shows three distinct rebound characteristics due to the effects of the impact velocity and angle. As impact angle increases, the restitution ratios for the three impact velocities converge to a critical angle beyond which the effects are less well defined. Generally, it shows that impact at higher velocity will result in a higher rebound angle for impact angles smaller than the critical angle. Comparison was also made with result obtained by other researchers (Ref 9) which shows good agreement in the directional coefficient,  $\beta_2/\beta_1$ , but a generally higher measured velocity ratio,  $V_2/V_1$ , was obtained. This is most likely to be due to the smaller particles ( $50 \mu\text{m}$  compared to  $200 \mu\text{m}$  particles used in Ref 9) used in the current tests. The effect of the impact velocity for the duralumin material, figure 12, is less well defined compared to those obtained for the aluminium material but similar characteristics were also found. In general, the restitution ratios of aluminium and duralumin materials are a function of the following parameters;

$$f\left(\frac{V_2}{V_1}\right), f\left(\frac{\beta_2}{\beta_1}\right) = f(V_1, \beta_1, D_p, M_{wall}, M_{pie})$$

#### FRAGMENTATION CHARACTERISTICS

Figures 13 and 14 show the effect of impact velocity and particle sizes on the amount of fragmented dust. They generally show that as particle impact velocity and size increase, the amount of fragmented dust also increases. For larger particles, figure 13, fragmentation occurs mostly at the lower end of the dust size spectrum whereas for smaller particles, figure 14, it is across the whole size bandwidth.

#### FURTHER APPLICATIONS OF THE TRAJECTORY CODE

The code is currently being used by a commercial firm in the design of particle separators and will also be used to assess the erosion in axial and centrifugal compressors in an on-going study, the results of which will be reported at later conferences. The following examples, however, show the capability of the trajectory code in simulating particle trajectories in a stationary and rotating geometries. Figure 15 shows the particle trajectories predicted in a compressor cascade which has no radial velocity component. Figure 16 shows the particle trajectories predicted in high speed impeller and the resulting predicted erosion parameter (Fig 17). Initial findings seems to show good agreement with experimental results especially in the area predicted to have a high level of erosion. Further results will be presented at later conferences.

#### CONCLUSIONS

A general insight of the particle trajectories studies has been presented including a facility to measure particle restitution ratios. The trajectory code was successfully validated against experimental data obtained in a helicopter inertial particle separator and good agreement was found especially with spherical particles. In the case of the irregular quartz particles, a shape factor, which accounts for the higher drag, had to be applied. The particle restitution ratio tests show that impact velocity, impact angle, type of particle and wall material has an effect on the results particularly with aluminum material. Particle fragmentation is also found to be an important parameter which must be taken into account when modelling particle trajectories. The capability of the code in simulating particle trajectories in rotating and stationary components has also been presented, and initial findings have shown promising results.

#### REFERENCES

1. PARAMOUR, M.D., JENNINGS, P.G., 'Operational Requirements for Helicopter Engines for UK Services', 82nd Symposium, Propulsion and Energetics Panel on Technology Requirements For Small Gas Turbines at Montreal, Canada, Oct 4-8, 1993

2. MANN, D. L., HUMPHERSON, D. V., 'Helicopter Engine/Airframe Integration - The Way Ahead', 82nd Symposium, Propulsion and Energetics Panel on Technology Requirements For Small Gas Turbines at Montreal, Canada, Oct 4-8, 1993
3. TAN, S. C., 'A Computer Code to predict Particle Trajectories in a Three-Dimensional Gas Turbine Intake', MSc Thesis, Cranfield University, 1984
4. LIVESLEY, R. K., 'Finite Element. An Introduction for Engineers', Cambridge University Press, Cambridge, 1983.
5. TAN, S. C., 'A Study of Particle Trajectories in a Gas Turbine Intake', PhD Thesis, Cranfield University, 1988
6. HEYWOOD, A., Proc. Inst. Mech. Engrs., (London), 140, 257 (1938), Chem. & Ind., (London), 56, 149 (1937)
7. AGHA-SEIED-MIRZBOZORG, 'Multichannel Analysis for the analysis of laser Anemometry (L2F) signal', PhD Thesis, Cranfield University
8. YEE, K. H., SHAYLEY, P. J., COLLINGS, N., 'Erosion of Metals by Flyash Particles', Wear 91 (1983) 161-170.
9. GRANT, G., TABAKOFF, W., 'Erosion Prediction in Turbomachinery Resulting from Environmental Solid Particles', Journal of Aircraft, Vol. 12, No. 5, May 1975, pp. 471-478.
10. BALL, R., TABAKOFF, W., 'An Experimental investigation of the Erosive Characteristics of 410 Stainless Steel and 6Al-4V titanium', University of Cincinnati

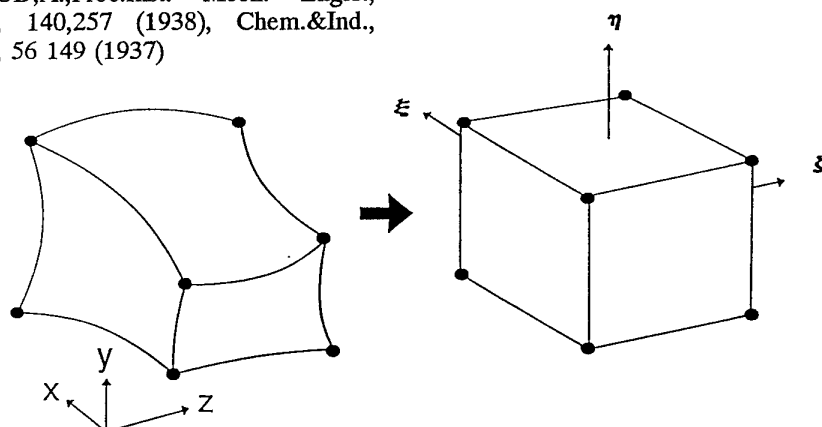


Fig.1 Transformation of an irregular tetrahedral element to a cubic element

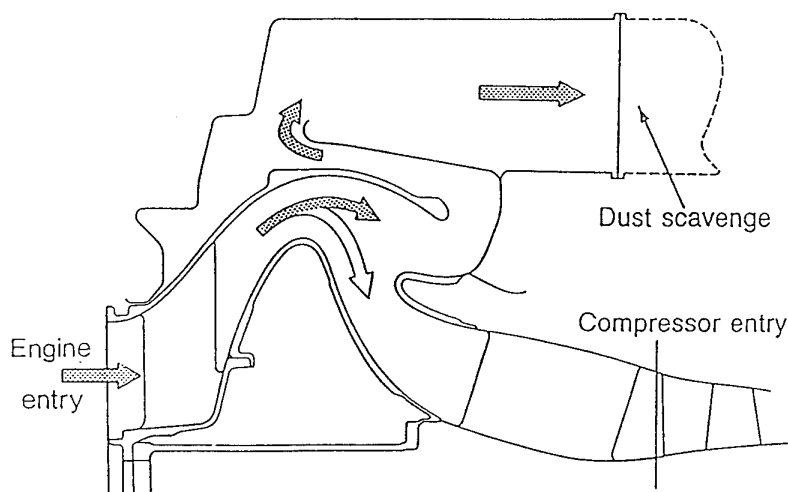


Fig.2 Inertial Particle Separator (IPS)

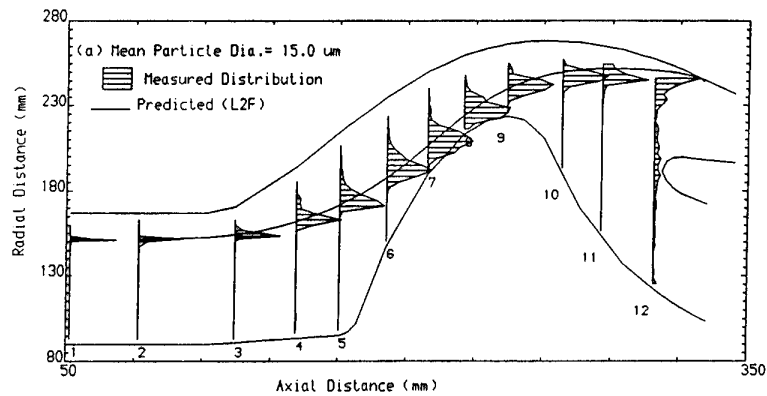
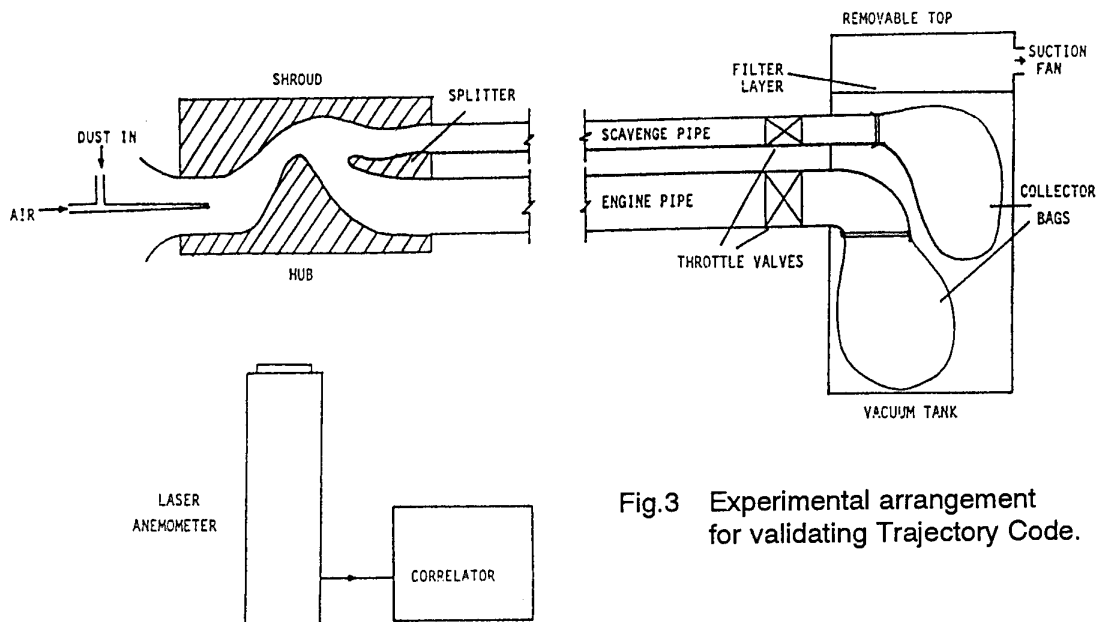


Fig.4 Particle distribution measured with a two-spot anemometer ( $d_p=15 \mu\text{m}$ )

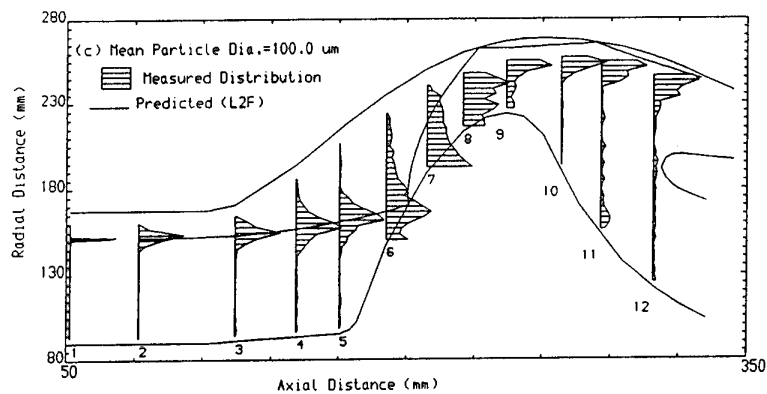


Fig.5 Particle distribution measured with a two-spot anemometer ( $d_p=100 \mu\text{m}$ )

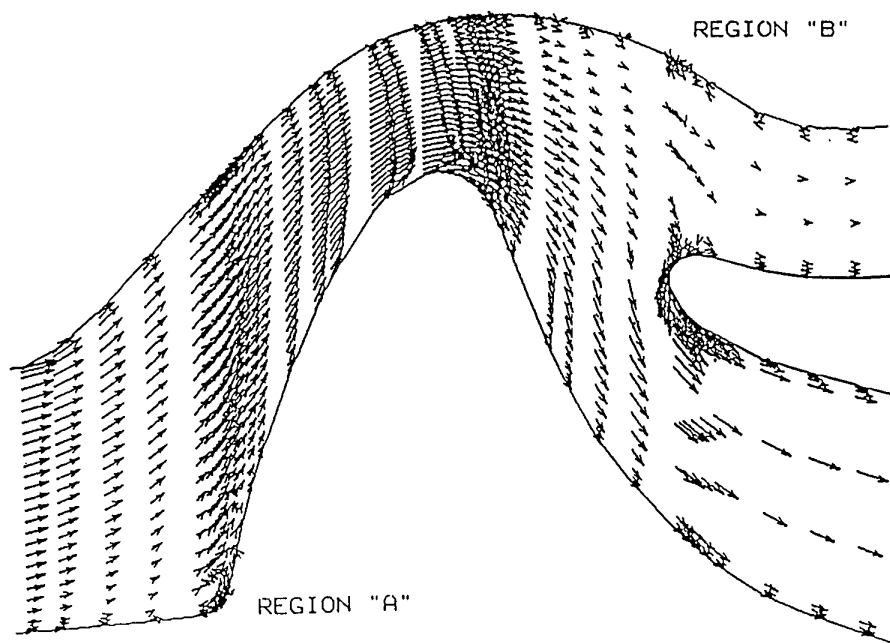


Fig.6 Predicted flow vectors in an Inertial Particle Separator



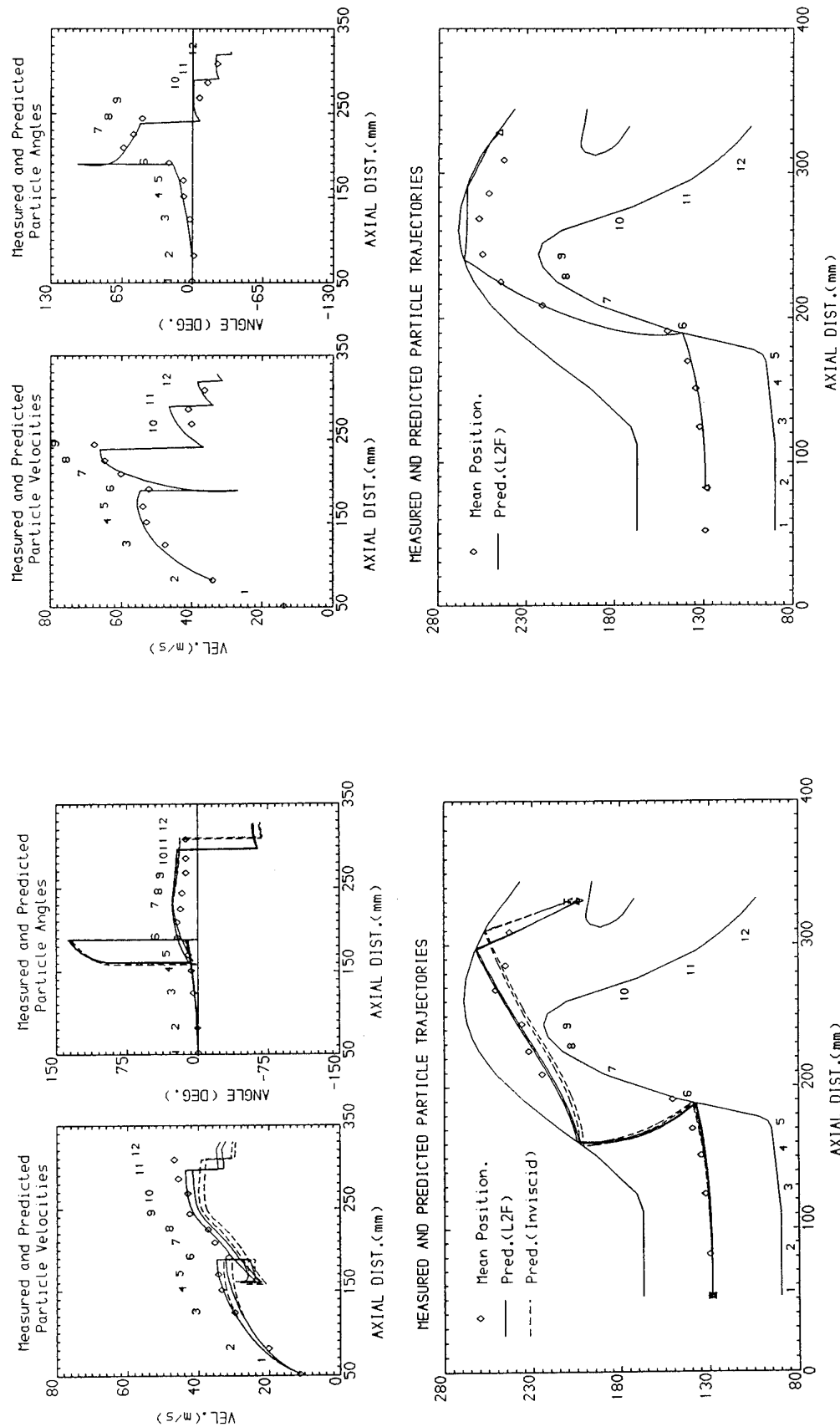


Fig. 7 Measured and predicted results for spherical particles

Fig. 8 Measured and predicted results for irregularly shaped (quartz) particles

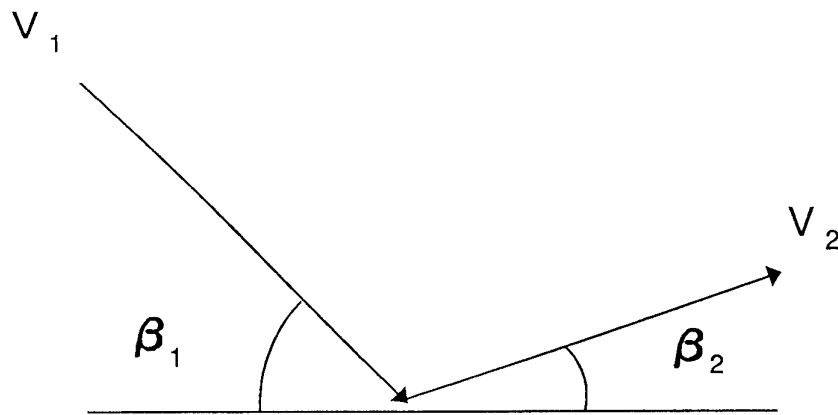


Fig.9 Impact and rebound velocity and angle

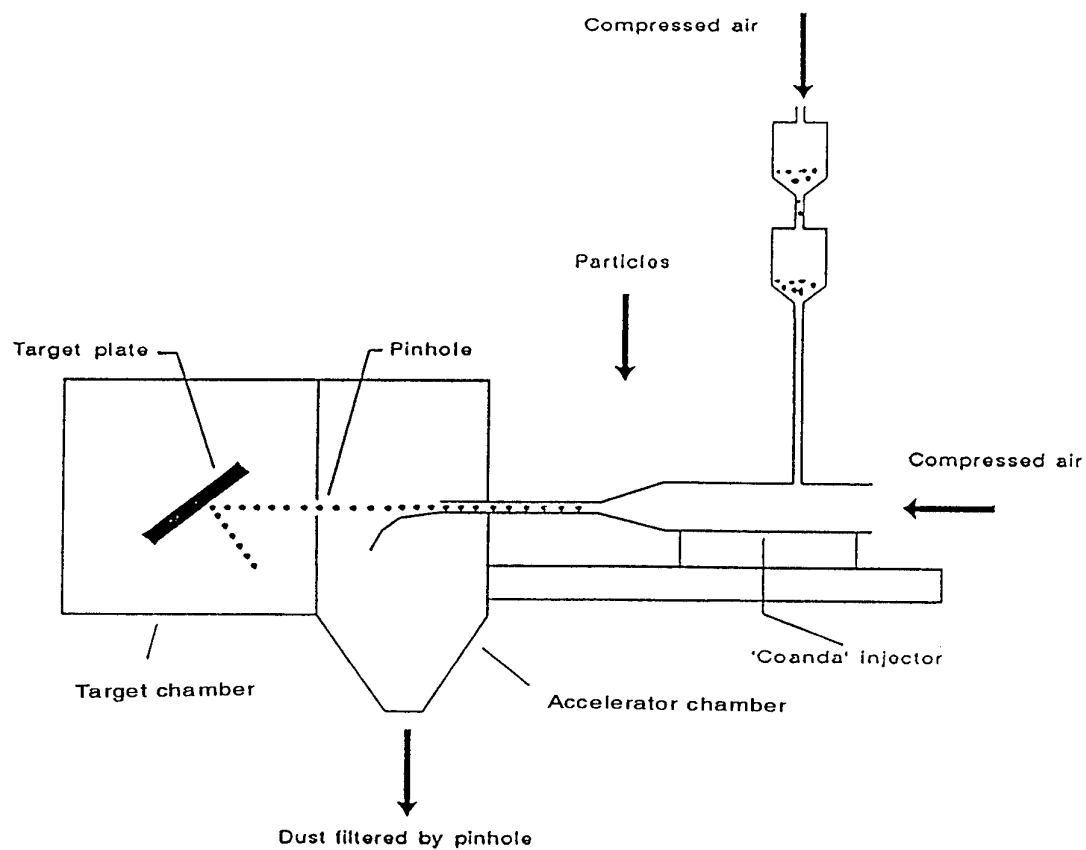


Fig.10 Experimental arrangement for measuring particle restitution ratios

Al-22 Gauge  
Dp = 50. (um)

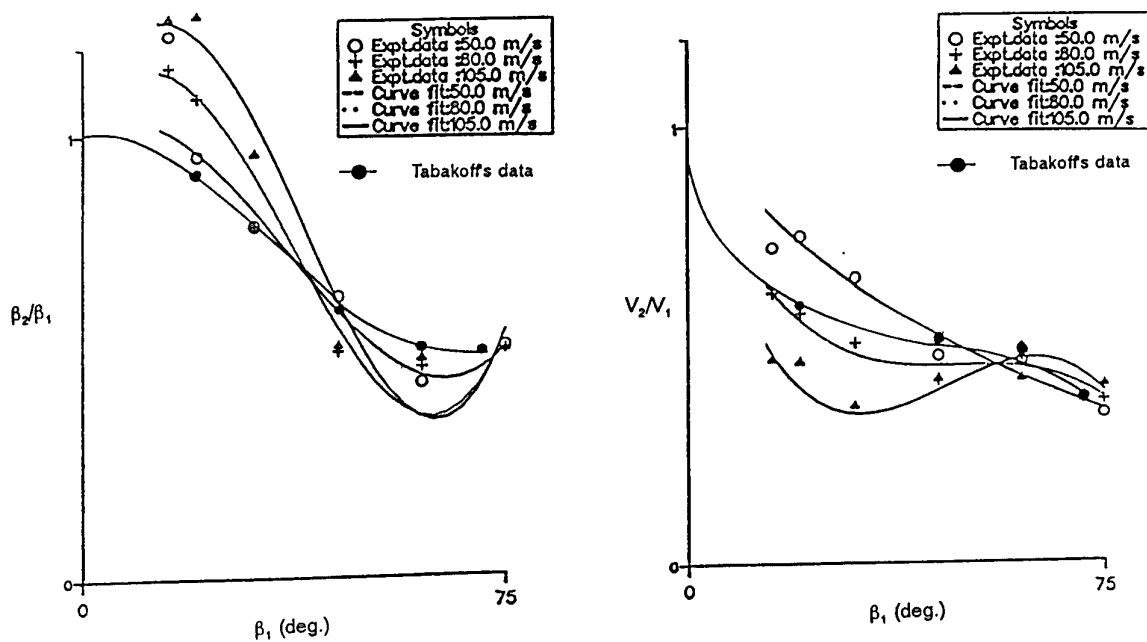


Fig.11 Measured restitution ratio for aluminium material

DURALUMIN - 22 Gauge.  
Dp = 200. (um)

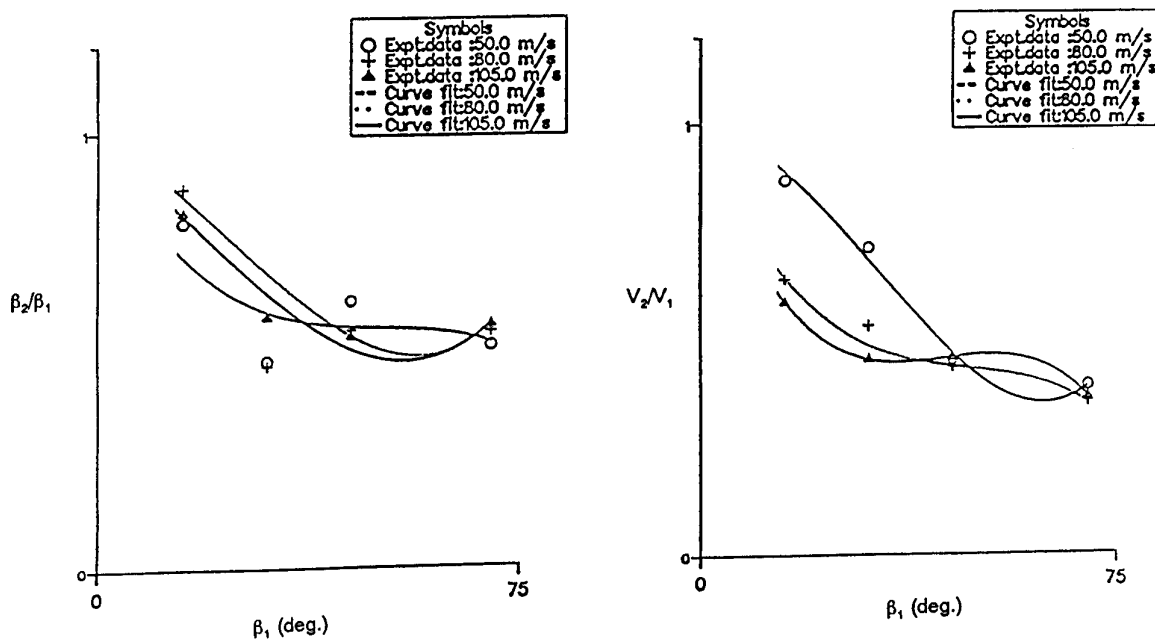


Fig.12 Measured restitution ratio for duralumin material

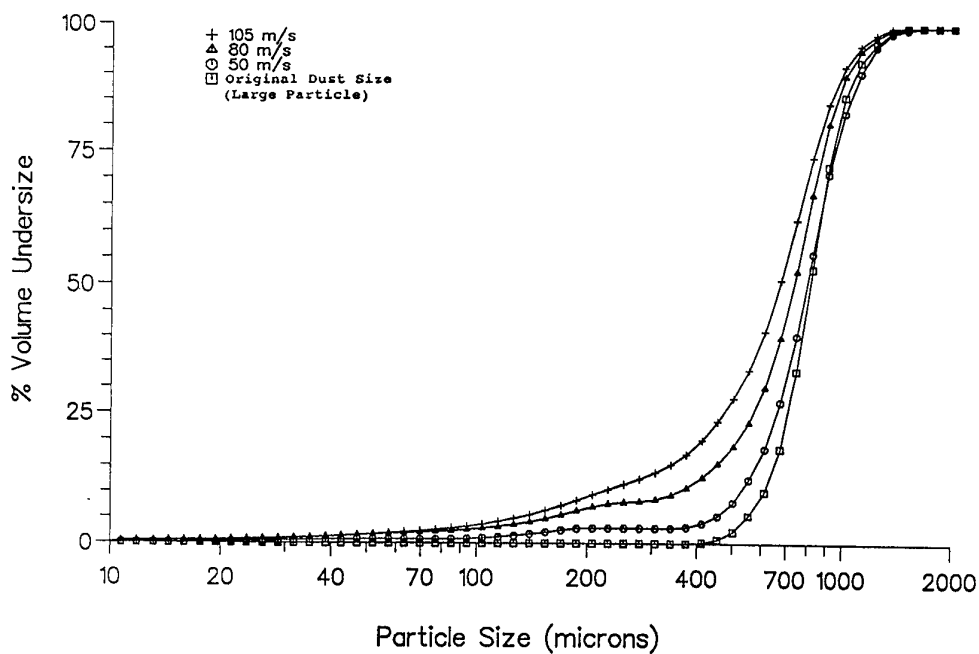


Fig.13 Effect of impact velocity on fragmentation (Large particles)

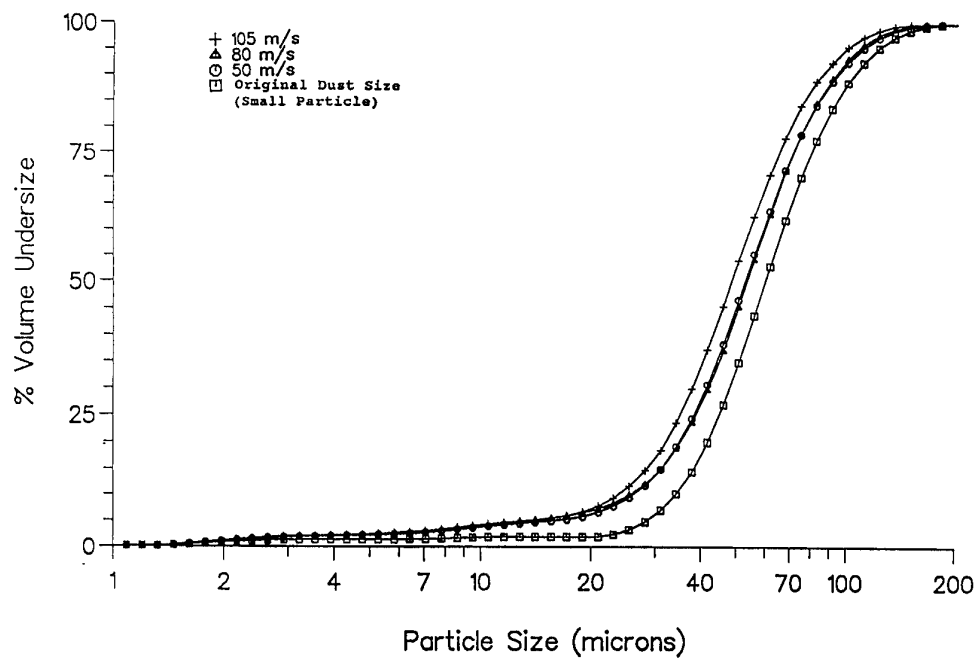


Fig.14 Effect of impact velocity on fragmentation (Small particles)

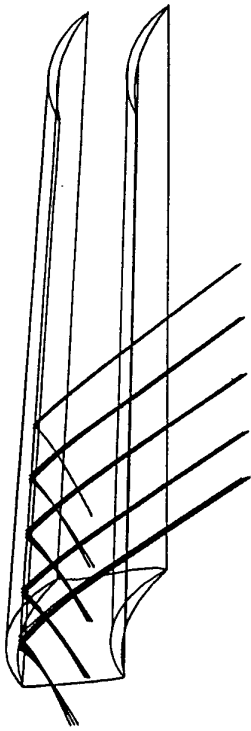


Fig.15 Typical predicted particle trajectories  
in a compressor cascade ( $V_r=0$ )

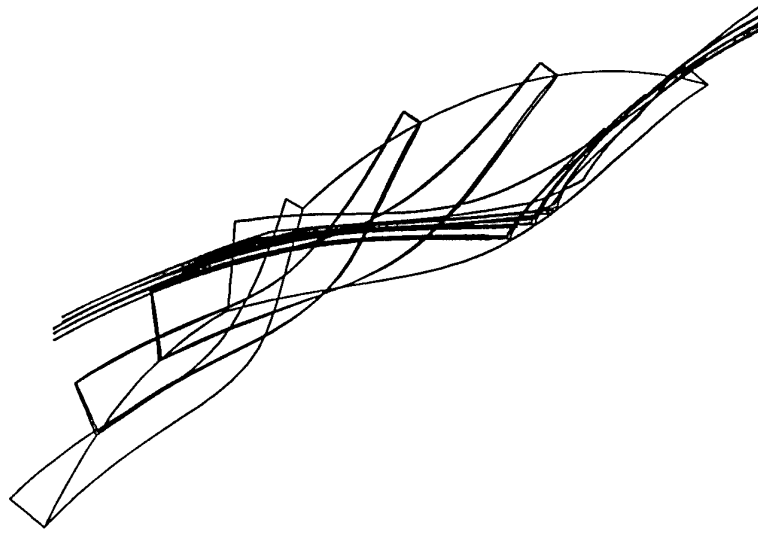
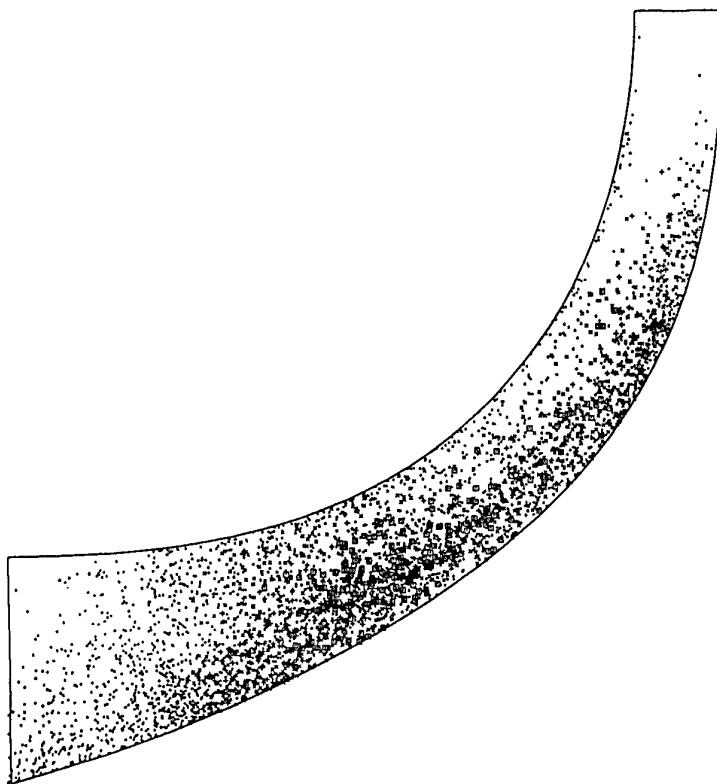


Fig.16 Typical predicted particle trajectories  
in a high speed impeller



Erosion parameter

- ▲ 0.393 – 0.491
- ▣ 0.295 – 0.393
- + 0.197 – 0.295
- × 0.099 – 0.197
- 0.001 – 0.099

Fig.17 Predicted erosion distribution in a high speed impeller

## QUESTIONS

### **K. BROICHHAUSEN (Ge)**

Q. Hamed and Tabakoff indicated the necessity of investigating the particle impact in combination with the flow. You are separating the flow from the particles. Could you give the background for this different experimental set-up?

A. We believe that to investigate particle impacts and include all the aerodynamic effects in order to simulate all possible flow scenarios will be impossible. In addition, we have also confirmed fragmentation of particles, therefore the rebound characteristics are even more sensitive to the aerodynamic effects. This is especially true for the smaller particles and measurement may not truly reflect the actual rebound phenomena.

### **M. FORDE (No)**

Q. Regarding the computation of particle trajectories, do you take special care of the particles in the boundary layer, and/or reflection of the particles into the flow?

A. We did not include the 'particle rolling' phenomenon in our modelling techniques because the flowfield already include viscous effects; thus, predicted trajectories of the very small particles (less than 1 micron) have shown the 'rolling' effects along the wall surfaces, which can only be due to the boundary layer effects.

### **P. KOTSIPOULAS (Gr)**

Q. Have you validated the trajectory code for particles other than spherical ones, i.e. like ash?

A. No, we did not. All the validations were carried out with quartz and spherical ballotini particles only.

# THE CALCULATION OF EROSION IN A GAS TURBINE COMPRESSOR ROTOR

by

G.C. Horton\*, H. Vignau\*\*, G. Leroy\*\*

\* Defence Research Agency, Farnborough, Hants, UK  
(on secondment at Turboméca May 1993 - April 1994)

\*\* Turboméca, 64511 Bordes Cedex, France

## ABSTRACT

Erosion of the turbomachinery and other components in helicopter gas turbines operating in a sandy environment is a significant problem. In order to better understand the mechanics of such erosion, and to enable the design of components better able to withstand it, a means of modelling erosion is needed.

Such a method has been developed at Turboméca. It consists of a method of predicting the trajectories of the particles within the component, on the basis of a prescribed aerodynamic field and taking into account rebounds from the walls, together with correlations for the erosion caused by impacts of the particles with the walls.

The various aspects of the method have been validated by comparison with available experimental data and these comparisons are presented. Predictions of particle trajectories in two types of particle separator and in two gas turbine compressors (axial and centrifugal) are also presented, together with some comparisons with experiment.

## RESUME

L'érosion des composants des moteurs d'hélicoptères évoluant dans un environnement chargé en sable est un problème crucial. Pour mieux cerner les mécanismes qui régissent cette érosion et pour concevoir des pièces plus tolérantes, il est nécessaire de modéliser ce phénomène. Un tel modèle a été développé à Turboméca. Il associe un calcul de trajectoire de particules dans chaque composant avec prise en compte des divers rebonds, sur la base d'un champ aérodynamique, et l'estimation, à partir de corrélations, de l'érosion résultant de l'impact des particules sur les parois.

Les différents volets de la méthode ont été validés sur la base des données expérimentales disponibles.

Les résultats obtenus dans la prévision des trajectoires pour deux types de séparateur de particules et deux sortes de roues de compresseur (axial et centrifuge) sont aussi présentés et comparés à quelques résultats d'essai.

## 1. INTRODUCTION

The operation of helicopter gas turbines in a sandy or dusty environment can result in serious erosion damage to the various engine components, particularly the compressor (figure 1), as a result of the ingestion of the sand particles into the engine and their consequent abrasive impacts with the components' surfaces.

This erosion can then result in a loss of performance of the engine and ultimately its catastrophic failure.

Several means of combatting this problem are possible, including :

- improved filtration of the particles at the engine inlet
- erosion-resistant coatings on the exposed surfaces [ref. 1]
- changes to the geometry of the engine components.

In each case, if the improvements are to be made without many hours of expensive experimental testing, it is important that a method of predicting the trajectories of the particles through the components and the erosion resulting from their impacts with the surfaces, is available. This paper describes such a method together with some of the results used to validate it and some predictions on gas turbine engine components.

## 2. METHOD

The method described here is based on that of Jarifi [ref. 2] with modifications to extend the range of geometries treated and to incorporate more recent models for some of the aspects of the calculation. This method solves the equations of motion for the particles in a relative frame and thus, in rotating components such as compressor rotors, includes terms for centrifugal and Coriolis forces. The particles are treated individually rather than as a continuum (ie a Lagrangian rather than Eulerian approach) and the equations for each particle are solved using a single step time-stepping technique. It is assumed that the particles are spherical and that their volume density is low enough for particle-particle interactions (collisions) to be ignored. Further, it is assumed that the effect of the particles on the surrounding fluid can be ignored.

### 2.1 Fluid-particle interaction

The effect of the fluid on the particles is modelled by applying drag-force correlations to a pre-defined aerodynamic field. Several different methods for calculating this aerodynamic field have been used. They will be indicated, though not discussed in detail, in the presentation of the results in section 3.

Several models for the drag force on the particles have been obtained from the literature [ref. 3-7]. In each case they depend on a drag coefficient ( $C_d$ ) which varies with the particle Reynolds number (based on the relative speed between the fluid and the particle). The model used for the calculations presented here is that due to Wallis [ref. 6] and takes the form :

$$C_d = 24.0(1.0 + 0.15REp^{0.687})/REp \quad REp < 1000$$

$$C_d = 24.0(1.0 + 0.15REp^{0.687})/1000 \quad REp > 1000$$

where  $REp$  is the particle Reynolds number. This formula for  $C_d$  is shown graphically in figure 2. The drag force itself is calculated by

$$F = 0.75 \rho_a / (\rho_p d) C_d |V_a - V_p| (V_a - V_p)$$

where the subscripts a and p denote the air and particle properties respectively. This model has been checked by comparison with

calculations for the acceleration from rest of a particle in a constant velocity flow as presented by Tabakoff and Hamed [ref. 8]. The comparisons of the results for different particle sizes in different flow velocities are shown in figure 3 and a good level of agreement between the two (admittedly rather similar) prediction methods is found.

### 2.2 Particle-wall interactions

A key feature of calculation methods of this type is their treatment of the impacts of particles with the walls and the subsequent rebounds. In order to determine the point of impact, once such an impact has been detected, the program iteratively reduces the size of the time step until the particle is predicted to be within one particle diameter of the wall. The impact location is then given by constructing a perpendicular from this location to the wall.

In reality, of course, the impact itself is a highly statistical process with such influences as the size and shape of the particle, its speed of rotation and orientation at the point of impact as well as the local roughness of the wall. This is in addition to considerations such as the material properties of the particle and wall and the speed and direction of the particle at impact. Other researchers have reported attempts to treat all of these variables but most of them introduce too great a complexity for calculation methods such as presented here, with its requirement to treat a large number of particles (and hence rebounds) in a short time. On a statistically averaged basis the important parameters are the materials of the particle and wall together with the speed of the particle and the angle between its trajectory and the wall surface before impact. The program, like many similar ones, uses correlations to determine the speed and direction (relative to the wall surface) after the impact as functions of the same parameters beforehand. A different correlation is therefore required for each wall-particle material pair; those used have either been found in the literature or obtained by fitting a curve (using a least squares method) to the published experimental data. These correlations have either of the two following forms :

$$\begin{aligned} V_{n2}/V_{n1} &= F_n(\beta_1) \quad \text{or} \quad V_2/V_1 = F_n(\beta_1) \\ V_{t2}/V_{t1} &= G_n(\beta_1) \quad \beta_2/\beta_1 = G_n(\beta_1) \end{aligned}$$



where  $V_{n1}$  and  $V_{n2}$  are the velocities normal to the wall before and after the impact,  $V_{t1}$  and  $V_{t2}$  are the velocities parallel to the wall.  $V_1$  and  $V_2$  are the relevant total velocities while  $\beta_1$  and  $\beta_2$  are the angles between the particle trajectory and the wall.  $F_n$  and  $G_n$  are usually of the form of quartic relations. The dependence of the above ratios on either  $V_1$  or the particle size is very small and hence neglected. Figure 4 shows one such correlation, for quartz particles rebounding from a stainless steel target, obtained from reference 9. The speed and angle of the particle's trajectory after the impact is plotted against the angle before. Also shown on this figure are the experimental results from which the correlation was obtained.

### 2.3 Particle size distributions

For the majority of calculations performed with the program a single size is used for all the particles. However, when aero engines and their components are tested for susceptibility to sand ingestion a single particle size is not used, but rather a grade of sand with a known frequency distribution for the size. Two different approaches have been used to allow for this. In the first approach a large number of particles are used each with a different diameter, chosen by generating a random number and then using that, in conjunction with the particle size distribution to calculate the diameter. In the other approach a number of runs of the particle trajectory program are performed, each with a different size for the particles. The final result (e.g. filtration efficiency or erosion rate) is then calculated by combining the results for the individual particle sizes, again in conjunction with the particle size distribution. The first method has the advantage of only requiring a single run of the program but, for certain types of sand, the particle size distribution is so biased to the small particles that a very large number of particles need to be considered in order to have an adequate number of large particles for the results to be realistic. In such cases it has been found to be faster to use the second approach.

Figure 5 illustrates two of the particle size distributions that have been used, MIL-SPEC-C and AC Coarse. Both the calculated distributions (using the first approach with 100000 particles) and the data on which the calculations were based are shown, showing

the validity of the approach for the MIL-SPEC-C sand. The discrepancy at the top end of the AC Coarse distribution indicates a requirement for an increased number of particles if this data is to be fitted correctly.

### 2.4 Erosion calculation

The erosion rate of the material is calculated after the trajectory calculation by applying correlations to each individual impact. The individual contributions for all of the impacts are then combined to give a description of the erosion rate for the surface. Figure 6 shows the correlation [ref. 10] for the erosion of Ti6Al4V alloy subject to the impact of quartz particles. The erosion rate,  $E$ , gives the amount of material eroded (in mgm) per gram of impacting erodant. For later display as contours of erosion,  $E$  is related to the total mass of erodant entering the geometry during the trajectory calculations.

## 3. RESULTS

The method described above has been applied to several different geometries, some of which will be described here. The first serves as a validation case for the trajectory predictions.

### 3.1 Tube with Abrupt Contraction

This geometry, as described by Ye and Pui [ref. 11] is used to model a variety of particle filters, different filters being treated by using different tube diameters and contraction ratios. The fluid flow in these geometries was calculated using a viscous, compressible, axisymmetric finite-volume method.

Figure 7 shows both the predicted fluid flow and the calculated particle trajectories in one such case, with a contraction ratio of 9. The particles which impacted the wall were considered to have been filtered off and so the calculation of the trajectory stopped. The results are presented in figure 8 as a comparison of the variation of filtration efficiency plotted against the square root of Stokes' number,

$$Stk = \rho_p d^2 V_a / (18 \mu D)$$

where

$V_a$  is the inlet fluid velocity  
 $D$  is the outlet tube diameter  
 $d$  is the particle diameter.

The filtration efficiency is defined as :

$$\frac{(\text{Mass of particles filtered})}{(\text{Mass of particles injected})}$$

As  $Stk$  includes a  $d^2$  term, the square root of  $Stk$  forms a non-dimensional measure of the particle diameter. The calculations were performed for each geometry over a range of Stokes' numbers from 0.01 to 4.0 giving an overall range of particle sizes from 0.1  $\mu m$  to 16  $\mu m$ . The results show good agreement over this range of Stokes' numbers for the case with the lowest tube Reynolds number and reasonable agreement for the other two cases. As a result it is possible to have confidence in the ability of the program to correctly predict the particle trajectories for this class of particle sizes. The trajectories of larger particles are generally dominated by rebound effects, rather than aerodynamic effects, and so the validation for this range of particle sizes is considered adequate for the majority of calculations.

### 3.2 Inlet Particle Separator (IPS)

The airflow through the axisymmetric IPS geometry was calculated using a finite volume Navier Stokes code. For the particle trajectory calculations a degree of randomness was added to the rebound model, similar in principle to the probabilistic bounce model used in ref. 12. In addition a modified form of the  $C_d$  correlation was used in which a factor, varying with particle size, was introduced to obtain an improved correspondence with the experimental results for one case.

The predicted trajectories for two different particle sizes are shown in figure 9. The large particles rebound from the inner and outer walls and all exit via the scavenge duct. The small particles tend to follow the flow to a much greater extent and a large fraction are swept into the engine. In this case it is clear that the position and shape of the splitter lip will have a significant effect on the separation efficiency of the IPS as there is a clearly defined point on the splitter whereby particles impacting to one side of it exit via the scavenge duct. Those impacting to the other side of this point enter the engine.

Two different designs of IPS have been studied, the two differing only in the shape of the splitter lip. Calculations of particle trajectories have been performed for a range

of particle sizes for both these geometries and the variations of separation efficiency, derived from these calculations, are compared in figure 10. For the IPS geometry the definition of efficiency that is used is that of concentration efficiency

$$\eta = 1 - \frac{(\text{Sand concentration entering engine})}{(\text{Sand concentration at entry to the IPS})}$$

Geometry 1 has the greater efficiency for small particle sizes. For large sizes the efficiencies of the two geometries are the same but between these two extremes is a region where geometry 2 has the higher efficiency. It is evident that for particle sizes greater than about 10  $\mu m$  the method is predicting too high an efficiency. On test geometry 1 gave an efficiency which was 3 percentage points higher than that of geometry 2. This difference has not been reproduced in the calculations, though the efficiency of geometry 1 is predicted to be higher than that of geometry 2 in the region where there is better agreement with the experimental results.

The performance of geometry 1 has also been predicted at two other scavenge ratios and the results for all three are shown in figure 11. It is evident that the efficiency increases with increasing scavenge ratio. This result is in accord with that found in the experiment.

### 3.3 Inertial Air Filter

The geometry of this device is illustrated in figure 12. The airflow through it was calculated in two parts. The helical part was calculated as a three-dimensional field while the rear part of the filter was calculated as an axisymmetric field ; both calculations used the same finite-element Navier Stokes code. The two fields were joined together for the trajectory predictions. Two versions of this filter exist, the difference between the two concerns the length of the helical portion. As for the IPS, a number of calculations have been performed for the two geometries using a range of particle sizes. The results of these calculations are presented as curves of filtration efficiency plotted against particle size for both geometries in figure 13, together with the experimental results for one of the geometries. The definition of filtration efficiency used here is the same as section

3.1. The prediction shows a more rapid rise in efficiency with particle size than the experiment, but generally there is good agreement between the prediction and the experiment. The superior performance of geometry 1 is evident from this figure. In overall efficiency the calculations predict a difference of 6.3 percentage points between the two geometries.

### 3.4 Axial Compressor Rotor

For this case the flowfield was calculated using a three-dimensional time-marching Euler code. The predicted particle trajectories for two different sizes of particle, 10  $\mu\text{m}$  and 100  $\mu\text{m}$ , are shown in figure 14. For clarity only 30 trajectories are shown in each; normally a prediction would involve many more particles.

In the results with the 10  $\mu\text{m}$  diameter particles it can be seen that some particles travel straight through the compressor without any impact. Others however impact the blade pressure surface and then travel towards the casing as a result of the influence of the centrifugal force. Certain of these particles then impact the casing downstream of the blade trailing edge. With the 100  $\mu\text{m}$  particles the influence of the fluid is reduced and, rather than following the fluid, they all impact the pressure surface. The effect of the centrifugal force is greater than with the smaller particles resulting in an increased number of impacts on the casing downstream of the trailing edge. The results of these differences in the trajectories can be seen in figure 15 as contours of erosion on the various surfaces for the two particle sizes. For these plots the trajectory computations were reformed with 10000 particles each to give more realistic results. In each case the pressure surface and casing are subject to the most significant erosion. With the 100  $\mu\text{m}$  particles the peak erosion is found on the pressure surface, though not all of the surface is eroded. Near the hub only about 50% of the blade chord is eroded as a result of the shielding effect of the adjacent blade. The peak erosion occurs near the ends of the blade as these regions suffer impacts from particles which have already impacted the endwalls as well as those particles which strike the pressure surface directly. For the 10  $\mu\text{m}$  particles the magnitude of the erosion is considerably reduced but it now affects

almost the whole of the surface. The erosion of the casing with the 10  $\mu\text{m}$  particles is very light and mainly confined to a region downstream of the trailing edge whilst the 100  $\mu\text{m}$  particles cause the area eroded to be more extensive with a small peak occurring approximately one chord downstream of the trailing edge.

A comparison of the erosion contours on the pressure surface predicted using the AC Coarse distribution of particle sizes with those from experiment is shown in figure 16. The extent of the eroded area has been well modelled, as has the overall erosion level. The peak erosion levels also compare well, though in the prediction this occurs near the endwalls whereas the experiment shows it occurring at about 50% blade height. The most probable reasons for this difference are an uncertainty which exists in the initial conditions for the particles and a difference in the endwall shape between the prediction and the experiment.

### 3.5 Centrifugal Compressor Rotor with Splitter Blade

The flowfield in this geometry was predicted using a similar method to that used for the axial compressor. Particle trajectories have again been calculated for both 10  $\mu\text{m}$  and 100  $\mu\text{m}$  diameter particles and they are shown in figure 17. The 10  $\mu\text{m}$  particles follow the flow to a greater extent than the 100  $\mu\text{m}$  ones and so undergo fewer collisions with the blade and endwall surfaces. With the 100  $\mu\text{m}$  diameter particles all the particles impact the main pressure surface of the blades near the leading edge and then impact the same surface again at about 50% axial chord. The second impact is then followed almost immediately by an impact with the casing. The particles then experience several further impacts with the blades and endwalls before exiting from the rotor passage. This particular compressor features single splitter blades in each rotor passage and, although the particles pass very close to the splitter leading edge, there are no impacts on the splitter blades in this calculation.

A calculation has also been performed for this geometry with a considerably increased number of particles with sizes obtained from an AC Coarse size distribution. As for the axial compressor the majority of the erosion occurs on the pressure surface, with none at

all on the hub or the suction surface and only very little on the casing. The erosion on the pressure surface is shown in figure 18.

The region of erosion which results from the initial impacts near the leading edge can be clearly seen as can the extended region caused by the various subsequent impacts.

#### 4. CONCLUSIONS

A method has been developed and validated for the prediction of the trajectories of sand particles in gas turbine engine components. In addition it can calculate the erosion which arises from the impacts with the surfaces.

This method has been used to calculate the particle trajectories and erosion in two different gas turbine compressors and also the separation efficiencies of two different types of filter. Where available these results have been compared with those from experiment. The comparisons are generally good, showing that the method can be used for the optimisation of gas turbine engine components.

#### ACKNOWLEDGMENTS

The authors wish to thank SOFRANCE (LABINAL Group (F)) for providing geometries, aerodynamic computations and experimental results. They also thank ROLLS-ROYCE (GB) for their provision of geometries and experimental results.

#### REFERENCES

1. P. MONGE-CADET, F. PELLERIN  
Revêtements Anti-Erosion Multicouches  
Paper31, AGARD Symposium on  
Erosion, corrosion and foreign object  
damage effects in small gas turbines,  
April 1994
2. M. JARIFI  
Prédiction des trajectoires de particules  
transportées par le fluide traversant une  
turbomachine, en vue de l'étude de l'éro-  
sion des parois.  
Thèse de l'Ecole Nationale Supérieure  
des Mines de Paris, 1982
3. A. HAMED  
An investigation in the variance in  
particle surface interactions and their  
effects in gas turbines.  
ASME Journal of Engineering for Gas  
Turbines and Power, Vol 114, pp235-  
241, April 1982
4. W. TABAKOFF, A. HAMED  
Effect of environmental particles on a  
radial compressor.  
AIAA paper AIAA-88-0366, 1988
5. W. TABAKOFF, A. HAMED  
Three-dimensional particle trajectories in  
turbomachinery.  
I.Mech.E paper C63/81, 1981
6. G.B. WALLIS  
One-dimensional and two-phase flow.  
Magraw-Hill, New York, 1969
7. M. SOMMERFELD, G. ZIVKOVIC  
Recent advances in the numerical  
simulation of pneumatic conveying  
through pipe systems.  
Computational Methods in Applied  
Sciences, pp201-212, 1992
8. W. TABAKOFF, A. HAMED  
Aerodynamic effects on erosion in  
turbomachinery.  
Proceedings of the 1977 Tokyo Joint Gas  
Turbine Congress, pp574-581, 1977
9. S. ELFEKI, W. TABAKOFF  
Erosion study of radial flow compressor  
with splitters  
ASME paper 86-GT-240, 1986
10. B.R. VITTAL  
A design system for erosion tolerant  
helicopter engines  
Presented at the Specialists' Meeting on  
Rotary Wing Propulsion Systems,  
Williamsburg, Va. Nov 1986
11. Y.YE, D.Y.H. PUI  
Particle deposition in a tube with an  
abrupt contraction.  
J. Aerosol Sci., Vol 21, No.1, pp29-40,  
1990
12. A. HAMED, Y.D. JUN, J.J. YEUN  
Particle dynamics simulations in inlet  
separator with an experimentally based  
bounce model  
AIAA paper AIAA 93-2156

## QUESTIONS

### A. HAMED (US)

Q. You mentioned modifications to the drag coefficient and the particle restitution ratio. Can you explain:

- i) what are the modifications to  $C_d$ ?
- ii) what type of randomness was introduced in the particle rebound?
- iii) what is the basis of these modifications?
- iv) how were they validated compared with your initial validations for the original  $C_d$  and rebound models?

A. The modifications to the  $C_d$  model were developed in an attempt to determine whether the discrepancy between the initial predictions and the experimental results could be accounted for by inaccuracies in the  $C_d$  model. It consists of a factor, dependent on the particle size, which is applied to the  $C_d$ , as calculated by the correlation. The factors for a few particle sizes were obtained by trial and error to obtain good agreement with experiment for the datum case (Geometry 1, design scavenge ratio). The factors for other sizes were obtained by fitting a curve through the initial points. The same factors were then used for all the IPS calculations.

The random rebound was introduced to provide some modelling of the effects on the rebound of surface roughness and the non-sphericity of the particles. It consists of a factor (generated randomly, centred about 1.0) which is applied to the changes in the velocities, normal and tangential to the surface, as calculated using the correlations.

The modifications have not been further validated. Obviously the lack of physical justifications for the modifications is not very satisfactory, but they have served to indicate that modifications to the  $C_d$  and rebound models can correct most, if not all, or the discrepancies with the original results.

### V.R. PARAMESWARAN (Ca)

Q. The last three papers talked about the use of inertial particle separators. What are the possibilities of these being eroded themselves and particulates from these ingested into the engine? What materials are used for the inertial separators?

A. The IPS is mainly titanium alloy, with some parts made of stainless steel. The air velocities in the IPS are considerably lower than the relative velocity at entry to the compressor. It would be expected that the particle velocities would also be much lower and the erosion of the IPS would be very small.

**P. STALLARD (UK)**

- Q. For the IPS work, what were the 'small' and 'large' particle sizes, as discussed in the text and Figure 9?  
For the vortex tube separator, what was the diameter of the vortex tube?  
Was the experimental work for single tube, not multi-tube panel?
- A. The small particle size was about 3 micron, the large particle size was about 50 micron.  
The vortex tube had a diameter of approximately 1 cm.  
Yes, the experimental efficiencies quoted are for a single tube.

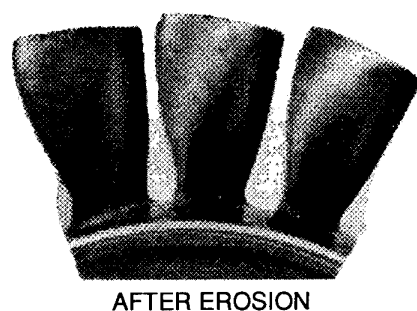
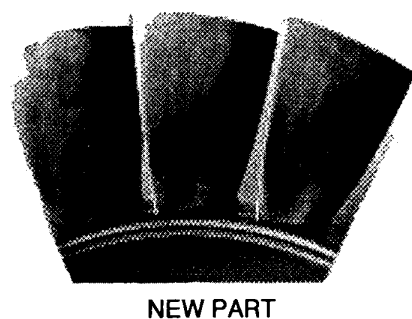


Figure 1 - Illustration of erosion in axial compressor

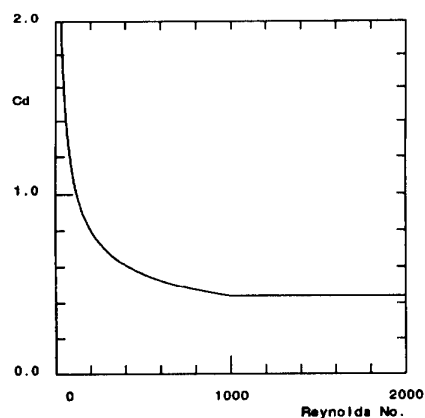


Figure 2 - Correlation for drag force coefficient

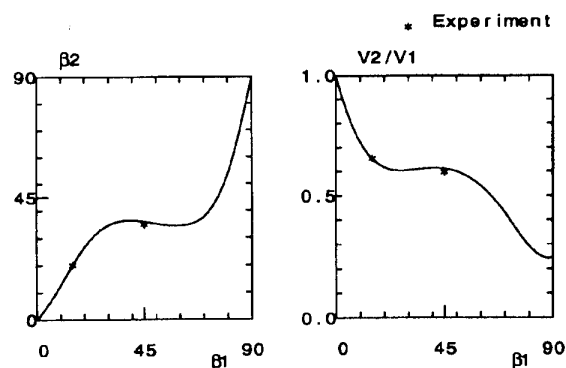


Figure 4- Rebound correlation for quartz particles impacting stainless steel target

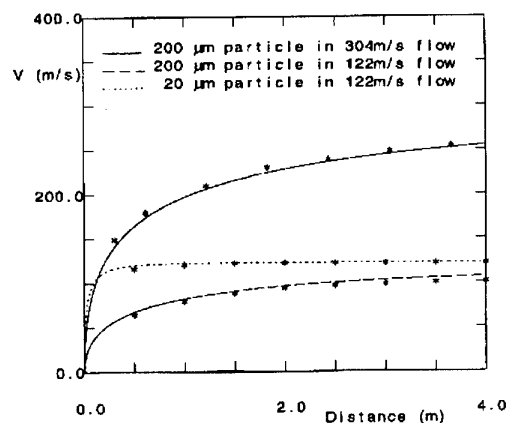


Figure 3 - Comparisons of predictions for particle acceleration with the results of Tabakoff and Hamed

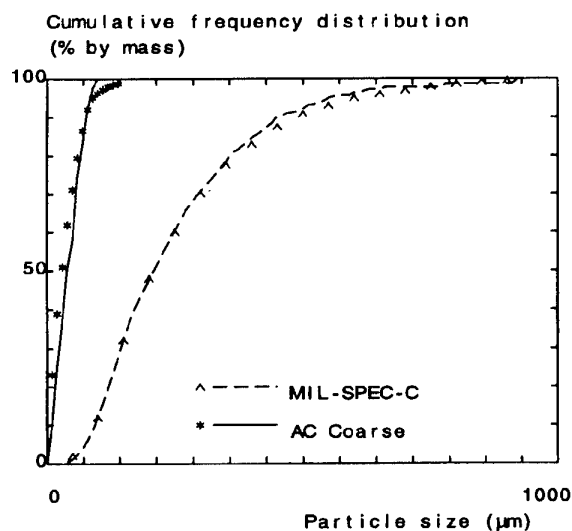


Figure 5- Particle size distributions for two standard sands

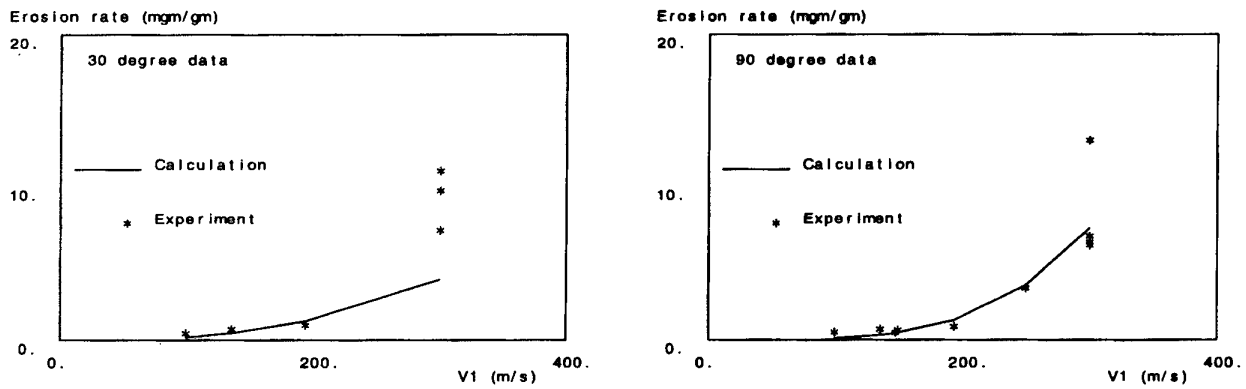


Figure 6 - Erosion rate correlation for quartz impacting a titanium alloy target

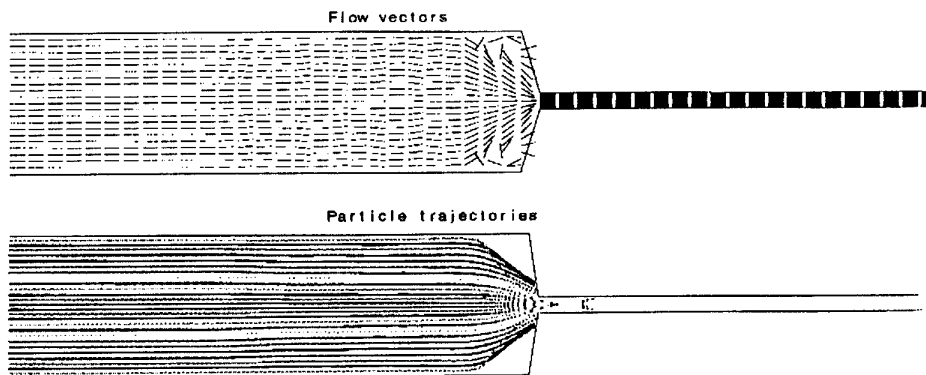


Figure 7 - Flow field and particle trajectories for contraction tube

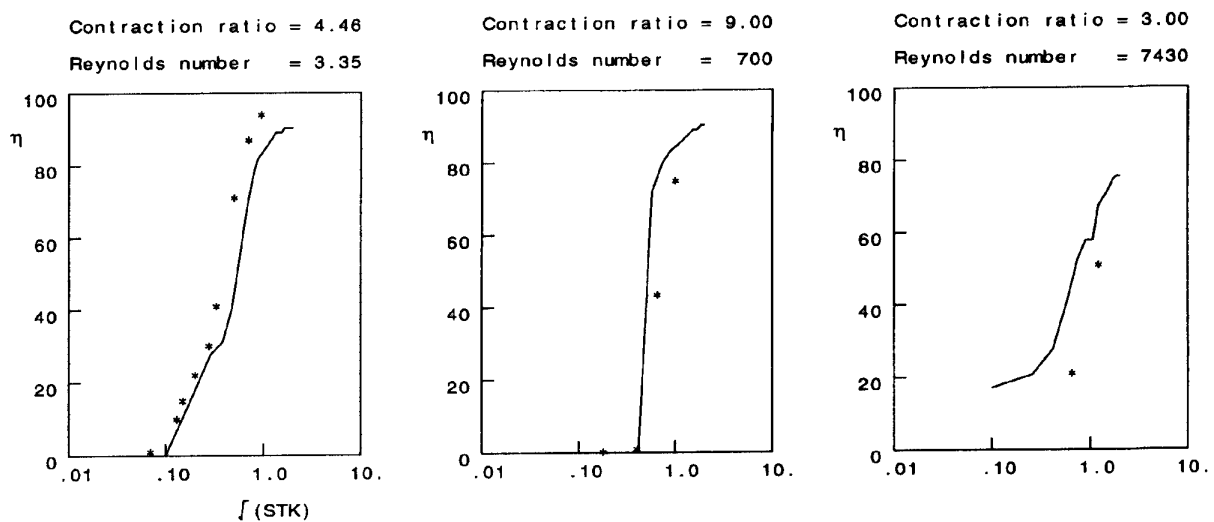


Figure 8 - Predictions of filtration efficiency for three contraction tube cases



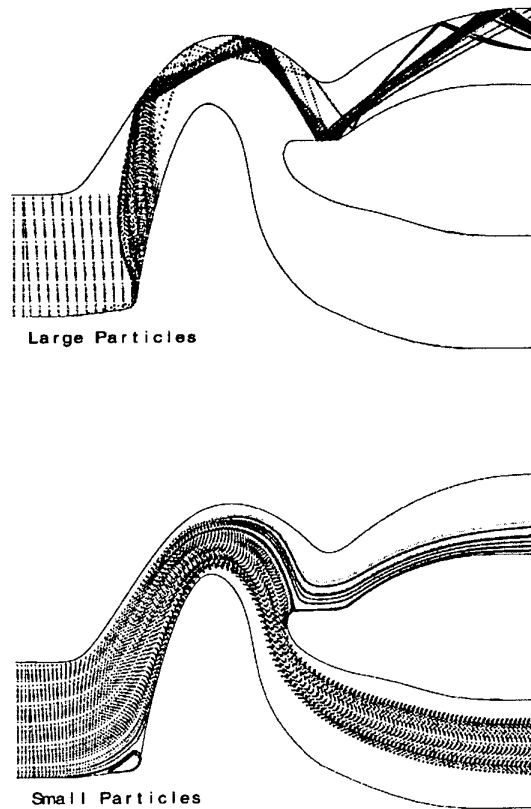


Figure 9 - Predicted particle trajectories in IPS geometry

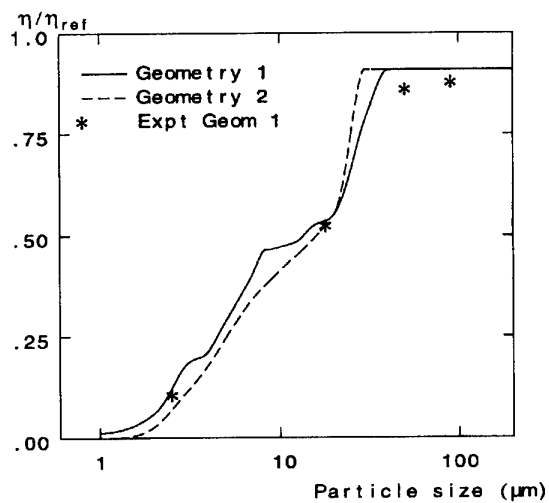


Figure 10 - Predicted variation of concentration efficiency with particle size for two IPS designs

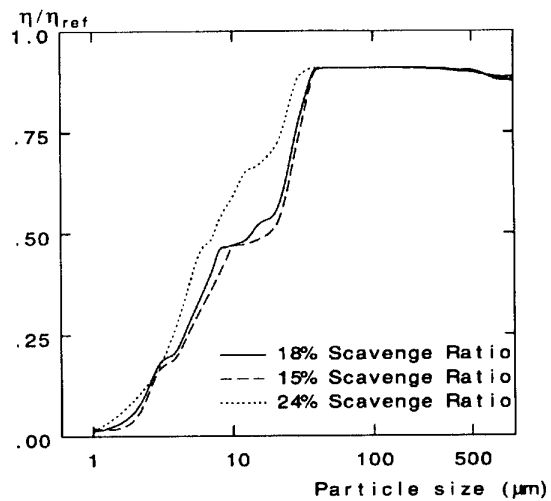


Figure 11 - Predicted variation of concentration efficiency for three scavenge ratios for IPS

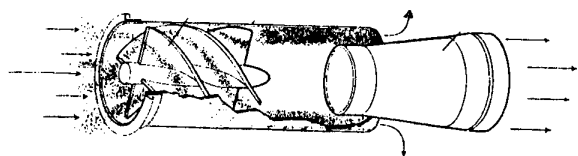


Figure 12 - Geometry of inertial air cleaner

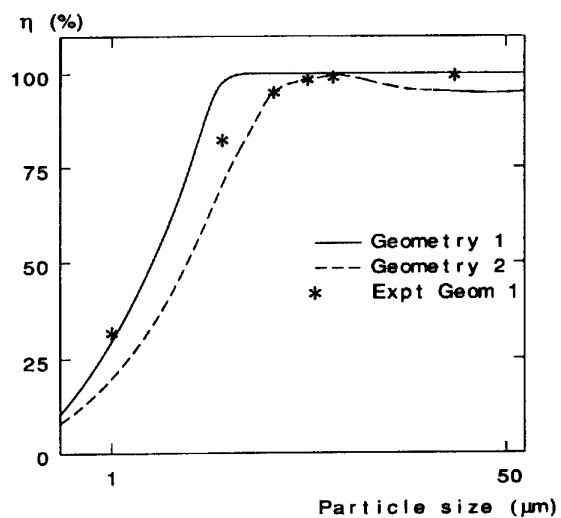


Figure 13 - Predicted separation efficiency variations for two inertial air cleaners

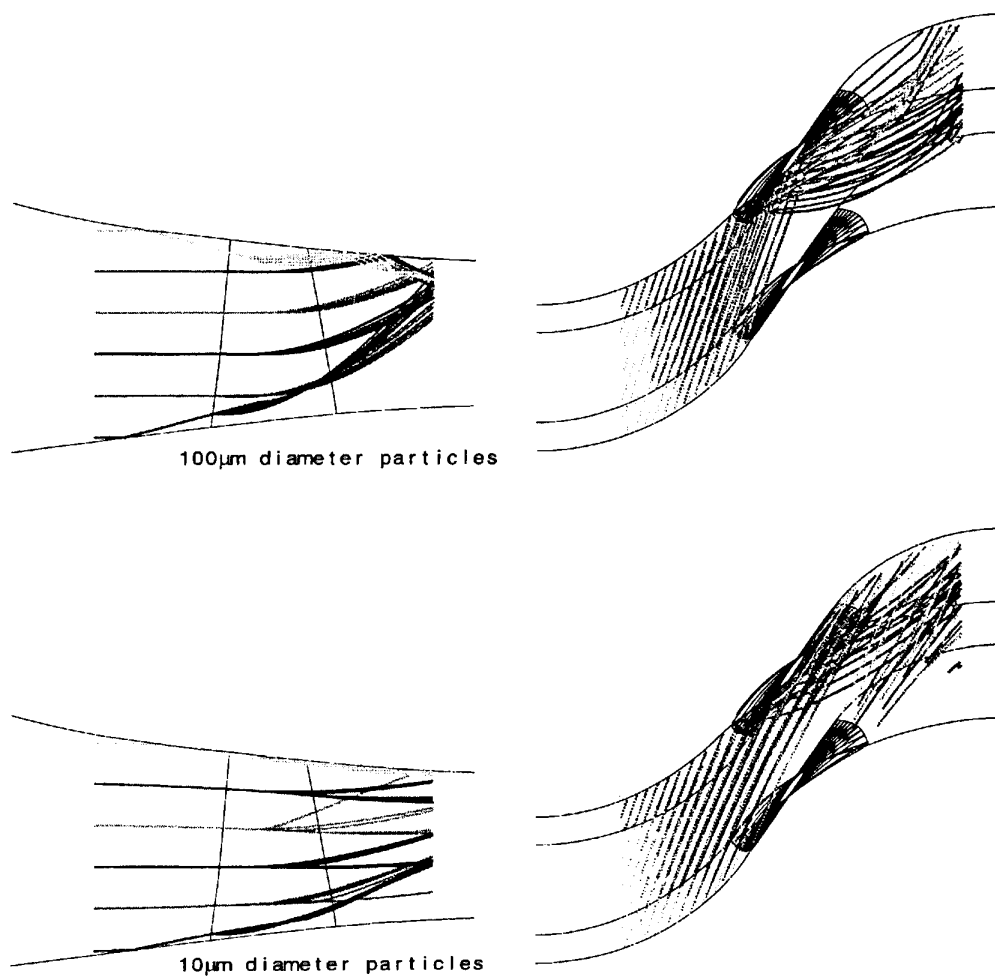


Figure 14 - Predictions of particle trajectories in axial compressor

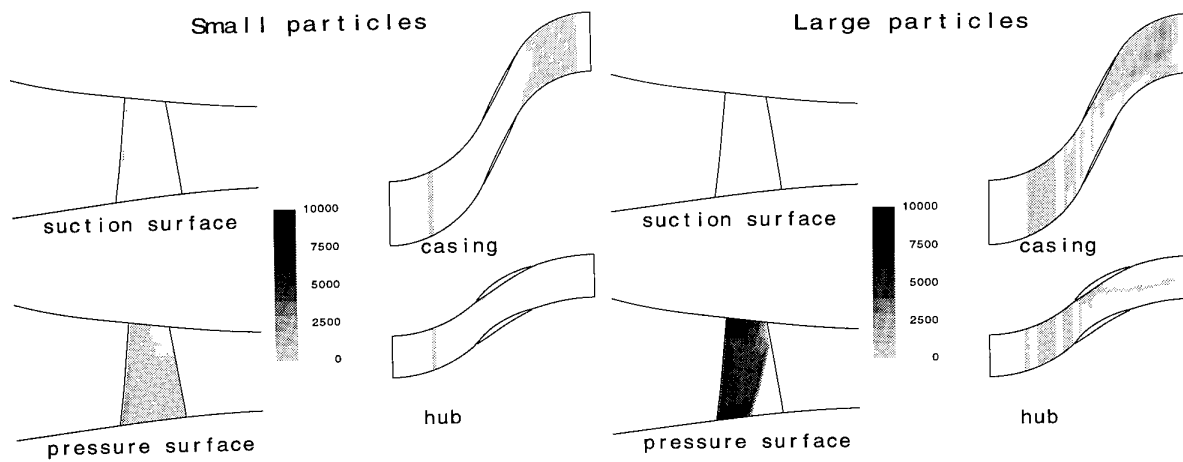


Figure 15 - Predicted erosion contours for two different particle sizes in axial compressor ( $\text{mgm/gm/m}^2$ )

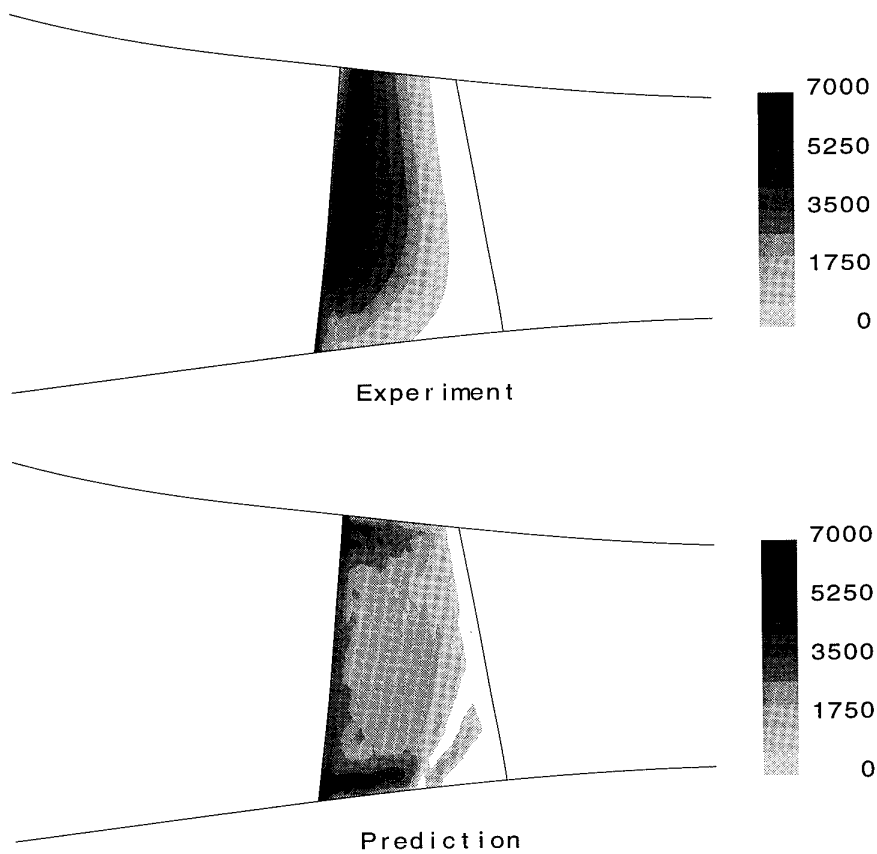


Figure 16 - Comparison of prediction for AC Coarse sand with experiment ( $\text{mgm/gm/m}^2$ )

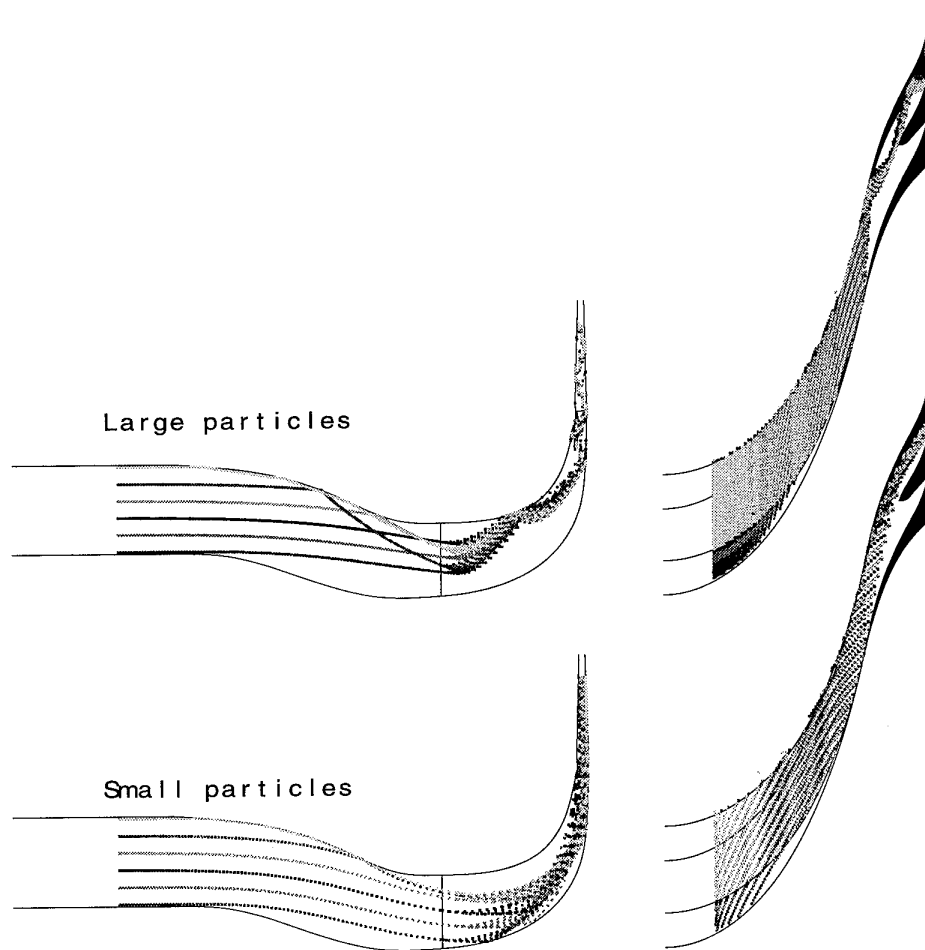


Figure 17 - Predicted trajectories in centrifugal compressor

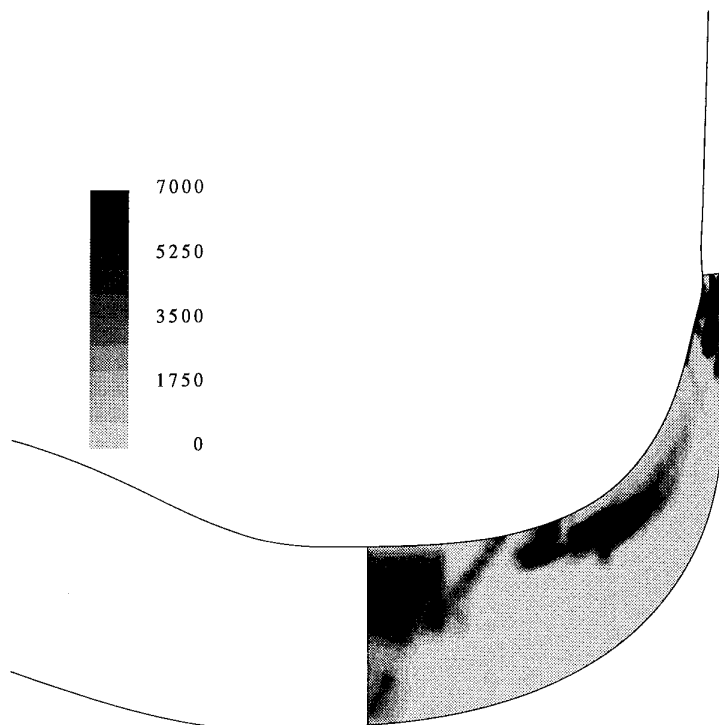


Figure 18 - Predicted erosion on pressure surface of centrifugal compressor ( $\text{mgm/gm/m}^2$ )

## Performance Deterioration of Axial Compressors Due to Blade Defects

J. Schmücker

A. Schäffler

MTU München

Dachauer Str. 665, 80976 Munich  
Germany

### Summary

During flight operation the engine swallows sand or other hard particles usually from the runway. Passing through the compressors they will damage the blades, erode the coating and deteriorate seals.

The submitted paper presents some measurements, which show the effect on compressor performance due to the most important and frequent defects.

The investigation - conducted at high pressure compressors - comprehend tests with reworked blades at leading and trailing edges, rounded rotor tips and increased tip clearances. The results are summarised in easy to handle correlations, which enables the user to estimate the deterioration and to fix repair rules within the allowed performance loss range.

For example the dominant role of tip clearance effects may force the designer to provide passive or active clearance control or to choose special materials for blades and coatings.

Later on the engines return from the customer to the shop for overhaul. Then the permitted extent of repair work has to be fixed due to the allowed shortfall in performance of a used engine.

In order to know the effect of defects as damaged leading and trailing edges, rounded tips or rubbed coatings i.e. increased clearances several test were conducted in the past, from which repair rules were derived. The most important results from measurements at HP-compressors are presented in this paper.

### List of Symbols

A	tip clearance factor	-
F	area	m <sup>2</sup>
h	blade height	m
Kv	blade area loss parameter	-
l	chord length	m
M	mass flow	kg/s
Ma	Mach number	-
Re	Reynolds number (chord)	-
r	radius	m
s	tip clearance	m
SM	surge margin $((\pi_{SL} - 1)/(\pi_{WL} - 1))$ at constant flow	-
z	number of stages	-
$\Delta$	difference	-
$\eta$	efficiency (isentropic)	-
$\pi$	pressure ratio	-

### Suscripts

R	rotor
S	stator
SL	surge line
WL	working line

### 1 Introduction

In the time of the design and development of an engine it is necessary to get as early as possible informations on the behaviour of the compressors in engine under running conditions.

### 2 Rigs and test set up

The investigated compressors are of very small size and of low transonic flow high pressure compressors without inlet guide vanes or variable stators. The five-stage version is a research compressor, while the six-stage machine is provided for the RB199 engine. A rough scheme of the compressor is given in figure 1. The small dimensions of the blading can be seen by the values of chord length and blade height being 26/34 at rotor 1 and 11.5/19 [mm] at rotor 6.

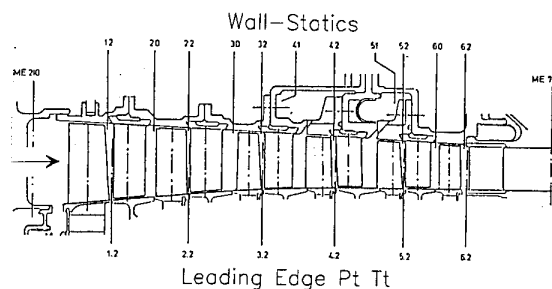


Fig. 1: Six-Stage Rig Compressor

Both are at that time (about 1968) highly loaded and designed without preswirl to all stages. The flow path is characterized by a high hub to tip ratio and the blades by a high aspect ratio. Table 1 reviews the main parameters.

	Rig 212/208	Rig 207/211/220
No. of stages	5	6
Mass flow per front area [kg · √k / (s · kPa · m <sup>2</sup> )]	26	29
Pressure ratio	2.87	3.68
Hub to tip ratio at inlet	0.84	0.82
Tip Mach-number	.92	1.01
Blade typ: Rotor Stator	DCA NACA65	DCA NACA65

Tab. 1: Design Values of the High Pressure Compressors

The rig testing was done with the swan neck duct in front of the compressor including the struts and simulators to create the boundary layer and the stator wakes coming from the intermediate pressure compressor in the engine. At first the outlet channel was cylindrical, but later replaced by the dump diffusor and the combustor.

The overall performance map was measured by use of a Venturi flowmeter at inlet and total pressure and temperature rakes both radially and circumferentially arranged.

The cold tip clearances were determined during the assembly in the shop and at some tests by a capacitive distance measuring system over the second and last rotor.

### 3 Results and Discussion

#### 3.1 Reworked leading and trailing edges of rotors and stators

During flight operation small hard particles (usually sand from runways) pass through the core engine, leading to foreign object damage (FOD) on the compressor blading. Statistical evaluation of flight engines which came into MTU for repair gave the following broad picture:

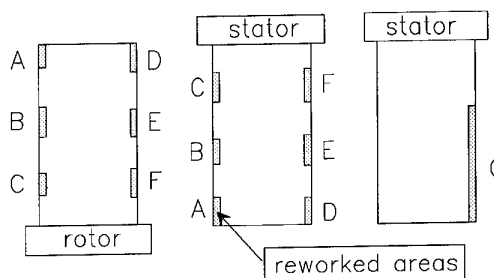
- damage is spread equally over all stages
- 2/3 of the rotor blades are hit at the leading edge and 1/3 at the trailing edge
- 1/3 of the stator blades are hit at the leading edge and 2/3 at the trailing edge
- cracks are equally distributed over the blade height

For overhaul of the engines these damaged blades will be reworked by blending of the leading and trailing edges. Especially the rounding of the leading edges after blending is inspected closely. The range of blending per blade is mainly due to mechanical reasons.

Assuming that the permitted amount of blending - fixed in the repair rules - will not change, the only degree of freedom is the number of reworked blades which can be mixed into each blade row.

Therefore a test programme was scheduled in order to evaluate the effect of reworked blades on the compressor performance. The programme at the six-stage high pressure compressor rig started with a new engine module which gives the basic performance calibration, called build 1.

Then in two steps (build 2 and 3) the number of reworked blades was increased from 10% to 22%. The damage types (Fig. 2) reflects typical mixes as normally experienced. The amount of rework goes to the maximum allowed level and is spread equally over all blade rows, except stator 6 (Tab. 2).



	% of blade height reworked (only one typ of rework per blade)		
	Leading edge	Trailing edge	
	Typ A, B, C	Typ D, E, F	Typ G
Rotor	28,3	28,3	--
Stator	26,6	26,6	65,0

Fig. 2: Description of Rotor and Stator Blades Reworked

		% of reworked blades						
Build		2			3			4
Typ		A,B,C	D,E,F	G	A,B,C	D,E,F	C <sub>j</sub>	A,B,C
Rotor	1	5.8	3.8	-	15.4	7.7	-	50.0
	2	6.9	3.4	-	13.8	8.0	-	49.4
	3	6.2	2.7	-	14.2	8.0	-	50.4
	4	6.7	3.7	-	13.3	8.9	-	49.6
	5	6.5	3.6	-	13.7	8.6	-	50.4
	6	6.4	3.5	-	14.2	8.5	-	49.6
All Rotors		6.4	3.5	-	14.1	8.3	-	49.9
Stator	1	3.3	3.3	3.3	7.8	7.8	6.7	-
	2	3.0	3.0	4.0	8.1	6.1	8.1	-
	3	3.3	3.3	3.3	7.3	8.1	6.5	-
	4	3.3	3.3	3.3	7.2	7.8	7.2	-
	5	3.1	3.8	3.1	7.5	8.8	6.3	-
All Stators		3.2	3.3	3.4	7.6	7.7	7.0	-

Tab. 2: Summary of Rework at Rotors and Stators

A fourth test should cover a high percentage (50%) of a specific type of damage i. e. rework of rotor leading edges but no other blending. This is usually thought to be the most detrimental to surge margin. All four tests are run with the same tip clearances. The test results of build 1, 2 and 3 are illustrated in Fig. 3 for the typical engine bleed flow case at atmospheric inlet conditions. Average rotor Reynolds number is  $Re=3 \cdot 10^5$  which corresponds for instance to 42 000 feet/Ma=0.5 flight condition.

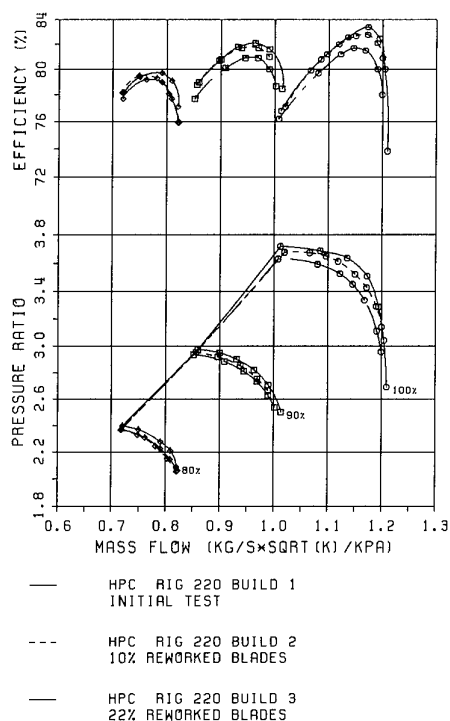


Fig. 3: HPC-Rig 220, Build 1, 2, 3 Influence of Reworked Blades on Performance

The plotted speed lines 80, 90 and 100% represent the normal engine operating range.

A steady decline of mass flow function and efficiency can be seen which amounts to a loss of 1.5% in build 3 at 100% non-dimensional speed on an engine running line. The corresponding values for build 2 are 0.8% and 0.6%.

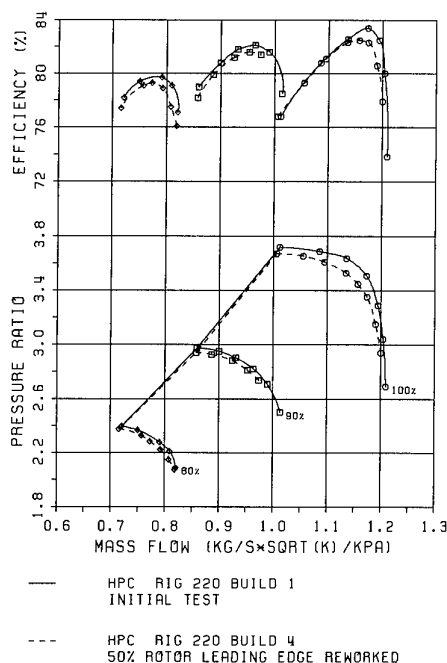


Fig. 4: HPC-Rig 220, Build 1, 4 Influence of Rework Rotor Blades on Performance

Surprisingly little reduction of surge margin could be noticed. Only a 2-3% decrease was encountered at 100% r. p. m. reducing to zero at 90% and lower speeds.

The effect of reworked rotor leading edges in build 4 (fig. 4) yielded a similar result as build 2. The well rounded leading edge thickening and the decreased chord length reduce flow and efficiency by 1.2% and 0.8% respectively whereas the effect on surge margin is very small.

At the 100% speed line the builds 1 to 4 were measured with different bleed flows. With bleed port closed additionally the Reynolds number was lowered in several steps down to  $Re = 1,4 \cdot 10^5$ . The results of these test series indicate the same behaviour of mass flow, efficiency and surge margin as found out with the basis series described above.

In order to correlate the test results, a simple, easy to handle parameter is needed which at least describes the basic effects of blade rework.

Blade rework acts in various ways on the compressor flow:

Rework of leading edges reduces chord length, increases incidence angle and thickness of the leading edge radii.

This combination of effects leads to the following effects:

- increased losses due to higher incidence at the stall end of the loss curves and increased supersonic losses
- reduced blade turning
- possible earlier stall due to higher loading (reduced blade area) or distinct incidence stall.

Blade rework at the trailing edges reduces chord length, increases pitch/chord ratio, reduces exit flow angle directly and increases trailing edge thickness.

This combination of effects leads to the following effects:

- increased losses due to thick trailing edges (especially effective on stators due to the unsteady effects of wake boundary layer interaction on the following rotors)
- significantly reduced flow turning in the whole operating range.

As it is difficult to describe the different effects of all the variety of blade rework encountered, a very simple correlation parameter can be a description of the total blade area lost in relation to the overall blade surface of a new compressor, disregarding whether rotor or stator blades are reworked.

The blade area loss parameter  $K_v$  is defined to:

$$K_v = \frac{\Sigma \Delta F_R + \Sigma \Delta F_S}{(F_R + F_S)_{new}} \cdot 100 (\%)$$

Table 3 summarizes the blade area loss parameter  $K_v$  for the test series, showing that in builds 3 and 4 about 0.4 % of the total blade area was removed.

build	1	2	3	4
blade area Kv	0	0.196	0.429	0.380
loss factor [%]				

Table 3: Area Loss Parameter

If the blade area loss parameter is used straight forward the result plotted on fig. 5 can be obtained for the test series.

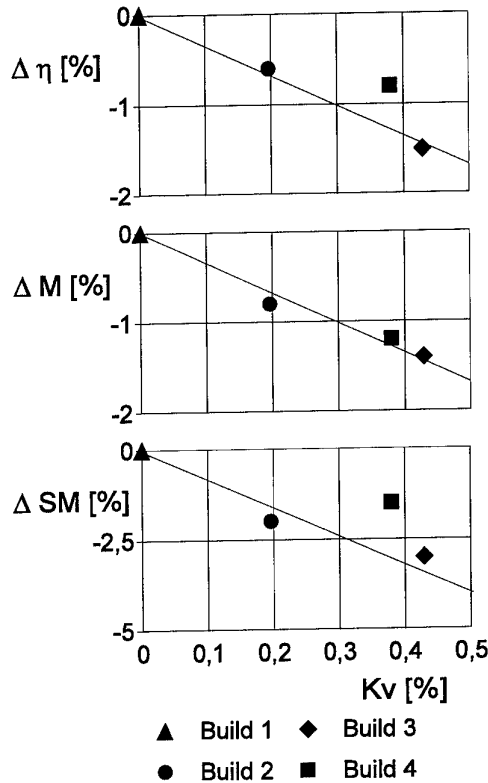


Fig. 5: HPC-Rig 220  
Loss in Efficiency, Mass Flow and Surge Margin  
versus Blade Area Loss Parameter

A linear degradation of mass flow and efficiency appears for builds 1 - 2 - 3, which is very much the expected result due to the same distribution and type of blade rework.

A somewhat smaller effect on efficiency and surge margin reduction was experienced for the pure rotor leading edge rework in build 4 which produced almost the same blade area loss as build 3.

Nevertheless, the simple parameter can describe in first order the performance loss to be expected for a rework of that amount. The reduced performance loss in build 4, however, does lead to four important conclusions:

- rotor leading edge rework does only moderately impair the relatively low Mach Number compressor if the rework is done properly, i. e. the leading edges are well rounded,
- the compressor is stalling due to blade loading and not in a plain incidence stall mode,

- the damage and rework to the trailing edges of the stators are probably more harmful to the compressor than the leading edge rework of the rotors,

- the resulting internal stagewise mismatch due to the rework is small due to the low pressure ratio and Mach Numbers and the generous choke margins applied in the design, leading to wide efficiency islands.

### 3.2 Tip rounded rotor blades at leading and trailing edges

In service the engine will swallow dust and small sand particles. They pass through the compressors and lead besides other disadvantages to erosion at the rotor tips and the blades show rounded leading and trailing edges at the tips. Also rubbing in the coating in connection with axial movements of the rotor tips result in such damages. On the other hand this type of blade error is some times encountered due to manufacturing accidents and the blades are mostly not long enough to overcome the problem by grinding.

In order to get an idea of the effect of tip rounded rotor blades on the performance tests with the 6-stage HP-compressor were carried out. The basic calibration test (build 5) used rotor blades with nearly sharp edges of 0.5mm radius which is the usual rounding. Then for the second test (build 6) the rotor blades of the stages 2, 3, 4 and 5 were rounded by a radius of 1.5mm. The other blades were as build 5 and also the test conditions as inlet pressure and temperature (same Re-No. level) or the bleed flow rate remained unchanged.

The test results in fig. 6 show an efficiency drop between 0.4 and 1% depending on speed and a constant loss in surge margin over the investigated speed range with a value of 4%, while the mass flow is nearly unaffected (-0,3%).

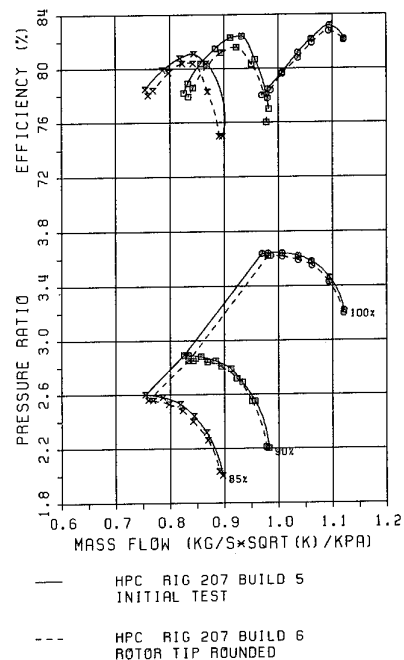
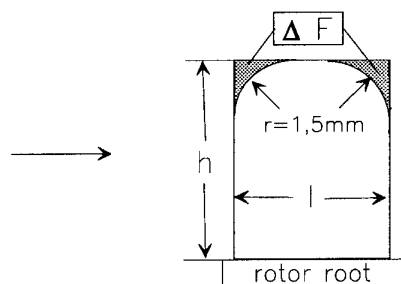


Fig. 6 HPC-Rig 207, Build 5 and 6  
Influence of Rotor Tip Rounding on Performance



As the rounding of 1.5mm is a large value (rotor 5 has  $l = 11.5$  and  $h = 21$ mm) the results indicate that a smaller amount can be allowed without a remarkable deterioration in performance. In order to have an easy to handle tool for estimating the effect of rounded tips or similar tip defects a correlation was established. It is assumed that the performance loss depends on the reduced blade area. So the missed area ( $\Delta F$ ) compared to the ideal blade is divided by the chord length and the blade height. The mean value for the whole compressor is defined in fig. 7.



$$(\Delta F / F)_{eq} = \frac{1}{z} \sum_1^z \left( \frac{\Delta F}{h \cdot l} \right)$$

Fig. 7: Definition of Area Loss Parameter

In fig. 8 the correlation is illustrated for the loss in efficiency and surge margin. As there is only one test result available a linear dependence was assumed.

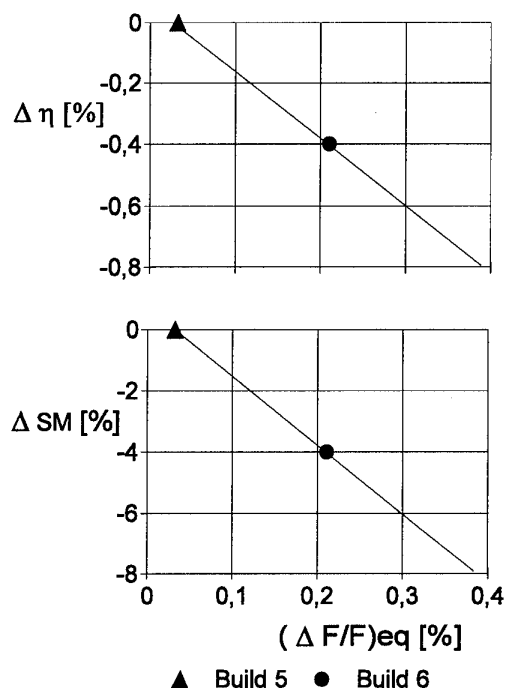


Fig. 8: Efficiency and Surge Margin Loss Versus Area Loss Parameter

### 3.3 Radial Tip Clearance

In service the compressor performance will deteriorate as rotor and stator tip clearances increase. Depending on the hardness of the material used for the abrasive coating the blade length is shortened when rubbing at the casing. The coating is rubbed out in form of trenches, which have sharp edges or - if the rotor undertakes larger axial excursions - a shallow transition to the untouched coating will be formed.

Also in the case that the blade does not contact the casing the clearance may be increased by erosion.

In order to establish a correlation between radial clearance and performance loss several tests with different HP-compressor rigs had been conducted. Results of a very early test in 1970 is presented on fig. 9 for a 5-stage compressor (rig 208). From build 1 to build 2 all rotor blades were shortend by 0.4mm.

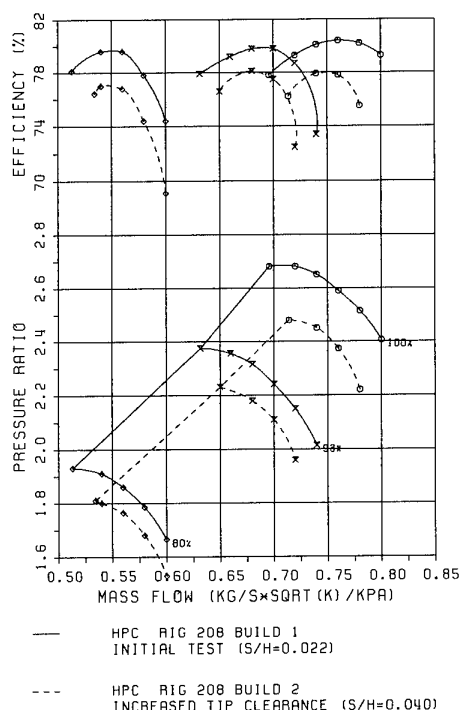


Fig. 9: HPC-Rig 208, Build 1 and 2  
Influence of Tip Clearance on Performance

The equivalent mean tip clearance, defined as

$$\left( \frac{\bar{s}}{h} \right)_{eq} = \frac{1}{1 + A} \left[ \left( \frac{\bar{s}}{h} \right)_R + A \cdot \left( \frac{\bar{s}}{h} \right)_S \right]$$

(with  $A=0.5$  for efficiency and mass flow and  $A=0.2$  for surge margin) was changed from 1.1% to 2.4% for the compressor running at 100% speed. At atmospheric inlet conditions a loss in mass flow of 4.1% (at engine working line), in efficiency of 2.6% and in distance from surge of about 15% was measured.

Since that test several HP-compressor rigs were tested including variation of rotor and/or stator clearance. In the fig. 10, 11, 12, all results are summarised in terms of the change

in equivalent tip clearance versus the loss of three main performance parameters. The investigated tip clearance range reaches from 1 to 3% and so comprise the usual values. Within this scope a linear relationship is reasonable, which is marked by straight lines in the plots. The mean loss for a 1% change in tip clearance is 2% in efficiency and mass flow and 7.5% in surge margin.

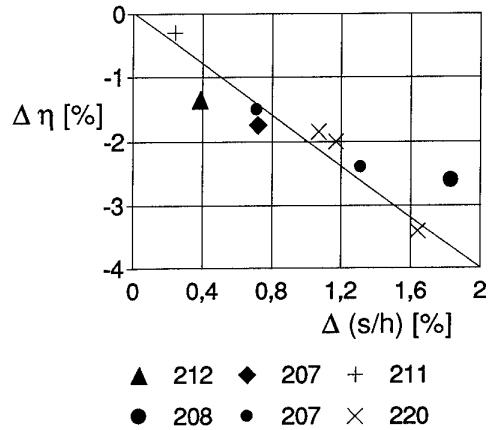


Fig. 10: Efficiency loss versus equivalent Tip Clearance

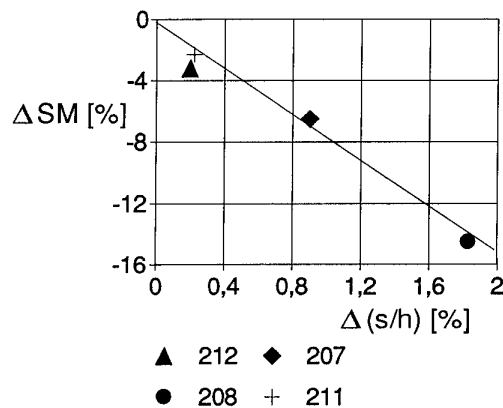


Fig. 12: Surge Margin Loss versus equivalent Tip Clearance

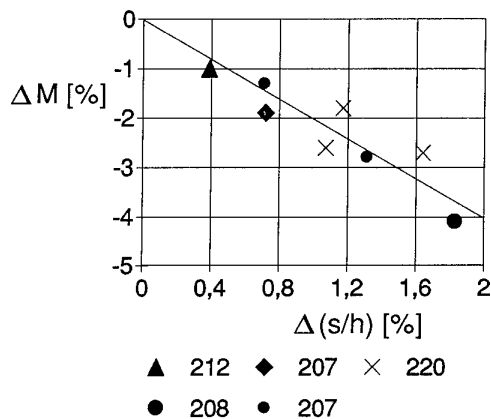


Fig. 11: Mass Flow Loss versus equivalent Tip Clearance

At the 6-stage compressor also a test series with trenches was conducted and the results fit quite well to the tests with a plane coating for efficiency and mass flow. The leading parameter is obviously the distance between rotor tip and coating.

#### 4 Conclusions

The results of several tests - conducted at high pressure compressors - lead to the following statements:

- If reworked blades are mixed together with new blades for a repair compressor even ten percent (corresponding to  $K_v = 0.2\%$ ) reduce the performance by more than half a percent in efficiency and mass flow and by two percent in surge margin. The effect is higher in the case of rework at stator trailing edges than at rotor leading edges.
- Tip rounded rotor blades of 1.5mm radius i.e.  $\Delta FIF = 0.18\%$  result in high surge margin loss of 4% and 0.4% in efficiency.
- The change in equivalent radial tip clearance by 1% reduces mass flow and efficiency by 2% and surge margin by 7.5%.

#### 5. Acknowledgements

The authors wish to thank MTU for the permission to publish this paper and all colleagues for their help.

# EROSION OF T56 5th STAGE ROTOR BLADES DUE TO BLEED HOLE OVERTIP FLOW

B. C. Barry  
T.C. Currie

Institute for Aerospace Research  
National Research Council of Canada  
Building M-7, Montreal Road  
Ottawa, Ontario, Canada K1A-0R6

## SUMMARY

Severe trailing edge erosion of ALLISON T56 gas turbine 5th and 10th stage compressor blades has been observed in Field Service Evaluations and sand ingestion tests. The erosion typically occurs within 3 mm of the blade tip and has been attributed to overt看 flow produced by the bleed holes present over the 5th and 10th stage rotors.

The overtip flow through the 5th stage bleed holes of an operating T56 has been surveyed with a laser two-focus (L2F) velocimeter in order to identify the features of the flow field responsible for the tip erosion. Two-dimensional measurements were made at 4 spanwise locations in the outer 25% of the span. Three-dimensional measurements were made at three spanwise stations within 7mm of the blade tip (15% of span).

The flow was found to be unaffected by the bleed holes beyond 3-4 mm from the blade tip. This result is consistent with erosion patterns observed on service-exposed blades and blades subjected to accelerated erosion in sand ingestion tests.

## NOMENCLATURE

$x$	coordinate parallel to engine axis (see <b>Figure 7</b> )
$y$	radial coordinate (see <b>Figure 7</b> )
$z$	tangential coordinate (see <b>Figure 7</b> )
$x', y'$	axial and radial coordinates respectively in bleed hole local coordinate system
$M$	Mach number
$Tu$	turbulence intensity
$V_{abs}$	absolute velocity, m/sec
$V_x$	velocity component in the axial ( $x$ ) direction, m/sec
$V_y$	velocity component in the radial ( $y$ ) direction, m/sec
$V_z$	velocity component in the tangential ( $z$ ) direction, m/sec
$\alpha$	absolute flow angle
$\delta X$	uncertainty in variable $X$

$\theta$	optical head angle in the $x$ - $y$ plane (see <b>Figure 7</b> )
$\Omega$	angle between laser beams for 3-D measurement

## 1 INTRODUCTION

In late 1991 the Canadian Forces conducted a study to establish the attrition rates for various T56 engine components that were being considered for either repair development or durability enhancement. The results indicated that there was a significant increase in compressor rotor blade rejection for the 5th and 10th stages, in comparison with adjacent stages. For instance, the rejection frequencies for the T56-A-14 LFE engine, installed on the CP 140 Aurora, were 97% and 96% for the 5th and 10th stages respectively, while the attrition rates for the 4th and 9th stages were 63% and 75% respectively (**Figure 1**). In all cases the primary contributor to component rejection was airfoil erosion near the blade tips. The Canadian Forces statistics were based on a sample of 25 engines [1], [2].

Further evidence that the 5th stage rotor blades, in particular, experience abnormally high rates of erosion can be found in the results of titanium nitride (TiN) coating tests reported in reference 1. Two pertinent tests documented in that reference are a 2200 hour Field Service Evaluation (FSE) performed by the Canadian Forces and a sand ingestion test performed on an uncoated compressor by Detroit Diesel Allison. Erosion of the TiN coating on the 5th stage rotor was observed in the former while severe erosion of the 5th stage rotor blade tips was observed in the latter. The coating erosion observed in the FSE was limited to a strip on the pressure surface extending ~3mm from the blade tip.

The 5th and 10th stages of the T56 are equipped with a compressor air bleed band: effectively a series of holes around the compressor casing which permit unloading of the compressor during acceleration. Since the T56 operates at a constant (governed) speed of 13820 rpm and the bleed valves close at 94% of this speed during normal acceleration, the valves are open only a small

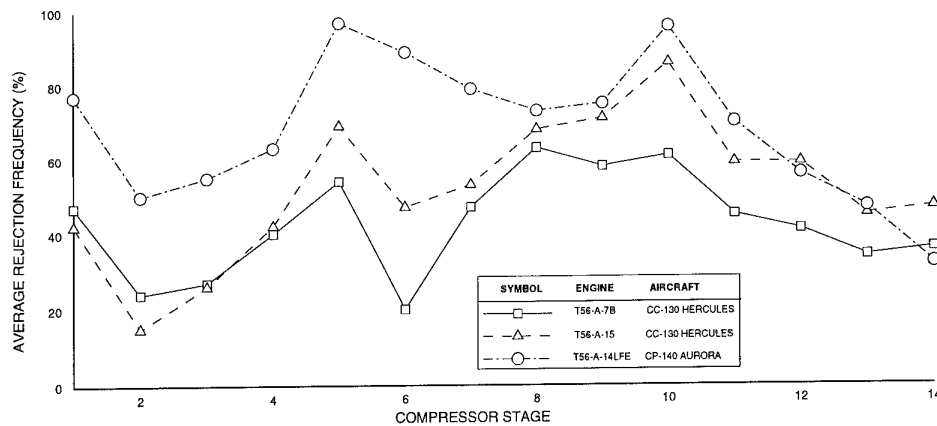


Figure 1: Compressor blade rejection frequency

fraction of the engine operating time. It was therefore felt unlikely that the blade erosion referred to previously was occurring while the valves were open. To test the hypothesis that the erosion was occurring while the valves were closed, the overtup flow resulting from the bleed holes was surveyed with a laser two-focus (L2F) velocimeter while the engine was operating at maximum continuous power at sea-level conditions.

A secondary objective of the tests was to gain experience applying the L2F to flowfield measurement in an operating gas turbine. To the authors' knowledge, these tests represent one of the first applications of an L2F to non-intrusive velocity measurement in a gas turbine, as opposed to a test rig.

## 2 ENGINE AND INSTRUMENTATION

### 2.1 Engine Description

The test vehicle for this study was an Allison T56-A7B single spool turboprop engine from a C-130 Hercules cargo aircraft. The T56 engine has a fourteen stage compressor, a six can combustor, and a four stage turbine. The single shaft is coupled to a reduction gearbox mounted forward of the compressor. Power is transmitted through the gearbox to a flywheel and a Froude waterbrake dynamometer. A schematic of the engine test facility is shown in Figure 2.

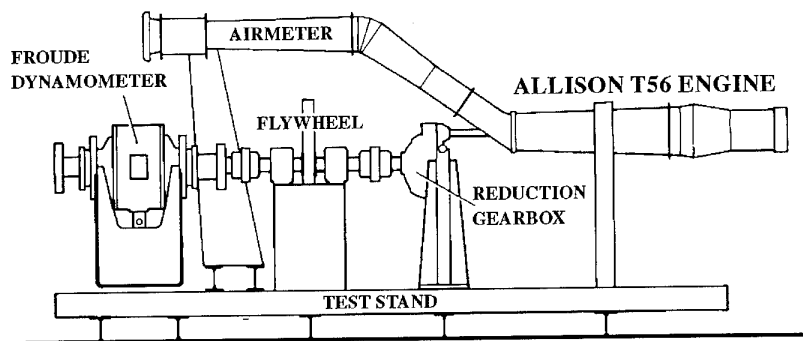
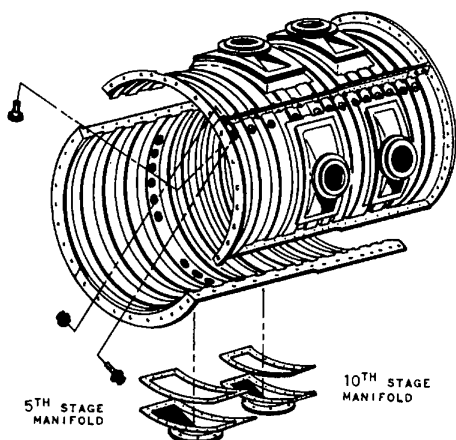


Figure 2: Engine test facility

## 2.2 Compressor Bleed Hardware

As mentioned previously, the T56 compressor casing contains a series of bleed holes over the 5th and 10th stage rotors. The 5th stage bleed air enters four valves, attached to collection manifolds, through 24 holes in the casing, 6 for each quadrant. The bleed holes and manifolds are shown in **Figure 3**.



**Figure 3: T56 compressor casing**

The bleed hole diameter and pitch are 25.4 mm (1") and 29.2 mm (1.15") respectively. The hole diameter is approximately equal to the axial tip chord of a 5th stage blade, so the hole spans almost the entire blade tip (**Figure 4**). The pitch of the 41 rotor blades is 28.63 mm (1.127") at the tip and is thus closely matched to the hole pitch.

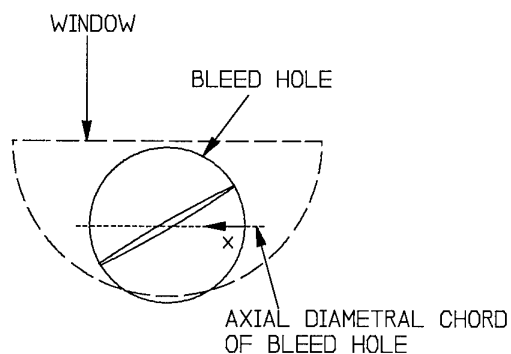


**Figure 4: Bleed hole and rotor blade**

Optical access to the 5th stage rotor was achieved by replacing one of the bleed valves with a 9.5 mm (3/8") thick semi-circular quartz window. The window was

mounted in a steel frame and attached to a modified manifold. The manifold, with the window removed, is shown in **Figure 5**. The 1 inch bleed hole and 5th stage blade are visible in the background.

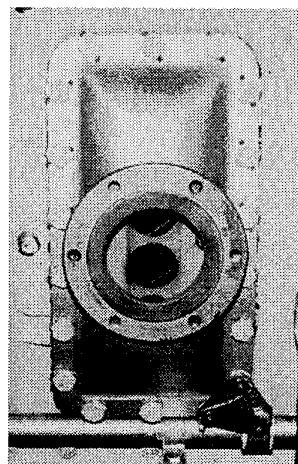


**Figure 5: 5th stage bleed valve manifold**

## 2.3 Instrumentation

Instrumentation on the T56 includes a high Mach number (0.8) airmeter in front of the engine, compressor inlet pressure and temperature rakes, a tailpipe airmeter mounted after the turbine, vibration sensors on the engine carcass, and turbine-type fuel flowmeters. The engine is also equipped with total temperature and pressure probes in every stage of the compressor, as well as compressor discharge and turbine inlet pressure and temperature rakes.

## 2.4 Laser Velocimetry Equipment

A Polytec Model L2F-0-2100 laser two-focus system was used for the flow field investigation. The L2F optical head, shown in the system schematic included as **Figure 6**, was mounted on an Aerotech three-axis traversing system to permit movement in the axial (x) and radial (y) directions, as well as rotation ( $\theta$ ) in the x-y plane (**Figure 7**). The traversing system was controlled remotely from the L2F PC (**Figure 6**).

Testing was scheduled to begin during the winter months, when ambient temperatures are typically well below the operational limits of the L2F optical head. To prevent damage, the head was encapsulated in a temperature-controlled enclosure.

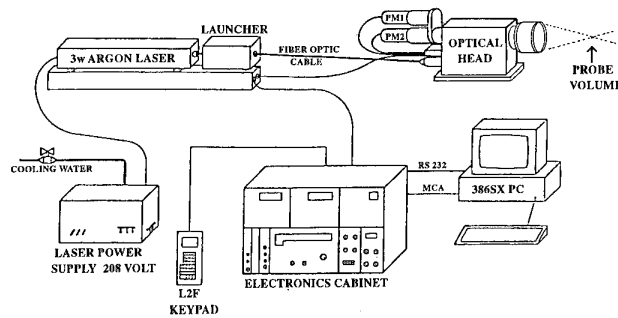


Figure 6: L2F system components

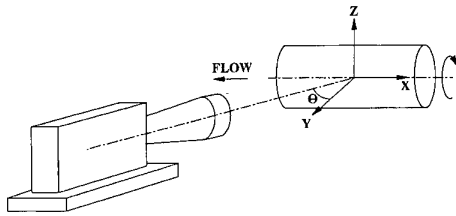


Figure 7: Reference coordinate system for velocity measurements

A Bently Nevada proximity probe was mounted on the window housing to provide a once per blade trigger signal to the L2F synchronizer, which is needed to make measurements in rotating blade rows. Some initial conditioning, including the removal of a DC offset, pre-amplification, and filtering were performed before the signal was suitable for use by the synchronizer.

A Polytec L2F-A-1000 sub-micron aerosol generator was used to seed the flow. A mixture of glycerol and alcohol yielded particle production rates in excess of  $10^9$  particles/second. The flow was bulk seeded by connecting the aerosol generator to the anti-icing struts located in the engine front frame.

### 3 L2F Operation and Data Reduction

#### 3.1 2-D Measurements

The L2F uses statistically-averaged and correlated time-of-flight (TOF) data for airborne particles travelling between the focal volumes of two closely-spaced laser beams to calculate the magnitude and direction of the absolute velocity component perpendicular to the beams [3]. In the NRC system, light from a 3W laser is carried by a fiber-optic cable to the optical head (Figure 6), where it is split into two beams by a Rochon prism. The two beams are then focused by a transceiver lens to obtain the two intensely illuminated focal volumes

comprising the probe (measurement) volume. Light backscattered from particles passing through the focal volumes is collected by the transceiver lens, focused into the focal plane of a second lens, and then imaged onto two pinholes in front of the two photomultiplier (PM) tubes seen at the rear of the optical head in Figure 6. Tube PM1 detects light backscattered from one of the focal volumes, designated the start beam, while PM2 detects light backscattered from the other, designated the stop beam. An electronic timer is started when backscattered light is detected by PM1 and stopped when light is detected by PM2, thereby recording a single TOF<sup>1</sup>. An operator-specified (> 500 typically) number of TOF measurements are averaged and correlated by software resident on the PC (Figure 6) to obtain the velocity in a single measuring direction in the plane normal to the beams. Velocities are measured over a range of directions to determine the direction and magnitude of the velocity component normal to the beams. The measuring direction is varied by rotating the plane of the start and stop beams about the start beam.

In addition to the mean values of flow speed and direction, the statistical processing of the TOF data yields the random uncertainties in these measurements as well as higher-order statistics of the flow, such as turbulence intensities. The turbulence intensity<sup>2</sup>  $Tu$  and the uncertainties are related, however, since the relative

1. Time-of-flight measurements obtained when the same particle passes through the start and stop beams are more highly correlated than false measurements obtained when the particles are different.

2. For the 2-D measurements,  $Tu = \sqrt{((u^2 + v^2)/2) / V_{abs}}$ , where  $u$  and  $v$  are the turbulent velocity components parallel and normal to the 2-D flow direction respectively.

error of the velocity components is less than  $\sim 1.5\%$  when  $Tu < 20\%$ , for example [3]. Similarly, the uncertainty in the flow angle is less than  $\sim 1^\circ$  when  $Tu < 20\%$ .

The L2F measurements are synchronized to the rotor speed to make measurements in a rotating blade row. The multi-windowing feature of the L2F divides each blade pitch into  $N$  partitions or windows ( $N \leq 16$  typically) and then stores each TOF in a separate buffer assigned to the window in which the measurement was made. This procedure yields a circumferentially-averaged velocity for each of the  $N$  windows across the blade passage at the  $x$  and  $y$  coordinates of the probe volume. Velocity variations across the width of a window are interpreted as turbulence.

For flows which are time-periodic at the blade-passing frequency, such as the bleed hole overtip flow, the L2F measurements are actually synchronized with the blade passing frequency instead of the rotor speed. Time-of-flight measurements are made for each blade passage in succession in this case, so the buffer for each window receives data from every blade passage on the rotor. This procedure speeds up measurements considerably.

### 3.2 3-D Measurements

Although a 2-D L2F only measures velocities in a plane normal to the laser beams, it is possible to measure all 3 components of velocity by making two 2-D measurements at the same point in space but in planes separated by an angle  $\Omega$ , as shown in **Figure 8**. For sufficient resolution,  $\Omega$  should not be less than  $30^\circ$  [3].

The two 2-D measurements yield two flow angles  $\alpha_1$  and  $\alpha_2$  and two absolute velocities  $V_{abs1}$  and  $V_{abs2}$  corresponding to measurement planes 1 and 2 respectively<sup>3</sup>. If the corresponding beam angles in the  $x$ - $y$  plane are  $\theta_1$  and  $\theta_2$  ( $\theta$  is defined in **Figure 7**), the three components of velocity in the directions defined in **Figure 7** can be obtained from the expressions:

$$V_x = \frac{V_{abs2} \sin(\alpha_2) \sin(\theta_1) - V_{abs1} \sin(\alpha_1) \sin(\theta_2)}{\sin(\theta_1 - \theta_2)} \quad (1)$$

$$V_y = \frac{V_{abs2} \sin(\alpha_2) \cos(\theta_1) - V_{abs1} \sin(\alpha_1) \cos(\theta_2)}{\sin(\theta_1 - \theta_2)} \quad (2)$$

3. By convention,  $\alpha$  is positive counterclockwise and zero at bottom dead center (ie. at the base of the optical head) when viewed along the beam axis from the focusing lens.

and,

$$V_z = -V_{abs2} \cos(\alpha_2) \quad (3)$$

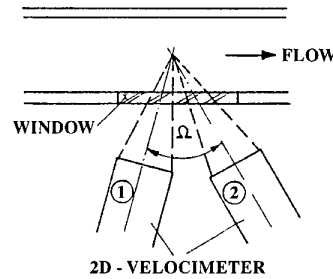


**Figure 8: Three-dimensional velocity measurement**

The velocity component  $V_y$  corresponds to the radial component in the T56 application. Since the angles  $\theta_1$  and  $\theta_2$  were set to  $+15^\circ$  and  $-15^\circ$  respectively in the T56 tests, Equation 2 can be rewritten for this case as

$$V_y = C(V_{abs2} \sin \alpha_2 - V_{abs1} \sin \alpha_1) \quad (4)$$

where  $C = \cos 15^\circ / \sin 30^\circ = 1.932 (\approx 2)$ .

For flow angles  $\alpha$  near  $0^\circ$  or  $180^\circ$ , which would require flow through the measurement volume which was predominantly tangential with the optical head oriented as shown in **Figure 7**,  $\sin(\alpha) \approx \alpha$  and Equation 4 simplifies to

$$V_y \approx C \bar{V}_{abs} (\alpha_2 - \alpha_1),$$

with

$$\bar{V}_{abs} = (V_{abs1} + V_{abs2})/2.$$

This assumes  $V_{abs1} \approx V_{abs2}$ , as will invariably be the case provided  $V_y$  is relatively small. The uncertainty in  $V_y$  is

$$\delta V_y \approx 2 \bar{V}_{abs} \sqrt{2} (\delta \alpha)$$

in this case for small values of  $\alpha_2 - \alpha_1$ . For the flow angle uncertainty  $\delta \alpha$  of  $\sim 1^\circ$  given previously,

$$\delta V_y \sim 5\% \text{ of } \bar{V}_{abs}.$$

For flow angles  $\alpha$  near  $90^\circ$  or  $270^\circ$ , on the other hand, which would require predominantly axial flow through the measurement volume, Equation 4 simplifies to

$$V_y \sim C(V_{abs2} - V_{abs1})$$

and the corresponding uncertainty is

$$\delta V_y \sim 2\sqrt{2} \delta V_{abs} \text{ or } \sim 4\% \text{ of } V_{abs} \text{ for } \delta V_{abs}/V_{abs} = 1.5\%$$

Provided the underlying assumptions are valid, the preceding simplified analysis indicates that  $\delta V_y$  is not strongly dependent on  $\alpha$ . It also indicates that the optical head orientation shown in **Figure 7** is probably as suitable as the alternate orientation in which the rotary traversing stage and the attached optical head are mounted vertically on the x-y stage instead of horizontally. Since the direction of the flow was typically midway between axial and tangential in the T56 tests in any case, the decision to mount the rotary stage horizontally was largely based on convenience.

## 4 EXPERIMENTAL PROCEDURE

### 4.1 Test Plan

Although it was originally planned to obtain 2-D measurements at all of the  $i,j$  grid points shown on the meridional plane in **Figure 9**, the points with  $j \geq 5$  were dropped when preliminary measurements indicated that the flow at those locations was largely unaffected by the bleed hole. Three-dimensional measurements were made on radial planes  $j \leq 3$ , although at somewhat different axial coordinates than those indicated in **Figure 9** because of problems with window housing/laser beam interference. Planes  $j=1,2,3$  and 4 were located 0.64, 3.84, 7.04 and 10.24mm respectively from the tip. The last distance (ie. 10.24mm) corresponds to  $\sim 23\%$  of the blade height, which is 44.2mm at mid-chord.

All measurements were made along the axial diametral chord (**Figure 4**) of the third bleed hole in the group of six, in the direction of turbine rotation. The tests were performed at maximum continuous power at sea-level conditions, as mentioned previously.

### 4.2 2-D Measurements

The multi-windowing feature of the L2F was used to divide the blade pitch into 16 windows. At any given location  $i,j$ , the number of windows in which measurements could be made was always less than 16, however, because some windows were obscured by the thickness of the blades and others were obscured by

blade shadow. To avoid damaging the photomultiplier tubes with intense light backscattered from the blade surfaces (ie. flare), the light chopper of the L2F was used to turn off the laser beam when the blades passed through the measurement volume.

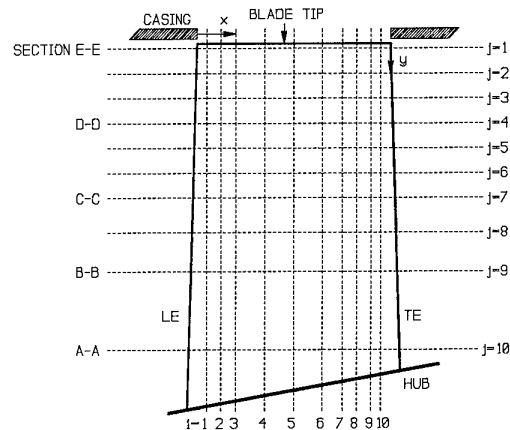


**Figure 9: Original grid of measurement points in the meridional plane**

The measurement window locations at each axial station  $i$  ( $i=1,2,\dots,10$ ) are shown in **Figure 10**. The windows are the vertically stacked boxes. The number of windows used at each point  $i,j$  ranged from 11 -> 14.

### 4.3 3-D Measurements

The 3-D measurements were obtained with beam angles  $\theta_1$  and  $\theta_2$  of  $+15^\circ$  and  $-15^\circ$  respectively (ie. the angles were  $15^\circ$  either side of the window normal), as noted previously. To avoid having to correct for the beam displacement which occurs because of refraction when a light beam passes through a flat window at any angle other than normal, the probe volume was focused onto a datum on the blade tip every time the beam angle was changed. All subsequent  $x$  and  $y$  translations of the optical head at the same beam angle were referenced to its location when the probe volume was focused on the blade tip datum.

Three-dimensional measurements were made at three radial locations,  $j = 1A, 2$ , and 3. High turbulence at station  $j=1$ , 0.64 mm in from the blade tip, resulted in poor data quality and unacceptably long testing times. Station 1A, 1.5 mm in from the blade tip was chosen to reduce the testing times and provide more useable data.

For a window of a given size, the envelope of points accessible by the probe volume is reduced when 3-D measurements are required because of increased



interference between the window housing and the off-normal laser beam. In the case of the T56 tests, this interference prevented making 3-D measurements at axial stations near the edges of the bleed hole (ie. near the blade leading and trailing edges). In the revised grid of measurement locations, data were obtained at 8 axial stations, spaced 1 mm apart, starting at 9 mm from the leading edge (**Figure 11**).

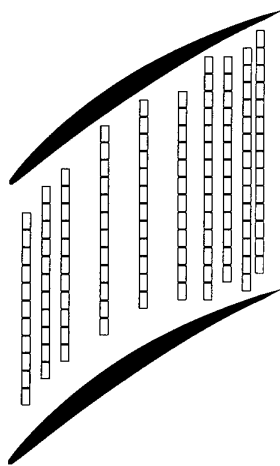


**Figure 10: 2-D pitchwise measurement windows**

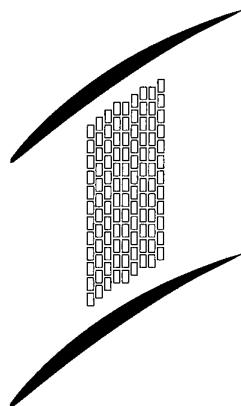


**Figure 11: 3-D Measurement Windows**

## 5 RESULTS

**Figures 12-15** show contours of relative Mach ( $M$ ) number<sup>4</sup> for the 2-D measurements obtained at  $j=1,2,3$  and 4 respectively. Streamlines of the flow in the

corresponding blade-to-blade planes are superimposed on the Mach contours. The streamline plots show that the flow is only slightly affected by the bleed holes at  $j=2$  and largely unaffected in planes further from the tip. The streamlines at 0.64mm from the tip (**Figure 12**) reveal a large velocity component in the direction of the pressure surface. It is this component which causes the erosion observed in FSE and sand ingestion tests.

**Figures 12-15** show that Mach numbers are highest near the suction surface and lowest near the pressure surface in all but the outermost blade-to-blade plane ( $j=1$ ), where Mach numbers are lowest at mid-passage near the trailing edge. Although the Mach number distribution at  $j=1$  shows a significant increase in the level of axial diffusion from mid-chord to the trailing edge on the suction surface compared to other planes, there is insufficient data close to the blade surface to estimate the extent of flow separation, if any, in that region. Flow separation from the suction surface near the trailing edge would likely accelerate erosion in that area.

**Figures 16-18** show contours of radial velocity  $V_y$  (+ve outwards) for the 3-D measurements obtained in the windows shown in **Figure 11** at  $j=1A, 2$  and 3. At  $j=1A$  and  $j=2$ , the contours indicate that the flow is moving outwards when a blade is underneath the axial diametral chord (**Figure 4**) of the bleed hole and inwards when the probe volume is at mid-passage. As might be expected from the 2-D results,  $V_y$  is small at 7.04mm from the tip ( $j=3$ ) but exceeds 75m/s (ie.  $M_y > 0.2$ ) near the blade surface at the tip.

$J=1, 0.64 \text{ mm FROM BLADE TIP}$

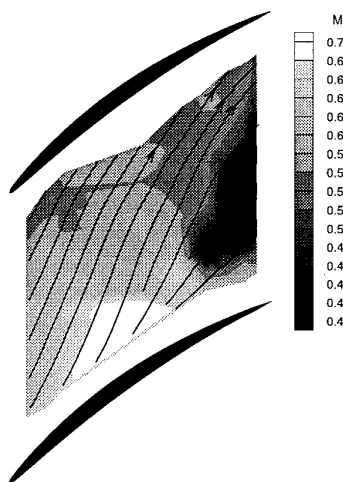


**Figure 12: Mach contours and streamlines for 2-D measurements at  $j=1$**

4. Calculated from velocities in the blade-to-blade planes by assuming constant rothalpy.

J=2, 3.84 mm FROM BLADE TIP

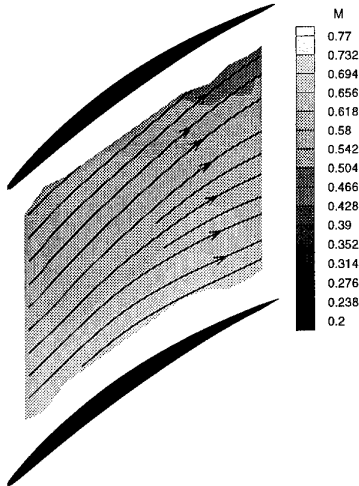


Figure 13: Mach contours and streamlines  
for 2-D measurements at j=2

J=4, 10.24 mm FROM BLADE TIP

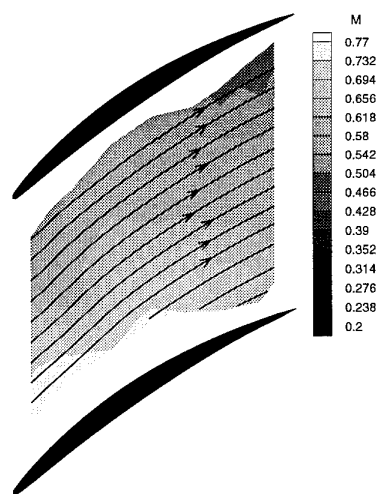


Figure 15: Mach contours and streamlines  
for 2-D measurements at j=4

J=3, 7.04 mm FROM BLADE TIP

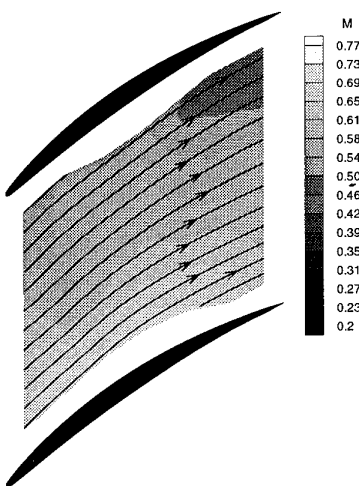


Figure 14: Mach contours and streamlines  
for 2-D measurements at j=3

J=1A, 1.5 mm FROM BLADE TIP

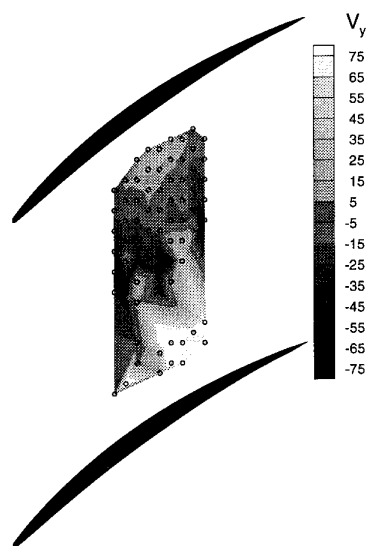


Figure 16: Radial velocity contours at j=1a

J=2, 3.84 mm FROM BLADE TIP

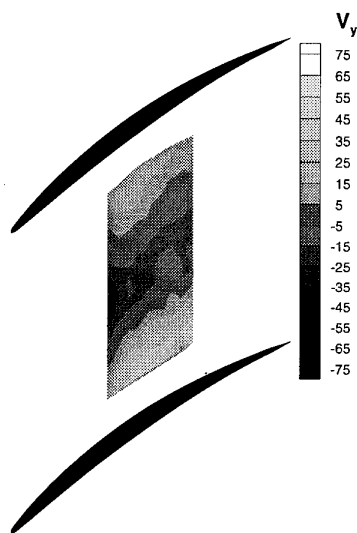


Figure 17: Radial velocity contours at j=2

J=3, 7.04 mm FROM BLADE TIP

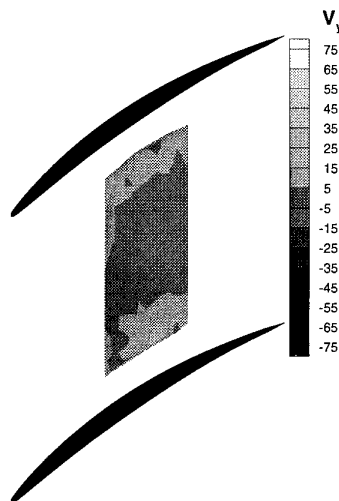


Figure 18: Radial velocity contours at j=3

Some of the measurement windows shown in Figure 11 had to be excluded at j=1A because the local turbulence (unsteadiness) level was too high to obtain a measurement. The windows where measurement of the velocity was possible are displayed as small circles in

Figure 16. The highly turbulent region also caused problems in the 2-D measurements at j=1, where, once again, some of the 2-D measurement windows shown in Figure 10 had to be excluded. Confirmation that there was a core of highly turbulent fluid in that area is seen in the plot of turbulence intensity distribution at j=1 included as Figure 19. Turbulence intensities (Tu) are much smaller further from the tip, as shown in Figure 20 for the plane at j=4. The level of turbulence seen in Figure 20 is still unusually high, however, since Tu is typically 5-10% in the repeating stages of a multi-stage axial compressor.

J=1, 0.64 mm FROM BLADE TIP

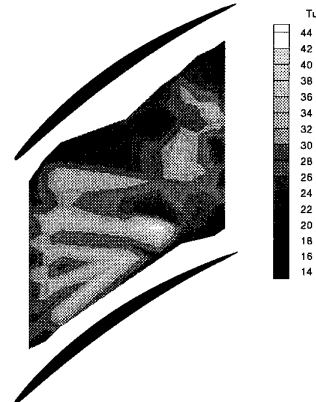


Figure 19: Turbulence intensity contours at j=1

J=4, 10.24 mm FROM BLADE TIP

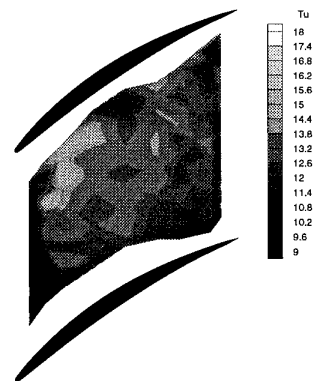


Figure 20: Turbulence intensity contours at j=4

## 6 CONCLUSIONS

The flowfield underneath a casing bleed hole in the 5th stage rotor of an Allison T56 gas turbine has been surveyed with a laser two-focus velocimeter. The flow within 3-4mm of the tip was found to have a large velocity component in the direction of the pressure surface, which explains why blades are being eroded in this area. Based on the results, erosion would be expected even when the bleed valves are closed, so there would be little benefit in attempting to reduce the amount of time the valves are open. Short of applying blade coatings, which have been shown to have some benefit [1], there is probably little that operators can do to reduce erosion in this case.

Since there are 24 bleed holes in the casing and the pitch of the holes is slightly greater than the tip pitch of the 41 blades on the 5th stage rotor, roughly 60% (ie.  $(24/41) \times 100$ ) of the casing circumference is occupied by bleed holes. It seems unlikely, therefore, that the 5th stage is contributing significantly to the overall pressure rise of the compressor, in which case it may not matter whether the blades are eroded or not. If erosion beyond the current repair limits did not significantly degrade

performance, which would require further testing to confirm, blade rejection rates could be reduced by relaxing the rejection criteria. These criteria are currently the same as those applied to neighbouring stages without bleed holes.

The L2F data will be compared to the results of a CFD simulation of the bleed hole overtip flow in future work.

## 7 ACKNOWLEDGEMENT

This research project was sponsored by the Canadian Department of National Defence, Chief of Research and Development. Their continuing support is gratefully acknowledged.

## 8 REFERENCES

- [1] 1990 T56 Component Improvement Program (CIP) Conference, Allison Gas Turbine Division, Detroit, Oct. 1990 : Subject: "Erosion/Corrosion Coatings"
- [2] Donaghy, Capt.M.J, Private Communication , Propulsion Systems Manager, T56 Series II and III, CF34-1A and ALF 502L-2C Engines, Canadian Forces
- [3] Schodl, R., "Measurement Techniques in Aerodynamics", VKI Lecture Series 1989-05, 1989

# INVESTIGATION OF MECHANICAL EROSION IN FUEL PIPELINES

M.Founti and A.Klipfel

National Technical University of Athens  
Mechanical Engineering Department  
Thermal Engineering Section  
Patission 42, Athens - 10682, Greece

## 1. SUMMARY

The aim of this work is to investigate the characteristics of mechanical erosion in a vertical sudden expansion turbulent two-phase flow. The flow field in an axisymmetric sudden expansion flow laden with round glass particles at 3% per volume and flowing in the direction of gravity was examined both experimentally and computationally. Velocities of particles and fluid were simultaneously measured at  $Re = 6 \times 10^4$  using a single component laser Doppler anemometer and a burst peak detector which discriminates the amplitude of the Doppler bursts resulting from the two discrete phases. The test facility was refractive index matched, allowing measurement of the  $\bar{U}$ ,  $V$ ,  $\bar{u}^2$ ,  $v^2$  and  $w^2$  components throughout the whole velocity flow field. Computations were performed using a Eulerian/Lagrangian approach considering drag, lift and gravity forces acting on a particle as well as modelling of particle-dispersion by turbulence, particle-wall and particle-particle collisions. Mechanical erosion of the pipe wall was determined via an empirical formula, using the predicted impact velocities and angles.

## 2. INTRODUCTION

Material erosion is a commonly met problem in pipelines transporting fuels with suspended solid residuals. Particle-wall collisions can lead to erosion of the wall-material, usually called material or mechanical erosion. By tracking the trajectory of a particle that travels in a pipe flow and that ultimately strikes a surface, it is possible to compute the particle impact and rebound velocities and angles. Erosion can be then defined as the ratio of the material mass removed from the surface due to the collision over the total mass of the particles impinging on the surface.

## 3. EXPERIMENTAL TECHNIQUE

The experiments were conducted in the vertically mounted sudden expansion test facility, also used by (Ref 1) and pictured in Figure 1. The closed-loop circuit has been modified to operate with diesel oil and to prevent the solid particles from entering the sump tank in order to avoid their sedimentation. A centrifugal particle separator retained all particles larger than  $100 \mu m$  prior to entering the sump tank. The retained particles, via a venturi-type pump, were re-united with the fluid without entering the pump (to avoid their

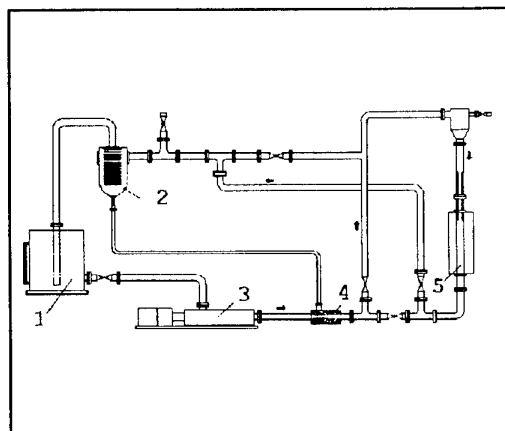


Figure 1: The Experimental Set-up

1) Sump Tank, 2) Centrifugal Filter (Particle separator)  
3) MOHNO-helical Pump, 4) ANGUS-venturi type fluid inductor, 5) Test Section with sudden expansion

crushing), at a constant rate of 3% of the fluid volume flow rate.

The test-section comprised a 1 m long, 51 mm inner diameter (D) DURAN-glass pipe, inserted in a rectangular trough, and a smaller diameter brass-pipe, with inner diameter (d) of 25.5 mm which ends up to a block of 50.5 mm outer diameter, thus creating the sudden expansion geometry (expansion ratios: 1:2). The small diameter brass-pipe provided an inlet to the test-section of ca. 20 D. The glass particles used were spherical with mean diameter  $d_p = 450 \mu m$ , size range 400 - 520  $\mu m$ , density equal to 2500 Kg/m<sup>3</sup> and refractive index equal to 1.52. The experiments have been performed at Reynolds numbers, based on the large pipe diameter and the maximum inlet axial mean velocity, equal to  $5.17 \times 10^4$  and  $6 \times 10^4$  for the single phase and two phase flows respectively.

Integration of the measured axial mean velocity profiles for the single and two-phase flows has yielded an average value of the mass flow rates equal to 1.7304 kg/sec, and the bulk flow velocity, ( $U_b = m_w / \rho_w A$ ,  $A = \pi d^2 / 4$  where D = large pipe diameter) has been

Fluid massflow rate: Particle massflow rate:	$m_f =$ $m_p =$	1.7303 170	Kg/s g/s	$U_{b,d} =$ 4.08m/s	$U_{b,D} =$ 1.021m/s
Slip velocity (m/s)	$Re_p$	CD	St	$\tau$ (ms)	$t_r$ (ms)
Inside recirculation: 0.35	13.6	3.4	8.66	1.8	15.6
Outside recirculation: 0.06	5.1	6.9	7.90 2.26	1.8	8.3 4.07

**Table 1:** Particle flow characteristics

calculated equal to 1.021 m/sec. Errors in the calculation of the average mass flow rate can be upto 15%. The bulk velocity in the two-phase flow cases may be affected by the variation of the mixture density/viscosity from that in the single-phase flow, but no account has been taken here.

Values of the particle Reynolds number ( $Re_p = d_p |U_f - U_p| / \nu$ ) have been selectively calculated at various locations in the flow field. Appropriate time scales ( $t_r$ ) of the flow have been calculated based on the step height (12.5 mm), and the maximum particle inlet axial mean velocity (6.14 m/s) as well as the maximum negative axial mean velocity measured in the recirculation zone (-0.8 m/s). As Table 1 shows, Stokes numbers corresponding to the above flow conditions have been calculated to be between 2.3 and 9. The characteristic response time of the pipe flow and the corresponding particle Stokes numbers suggest that the particles can be expected to follow any flow fluctuations, and that they are capable of greater lateral dispersion than the fluid elements.

The laser-Doppler anemometer comprises a 50 mW He-Ne laser, a TSI optical module with double Bragg-cells (freq. shift used 2-5 MHz), and a 150 mm focusing lens (incident beam spacing 50 mm) resulting to a control volume of 0.918 mm length and 0.15 mm diameter. A 350 mm collection lens (magnification equal to 1.1) and an avalanche Photo Diode were used for the collection of the scattered light.

The Doppler signals after being band-pass filtered were processed by a 175 MHz, LeCroy-9400A (LeCroy, Spring Valley, USA) transient recorder interfaced to a 386-SX P.C. The transient recorder was operated in a sequential mode, as described by (Ref 2). The digitizing frequency was 12.5 MHz. The total storage of the LeCroy was divided into 250 segments and after the storage of 250 bursts the data were transferred to the P.C. in a sequential mode via an IEEE-488 (National Instruments, USA) interface card. While the data were processed in the PC the next 250 bursts were stored in the transient recorder. Mean and rms velocities were calculated from approximately 10,000 samples based on

a F.F.T. The amplitude of each filtered Doppler burst was recorded with the help of a burst peak detector, developed by (Ref 3) that evaluated the location of maximum amplitude corresponding to the centre of Doppler burst. Once a burst is detected the transient recorder is triggered only once using a trigger generation logic. The two phases were distinguished by setting a low and a high amplitude limit whereby bursts with amplitude below the low amplitude limit were classified as the carrier phase and bursts with amplitude above the high amplitude limit were seen as the discrete phase (particles). At the overlapping amplitude region, bursts cannot be easily classified, especially if they cross the measuring volume outside its centre, and as a result an error up to 4% may be introduced to the measured velocities. The data evaluation was performed by a Digital Signal Processing Board (DSP) mounted in the P.C. The approach is a simplification of the method used by (Ref 3) for the determination of the measurement volume size and for measuring particle mass fluxes in phase Doppler anemometry.

The refractive index of the carrier phase has been matched to the refractive index of the material of the enclosing pipe, and partly to that of the solid phase. At 25°C, the refractive index of the mixture of the two diesel oils (light fuel,  $\rho = 830$  kg/s,  $\nu = 5.205$  cSt) has been matched to the refractive index of the pipe (equal to 1.473) and hence the matching with the refractive index of the glass particles has not been optimum. The temperature of the diesel mixture has been controlled to within 0.5°C throughout the experiments. Refractive index matching allowed measurements at high particle concentrations and prevented refraction displacement of the measuring volume inside the test-section due to curvature of the pipe walls.

Measurement errors were expected to be higher in regions of steep velocity gradients, where the glass-particle arrival data rates were measured to be the lowest. Measurement errors upto 3% in the mean and 5% in the normal stress values were expected in these regions.

#### 4. COMPUTATIONAL APPROACH

The predictions have been performed using as inlet conditions the measured axial, radial and azimuthal velocity profiles at 2 mm and 9 mm from the inlet plane for the particle and fluid conditions shown in Table 1. The measured profiles have been extrapolated at  $z = 0$  mm, in order to be serve the calculation purposes. The inlet turbulent kinetic energy was set according to the experimental data and the dissipation rate was defined by trial and error. A modified version of the TEACH code (Ref 4) as described by (Ref 5) has been used for the computations which have been performed at a 486-AT computer.

For the present flow configuration which is steady, incompressible, turbulent, axisymmetric, the standard time-averaged continuity and momentum equations were solved. A modified version of the  $k-\epsilon$  turbulence model, as described by (Ref 6) was employed for the modelling of the turbulence quantities. The model modifies the  $C'_\mu$  [ $= C_\mu / \{1 + a\tau_v/\tau_c\}$ ] and  $C'_2$  [ $= C_2 / \{1 + b\tau_v/\tau_c\}$ ] constants of the standard  $k-\epsilon$  model to account for the radius of curvature of the flow. (where  $\tau_v = k/\epsilon$  and  $\tau_c = \epsilon/N_c^2 k$  and  $N_c$  is the Brunt-Vaisala frequency for the fluid). The resulting system of equations was solved via a finite difference method based on a staggered grid arrangement, using the SIMPLE (Ref 7) algorithm, the upwind differencing discretization scheme, and the Tri-Diagonal Matrix Algorithm.

For the two-phase flow, the calculation of the particle trajectories was performed using a Lagrangian formulation, (Ref 8) and the equations of the continuous phase transport were solved using a Eulerian treatment.

The particle trajectories have been calculated by solving instantaneous particle motion (momentum) equations:

$$\frac{d\mathbf{x}}{dt} = \mathbf{u}_P \quad (1)$$

$$m_P \frac{d\mathbf{u}_P}{dt} = \mathbf{F}_D + \mathbf{F}_S + \mathbf{F}_R + \mathbf{F}_G \quad (2)$$

$$I_P \frac{d\bar{\omega}_P}{dt} = \mathbf{T} \quad (3)$$

where the drag force, lift force due to shear stresses (Ref 9), lift force and torque due to particle rotation (Ref 10) and gravitational force are taken into account.

$$\mathbf{F}_D = \frac{3}{4} \frac{\rho_F}{D_P} m_P C_D (\mathbf{u}_F - \mathbf{u}_P) |\mathbf{u}_F - \mathbf{u}_P| \quad (4)$$

$$\mathbf{F}_S = 3.0844 m_P \frac{\sqrt{\rho_F \mu}}{\rho_P D_P} \sqrt{\frac{1}{|\bar{\omega}_F|}} (\bar{\omega}_F \times (\mathbf{u}_F - \mathbf{u}_P)) \quad (5)$$

$$\mathbf{F}_R = \frac{\pi}{8} \rho_F D_P^3 \left[ \frac{1}{2} \nabla \times \mathbf{u}_F - \bar{\omega}_P \right] \times (\mathbf{u}_F - \mathbf{u}_P) \quad (6)$$

$$\mathbf{F}_G = m_P g \left( 1 - \frac{\rho_F}{\rho_P} \right) \quad (7)$$

The lift force and torque for a rotating sphere in a stagnant fluid is derived by (Ref 10) and extended to include the relative motion between the particle and the fluid (Ref 11)

$$\mathbf{T} = -\pi \mu D_P^3 \left[ \frac{1}{2} (\nabla \times \mathbf{u}) - \bar{\omega}_P \right] \quad (8)$$

The drag coefficient of the spherical particles was calculated using values according to (Ref 12) and which closely simulate experimental data.

The model of (Ref 13) has been used for the simulation of the particle dispersion due to the fluid turbulence. The instantaneous fluid velocity is considered to comprise of a mean and a fluctuating component, which is introduced as a stochastic process, considering local turbulence isotropy. Fluid fluctuations are modelled as random numbers following a Gaussian distribution with zero mean value and standard deviation set from  $U_{r.m.s} = (2/3k)^{1/2}$ . Particles are considered to interact with the fluid eddy for a specified period of time.

Interaction ends if:

a) the particle remains in the eddy for a longer time period (TINT) than the eddy life-time ( $T_E$ ), where  $T_E = C_T k/\epsilon$  and  $C_T = 0.6$ .

b) the particle exits the specific eddy (crossing-trajectories effect). The distance travelled by the particle through the eddy ( $x$ ) is compared to the characteristic length scale of the eddy ( $L_E = T_E U_{rms}$ ). If  $x > L_E$  it is considered to be the end of the interaction time.

When either of the above two criteria is fulfilled, it is considered that the particle starts to interact with a new

eddy. For this purpose a new fluctuation component is sampled from the Gaussian distribution function. The sampling is performed for the two velocity components and the fluctuations are temporally and spatially uncorrelated.

In the present study the interparticle collision model of (Ref 11) is employed and extended to take account of the particle angular momentum exchange considering sliding and non-sliding collision according to (Ref 14). The collision process of the particle being tracked through the flow field is calculated based on the averaged values of particle velocities and concentration in the control volume under consideration. The main idea is to calculate the probability of collisions for a given particle with any other particle during the time step considered. This probability exists, since for higher particle loadings the collision between particles can be regarded as a stochastic event, similar to collisions between molecules in gases which can be described by the kinetic theory of gases. On the basis of this probability, it is possible to decide in every time step, by generating some random number, whether a collision of a given particle will take place or not. In the case that a collision occurs, a stochastic collision model is employed in order to obtain the post-collision velocities of this particle. Three main steps are executed:

1. Calculation of the fields of parameters which are necessary to calculate collision probability (i.e. particle mean velocities, RMS values and concentration).
2. Calculation of the collision probability.
3. Application of the stochastic collision model.

By assuming that:

- a particle may collide only with another particle in the same control volume
- one collision occurs during a given time step  $\Delta t$
- a Gaussian velocity distribution exists for the particles
- the particle velocity fluctuations are isotropic, the interparticle collision probability can be expressed as follows :

$$P_{coll} = \frac{2^{3/2} \pi^{1/2} N_p \Delta t}{4 V_U} (D_p^2 + 2 D_p \frac{D_m^{3/2}}{D_{N,m}^{1/2}} + \frac{D_m^4}{D_{N,m}^2}) \sqrt{2 u'^2} \quad (9)$$

where  $N_p/V_{ij}$  is the number of particles per unit volume,  $\Delta t$  is the time step,  $D_p$  is the diameter of the considered particle,  $D_m$  is the number averaged particle diameter,  $D_{N,m}$  is the particle diameter with the highest probability and

$$\overline{u'^2} = \frac{1}{3} \sum_{k=1}^3 \overline{u_k'^2} \quad (10)$$

where  $u_k'$  is the particle velocity fluctuation in the  $k$  direction.

The local particle concentration and velocity variance are calculated by tracing a sufficient number of particles into the flow field.

As mentioned above, the collision probability is calculated in each time step. A collision is simulated only when a uniform distributed random number in the range  $[0,1]$  becomes smaller than the collision probability.

When a collision takes place, it is considered that a fictitious particle hits the one which is currently traced. The size and the velocities (translational & rotational) of the fictitious particle are chosen on the basis of the calculated statistics for the control volumes considered. By transferring the problem into a coordinate system where the fictitious particle is fixed, the collision location can be randomly set at a point in the front half of the particle surface, when the front half is considered to be in the direction of relative motion. Next, the particle velocity vectors are transformed into an appropriate coordinate system in order to obtain a central collision. After that, a sliding or non-sliding collision is considered and the rebounding translational and rotational velocity vectors are calculated according to the momentum conservation laws and re-transformed to the original coordinate system.

The interparticle collision phenomenon influences the particle velocity fluctuations and subsequently the collision probability. Hence, an iterative procedure is implemented for the evaluation of these effects. First, the particle trajectories are tracked without taking into account the collisions. Next the trajectories are continuously re-calculated until the change of the particle RMS velocity becomes smaller than a certain value (e.g. 5 %)

Particle trajectories are calculated considering the following boundary and initial conditions:

- a) At the inlet, the particle velocity is modelled as the sum of a mean (set from the measured data) and a fluctuating component, which is introduced as a random number following a Gaussian distribution with zero mean value and standard deviation equal to the local experimental values of the particle r.m.s. velocities.
- b) Particles are introduced at a finite number of starting locations along the inlet radius of the pipe. A random number RN that follows a uniform distribution is used to vary the particle position within each cell. On average 9000 particle trajectories are calculated.
- c) When a particle approaches a wall, it is examined whether its new position lies within the boundaries of the flow or not. If the new particle position lies outside the boundaries, it is set on the wall, and it is considered that the particle collides with it. The new axial position is based on the new radial position and the tangent of the resulting angle, the collision angle. The model of (Ref 15) is used in order to obtain the particle translational and rotational velocities after a wall collision. The model distinguishes and takes account of two types of collision: a collision with and without



sliding. The empirical restitution coefficients are provided by the work of (Ref 16). For the calculations the particles have been simulated as glass with the rest of the properties being those of quartz-sand and the pipe walls were assumed to be 2024-Al alloy.

The mechanical erosion caused by the particle impact is calculated as suggested by (Ref 17,18):

$$\epsilon = K_1 f(\beta_1) (V_1 \cos \beta_1)^2 (1 - R_T^2) + f(V_{IN}) \quad (11)$$

where  $\epsilon$ : Erosion in terms of mass removed per unit mass of incidence particle (mgr/gr)

$R_T = 1 - 0.0016 V_1 \sin \beta_1$  for aluminum alloys

$$f(\beta_1) = \{1 + CK [K_{12} \beta_1 \sin(90/\beta_0)]\}^2$$

$$f(V_{IN}) = K_3 (V_1 \sin \beta_1)^4$$

$\beta_0$ : the angle of attack where maximum erosion occurs.

$CK = 1$  when  $\beta_1 < 3\beta_0$ .

$CK = 0$  when  $\beta_1 > 3\beta_0$ .

$K_1 = 3.67 \times 10^{-6}$ ,  $K_{12} = 0.585$ ,  $K_3 = 6.0 \times 10^{-12}$  for quartz particles eroding aluminum alloy surfaces.

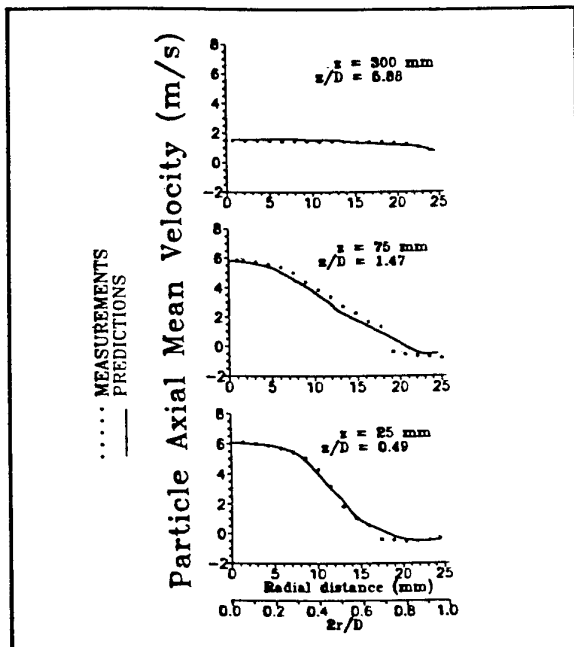


Figure 2: Predicted and measured particle axial mean velocity profiles at location  $z=25, 75$  and  $300$  mm from inlet.

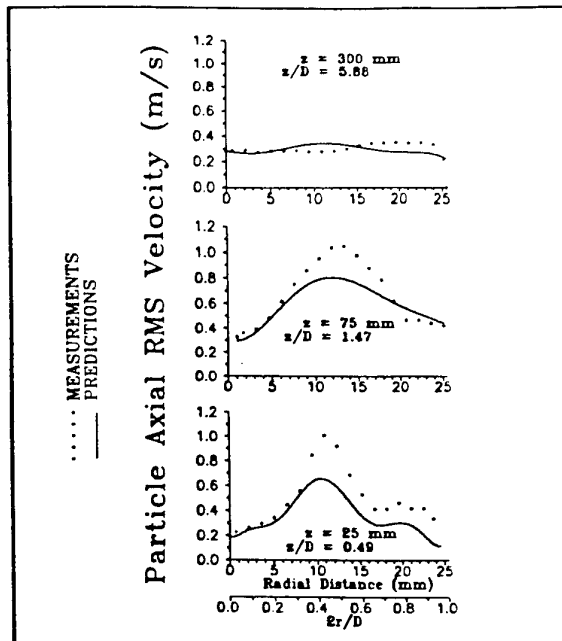


Figure 3: Predicted and measured particle axial RMS velocity profiles at location  $z=25, 75$  and  $300$  mm from inlet.

## 5. RESULTS

The prediction of the discrete phase velocities is compared to experimental data as shown in Figure 2 and 3. Figure 2 presents the particle axial mean velocity profile at three different downstream locations ( $z=25, 75, 300$  mm), while Figure 3 presents the particle axial RMS velocity profile at the same downstream locations. As it is shown the predictions of the mean quantities agree well with the measurements. On the other hand, the RMS quantities are underpredicted. The underprediction is partly caused due to the assumption of turbulence isotropy and probably due to the simulation of the particle-particle collisions which tends to diminish the particle velocity fluctuations. The latter denotes that the interparticle collision model needs further improvement and enhancement.

A sample of the calculated particle trajectories and their behaviour in the wall region are presented in Figure 4. It can be observed that particles tend to collide with the pipe wall and slide along it. Particles injected in the potential core of the flow have higher velocities and they do not enter the recirculation zone. When they reach the pipe walls, they collide several times and thereafter remain in the vicinity of the wall and slide. Figure 5 presents calculated values of mechanical erosion that can be caused to the pipe walls due to the multiple particle collisions. As it is shown, the location where the flow reattaches (in this case at  $z=140$  mm) determines the distribution of the erosion along the pipe wall. Erosion reaches its maximum values upstream and downstream of the reattachment point. Most of the particles that enter the recirculation zone are getting

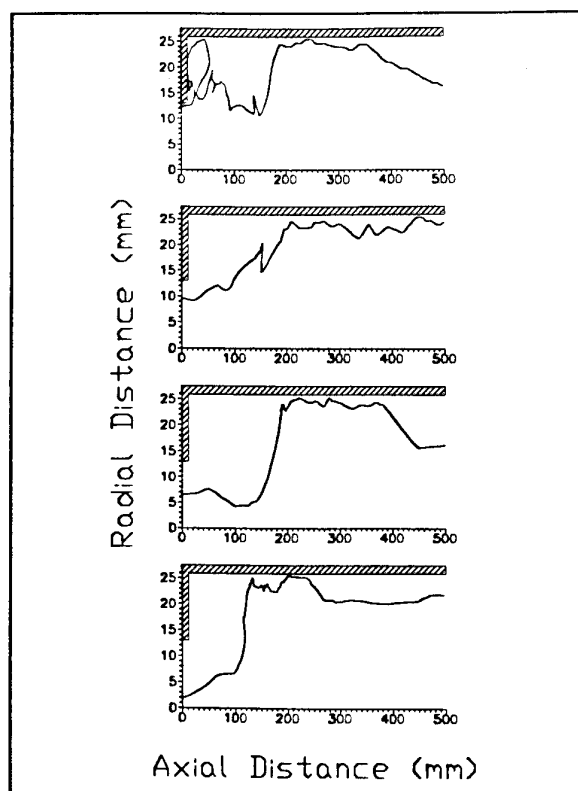


Figure 4: Calculated particle trajectories

trapped, recirculate and collide with the pipe walls. Subsequently the particle-wall collisions are more frequent in this region and therefore the erosion increases. Furthermore, particles that do not manage to enter the recirculation zone collide with the wall in the region downstream the reattachment point. These particles hit the wall with an impinging angle close to the one where maximum erosion occurs.

## 6. REFERENCES

1. Founti, M. and Papaioannides, G., "Influence of expansion ratio on the size of recirculation zone in two-phase sudden expansion flows", Proc. 6th Intern. Symposium on Applications of Laser Techniques to Fluid Mechanics, Lisbon, Portugal, 1992.
2. Sommerfeld, M., Qiu, H.-H., and Durst, F., "High resolution data processing for phase - Doppler measurements in a complex two-phase flow", Proc. of the 4th Intern. Symp. on Applications of Laser Anemometry to Fluid Mechanics, Lisbon, Portugal, 1990, paper 3.8.
3. Qiu, H.-H., and Sommerfeld, M., "A reliable method for determining the measurement volume size and particle mass fluxes using phase-Doppler anemometry", Exps. in Fluids, 13, 1992, pp. 393-404.
4. Gosman, A.D., and Ideriah, F.J.K., "TEACH-T: A general computer program for two dimensional turbulent, recirculating flows", Int. Report, Fluids Section, Mech. Eng. Dept., Imperial College, London, 1976.
5. Founti, M., and Klipfel, A., "Measurements and predictions in vertical, two-phase sudden expansion flows", Proc. of the 2nd International Symposium on Engineering Turbulence Modelling and Measurements, Florence, Italy, 1992.
6. Sung, H. J., Jang, H. C. and Cho, C. H. "Curvature-dependent two-equation model for recirculating flows", Proc. of the Intern. Symposium on Engineering Turbulence Model. Exp., Rodi and Ganic-Editors, 1990, pp. 33-42.
7. Patankar, S.V., "Numerical heat transfer and fluid flow", Hemisphere Publis. Co., 1980.
8. Durst, F., Milojevic, D. and Schoenung, "Eulerian and Lagrangian Predictions of Particulate Two-Phase Flows: A Numerical Study", Appl. Math. Modelling, 8, 1984, pp. 101-115.
9. Saffman, P.G., The lift on a small sphere in a slow shear flow, J. Fluid Mech., 22, 1965, pp. 385-400.
10. Rubinow, S.I. and Keller, J.B., "The transverse force on a spinning sphere moving in a viscous fluid", J. Fluid Mech, 11, 1961, pp. 447-459.
11. Sommerfeld, M. and Zivkovic, G., "Recent advances in the numerical simulation of pneumatic conveying through pipe systems", Computational Methods in Applied Sciences, Elsevier Science Publishers, 1992, pp. 201-212.

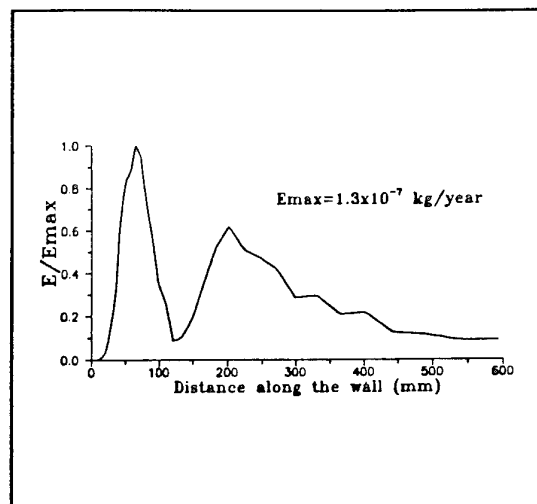


Figure 5: Predicted distribution of mechanical erosion along the pipe wall.

12. Morsi, S.A., and Alexander, A.J., "An investigation of particle trajectories in two-phase flow systems, J. Fluid Mech., 55, part 2, 1972, pp. 193-208.
13. Gosman, A.D., and Ioannides, E., "Aspects of computer simulation of liquid fueled combustors", J. of Energy, 7, 1983, pp. 482-490.
14. Oesterle, B., and Petitjean, A., "Simulation of particle-to-particle interactions in gas-solid flows", Int. J. Multiphase Flow, 19, 1, 1993, pp. 199-211.
15. Matsumoto, S. and Saito, S., "Monte Carlo simulation of horizontal pneumatic conveying based on the rough wall model", J. Chem. Engng. Japan, 3, 1970, pp. 223-230.
16. Tabakoff, W., Malak, M.F. and Hamed, A., "Laser measurements of solid-particle rebound parameters impacting on 2024 Aluminium and 6Al-4V Titanium alloys", AIAA -Journal, 25, 5, 1987, pp. 721-726.
17. Tabakoff, W. and Hamed, A., "Aerodynamic effects on erosion in turbomachinery", Tokyo joint gas turbine progress, 1977, pp. 574-581.
18. Tabakoff, W., Kotwal, R. and Hamed, A., "Erosion study of different materials affected by coal ash particles", WEAR, 52, 1979, pp. 161-173.

## QUESTIONS

### J. TAN (UK)

- Q. Do you calculate the diffusion coefficient from the Lagrangian computation of the particle trajectories? And do you update these diffusion coefficient values in the Eulerian calculations?
- A. No, we did not take account of the diffusion coefficient. Instead, we used the model of Gosman and Ioannides.

## AN AIRBORNE MONITORING SYSTEM FOR FOD AND EROSION FAULTS

Giuseppe Lombardo\* Giovanni Torella\*\*

\* University of Palermo

Dipartimento di Meccanica e Aeronautica  
Viale delle Scienze 90128 - Palermo - Italy

\*\* Italian Air Force Academy

Dipartimento di Scienze applicate al volo  
80078 - Pozzuoli - Napoli - Italy

### SUMMARY

FOD and erosion are the events causing the most part of accidental damages in gas turbine engines. When FOD is not destroying or when erosion is in progress the performance level decreases and the necessity of unscheduled maintenance actions becomes quite real. Moreover when there is a light FOD, or the erosion process is constant in time, it may be difficult to detect the exact cause of performance decrease and to plan the most effective maintenance action. This paper deals with the results of a study carried out for developing an Engine Condition Monitoring system particularly suitable for detecting the MicroFOD and erosion effects in gas turbines. The developed numerical codes has been applied to a single spool turboshaft engine with free power turbine. The obtained results are presented and discussed.

### LIST OF SYMBOLS

PW	power
W	mass flow rate
T	temperature
$C_p$	specific heat at constant pressure
$\eta$	efficiency
P	pressure
$\gamma$	ratio of specific heats
$\Gamma$	corrected mass flow
k	fuel calorific value
K	pressure coefficient

### SUBSCRIPTS

1..5	engine station
C	compressor
B	burner
F	fuel
GGT	gas generator turbine
PT	power turbine
M1	GGT driving shaft
M2	PT driving shaft
S1	GGT power extraction
S2	PT power extraction
s	bleedings

### 1. - INTRODUCTION

The gas turbine engines are characterised by the use of large quantity of air. The air necessary for both the engine working and the thrust or power production is drawn from the external environment.

The mass flow rate may contains many different objects that cause dangerous effects on the engine.

Usually the engines have not tools for filtering the incoming air. The presence of suitable filters causes the decrease of performance and the growth of both weight and drag. Therefore filters are used only for special operations.

The objects contained in the incoming air cause FOD and erosion of engine parts. The nature and the size of the objects is quite wide. Sand, stones, dust, little bolts and nuts and similar object that is on the runway may be ingested by the engine. Moreover, owing to human negligence, the engine may swallows screw-drivers, monkey-wrench, gloves and any other object put in or near the intake.

The FOD possibility increases during the take-off and the landing. As an example, before the take-off of the F117 Night Hawk, the stealth bomber of USAF, the runway is carefully controlled in order to avoid the presence of any object that may ingested by engines.

Last but not least the bird ingestion is another important cause of FOD. The impact of birds against the intake or their ingestion may cause severe problems to the engine [1].

The FOD probability during engine operating life is very high therefore, the engine must tolerate the effects within fixed limits. For this aim the procedures for engine certification require the getting through specific tests as stones, ice, birds and water ingestion [2].

Moreover the FOD is one of the most important cause of unscheduled maintenance action. Sometimes, when a MicroFOD is occurred and/or an erosion is in progress, it may be difficult to understand the reasons of engine behaviour and to plan the right intervention.

A tool for controlling the development of MicroFOD effects might reduce the maintenance costs and might help the diagnostics. Tools for Engine Condition Monitoring (ECM) may be based on Gas Path Analysis (GPA) engine simulation [3].

This paper shows the results of a study carried out for developing suitable methods and numerical codes for monitoring the engine performance and behaviour when FOD and erosion are in progress.

The work has been split in different steps.

The first one has dealt with the study of FOD and erosion effects on engine working, performance and behaviour.

The successive step has been dedicated to the development of a theoretical method and to the set-up of the pertinent computer codes for Engine Condition Monitoring and for FOD and erosion progress analysis.

At last the developed codes have been used for simulating and analysing the effect of FOD on a single spool turboshaft engine with free power turbine. The obtained results are presented and discussed.

## 2. - FOD EFFECTS IN GAS TURBINE

The various type of FOD and the erosion linked to continuous MicroFOD are quite frequent events.

Fig. 1-3 show the FOD occurrence in Italian Air Force from 1988 to 1993.

FIG. 1 - FOD EVENTS vs YEARS

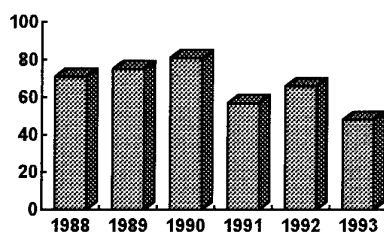


FIG. 2 - CAUSES OF FOD

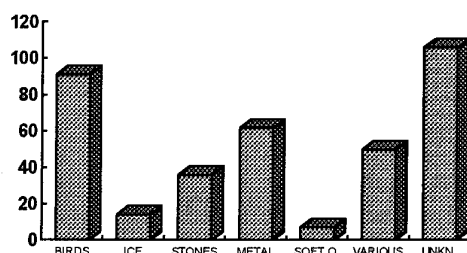
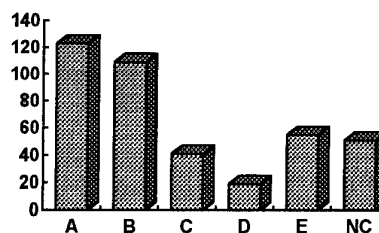


FIG. 3 - FOD DAMAGES



where:

**A** Blade surface repairing without replacement;

**B** Blade surface repairing with replacement up to 5% of blade;

**C** Blade surface repairing with replacement up to 50% of blade;

**D** Blade surface repairing with replacement beyond 50% of blade;

**E** Compressor / engine destroyed.

Every object entering into engine strikes against the blades of compressor. This component is very delicate and it is mainly responsible for the behaviour of the whole engine. Different studies [4] have shown that the 60-70% of the causes leading to engine performance decrease are due to the Fan-Compressor section. Obviously the FOD is responsible for a large part of the problems.

The effects of FOD on engine are strictly linked to the size, the nature and the velocity of ingested objects. The consequence of strong FOD is the destruction of the engine. Less serious events cause blade deformation and loss of blade pieces so that there is the reduction of efficiency and of compression capacity and the decrease of mass flow rate delivered by the compressor.

The final consequences are the augmentation of fuel consumption and malfunctions during transient operation. The trouble-shooting section of engine maintenance manuals are full of malfunction due to FOD and erosion.

For a large FOD, with the partial destruction of a large number of blade rows, the engine behaviour is not ambiguous: a strong stall is followed by the fast decrease of thrust or power level and a possible engine shut-down.

For a light FOD or erosion the fault selection and the choice of correct maintenance action may be difficult because there are little variations of blade geometry in the different compressor stages. The effect may increase with time and the decrease of engine performance is slow. Anyway both the performance and security delay are constant and may lead to unacceptable situations.

Beside the security of engine working, the FOD and the erosion strongly affect the maintenance activity. This way FOD, MicroFOD and erosion

are responsible of the utilization of both human and economical resources and they contribute to the increase of management costs. Therefore the possibility of having tools for detecting, studying and monitoring continuously the effects of light FOD and the growth of erosion should be very useful for engine management.

The final target of this study is to carry out a tool for the detection and the control of any kind of FOD, including light FOD and erosion. The main features of the system should be:

- reliability;
- sensitivity;
- simplicity;
- flexibility.

Moreover the obtained integrated package should be airborne.

### 3 - ECM AND GPA REQUIREMENTS

During the past years the maintenance criteria of gas turbine engines have been changed. The old and expensive Time Between Overhaul (TBO) criterion has been replaced by the more effective and less expensive "Condition Monitoring" philosophy.

Obviously, in order to put in practice this philosophy, to assure both low cost maintenance and high security margins, some techniques for monitoring the engine health have been developed, [5], [6].

Gas Path Analysis is an important support of Engine Condition Monitoring.

It groups methods that allow the determination of the thermo-fluid-dynamic parameters in any engine section so it is possible to evaluate the performance level of the whole engine and of each component, [7] - [10].

The component efficiency decrease, caused by engine wear or failures, implies the reduction of engine performance. Therefore the behaviour of engine with faults in progress may be detected by the changes of some engine parameters with respect to the corresponding values of healthy engine.

Unfortunately, most of the parameters useful for revealing the condition of the engine components cannot be measured.

Nevertheless, mathematical models based on GPA techniques allow the evaluation of parameters not directly measurable so the development of airborne Engine Condition Monitoring system for FOD and erosion faults diagnostics is possible.

The current applications of GPA are characterized by several linearizations of the equations of the model in order to simplify and speed up the calculations. The linearized applications are intrinsically approximated and don't meet the main features of the ECM system for FOD and erosion: the sensitivity and the reliability.

The present work shows the development of a real time model of the engine based on a non linear GPA approach [11].

The model is able to simulate the engine behaviour in case of FOD, erosion or different failure and is valid for both severe faults, requiring a non linear approach, and for less severe phenomena usually not detectable by the ordinary airborne instrumentation.

The model is based on a vectorial non linear formulation that will be described in the following section. The method allows to set up a computerized diagnostic system able to supply in flight information about engine efficiency and failure evolution.

Such a model provides accurate results for the diagnostics even when different faults are in progress. Moreover, by an Artificial Intelligence post-processor system, it allows separation of and monitoring of the evolution of an initial failure (e.g. FOD), independently of additional or consequential failures [12].

This way a complete real time knowledge of the state of engine is obtained and the results may be used for different aims. The in-flight information about the real condition of the engine may help the pilots to make decision about the mission, improving the effectiveness of the operative action.

For land based facilities the information allows a choice of the most effective maintenance interventions.

### 4 - THE GPA MODEL

The GPA model is based on a set of equations describing the thermo-fluid-dynamics transformations of gas, the balance of energy and mass for each engine component (inlet, axial compressor, burner, high and low pressure turbines, shafts, nozzle).

By a correct arrangement of the engine modules and by taking into account the bleeds and the power extractions it is possible to build up the mathematical model of a gas turbine engine with different configurations. This feature meets one of the desired characteristics of the system: flexibility. In the present paper, a single spool engine turboshaft with free power turbine will be studied.

The main equations for this engine configuration are [13]:

$$PW_C = W \cdot CP_C (T_2 - T_1) \quad (1)$$

$$\eta_C = \left[ \left( \frac{P_2}{P_1} \right)^{\frac{\gamma_C - 1}{\gamma_C}} - 1 \right] \frac{T_1}{(T_2 - T_1)} \quad (2)$$

$$\Gamma_C = \frac{W \sqrt{T_1}}{P_1} \quad (3)$$

$$\eta_B = CP_B (W_B + W_F) \frac{(T_3 - T_2)}{kW_F} \quad (4)$$

$$P_2 (P_2 - P_3) = K_B T_2 W_B^2 \quad (5)$$

$$PW_{GGT} = W_{GGT} CP_{GGT} (T_3 - T_4) \quad (6)$$

$$\eta_{GGT} = \left[ 1 - \left( \frac{P_4}{P_3} \frac{\gamma_{GGT}^{-1}}{\gamma_{GGT}} \right) \right]^{-1} \frac{(T_3 - T_4)}{T_3} \quad (7)$$

$$\Gamma_{GGT} = \frac{W_{GGT} \sqrt{T_3}}{P_3} \quad (8)$$

$$\eta_{M1} = \frac{PW_{CA} + PW_{S1}}{PW_{GGT}} \quad (9)$$

$$PW_{PT} = W_{PT} CP_{PT} (T_4 - T_5) \quad (10)$$

$$\eta_{PT} = \left[ 1 - \left( \frac{P_5}{P_4} \frac{\gamma_{PT}^{-1}}{\gamma_{PT}} \right) \right]^{-1} \frac{(T_4 - T_5)}{T_4} \quad (11)$$

$$\Gamma_{PT} = \frac{W_{PT} \sqrt{T_4}}{P_4} \quad (12)$$

$$\eta_{M2} = \frac{PW + PW_{S2}}{PW_{PT}} \quad (13)$$

The balance of bleed mass flow used for turbine cooling and for the pressurization of lubrication system, is represented by the following equations:

$$\begin{aligned} W_{GGT} &= W_B + W_F \\ W_B &= W_A - W_{s1} - W_{s2} \\ W_{PT} &= W_{GGT} + W_{s3} \end{aligned} \quad (14)$$

The GPA non linear equations system, can be described by the vectorial relation:

$$F(Z) = 0 \quad (15)$$

where  $Z$  is a vector whose  $n$  components are the engine characteristic parameters ( $T$ ,  $P$ ,  $PW$ ,  $W$ ,  $\eta$ ,  $\Gamma$ , etc., at the different engine sections) and  $F$  is a non linear vectorial function of  $m$  components where  $m$  is the number of equation. In the usual GPA applications, the system (15) is solved by Taylor formula rounded off at the

first term. Such approximation produces a linearization of the mathematical model given by:

$$F'(Z_0)(Z - Z_0) = 0 \quad (16)$$

where  $Z_0$  is an engine working point so that  $F(Z_0) = 0$ .

This method is intrinsically approximated and doesn't meet the sensibility level requirements of ECM system. In the present paper, the system (15) is solved iteratively, so the linearizations are totally eliminated.

The research of the solutions of the system involves, if  $n > m$ , a restriction of  $F(z)$  from  $S^n$  to  $S^m$ , by imposing proper values of  $n-m$  vectorial components and produces the following system [14]:

$$\begin{cases} F^*(x) = 0 & S^m \rightarrow S^m \\ x_{n-m+1} = k_{n-m+1} \\ x_{n-m+2} = k_{n-m+2} \\ \dots\dots\dots \\ x_n = k_n \end{cases} \quad (17)$$

The iterative solution of  $F^*(X) = 0$  in system (17) is performed by the Robinson's method that for the current application, shows a very fast convergence [15]. The solution of (17) is determined by the following iteration

$$X^{k+1} = X^k + \Delta^{k+1} \quad (18)$$

where:

$X^*$  is a solution of  $F^*(X)$ ,

$$\Delta^{k+1} = -[G(X^k, X^{k+1}) * U^{-1}(X^k, X^{k+1})]^{-1} * F(X^k) \\ k = 1, 2, 3, \dots$$

$$\text{with } U^{-1}(X^k, X^{k+1}) = X^k - X^{k+1} * H^k,$$

$$G(X^k, X^{k+1}) = F[X^k + U(X^k, X^{k+1}) * e^J] - F(X^k)$$

$$\text{and } G(X^k, X^{k+1}) * U^{-1}(X^k, X^{k+1})$$

is just a difference approximation to the jacobian  $J(X^k)$ ,  $H^k$  is a suitable orthogonal matrix so as to minimize the calculations.

The iterative procedure stops when the various convergence tests are verified.

The values of specific heat in the equation describing the engine modules depend on the gas temperature and on the fuel/air ratio value. In each component, their evaluation, has been carried out by an integral mean of a function depending on the gas composition and temperature [16]. The variation of the specific heat with pressure has not been taken into account since it is very small.

## 5. - THE ECM SYSTEM

The theoretical method described in the previous section has been used for developing a computer code for ECM that allows to study the FOD, MicroFOD and erosion effects.

Besides the already specified characteristics, the numerical ECM system must be airborne and must be mainly used during the actual running of engine as an aircraft power plant.

The ECM system is based on two parallel and simultaneous simulations of the real engine subject to monitoring. These parts of system, *THE SIMULATOR 1* and *THE SIMULATOR 2* are depicted in fig. 4.

Even if the two codes calculate the values of the same parameters of the engine, they are conceptually different. The necessity of utilizing two different simulation codes is justified by the following considerations.

Every ECM system, based on the Gas Path Analysis criterion, evaluates the variations of some engine thermodynamics and performance parameters. The deviations, computed with respect to baseline values, allow the detection of the origins of performance deterioration.

The usefulness and the reliability of conclusions about the probable sources of engine deterioration are strictly linked to the baseline values.

The baseline values are the typical performance and thermodynamic values shown by the engine when there are no faults in progress and no reasons of performance decays. During the development of an ECM system a difficult problem is to obtain sure and reliable values of main engine parameters in order to construct right baselines.

The baselines may be obtained from theoretical calculations or from information delivered by the engine manufacturer. Former data is quite unuseful for ECM system owing to the different behaviour between the theoretical and actual engine. The latter data is obtained from experimental tests carried out on land-based test beds. These data represent a 'mean engine' and are not usable for all engines because, even if they all show the same health conditions, the behaviour is different for each one engine.

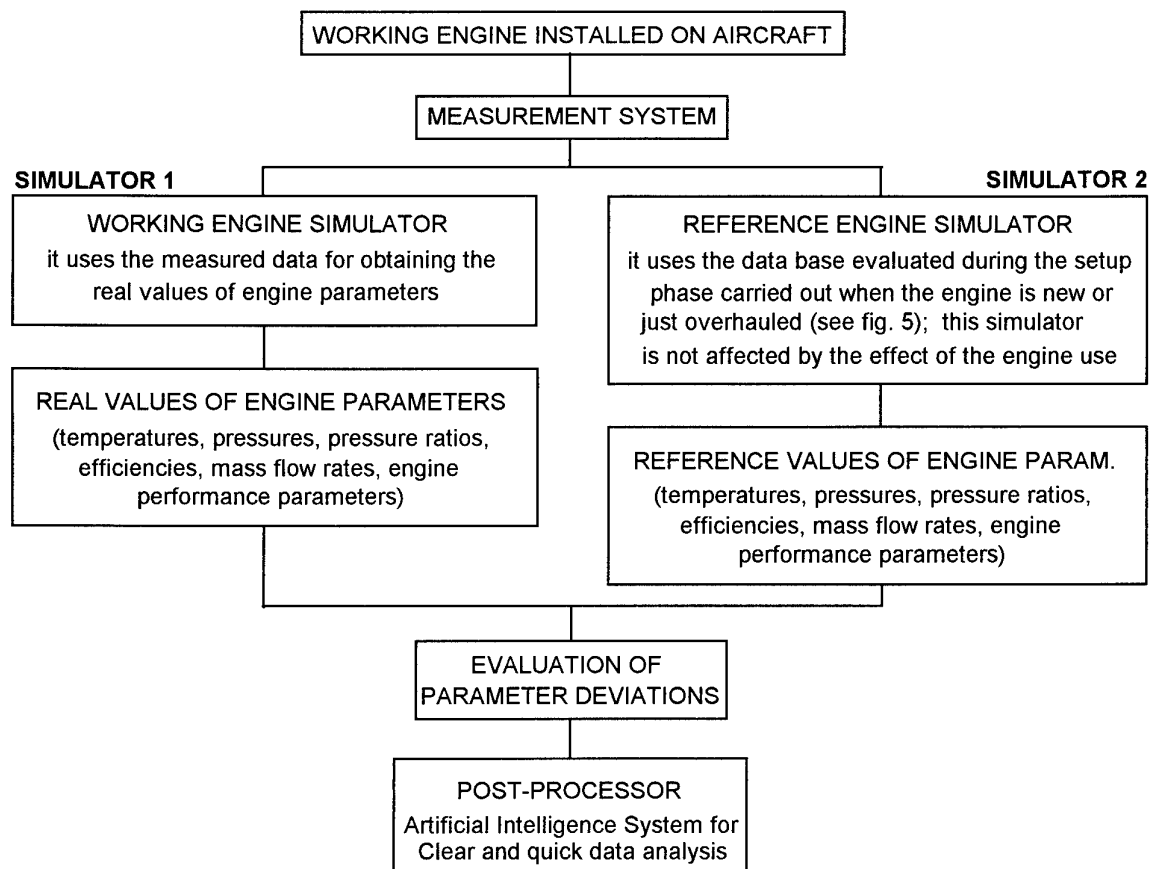


Fig. 4 - Main parts of ECM system developed for FOD and erosion effects monitoring



Moreover, if the manufacturer should deliver the baseline for each engine, the data should be obtained from a test bed or by other installation different from the usual working environment of engine: the same engine shows different behaviour when it is running on a test bed and when it is the aircraft power plant.

In any case, even if the engine is healthy and there are no performance decay, the comparison of actual running data with respect to baseline values should lead to variations [17]. Unfortunately the order of parameter deviations is just similar to the order useful for carrying out ECM for light FOD and erosion. During this study the problem of constructing a suitable baseline has been solved by using two different simulators.

The airborne ECM system begins its working for a new or just overhauled engine, with a first operation phase.

In this phase, during the first flights, the main values parameters, used for successive baseline evaluation, are calculated.

The simulator evaluates the main performance of each components and the component maps. The main steps of this phase are depicted in fig.5.

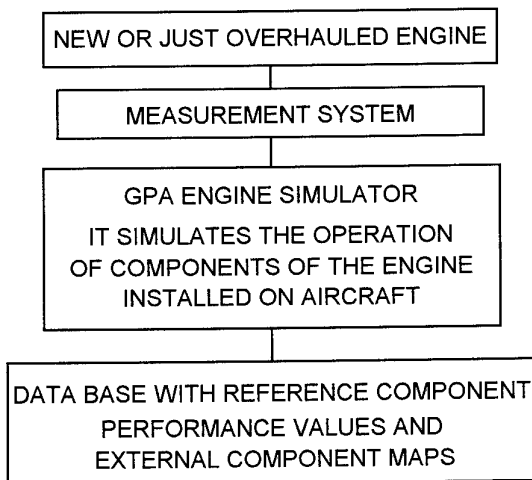


**Fig. 5 - The set-up phase of ECM system for evaluating the engine baseline values**

The reference database is used by *SIMULATOR 2*, by means a multi-dimensional local interpolation [18], during the working life, for the evaluation of baseline values of engine performances.

During usual engine operation, after the system has generated the reference database, a set of engine parameters is acquired, by a suitable measurement system.

The data are contemporary processed by both *SIMULATOR 1* and *SIMULATOR 2*.

*SIMULATOR 1* evaluates the performance and thermodynamic data of each engine component and of the whole engine. These values are the real data of the engine and may be affected by all responsible causes of engine deterioration (FOD, MicroFOD, erosion, etc.).

*SIMULATOR 2* evaluates the same parameters, but it uses the component maps that have been evaluated during the set-up phase. So the system evaluates a data set containing the values of engine parameters with no fault nor any cause of performance deterioration, i.e. a baseline. This baseline is very accurate and reliable because it has been evaluated by using the data obtained from the monitored engine in the current operating working conditions. It is a 'dynamic baseline' and, if any performance deviation is detected by the system, it is surely caused by a real problem and it is not due to the different behaviour of the actual engine to the engine used as reference.

When both actual and baseline values of engine parameters have been obtained, the ECM system evaluates the deviations.

Successively by a suitable tool, i.e. an expert system, the data are quickly and clearly shown to the pilot or to the flight engineer[19].

The comparison of the output of the two simulators, carried out in the envelope of the engine operation, provides a set of data that can be elaborated and analysed for F.O.D and erosion diagnostics and monitoring.

Moreover the data is stored in a file containing all information about the engine operating life.

## 6. - AN EXAMPLE OF SYSTEM APPLICATION

The developed code has been used for the simulation of FOD effects in a single spool turboshaft engine with free power turbine. For this study, owing to the difficulty in obtaining the data during the operating life of a real engine, a fictitious engine has been used.

The values of engine parameters necessary for the set-up phase have been derived from test bed data of different engines. This way a 'paper engine', mean of several engine, has been considered.

The main aim of the ECM system application is to test the sensitivity of the codes and the consistency of results obtained by typical variations of engine parameters due to FOD and erosion. Moreover the consistency of engine behaviour must be tested.

In order to simulate the FOD effects the following engine parameters have been changed:

-compressor exit temperature (T2);

- compressor exit pressure (P2);
- compressor delivered mass flow (W).

The study has carried out by supposing that, coherently with the simulated faults, there is the increase of T2 and the decrease of both P2 and W. The selected parameters have changed on a wide range. The T2 varies from 3% and 40% while P2 and W change from -3% to -40%. This way a large variety of FOD and erosion events may be simulated.

The parameters simultaneously change and the ECM system delivers the variations of engine parameters caused by the modifications of T2, P2 and W.

The obtained results are depicted in table 1.

Calculations have been carried out by considering a fixed value of both fuel flow and rotational speed. This choice is due to the necessity of selecting an engine operating condition for studying the consistency of obtained results.

The results of table 1 show that, for an increase of T2 and an decrease of both P2 and W, the compressor efficiency decrease. This is a good result because both FOD and erosion cause deformation of blades and alteration of compressor geometry.

The other results depicted in table 1 show that the variation of compressor parameters (T2, P2 and W) produces the diminution of:

- Compressor corrected mass flow rate (Comp. Crctd Mass Flow);
- Burner exit pressure;
- Burner mass flow rate;
- Gas Generator Turbine exit pressure (GGT Exit Press.);

- Gas Generator Turbine mass flow rate (GGT Mass Flow);
- Power Turbine mass flow rate (PT Mass Flow);
- Engine Power (Power).

The following parameters rise:

- Turbine Inlet Temperature (TIT)
- Gas Generator Turbine exit temperature (GGT Exit Temp.);
- Gas Generator Turbine corrected mass flow (GGT Crctd Mass Flow);
- Power Turbine corrected mass flow (PT Crctd Mass Flow);
- Exhaust Gas Temperature (EGT).

The increase of both Gas Generator and Power Turbine Corrected Mass Flow Rates are very strange. In fact during usual operations, also when there is some fault in other engine components, both values are constant.

The two results are a consequence of the assumed constant value of fuel flow and rotational speed. This is not at all an usual running of engine. It has been used here only for testing the robustness and consistency of model results.

Other results obtained for a fixed value of only fuel flow are presented in table 2. As it is shown the Gas Generator and Power Turbine Corrected Mass Flow Rates are constant.

The strong variation of T2, P2 and W (i.e. 30-40%), leading to stronger changes of compressor efficiency, have been used only for testing the non linear characteristics of the proposed method.

TABLE 1

	3%	6%	10%	15%	21%	30%	40%
COMP EFFICIENCY.	-7,59%	-14,38%	-22,42%	-31,15%	-40,10%	-51,26%	-61,43%
COMP CRCTD MASS FLOW	-3,00%	-6,00%	-10,00%	-15,00%	-21,00%	-30,00%	-40,00%
BURNER EXIT PRESS.	-3,06%	-6,11%	-10,17%	-15,23%	-21,29%	-30,34%	-40,34%
BURNER MASS FLOW RATE	-3,27%	-6,53%	-10,89%	-16,33%	-22,86%	-32,66%	-43,55%
T I T	3,17%	6,48%	11,10%	17,28%	25,43%	39,59%	59,32%
GGT CRCTD MASS FLOW	1,41%	2,85%	4,78%	7,26%	10,32%	15,18%	21,05%
GGT MASS FLOW	-3,21%	-6,42%	-10,70%	-16,04%	-22,46%	-32,09%	-42,78%
GGT EXIT TEMP.	2,39%	4,93%	8,57%	13,59%	20,45%	33,00%	51,59%
GGT EXIT PRESS.	-6,52%	-12,45%	-19,54%	-27,26%	-35,15%	-44,72%	-52,97%
PT MASS FLOW	-3,00%	-6,00%	-9,99%	-14,99%	-20,99%	-29,98%	-39,98%
PT CRCTD MASS FLOW	5,00%	9,98%	16,55%	24,56%	33,71%	46,08%	57,14%
E G T	3,90%	8,00%	13,83%	21,75%	32,40%	51,43%	78,88%
POWER	-6,16%	-12,19%	-20,00%	-29,41%	-40,16%	-55,17%	-70,31%

TABLE 2

	3%	6%	10%	15%	21%	30%	40%
COMP EFFICIENCY.	-7,02%	-13,92%	-21,9%	-30,9%	-40,47%	-52,38%	-64,28%
COMP CRCTD MASS FLOW	-2,77%	-5,58%	-9,13%	-15,88%	-21,23%	-30,57%	-38,9%
BURNER EXIT PRESS.	-2,24%	-5,96%	-9,76%	-14,69%	-18,01%	-26,51%	-38,25%
BURNER MASS FLOW RATE	-3,85%	-7,08%	-13,71%	-18,52%	-30,31%	-42,3%	-48,38%
T I T	6,31%	9,84%	11,23%	15,46%	23,07%	29,4%	33,3%
GGT CRCTD MASS FLOW	0%	0%	0%	0%	0%	0%	0%
GGT MASS FLOW	-6,3%	-8,78%	-14,48%	-21,17%	-29,75%	-41,46%	-52,24%
GGT EXIT TEMP.	2,13%	3,72%	7,69%	11,16%	21,66%	21,85%	25,4%
GGT EXIT PRESS.	-3,13%	-6,12%	-9,68%	-14,66%	-17,6%	-25,96%	-38,26%
PT MASS FLOW	-6,23%	-7,92%	-13,4%	-20,2%	-27,94%	-40,12%	-50,11%
PT CRCTD MASS FLOW	0%	0%	0%	0%	0%	0%	0%
E G T	2,43%	6,58%	11,63%	19,81%	28,66%	40,69%	56,27%
POWER	-5,71%	-11,52%	-19,38%	-27,47%	-37,2%	-51,92%	-65,43%

Such values are usually not realistic; However the results of tables 1, 2 useful for testing the model consistency, are justified by the following considerations.

The mass flow rate worked out by engine components decreases owing to the reduction of compressor delivered mass flow rate caused by the deformation of compressor geometry.

Also the decrease of pressures in all engine sections is justified by the damages suffered by the compressor. The alteration of blade geometry causes the decrement of compression capacity of component, so the compressor pressure ratio, for a fixed rotational speed, decreases.

The reduction of compressor corrected mass flow rate is due to the decrease of W. Owing to the decrement of compressor mass flow rate and to the constant value of compressor inlet total pressure and temperature, the corrected mass flow decreases.

Finally the power reduction is due to the decrement of mass flow rate and compressor efficiency.

The rise of Turbine Inlet Temperature is justified by thinking that the fuel flow is constant and there is a decrease of burner mass flow rate. The increment of TIT is the main reason of the augmentation of gas generator turbine exit temperature and of EGT. The decrement of pressure and mass flow is overcome by the increment of TIT and of the other temperatures.

Fig. 6-10 show the data obtained by simulation with the ECM codes. The graphs depict the engine response to the contemporary variations of T<sub>2</sub>, P<sub>2</sub> and W

The results are useful because they allow evaluation of the behaviour of both engine and components performance due to assigned variations of compressor parameters. The graphs represents the surfaces obtained by the 4D space surfaces representing the variation of single parameters by the contemporary variations of T<sub>2</sub>, P<sub>2</sub> and W. The presented graphs are concerning with a fixed value of compressor mass flow only for practical problem of results presentation. Obviously it is possible to obtain other graphs for different values of W.

The engine parameter trends, shown in fig. 6-10 may be justified by the same considerations made for the results contained in table 1.

It is interesting only from a theoretical point of view to consider the influence of each selected compressor parameter.

The calculations may furnish results whose analysis may confirm and support the reliability and the sensibility of codes.

Moreover the simulation is useful for studying the partial influence of each parameter on the engine behaviour even if, in actual operation, it is quite improbable that a fault will cause the variation of a single parameter.

It is not realistic to suppose that a FOD or an erosion affect only the T<sub>2</sub> or P<sub>2</sub> or W.

The main results are depicted in fig. 11-15.

FIG. 6 - G.G.T. EXIT PRESSURE

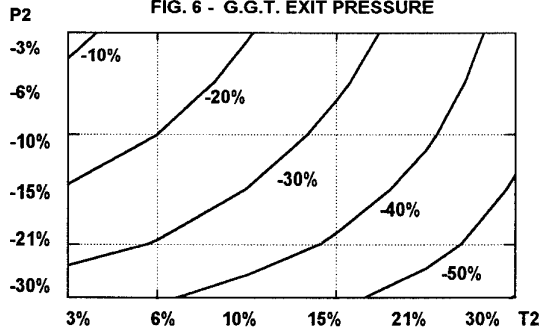


FIG. 7 - E. G. T.

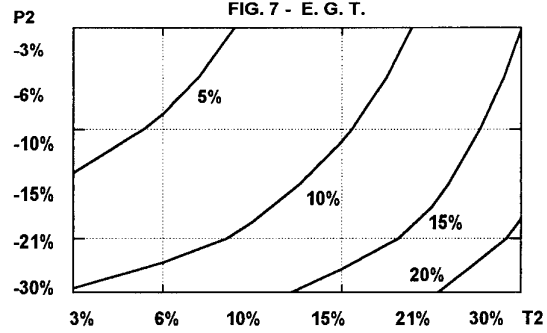


FIG. 8 - POWER

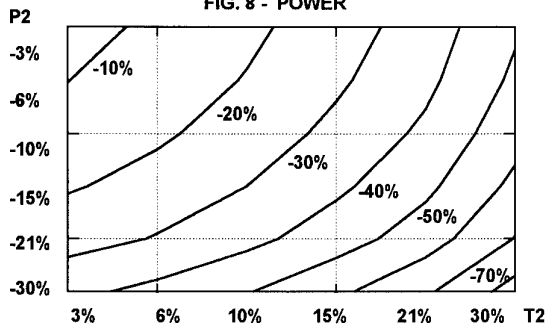


FIG. 9 - COMPRESSOR EFFICIENCY

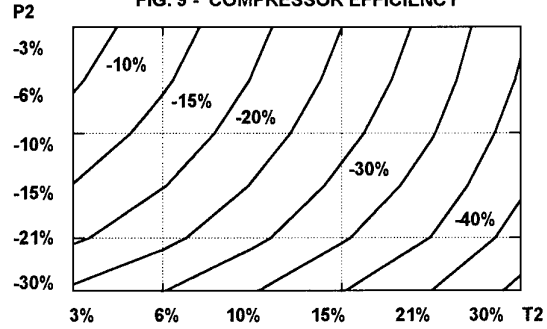


FIG. 10 - BURNER EXIT PRESSURE

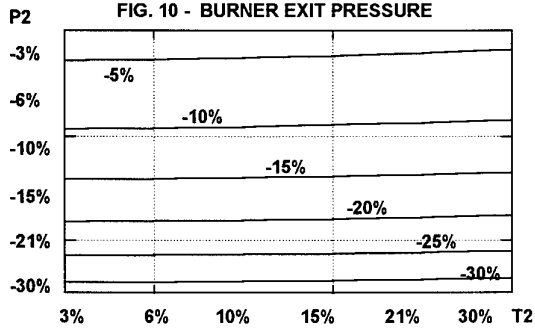


FIG. 11 - COMPRESSOR EFFICIENCY

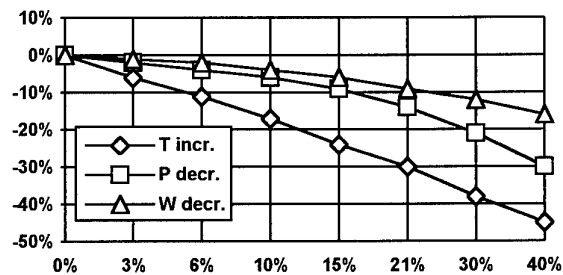


FIG. 12 - G.G.T. MASS FLOW

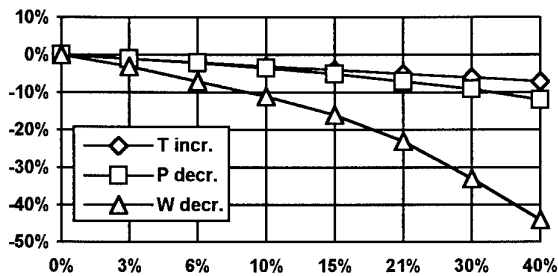


FIG. 13 - POWER

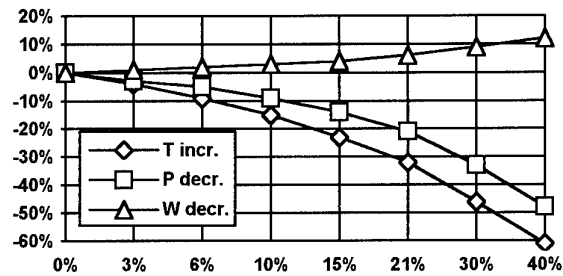


FIG. 14 - TIT

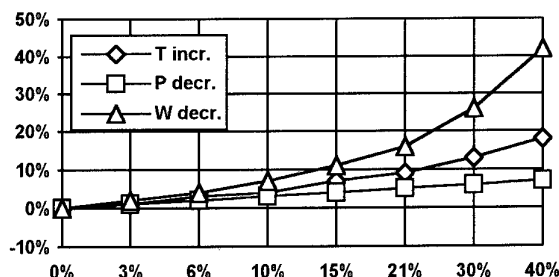


Fig.11 shows the trend of compressor efficiency and it is interesting to note that this parameter is affected by T2, P2 and W. This behaviour may be justified by considering that the increase of T2 and the decrease of P2 and W are the symptoms of efficiency decrement due to alteration of compressor aerodynamics. Moreover the influence of T2 is obviously predominant with respect the influence of P2 and W.

In the real working, if a fault in progress is present, the operating point of compressor shifts and there is a variation of all parameters; but it is important to underline that the obtained results are consistent with the actual working of compressor.

The results dealing with the mass flow rate of gas generator, fig.12, are quite consistent to the actual working.

The parameters are less sensitive to the variations of P2 and T2 than to W variation. This behaviour may be justified by considering that, if there is only a diminution of compressor mass flow rate it is quite logical to find the decrement of the mass flow worked out by each component.

Finally it is important to examine the separate influence of T2, P2 and W on engine power, fig.13

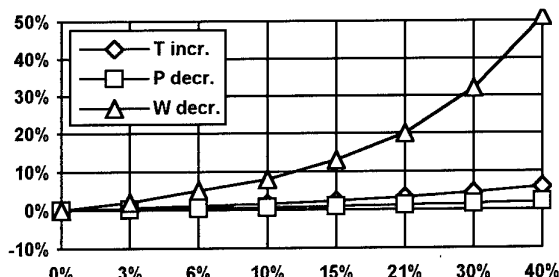
The simulation has shown that the power decreases with both T2 increment and P2 decrement. These trends may be justified by observing that both parameters cause the decrement of compressor efficiency and this leads to power diminution.

The surprising result is that, by decreasing the mass flow rate delivered by compressor, the power increases.

The reason of this behaviour may be obtained by the analysis of fig.14 where the turbine inlet temperature trends are depicted. Owing to the diminution of compressor mass flow the TIT increases. This augmentation is dominant with respect to W decrement therefore the power engine rises.

The increment of TIT with T2 and P2 is not enough for dominating the reduction of

FIG. 15 - G.G.T. EXIT TEMPERATURE



compressor efficiency so the global effect is the decrease of power.

The trend of temperature depicted in fig.15 may be explained in the following way. The increment of parameter is mainly due to the decrement of compressor mass flow and to the consequent increase of TIT. The few sensitivity to the variation of T2 is caused by the simultaneous decrement of compressor efficiency and the increase of compressor power. So the enthalpic drop in the gas generator turbine increases. This attenuates the variation of gas generator turbine exit temperature.

## 7. - CONCLUSIONS

A Gas Path Analysis real time non linear model of gas turbine engine is formulated.

This model is able to simulate the engine behaviour in case of FOD, erosion or different failure. The model is valid not only for severe fault phenomena requiring non linear approach, but also for less severe fault phenomena usually not detectable by the ordinary airborne instrumentation.

The vectorial non linear formulation of the model allows setting up of a computerized diagnostic system able to supply pilots with information on current engine efficiency and failure evolution.

This diagnostic system calculates in real-time the engine reference operational parameters, representative of its nominal conditions as just installed or overhauled. These parameters are then compared with the current real-time values computed for the working engine in order to extract the diagnostic information of the engine and its components.

This system may be used as a robust support for on condition maintenance. The system, because of its sensitivity detects impending failures during maintenance and failures that have occurred during the flight even when they are simultaneous and/or of low intensity.

Effects of various cases of FOD and erosion on gas turbine performance, simulated by the model discussed here, have been presented. Even if the applications of developed ECM system has concerned with a 'paper engine', the obtained results have shown consistent behaviour of engine.

At the present works are in full progress for further testing of codes by using actual experimental data from different sources. Moreover the monitoring of some engines are in progress.

## REFERENCES

- [1] Blokpoel, H., "Bird Hazards to Aircraft", Clarke Irwin, Min. of Supply and Services Canada, 1976
- [2] Dini, D., and Giorgieri, L., "Testing Simulation of Damages Occurred in Service", Paper No. 13, AGARD CP 215, 1977
- [3] Urban, L. A., "Gas Path Analysis Applied to Turbine Engine Condition Monitoring", J. of Aircraft, AIAA, Vol 10, No 7, 1973
- [4] Sallee, G.P., Kruckenberg, H.D., and Toomey, E.H., "Analysis of Turbofan Engine Performance Deterioration and Proposed Follow-On Tests", NASA CR 134769, 1975
- [5] Krupa, W., Hamilton, K., "An Advanced Diagnostic Engine Monitoring System Approach", Paper No. 13, AGARD CP 165, 1975.
- [6] Geer, D. H., Johnson, D., Pilcher, J.A., "A Modern Condition Monitoring and Gas Turbine Control System", ASME 84 GT 220.
- [7] Mentana, F. O., "Turbojet Engine Gas Path Analysis", Paper No. 16, AGARD CP 165, 1975.
- [8] Lunderstadt, R., Fiedler, K., "Gas Path Modelling, Diagnosis, and Sensor Fault Detection" Paper No. 34, AGARD CP 448, 1988.
- [9] Stamatis, A., Papailiou, K., "Discrete Operating Conditions Gas Path Analysis", Paper No. 33, AGARD CP 448, 1988
- [10] Stamatis, A., Mathioudakis, K., "Jet Engine Fault Detection With Differential Gas Path Analysis at Discrete Operating Point", 7133 ISABE 1989.
- [11] Lombardo, G., Caprili, M., "A Non Linear Gas Path Analysis Model for Gas Turbine Diagnostics", Proceedings of 12<sup>o</sup> Congress of A.I.D.A.A., Italy, 1993
- [12] Dietz, W. E., Kiech, E. L., Ali, M., "Jet and Rocket Engine Fault Diagnosis in Real Time", J. of Neural Network Computing, 1, 5-18, 1989
- [13] Gordon C. Oates, "Aerothermodynamics of Gas Turbine And Rocket Propulsion", AIAA education. series 1988
- [14] Broyden, C. G., "A Class of Methods For Solving Non Linear Simultaneous Equations", Math. Comp. 19, 1965.
- [15] Robinson, S. M., "Interpolative Solution of System of Nonlinear Equations", SIAM J. Numer. Analysis. Vol. 3, No 4, 1966.
- [16] Reynolds, W. C., "Thermodynamic Properties in SI", Dept. of Mechanical Engineering, Stanford University, 1979.
- [17] MacLeod, J. C., Laflamme, J. C., "The Effects of a Compressor Rebuilt on Gas Turbine Performance", Paper No. 26, AGARD CP 448, 1988
- [18] Shepard, D., "A Two-Dimensional Interpolation Function For Irregularly-Spaced Data", Harvard College, Cambridge, Massachusetts, 1968.
- [19] Timo, S., Heikki, N., "Application of Artificial Neural Networks in Process Fault Diagnosis", Automatica, Vol. 29, No. 4, 1993
- [20] Dundas, R. E., "The Use Of Performance-Monitoring To Prevent Compressor And Turbine Blade Failures", ASME 82 GT 66.
- [21] Saravanamuttoo, H.I.H., "Overview on Basis And Use Of Performance Prediction Methods" Paper No. 1, AGARD-LS-183, 1992

## QUESTIONS

### **G.D. XISTRIS (Ca)**

- Q. What deviations have you encountered in the performance baselines established on the testbed for the same family of engines?  
What has been your operational experience with the Engine Condition Monitoring system to date?
- A. About 2 - 3%; this is comparable to the amount of deviation necessary for fault detection.  
We are now starting to test the system using data obtained from some maintenance centres.

## CONCEPTION DES AUBES FAN SOUMISES A L'IMPACT D'OISEAUX

P. VIGNOLLES - P.X. BUSSONNET - J. TALBOTEC  
SNECMA  
77550 MOISSY CRAMAYEL  
FRANCE

### RESUME

La qualité des aubes fan en terme de tenue à l'impact est un des paramètres majeurs intervenant dans la sécurité des avions modernes équipés de moteurs à fort taux de dilution. Les renforcements définis comme nécessaires dans certaines zones des profils d'aubages fan, doivent faire l'objet de compromis entre les objectifs de tenue mécanique et de performances aérodynamiques.

Snecma a développé dans ce domaine une méthodologie de prévision de tenue à l'impact des aubes basée sur des modèles de calcul.

Parallèlement, les progrès faits en aérodynamique ont permis de prévoir les conséquences sur les performances aérodynamiques de ces contraintes liées à l'ingestion et de maintenir des niveaux de performances très élevés.

### INTRODUCTION

Pour le motoriste, l'obligation de satisfaire des clients de plus en plus exigeants tant en terme de performance que de "maintenabilité" passe par une amélioration des capacités des fans modernes. Cette amélioration de performances associée à des impératifs économiques demandant de faire bien du premier coup tout en réduisant les durées de conception et de développement, oblige à parfaitement maîtriser toutes les étapes du dimensionnement d'une aube fan. Ceci se traduit par la nécessité de concevoir des soufflantes optimisées suivant des critères parfois antinomiques.

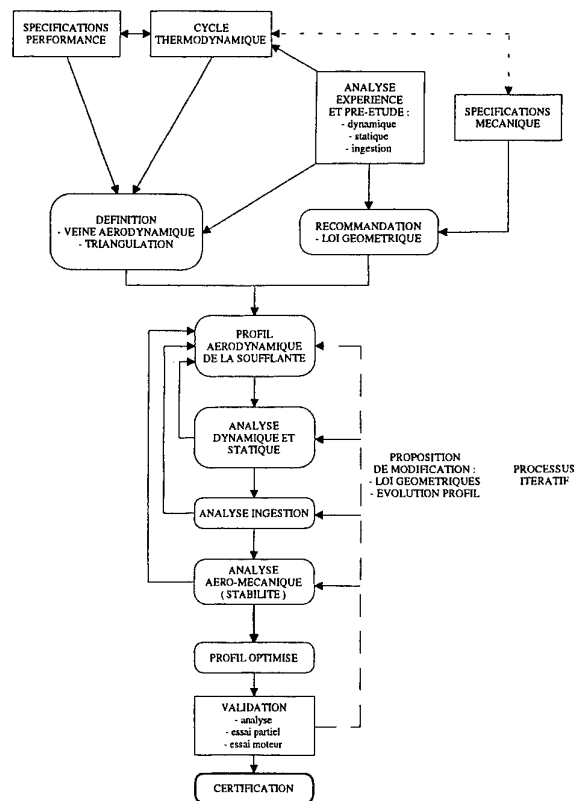
Ainsi, il est important de prévoir très correctement les déformations et les contraintes subies par la pale lors d'ingestion de corps étrangers afin d'éviter d'une part une trop forte dégradation des aubes en fonctionnement et d'autre part un surdimensionnement qui occasionnerait une augmentation significative de la masse du moteur et une baisse du niveau de performance.

Ce souci d'obtenir le meilleur compromis entre une résistance suffisante aux chocs et une bonne définition aérodynamique a donc conduit Snecma à disposer d'outils de calculs performants. Principalement, le besoin de bien prédire la tenue à l'impact des aubes est d'autant plus

nécessaire que les spécifications officielles actuellement en vigueur sont sujettes à modifications (avec des réglementations évoluant vers une plus grande sévérité à l'ingestion) et que le coût des essais réels sur moteur est prohibitif.

### 1. PROCESSUS DE DIMENSIONNEMENT AERODYNAMIQUE ET MECANIQUE D'UNE SOUFFLANTE DE MOTEUR CIVIL

#### Organigramme de conception d'une soufflante



Le processus de conception d'une roue fan (fig. 0) est régi par les besoins clients ; ce sont les demandes de ces derniers qui décident des spécifications performance et mécanique qui conduisent à la définition aérodynamique des veines. Sur la base de certaines recommandations (lois géométriques), une première version de l'aube est



ainsi introduite dans un processus itératif vérifiant successivement son comportement aérodynamique, vibratoire et statique, à l'ingestion et aéromécanique. A chaque étape, l'ingénieur de conception peut être amené à suggérer des modifications de profil ou de géométrie, conduisant à renvoyer le fan au début de la chaîne itérative. Au terme de ce cycle, un profil optimisé est proposé à la validation puis, si toutes les vérifications (analyses, essais partiels, essais moteur) s'avèrent positives, soumis à la certification (si les validations soulèvent certains problèmes, le profil est réintroduit dans la chaîne de conception pour des modifications plus ou moins profondes).

Nous ne présentons dans cet article que les 4 étapes du processus itératif en développant particulièrement l'aspect dynamique (vibratoire et ingestion).

## 2. DIMENSIONNEMENT AERODYNAMIQUE

D'un point de vue aérodynamique, la méthodologie de conception des soufflantes actuelles bénéficie des progrès récents dans le domaine des méthodes numériques élaborées. Ces dernières, et en particulier le code tridimensionnel CANARI qui résout les équations de Navier-Stokes moyennées associées à un modèle de turbulence [1], constituent une approche efficace pour la définition et la recherche de performances optimales.

En outre, cette recherche de performances de plus en plus élevées (fig. 1) -notamment le rendement, dans des plages de fonctionnement où est consommée une majeure partie du carburant- s'accompagne d'un accroissement de la sévérité des règlements dans la certification aéronautique.

Une des réglementations les plus contraignantes (au sens où elle induit la contrainte géométrique la plus pénalisante), consiste en la tenue des aubes de soufflantes à l'ingestion d'oiseaux moyens. La zone critique d'application de ce critère interfère souvent avec la partie de fonctionnement supersonique de la soufflante. Ainsi, le dimensionnement des profils à l'ingestion d'oiseaux conditionne en grande partie la valeur du dièdre du bord d'attaque et l'évolution de l'épaisseur dans une grande partie de la zone de captation. Or, la forme du bord d'attaque influence directement l'inclinaison du choc détaché et son intensité, donc le rendement. La zone de captation des profils quant à elle, régit le débit, en fonctionnement supersonique amorcé.

Il s'avère donc primordial d'être en mesure d'apprécier les conséquences sur les performances aérodynamiques de ces contraintes d'épaisseur liées à l'ingestion. L'utilisation du code CANARI associé à un maillage structuré permettant une représentation très fine du bord d'attaque (figures 2 et 3), s'impose aujourd'hui comme

une étape essentielle dans la prédiction des performances et du fonctionnement aérodynamique des aubages de soufflantes.

## 3. DIMENSIONNEMENT DYNAMIQUE

Les phénomènes vibratoires sont l'un des principaux risques de défaillance des aubes mobiles dans leur ensemble.

La conception dynamique des aubes de soufflante consiste à éviter les coïncidences entre les modes propres de l'aube et les sources d'excitation environnantes.

Pour ce faire, la géométrie des aubes est optimisée afin de positionner ses modes propres sur un diagramme de CAMPBELL (fig. 4) dans des plages de fréquences qui sont fonction :

- des fréquences et des amplitudes des sources d'excitation identifiées (sillage, distribution.....)
- de la sensibilité des modes à être "excité"
- des plages d'utilisation du moteur.

La prédiction des modes propres (fig. 5) est faite au niveau dimensionnement par des calculs éléments finis.

Le degré de fiabilité nécessaire à ce jour pour "faire bien du 1er coup" exige des analyses intégrant :

- l'utilisation de maillage fin (fig. 6)
- la prise en compte du raidissement introduit par le champ centrifuge (fonction du régime)
- la prise en compte de conditions limites les plus réalistes possibles :
  - \* schématisation de l'attache du disque avec des conditions de contact au niveau des portées.

Dans le cas de la soufflante, le disque influence fortement la dynamique de l'aube et par conséquent doit être intégré à l'analyse. Des conditions limites de répétitivité cyclique permettent de mettre en évidence tous les modes couplés (aube + disque) à partir du maillage d'un seul secteur de la soufflante ( $1/N_{\text{ième}}$ ,  $N$  étant le nombre d'aubes).

L'ensemble de ces sophistications permet d'atteindre à ce jour des précisions dans la prédiction inférieure aux dispersions d'aubes à aubes (dues aux tolérances géométriques et aux variations des caractéristiques matériaux).

L'optimisation dynamique vise donc à placer au mieux l'ensemble des fréquences propres de l'aube de soufflante en modifiant les lois géométriques sur la hauteur de l'aube (épaisseur relative, corde, fig. 7) et plus

récemment les formes de profil (évolution de l'épaisseur en fonction de la corde, fig. 8).

L'utilisation dans cette phase de la conception d'un optimiseur couplé au calcul dynamique permet une convergence rapide vers un aubage satisfaisant.

Le dimensionnement dynamique de l'aube de soufflante est validé au cours du développement par :

- une corrélation des fréquences propres de l'aube
- une mesure des niveaux de contraintes au cours d'essais moteur au sol avec et sans distorsion (vent de travers) et en vol.

#### **4. DIMENSIONNEMENT AERO-MECANIQUE**

Snecma utilise en conception des méthodes numériques pour prédire le comportement aéroélastique des roues aubagées. Un secteur aube-disque est modélisé en 3D par éléments finis. L'utilisation des propriétés de symétrie cyclique permet d'obtenir une base modale en rotation. Le couplage avec un code d'aérodynamique instationnaire (résolution des équations d'Euler tridimensionnelles dans un canal inter-aube) permet d'étudier la stabilité du système. Pour la prédiction des réponses forcées à des sillages aérodynamiques provenant des étages amont, le terme d'excitation forcée a été ajouté aux équations précédentes. Ce terme supposé indépendant du mouvement des aubes est calculé par le même code d'aérodynamique instationnaire auquel on fournit le déficit de pression total en amont de la roue. La résolution en base modale du système couplé aéromécanique fournit les contraintes dynamiques sur la pale, et permet ainsi de juger de la criticité relative de différentes coïncidences dans le diagramme de Campbell.

#### **5. DIMENSIONNEMENT A L'INGESTION DE CORPS ETRANGERS**

Le dimensionnement des aubes de soufflante moderne à l'ingestion de corps étrangers nécessite de vérifier leurs tenues aux différents risques d'impact qu'elles pourraient rencontrer en fonctionnement (impact d'oiseaux, de morceaux de pneumatiques et de glace.....). A cet effet, les spécifications officielles imposent l'intégrité de ces pièces lors de la plupart des chocs qu'elles subissent, tout en permettant de conserver une partie des performances du moteur et ce, pendant un certain laps de temps ; le respect de ces spécifications étant, évidemment, une obligation pour le motoriste.

C'est ainsi que la réussite à l'essai d'ingestion de glace (grêlons de 1" et 2" ; barreau de glace de 1" x 4" x 8")

passse par une absence de perte de poussée prolongée ; les dommages résiduels devant être tolérables par le "Shop-manuel".

Pour les essais d'ingestion de morceaux de pneumatique (masse = 4 lb), il est demandé, en particulier, de démontrer l'aptitude du moteur à contenir les débris occasionnés par l'impact ainsi que le parfait contrôle de l'arrêt moteur.

La réglementation concernant l'ingestion d'oiseaux peut se décomposer en trois niveaux de sévérité : ingestion de petits oiseaux (55 à 110 g), ingestion d'oiseaux moyens (1.5 lb et 2.5 lb) et ingestion d'oiseaux lourds (4 lb).

Pour les petits oiseaux, les critères de certification sont sensiblement similaires à ceux demandés pour les essais d'ingestion de glace.

Pour les oiseaux moyens, les autorités certifiantes demandent de démontrer l'intégrité des diverses pièces ainsi que le parfait contrôle du moteur après impact. Consécutivement à ces essais, le moteur doit alors pouvoir respecter, pendant 20 mn, un cycle de fonctionnement pré-établi l'obligeant principalement à assurer une poussée résiduelle supérieure à 75% de sa poussée initiale.

Pour les oiseaux lourds, le motoriste doit garantir la rétention des débris, l'intégrité des suspensions, l'absence de feu moteur, le contrôle de l'arrêt moteur, la non-pollution de l'air cabine et la non inversion de poussée.

Lors des essais de certification à l'ingestion, le nombre de projectiles envoyés sur une même roue dépend de la surface frontale du moteur et les vitesses retenues (vitesse de rotation du moteur et vitesse du projectile) doivent correspondre aux cas les plus critiques.

Le motoriste est donc ainsi amené à rechercher lors du dessin des aubes de soufflante de ses moteurs, le meilleur compromis entre une résistance suffisante aux chocs et une bonne définition aérodynamique sans laquelle les niveaux de performances ne seraient pas suffisants. Pour ce faire, il importe de pouvoir prédire par analyse le comportement mécanique d'une aube sous impact ; ce besoin étant d'autant plus nécessaire que les réglementations actuellement en vigueur sont sujettes à évolutions et que le coût des essais réels sur moteur est extrêmement élevé.

Dans ce qui suit, nous nous intéresserons exclusivement aux impacts d'oiseaux sur aubes métalliques pleines en présentant le phénomène à modéliser ainsi que "l'outil de prédiction" dont dispose Snecma : PLEXUS.

### 5.1. Choc mou : interaction fluide structure

La réponse dynamique des aubes fan soumises à un impact d'oiseau dépend de nombreux facteurs ; les principaux étant très certainement la vitesse et le poids du volatile, la géométrie de l'aube, la vitesse de rotation de la roue et la localisation de l'impact.

Pour le dimensionnement d'une pale, le cas le plus pénalisant reste l'ingestion d'oiseaux moyens (actuellement à 1.5 lb mais que la future réglementation va faire passer à 2.5 lb) du fait des niveaux de performances à respecter après impact. Le régime moteur retenu pour les certifications correspond au décollage, phase au cours de laquelle la probabilité d'ingérer des oiseaux est relativement élevée et où la vitesse (axiale) d'entrée du volatile est faible (cette vitesse d'ingestion est en fait estimée égale à la vitesse avion et peut varier de 70 m/s à 110 m/s). Cette différence considérable entre la vitesse de rotation du moteur (on peut atteindre en sommet de pale des vitesses supérieures à 400 m/s) et la vitesse du projectile conduit à des efforts normaux appliqués à l'aube importants.

Les films d'essais d'ingestion ont mis en évidence que l'oiseau est découpé en tranches par les pales et que la masse d'une tranche est une fonction du pas entre deux aubes et de l'angle d'incidence de la vitesse relative de l'oiseau par rapport à l'aube [2]. Le niveau de cette vitesse relative (entre 350 m/s et 450 m/s) conduit à assimiler ce type d'impact à un choc mou, le projectile se comportant pendant toute la durée du choc comme un fluide [3-4]. La durée de l'impact est estimée équivalente au temps mis par l'oiseau pour "traverser" la roue (de 0.5 ms à 1 ms suivant la largeur de corde).

L'importance des forces d'ingestion conduit généralement à une plastification des zones impactées avec formation d'une poche résiduelle voire à leur rupture ; la limite élastique du matériau étant largement dépassée (fig. 9). Schématiquement, ces efforts peuvent être estimés comme étant la somme de 4 types de force :

- forces d'arrêt du projectile, résultant de l'onde de compression créée lors de l'impact (pression d'Hugoniot).
- forces d'écoulement du fluide le long de la pale, provenant de la déviation du projectile (pression de Bernouilli).
- forces de frottement visqueux entre aube et projectile.
- force de décohéssion au sein du projectile (forces de découpe ; elles correspondent au passage entre une phase quasi-solide et une phase quasi-liquide).

L'observation de ce phénomène d'ingestion d'oiseau a amené Snecma à utiliser un code de résolution numérique possédant les caractéristiques suivantes.

- La formulation du code doit être explicite-explicite afin d'être bien adaptée au phénomène transitoire rapide.
- Elle doit être de type ALE (Arbitrary Lagrangian-Eulerian) pour s'adapter à la fois à une formulation de type fluide (Eulérienne) pour le projectile et solide (Lagrangienne) pour la structure impactée.
- Les lois de comportement matériaux pour la structure doivent être du type élasto-plastique ou visco-élastoplastique pour tenir compte à la fois des déformations résiduelles et de l'influence de la vitesse de déformation sur les caractéristiques matériaux.
- Le fluide doit avoir un comportement compressible pour mettre en évidence la pression d'Hugoniot.
- La structure doit être capable de prendre en compte un chargement initial en contrainte pour pouvoir tenir compte du raidissement centrifuge dû à la rotation de l'aube.
- Le logiciel doit être capable de prendre en compte des conditions de glissement entre structures pour modéliser les conditions de contact entre d'éventuelles nageoires.

### 5.2. PLEXUS et la formulation A.L.E. [5-6]

Le programme PLEXUS permet le calcul de structures composées de solides et de fluides soumises à des chargements dynamiques rapides pouvant aller jusqu'à la ruine. Il tient compte de la non-linéarité géométrique (grands déplacements) et éventuellement du comportement non linéaire des matériaux. La discrétisation spatiale est basée sur la méthode des éléments finis et l'algorithme de résolution est explicite. Ce logiciel fait partie du système CASTEM développé par le Commissariat à l'Energie Atomique (C.E.A.) de Saclay et la CISI.

La méthode implantée dans PLEXUS pour le traitement des problèmes hydrodynamiques avec interactions fluide-structure (interaction oiseau-aube) est la méthode A.L.E. (Arbitrary Lagrangian Eulerian). Cette modélisation a été développée par NOH [7] ; HIRT, AMSDEN et COOK [8] en formulation différences finies et par DONEA [9], BELYTSCHKO [10] en éléments finis.

Dans la description Lagrangienne, les noeuds du maillage (ou de la grille) suivent les points matériels. Ils se déplacent donc au cours du temps avec une vitesse égale à la vitesse des particules. Dans nos simulations, ce modèle

servira à décrire les structures impactées à savoir les aubes fan.

En Eulérien, la grille reste fixe ; on calcule à chaque instant les paramètres du point matériel qui était confondu avec le noeud de la grille à cet instant.

La méthode A.L.E. permet à la grille de se déplacer avec une vitesse arbitraire indépendante de la vitesse des particules.

Ainsi, une des caractéristiques du code PLEXUS réside dans le fait que l'on maille toute la position de l'espace dans lequel le projectile fluide est susceptible de transiter, ce qui implique qu'à l'instant initial du calcul, la plupart des éléments sont vides sauf ceux correspondant à la position du projectile juste avant l'impact. La réponse temporelle se détermine pour chaque pas de temps, par un calcul de transfert de masse à travers les facettes de chaque élément.

Le mouvement des noeuds définissant l'espace fluide est déterminé à partir de celui de noeuds structure permettant ainsi de tenir compte de l'influence de la déformation de la pale sur l'écoulement du fluide et sur les pressions qui en résultent. Ces pressions sont transmises à la structure (aube) par des éléments appelés "éléments fluide-structure" (ce sont en fait des éléments d'interface séparant la zone impactée de la pale et le canal fluide dans lequel va "s'écouler" l'oiseau).

La discrétisation temporelle utilise une méthode de différence centrale, l'algorithme d'intégration dans le temps différant sensiblement de celui utilisé en Lagrangien pur.

Pour assurer la stabilité de l'algorithme, nous imposons au pas de calcul d'être inférieur au pas de stabilité défini par :

$$\Delta t_{stab} = \frac{L}{C + \max(V_i)}$$

$L$  = la plus petite dimension de l'élément

$c$  = célérité du son

$V_i$  = composantes de la vitesse matérielle ( $i=1, 2, 3$ )

### 5.3. Simulations numériques

Dans toutes nos simulations, nous ne considérons que l'impact d'une tranche d'oiseau (correspondant à la coupure des aubages) au niveau du bord d'attaque de la pale ; les dimensions de la tranche étant déterminées avant de lancer un calcul PLEXUS. Le matériau modélisant l'oiseau est un fluide homogène ayant des caractéristiques proches de l'eau ( $\rho=1000 \text{ kg/m}^3$  ;  $c=1000 \text{ m/s}$ ). Le fait de maille l'espace dans lequel peut transiter le projectile conduit à des "maillages fluide"

relativement importants (de 2000 à 5000 éléments volumiques à 6 ou 8 noeuds. Les quantités scalaires (masse volumique, pression, énergie interne) sont définies au centre de gravité de l'élément et sont supposés uniformes dans tout l'élément.

La structure impactée (aube fan pleine en titane avec ou sans nageoire) est modélisée par un matériau élasto-plastique ; la loi introduite dans le code correspondant à une vitesse de déformation de  $1000 \text{ s}^{-1}$ . La rupture est estimée lorsque la contrainte équivalente de Von Mises atteint  $1600 \text{ MPa}$  (ce qui équivaut à des allongements admissibles de 16%). Nos simulations sont réalisées en maillant la pale en éléments coques à 3 ou 4 noeuds et en raffinant tout particulièrement la zone impactée ainsi que la zone d'écoulement de l'oiseau. Cela nous conduit à des tailles de "maillage structure" pouvant aller jusqu'à 800 éléments.

Cette finesse de maillage aboutit à des pas de calcul avoisinant les  $10^{-7} \text{ s}$ .

Dans nos calculs, seuls les "noeuds fluide" sont animés d'une vitesse initiale, vitesse initiale correspondant à la vitesse relative de l'oiseau par rapport à l'aube ; les "éléments structure" étant, quant à eux, soumis à un champ de contraintes initiales dues au raidissement centrifuge.

Les résultats reportés sur les figures 9, 10 et 11 s'ils ne représentent que des simulations de cas tests bien particuliers (impact d'oiseaux de 2.5 lb au niveau du panneau supérieur) n'en sont pas moins représentatifs du phénomène généralement observé lors d'un impact sur une aube métallique, tant au niveau déplacements qu'au niveau zones endommagées.

Ainsi, la localisation des déformées résiduelles (fig. 9) obtenues par le calcul est sensiblement similaire à celle observée expérimentalement, à savoir :

- bord d'attaque (niveau de l'impact) ; c'est l'endommagement le plus critique avec création d'une poche résiduelle et parfois retournement du bord d'attaque (avec des niveaux de plasticité allant de 3 ou 4 % lors de tirs "bas de pale" à plus de 10% pour des tirs "haut de pale" avec des oiseaux de 2.5 lb).
- haut de pale (proche du bord d'attaque) : ce type de dommage qui entraîne un dévissage du panneau supérieur est classiquement observé lors d'impact haut de pale.
- bord de fuite : ce phénomène très localisé se traduit par de "petites ondulations" résiduelles du bord de fuite.
- bord de fuite (coin du panneau supérieur) ; cet endommagement se traduit par un dévissage du panneau supérieur (niveau bord de fuite).

En terme de durée d'impact, l'évolution du niveau de plasticité d'éléments voisins de la zone impactée (fig. 10) montre que la poche résiduelle est définitivement formée après 0.32 ms alors qu'expérimentalement, on l'estime définitivement acquise vers 0.3 ms ; les temps de "traversée" calculés et observés de l'oiseau étant également sensiblement identiques (aux alentours de 0.6 ms pour les aubes à petites cordes et supérieures à 1.2 ms pour les aubes à grandes cordes).

## 6. CONCLUSION

La difficulté majeure que rencontre le motoriste lors de la conception d'une aube fan est de parvenir à converger vers une pale satisfaisante vis-à-vis de l'ensemble des critères aérodynamique, dynamique, aéromécanique et d'ingestion. Ceci est particulièrement vraie pour les coupes de têtes qui sont :

- les plus dures à optimiser aérodynamiquement
- les plus instables
- les plus critiques en ingestion
- prépondérantes pour la masse des rotors de soufflante et de l'ensemble des carters (dimensionnés aux charges de perte d'aube).

Aussi, Snecma continue à investir dans le développement et la fiabilisation de ces codes de calculs notamment en ingestion et en aéromécanique afin de réduire les temps de conception et donc les coûts en faisant "bien du premier coup" ; la finalité des ces investigations étant de disposer d'un outil d'optimisation intégrant les différents critères (dynamique, aérodynamique, aéromécanique et ingestion).

## BIBLIOGRAPHIE

- [1] V. COUAILLIER - A.M. VUILLOT - Ph. VEYSSEYRE  
"Validation d'un code Navier-Stokes 3D sur une soufflante expérimentale"  
Revue scientifique Snecma n° 4.
- [2] H.C. TEICHMAN - R.N. TADROS  
"Analytical and experimental simulation of fan blade behavior and damage under bird impact"  
ASME paper number 90-GT-126.
- [3] R.L. PETERSON and J.P. BARBER  
"Bird impact forces in aircraft windshield design"  
AFFDL-TR-75-150, March 1976.
- [4] J.S. WILBECK and J.L. RAND  
"The development of a substitute bird model"  
ASME Journal of engineering for Power, vol 103, 1981, pp 725-730.
- [5] A. HOFFMANN - M. LEPAREUX - B. SCHWAB  
A. FORESTIER - H. BUNG  
"PLEXUS - A general computer for fast dynamic analysis"  
Congrès mécanique PORTO ALEGRE (1994).
- [6] H. BUNG - A. COMBESCURE - A. FORESTIER  
M. LEPAREUX - P. GALON  
"Lois de comportement et modélisation des impacts"  
Colloque C3 suppl. au journal de Physique III, vol 1, Octobre 1991.
- [7] W.F. NOH - CEL  
"A time independent, two-space dimensional, coupled Eulerian-Lagrangian Code"  
Methods in computational Physics, p 117.
- [8] C.W. Hirt - A.A. AMSDEN - J.L. COOK  
"An arbitrary Lagrangian-Eulerian computing Methods for all flow speed"  
Journal of computational Physics 14 (1974).
- [9] J. DONEA  
"Finite element analysis of transient dynamic fluid-structure interaction"  
Advanced structural dynamics (applied science publishers 1988) pp 255-290.
- [10] T. BELYTCHKO - J.M. KENNEDY  
"Computer models for subassembly simulation"  
Nuclear engineering and design 49 (1978).

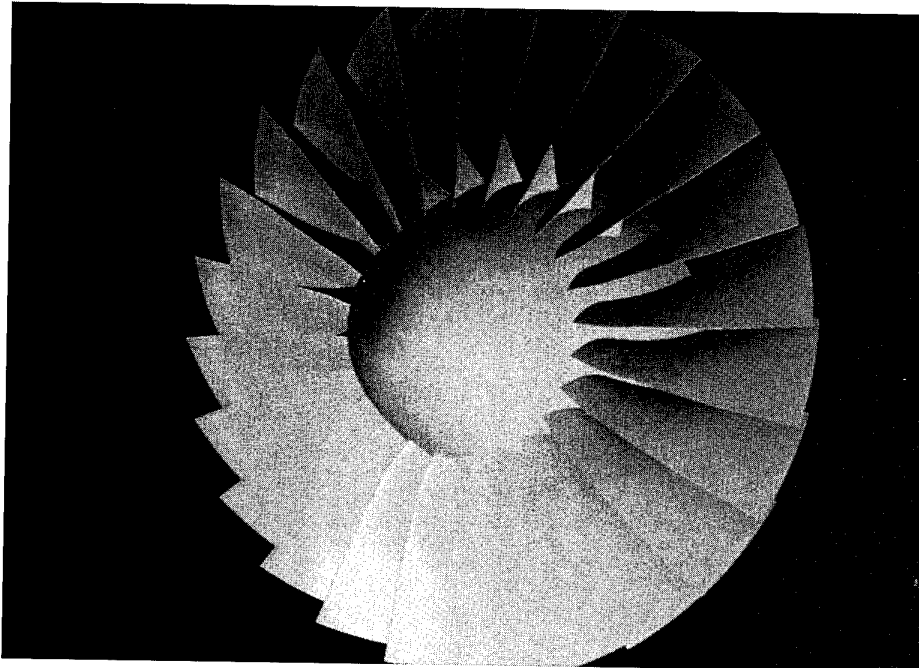


Figure 0 : soufflante civile vue globale

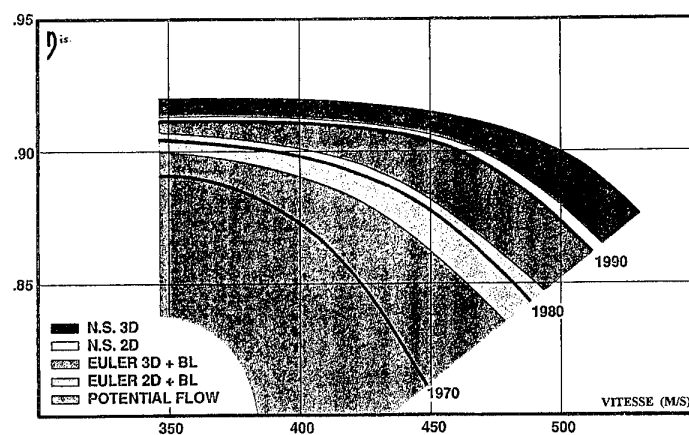
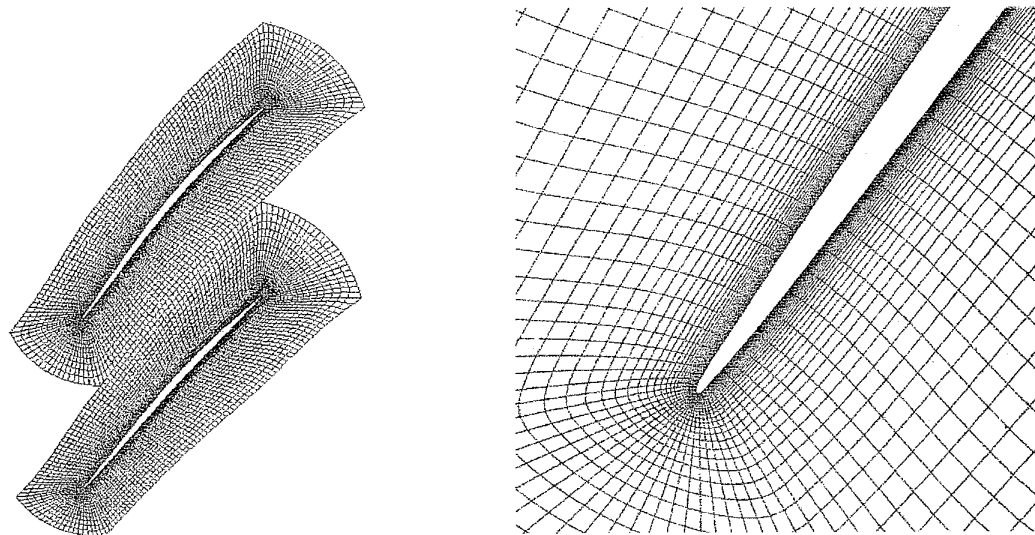
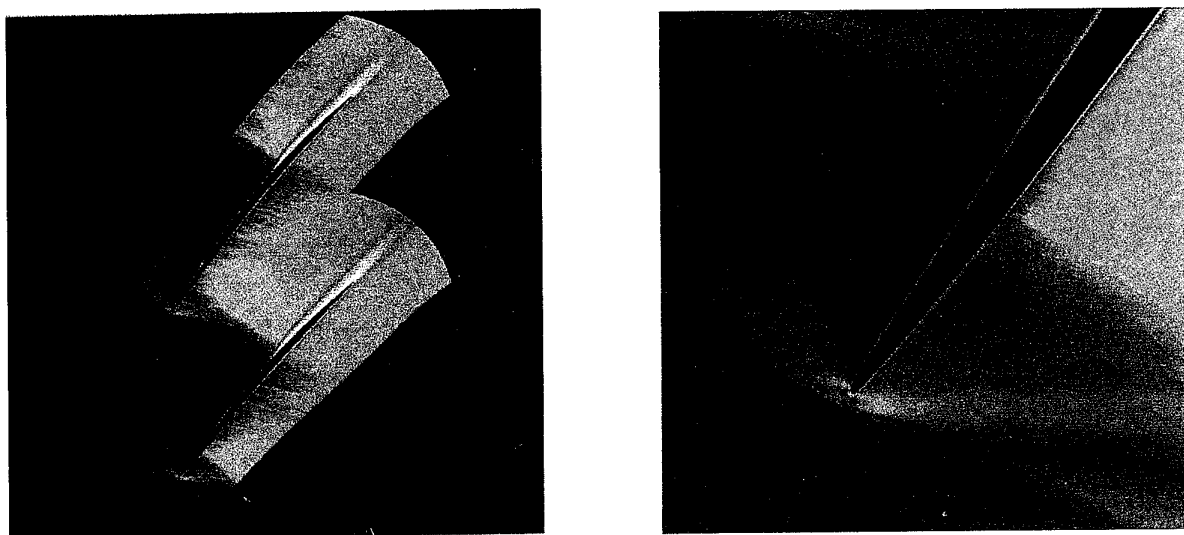


Figure 1 : évolution du rendement isentropique  
corrélée avec les méthodes numériques  
utilisées pour la critique aérodynamique



**Figure 2 :** maillage utilisé par le code CANARI :  
 - vue globale (coupe à 86% de hauteur)  
 - détail du bord d'attaque



**Figure 3 :** cartographie de l'écoulement  
 (nombre de Mach relatif)  
 - vue globale (coupe à 86% de hauteur)  
 - détail du bord d'attaque ( $Mw_1 = 1.33$ )

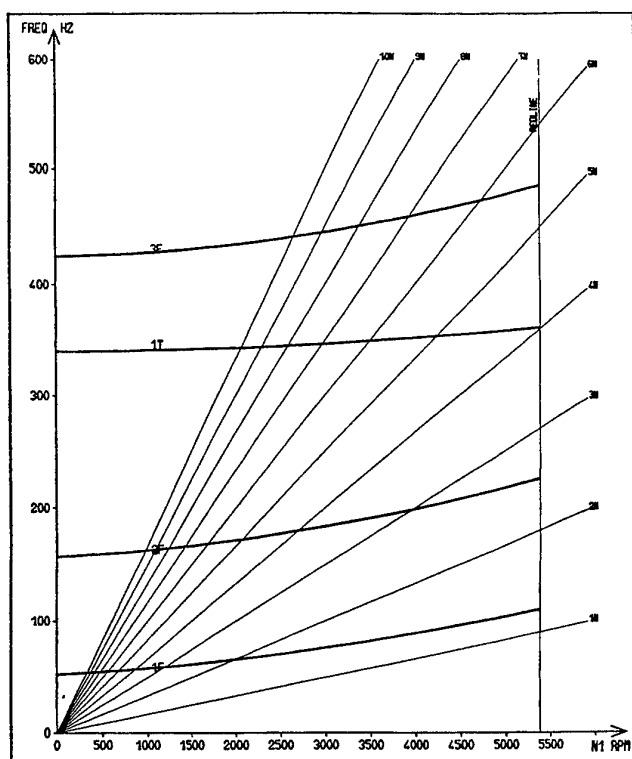


Figure 4 : diagramme de CAMPBELL

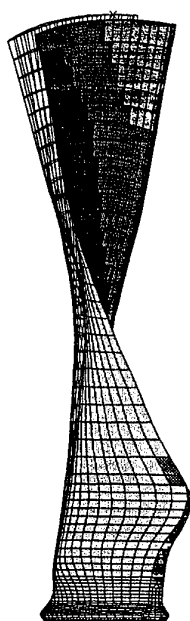


Figure 5 : déplacements vibratoires (mode 1F)

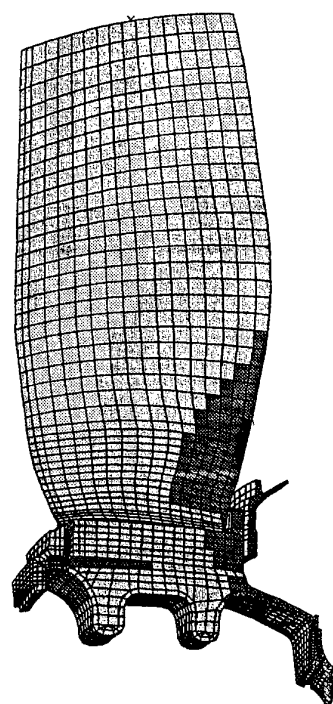


Figure 6 : exemple de maillage



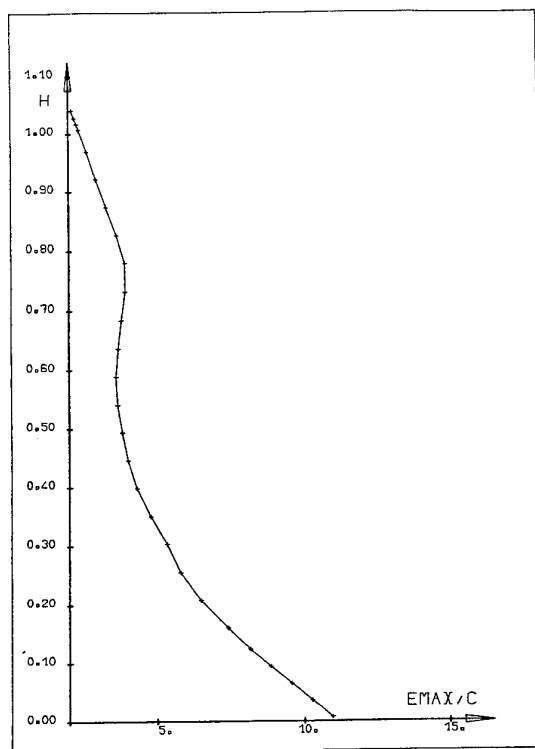


Figure 7 : évolution de emax/corde en fonction de la hauteur

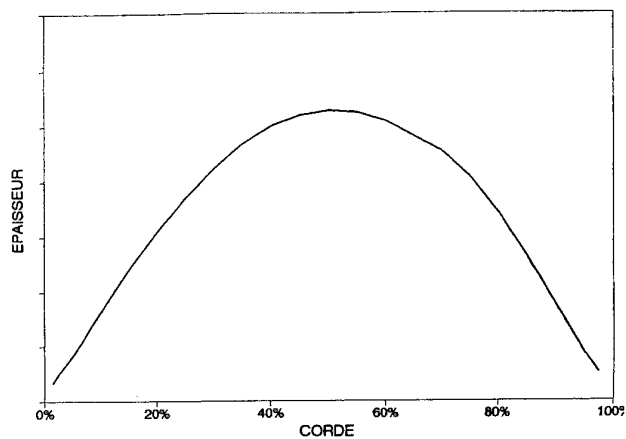


Figure 8 : épaisseur en fonction de la corde

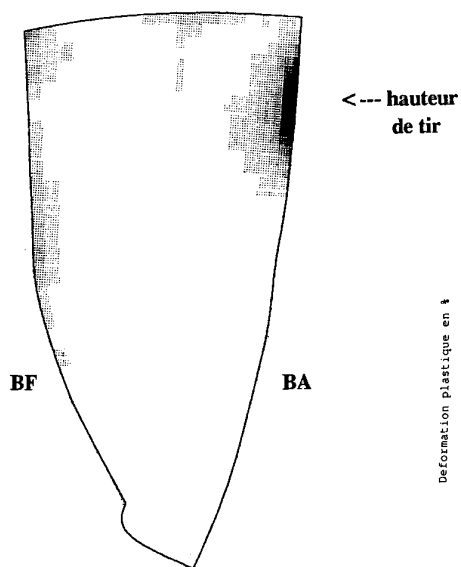


Figure 9 : déformations plastiques

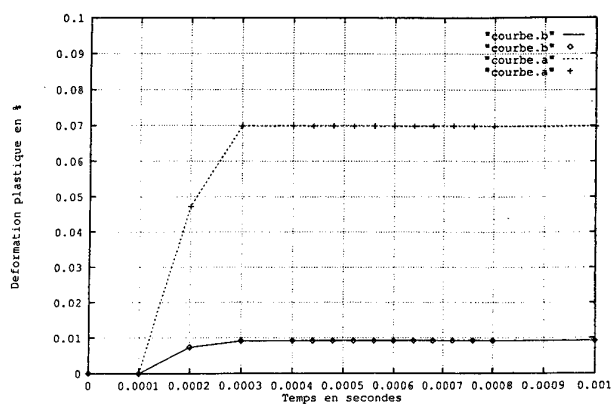
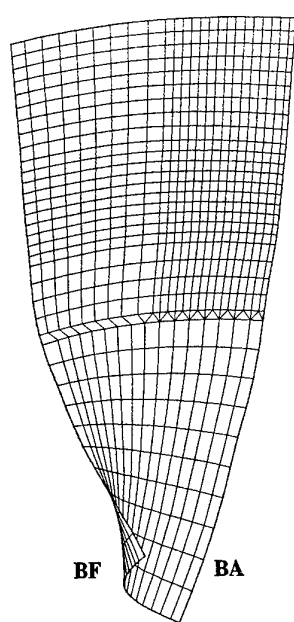
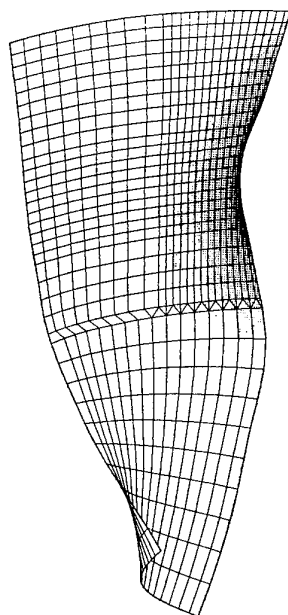


Figure 10 : évolution de la déformation plastique de deux éléments appartenant à la poche résiduelle (a. élément du BA - b. élément de fond de poche)

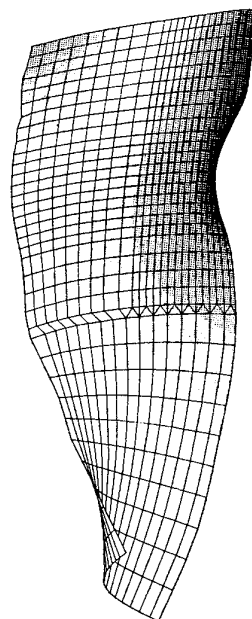


BF BA

a)  $t=0s$



b)  $t=0.4ms$



c)  $t=0.8ms$

Figure 11 : Déformée de l'aube

( $M=2.5$  lb ;  $V=90$  m/s ;  $N=5300$  tr/min ; Hauteur=70%)

# **IMPACT LOADING OF COMPRESSOR STATOR VANES BY HAILSTONE INGESTION**

**J. Frischbier**

**MTU München GmbH  
Postfach 50 06 40  
D-80976 München  
Germany**

## SUMMARY

Impacts of 1 inch diameter ice bullets onto stator vanes of the first stage of an axial compressor were investigated at an impact velocity of  $v = 257$  m/s. The analytical and experimental simulations of typical hailstone ingestions were performed with special emphasis on damage effects of the thin leading edges of the hidden titanium vanes. The paper includes a comprehensive overview of the ice properties used in the analytical model regarding elastic constants, strain rate dependent strength and crack propagation under compression. The influence of different impact positions and ice properties was investigated in the analytical simulations. In all cases the highest stresses occur at the leading edge of the hidden vane. When the centre of impact is placed on the leading edge plastic deformations are expected and localized microcracks cannot be excluded. When the target point is positioned on the suction side of the vane (air foil flank) the energy transfer and the loading is high, but the deformations remain elastic. For verification shooting tests of ice bullets on a complete stator were performed. The ice balls were made by freezing water in liquid nitrogen and the impacts were recorded with a high speed camera. The observed leading edge deflections are in good agreement with the calculated values, but in no case plastic deformations or cracks were detected.

## 1 INTRODUCTION

Hailstone ingestion may cause critical damage in the first stage of jet engine compressors. Therefore in the certification process of a new engine the structural integrity of the engine under hailstone ingestion usually has to be proven in a full scale engine test. The present paper does not deal with these certification tests, but it will give an overview of fundamental ice ingestion investigations at MTU during the development process of a new axial compressor.

In the case of hailstone ingestion mainly the fan rotor blades are affected. The high rotational speed of the fan blades can create high impact velocities between hailstone and blade. When the blade flank is hidden this gives a considerable energy exchange between both impact partners. In this case the global bending potential of the blade is affected.

A second, sometimes more critical local effect happens when the leading edge is

hidden. Due to the early state elastic behaviour of the ice, the high impact velocity and the small contact curvature radii (hailstone radius versus leading edge radius) high Hertzian pressures are transferred during the first few microseconds. Local plastifications and microcracks can be created. This can affect the high cycle fatigue potential of the blade - especially when it is made of titanium.

In general however the resistance of modern wide chord fan blades is significant higher than that of older narrow chord fans. The leading edges are much thicker and the elastic deformation potentials of the individual blades are higher. So for modern wide chord fan blades the ingestion of hailstones of the 1 inch size range need not necessarily be really critical. In shooting tests at MTU (1 inch, 350 m/s) the hidden rotor blades indeed showed some moderate elastic deflections of the leading edge regions, but all impacts were far from creating serious damage.

So far some aspects of hailstone impacts on rotor blades. When stator vanes are hidden the situation may be different. Under certain conditions hailstones can pass the first rotor stage without any interaction with the rotating blades. Fig. 1 shows the general scheme of such a high speed impact condition, which is typical for an aircraft operating close by  $Ma = 1$ . The axial ice inlet velocity  $u$  and the blade circumferential speed  $c$  are giving a relative velocity  $w$  and a corresponding direction, which is parallel to the main blade chord. Under these circumstances hailstones can pass the rotor stage and hit the stator vanes as intact ice balls.

Due to the higher number of blades stator vanes typically are much thinner than the wide chord rotor blades of the corresponding stage. Also the leading edges of the vanes are sharper than those of the rotor blades. In other words the probability of serious damage may be higher for stator vanes than for rotor blades. Although an immediate complete blade loss is rather unlikely the vibration strength especially in titanium decreases significantly with local defects. Parts of single vanes may be lost by high cycle fatigue with serious consequences for the structural integrity of the high pressure compressor. Also the excitation energy of several engine harmonics may increase significantly.

In the present paper the impact of 1 inch

diameter ice bullets with a mass of 0.22 oz. onto stator vanes is being investigated analytically and experimentally. The size of the ice balls was taken from the test specification for the engine certification and the radial target positions were chosen to be at 35 % blade span from the inner diameter shroud of the stator.

Referring to the specific velocity conditions described above the possible impact velocity was calculated to be 257 m/s. Two different circumferential target positions were investigated - a central leading edge impact with possible local damage and a flank impact onto a vane suction side to create a significant bending impulse. An overview of the main test parameters is given in Tab. 1 below.

Hailstone diameter	1 inch
mass	0,22 oz
Impact velocity	257 m/s
Impact position	35 % span from IDS leading edge suction side

Table 1. Test parameters

## 2. Elasticity, Strength and Fracture of Ice

Ice belongs to the system of hexagonal crystals. Experimental values of the anisotropic elastic constants at a temperature of  $-16^{\circ}\text{C}$  are given in /1/,/2/:

$$\begin{aligned} C_{11} &= 13850 & \text{MPa} \\ C_{33} &= 14990 & \text{MPa} \\ C_{44} &= 3190 & \text{MPa} \\ C_{12} &= 7070 & \text{MPa} \\ C_{13} &= 5810 & \text{MPa} \end{aligned} \quad (1)$$

In this notation  $C_{ij}$  are the elastic constants of the generalized Hookes Law

$$\begin{aligned} \sigma_x &= \begin{bmatrix} C_{11} & C_{12} & C_{13} & 0 & 0 & 0 \\ & C_{22} & C_{23} & 0 & 0 & 0 \\ & & C_{33} & 0 & 0 & 0 \\ & & & C_{44} & 0 & 0 \\ & & & & C_{55} & 0 \\ & & & & & C_{66} \end{bmatrix} \begin{bmatrix} \epsilon_x \\ \epsilon_y \\ \epsilon_z \\ \gamma_{yz} \\ \gamma_{xz} \\ \gamma_{xy} \end{bmatrix} \quad (2) \end{aligned}$$

for an orthotropic continuum with 3 normal planes of elastic symmetry. With the additional symmetry conditions

$$\begin{aligned} C_{22} &= C_{11} \\ C_{23} &= C_{13} \\ C_{55} &= C_{44} \end{aligned} \quad (3)$$

and

$$C_{66} = (C_{11} - C_{12})/2 \quad (4)$$

for hexagonal crystal systems the 5 independent elastic constants of Eqn (1) remain for the single ice crystals.

The relation between the elastic properties of single crystals and of 'quasi-isotropic' bodies made up of a large number of small single crystals disposed at all possible orientations has

been investigated by many workers. A physically and mathematically exact solution of this problem does not exist until now.

An approximation method has been proposed by Voigt /3/. The procedure is based on the assumption that the stiffnesses of the aggregate are the space averages of the stiffnesses of the crystallites, a procedure equivalent to assuming that the strain is uniform throughout the assemblage, but the stress is not. With this procedure the following equations can be derived for the youngs modulus E and the shear modulus G of the isotropic polycrystalline aggregate:

$$\begin{aligned} E &= (A+B+3C) (A+2B)/(2A+3B+C) \\ G &= (A-B+3C)/5 \end{aligned} \quad (5)$$

with

$$\begin{aligned} 3A &= C_{11} + C_{22} + C_{33} \\ 3B &= C_{23} + C_{13} + C_{12} \\ 3C &= C_{44} + C_{55} + C_{66} \end{aligned}$$

With these equations and the elasticities given by Eqn (1) and (4) the following values

$$\begin{aligned} E &= 9500 \text{ MPa} \\ G &= 3600 \text{ MPa} \end{aligned}$$

are calculated. Measured values for youngs modulus of pure ice are given in Ref. /4/, /5/. The measurements were performed at temperatures between  $-40$  and  $-45^{\circ}\text{C}$  and the values vary between 9100 and 9800 MPa. In the analytical simulation these values were used as 'upper boundaries' taking into account that the elasticity of hailstone ice is reduced by impurities and air inclusions.

A great number of publications exist regarding the strength and crack propagation behaviour of ice. Fig. 2 gives a comprehensive overview of strength values of pure ice as a function of strain rate  $d\epsilon/dt$ . Beside loading velocity and type of loading (tension or compression) the strength of ice also depends on parameters like temperature (Ref. /8/) and grain size. The maximum value for the strength of pure ice is at 10 MPa. This value is valid only for slow events with strain rates between  $10^{-4}$  and  $10^{-2} \text{ s}^{-1}$ . For high speed loading such as hailstone ingestion with strain rates of more than  $100 \text{ s}^{-1}$  a value of 3 MPa for the compressive strength seems to be likely.

At high rates of strain ice fails in a brittle manner through crack nucleation and propagation. While the crack nucleation is similar for tensile and compressive loading, the crack propagation differs for both types of loading (Ref./8/). For compressive loading (early state of hailstone impact) the crack propagation is a stable process. It differs from tensile fracture in that the ice fails through a combination of a large number of cracks rather than through the instable growth of a single crack. With Ref. /8/ the stress leading to fracture can be expressed by

$$\sigma = 3.5 K_{IC} (2/L)^{1/2}, \quad (7)$$

where  $L$  notates the initial flaw separation. Experimental values of the fracture toughness  $K_{IC}$  are given in Ref. /9/: for sea ice a mean value of 113 kN/m<sup>3/2</sup> (80 specimens, standard deviation 38 kN/m<sup>3/2</sup>).

So only for crack lengths of more than 10 mm the theoretical stress level needed for crack propagation falls below the actual compressive strength given above.

For 1 inch size hailstone ingestion simulations this means, that an analytical material model can be used as an appropriate tool, in which the ice ball solid finite elements behave like elastic bodies until the fracture stress is exceeded.

### 3. ANALYTICAL SIMULATION OF ICE INGESTION

The ice ingestion calculations were performed with the commercial program system DYNA3D. DYNA3D is an explicit three-dimensional finite element code for analyzing the large deformation dynamic response of inelastic solids and structures. A contact-impact algorithm permits gaps and sliding along material interfaces with friction. The equations-of-motion are integrated in time by the central difference method. At MTU DYNA3D is used especially for studies of bird strike, blade-off accidents and blade-casing adradable interactions.

Fig. 4 shows the relevant segment of the finite element model used here and the two investigated impact situations (leading edge impact, suction side flank impact). The model consists of the complete stator blading and the relevant casing structures. Originally this model was used for high speed bird strike investigations. The two relevant stator vanes are modelled with a relatively fine mesh of eight-node solid elements. Each of the both stator vane segments contains 2046 solid elements and 2558 nodes with 3 degrees of freedom per node. The rest of the stator and of the casing structures are modelled with a quite coarse mesh of plate elements, just to get a good approximation of the boundary conditions and the global stiffnesses. The ice bullet after all consists of 1000 solid elements with 1320 nodes. Such a relatively fine mesh was necessary to enable a progressive fracture simulation in small discrete steps.

For the ice an isotropic elastic oriented crack material model was used. Each finite element behaves elastic until the maximum principal stress exceeds the fracture stress. The element then fails on a plane perpendicular to the direction of the maximum principal stress. In tension the element does not carry any stresses on the fracture plane, but in compression it carries both normal and shear stresses. If the fracture stress is exceeded in another direction, the element fails isotropically and behaves as a fluid. This material model was valued to be a relatively good

approximation of the real situation with due regard to the available computer capacity. To estimate the influence of the constitutive parameters of the ice material model on the simulation results, comparative calculations with variations of ice density, youngs modulus and strain to failure were performed.

For the titanium stator vanes a strain-rate dependent elastic-plastic material model with combined kinematic and isotropic hardening behaviour was used. In this model youngs modulus, Poissons ratio and hardening modulus are constant parameters, while the yield stress is a function of strain rate  $d\epsilon/dt$ :

$$\sigma_{0,2} = \sigma_{0,2 \text{ quasistatic}} [1 + (\dot{\epsilon}/k_1)^{1/k_2}] \quad (8)$$

$K_1$  and  $k_2$  are free parameters to adapt Eqn (8) to measured stress-strain characteristics.

For the special titanium alloy used in the stator the strain-rate dependent stress-strain curves have been measured at the Institute for Applied Material Research (IFAM/FhG) of the Fraunhofer-Institute in Bremen. Fig. 3 shows the general test arrangement and gives a qualitative impression of the measured curves. While measuring the stress/strain-relation the bending specimens were loaded to failure with different loading velocities  $d\epsilon/dt$  as test parameters. As to be seen in Fig. 3 mainly the yield stress is influenced by the strain rate, so that Eqn (8) enables a good analytical fit of the measured stress-strain characteristics.

So far some details of the analytical simulation model. The calculation were performed on an IBM RS6000 Risc workstation, taking typically one hour cpu-time and a total storage amount of about 70 Mbyte per run.

### 4. ANALYTICAL RESULTS

Fig. 7 shows a typical sequence of a flank impact analyzed first. In this simulation values at the upper boundary of the theoretical range were taken for the ice properties

$$\begin{aligned} \rho &= 800 \text{ Kg/m}^3 \\ E &= 9800 \text{ MPa} \\ \epsilon &= 0.001 \text{ (fracture strain)} \end{aligned}$$

to get an estimation of the maximum loads. Under these conditions the maximum radial tensile stress was analyzed at the leading edge of the hidden cross section on the pressure side. Fig. 8 shows the time histories of the calculated radial stresses at different chordwise positions on the pressure side of the hidden cross section. The maximum stress of 1100 MPa at the leading edge is reached 90  $\mu$ s after the first contact, taking into account, that the whole impact takes about 200  $\mu$ s. This stress level is associated with a very slight local plastification (total strain maximum 0.012 in Fig. 5), but from a global point of view the whole accident remains elastic. This is due to the high corresponding rate of strain with a peak

value of  $375 \text{ s}^{-1}$ , given in Fig. 6. In quasi-static loading of titanium a stress level of 1100 MPa usually is associated with a total strain of 0.1.

In spanwise direction a considerable amount of deformation energy is transferred to the hub cross section at the inner diameter shroud. Here the radial stresses still reach a level of 1000 MPa, to be seen in Fig. 9.

Also a significant amount of energy is transferred to the neighbouring vanes. Viewing in the impact direction at the left hand neighbour vane stress levels of still up to 320 MPa are calculated at the leading edge position of the hub cross section.

Altogether the whole accident is valued to create high but not really critical stress levels. Serious defects such as local cracks or major plastic deformations are not expected.

In the second case a central impact of the ice ball onto the leading edge was analyzed. Here it is expected that the whole accident is predominantly controlled by the Hertzian elastic contact pressures between ice ball and vane leading edge in the very early state of the impact until the ice ball fails by brittle fracture.

Indeed already 25  $\mu\text{s}$  after the first contact the final level of 0.18 for the effective plastic strain is reached at the impact centre on the leading edge (see Fig. 11). This is a value quite close to the strain to failure for titanium. Fig. 14 shows the deformation plot for  $t = 36 \mu\text{s}$  immediately before the ice ball fails completely.

At this time step the theoretical intersection between the periphery of the ice bullet and the leading edge is 9 mm and about one third of the solid elements of the ice bullet have already failed. On the stator vane the plastified region is quite localized. Figures 12 and 13 show the corresponding local plastification distributions for  $t = 36 \mu\text{s}$ . The region with effective plastic strain values of more than 0.1 is restricted to 10 % relative chordlength in chordwise direction and to 17 % of the total span in spanwise direction.

After the first 100 microseconds the calculation had to be stopped due to numerical problems with the finite elements of the ice ball. In the analytical model after failure the ice finite elements behave as a fluid, but the ice ball does not separate into several parts as it does in reality. So after the failure of the complete ice ball a further calculation makes no sense due to absolute unrealistic numerical hydrodynamic effects of the extremely deformed but not separated analytical ice ball. On the other hand, within the simulated time range, the local plastification is calculated to reach its final level after 25  $\mu\text{s}$ , where the simulation is valued to be still realistic.

The results presented until now were

calculated with the analytical ice properties given above. To get a feeling how the results depend on the assumed ice properties further calculations with ice properties at the lower boundary of the estimated range were performed. In this case, with

$$\begin{aligned}\rho &= 700 \text{ Kg/m}^3 \\ E &= 8300 \text{ MPa} \\ \epsilon &= 0.0003 \text{ (fracture strain),}\end{aligned}$$

a maximum effective plastic strain of 0.16 is calculated, which has to be compared with the value of 0.18, calculated before. This means that the sensitivity of the calculated maximum strain to variations of the ice properties is rather moderate. This seems to be plausible, taking into account, that in Hertz theory of contact for elastic bodies with different youngs moduli ( $E_{\text{ice}} \ll E_{\text{titanium}}$ ) the contact force approximately is a linear function of the lower module ( $E_{\text{ice}}$ ).

On the other hand the calculated results for the central leading edge impact are just to be seen as rough indications of the real situation, because the finite element mesh of the stator vane is too coarse in comparison to the calculated strain gradients to give accurate quantitative results.

Summarizing the results of the analytical simulations the ingestion of an 1 inch hailstone seems to be uncritical, when the vane flank (suction side) is hidden. The loading is high, but the main deformations are elastic. When the leading edge is hidden, high but localized plastifications are likely, but the situation still is valued to be tolerable, because an immediate complete crack of the hidden cross section is rather unlikely.

The possible damage area is rather localized and the elastic strain energy in the blade is much too low to force a crack propagation.

#### ICE INGESTION TESTS

Fig. 15 shows the MTU test arrangement for the ice ingestion tests, which is also used for bird strike investigations. The cartridge with the ice ball is positioned at the end of a 12 metre acceleration tube. It is accelerated to the nominal impact velocity by a sudden expansion (valve) of the helium pressure vessel behind. Before leaving the tube the velocity of the cartridge is measured with optical sensors. The relation between vessel pressure and final impact velocity is determined with calibration tests. At the end of the tube the cartridge is caught and after another two metres distance the free ice ball hits the stator. The tests were observed with a high speed camera with a capacity of 7000 pictures per second.

The ice balls were made by freezing water two minutes in liquid nitrogen. Immediately afterwards the ice balls were put into the cartridge to perform the shots. This freezing method had the advantage to be fast and uncomplicated, so

that the whole test series could be performed within a few days. On the other hand the strength of the test ice was unknown and a reduction of the strain to failure of the ice ball due to the shock freezing method is rather likely. Nevertheless the ice bullets were valued to be representative in some way with due regard to the fact that, under the impact conditions tested here with rates of strain of more than  $300 \text{ s}^{-1}$ , ice always fails in a brittle manner and creep properties are not requested.

In the test series the same conditions as in the analytical investigation were chosen and the target accuracy of the shots was in the range of a few millimeters. Fig. 16 shows a photo sequence of the high speed camera recording of an impact onto a vane suction side (flank impact). The ice projectile is followed by fragments of the cartridge.

In the photo sequence the fifth picture corresponds to the third state of Fig. 7. The maximum leading edge deflection of 4-5 mm, derived from the camera recording, is in good agreement with the calculated values of Fig. 10. Also a significant vibration excitation of the neighbouring vanes can be clearly seen. So for the energy controlled flank impact the analytical predictions of the global deformations and of the energy exchange are verified quite well by the ingestion tests.

In the test series of central leading edge impacts the predicted plastic deformations of the analytical simulation could not be verified. No plastic deformations or local cracks were detected afterwards.

Additional to the test conditions, analyzed in the theoretical section, further ingestion tests with different impact angles and impact velocities were performed. At an incidence angle between  $18^\circ$  and  $39^\circ$  with respect to the engine rotation axis hailstones also can pass the rotor stage without fracture, when their absolute inlet velocity is in the range of 340 m/s. Under these test conditions similar effects as presented before were observed. When the suction side is hidden a significant bending vibration is forced, but no local damage is detected, when the leading edge is hidden.

#### CONCLUSIONS

Impacts of 1 inch size hailstones onto stator vanes of the first stage of an axial compressor have been investigated analytically and experimentally. When the suction side (vane flank) is hidden, significant deflections are caused with bending stresses of up to 1100 MPa. The global deformations and the energy transfer to neighbouring vanes in the analytical simulations could be verified quite well by the high speed camera recordings of the corresponding shooting tests. When the impact is placed directly on the leading edge of a vane, quite localized plastifications are predicted by the analytical simulation, which could not

be verified by the test results. The reason for this discrepancy may be either an incapability of the analytical model to predict correctly the local Hertzian contact pressures due to an insufficiently refined finite element model, or on the experimental side an insufficient strength of the test ice bullets due to the shock freezing process. This has to be clarified by future investigations.

For the immediate structural integrity of the engine the one inch hailstone impact onto the investigated stator is valued to be tolerable since an immediate fracture of a complete stator vane can be excluded due to an insufficient amount of strain energy, no matter, whether the calculated plastifications are true or not.

On the other hand, even in the case, when the vane flank is hidden, the bending stresses are so high, that critical damage must be expected for ice bullets bigger than 1 inch. For the compressor stator investigated here this is a hypothetical case, since ice bodies larger than 1 inch are fractured in the rotor stage.

#### REFERENCES

- /1/ Hearmon, R.F.S., "An Introduction to Applied Anisotropic Elasticity", Oxford University Press, UK, 1961
- /2/ Hearmon, R.F.S., "The Elastic Constants of Anisotropic Materials - II", *Advances in Physics*, 5, 1956, pp. 323-382
- /3/ Voigt, W., "Lehrbuch der Kristallphysik", Teubner Verlag, Leipzig, 1910, Neudruck 1928
- /4/ Sinha, N.K., "Ice and Steel - A Comparison of Creep and Failure", in "Proceedings of the European Mechanics Colloquium 239", Leicester University, UK, 1988, pp. 201-212
- /5/ Sinha, N.K., "Rheology of Columnar-Grained Ice", *Experimental Mechanics*, 1978, 18, pp. 464 - 470
- /6/ Hallam, S.D., "The Role of Fracture in Limiting Ice Forces", 8th IAHR Ice Symposium, Iowa, 1986
- /7/ Riley, S.J., "Icing Research Related to Engine Icing Characteristics", AGARD CP 480, 29, pp. 1-12
- /8/ Mills, M.R., Hallam, S.O., "Ice Loading on Offshore Structures: The Influence of Ice Strength", in "Proceedings of the European Mechanics Colloquium 239", Leicester University, UK, 1988, pp. 152-167
- /9/ Parsons, B.L., Snellen, J.B., Muggeridge, D.B., "The Double Torsion Test Applied to Fine Grained Freshwater Columnar Ice and Sea Ice", in "Proceedings of the European Mechanics Colloquium 239", Leicester University, UK, 1988, pp. 188-200

## QUESTIONS

### **P. RAMETTE (Fr)**

Q. How do you evaluate the probability that a hailstone could impact Stator 1 without impacting Rotor 1?

A. In detail the statistical probability was not evaluated. My estimation is that the absolute probability is comparatively low. For related situations, such as specific bird strike situations, we have evaluated such statistical probabilities. Here for the hailstone impact situation of the stator vanes, a statistical probability investigation would have to take account of the combination of probabilities such as:

- probability of the aircraft having a hailstorm event with respect to a certain number of flight hours (expected flight missions, experience with hailstorm events in the past);
- probability for hailstones to pass the aircraft intake (several metres, curved) without being fractured (probability of flight missions with specific flight incidence angles);
- probability of the hailstones to pass the rotor stage without being fractured (assumptions for hailstone distributions - spanwise, circumferential; probability for a specific hailstone inlet velocity with respect to a certain rotor circumferential speed).

Despite these probabilities, you will always have a number of related situations, when larger ice structures are just separated in the rotor.



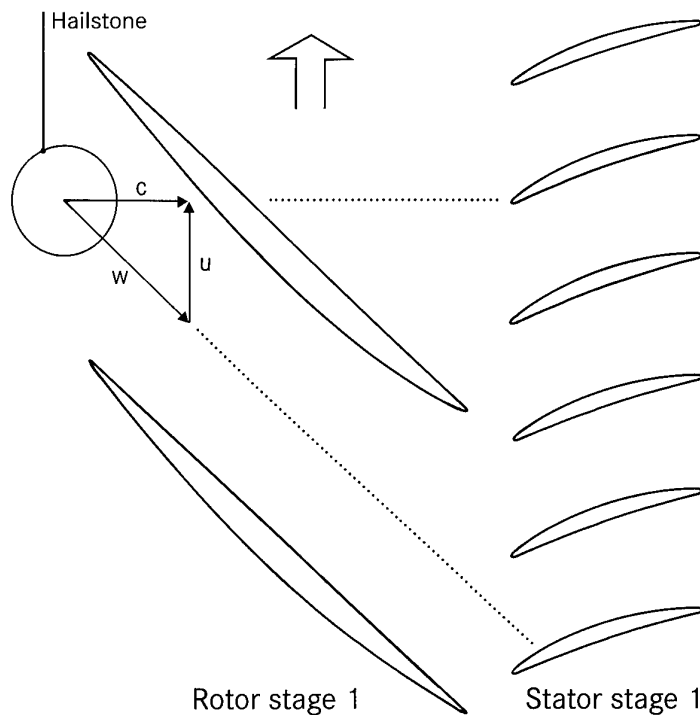


Figure 1. Scheme of an ice high speed impact onto stator vanes

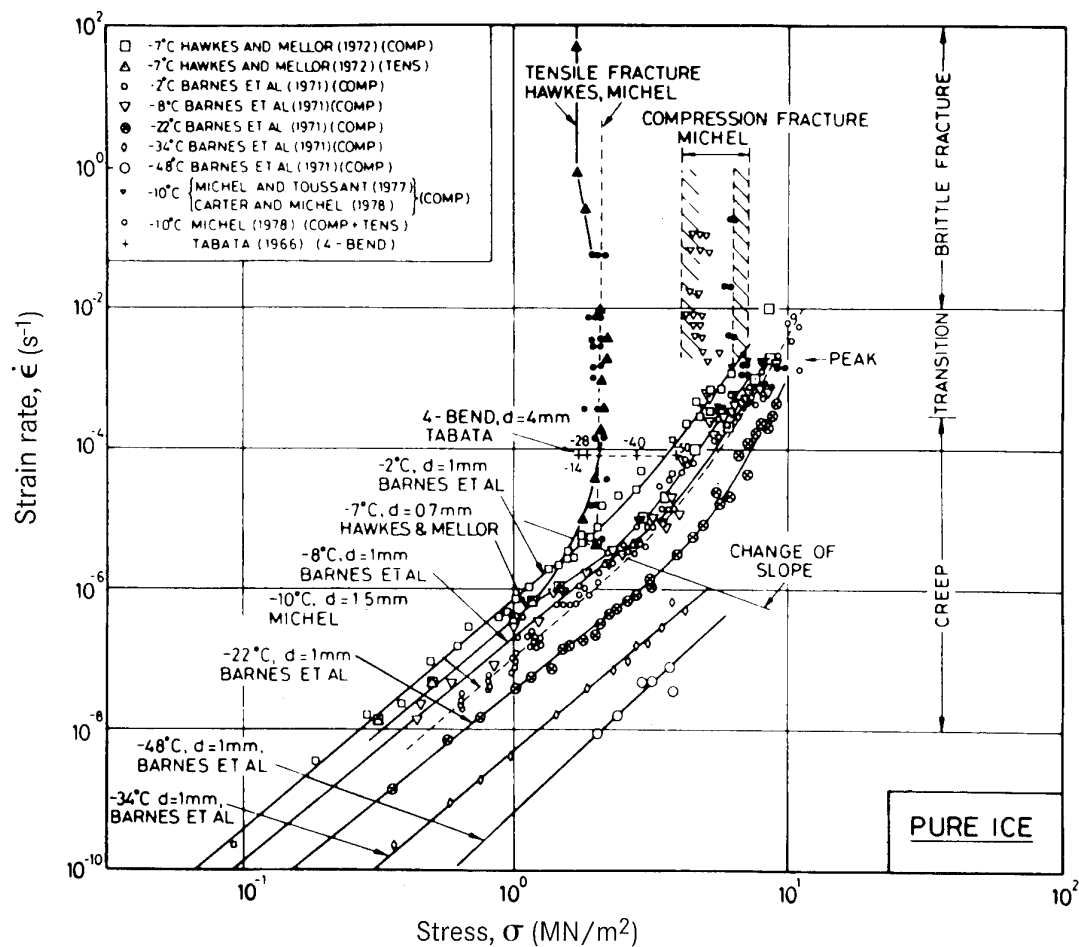


Figure 2. Strength of pure ice as a function of strain rate and type of loading (from Ref. /8/).

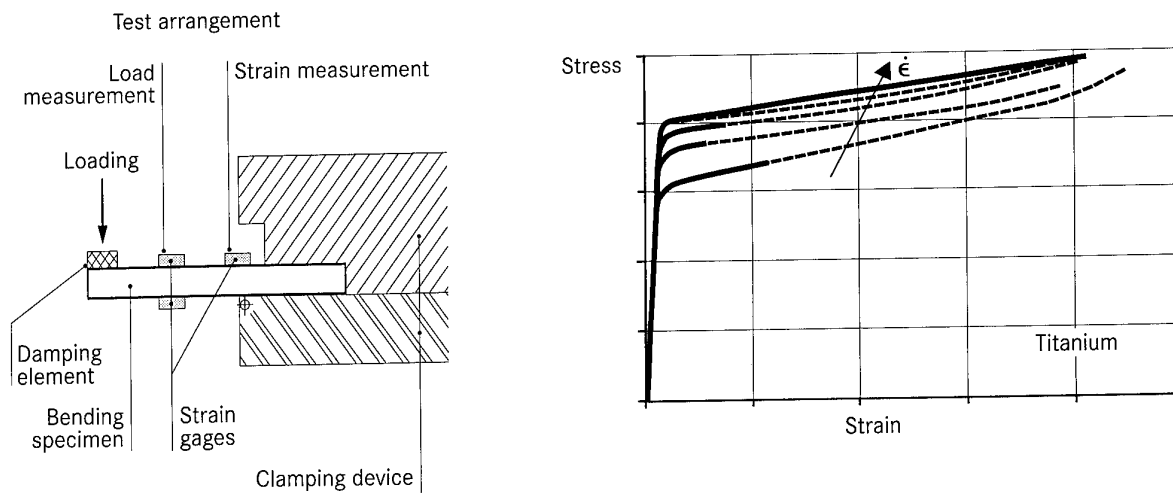


Figure 3. Measurement of the strain rate dependent elastic-plastic stress-strain behaviour of titanium

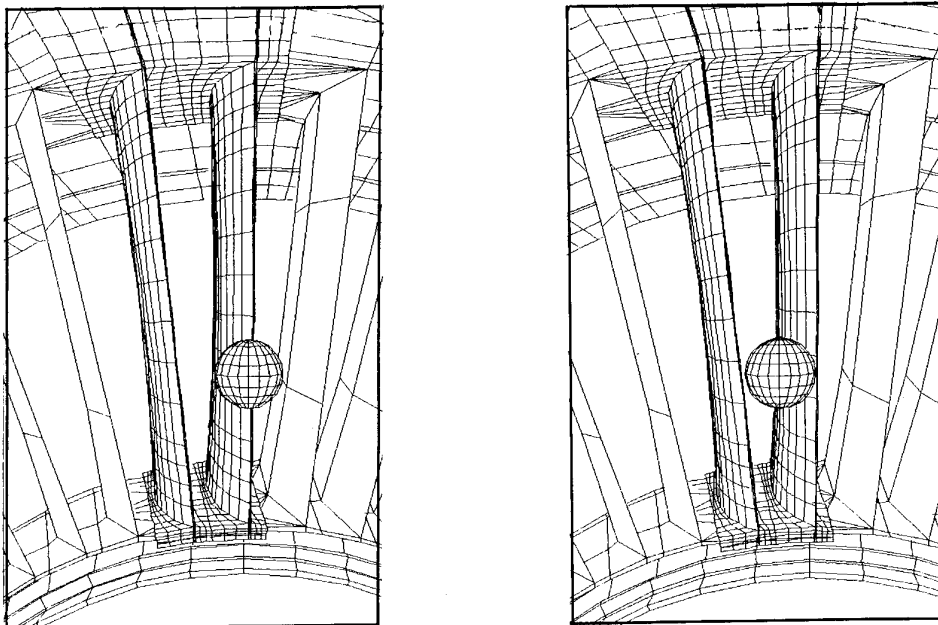


Figure 4. Section of the finite element model (leading edge impact, flank impact)

Radial strain

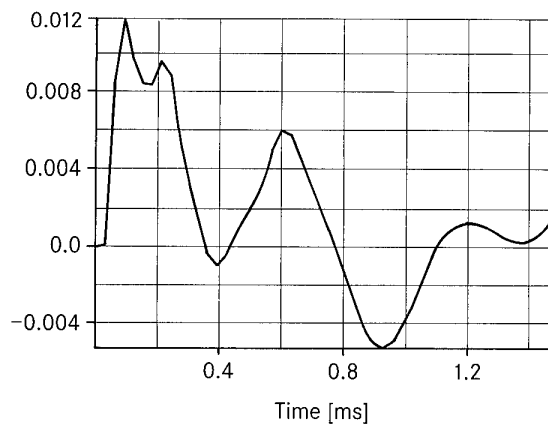


Figure 5. Time history of radial strain (infinitesimal total strain) at the leading edge of the hidden cross section (flank impact).

Strain rate

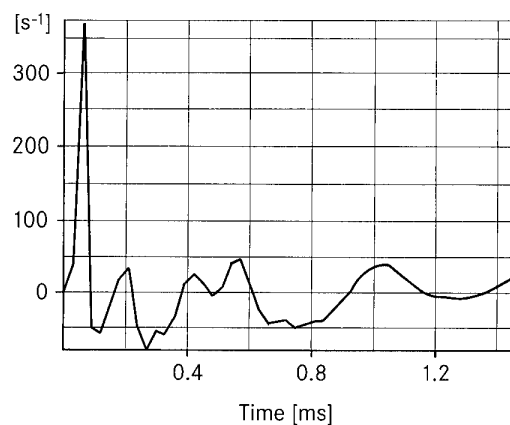


Figure 6. Time history of strain rate (position and impact conditions as Fig. 5)

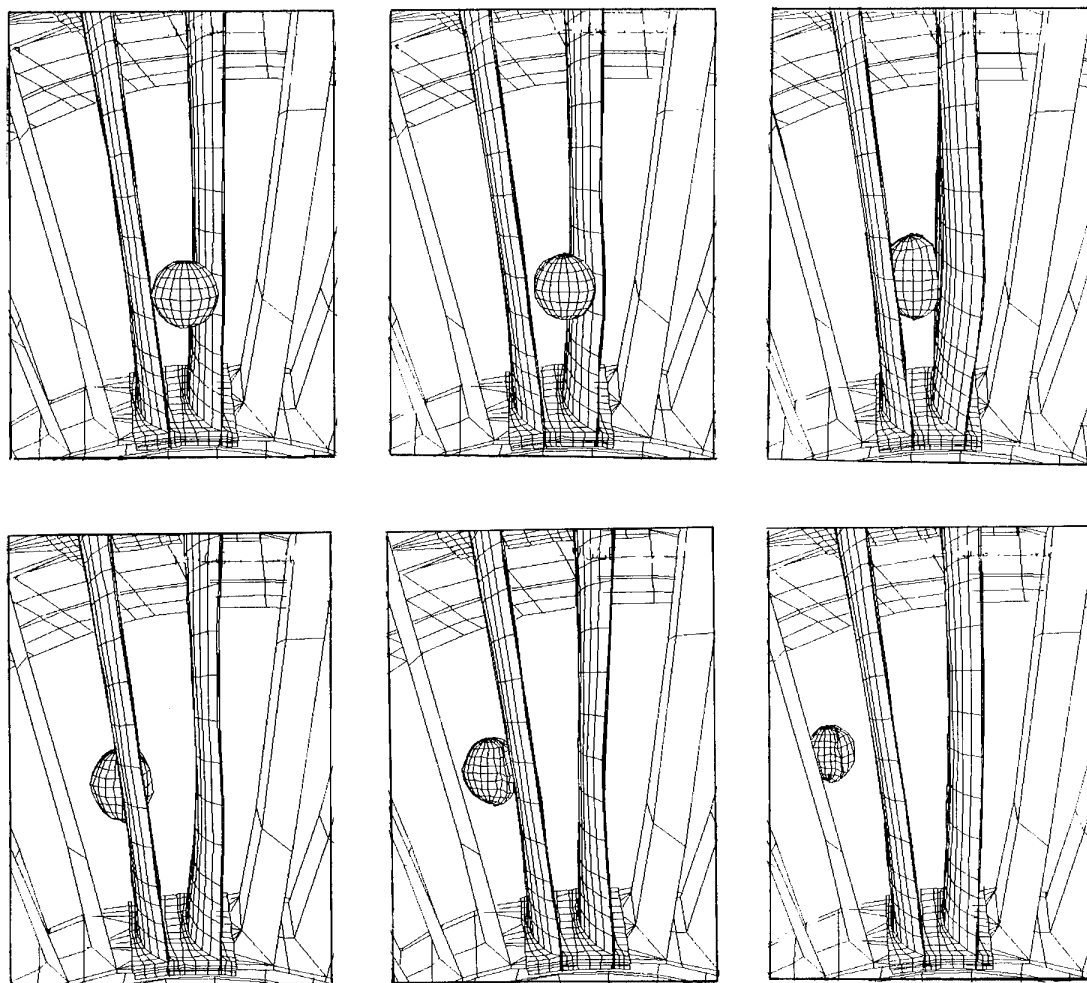


Figure 7. Sequence of analytical simulation of a flank impact

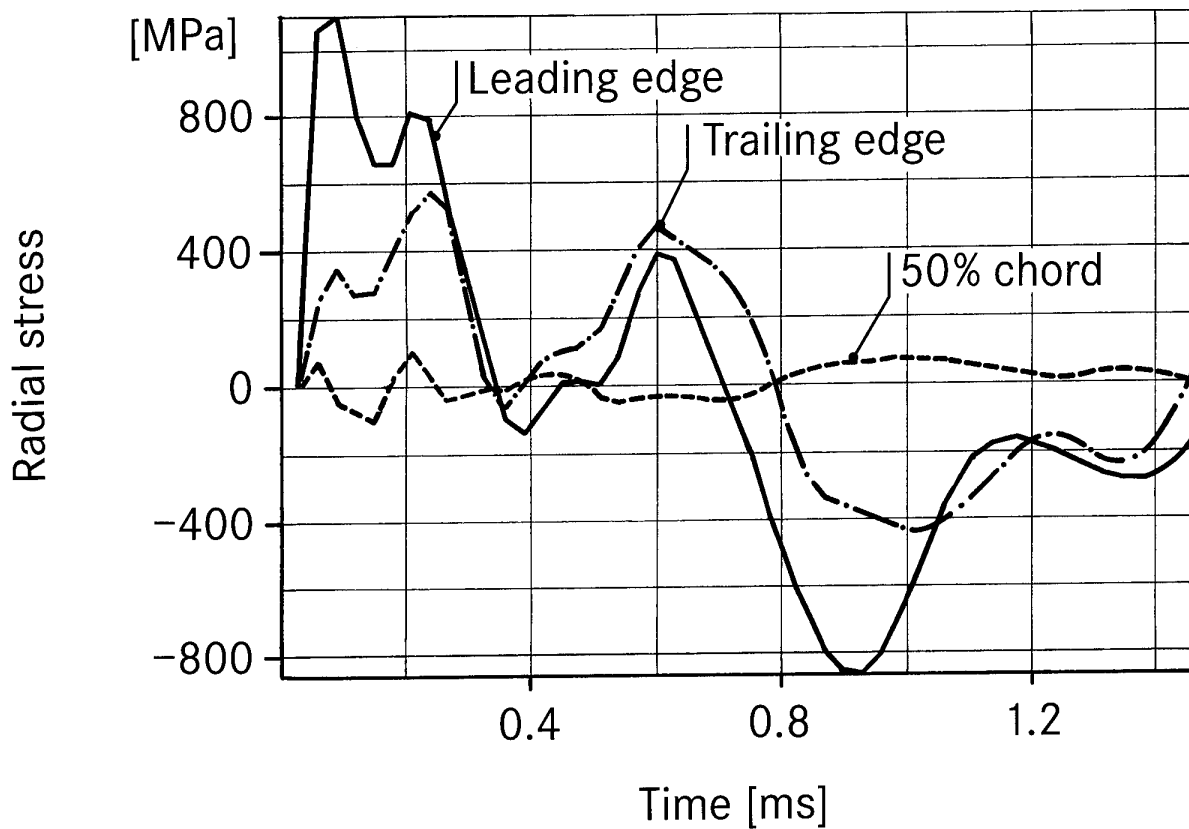


Figure 8. Time history of radial stresses on the pressure side of the hidden cross section (flank impact).

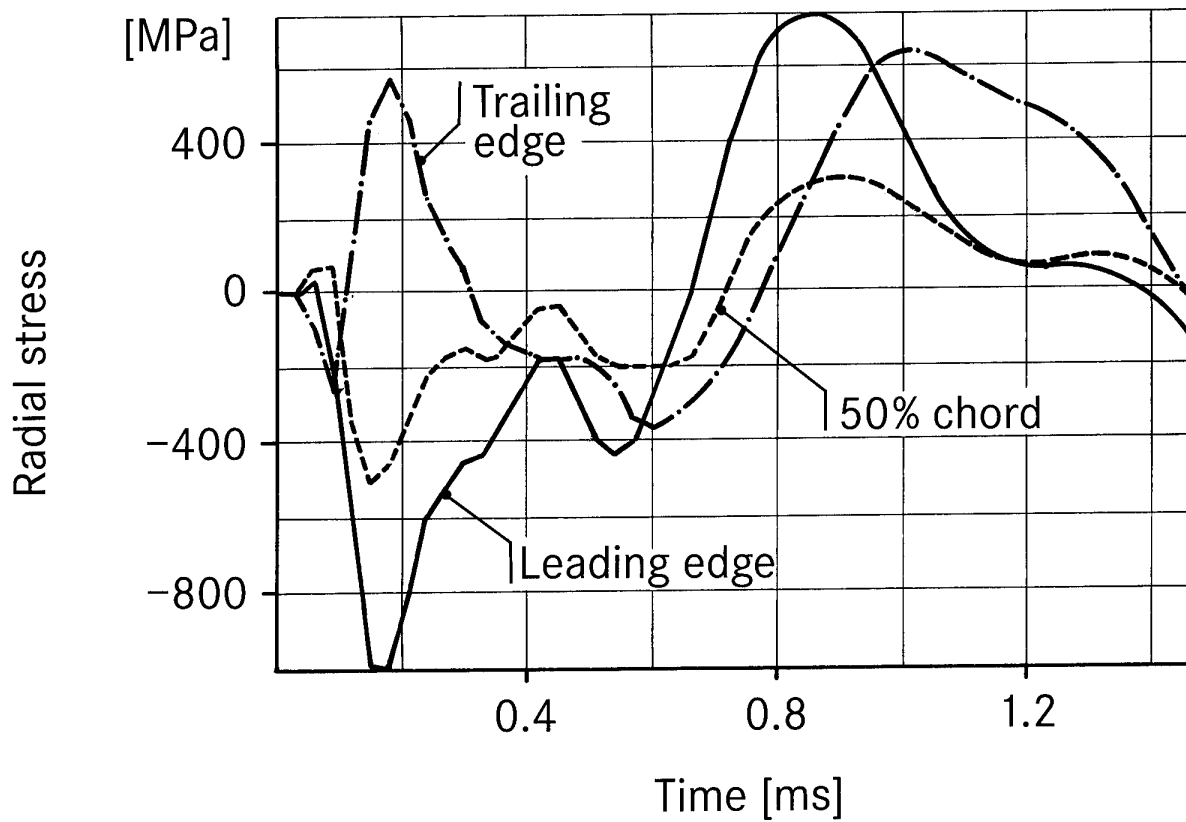


Figure 9. Time history of radial stresses on the pressure side of the hub cross section (flank impact)

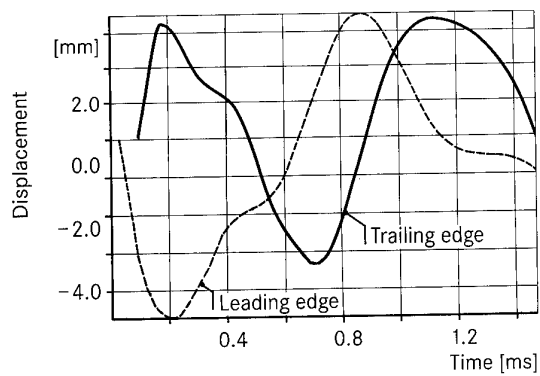


Figure 10 Time history of the tangential leading and trailing edge deflections of the hidden cross section (flank impact)

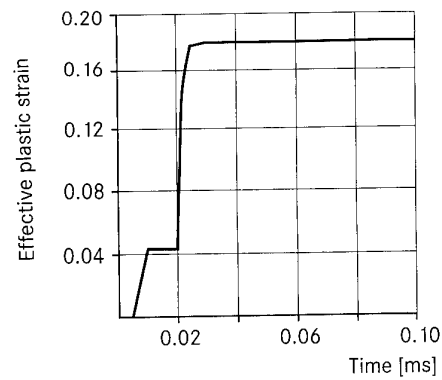


Figure 11 Time history of the effective plastic strain at the leading edge position (impact centre, leading edge impact)

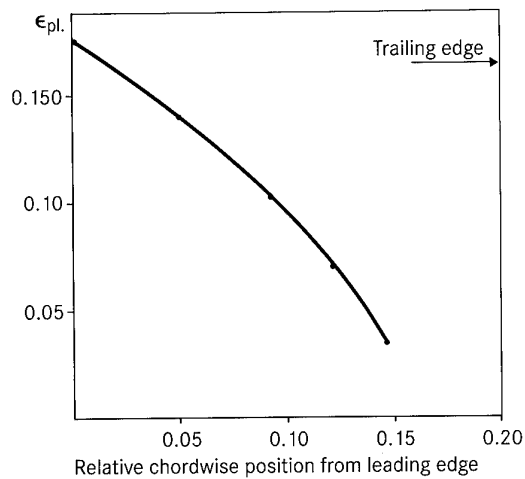


Figure 12 Chordwise distribution of effective plastic strain near the centre of impact ( $t = 36 \mu s$ , leading edge impact)

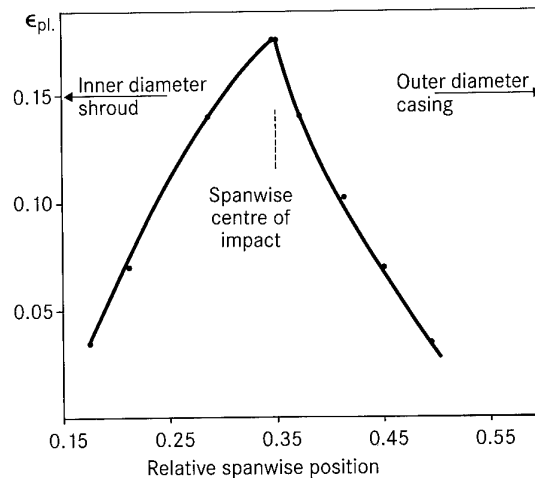


Figure 13 Spanwise distribution of effective plastic strain

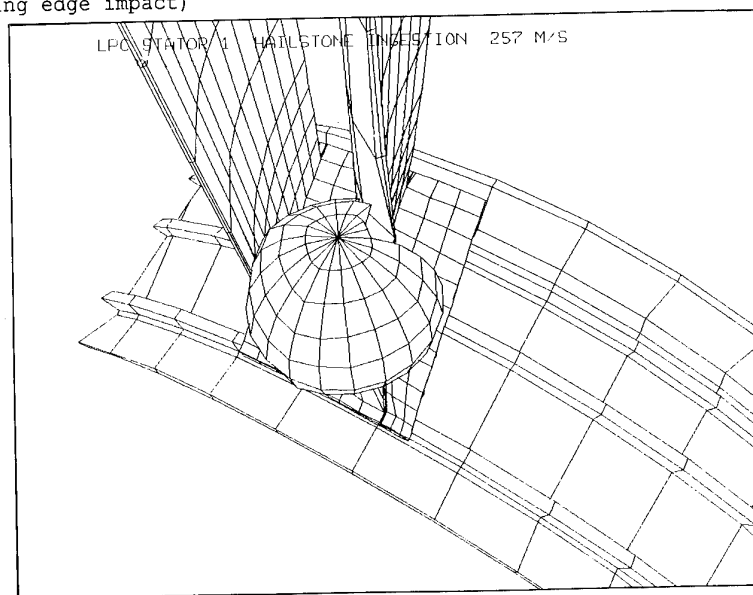


Figure 14 Deformed shape at  $t = 36 \mu s$  (leading edge impact)

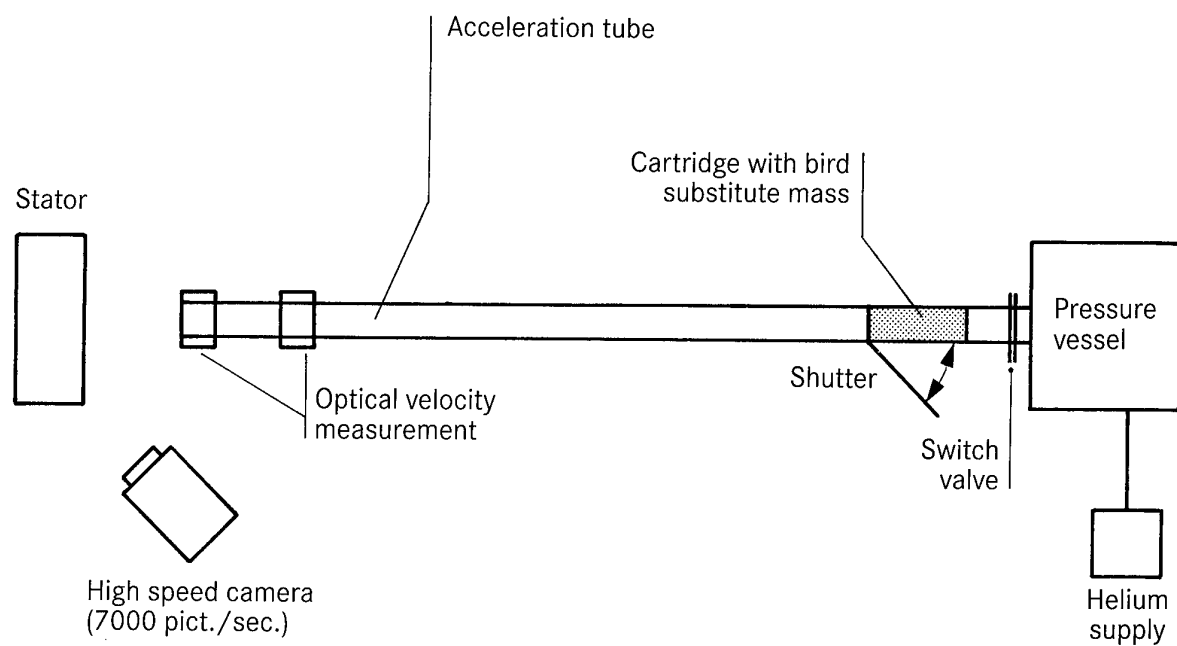


Figure 15 Test arrangement for ice ingestion

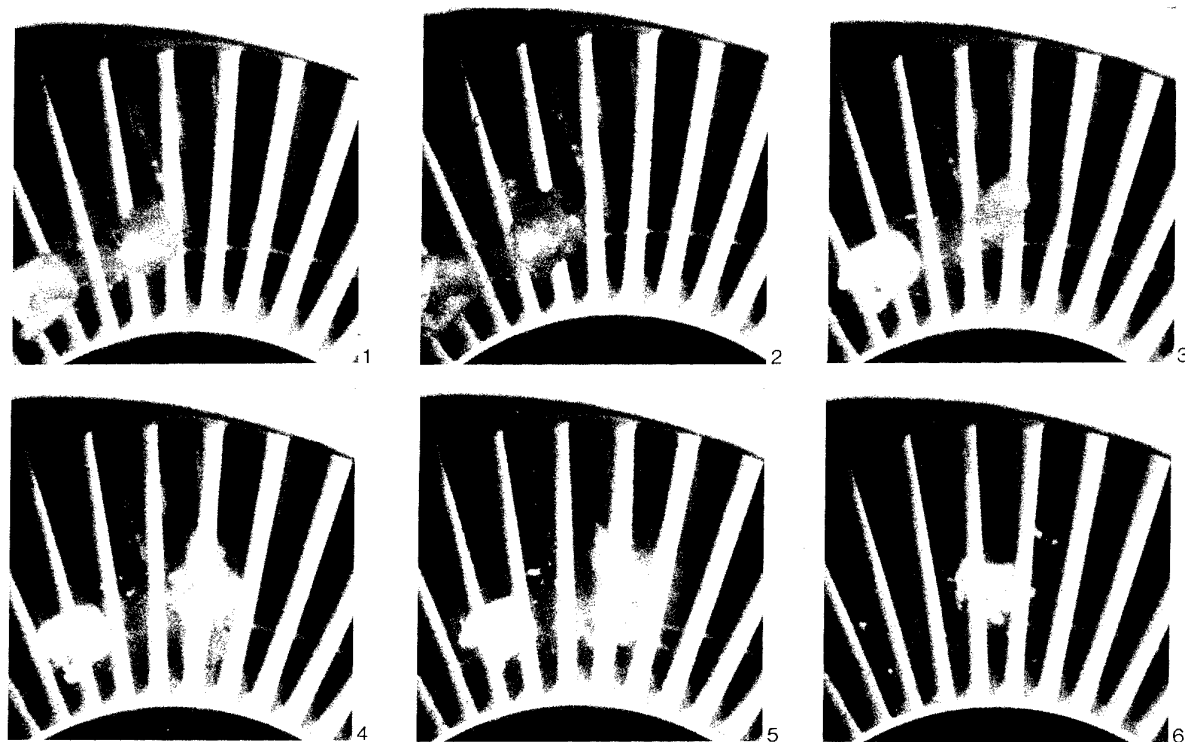


Figure 16 Sequence of high speed camera recording (flank impact, 257 m/s)

## Soft Body Impact on Titanium Fan Blades

D.A. Hughes \*

I. Martindale +

C. Ruiz \*

\* University of Oxford

Dept. Eng. Science

Parks Road

Oxford OX1 3PJ

England

+ Rolls-Royce plc

PO Box 31

Derby DF24 8BJ

England

### 1. ABSTRACT

The strength of titanium fan blades under soft body impact has been studied by means of panel tests. The panels, representing blades with various leading edge profiles, were exposed to oblique impact in a gas gun facility by launching a block of gelatine at speeds of up to 600 m/s. High speed photography, at 100,000 f.p.s. and strain gauges provide a record of the deformation. Failure occurred either as a result of extensive deformation or localised tearing. Tearing was taken as determining the limiting strength of the blade, which was found to be strongly dependent on the leading edge profile.

### 2. INTRODUCTION

One of the most crucial aspects of jet engine design is the profile of the front fan blade and consequently any changes in the actual aerofoil profile have an effect on both the fuel economy and the impact resistance of the engine. There exists however, a conflict of objectives in the specification of this fan blade in that high fuel economy requires a very thin leading edge whilst high impact resistance requires a thicker leading edge.

Historically, comparisons in impact resistance for fan blades have been conducted using large rotating test facilities whereby soft body projectiles are fired or dropped into either a full rotating fan blade set or a single rotating arm configuration. This type of facility is useful as a pre-cursor to full certificate testing but is prohibitively expensive if a large number of comparison tests are required for design studies. The objective of this paper is to outline a technique which will enable a comparison to be made into the effect the leading edge geometry has on the failure mode of the blade. This is achieved by the combination of soft body impacts on static wedge shaped titanium panels (machined to represent a leading edge profile) and finite element modelling of the impact situation.

Two modes of failure have been studied - Mode A purely plastic deformation and Mode B plastic deformation with localised tearing originating from the leading edge.

### 3. EXPERIMENTAL PROGRAMME

In the experimental programme use was made of the gas gun facility at the Oxford University Technology Centre. This has the capability of enabling fully instrumented impacts of soft body projectiles up to 600 m/s with both high speed photographs and strain gauge histories.

The facility consists of a reservoir, breach block, sabot, barrel and containment vessel housing the specimen to be impacted.

A schematic diagram is shown in figure 1.

The soft body projectiles used in all the impact tests were a mixture of water and bovine hide gelatine. Wilbeck and Rand [1] demonstrated that gelatin is a good substitute bird material and is generally used by most aero-engine manufacturers. For all tests both the gelatine and water were accurately measured by weight, thoroughly mixed, poured into moulds and allowed to set. This particular mix of gelatine produced a close approximation to the density of real birds as outlined by Wilbeck [2]. However, the use of phenolic micro-balloons to provide a more "bird like" compliance to the projectiles was not undertaken in the tests. This was deemed unnecessary due to each projectile having initially identical dimensions, mass and density. The objective being to produce a highly deformable projectile which although not exact replicas of actual birds provided a means of comparing the impact response of a panel to a standard projectile.

The projectiles were cylindrical in shape and were encased in polystyrene before being packed in to a cylindrical nylon sabot. The sabot was designed to form part of the firing mechanism of the gun as shown in figure 1. Once the sabot was placed into the breach four pressurised clamps were located around the circumference of a groove towards the end of the sabot and an "o" ring formed a gas tight seal between the sabot and breach. This complicates the design of the sabot in that it must be strong enough to withstand the firing pressures but weak enough to be removed before impact with a specimen. The sabot was stripped away or fragmented before it hits the specimen with the use of an arrester. Considerable amount of development work was conducted on the sabot to achieve the correct fragmentation to prevent a plug of nylon from the base of the sabot causing a double impact on the specimen. This was checked by the use of witness plates and no structural damage was recorded when an empty sabot was fired.

The procedure for firing the gun was as follows, the projectile was placed into the sabot and then loaded into the breach. Both the clamps and the reservoir were pressurised with nitrogen gas. Once the firing pressure was achieved the pressure on the clamps was vented and the full reservoir pressure propelled the projectile down the barrel.

All tests were conducted under vacuum to reduce the shock front ahead of the projectile.

At the end of the barrel was positioned a velocity measurement device consisting of two infra-red detectors connected to a digital counter timer. As the sabot emerged from the barrel, it

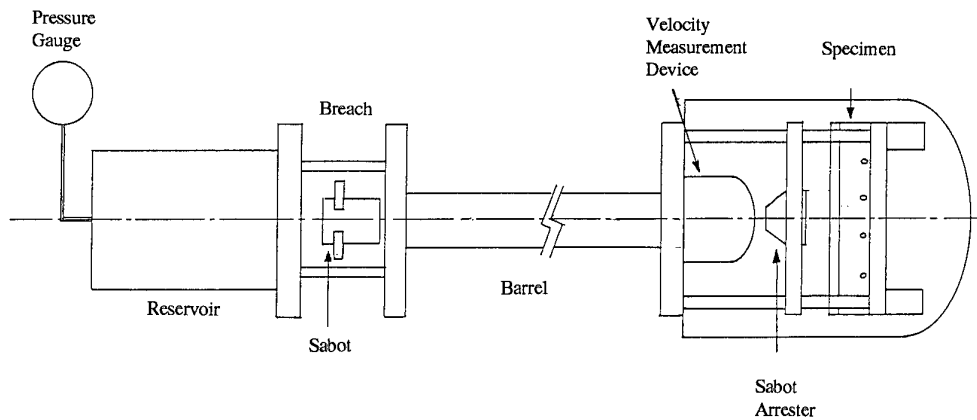


Figure 1. Schematic view of large gun

broke the infra-red beam enabling the velocity to be calculated. The camera used in all the experiments was a Cordin rotating drum framing camera. Normal 70mm wide photographic film is placed around a drum inside the camera and a series of both static and rotating mirrors reflect images onto the rotating drum. The camera was set to record 100,000 f.p.s. in all the tests. Images were recorded by illuminating the impact using a flash gun triggered by the velocity measurement device. The flash gun gives a very intense beam of light using a shaped pulse with an almost instantaneous rise time. The exposed film is then processed in a normal way. Typical results are shown in figure 2.

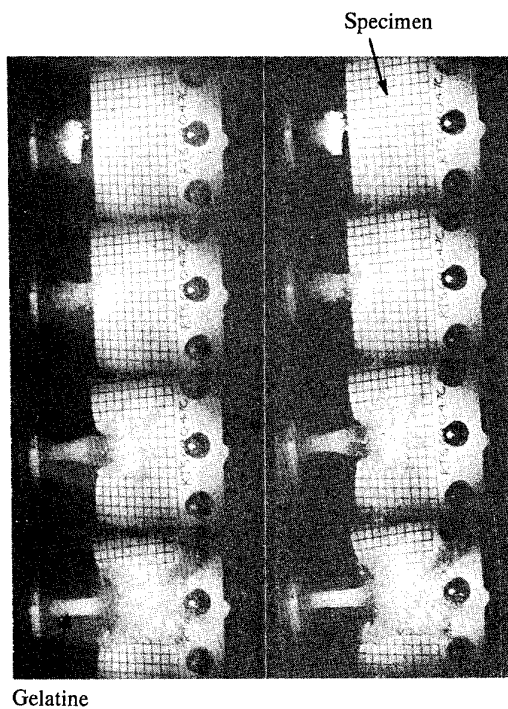


Figure 2. High speed photographs of impact event

### 3.1 Leading Edge Specimens

The specimens were manufactured from standard rectangular titanium alloy Ti-6Al-4V plate. To the flat plate was added a initial chamfer angle from the leading edge. This represented the basic blank specimen to which a ground leading edge profile was added. The specimens tested were of six different geometries classed in terms of both leading edge thickness and chamfer length. The leading edge thickness is defined as a radius added to the leading edge and the chamfer length, a supplementary chamfer measured from the leading edge as shown in figure 3.

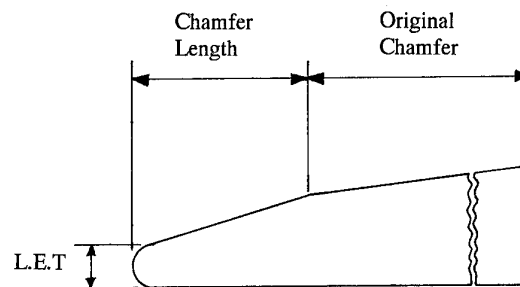


Figure 3. Leading edge geometry

The specimens could be classified into three distinct types, specimen type 47 was termed the datum profile because it was the standard profile with a leading edge thickness (radius) but without any leading edge chamfer. Specimens type 25 and type 27 were both double chamfer (machined on both sides of the leading edge) with type 27 having the thinner leading edge thickness. Type 48, 49 and 50 were each single chamfer with type 48 and 49 being of the same leading edge thickness but type 49 had a longer chamfer length. Specimen type 50 had the same size of leading edge thickness to type 27 but was a single chamfer. Table 1 summarises the various dimensional differences between the types of profiles.

The method of restraining the specimens during each test was by bolting the specimen along three edges to a solid clamping block with the leading edge remaining free. The size of specimen was chosen to cause failure at the centre of the leading edge before the stress waves had time to travel to the clamps and be reflected. Providing the clamps are a sufficient distance from the clamps, Bertke and Barber [3] showed that actual method of clamping has relatively little effect on the impact results.



Profile Number	Leading Edge Thickness	Chamfer		Lower Velocity	Upper Velocity	Critical Velocity
		Type	Length			
47	100 %	Single	0	113	145	123
48	29 %	Single	1.2 %	2	74	48
49	29 %	Single	3.3 %	0	39	23
50	50 %	Single	2.5 %	68	87	78
25	72 %	Double	3.3 %	41	93	88
27	50 %	Double	3.3 %	46	77	63

Table 1. Experimental details of leading edge specimens.

The clamping block itself was also inclined at an angle to the centre line of the gun. This produced a slicing effect on the gelatine projectile as it flowed over the leading edge and also as the specimen deformed it would take a larger slice out of the projectile.

### 3.2 Results of Soft Body Impacts

The results generally fall into three distinct categories. At low impact velocities all the various profiles deform plastically resulting in the classical "bird impact cupping" at the leading edge. This gives a very close resemblance to the type of damage observed in a real "birdstrike". As the impact velocity increases the localized necking or stretching of the material at the leading edge around the point of impact becomes more pronounced. This phenomenon is also observed in actual bird impacts to "in service" fan blades.

Finally, as the velocity increases further, the single chamfer type 49 fails with a tear initiated at the centre of the leading edge. The same type of failure occurs in all the various profiles at increasing velocity and a summary of results normalised to the type 49 velocity are shown in table 1.

In table 1 the terms "Lower level" refers to the highest impact velocity for each profile measured during the experimental tests that resulted in Mode A failure (plastic deformation). The term "Upper Level" refers to the lowest measured impact velocity to cause Mode B failure (tearing). Thus, the upper and lower levels define a "bracket" to the velocity of Mode A to Mode B failure in terms of the impact velocity and consequently there must exist a critical impact velocity to initiate Mode B failure. In conducting a post-impact analysis on the failed specimens and using the knowledge of necking at lower velocities it is observed that the maximum tensile strain on the reverse of the plate initiates failure and not the bending effects perpendicular to the line of the leading edge. The shear or tearing is then propagated by the loading, perpendicular to the leading edge. Also, another important aspect is that the velocity increases and so does the maximum specimen displacement. Once the velocity increases sufficiently to cause failure, the resulting maximum displacement is reduced.

Ultimately, it should be possible to reduce the size of the failure bracket in order to obtain the critical impact velocity by further impact tests. This could prove to be an expensive and time consuming exercise. Therefore, it is prudent to develop a finite element technique to analyze the impact situation.

## 4.0 MATERIAL TESTING AT HIGH RATES OF STRAIN

In order to conduct numerical analysis in support of the experimental programme it has been necessary to obtain material data as input to the finite element programme. Workers such as Mayer [5] and Mayer and Chiem [6] established that a

typical titanium alloy Ti-6Al-4V exhibits an increase in yield stress with an increase in strain rate. In terms of this investigation the soft body impact energies are such that the material impacted undergoes large scale plastic deformation in a few microseconds.

Therefore, tensile impact tests have to be performed on the titanium alloy Ti-6Al-4V cut from the panel specimens and tested at various rates of strain from quasi-static to impact rates. The test specimen used is shown in figure 4. This particular design was developed for use with the Split-Hopkinson Bar impact apparatus and although similar, does not conform exactly to the British Standards for tensile testing. Therefore, it is not possible to compare directly the values of fracture elongation of the specimen with the B.S. specimens but in general the effects of strain rate will be similar.

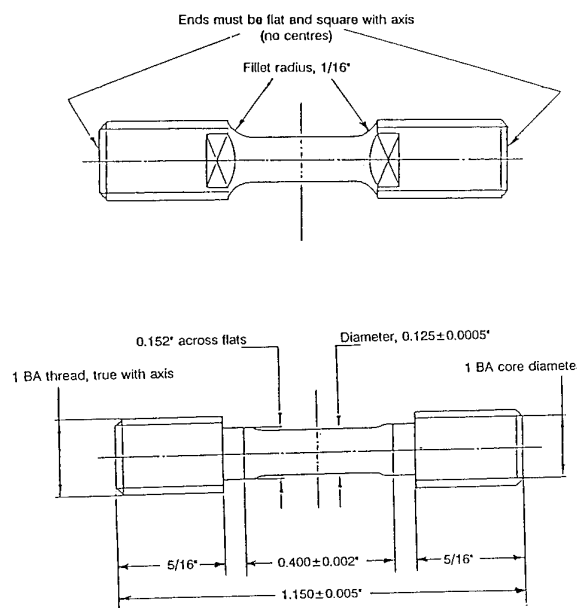


Figure 4. Standard design of tensile specimens

Stress-strain curves have been obtained for a minimum of four tests at different strain rates and are shown in figure 5. Each curve represents the mean of a number of specimens at the same strain rate. From the curves in the quasi-static tests once the material has begun to yield it then begins to work harden up to an ultimate tensile stress occurring between 7 and 8 % strain.

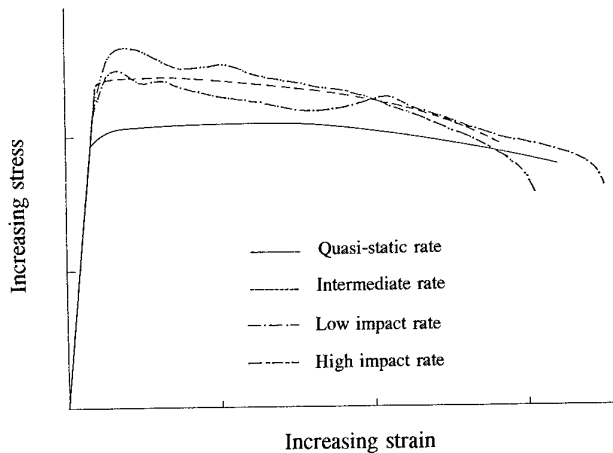


Figure 5. Stress-strain curves of Ti-6Al-4V at increasing strain rates

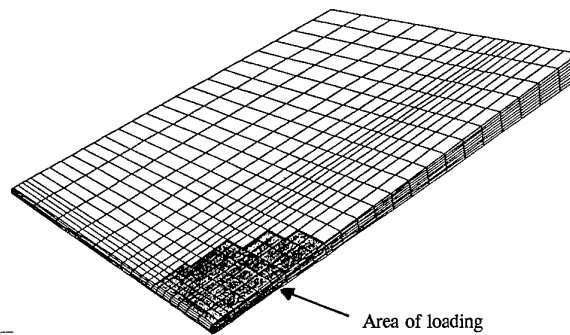


Figure 6. Specimen mesh

This is effectively an elastically perfectly plastic material response. Increasing the strain rate to an intermediate level raises the yield stress. The amount of work hardening has now been eliminated such that the upper yield stress corresponds to the ultimate tensile stress. Also, the material exhibits a more pronounced work softening until failure occurs at a low value of 12.6 % strain. Considering the impact tests, the increased upper yield point is now even more pronounced.

In using this material data great care must be taken in choosing the correct constitutive equation to fit the data. From the tests using cylindrical tensile specimens cut from the plate material the response of the titanium alloy varied with increasing strain rate. However, the response at a strain of up to 6-7 % could be described, very approximately as elastic-perfectly plastic but with a rate dependent flow stress.

Consequently, using this material data enables a strain rate dependent elastic-perfectly plastic model to be used requiring the specification of yield stress with strain rate. A caveat must be placed on the use of this model as it will only accurately predict the material behaviour up to strains of approximately 6 %, which equates to the initial portion of the impact. Fortunately it is the initial few microseconds which is of most interest in the mathematical modelling

## 5.0 MATHEMATICAL MODELLING

To model the exact impact situation requires the use of an explicit finite element code to simulate the large plastic deformation in the plate and the flow of the gelatine during the impact. A number of workers such as Niering [7], Lawson [8] and Terrier [9] have attempted to model the interaction between the flow of the bird and the deformation of the plate. In doing so penalties have occurred in terms of increased effort in modelling and a considerable increase in solution time. The objective of the analysis was to develop a simplified method to assess the impact resistance of a panel in terms of the calculation of the critical impact velocity to cause Mode B failure.

The analysis code used was DYNA3D and a typical mesh is shown in figure 6. Due to the symmetry of the impact only half of each leading edge specimen was modelled. The boundary conditions consisted of symmetry applied to one side, "encastre" conditions applied to the other two sides, with the leading edge remaining free.

The actual size of the model was chosen to provide a reasonable approximation to the actual response of the actual panel tests. Although the model was smaller than the actual plates tested it was assumed that the loading would be applied

over a short period of time (microseconds) and therefore, the stress waves would have insufficient time to reach the boundaries and be reflected.

From the post impact analysis of the experimental tests it was noted that panels that had failed by tearing (Mode B) had significantly less overall deformation than profiles which had undergone plastic deformation (Mode A), indicating that failure occurs early in the load cycle.

Therefore, in order to conduct a simplified analysis it appears reasonable to limit the analysis to the initial part of the analysis. Assuming this to be true the loading can be simulated by a shock pressure applied to the plate. Also reducing the solution time removes the need to model the flow of the gelatine. The shock pressure was applied to the model over an area of a quarter ellipse to take account of the oblique nature of the impact. The magnitude of the applied pressure was calculated based on the shock pressure formula developed by Barber [10] for gelatine impacts on flat plates. Due to the dynamic nature of this load it was necessary to adopt a dynamic loading in terms of a step function. The shock pressure was applied for a given length of time - typically microseconds - until the maximum velocity of the plate reach the same maximum velocity as the velocity component of the input pressure. The loading was then rapidly reduced to zero and the analysis continued at zero pressure.

The material model used in all calculations was material type 19 - strain rate dependent isotropic elastic plastic. This material type allows behaviour which is elastoplastic with strain rate dependent isotropic hardening/softening. However, from the material tests conducted using cylindrical test specimens, the response of the titanium at strains up to 6-7 % could be described as approximately elastic-perfectly plastic but with a rate dependent flow stress.

The input parameter for the pressure loading were derived from the experimental soft body impact tests. For each profile two different load cases were studied. The first based on the lower velocity ie. the point at which Mode A failure occurred and the second loadcase based on the upper velocity ie Mode B of the failure bracket.

In processing the results one important parameter calculated was the strain along the leading edge. As mentioned earlier it was this parameter observed in the experimental programme on the reverse of the blade to the impact which caused an elongation of the leading edge until shear failure occurred.

Therefore, plotting this value of maximum strain against time for all profiles leads to an observation as shown in figure 7.

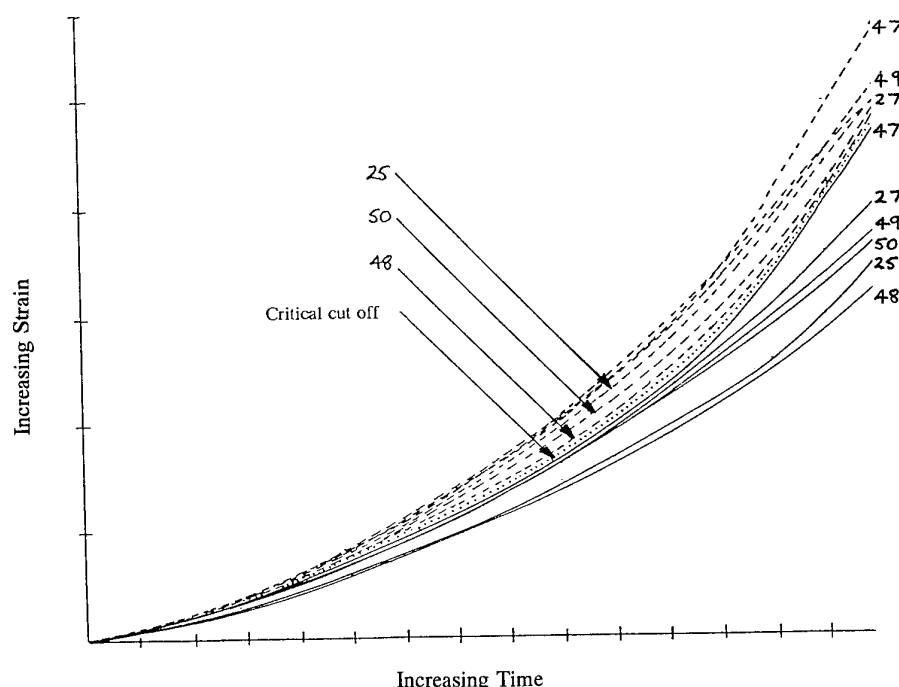


Figure 7. Graphical representation of profile responses

The responses for each profile at the lower velocity were defined within a particular region and conversely the responses at the upper velocity were all within a higher region. Therefore, the two regions defined the bounds to a critical response which defines the transition between Mode A and Mode B failures. Hence by adjusting the impact pressure for each profile until its response fell within the critical region enabled the critical impact velocity to be defined.

## 6.0 CONCLUSIONS

A simplified numerical analysis that has been described which offers advantages over a complete projectile/blade interactive analysis in terms of computing time, effort and general resources. It provides a solutions in good agreement with the experimental observations and can be used as a design tool, either with or without any experimental backing or, better still, as a means to derive from one or more tests enough information on which to estimate the impact strength of a given profile. It has been shown that from the material used in the current set of experiments, a critical cut off exists in a strain-time graph. Following the analytical procedure described it is easy to calculate the strain-time curve for any profile under a given impact condition and hence identify the corresponding shock pressure to cause tearing.

## 7.0 REFERENCES

- [1] Wilbeck. J.S. and Rand. J.L. "The development of a substitute bird model". Journal of Engineering Power. (103). p725-730. (1981).
- [2] Wilbeck. J.S. "Bird impact loading". Proc. Shock and Vibration Bulletin. (48). (1978).
- [3] Bertke. R.S. and Barber. J.S. "Impact damage on titanium leading edges from soft body impacts". AFML-TR-79-4019. (1979).
- [4] Bertke. R.S. "Local leading edge damage from hard particle and soft body impacts". AFWAL-TR-82-2034. (1982).
- [5] Mayer. L.W. "Strength and ductility of a titanium alloy Ti-6Al-4V in tensile and compressive loading under low, medium and high rates of strain". Proc. 5<sup>th</sup> Int. Conference on Titanium, Munich (1984).
- [6] Mayer. L.W. and Chiem. C.Y. "Conditions of adiabatic shear in dynamic torsional and compressive loading". Proc. 5<sup>th</sup> Int. Conference on Titanium, Munich (1984).
- [7] Niering. E. "Simulation of birdstrikes on turbine engines" Dyna3d User Group Conference. London (1988).
- [8] Lawson. M. and Tuley. R. "supercomputer simulation of a birdstrike on a turbofan aero-engine" Finite Element News (1987)
- [9] Terrier. J.M. "Bird and hailstone strikes on Rafale's raydome". Int. LS-DYNA3D Conference. Birmingham (1993)
- [10] Barber. J.P. Taylor. H.R. and Wilbeck. J.S. "Bird impact forces and pressures on rigid and compliant targets". AFFDL-TR-77-66. (1978)

## 8.0 ACKNOWLEDGEMENTS

The authors wish to acknowledge the technical and financial support of Rolls-Royce plc and the MOD/DRA.

British Crown copyright 1994

Published with the permission of the controller HMSO

## ICE-IMPACT ANALYSIS OF BLADES

C. C. Chamis and P. L. N. Murthy  
NASA Lewis Research Center  
Cleveland, Ohio 44135, U.S.A.

and

S. N. Singhal and E. S. Reddy  
NYMA, Inc.  
2001 Aerospace Parkway  
Brook Park, OH 44142, U.S.A.

### ABSTRACT

A computational capability is described for evaluating the ice-impact on engine blades made from composites. The ice block is modeled as an equivalent spherical object and has the velocity opposite to that of the aircraft with direction parallel to the engine axis. A finer finite element mesh is used for a portion of the blade near the impact region compared to the course mesh for the rest of the blade. The effects of ice size and velocity on the average leading edge strain are evaluated for a simulated unswept composite propfan blade. Parametric studies are performed to assess the blade structural responses due to the ice-impact at various locations along the span. It is found that: (1) for a given engine speed, a critical ice speed exists that corresponds to the maximum strain and (2) the tip bending type frequencies increase after impact while the torsion frequencies decrease.

### INTRODUCTION

At high altitudes, when aircraft flies through clouds of super-cooled water droplets, ice formation occurs on forward facing structural components. One such component is the engine inlet. With time, the ice accretes on the inlet and eventually sheds due to structural vibrations. A schematic of this phenomenon is shown in Figure 1. As a result, blocks of ice travelling at the speed of aircraft impact the engine blades rotating at high speeds. This process may cause severe damage to the blade and subsequently to the engine. In order for the blade to sustain the ice impact, it is necessary to properly account for ice-impact during the design.

Fibrous composites are ideal for structural applications such as high performance aircraft engine blades where high strength-to-weight and stiffness-to-weight ratios are required. These factors along with the flexibility to select the composite layup and to favorably orient fiber directions help limit the impact damage and stresses arising from large rotational speeds.

The objective of this paper is to simulate ice-impact on engine blades. A simulated unswept composite propfan blade is used to demonstrate the computational capability. The ice-impact analysis is carried out by modifying the foreign object damage option provided in Reference [1]. It is assumed that the damage is severe near the impact site (local region) and hence only a portion of the blade around the impact region needs to be modeled using a finer finite element mesh. Furthermore, large scale deflections accompany the impact event in the impact region [Ref.2]. In order to simulate the behavior near the impact region and along the leading edge, the analysis of the blade must include fully stressed states and large deflection. This is accomplished in the code by modifying the membrane stiffness in the radial direction to reflect a fully yielded condition for a metallic blade and an equivalent state for a composite blade. The details are described in Reference [2].

The effectiveness of the computerized capability is demonstrated by using it to perform parametric studies of post-impact blade structural performance. The effects of ice size and velocity on the average leading edge strain, maximum impact displacements, maximum root stress, vibration frequencies and flutter boundaries are investigated.

### FUNDAMENTALS OF ICE-IMPACT SIMULATION

A brief description of ice-impact simulation is provided in this section.

#### Geometry of Ice-Impact

The geometry of ice-impact on the leading edge of the blade is shown in Figure 2. The impact velocity direction relative to the blade is a function of aircraft speed and rotational speed of the blade (Fig. 2(a)). The resulting impact force depends on the magnitude and direction of relative velocity and also on the mass of ice size. Depending on the spacing (i.e., number of blades) and relative velocity as shown in Figure 2(b),

only a portion of the ice size hits the blade. The ice "sphere" that is approaching the blade under consideration is sheared off by the adjacent blade and only a part of it impacts the leading edge. Therefore, the size of the ice sphere that finally impacts the blade depends on the blade spacing, blade speed and aircraft speed.

#### Blade Modeling

The damage due to impact is considered to be localized and hence only a local portion of the blade around the impact region (Fig. 3) is modeled using a finite element finer mesh. In the code, the blade geometry is input in the form of finite element grid and nodal thicknesses. The spanwise impact region is specified with two parameters, namely, lower and upper bounds of radial fractions,  $a$  and  $b$ . However, the modeled impact span is approximated to be the region between the two finite element radial stations that are defined in the blade geometry and are nearest to  $a$  and  $b$ . Along the chord, only half of the blade is included in the impact region. The finite element used is similar to NASTRAN (TRIA3) three node triangular plate element [3,4]. A total of 35 nodes and 48 elements are used (Fig. 3). The impact is considered at the midpoint of the local region (finite element node 16) (Fig. 3) along the leading edge.

Large scale deflections usually accompany the impact event. This phenomenon is simulated in the elements that are close to the impact node by modifying the membrane stiffness in the radial direction as described in Reference [5]. A computer code has been developed at NASA Lewis Research Center, specifically for ice-impact simulation as described in the next section.

#### COMPUTER CODE DESCRIPTION

The computer code developed specifically for engine blade ice-impact is identified as BLASIM (Blade Assessment for Ice-Impact). BLASIM is open-ended, portable and transportable. The simulation capabilities in BLASIM are summarized in this section.

#### BLASIM Structure

Blasim consists of several functional modules as shown in Figure 4. These modules provide the simulation capability in BLASIM. Starting from the 12 o'clock position in Figure 4 and proceeding clock-wise, the BLASIM simulation capability includes: (1) analysis for blade displacement, (2) blade root stress due to impact, (3) flutter, (4) free vibrations, (5) fatigue, (6) single and multiple ice-impacts, (7) resonance margins, (8) local damage due to impact, and (9) stresses throughout the blade as well as modules for composite mechanics and for finite element model generator. It is important to note that additional modules can be readily added when augmented capability becomes necessary.

The flow chart for BLASIM is shown in Figure 5. Note that the post-impact blade geometry is updated in order to properly simulate the effects of impact on the post-impact structural performance of the blade.

#### Blade Construction and Modeling

A computationally efficient triangular coarse mesh with five chordwise stations and eleven spanwise stations is used to model the blade. The model has a total of 55 nodes and 80 NASTRAN TRIA3 type triangular finite elements (Fig. 6). For local impact analysis, a model consisting of 35 nodes and 48 elements is used (Fig. 3). The blade model is generated using the model generator module by using a NASTRAN type finite element grid or description of stacked airfoil sections, or by using a preprocessor where the user selects one of the built-in symmetric airfoils at three (root, midspan and tip) or more blade input stations. A user friendly option is also available to input finite element grid through a file instead of selecting an airfoil.

The composite mechanics in ICAN [Ref. 6] module is called to generate composite material properties which can be specified by inputting individual ply properties or specifying fiber/matrix combinations from a BLASIM-resident data bank. The data bank contains a wide spectrum of fibers and matrices and corresponding properties. When fibers and matrices are input, ICAN is used to generate temperature and moisture dependent ply properties of the blade material.

#### Analysis Types

As was already mentioned, the analysis capabilities supported by the BLASIM code include: local and root ice impact damage, local and root Foreign Object Damage (FOD), static, dynamic, resonance margin calculations, flutter, and fatigue. Only the analyses requested in the input are carried out as shown in Figure 5. Several types of loading, namely, pressure, temperature, moisture and centrifugal, can be included in these analyses. BLASIM can also be used to perform the above analyses for multiple (identical) ice-impacts with geometry update after each local ice-impact. Further details of ice-impact analyses are given in a later section.

#### Computer Systems

The BLASIM code and the interactive preprocessor have been installed and tested on VAX, CRAY and Silicon Graphics workstation at NASA LeRC. A typical single impact analysis requires approximately 10 seconds on CRAY XMP. Hence, the code provides a quick estimate of the ice-impact response and can be interfaced with an optimization module for design optimization purposes.

### Blade Types

As mentioned in a previous section, the BLASIM code can be used to analyze solid, hollow, superhybrid and composite blades. The solid blade is composed of a single material whereas hollow and superhybrid blades are constructed with prescribed composite layups. BLASIM composite blade models can have a maximum of seven different material layers. Each layer is made from a different composite and may include one or more plies depending on the overall blade thickness at that point. Hollow blades have a titanium surrounding a borsic/titanium composite, with a hollow region at the center (Fig. 7). The location and size of the hollow region can be defined by the user. Superhybrid blades have a special composite layup: [Titanium (skin)/Borsic-Aluminum Graphite-Epoxy /Titanium]<sub>s</sub> (Fig. 8) For general composite blades, users can specify ply constituent materials, corresponding layer thicknesses and fiber orientations. The layup is assumed to be symmetric and in each material layer, the plies are laid with alternating angles as shown in Figure 9. The last material in the input (usually a metal) is considered to be a core with a variable thickness. The blade is constructed from elements having variable thicknesses and material layup of each element is subject to following considerations:

- (i) If total thickness of an element can accommodate 1 to ( $n-1$ ) materials to their specified maximum limit, the remaining element thickness is assigned to the  $n^{\text{th}}$  material (core).
- (ii) If the total thickness cannot accommodate all material layers to their thickness limit, plies are deleted from material layers in the order ( $n-1$ ), ( $n-2$ ), ..., 2. That is, material 1 is always present and plies in ( $n-1$ )<sup>th</sup> material are deleted first.
- (iii) If the element thickness is less than twice the thickness of material 1 (skin), element thickness is adjusted to be equal to that value.

### ILLUSTRATIVE EXAMPLE

In this section, application of BLASIM to a specific case is described. The impact conditions for this case are shown in Figure 10. The respective material properties are listed in Table 1. The various aspects evaluated are described below.

#### Blade Root Stress

The blade root damage versus ice-impact span location is shown in Figure 11 [Ref. 7]. Note that the damage initiation is evaluated using a modified distortion energy function. Other points to note include: (1) the damage is relatively insignificant for engine speeds below 3000 revolutions per minute; (2) the damage increases linearly with span impact; and (3) the damage increases nonlinearly with engine speed.

The blade root damage in terms of energy speed and impact angle is shown in Figure 12 [Ref. 7]. Note that the ice size is also shown in the figure. The points to observe in this figure are: (1) the impact angle increases very rapidly at engine speeds up to about 2000 RPM and levels off at engine speeds greater than 4000 RPM; and (2) the damage induced at the root is negligible at engine speeds below 5000 RPM, then increases very rapidly and peaks at about 8500 RPM, and drops suddenly to about 1/3 its peak value. It may, therefore, be concluded that a critical speed exists beyond which the blade will sustain severe damage at the root. For this case, that engine critical speed is about 7000 RPM. These cases demonstrate BLASIM's usefulness to evaluate ice-impact blade root damage.

### BLADE LOCAL DAMAGE

Local damage in terms of localized strain at the leading edge and its effects on the blade untwist are shown in Figure 13 versus ice size radius [Ref. 8]. Ice size smaller than 0.2 inch radius equivalent sphere has negligible effect on the localized strain. Sizes greater than 0.2 inch induce substantial strains which increase rapidly with size. For example, a 0.4 inch radius will induce about 1% strain which is large enough to cause local indentation and failure.

Ice sizes up to 0.5 inch radius cause negligible blade untwist. However, sizes greater than that, cause rapid changes in blade untwist which bottoms out at about 0.65 inch radius and decreases rapidly as the ice size becomes larger than 0.65 inch radius. Both of the above assessments demonstrate that BLASIM can be used effectively to evaluate ice-impact local damage.

### BLADE VIBRATION FREQUENCIES

The ice-impact affects post-impact vibration frequencies of the blade. These effects are shown in Figure 14 for the first three vibration frequencies and their respective mode shapes [Ref. 9]. It can be seen that: (1) the first frequency increases slightly, the second frequency, which is primarily a tip bending mode, increases by about eight percent. This increase is mainly due to local indentation which causes a local type partial support. And (2) the third frequency, which is primarily a twisting mode, decreases by about eight percent. It is well known that decreases in torsional vibration modes decrease flutter resistance [Ref. 10]. Therefore, the impact effects on flutter resistance need to be evaluated.

Evaluation of post-impact vibration frequencies demonstrate that BLASIM can be readily used to evaluate post-impact overall (global) blade structural dynamic performance.

### BLADE FLUTTER

It was mentioned in the previous section that ice-impact effects on vibration frequencies also affect the

flutter resistance.

The blade flutter regions (stable, unstable) are plotted in Figure 15 versus Mach number and for the conditions investigated. As can be seen, the blade is stable and will not flutter if it is operating at subsonic regimes (Mach number less than 1) [Refs. 9 and 11]. The important observation is that BLASIM can be used to evaluate post-impact effects on flutter.

The discussion was limited to some specific post-impact effects, BLASIM has sufficient versatility to evaluate other effects as well [Ref. 12].

## SUMMARY

The significant results from an investigation on ice-impact simulation of blades are summarized below.

1. A computer code (BLASIM -BLade ASsessment for Ice iMPact) has been developed.
2. The code is user friendly, portable, quite versatile, and has been documented.
3. The code handles single and multiple impacts.
4. The code handles a variety of blade internal construction such as spar-shell, monolithic, monolithic with composite surfaces patches, all types of composites and including hybrids and superhybrids.
5. The code can be used to assess blade designs for different types of ice impacts, design blades for specified ice impacts, and even tailor blades to meet specified ice impact and other mechanical design requirements simultaneously.
6. The code can be used to evaluate its response during the impact event as well as post impact structural performance (vibration, flutter, displacement, twist, local and root damage).
7. Post-impact blade evaluation showed that: (1) a critical speed exists which induces maximum local strain; (2) post-impact tip type vibration frequencies increase while torsion-type decrease; and (3) the blade will not flutter for subsonic speeds.
3. MacNeal, R.H: A Simple Quadrilateral Shell Element. Computers and Structures, Vol. 8, Pergamon Press, Great Britain, 1978, pp. 175-183.
4. MSC/NASTRAN, Version 65C, User's Manual. The MacNeal-Schwendler Corporation, 1987.
5. Reddy, E.S., et. al: Analysis of Aircraft Engine Blades Subjected to Ice-Impact. NASA TM 105336, 1991.
6. Murthy, P.L.N. and Chamis, C.C: Integrated Composite Analyzer (ICAN), User's and Programmer's Manual. NASA TP 2515, 1986.
7. Reddy, E.S., Abumeri, G.H., Chamis, C.C., and Murthy, P.L.N: Root Damage Analysis of Aircraft Engine Blade Subject to Ice-Impact. NASA TM 105779, August 1992.
8. Reddy, E.S., Abumeri, G.H., Chamis, C.C., and Murthy, P.L.N: Analysis of Aircraft Engine Blade Subject to Ice-Impact. NASA TM 105336, November 1991.
9. Abumeri, G.H., Reddy, E.S., Murthy, P.L.N and Chamis, C.C: Dynamic Analysis of a Pre-and-Post Ice Impacted Blade. NASA TM 105829, August 1992.
10. Reddy, T.S.R. and Kaza, K.R.V: Analysis of an Unswept Propfan Blade With a Semiempirical Dynamic Stall Model. NASA TM 4083, 1989.
11. Reddy, E.S., Abumeri, G.H., Murthy, P.L.N. and Chamis, C.C: Structural Tailoring of Aircraft Engine Blade Subject to Ice Impact Constraints. NASA TM 106033, September 1992.
12. Reddy, E.S. and Abumeri, G.H: BLade ASsessment for Ice iMPact (BLASIM) User's Manual, Version 1, NASA Contract NAS3-25266, 1992.

## REFERENCES

1. Brown, K.H: Structural Tailoring of Engine Blades (STAEBL), User's Manual. United Technologies, Pratt & Whitney Report No. PWA5774-39, March 1985.
2. Brown, K.H: Structural Tailoring of Engine Blades (STAEBL), Theoretical Manual. NASA CR 175113, 1986.

Table 1. Properties of the Blade Constituent Materials

Material Type	$E_{11}$ (psi)	$E_{22}$ (psi)	$G_{12}$ (psi)	$\nu_{12}$	$\rho$ (lb.sec <sup>2</sup> /in <sup>4</sup> )	ply thickness (inches)
Titanium (Ti6)	$16.5 \times 10^6$	$16.5 \times 10^6$	$6.4 \times 10^6$	0.30	0.00044	----
Graphite-Epoxy	$32.0 \times 10^6$	$1.0 \times 10^6$	$0.7 \times 10^6$	0.25	0.00015	0.005

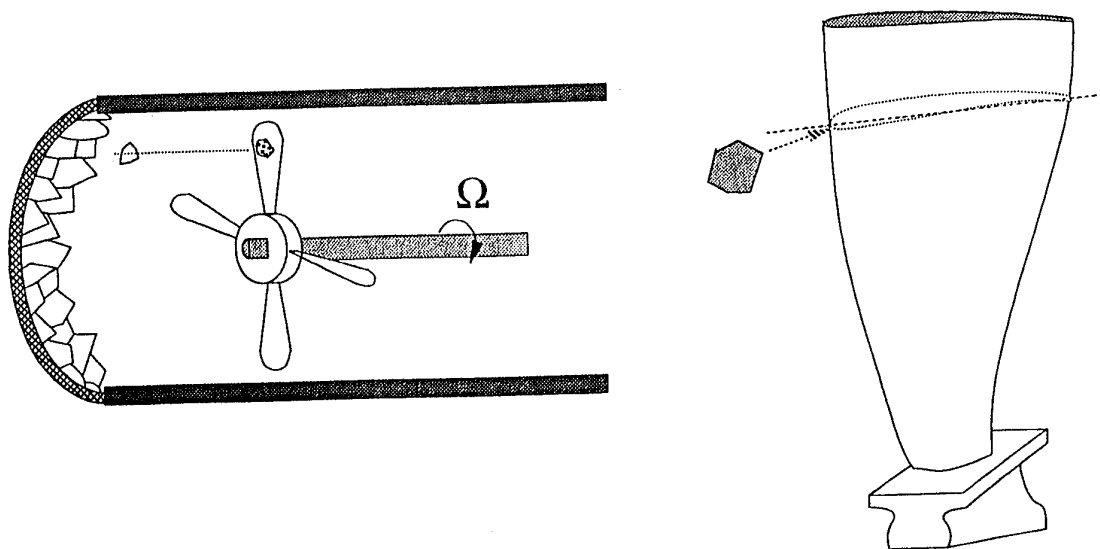


Figure 1. A Schematic of Ice-Impact on an Engine Blade

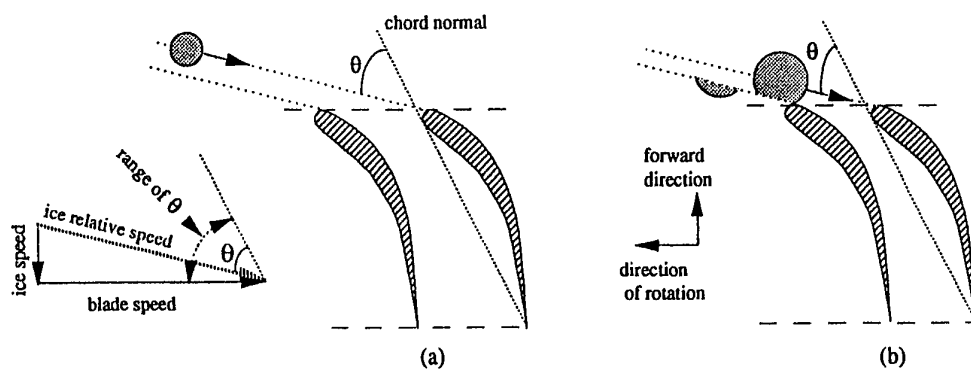


Figure 2. Geometry of Ice-Impact on an Engine Blade



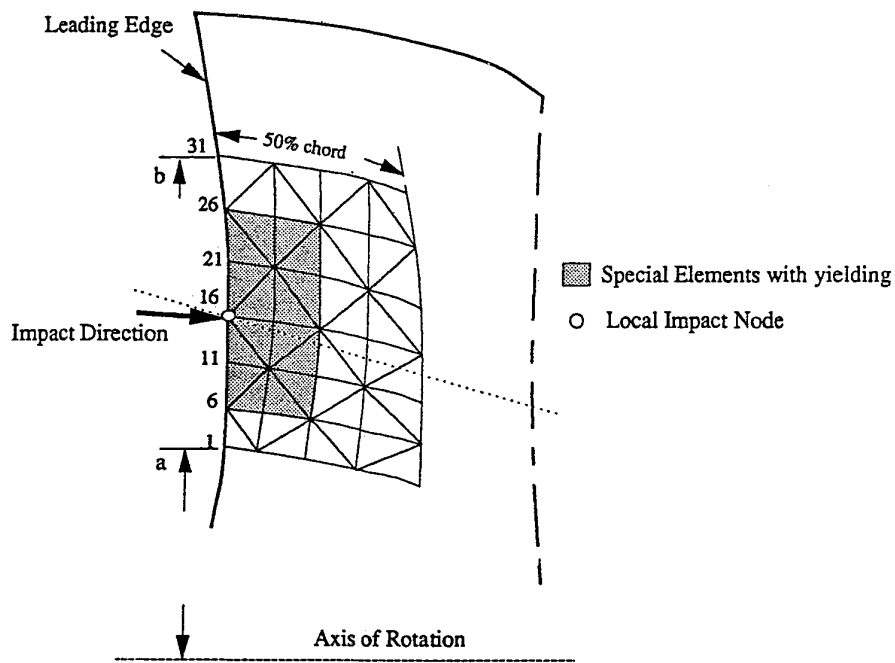


Figure 3. Finite Element Model for Local Ice-Impact Analysis

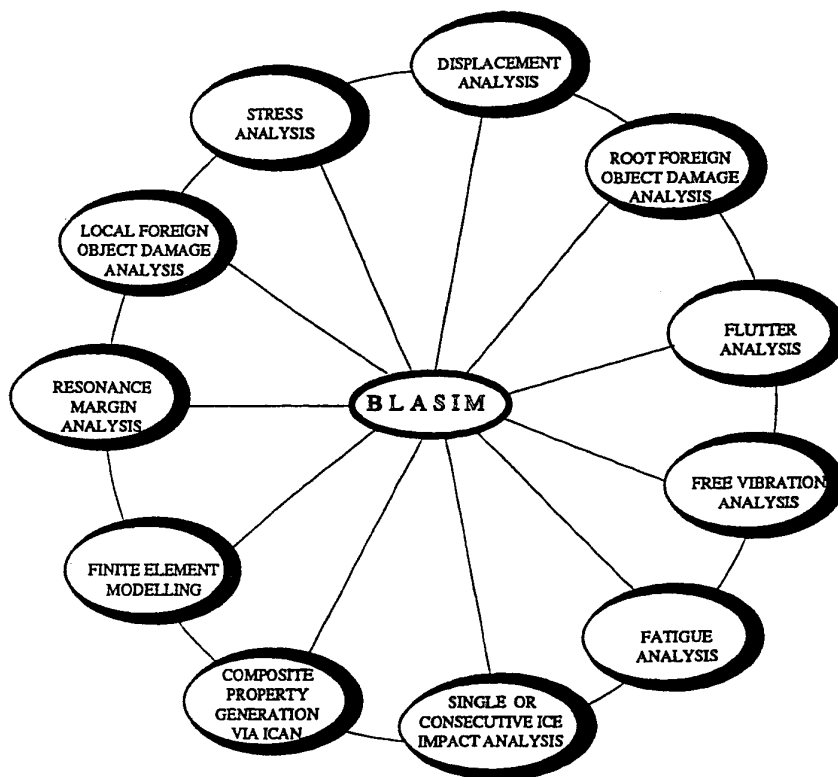


Figure 4. BLASIM Code Analysis Modules

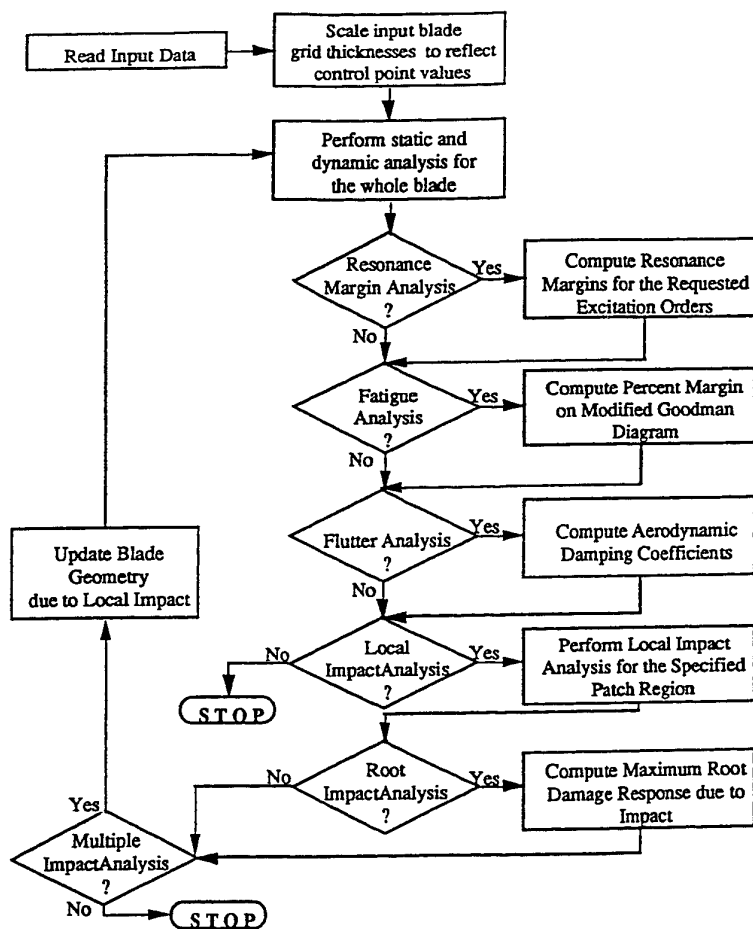


Figure 5. BLASIM Code Flowchart

#### Analysis Degrees-Of-Freedom

- Normal, Tangential and Radial Motion
- Normal Motion

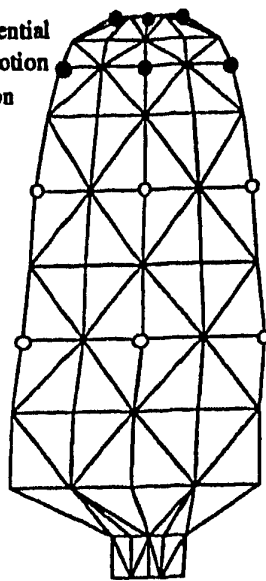


Figure 6. Blade Finite Element Model and Analysis Degrees-of-Freedom

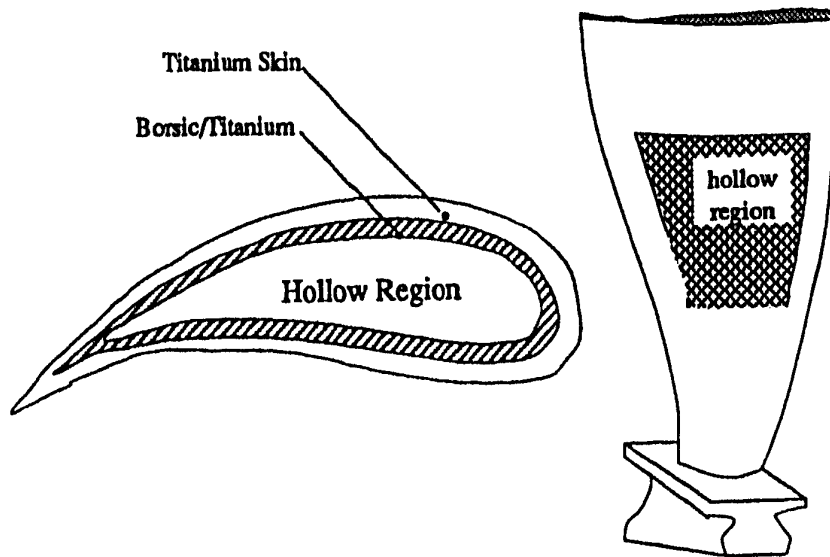


Figure 7. Hollow Blade and the Associated Layup

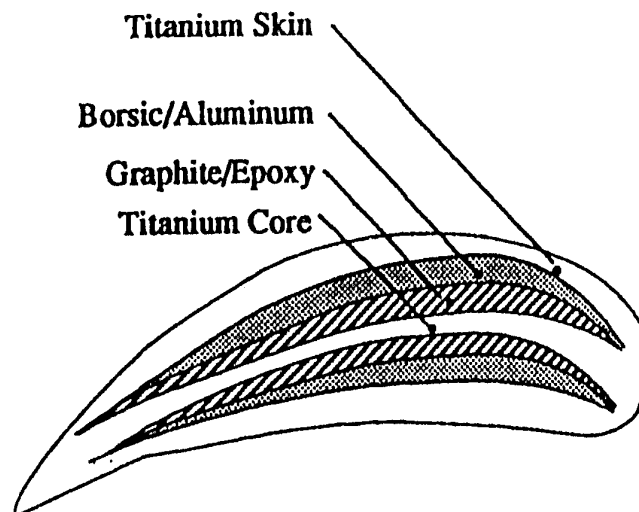


Figure 8. Cross Section of a Superhybrid Blade

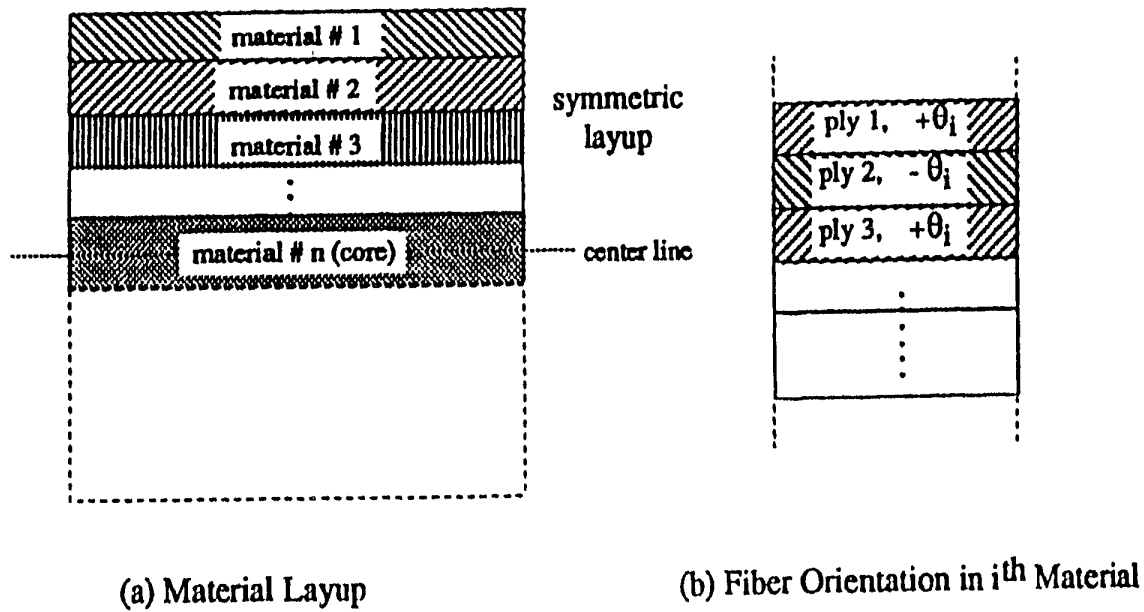


Figure 9. Composite Blade Layer Configuration

### LOCAL IMPACT RESPONSE - Example Description

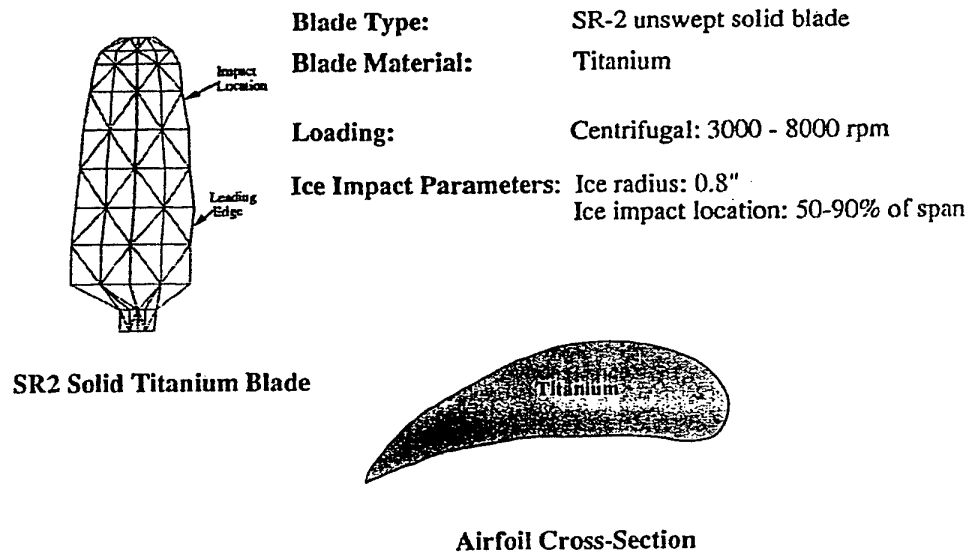


Figure 10. Impact Conditions for Illustrative Example

## EFFECT OF IMPACT LOCATION ON ROOT RESPONSE

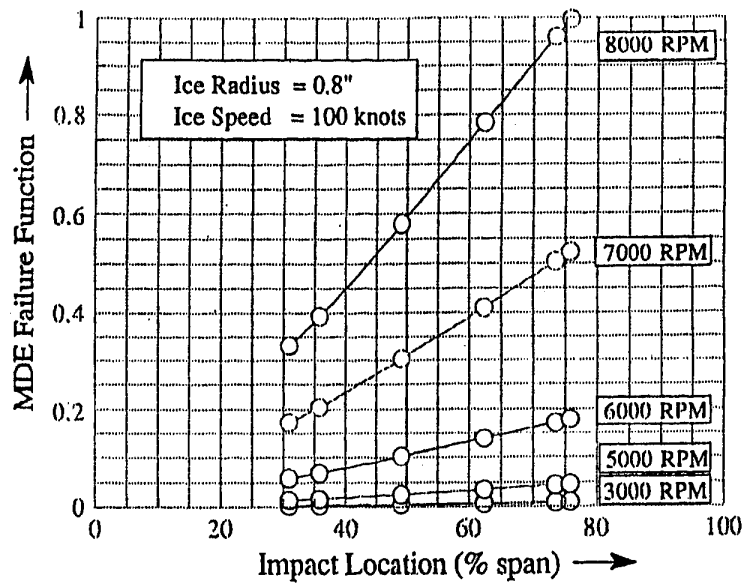


Figure 11. Blade Root Damage

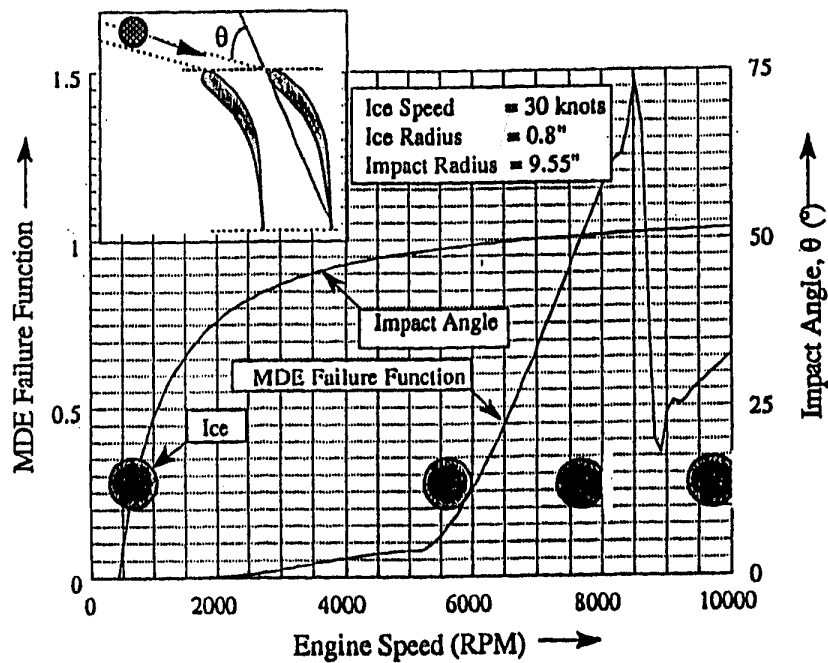


Figure 12. Effect of Engine Speed on Blade Root Damage

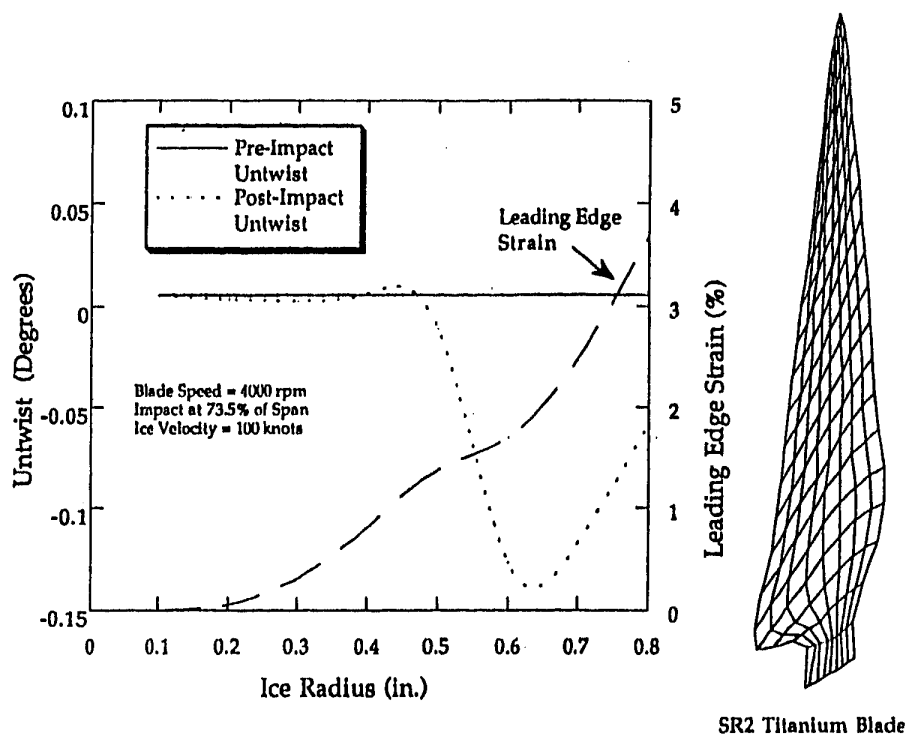


Figure 13. Ice-Impact Effects on Blade Local Damage

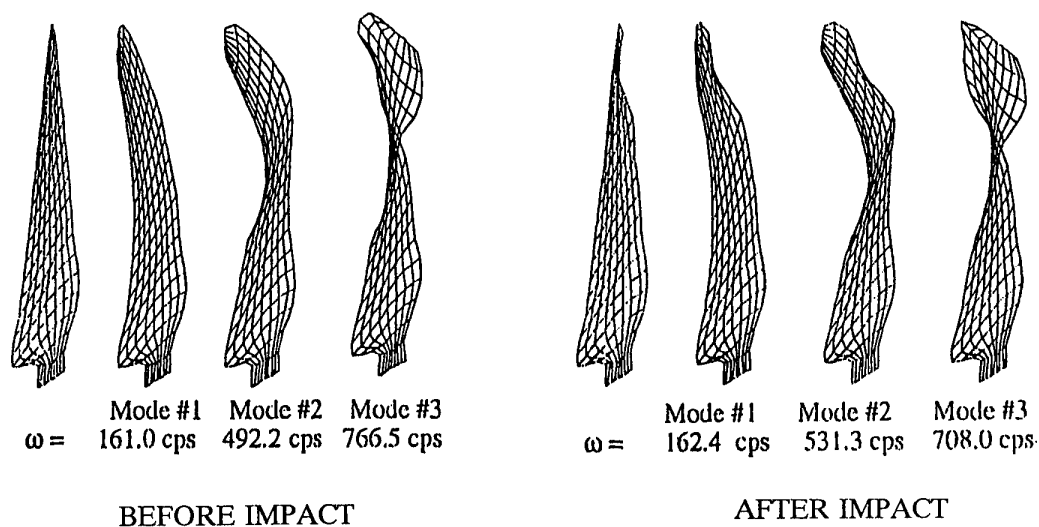


Figure 14. Ice-Impact Effects on Vibration Frequencies (Engine Speed = 4000 RPM; Ice Velocity = 120 knots; Ice radius = 0.8 in.)

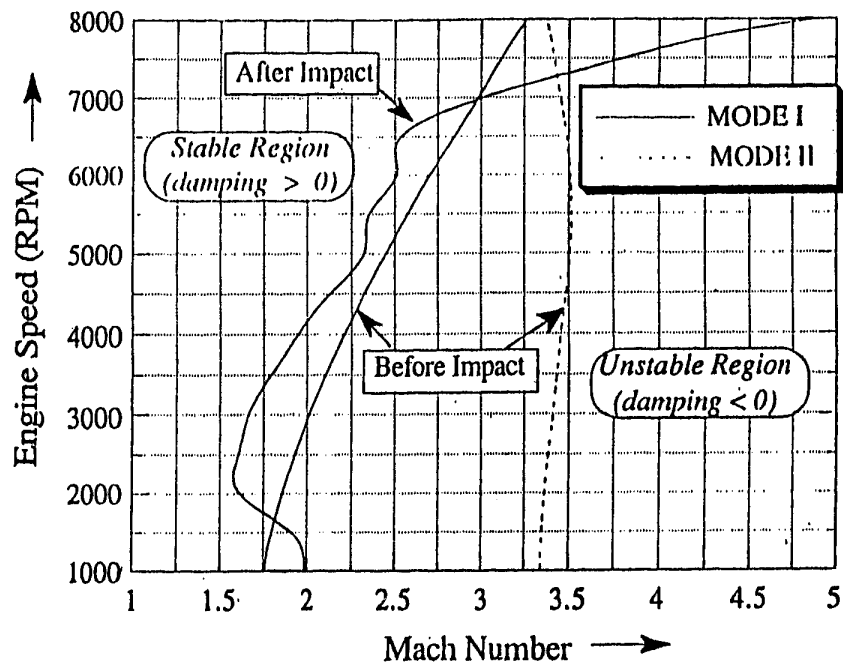


Figure 15. Ice Post-Impact Effects on Blade Flutter

## Damage of High Temperature Components by Dust-Laden Air

P. König, T. Miller, A. Roßmann

Motoren und Turbinenunion GmbH

Postfach 50 60 40

D-80976 München

Germany

### 1. Introduction

Turbine engine operators are familiar with damage to components due to dust-laden air in the compressor, but they are less aware that such damage can also occur to high temperature components, especially turbine rotor blades. Nevertheless, the frequency of occurrence of this type of damage as well as the related costs and effects on turbine performance are also of major concern.

Higher efficiency in turbine engines can be obtained by increasing operating temperatures, in particular, the gas temperature in the turbine. This brings with it a number of major materials problems which can be exacerbated by dust transported into the turbine by the gas stream or cooling air. Current turbine blade materials are close to their limits in strength. A general rule of thumb states that for such materials operating close to their temperature limits, a 15° C increase in material temperature reduces life by a factor of 2 for the same operating load. In addition, a significant increase in the damaging effects of a number of temperature dependent processes including oxidation, corrosion, erosion and erosion/corrosion is to be expected.

These problems have lead to the necessity for more intensive cooling of blades and/or for the use of thermal barrier coatings. Recent experience has shown, however, that oxidation and corrosion in combination with the effects of dust-laden air can still contribute to failure in the turbine area. These problems have often been shown to be due to local overheating related to the geometry of the blade cooling system. Such damage has often not been easily recognized or understood, because the initial effects are often a slow, unnoticed local increase in temperature. An addition complication is that the final failure often obliterates evidence of these initial effects.

The purpose of this paper is to describe the types of damage which can occur in the turbine area due to dust-laden air. Important effects and mechanisms will be described using examples of

typical forms of damage, and suggestions toward avoiding these problems will be given.

### 2. Dust-Laden Air: Origins and Types of Damage

There are two major sources of particles which can lead to damage of high temperature turbine components. Each source leads to different types of damage, especially on turbine rotor blades.

The first type relates to dust found in the main air/gas stream. Foreign particles such as dust or foreign objects can be ingested in the compressor. These are known sources of erosion damage in the compressor itself. During passage through the compressor, these particles are reduced to fine dust. The dust then passes through the combustor. Of particular significance are the hottest zones. The dust particles melt in these hot combustion zones and are carried out in the hot gas stream. They impinge and condense or solidify on blade surfaces which are cooler in comparison.

The damage due to dust in the main air/gas stream is thus corrosion related and depends strongly on the chemical composition of the dust. A significant corrosive effect is to be expected from dust particles with high sulfur and/or chloride contents (danger of hot corrosion/sulfidation) such as dust containing gypsum and/or salt containing dust. It should be noted that particle compositions, for example, containing SiO<sub>2</sub>, can also lead to damage of thermal barrier coatings through reactions with zirconia. These coatings are currently applied on many hot components in production engines.

The second source of particles and dust is located within the engine itself. Such particles are primarily a product of wear due to abrasive contact, erosion or fatigue spalling of abrasive coatings used to minimize blade tip clearances in the compressor and in the labyrinths. Typical materials used for these applications are sprayed nickel-graphite or silicon rubber layers for the sealing of rotor and stator blade roots, or



abrasive coatings in the low pressure compressor.

These particles are transported in the cooling air stream for the turbine blades. Cooling air for high pressure turbine components is normally taken out of the main stream behind the compressor, Fig. 1, and lead into the internal cooling structure of the blades. It is not uncommon that the air is first brought into a precompressor (coverplate) before entering the high pressure turbine blading in order to bring it to a sufficiently high pressure level so that it can be used for the film cooling of rotor blades.

The engine design plays an important role in determining the amount of dust carried by the cooling air. The cooling air stream is often collected from leakage air from the various labyrinths or comes in contact with the labyrinths, thus loading it with wear particles. In triple shaft engines cooling air for hot parts is first lead through the outer wall of the compressor casing where a high dust concentration is often found due to centrifugal effects.

The life of high temperature components can be influenced in a number of ways by dust-laden air.

- The openings to film cooling channels can be partially or fully blocked by dust particles carried by the hot gas stream. Experience indicates, for example, that particles containing high contents of iron oxide such as rust, or filled silicon rubbers lead to blockage of narrow cooling channels.
- The cooling air stream within the blade or behind the overheated zone can also be partially or totally blocked. Blockage of tip caps can lead to a reduction in cooling air and burning of the leading edge in front of them.
- Isolated deposits and/or oxidation layers can form within the hot part.
- Cooling air can be lost through leakage caused by local overheating due to blockage in other areas of the component.

### 3. Case Histories

Two examples typical failures in operation are

presented in the following section to show the effects and mechanisms of damage due to dust-laden air. The following steps were taken in each case to determine the damage mechanism and to provide information leading to possible remedies:

- Failure investigation and analysis
- Failure simulation: experimental reproduction of the damage to test hypotheses for the damage mechanism
- Remedies: development and proving of the effectiveness of possible remedies in the test rig.

#### 3.1 Damage to a convection cooled turbine rotor blade by particles carried in the main air stream (Case 1)

##### 3.1.1 Failure Analysis (Case 1)

In this case, turbine rotor blades made of uncoated, cast IN 100 were found to be heavily damaged after only a few hundred operational hours, Fig. 2. A diagram showing the location of the damage is shown in Fig. 3 and a macrograph of the damage can be seen in Fig. 4. An area of significant material loss at the leading edge along 2/3 of the blade length can be seen and is characterized by discoloring and roughness. Light colored dust deposits with a high sulfur content were found around the blade root and in the area near the cooling air inlets. The sulfur content is typical for engines running in this environment.

The initial evidence would lead to the conclusion that the damage mechanism was concurrent particle erosion and oxidation/corrosion attack. However, closer examination of the damaged area indicates that this hypothesis is not sufficient to explain the damage. Significant damage by erosion was not found and would not be expected in such short operating times, even though the presence of fine dust could be suspected. On the other hand, a pure corrosion mechanism would also not account for such heavy damage in such a short time.

Further work was deemed necessary to determine the cause of damage. Metallographic investigations were conducted on the damaged blades. Typical signs of oxidation and corrosion attack for the base material, IN 100, a cast nickel-base alloy were found. However, the microstructure showed no

signs of overheating (up to 50 °C) which would cause a significant reduction in life for the leading edge area (in the temperature range above 1100 °C). No evidence for significant particle erosion was found.

A number of blades were ground parallel to the profile. It was found that dust deposits with the same chemical composition had significantly narrowed the radial cooling channels. The cooling air throughput was measured for typical blades. The measurements showed no significant reduction in the amount of cooling air which agrees with the results of the investigation of the microstructure.

On the other hand, it should be recalled that deposits in the cooling channels can have a local effect on component temperature which may not be large enough or broad enough in area to be located in a single section. Partial blockage of cooling channels can have a thermal barrier effect, enhancing damage by changing the heat flow and cooling effect. This can be seen in Fig. 5, where a thermograph shows a local increase in blade temperature of 10° C as compared to a blade without internal deposits. (This thermograph was obtained by heating the blade with hot air in the cooling channels and measuring the surface temperature.)

Based upon the evidence found to this point, erosion or corrosion alone as well as combined erosion/corrosion, could not be considered to be the main cause of damage. In order to cast further light on the damage mechanism, an experiment was developed to simulate the damage observed in operation.

### 3.1.2 Failure Simulation and Mechanism (Case 1)

A test rig, Fig. 6, was designed and built whereby a cooled turbine rotor blade is statically mounted behind a tube combustor. The blade can be alternately cycled between the combustor and a compressed air stream for cooling. Fixed doses of dust (chemical composition given in Fig. 7) can be injected in the primary zone in the combustion chamber. The mechanical loading by centrifugal forces on the blade was not simulated. This was considered to have only a negligible effect on the expected buildup of particle deposits.

The blades were thermally cycled under particle loading with a typical thermal cycle consisting of a 5 minute hold time at 1090° C (component temperature measured in the first radial cooling channel at blade half height), 5 minutes at 940° C, and then ca. 10 seconds rapid cooling to 600° C (Fig. 8). These conditions were obtained under combustor settings which were shown by thermal paint tests to provide a distribution of temperatures at the leading edge similar to those in operation. The blades were optically examined for damage every 10 cycles.

Fig. 9 shows a typical uncoated IN 100 blade after 40 cycles. A significant amount of material removal is clearly seen at the leading edge in Fig. 10 (Area 1 in Fig. 9). A crust of sand consisting of at least two layers can be seen in the adjoining Area 2. Further layers are to be found further back toward the trailing edge.

A metallographic section of the damaged zone clearly shows high temperature corrosion. This area shows a large amount of corrosion products which are to some extent still bound to the base material. In the interfacial region of the base material, the grain boundaries show c'-phase depletion. In this area, fine precipitates typical of sulfidation are found.

The evidence from the simulations indicates that material removal could be related to a combination of corrosion and thermal cycles and is not only a result of the test time at temperature as would be expected for pure corrosion, erosion or erosion/corrosion. The following model could best describe the results. Molten dust particles from the combustor impinge on the relatively alicold blade surface and remain as a doughy mass. If the protective  $Al_2O_3$  layer has not yet formed, the sand melt can preferentially react with aluminum from the blade material. An existing  $Al_2O_3$  layer can also be dissolved by the melt. The melt is corrosive due to the presence of gypsum ( $CaSO_4$ ) in the sand. A relatively thick layer of corrosion products and sand form on the leading edge at the impingement sites which acts brittly upon cooling. The sand layer and the corrosion products spall off with each thermal cycle due to thermal stresses built up due to the difference in thermal expansion between the base material and the layer. New reactive surfaces are formed which allow this

process to continue. This loss of material thus leads to a rapid change in blade profile.

### 3.2 Damage to a film cooled turbine rotor blade (Case 2)

The following case is typical of damage due to dust transported by the cooling air. Turbine rotor blades, SR99 S.C. showed heavy damage after an operating time for the blades of only about 200 hours. All blades from the stage had the same appearance (Fig. 11). A zone with a green colored glassy layer can be seen on the convex (suction) side in the flow direction behind the cooling channels. Radial cracks running to the first cooling channel with significant plastic deformation were found underneath the shroud on the suction side. A large number of blades showed only crack formation without significant deformation. A powdery green layer was found in the root region around the cooling air inlet and under the platform. An analysis of the glassy layer on the blade surface and of the powdery layer at the root showed similar compositions with a high nickel content. The composition is typical of wear particles from abrasive coatings for compressor blades and labyrinths of the engine type in this case.

A metallographic investigation of the material in the damaged area showed no microstructural changes and no evidence of extreme overheating. This does not, however, rule out the possibility of long term effects of overheating in the range of 50° C. No evidence for erosion was found. The deformation as seen in cross section could not be satisfactorily explained by "soft body impact" typical, for example, for coke particles (carbon impacts) coming from the combustor. A further section through the cooling channels near the leading edge showed that they were partially filled with dust apparently carried in by the cooling air. The cooling effect could therefore have been significantly affected (Fig. 12).

#### 3.2.2 Failure Simulation and Mechanism (Case 2)

Previous experience indicated that the coincidental occurrence of two apparently unrelated effects such as deposit formation on the blade and crack formation is unlikely. In this case, simulation of the damage could not yet be

carried out. However, based to some extent on Case 1, the following hypothesis for the damage mechanism was deemed plausible.

Wear particles from a nickel-graphite abrasive coating enter the cooling air stream and are carried into the blades. Upon entry in the film cooling channels, these particles are baked into the channels resulting in poorer cooling of the leading edge. The leading edge is overheated, leading to radial crack formation and at times to collapse of the blade surface (Fig. 13). The damage appears similar to foreign object damage. The glassy layer found on the suction side formed through the melting of the abrasive coating particles after they exited the film cooling channels and entered the hot gas stream. It is possible that this layer had a thermal barrier effect on this area of the - blade, thus increasing the temperature gradient towards the overheated leading edge area. This gradient could locally be higher than 50° C and thus exacerbate the effects of operational thermal cycling. The result is a continuous process of corrosion due to the deposit and spallation due to thermal cycling.

### 4. Remedies

There are a number of possible remedies to the problem of damage to hot section components by dust-laden air. From a construction standpoint, the use of suitable filters or separators in the cooling air stream, or also a precompressor (coverplate) with the function of a separator may be possible. Such equipment has, however, not yet found its way into production engines. This may lie in the fact that it presents too large a disturbance in the cooling air stream. Further basic design studies are required in this area.

If the use of filters or separators is not possible, and it is not possible to operate in dust free environments, the use of sufficiently corrosion and oxidation resistant base materials or coatings is required. Much work is required in this area. This includes a better understanding of the damage mechanism in detail as well as the properties of the base material and the coating under complex loading. Furthermore possible blockage and damage in high temperature regions should be considered when developing abrasive coatings as clearance seals for blade tips and labyrinths.

## 5. Literature

- S.W. Kandelbo, Aviation Week and Space Technology, Aug. 20, 1990, pp. 25-26.
- J.A. Goebel, F.S. Petit, G.W. Goward. "Mechanisms for the Hot Corrosion of Nickel-Base Alloys", Metallurgical Transactions, Vol. 4, 1973.

This paper also makes use of unpublished work from the following authors:

F. Brungs, W. Hoffmüller, J. Eichner, M. Pierro.

Fig. 1 - Typical military triple-shaft engine

Fig. 2 - Rotor blades chord length reduction versus running time

Fig. 3 - Damage to a turbine rotor-blade from Case 1

Fig. 4 - Service engine

Fig. 5 - Influence of sand deposits on heat transfer

Fig. 6 - Test rig

Fig. 7 - Composition of dust from Case 1

Fig. 8 - Test cycle

Fig. 9 - Typical condition of a blade after testing

Fig. 10 - Leading edge of the blade shown in Fig. 9

Fig. 11 - Typical blade from Case 2

Fig. 12 - Longitudinal section through cracked cooling channels showing nickel containing deposits in the channels. Deposit thickness approx 80  $\mu\text{m}$ , channel width at this position approx 260  $\mu\text{m}$

Fig. 13 - Section through the damage region. Top: Collapse of cooling channel, bottom: thermal fatigue cracking of corroded layer reaching into base material

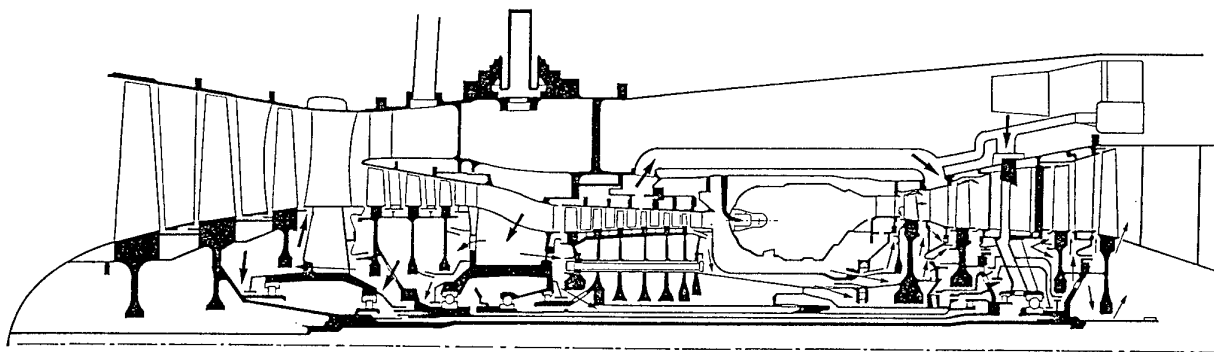


Fig. 1 Typical military triple-shaft engine

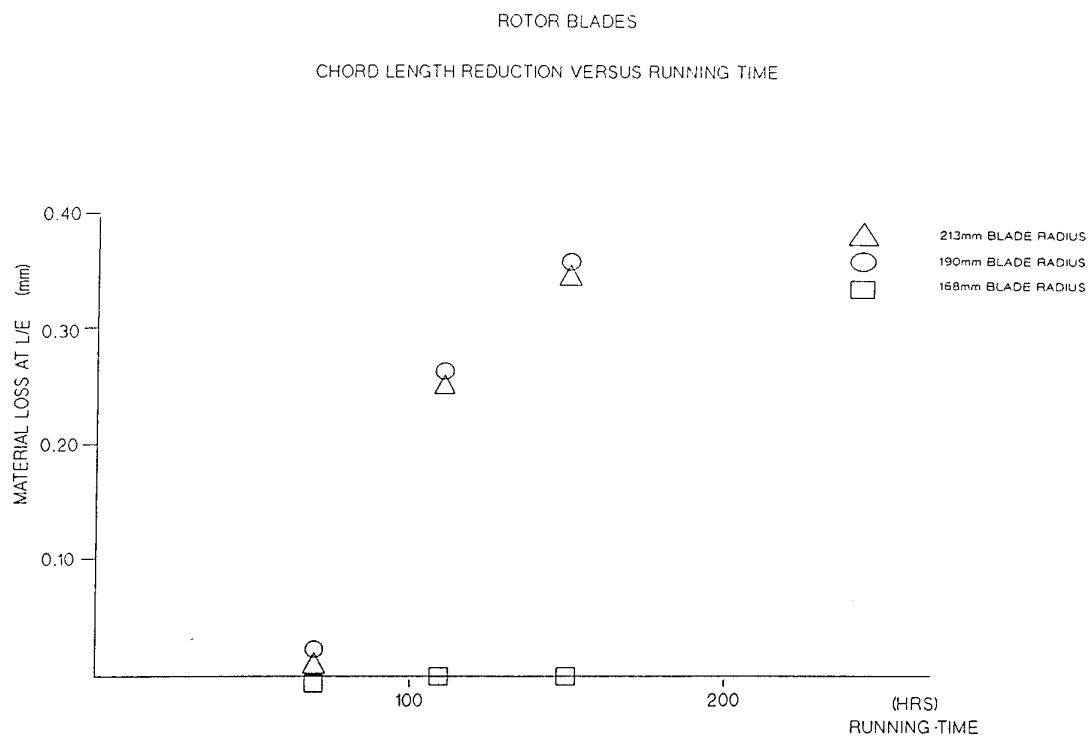


Fig. 2 Rotor blades chord length reduction versus running time

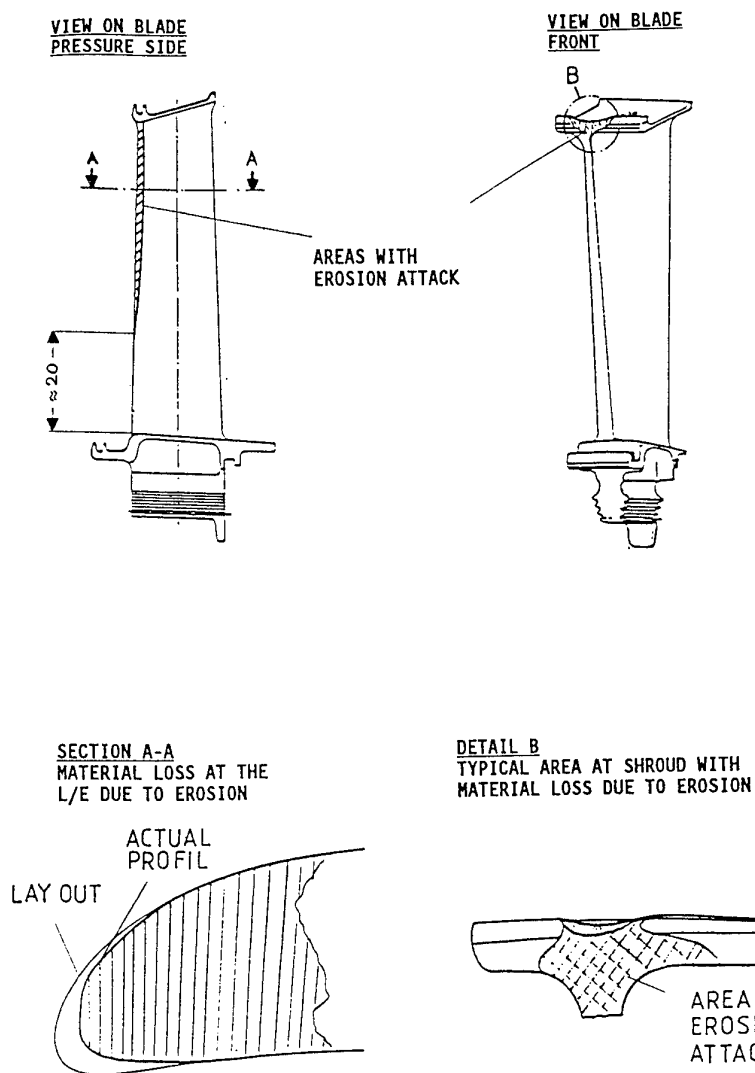


Fig. 3 Damage to a turbine rotor-blade from Case 1

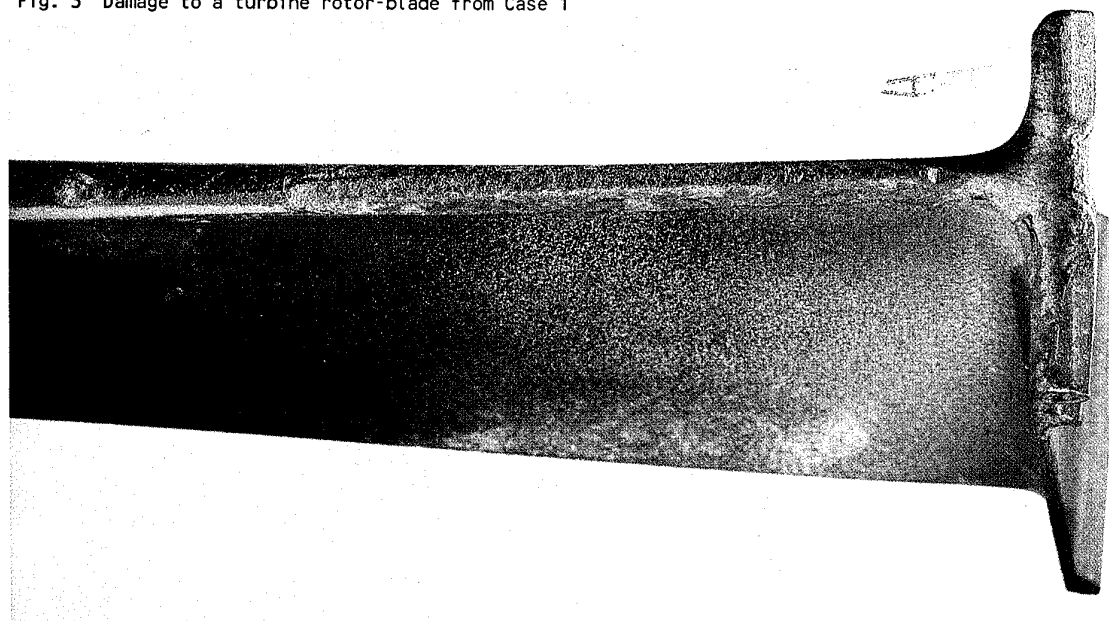


Fig. 4 Service Engine 160 h

## INFLUENCE OF SAND DEPOSITS ON HEAT TRANSFER

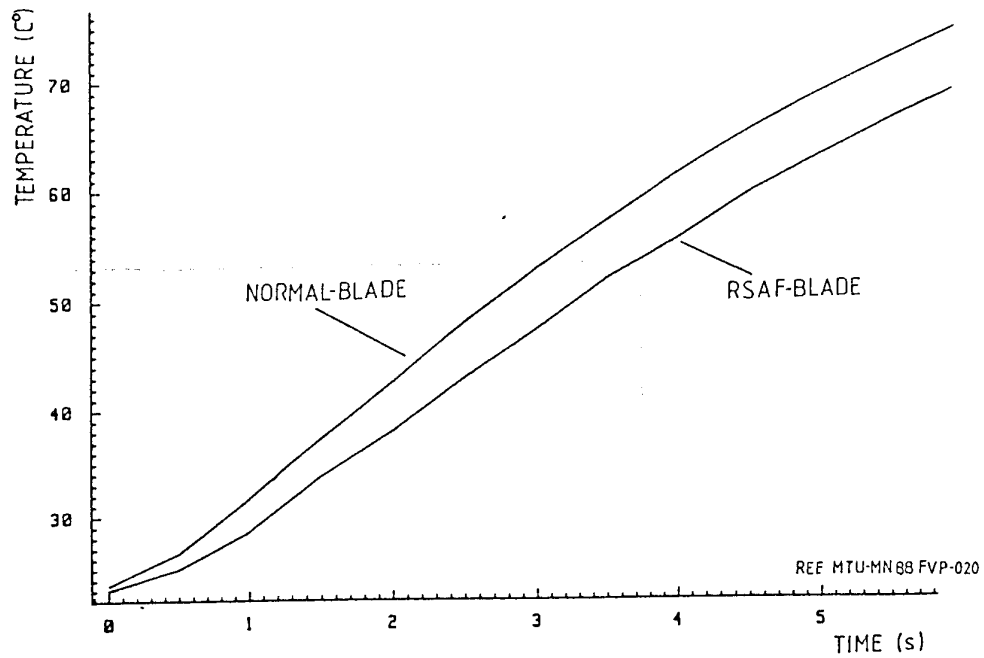


Fig. 5 Influence of sand deposits on heat transfer

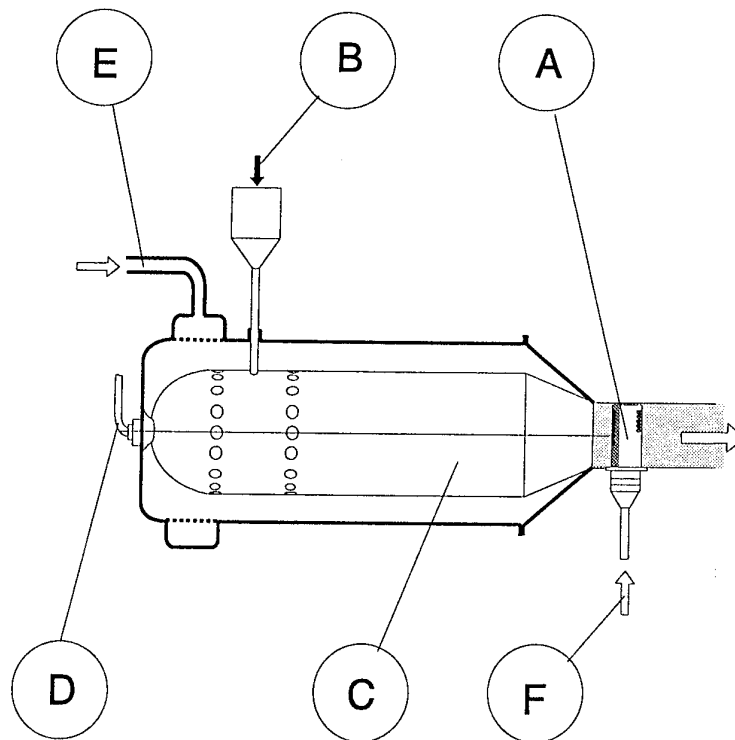


Fig. 6 Test rig

- A = Test blade
- B = Dust injection
- C = Combustion chamber
- D = Fuel
- E = Combustion air
- F = Cooling air

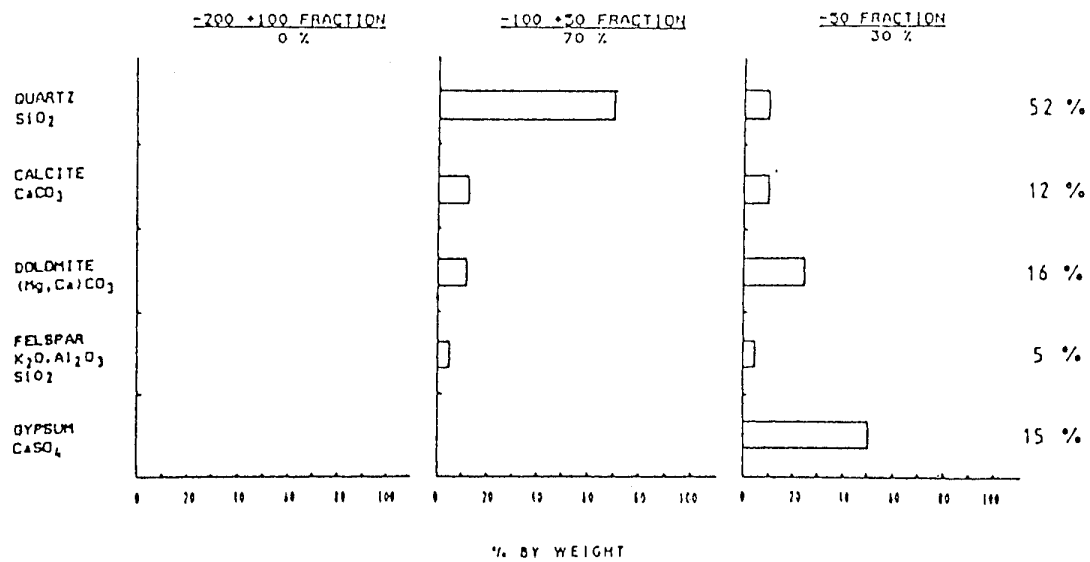
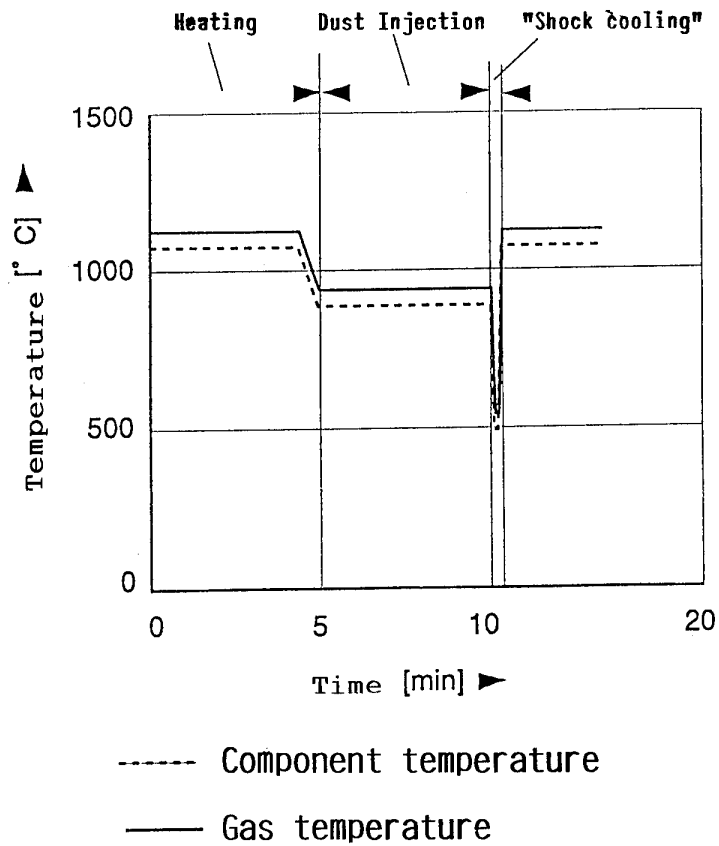


Fig. 7 Composition of dust from Case 1



Typical Cycle

Fig. 8 Test cycle



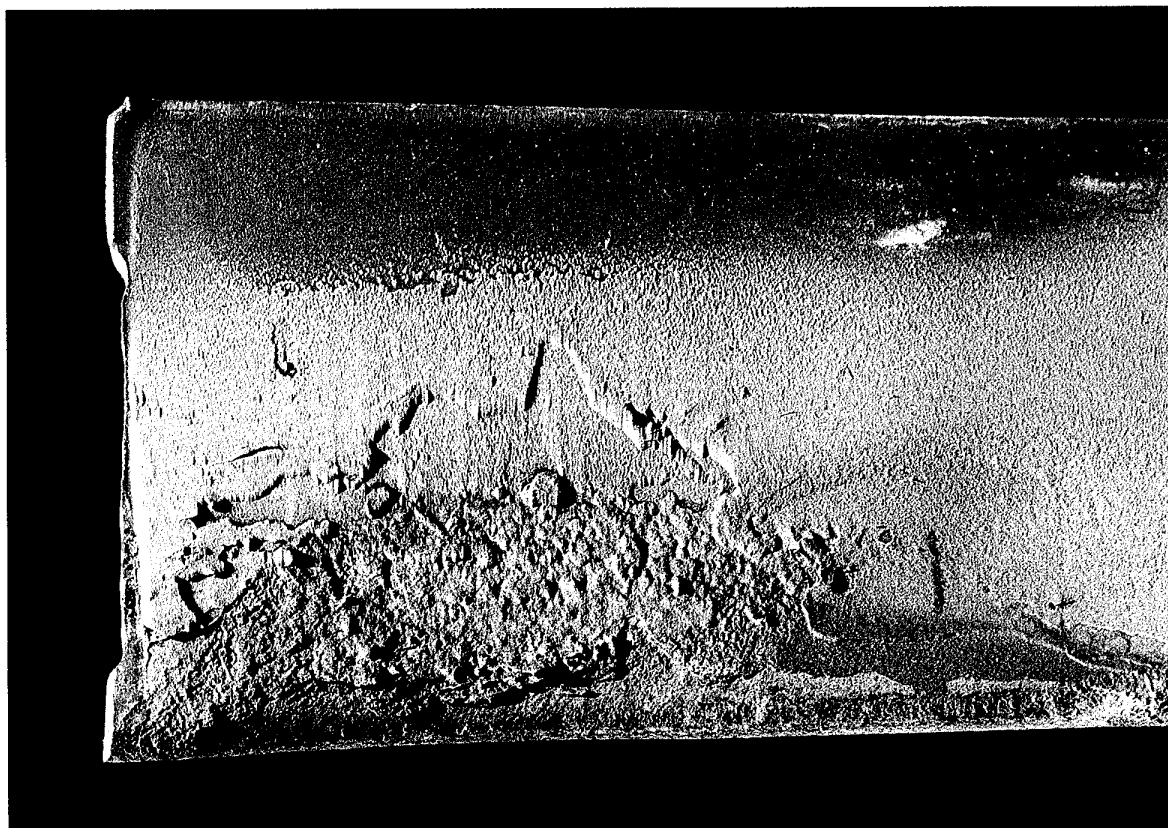


Fig. 9 Typical condition of a blade after testing

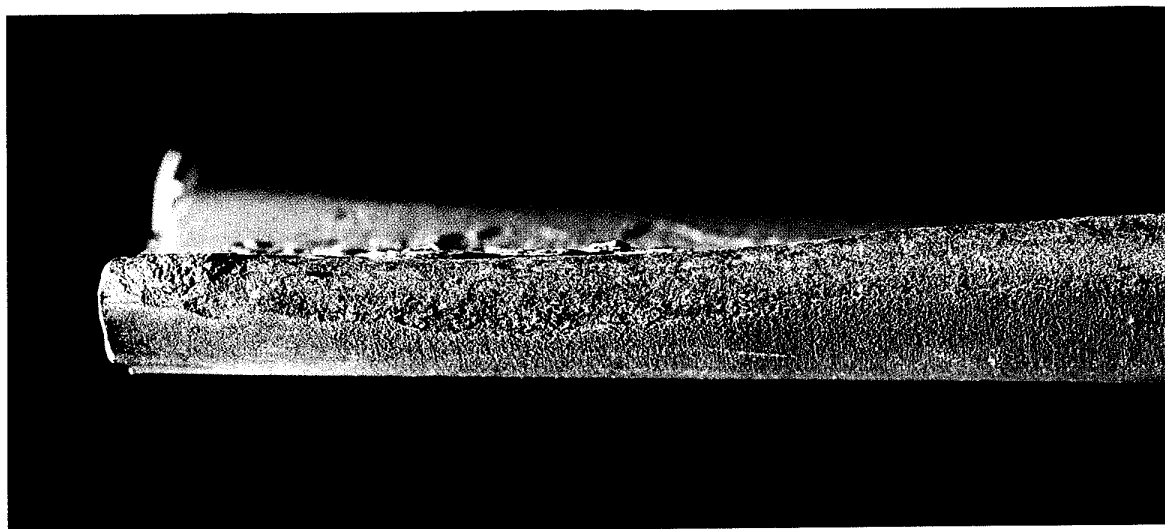


Fig. 10 Leading edge of the blade shown in Fig. 9



Fig. 11 Typical blade from Case 2



Fig. 12 Longitudinal section through cracked cooling channels showing nickel containing deposit in the channels. Deposit thickness approx.  $80\ \mu\text{m}$ , channel width at this position approx.  $260\ \mu\text{m}$ .

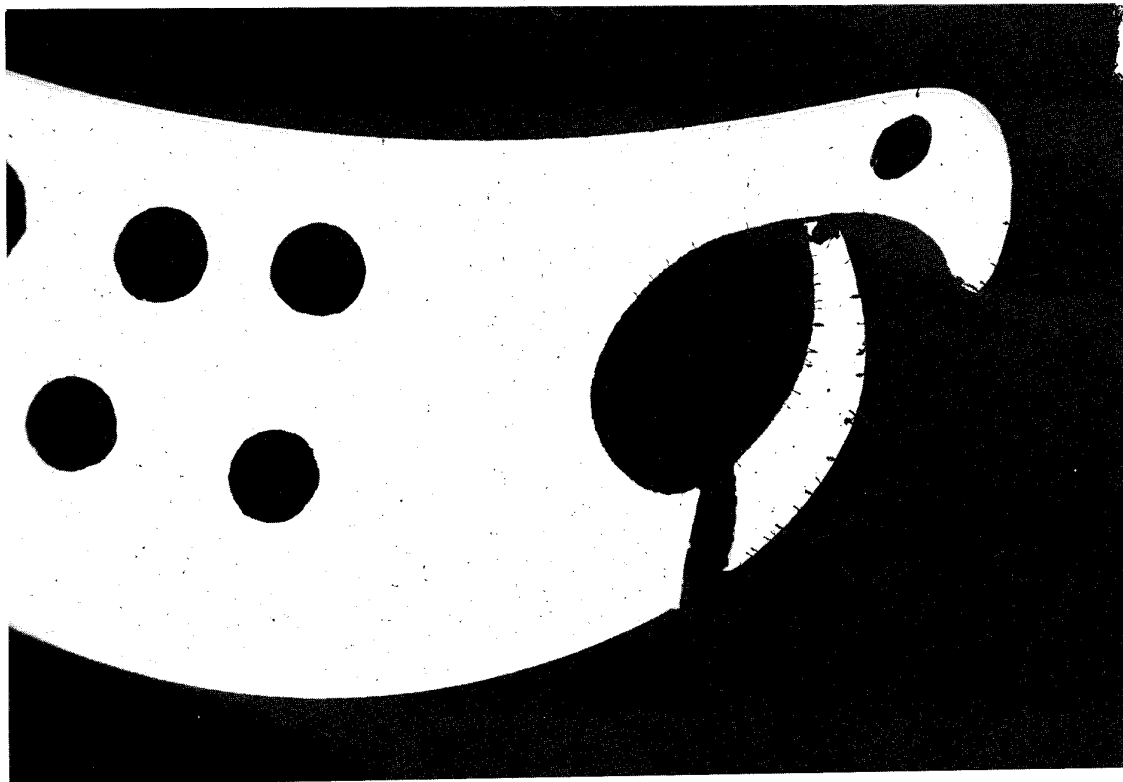


Fig. 13 Section through the damage region. Top: Collapse of cooling channel, bottom: thermal fatigue cracking of corroded layer reaching into base material

## ANALYSE DE L'ÉROSION DE MATERIAUX METALLIQUES DE STRUCTURES CUBIQUES CENTREE ET FACE CENTREE

A. Magnée

Université de Liège, Faculté des Sciences Appliquées, Département. Métallurgie et Science des Matériaux  
Rue A. Stévant, 2 - 4000 LIEGE  
BELGIUM

### RESUME

Une loi généralisée d'usure par érosion, sous forme non dimensionnelle, est proposée. Celle-ci rend compte explicitement de la nature et de la microstructure du matériau impacté, de l'angle d'impact des particules, de leur acuité et de leur dureté.

Le comportement à l'érosion de divers aciers et fontes est examiné ainsi que la tenue de nouveaux matériaux intermétalliques ordonnés Fe-25%Al - (Zr, Cr, B).

L'intérêt de tels alliages dans des environnements agressifs du type érosion-corrosion est montré.

**Mots clés :** usure, érosion, modèle, matériaux métalliques, intermétalliques Fe-Al

### 1. INTRODUCTION

L'érosion par un flux de particules solides concerne de nombreux secteurs d'activités humaines dans le domaine de la construction aéronautique (engins spatiaux, aubes de turbines, pales d'hélicoptères en présence de poussières abrasives) et de la construction mécanique (conception des équipements pour le transport pneumatique de solides pulvérulents, dépoussiérage des fumées, concassage et broyage de minerais et de matières diverses).

Cette dernière frange d'applications est particulièrement importante et couvre un domaine élargi d'industries minérales, minières, cimentières, de transformations et d'équipements.

L'amélioration des performances des pièces d'usure dans de tels secteurs pose des problèmes métallurgiques délicats et ce d'autant plus que l'on appréhende généralement mal les paramètres importants qui gouvernent ce type d'endommagement, le recours à des essais in situ étant souvent très aléatoire et les moyens de simulation étant par ailleurs pratiquement inexistant.

Cet état des choses nous a amené à déployer des moyens d'études spécifiques que nous décrirons par la suite.

### 2. ENDOMMAGEMENT TRIBOLOGIQUE ET ÉROSION

On a mentionné à de multiples reprises, que l'usure constitue un phénomène complexe souvent mal perçu.

Cependant, on peut affirmer que les dégradations observées pour un matériau donné sont nécessairement le résultat d'un collectif déterminé de sollicitations dont, en définitive, il faut identifier les paramètres directeurs, non négligeables, dans les conditions particulières de fonctionnement du système, de sorte que l'on peut postuler l'existence d'une relation générale liant l'usure à un ensemble de variables significatives  $v_i$  ( $i = 1, n$ ), qui pilotent la cinétique des phénomènes, soit :

$$W = F(v_1, v_2, v_3, \dots, v_n)$$

En procédant alors à une analyse conceptuelle en théorie des systèmes, on aboutit à définir cinq modes principaux d'endommagement tribologique gouvernés par un ensemble de 12 variables généralisées d'usure (1).

Les modes fondamentaux mis en évidence sont les suivants (Fig.1) :

- l'usure adhésive
- l'usure tribochimique
- l'usure par fatigue
- l'usure abrasive
- l'usure érosive.

Par ailleurs, les variables généralisées, gouvernant l'usure, correspondent à :

- la vitesse relative du mouvement  $V$ , [ $L T^{-1}$ ]
- la longueur de déplacement  $L$ , [ $L$ ]
- la masse des particules  $M$ , [ $M$ ]
- la dureté du matériau  $H$ , [ $L^{-1} M T^{-2}$ ]
- la dureté de l'abrasif (ou du corps antagoniste)  $H_a$ , [ $L^{-1} M T^{-2}$ ]
- la force de contact  $F$ , [ $L M T^{-2}$ ]
- l'angle de contact  $\alpha$ , [ $^\circ$ ]
- l'acuité de l'abrasif (ou du corps antagoniste)  $\lambda$ , [ $^\circ$ ]
- le coefficient de friction  $f_0$ , [ $^\circ$ ]
- le coefficient d'adhérence :

$$\gamma^* = \frac{\gamma_{ad}}{HR_q}, [^\circ]$$

$\gamma_{ad}$  est l'énergie d'adhérence des corps en contact ( $J/m^2$ )

$R_q$  caractérise la rugosité quadratique du corps principal [ $L$ ]

- le coefficient d'activation :

$$Q^* = \frac{Q}{RT}, [^\circ]$$

$T$  est la température de contact [ $K$ ]

$R$  la constante universelle des gaz parfaits [ $J/K \text{ mole}$ ]

$Q$  l'énergie d'activation du processus tribochimique [ $J/\text{mole}$ ]

- le coefficient de déformation tribo-oligocyclique

$$\epsilon^* = \frac{\epsilon_p}{\epsilon_r}, [^\circ]$$

$\epsilon_p$  est la déformation microplastique de la surface lors d'un cycle de mise en charge [ $^\circ$ ]

$\epsilon_r$  la déformation plastique totale à la rupture du matériau [ $^\circ$ ]

Procédant alors à un examen de l'équation d'endommagement basé, d'une part, sur le théorème de l'analyse dimensionnelle, qui indique que toute corrélation quantitative entre des grandeurs physiques s'exprime par une relation fonctionnelle entre les combinaisons sans dimension de ces grandeurs et, d'autre part, sur le théorème de Buckingham qui précise le nombre de quantités non-dimensionnelles attachées au système, on aboutit à une équation d'usure unifiée qui a pour expression :

$$W = K \frac{\Delta}{H}$$

$\Delta$  représente l'énergie potentielle emmagasinée dans le corps à partir de son état naturel, soit :

$$\Delta = \frac{FL}{2} = \frac{MV^2}{2} \quad [ML^2T^{-2}]$$

La source d'énergie potentielle sera, selon le cas, liée, soit à l'action d'une force  $F$  agissant sur le contact en mouvement relatif à la vitesse ( $V$ ) sur une distance de glissement ( $L$ ), situation qui décrit les quatre premiers modes fondamentaux d'usure (adhésive, tribochimique, par fatigue, abrasive), soit à l'action de la "force vive" de la particule, c'est-à-dire à son énergie cinétique pour le dernier mode fondamental d'usure (érosion). Dans ce dernier cas, le coefficient  $K$  est de la forme :

$$K = K(\alpha, \lambda, \frac{Ha}{H}, f_0, k)$$

Le coefficient  $K$ , outre les variables généralisées déjà mentionnées, est dépendant d'une ou de plusieurs variables internes microstructurales complémentaires contrôlant le processus de dégradation macroscopique du matériau, à savoir ici le paramètre ( $k$ ).

Ainsi, dans la situation d'une usure par abrasion, en plus de la dureté, différents auteurs ont montré que la ténacité  $K_{IC}$  de l'alliage pouvait jouer un rôle déterminant dans la dégradation du matériau (2, 3).

Dans le cas de l'érosion, on a pu établir (1, 4) que le coefficient  $K$  avait pour expression :

$$K = f_1(\alpha, n, k) \cdot \lambda \cdot f\left(\frac{Ha}{H}\right)$$

- $\alpha$  correspond à l'angle d'impact des particules
- $n$  définit l'angle de rebondissement des particules, en l'occurrence l'angle au-dessus duquel la vitesse tangentielle résiduelle des particules est nulle. Cet angle  $\alpha_0$  est tel que :

$$\alpha_0 = \frac{\pi}{2n} = \arctg \frac{1}{6f_0}$$

- $k$  est le paramètre microstructural qui tient compte du comportement élastoplastique du matériau érodé, soit :

$$k = \phi/\epsilon$$

- $\phi$  est l'énergie de coupe du matériau ( $J/m^3$ ) ; celle-ci est pratiquement équivalente à la dureté du matériau si l'on se réfère aux premiers travaux de Finnie (5).
- $\epsilon$  est l'énergie de déformation du matériau, c'est-à-dire l'énergie requise pour enlever une unité de volume de matière par déformation ( $J/m^3$ ) ; ce paramètre introduit par Bitter (6) est lié aux propriétés qui traduisent le niveau de fragilité du matériau (niveau de plasticité avant rupture, ténacité)
- $\lambda$  désigne l'acuité des particules impactant la surface ; si l'on considère que celle-ci indente la surface comme un cône d'angle au sommet  $2\theta$ , on a :

$$\lambda \simeq \frac{6}{\pi} \cotg \theta$$

On observera que pour des angles  $\theta$  de l'ordre de  $60^\circ$ , le facteur  $\lambda$  vaut pratiquement l'unité, ce qui correspond par ailleurs, au contact sphérique ou, par référence  $\lambda = 1$  ; le paramètre  $\lambda$  est l'équivalent de l'indice de sphéricité  $\xi$  introduit par Hutchings (2) pour tenir compte de l'angularité de particule ( $\lambda = \xi^{-3}$ )

- La fonction  $f\left(\frac{Ha}{H}\right)$ , traduit le fait, que la dureté de l'abrasif, tout autre paramètre de la configuration étant maintenu constant, influence l'amplitude du phénomène d'usure. Ce fait est bien connu et a été montré la première fois, dans le cas de l'abrasion, par Krushchov (7)(Fig.2).

La fonction  $f\left(\frac{Ha}{H}\right)$  a pour expression (8, 9) :

$$f\left(\frac{Ha}{H}\right) = 1 - \exp\left(-\ln 2 \left(\frac{Ha}{mH}\right)^{1+2m}\right)$$

$m$ , dénommé coefficient létal d'abrasion, caractérise la transition du phénomène d'usure ( $1 < m < \pi$ ).

Dès que la dureté de l'abrasif devient supérieure à la dureté du matériau, la fonction tend vers 1 ; cette valeur est obtenue pratiquement pour  $Ha \geq 2H$ .

- La fonction  $f_1$  rend principalement compte du transfert d'énergie qui s'opère entre les particules et le matériau, source du phénomène d'érosion. La composante normale de vitesse de la particule ( $V \sin \alpha$ ) provoque un effet de déformation du solide conduisant à un arrachement de matière, tandis que la composante tangentielle ( $V \cos \alpha$ ) est responsable d'un effet de coupe. (10). L'usure du matériau par effet de déformation est alors :

$$W_D = \frac{M}{2\epsilon} (V \sin \alpha - V_e)^2$$

$V_e$  est la vitesse d'impact limite où la réponse du solide est encore élastique ; elle est de l'ordre de quelque m/s pour les matériaux métalliques et peut être négligée.

L'usure du matériau par effet de coupe a pour valeur :

$$W_C = \frac{M}{2\phi} (V^2 \cos^2 \alpha - V_r^2)$$

$V_r$  est la vitesse tangentielle résiduelle de la particule après impact ; celle-ci est différente de zéro pour des angles rasants d'impact compris entre  $0^\circ$  et  $\alpha_0$  conformément à l'expression :

$$V_r = V \cos \alpha \sqrt{1 - \sin n \alpha}$$

On aboutit ainsi à formuler une loi généralisée d'érosion sous la forme non dimensionnelle suivante :

$$W^*(n, \phi, \epsilon, \alpha) = \frac{2W\phi}{MV^2 \lambda f\left(\frac{Ha}{H}\right)} = \cos^2 \alpha \sin n \alpha + k \sin^2 \alpha$$

La fonction  $\sin n \alpha$  devient égale à 1 dès que  $\alpha \geq \alpha_0$

### 3. SIMULATION ET ÉTUDE DES PHÉNOMÈNES D'ÉROSION

L'étude et l'analyse des processus d'usure passent nécessairement par une voie expérimentale qui, en dehors d'une observation directe sur site, nécessite le support de moyens d'essais sur des appareils de laboratoire ou sur des dispositifs "pilotes" à échelle réduite.

#### 3.1. Principes clés de simulation

Le choix et la conception du tribomètre repose sur un certain nombre de principes que nous synthétiserons comme suit :

- Le premier principe implique l'existence d'une symétrie physique fonctionnelle entre le tribomètre et le faisceau des applications de la classe d'usure concernée.
- Le deuxième principe est d'assurer un découplage effectif des principaux paramètres d'action des phénomènes que l'on veut étudier.
- Le troisième principe est d'effectuer des essais qui couvrent suffisamment l'intégralité de ces mêmes phénomènes.

Au niveau de la conception du tribomètre, ceci a pour conséquence :

- l'exigence d'un contrôle et d'un ajustement d'un ensemble de paramètres tels que la masse, la vitesse, l'angle d'impact, la température, ... à des valeurs de consigne dans une gamme étendue de réglages;
- la nécessité de l'absence de toute interdépendance entre les paramètres directeurs du collectif de sollicitations.
- l'obligation d'un maintien de la configuration évitant des dérives systématiques ou aléatoires de l'amplitude du processus d'usure.

Pour satisfaire à ces diverses impositions, nous avons cherché à identifier les variables internes qu'il est primordial d'assujettir : nous les dénommerons paramètres conceptuels. Il s'agit d'une démarche qui, à notre connaissance, n'a pas été abordée dans la littérature et qui confère au dispositif de simulation développé son originalité.

Les principales variables d'essais, qu'il est utile d'analyser dans le cadre d'un dispositif de simulation consacré à l'étude de l'érosion, sont les suivantes :

a) les conditions opératoires de service :

- masse impactante (M)
- vitesse d'impact (V)
- angle d'impact ( $\alpha$ )
- flux d'impact ( $\psi$ )
- température (T)

b) les données relatives aux matières fragmentées :

- granulométrie des particules ( $\phi$ )
- dureté de l'abrasif ( $H_a$ )
- acuité de la matière ( $\lambda$ ).

Compte tenu des desiderata énumérés ci-dessus, le principe de construction de l'appareillage réalisé est le suivant : les éprouvettes à étudier sont disposées verticalement à la périphérie et au-dessus d'un disque horizontal animé d'un mouvement circulaire uniforme. Ce disque est percé d'encoches rectangulaires destinées à la fixation des éprouvettes. Celles-ci sont placées à intervalle régulier et sont orientées de manière à réaliser un angle d'impact ajustable entre  $15^\circ$  et  $90^\circ$  (11).

La matière impactante s'écoule à travers l'orifice d'un distributeur réglable à débit constant dans le temps. Ce distributeur est disposé de telle sorte que la matière qu'il débite tombe par gravité en rideau quasi monoparticulaire sur la circonférence décrite par les échantillons lors de la rotation du disque. L'ensemble de l'appareillage est placé sous vide de façon à éviter les turbulences aérodynamiques résultant des réactions de l'ambiance sur les échantillons. Les particules impactantes sont projetées contre la paroi latérale de la cuve, conçue pour éviter autant que possible les impacts secondaires (Fig.3).

En ce qui concerne le dispositif d'érosion, il est nécessaire de satisfaire aux principes suivants :

- La masse impactante, la vitesse et l'angle d'impact doivent être maintenus constants au cours d'une expérimentation.
- Toute la matière déversée doit effectivement impacter les échantillons, quelles que soient les conditions d'essais.
- Le flux de particules doit être maintenu constant à travers les essais.

A ces trois principes sont attachés trois variables internes ou paramètres conceptuels du tribomètre érosion que nous analysons à présent :

- 1) La conception de l'appareillage permet de fixer la température, la masse impactante, la vitesse et l'angle d'impact à des valeurs précises : pour ce dernier, on dispose d'un plateau où les échantillons sont calés angulairement de manière fixe de  $15^\circ$  à  $90^\circ$  par pas de  $15^\circ$ . La masse impactante peut être ajustée entre quelques grammes et 30 Kg environ, compte tenu du volume disponible de la trémie (12 litres). Le paramètre de configuration qui sera maintenu constant ici sera, dans la mesure du possible, le nombre d'impacts supportés par un échantillon d'usure au cours d'un essai; pour des particules quasi sphériques de diamètre  $\phi$ , ce "paramètre d'impact"  $\theta$  a pour expression :

$$\theta = \frac{6}{\pi} m_s^{-1} \cdot \phi^{-3} \cdot \frac{M}{n_0}$$

$m_s$  est la masse spécifique de l'abrasif. A titre indicatif, le nombre théorique d'impacts encaissés par un échantillon soumis à l'érosion de 5 Kg de particules de quartz de 1 mm de diamètre moyen est de 3,6 millions.

- 2) Pour que toutes les particules abrasives impactent uniquement la surface de travail des échantillons, il est nécessaire que la hauteur de l'échantillon soit au moins égale à la distance parcourue par une particule érosive entre deux impacts consécutifs. Compte tenu de la chute libre des particules dans un conduit de profondeur h, la hauteur effectivement impactée est donnée par l'expression :

$$H = H(R, n_0, V, h) = \frac{2\pi R \sqrt{2gh}}{n_0 V}$$

où g est l'accélération de la pesanteur ( $9,81 \text{ m/s}^2$ ).

La hauteur impactée sera indépendante des conditions d'essais si nous choisissons un "paramètre de fonctionnement" zêta constant, défini par :

$$\zeta = \frac{30 n_0 N}{\pi R V h}$$

et l'on a :

$$H = 60 \sqrt{2g} \zeta^{-1}$$

La constance du paramètre  $\zeta$  est obtenue, d'une part, dans la construction du dispositif, où à la fois la hauteur de chute libre h (0,20 m) et le rayon de giration R (0,241 m) sont maintenus fixes, et, d'autre part, en ajustant le nombre d'échantillons  $n_0$  en raison inverse de la vitesse d'impact.

Dans le domaine exploré, nous avons retenu systématiquement 3 vitesses d'impact, soit 25, 50 et 75 m/s, pour lesquelles le nombre d'échantillons, dans la cuve de simulation, est respectivement de 6, 3 et 2 unités, de sorte que :

$$\zeta = 13288,33 \text{ s}^{-1} \text{ m}^{-1/2}$$

La hauteur impactée est alors constante et égale à la moitié de la dimension z de l'échantillon, soit 20 mm. Le paramètre de fonctionnement zêta "quantifie" en quelque sorte le dispositif en imposant une fréquence d'impact constante puisque :

$$f = \frac{\zeta \sqrt{h}}{60} = 100 \text{ Hz}$$

On notera, de plus, que l'intervalle de temps entre deux impacts consécutifs  $\Delta t = f^{-1}$  équivaut à  $10^{-2} \text{ s}$  et ne peut, dès lors, perturber le processus impulsif lui-même qui impose des temps de contact beaucoup plus courts.

- 3) Le flux de particules abrasives est un paramètre important à maintenir constant au cours d'essais où l'on étudie, soit l'influence de la vitesse d'impact, soit l'action de l'angle d'incidence des particules sur l'usure du matériau.

Nous avons choisi ici des conditions de flux maintenues constantes à  $1 \text{ g/s.cm}^2$ .

Le flux a pour expression :

$$\psi = \psi(D, \alpha, n_o, H, L) = \frac{D \sin \alpha}{n_o H L}$$

où  $L$  est la largeur de la fenêtre d'alimentation de l'abrasif.

Celui-ci sera constant si l'on maintient un troisième paramètre conceptuel indépendant des conditions d'essais, soit le "paramètre de débit"  $\delta$ , tel que :

$$\delta = \frac{D}{n_o / \sin \alpha}$$

### 3.2. Adéquation tribologique

Nous examinerons, en premier lieu, l'influence de la masse impactante, de la vitesse de percussion et de l'angle d'impact des particules en relation avec la loi non dimensionnelle d'usure par érosion.

La figure 4 montre l'évolution de l'usure d'un acier étiré en fonction de la masse impactante d'abrasif constitué par du quartz en impact frontal : le taux d'usure varie linéairement avec celle-ci, conformément à la loi d'érosion.

La figure 5 est relative à l'évolution du taux d'usure en fonction de la vitesse d'impact : l'exposant de la loi de vitesse est proche de 2; d'une manière générale, celui-ci peut être supérieur à cette valeur par suite d'une érosion secondaire introduite par la fragmentation.

Le tableau I fournit les paramètres d'érosion de différents matériaux impactés par du corindon à  $50 \text{ m/s}$ . On observe bien le comportement attendu pour des matériaux doux très ductiles comme l'aluminium (Fig.6), et de matériaux durs et plus fragiles comme un acier martensitique hypereutectoïde ou une fonte à haute teneur en chrome (fig. 7) :

- Les matériaux doux sont caractérisés par une usure maximale correspondant à des impacts sous incidences obliques et par une énergie spécifique de déformation plus élevée que l'énergie spécifique de coupe ( $k < 1$ ).
- Les matériaux durs présentent une usure maximale lors d'impacts sous incidences frontales, l'énergie spécifique de déformation devenant plus faible que l'énergie spécifique de coupe ( $k > 1$ ).

La morphologie des surfaces érodées, analysées en microscopie électronique à balayage, est illustrée pour la fonte à haut chrome à la Fig.8 : ces observations confirment les caractéristiques fondamentales du processus d'érosion qui résultent de la superposition d'un mécanisme d'usure par effet de coupe, prédominant pour les faibles incidences d'impact, et par effet de déformation de plus en plus marqué pour les angles proches de l'impact frontal.

La figure 9 montre l'évolution de l'usure de l'acier doux, d'un acier à 1,5 % Cr et d'une fonte à haut chrome en fonction de la direction d'incidence des particules constituées ici par du quartz. On met ici en évidence l'importance des conditions de travail des équipements industriels dans les conditions d'érosion : la connaissance de l'angle statistique d'impact est d'un intérêt primordial puisque l'on observe que le comportement en service d'un alliage peut se révéler favorable ou non, suivant précisément cet angle de travail.

L'influence du rapport  $(H_a/H)$  est illustré à la Fig.10 : le diagramme souligne le fait que les mérites respectifs d'un alliage vis-à-vis d'un autre dépendent également de la nature des produits que l'on est amené à traiter : une solution valable pour des matières de faible dureté ne le sera pas nécessairement dans le cas de matières plus dures.

Enfin, comme nous l'avons mentionné précédemment, une caractéristique importante des structures autre que la dureté est la ténacité des alliages : un exemple probant est fourni par des essais sur une fonte hypereutectique à haut chrome traitée à  $740 \text{ Hv}$ , qui présente une tenue à l'érosion par le quartz systématiquement plus faible que celle d'un acier doux de  $200 \text{ Hv}$ . Ce mauvais comportement de la fonte à 35% Cr est dû à un déchaussement et à une fracture préférentielle des carbures  $\text{M}_7\text{C}_3$  de la matrice martensitique comme l'indique la figure 11.

### 4. ÉTUDE DE MATÉRIAUX ORDONNÉS INTERMÉTALLIQUES

Dans de nombreux procédés industriels, les matériaux métalliques sont soumis à des atmosphères très agressives, par suite de la superposition de phénomènes de corrosion et d'érosion à haute température. De telles conditions sont notamment rencontrées dans les installations de gazéification du charbon en lit fluidisé, dans les systèmes antipollution, en pétrochimie et dans les moteurs thermiques.

L'érosion qui se combine à la corrosion, peut entraîner des dégradations catastrophiques des matériaux, puisque l'impact des particules est susceptible de détruire la couche d'oxyde protectrice et de favoriser, en même temps, l'ablation des surfaces métalliques.

Les alliages couramment utilisés dans ces secteurs sont des aciers inoxydables austénitiques (304, 310, 316L) ou des aciers au chrome ferritiques; on a recours également à des alliages spéciaux du type stellite 6B, 800H ou Inconel.

D'une manière générale, les aciers inoxydables austénitiques peuvent être utilisés à des températures supérieures à celles des aciers ferritiques, sensibles au grossissement du grain au-delà de  $600^\circ\text{C}$  et à l'effet d'entaille. Cependant, il a été montré que la corrosion peut fortement altérer les propriétés mécaniques des matériaux, notamment la tenue au fluage.

Compte tenu de ces constatations, il apparaît que la formulation de nouveaux matériaux à hautes performances, dans ce domaine d'utilisation, doit éviter l'apparition de diverses réactions, que nous synthétiserons comme suit :

- 1) formation d'une couche oxydée épaisse et friable de faible adhérence et de dureté réduite;
- 2) décroissance rapide des propriétés mécaniques de résistance avec la température;
- 3) instabilité structurale liée à l'apparition progressive de nouvelles phases ou de précipités fragilisants.

Ces constatations nous ont amené à étudier des compositions Fe-Al à haute teneur en aluminium (12). Le domaine centré sur une teneur massique de l'ordre de 25% Al, c'est-à-dire une composition atomique à 40% d'aluminium, est particulièrement intéressant : en effet, cette composition ne présente aucune transformation de phase et reste ordonnée jusqu'à une température de fusion élevée proche de  $1300^\circ\text{C}$ .

La tenue à l'érosion de ces matériaux a été examinée, à la fois, à température ambiante et à haute température ( $600^\circ\text{C}$  et  $900^\circ\text{C}$ ) (Fig.12) :

A température ambiante, nous observons que :

- a) Le comportement, à température ambiante, de l'acier 316L est bien celui d'un matériau doux et ductile

- ( $k < 1$ ), le maximum d'usure correspondant à un angle de  $45^\circ$  environ.
- b) A contrario, le comportement de l'alliage Fe-25Al est celui d'un "matériau dur", malgré que celui-ci soit de dureté modérée (280HV) ( $k \geq 1$ ) ; le taux d'usure devient pratiquement indépendant de l'angle d'impact au-delà de  $60^\circ$ .
- c) Pour un angle de  $30^\circ$ , le taux d'érosion volumique de l'alliage Fe-Al est 35% plus faible que l'acier 316L.

Pour les essais à hautes températures, on constate que :

- a) Le comportement des matériaux s'apparente à celui de solides ductiles, le maximum d'usure se situant aux environs de  $30^\circ$ .
- b) Le comportement de l'alliage FeAl vis-à-vis de l'acier 316L devient de plus en plus intéressant au fur et à mesure que la température d'érosion s'élève, atteignant un rapport de performances supérieur à 6, à  $900^\circ\text{C}$  en impact frontal. Ceci est à mettre en relation avec les excellentes propriétés de résistance à l'oxydation des alliages FeAl, les couches d'alumine formées constituant une barrière efficace de protection du matériau à hautes températures.
- c) Les faciès d'érosion à  $20^\circ$  et  $600^\circ\text{C}$ , observés en microscopie électronique par balayage pour l'acier 316L et l'alliage Fe-25Al, confirment les effets de coupe et de déformation de la loi d'érosion.

Il ressort donc de cette étude, le grand intérêt de tels alliages, dès lors que la maîtrise de leurs mise à forme et transformation est assurée.

Une représentation tridimensionnelle de la loi d'érosion généralisée  $W^*(n, k, \alpha)$  est représentée à la Fig.13, l'angle  $\alpha_0$  adopté ici correspondant à  $18^\circ$  soit la valeur particulière  $n = 5$ .

La courbe  $k = 1$  sépare deux régions typiques du comportement à l'érosion des matériaux métalliques :

- La surface  $W^*(5; 0 < k < 1; \alpha)$  correspond aux matériaux "doux et ductiles", caractérisés par une érosion maximale sous incidence oblique ( $\alpha_{\max} \approx 18^\circ$ ).
- La surface complémentaire  $W^*(5; k > 1; \alpha)$  constitue la zone des matériaux "durs et fragiles", l'érosion maximale apparaissant pour un angle d'impact frontal ( $\alpha_{\max} = 90^\circ$ ).
- La courbe  $W^*(5, 1, \alpha)$  a pour particularité de correspondre à un processus d'usure qui devient indépendant de l'angle d'impact au-delà de l'angle  $\alpha_{\max} \approx 18^\circ$ .

Enfin, nous avons représenté, à la Fig.14, une cartographie tridimensionnelle de la surface érodée d'un matériau métallique par des particules solides. Il s'agit de la reconstitution, à l'aide d'un profilomètre de haute résolution et de grande amplification, de la morphologie typique d'endommagement dans ce mode d'usure. On retrouve ici les aspects caractéristiques de la formation de "copeaux", en impacts obliques. Ces "images de synthèse" constituent des "clichés topographiques" originaux réalisés grâce aux techniques les plus récentes d'acquisition de données, faisant appel à la microscopie mécanique à balayage.

## 5. CONCLUSIONS

L'endommagement par érosion concerne de nombreux secteurs de la construction aéronautique et mécanique.

Un tribomètre original pour l'étude de l'érosion est décrit.

La démarche entreprise ici s'appuie sur une nouvelle notion de paramètres conceptuels, qui sont les "variables internes" du dispositif de simulation qu'il s'agit d'identifier et de maîtriser dans l'expérimentation.

Nous montrons que le tribomètre conçu offre un rapport de convenance parfaite avec le mode d'endommagement tribologique concerné.

Nous examinons ensuite l'usure par érosion en dégagant, parmi différentes formulations théoriques, un modèle dérivé de celui de Finnie-Bitter. Les examens microstructuraux, effectués en microscopie électronique à balayage, confirment l'intérêt du modèle adopté, qui rend compte des mécanismes d'endommagement par effets de déformation et de coupe du matériau érodé.

Une loi généralisée d'usure par érosion, sous forme non dimensionnelle, est proposée, celui-ci rend compte explicitement de :

- la nature et de la microstructure du matériau par les paramètres métallurgiques spécifiques ( $\phi, \epsilon, n$ )
- l'angle d'impact  $\alpha$  des particules ;
- l'acuité  $\lambda$  des particules impactantes ;
- la dureté  $H_a$  des particules érodantes.

Le comportement à l'érosion de divers aciers et fontes est tout d'abord examiné pour aborder ensuite de nouveaux matériaux intermétalliques ordonnés Fe-25%Al (Zr, Cr-B).

L'intérêt de tels alliages dans des environnements agressifs du type érosion-corrosion est mis en évidence.

Enfin, une représentation tridimensionnelle de la loi généralisée d'érosion, permet une synthèse entre les caractéristiques microstructurales et le comportement global à l'érosion de matériaux les plus divers.

## REFERENCES

1. Magnée, A., Thèse : "Etude des processus d'usure de matériaux métalliques soumis à l'abrasion et à l'érosion", Faculté des Sciences Appliquées, Université de Liège, mai 1991.
2. Ruff, A.W., "Erosion by solid particle impact", Treatise on materials science, vol.16, Acad. Press, 1979.
3. Magnée, A., "Considérations théoriques sur l'endommagement par abrasion de matériaux métalliques", Cetim, Mecamat, octobre 1989.
4. Magnée, A., "L'endommagement par abrasion et érosion", Colloque Concep. Meca. et Tribo., Cetim, mai 1991.
5. Finnie, I., "Erosion by solid particles", Wear, vol.3, p.87-103, 1960.
6. Bitter, J.G.A., "A study of erosion phenomena", Wear, vol.6, p.5-21, 169-190, 1963.
7. Khrushchov, M.M., "Resistance of metals to wear by abrasion as related to hardness", Jour. Mech. Eng. London, paper 48, p.65-659, 1957.
8. Magnée, A., "Matériaux résistants à l'abrasion", Pratique des matériaux industriels, chap.9.5, Dunod, Paris, juin 1992.
9. Magnée, A., "Modelization of damage by abrasion", Wear, n°162-164, p.848-855, 1993.
10. Magnée, A. et al., "Behaviour in impact-erosion of ductile and brittle materials", CRM Reports n°37, p.43-50, December 1973.
11. Magnée, A., "Amélioration de la tenue des aciers par durcissement sous chocs répétés", SBM, n°1404, p.5.1-5.9, Bruxelles, avril 1989.
12. Magnée, A. et al., "Wear resistance of the FeAl intermetallic alloy", Int. Symp. on Intern. Comp. (JIMIS-6), Jap. Inst. of Metals, p.725-730, June 1991.



## QUESTIONS

### **AXEL ROSSMANN (Ge)**

- Q.   a)    Were the tests conducted at high temperatures, also in vacuum?
- b)    For room temperature testing, would there be a change in erosion behaviour between vacuum and air (e.g. oxidation effects in Al-alloys)?
- A.   a)    No, in this case, we use a modified erosion tribometer: the particles (diameter, about 200  $\mu\text{m}$ ) are projected on a target, inside an air flow, through a propulsion nozzle.
- b)    There is no difference in erosion behaviour, between vacuum and air tests, of course.

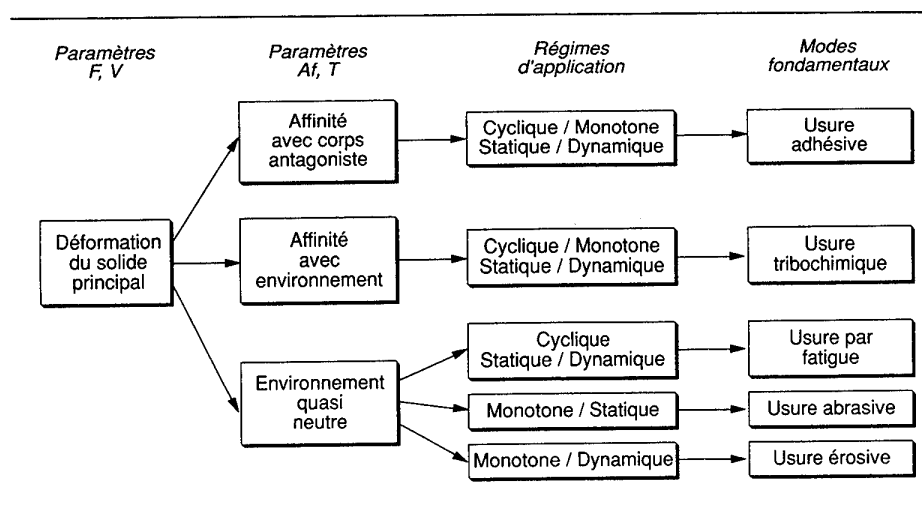


Fig.1. Modes fondamentaux d'endommagement tribologique (8)

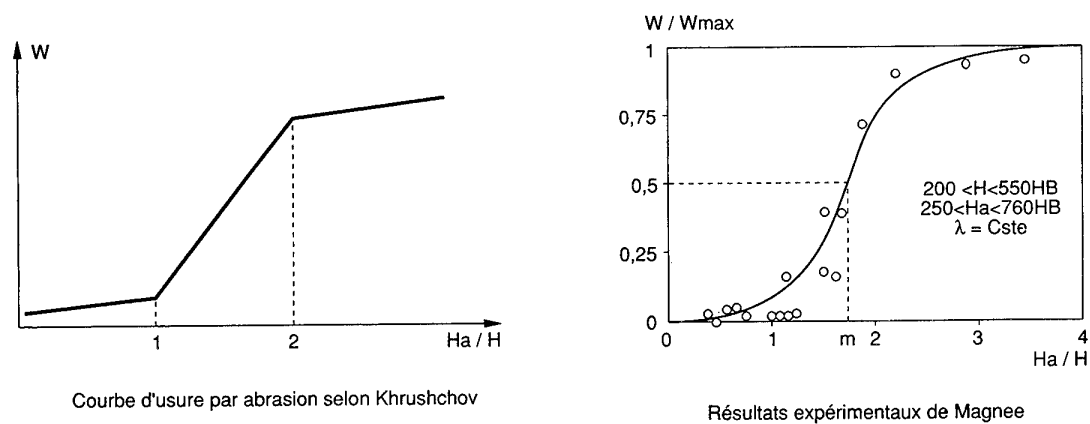


Fig.2. Influence de la dureté de l'abrasif sur le taux d'usure (8)

Matériau	Energie spécifique de coupe $\phi$ (KJ/cm <sup>3</sup> )	Energie spécifique de déformation $\epsilon$ (KJ/cm <sup>3</sup> )	k	n	$\alpha_{max}$	Dureté HV
Aluminium	16.3	95.7	0.17	5	18°	50
Acier étiré	23.6	71.5	0.32	2	33°	200
Acier Hadfield	18.2	39.7	0.46	2.25	40°	>200
Aciers 1%C-1.5%Cr	35.1	30.6	1.15	2.0	90°	620
Fonte 2.6%C-21%Cr	30.3	25.4	1.19	1.58	90°	700

TABLEAU I - Paramètres d'érosion de différents matériaux métalliques (abrasif :  $Al_2O_3$  ; 50 m/s)

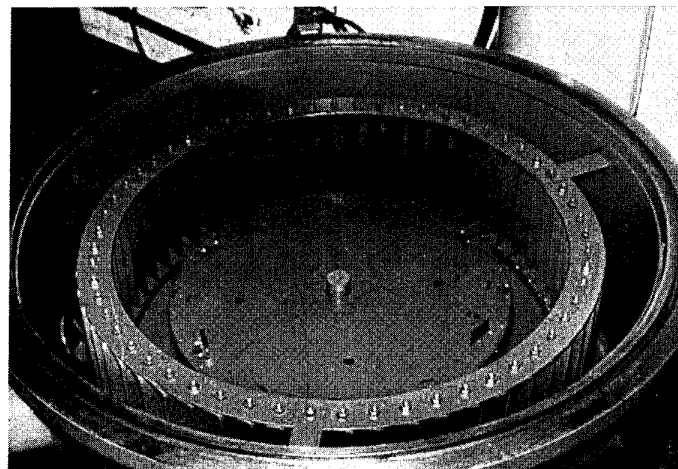
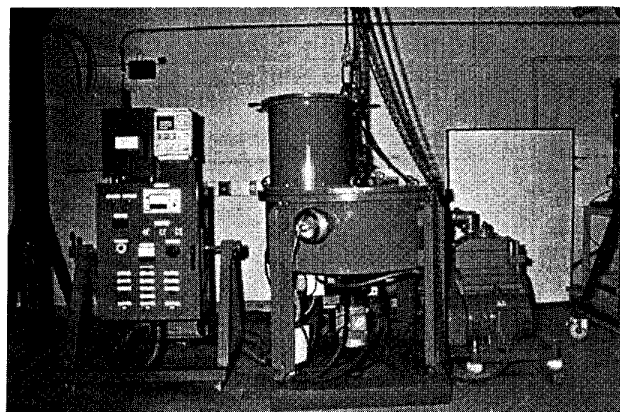
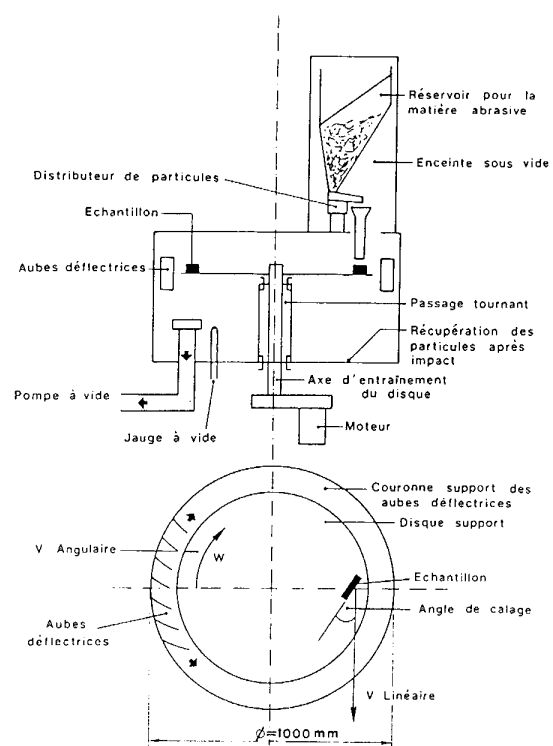


Fig.3. Principe du tribomètre érosion et vue du dispositif

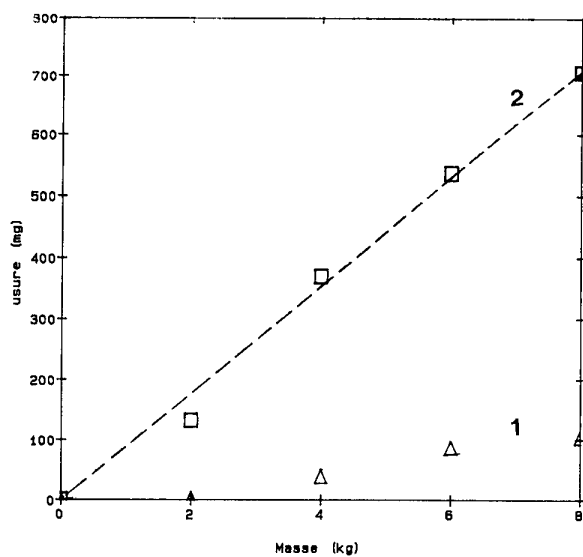


Fig. 4. Erosion de l'acier doux en fonction de la masse impactante ( $\alpha = 90^\circ$ ;  $\text{SiO}_2$ ;  $V(1) = 25 \text{ m/s}$ ;  $V(2) = 50 \text{ m/s}$ )

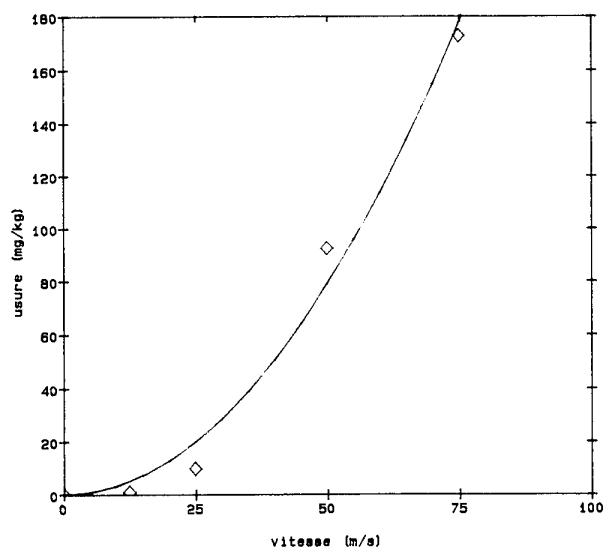


Fig. 5. Erosion de l'acier doux en fonction de la vitesse d'impact ( $\alpha = 90^\circ$ ;  $\text{SiO}_2$ )

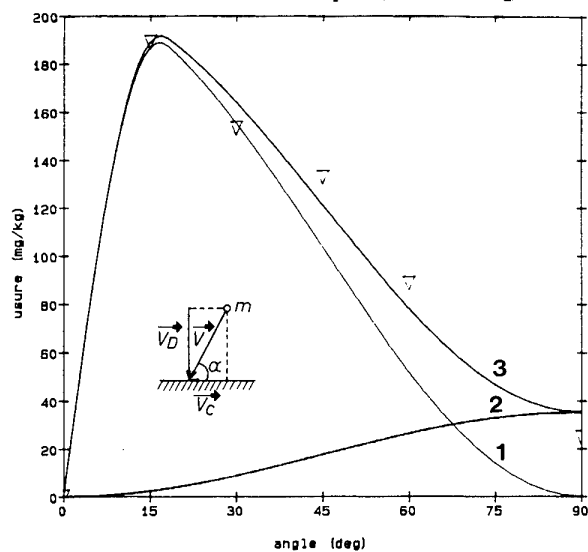


Fig. 6. Erosion de l'aluminium en fonction de l'angle d'impact ( $\text{Al}_2\text{O}_3$ ;  $50 \text{ m/s}$ ; (1) =  $W_C$ ; (2) =  $W_D$ ; (3) =  $W_C + W_D$ )

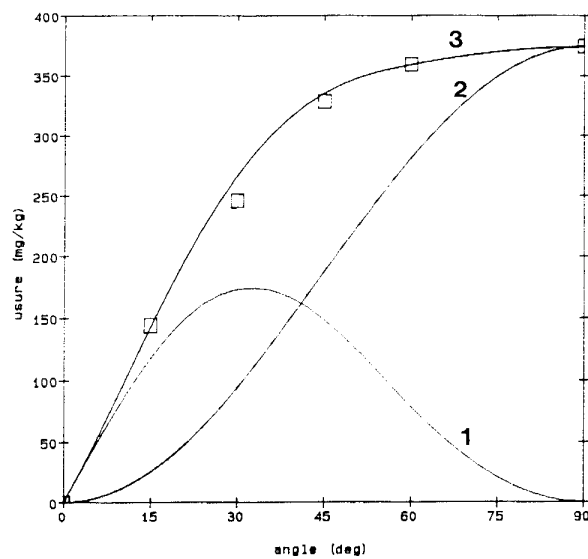


Fig.7. Erosion d'une fonte à haut chrome en fonction de l'angle d'impact ( $\text{Al}_2\text{O}_3$  ; 50 m/s)

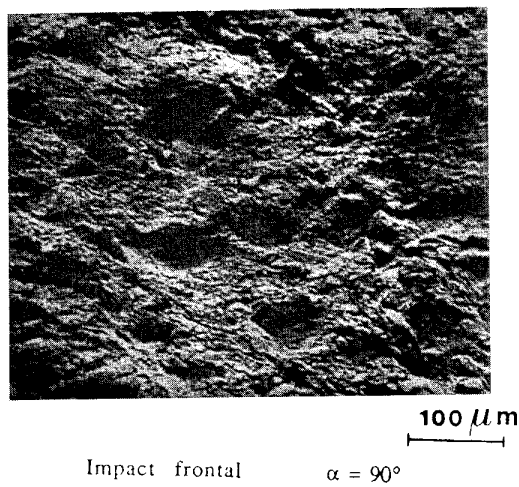
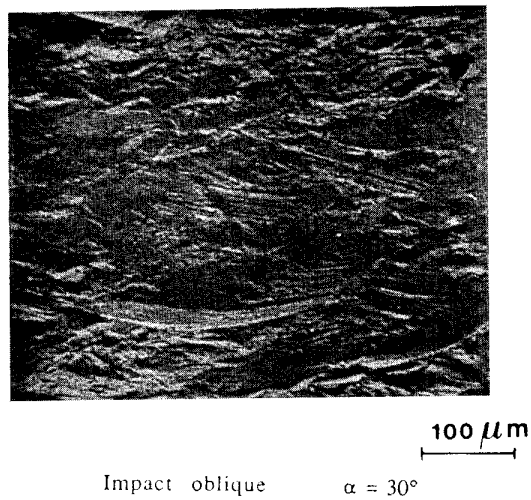


Fig.8. Surfaces érodées de la fonte à haut chrome observées en microscopie électronique à balayage ( $\text{Al}_2\text{O}_3$  ; 75 m/s)

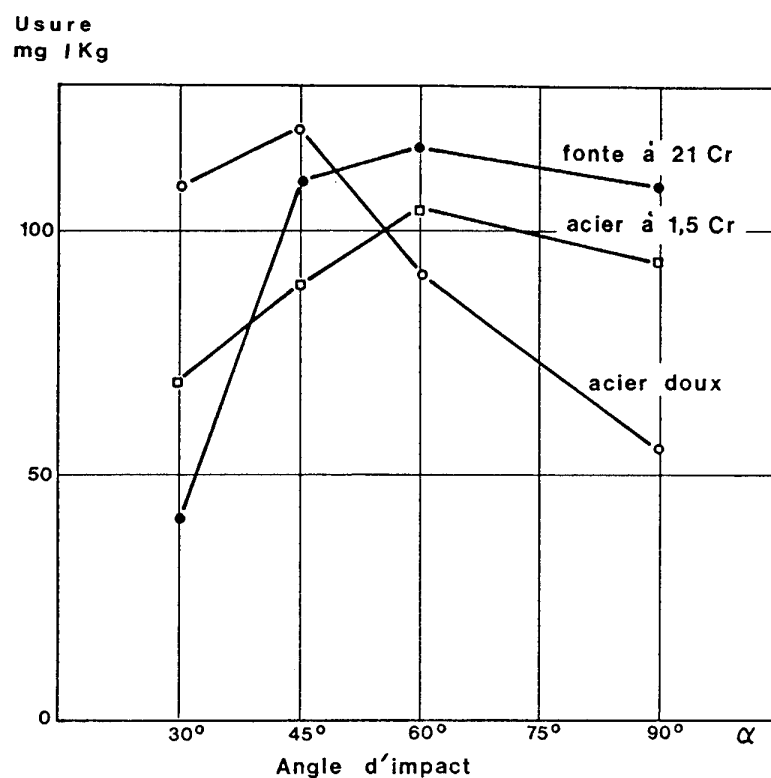


Fig.9. Influence de l'angle d'impact sur le comportement des matériaux ( $\text{SiO}_2$  ; 50 m/s)

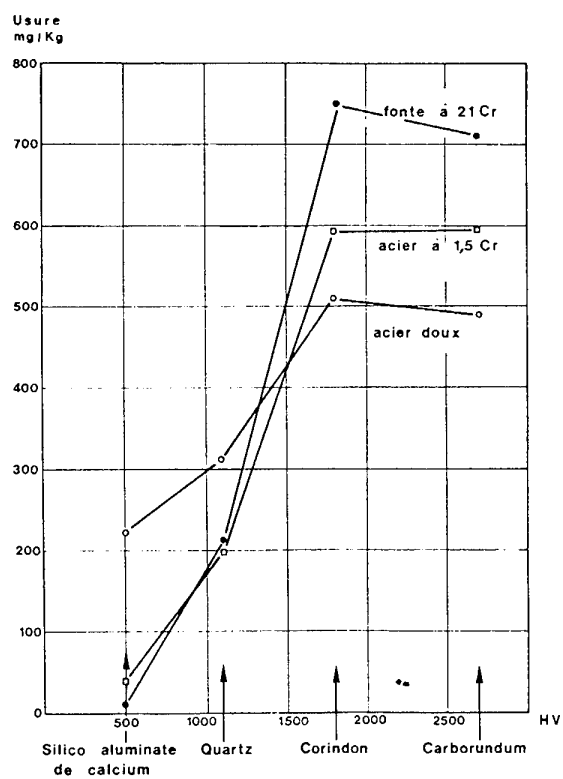
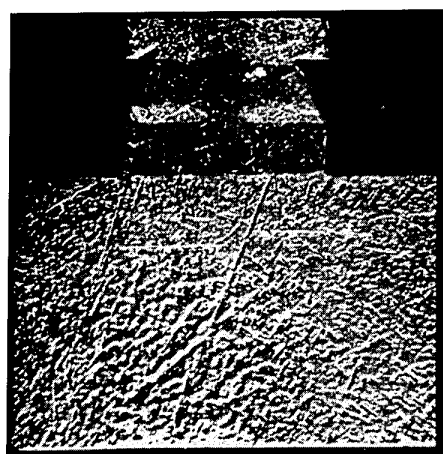
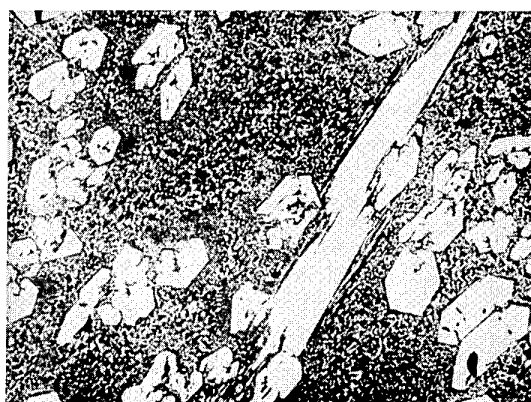


Fig.10. Influence de la dureté de l'abrasif sur le comportement des matériaux ( $\alpha = 30^\circ$  ; 75 m/s)



A



B

Fig.11. Influence de la ténacité sur le comportement des matériaux ( $\text{SiO}_2$  ;  $\alpha = 90^\circ$  ; 50 m/s)

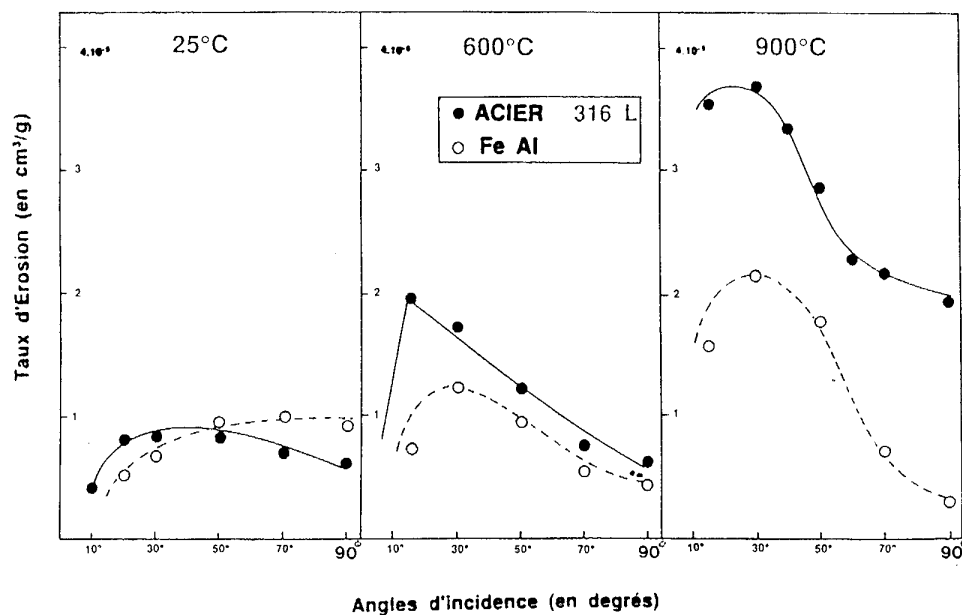


Fig.12. Essais d'érosion à différentes températures d'un acier inoxydable 316 L et d'un alliage intermétallique Fe-25Al-Zr ( $\text{SiO}_2$  ; 50m/s)

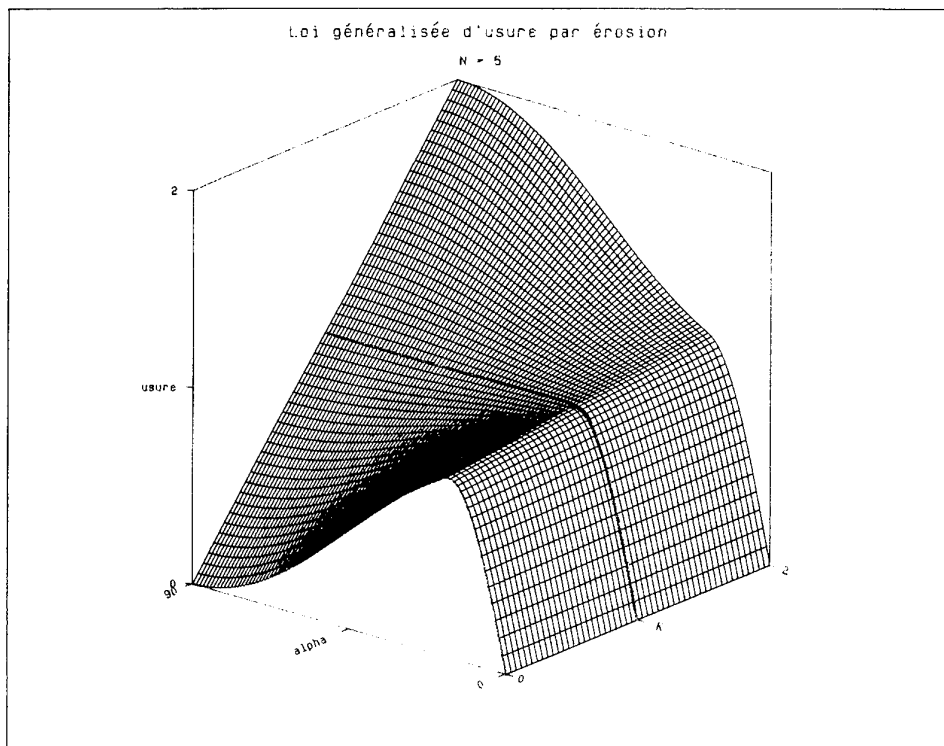


Fig.13. Loi d'érosion généralisée  $W^*$  ( $n, k, \alpha$ ) en variables adimensionnelles

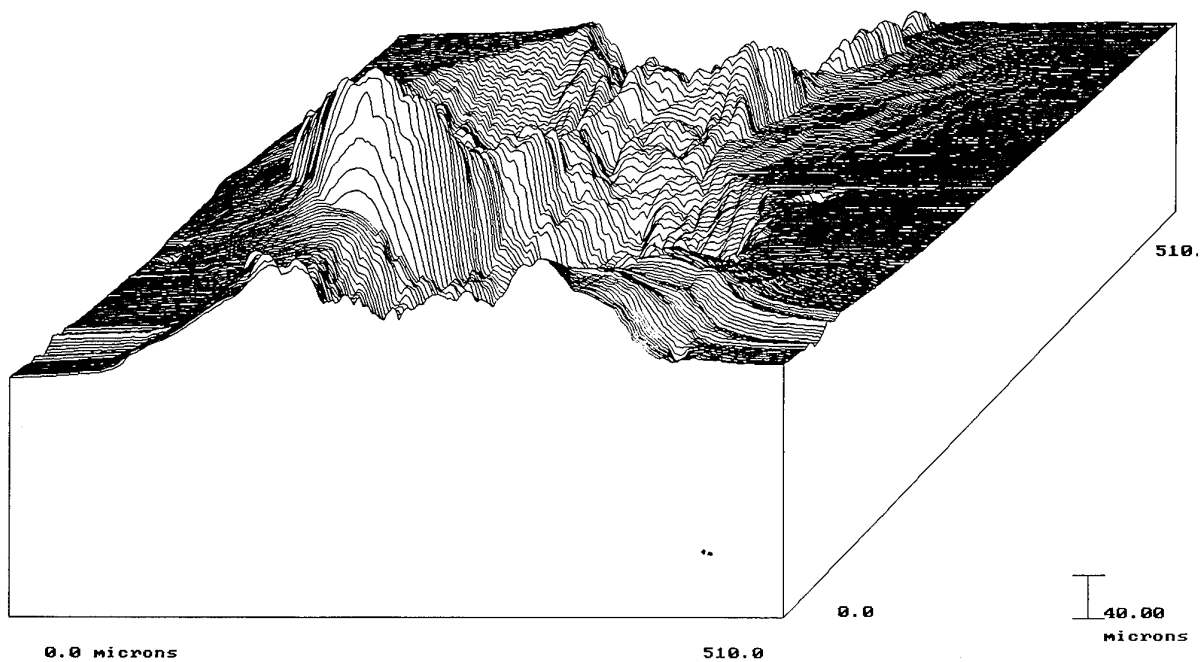


Fig.14. Cartographie tridimensionnelle de la surface érodée d'un acier Hadfield ( $\alpha = 15^\circ$ ; 50m/s ; sphères en carbure WC ;  $\varnothing = 0,93$  mm)



# PROTECTIVE COATINGS FOR COMPRESSOR GAS PATH COMPONENTS

D. R. NAGY \*  
 V. R. PARAMESWARAN \*\*  
 J. D. MacLEOD \*\*  
 J. P. IMMARIGEON \*\*

\* Liburdi Engineering Limited,  
 400 Highway 6, North,  
 Hamilton, Ontario, Canada, L9J 1E7

\*\* National Research Council of Canada,  
 Institute of Aerospace Research,  
 Ottawa, Ontario, Canada, K1A 0R6

## SUMMARY

The blades and vanes in gas turbine compressors operating in dusty environments are prone to degradation by solid particle erosion, which causes surface roughening and changes in airfoil geometry. This results in decreased compressor performance, and higher specific fuel consumption, leading to significantly increased operational costs. Erosion damage is more prominent in flight engines without air inlet filter protection.

Application of a thin ceramic titanium nitride (TiN) coating to improve the erosion resistance of compressor airfoils was thoroughly investigated. Coatings were applied to engine hardware by a Reactive Ion Coating (RIC) process and optimized to produce a very adherent erosion resistant coating. Computer modelling of the erosion process occurring on coated and uncoated airfoils suggested that the operational life of the compressor can be enhanced by a factor of two.

A complete set of compressor blades and vanes for an Allison T56 turboprop engine was coated for engine qualification tests. Laboratory tests showed that the thin coating had no significant influence on either the resonant frequency or the fatigue resistance of the blades and the instrumented engine tests confirmed that the performance was typical of overhauled engines, with no aerothermodynamic loss. Therefore, titanium nitride coatings are suitable for service and can be used on existing engines to improve the life of the compressors.

## INTRODUCTION

The compressor of a jet engine is designed to aspirate a large volume of air through the inlet and progressively pressurize it through various stages of blades and vanes. Any solid particles ingested in the airflow will be accelerated and impacted against the airfoil surfaces causing varying degrees of damage. The result is a progressive erosion of the airfoils that causes both surface roughening and metal loss.

This phenomenon is encountered in virtually all aero and ground based gas turbine engines to varying degrees of severity. Large amounts of dust and salts can be ingested into the engines of aircraft, especially those operating from unimproved airfields (figure 1). Helicopters manoeuvring in sandy fields will generate a dust cloud that surrounds the aircraft and the engine intakes<sup>1</sup>. Stationary turbines used for industrial and marine applications are often protected by high efficiency filtration against sand storms. However, in some environments the filters become clogged or inefficient causing operators to open intake bypass ducts and expose the compressor to erosion damage<sup>2</sup>.



Figure 1: A turboprop transport landing on a desert airstrip can generate a significant dust cloud around the intakes of the engines and expose the compressor components to severe erosion damage.

The damage resulting from airfoil erosion has serious consequences from both an engineering and an economic standpoint. As illustrated in Figure 2, erosion is the primary cause for an increase in the Specific Fuel Consumption (SFC) of modern turbofan engines<sup>3</sup>. The efficiency of a compressor decreases as the airfoils become roughened and erode away. To compensate for the power loss, more fuel is burnt with a resulting higher turbine inlet temperature. Therefore, it is not only more expensive to operate the engine, but the life of the expensive turbine hot section can be reduced. Additionally, more frequent overhaul cycles and increased downtime add to maintenance costs.

On jet engines, the ingestion of particulate matter initially causes a roughening of the airfoil surfaces. This leads to mild aerodynamic losses<sup>4</sup> and an increased tendency to foul. As the erosion progresses, significant material removal occurs not only leading to further aerodynamic losses but also resulting in blade structural weakening. In extreme cases, as the airfoil becomes thinner, a burr can develop on the edge causing airflow disturbances which, coupled with possible resonance shifts, result in increased failure risk.

By examining eroded compressor airfoils such as the one shown in figure 3, it can be observed that particle impact occurs at both high and low impingement angles depending upon the local airflow geometry. In general, small particles are swept along with the local airflow and hit the trailing edges at low angles. Conversely, larger particles tend to travel in straight lines, ricocheting from surface to surface. Radial plots of simulated particle trajectories show that the turning blades create a centrifuging action which progressively

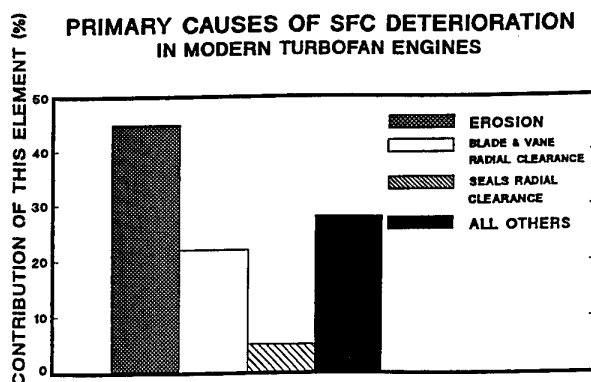


Figure 2: The loss in engine performance can be quantified in terms of specific fuel consumption (SFC) which is the additional quantity of fuel which must be burned to maintain the same output power levels. The data indicates that erosion of the airfoils has the largest influence on maintaining SFC performance in jet engines. (after reference 3)

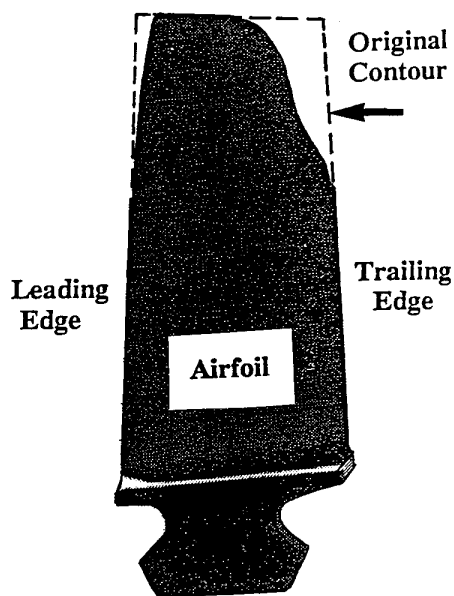


Figure 3: Eroded titanium compressor blades from an engine operated in a desert environment showing both leading and trailing edge chord loss. The dotted lines indicate the original airfoil contours.

concentrates the damage toward the outside diameter of the gas path annulus. Therefore, the initial stages tend to see a wide range of impact angles more or less uniformly across the airfoils; whereas the later stages will suffer more low angle impact at the outer radius<sup>5</sup>. It is this low angle trailing edge erosion which most seriously reduces the airfoil chord width and results in performance losses.

#### REVIEW OF EROSION MECHANISMS

The erosion response of engineering materials can be broken down into two broad types of behaviour. Materials which are softer than the eroding media and yield plastically undergo "ductile erosion." Most engineering alloys fall into the ductile erosion category. On the other hand, materials with little or no plastic behaviour, such as ceramics, which are often harder than the eroding media, undergo "brittle erosion." Many materials may exhibit a range of both kinds of behaviour depending upon the specific conditions involved. The

following discussion reviews basic models of both ductile and brittle erosion response under conditions similar to those expected in the turbine compressor environment.

#### I. Ductile Erosive Response

Metallic alloys such as those used for compressor airfoils are ductile in nature and resist erosion by absorbing the impact energy through plastic indentation. When hard particles hit smooth, solid and ductile surfaces, the surface is indented and the particle comes to a rest. The volume of material displaced by the particle is extruded in the form of a lip around the indentation as shown schematically in figure 4. Transformation of the kinetic energy into heat may locally soften and aid the extrusion mechanism. When a sharp particle impinges on the substrate at a low incidence angle, then the indentation becomes a ploughing effect. As additional particles hit the same local area, the extruded metal is subjected to a micro-cutting mechanism which results in material loss and high erosive wear rates. On the other hand, at high incident

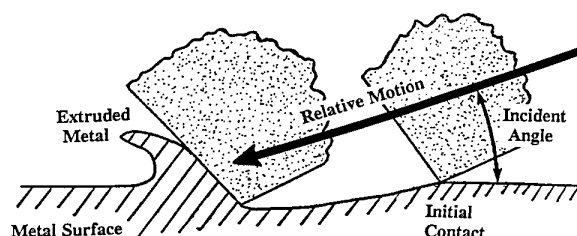


Figure 4: Schematic erosion mechanism for ductile metals. The incoming sand grain grazes the surface extruding metal ahead and to the sides. Subsequent impacts can shear off the exposed edges. (after reference 6)

angles, with smooth or large particles, the extruded material tends to be pushed back into the surface itself under multiple impacts with less material loss. As a result, the typical ductile erosion rate goes through a broad maximum at low angles near 20° while maintaining a lower rate at higher angles. The lowest erosion rate at very low angles is due to additional energy dissipation mechanisms arising from surface friction effects. The basic mechanism of erosion can be understood using Finnie's<sup>6</sup> kinetic energy erosion rate model for ductile materials. The erosion equation yields units of volume given as a function of incident angle, alpha,  $\alpha$ :

$$q = \frac{mV^2}{p\psi k} \left( \sin(2\alpha) - \frac{6}{k} \sin^2(\alpha) \right); \text{ for: } \tan(\alpha) < \frac{k}{6} \dots (1)$$

$$q = \frac{mV^2}{p\psi k} \left( \frac{k}{6} \cos^2(\alpha) \right); \text{ for: } \tan(\alpha) \geq \frac{k}{6} \dots (2)$$

where:

- q = volume of material removed by a single particle
- m = particle mass
- p = plastic flow stress
- $\psi$  = contact length to impact depth ratio
- k = tangential to normal impact force ratio
- V = impact velocity

This erosion model assumes the following conditions:

- 1) The contact length to depth ratio is constant for all angles.
- 2) The coefficient of friction is constant for all angles.

- 3) Cutting stops when the cutting tip of the particle leaves the surface.
- 4) At higher angles the particle may stop moving along the surface before it rebounds.
- 5) The erosion rate for a multiple impact situation is based on a single impact model. In actual practice this will increase the erosion rate at high angles.

The erosion curves predicted by equations 1 and 2 are plotted in figure 5. The two expressions predict the same weight loss when  $2\alpha = k/2$ . Maximum erosion rate occurs at an angle of  $2\alpha = k/3$  (18.5°). The only unknowns in the equations are  $\psi$  and  $k$ . Finnie uses  $\psi = 2$  and  $k = 2$  for angular abrasive particles.

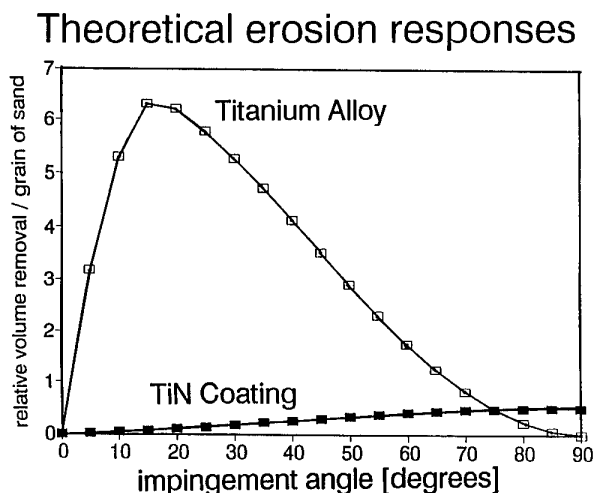


Figure 5: Erosion response curves generated the ductile and brittle erosion models exhibit somewhat complementary behaviour. Hard materials such as TiN have excellent low angle erosion resistance while ductile substrate alloys resist high angle erosion better.

## II. Brittle Erosive Response

Quantifying the erosion behaviour for hard brittle ceramic materials also requires an energy model to understand how the erosion rate changes as a function of impingement angle. In this case, hard, brittle materials are not appreciably indented and at low impact angles, the particles rebound elastically. Brittle materials, which undergo only limited plastic deformation, absorb the energy of high angle impact by the process of new surface generation. Localised crushing and fine networks of radial and lateral cracks develop shown as schematically in figure 6. During successive adjacent impacts, these cracks can grow and link to allow material loss<sup>7</sup>.

Evans and co-workers<sup>18</sup> developed an erosion model for material removal by a single round particle impacting on a solid, brittle surface. The erosion rate,  $\epsilon_1$ , is determined by the following mechanical factors:

- $V$  = velocity of impacting particles.
- $R$  = radius of impacting particles.
- $\zeta$  = density of impacting particles.
- $K_{IC}$  = toughness of target material.
- $H_t$  = indentation hardness of target material.

The erosion rate was found to be inversely proportional to the indentation hardness and the fracture toughness given by:

$$\epsilon_1 = V^m R^n \zeta^1 K_{IC}^\alpha H_t^\beta \dots \dots \dots (3)$$

where the exponents;  $m$ ,  $n$ ,  $1$ ,  $\alpha$ , and  $\beta$  have values of; 3.2, 3.7, 0.25, -1.3, and -0.25 respectively as predicted by the dynamic model of Evans.

Hockey et al<sup>9</sup> modified the Evans model to predict the total erosion rate at any given impact angle,  $\alpha$ , for a fixed velocity. This model assumes that the surface shear stresses due to an oblique angle impact may be neglected and only the vertical velocity component is considered. This relation is given by Sue<sup>10</sup>

$$\epsilon_\alpha = \epsilon_1 \sin^m(\alpha) \dots \dots \dots (4)$$

where the exponent,  $m$ , is equal to 1.62 for TiN.

In contrast to a ductile metallic substrate, the erosion rate of a brittle material is negligible at low angles and rises almost linearly with impingement angle, as shown in figure 5. There are deviations caused by the surface roughening "in situ," with a resultant change of actual incidence angles. If the material is sufficiently hard, some of the impact energy will be absorbed by the shattering or deformation of the particle rather than the surface. Similarly, high toughness is useful in limiting the extent of the crack networks and their growth rates. This mechanism works best for fully dense, smooth surfaces.

In practical terms, because the ductile and brittle erosive responses are largely complementary, then a compressor airfoil made of a combination of materials should perform better than one made of a single material type. A hard ceramic coating on a conventional metallic compressor airfoil would be expected to improve the erosion resistance of the airfoil to the predominantly lower angle impingement found in the compressor, even though at high angles the protection is possibly less effective.

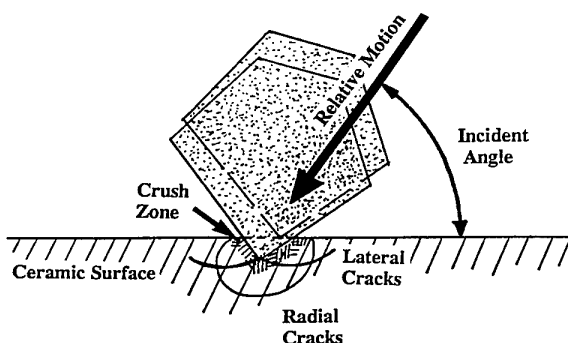


Figure 6: Schematic erosion mechanism for a brittle material illustrating the crushed zone, lateral and radial cracks caused by particle impact at the ceramic surface. The linking of these crack networks allows material loss.

## EROSION RESISTANT MATERIALS

Some basic properties of potential erosion resistant coating materials are listed in Table I. For example, ceramic oxides, typified by glasses and alumina, have medium hardness but low toughness, and generally exhibit poor adhesion when applied in thick layers. The plasma sprayed coatings such as tungsten carbide and chromium carbide tend to be heavy, thick, and have only moderate hardness. In addition, the sprayed coatings can have a rough surface that may be detrimental to the aerothermodynamic performance. Plated metals such as chromium and nickel are smooth but only marginally harder than the base metals. Alternatively, the vapour deposited

engineering ceramics, such as the nitrides, borides, and carbides have very high hardness and toughness, coupled with low density and smoothness. Coatings of TiN have been demonstrated to have good adhesion to compressor materials, which are also listed at the bottom of table I for comparison.

In order to be effective, a protective coating for compressor airfoils should, first of all, have good erosion resistance. This implies a hardness greater than silica which is the principal erodent, and a toughness as high as possible to improve the impact resistance at high angles. Secondly, the coating must adhere well to the base metals and ideally should also have a coefficient of thermal expansion (CTE) similar to that of the substrate material. In addition, the coating should be smooth and uniform in thickness, and capable of conforming to blade geometries and sharp edges without requiring additional grinding or polishing. Finally, the application process should not damage the substrate alloy by exposure to excessively high processing temperatures or corrosive chemicals.

By comparison, the compressor coatings used at present are primarily designed for corrosion protection or airfoil surface smoothing. As such, they are typically applied as slurries to form thick coatings which, can reduce the airflow area of small airfoils and may cause a significant shift in resonance frequency of blades. Furthermore, any improvement in airfoil smoothness could be short lived because these soft coatings have characteristically poor erosion resistance, compared to the ceramic materials or even the base alloys<sup>11</sup>.

In the present study titanium nitride was chosen as a first generation erosion resistant coating because it has many of the required properties, and has already proven effective against wear in the tool industry. Titanium nitride coatings are particularly attractive because of their high hardness, good toughness and a metal-like coefficient of thermal expansion. In addition, their relatively low density and coating thickness minimized any possibility of resonant frequency shifts or aerodynamic surface effects.

Table I

PROPERTIES OF CANDIDATE EROSION  
RESISTANT MATERIALS FOR TURBINE AIRFOILS

MATERIAL	DENSITY (g cm <sup>-3</sup> )	HARDNESS (HV)	TOUGHNESS (MPa·m <sup>1/2</sup> )	THERMAL EXPANSION (X10 <sup>-6</sup> /K)	BOND STRENGTH
Glass	2.5	500	0.8	3 - 5	poor
Alumina	4	2100	3 - 4	8	poor
Plasma Spray Zirconia	7.3	low	1 - 3	8 - 11	poor
D-Gun Tungsten Carbide	6.7	780-1000	-	10	excellent
Titanium Nitride	5.4	2300	3	9.4	excellent
Silicon Carbide	3.2	2600	6	5.8	poor
Silicon Nitride	3.2	1800	5	3	poor
Titanium Alloys	4.5	700	High	9	-
Stainless Steels	7.8	600	High	11 - 14	-

#### EROSION RESISTANT COATING LIFE MODEL

To test the potential for erosion prevention in a turbine compressor, a two dimensional computer simulation estimated the erosion behaviour of both conventional and TiN coated compressor airfoils<sup>12</sup>. In the simulation, quartz particles of

uniform size impinged on the airfoil surface at incident angles typical of the compressor blade shown in figure 7. Fixed masses of particles (40 kg/m<sup>2</sup> of 20 μm quartz per iteration) were evenly distributed over the surface with the erosion rate being governed by the appropriate equation discussed in the previous sections. For the coated blade, the brittle equation was applied using physical constants for TiN. After each iteration the surface recession was calculated, and if the ceramic to metal interface had been reached, then the governing equation switched to that of ductile titanium alloy. Calculations were terminated when the chord length was reduced by 1.8% as illustrated in figure 7 (1.8% is a typical erosion damage limit for the blade geometry utilized). For a conventional blade, the ductile equations were applied from the onset. When the chord loss limit was reached, the blade life was taken as the mass of sand,  $M_{max}$ , required to inflict the damage. The calculations were repeated for several coating thicknesses resulting in the component life curve shown in figure 8 which will be further discussed later.

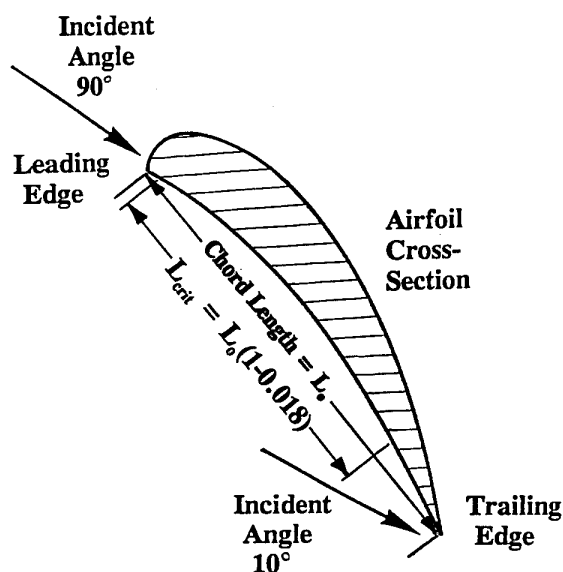


Figure 7: Schematic diagram of sand impingement upon a compressor blade showing the varying incidence angle and the chord length change associated with expiry of useful erosion life.

#### PROCESS DEVELOPMENT

TiN coatings can be produced using various deposition technologies. Reactive Ion Coating (RIC), a Physical Vapour Deposition (PVD) system, was chosen for compressor applications because of its ability to coat reasonably complex geometries at low temperatures<sup>13</sup>. A wide range of microstructure and stoichiometry can be produced using the RIC process<sup>14</sup> which allows the coating to be optimized for erosion. The use of an electron beam heated pool, instead of an arc source, results in fewer metallic splashes or defects being incorporated into the film<sup>15</sup>. Additionally, the electron beam can be used to melt various forms of stock materials and the process does not require expensive pre-manufactured targets as used by the arc and sputtering processes. The reactive ion coating (RIC) process uses relatively low temperatures (400-500°C) which do not alter the microstructure and mechanical properties of most compressor alloys,

As illustrated in Figure 9, the process takes place in a vacuum

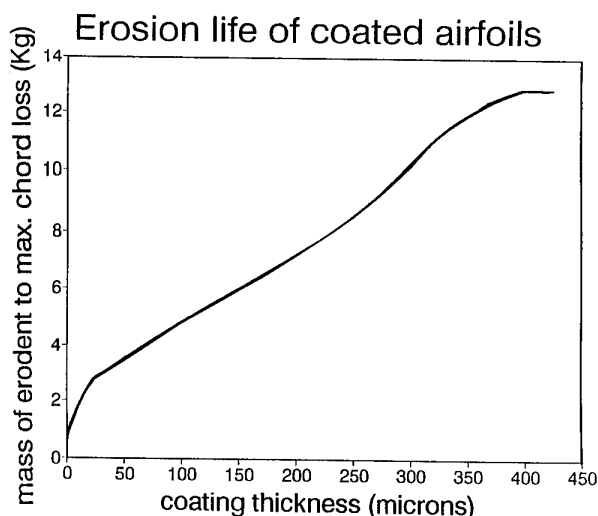


Figure 8: Calculated erosion life of titanium nitride coated airfoils. The erosion life limit was computed as mass of sand required to remove 1.8% of the original chord width. The tolerance of the uncoated blade (0  $\mu\text{m}$ ) was 0.7 kg of sand while the 10  $\mu\text{m}$  coated blade had double the life.

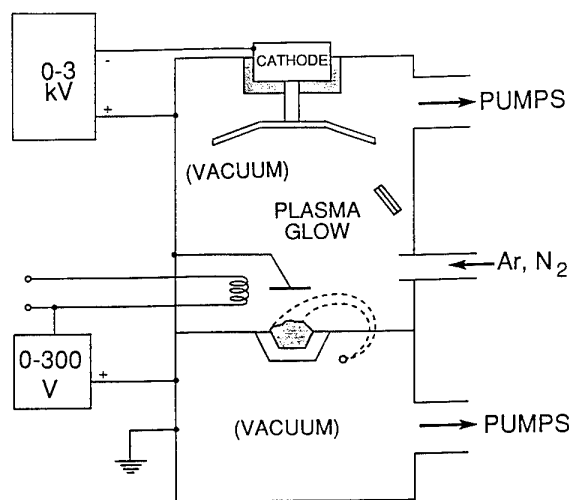


Figure 9: Schematic diagram of the Liburdi Engineering Reactive Ion Coating (RIC) apparatus illustrating the major features such as the electron beam evaporator and the additional filaments used to enhance the plasma conditions.

chamber with the components suspended from a rack above a titanium filled crucible. One unique feature of the RIC process is the additional tungsten filaments which act as thermionic emitters, injecting extra electrons into the process gas to generate a more stable plasma<sup>13</sup>. During operation, the titanium is melted by a focused electron beam originating from another tungsten cathode and magnetically deflected into the crucible. A shutter placed over the molten Titanium pool prevents splashing of molten titanium directly onto the components but allows the vapour to reach the component surfaces where it reacts with bombarding nitrogen atoms and ions to form titanium nitride<sup>14</sup>. An oscillating crystal deposition monitor is used to measure the coating growth rate while the coating conditions are controlled and recorded by a computer.

Before applying TiN to engine hardware, the coating's erosion resistance was optimized in a two step procedure. Starting from a recipe similar to standard TiN coating used on cutting tools<sup>16</sup>, the first optimization focused on adhesion and coating thickness, while the second optimization addressed stoichiometry and microstructural aspects. The overall result is a unique TiN coating with excellent erosion characteristics.

### I. Laboratory Characterization of TiN Coatings

The erosion response of the coatings was tested and confirmed to be of the brittle type. Plots of the erosion rate as a function of the incidence angle in figure 10 show similar curves to those predicted. These erosion results were generated by projecting angular alumina particles of an average size of 50 micrometers, through a nozzle, at impingement angles between 12° and 90° and measuring the resultant weight loss of coated metal coupons. Each test was carried out with only a small amount of sand to ensure that the coating was not penetrated. The mass of coating lost was converted to volume by assuming a density of 5.4 g/cm<sup>3</sup> for TiN. Plots of uncoated Ti-6Al-4V substrate are included to verify the ductile mechanism as well. The data show that significant improvements have been achieved when compared to uncoated material (similar results were achieved for 17-4ph stainless steel). By repeatedly erosion testing the same spot on a coated coupon, the erosion life of the titanium nitride was determined. The end of the erosion test was defined as a fixed mass loss of 15 mg, when the erosion area was showing essentially bare metal. The resulting plot, Figure 11, shows that the erosion rate is not strongly influenced by the coating thickness above a minimum of 5  $\mu\text{m}$ , and that the life extends roughly linearly with thickness, as predicted by the erosion model.

Samples of various TiN coatings were also examined by x-ray diffraction (XRD) to determine the crystalline phases present. The dominant peaks were of TiN, with smaller alpha titanium peaks which were attributed to the titanium substrate. On thin coatings, substrate peaks could also be recognised. Using the interplanar spacing from the XRD data, the lattice parameter for the titanium nitride was determined to be 0.4274  $\pm$  0.0010 nm on Ti-6Al-4V titanium substrates and 0.4262  $\pm$  0.0013 nm on 17-4 ph stainless steel substrates. By etching away the substrate, TiN powder samples were collected for analysis. The lattice parameter of the powder samples, 0.4239  $\pm$  0.0005 nm compares favourably with 0.4240  $\pm$  0.0005 nm, obtained for a commercial powder<sup>17</sup>.

### Experimental erosion responses

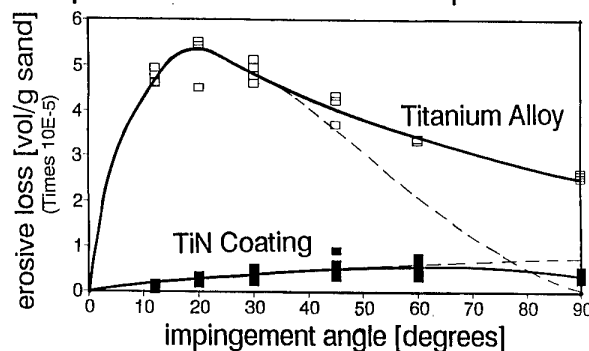


Figure 10: Experimental erosion tests of bare titanium alloy and titanium nitride coated titanium coupons. Care was taken to ensure that the coating was not breached during any of the tests at any angles. The dotted line illustrates the deviation from a theoretical erosion curve due to the influence of "in situ" surface roughening.

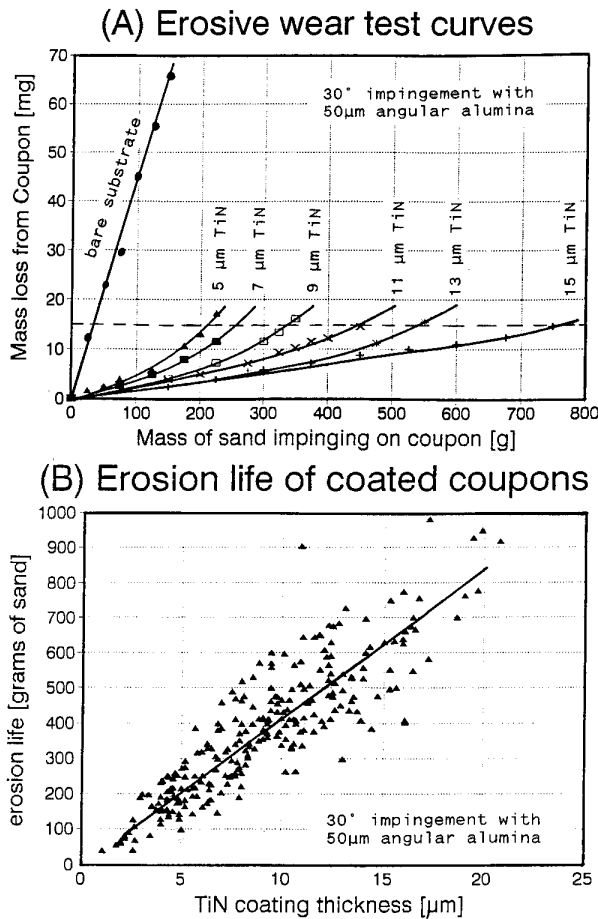


Figure 11: (A) The erosive wear rate of TiN coated coupons increases as the coating is consumed. A fixed mass loss of 15 mg was used as a reference point to define the "erosion life". (B) A plot of erosion life for coatings of various thicknesses shows a linear dependence above 5 μm.

The microhardness of the coating was measured on both the experimental and production batches using a conventional Vickers indentation hardness technique<sup>18</sup> with a 25g load. For experimental batches, a range of both hardness and erosion rates was observed (figure 12) with a parabolic relationship between them. For the optimised production batches, the measured microhardness was 3970 HV<sub>0.025</sub> with a standard deviation of 1230 HV<sub>0.025</sub>.

The influence of the coating on the natural frequency of compressor blades made of 17-4PH stainless steel was assessed and was found to be inconsequential. The coating caused a slight shift in frequency, of less than 1%, which is well within the range of scatter in natural frequency for new blades. This frequency shift is significantly less than that caused by blade erosion during service, as measured on service-exposed uncoated blades. The shift is also less than those associated with current thicker and/or heavier compressor coatings.

The influence of the coating on the fatigue properties of two blade alloys (17-4PH and Ti-6Al-4V) was also assessed through tests on both rotating bending bar specimens (for both alloys) and compressor blades (for 17-4PH blades only). The rotating bending fatigue test results indicated that there was no fatigue penalty associated with the coating. The 17-4PH compressor blades were tested by clamping their dovetails to

simulate the disc/dovetail contact loads arising from disc rotation and then by exciting the airfoils on a shaker table at their natural frequency. The tests were performed at constant root stress until failure or run-out ( $6 \times 10^7$  cycles) occurred. The Weibull distribution, shown in Figure 13, indicates that the coating has no deleterious effects on the fatigue strength of the blade at 90 ksi root stress. More recent fatigue test results indicate that the fatigue strength of the coated blades is marginally higher than that of uncoated blades.

## II. Engine Application

In collaboration with the Structures, Materials and Propulsion Laboratory of the Institute for Aerospace Research, National Research Council of Canada, RIC coatings were applied to the compressor of the medium-sized Allison T56 turboshaft engine<sup>19</sup>. The program involved coating the blades and vanes from a new engine and assessing the changes in aerodynamic performance, resulting from both the overhaul process and the addition of the TiN coating. After the compressor was stripped down, the blades and vanes were lightly glass bead blasted at 140 kPa to remove the black oxide layer present on the new parts, in order to improve the adhesion of the coating. The blades were fixtured for coating such that the complete airfoil, including the fillet and platform could be coated, while the shank and dovetail were protected by suitable masking. The various stages in the complete compressor set were grouped into similar sized airfoils and dovetails, and coated in several large batches. The T56 stator stages consisted of vane segments and were coated as half rings with the inner diameter masked to facilitate the subsequent seal brazing operation. Sample blades were included in each coating batch and tested for erosion and metallographic features.

Prior to coating, the parts were finished to the required surface smoothness and cleaned to remove any contaminants that could affect adhesion of the coating. The finishing and cleaning operations are particularly important since the thin coating will mirror the original surface and therefore the coated airfoils do not require any further polishing.

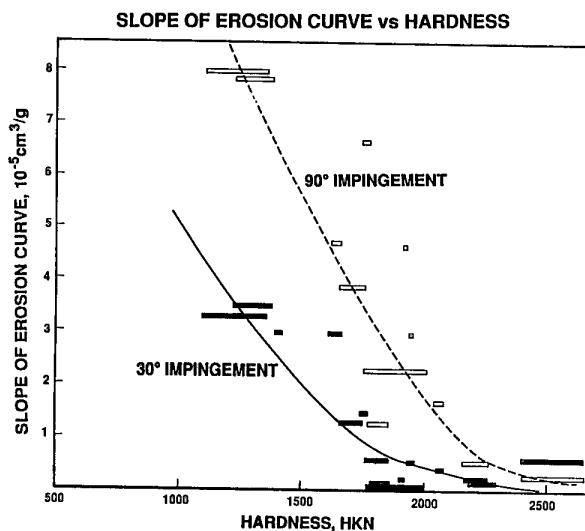


Figure 12: Erosion tests of various experimental coatings show the co-relation between the indentation hardness and the erosion rates found during the optimisation process.

## Weibull Analysis

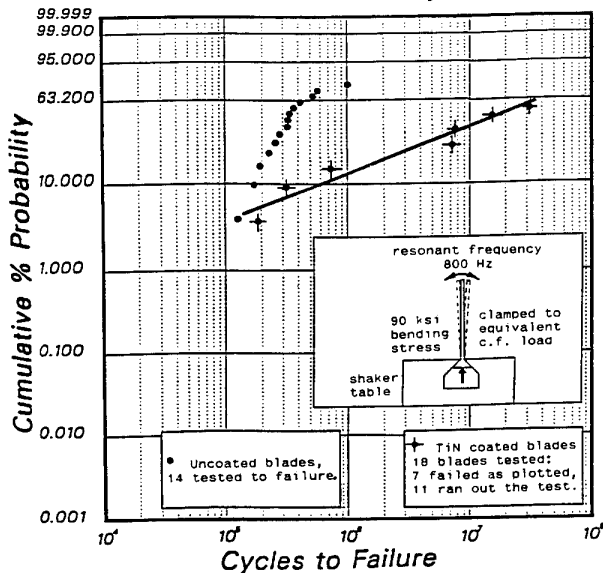


Figure 13: Weibull plot of fatigue test results for coated and uncoated stainless steel blades indicate that there is no significant change in fatigue life due to the thin RIC coating.

## DISCUSSION

### I. Erosion Model

The erosion lives of the titanium nitride coated airfoils, were estimated by the computer simulation. The blade life was determined on the basis of the total mass of sand,  $M_{max}$ , withstood in each case<sup>12</sup>. The simulation showed a non-linear variation of  $M_{max}$  with the coating thickness (figure 8). The non-linearity is caused by the shift in surface recession from mostly trailing edge damage for bare and thin coatings to mostly leading edge damage for thicker coatings. The trailing edge damage is consistent with blade erosion contours found in service as was shown in figure 1. Above a critical thickness of 28  $\mu\text{m}$ , the trailing edge metal was no longer exposed to the erosive media. In this case, chord loss was from the leading edge alone where high angle impingement is prevalent. No limit to the erosion life improvement was found until the coating became impractically thick from both a processing (cost) and application (airflow restriction) point of view.

This model is expected to be conservative because the experimental erosion rate for titanium was found to be larger at high angle than that predicted by the theory. Conversely the high angle erosion rate of the titanium nitride was found to be smaller than predicted from theory. This is shown in figure 10 where the dashed lines represent the theoretical behaviour to be compared to the actual behaviour.

### II. Characterization

The TiN coating's erosion response agrees qualitatively with the experimental models. Quantitative comparisons cannot be made because the model uses smaller quartz particles typical of that expected to be ingested into compressors, while the erosion tests were accelerated by using larger and more aggressive alumina grit. Slight deviations of the erosion response curves can be explained by inevitable changes from the initial erosion conditions caused by impact roughening and material loss.

The shift in lattice parameter measured on the experimental coatings from that of the detached powders could be attributed to a state of residual compressive stress which has both thermal and intrinsic components. The thermal component is derived from the CTE mismatch and temperature change from processing to ambient. After accounting for the thermal component, the coatings are still found to have an intrinsic compressive stress which probably arises from the atomic peening action of the plasma upon the growing film<sup>20,21</sup>. This residual compressive stress is thought to increase the coating hardness, and indeed, those films exhibiting higher residual stress levels in the pure TiN phase had the most favourable erosion resistant characteristics.

In future applications of TiN, special cleaning procedures have been implemented to ensure that the airfoil surfaces are smooth prior to coating so that the ceramic film can replicate and maintain an aerodynamically smooth surface. In service, the hard coating should protect the softer substrate against accelerated roughening and, possibly fouling, which would translate to improved SFC performance and reduced airfoil replacement frequency.

### III. Engine Performance Testing

As compressor coatings could potentially alter engine performance by virtue of their application thickness and surface quality, it was decided to quantify any performance changes that might occur on an Allison T56 turboprop engine, after coating the compressor blades and vanes with TiN. Engine performance testing was carried out in a test bed in the Institute for Aerospace Research, National Research Council, Canada, in Ottawa. The results of this study are detailed in a separate publication<sup>19</sup>.

To establish the effects of applying a coating the compressor on overall engine performance, it was first important to establish the effects of rebuilding the compressor. A comparison of three rebuilds was chosen. Baseline testing of the engine was performed to establish the "as received" condition of the engine. Performance signatures of the overall engine and its individual components were then quantified.

After the baseline testing was completed, the engine was sent to the overhaul contractor to be disassembled and rebuilt following normal procedures. The engine was retested using the same procedures used in the baseline tests. This process was repeated for a second and third rebuild. Following the third rebuild testing, the engine was returned to the overhaul contractor for rebuilding and TiN coating of the compressor. The testing after the third rebuild became the reference condition for the post-coating testing.

A total of fourteen engine parameters were used to evaluate the performance of the engine and its individual components. An overall repeatability for each parameter was established from the data gathered during the rebuild study. This repeatability represents the maximum variation in performance of the engine due to the random tolerance changes which occur during a normal compressor rebuild. The most significant tolerance changes were the blade tip to casing clearances. With this information, the effects of the compressor coating could be isolated from the effects of the rebuild process.

The actual performance deviations between the pre-coating and post-coating tests are given in Table II. For comparison, the overall repeatability and calculated measurement uncertainties are also listed. The results indicated that for most parameters, the performance changes were less than the overall

Table II  
EFFECTS OF TiN COATING ON ENGINE PERFORMANCE  
(MacLeod and Laflamme, ref. 19)

	OVERALL DEVIATION (%)	DEVIATION (%)	PARAMETER UNCERTAINTY (%)
Compressor efficiency	0.41	-0.20	0.87
Corrected airflow	0.43	-1.00	0.27
Corrected fuel flow	0.44	+0.23	0.43
Corrected output power	0.97	+0.38	1.42
Specific fuel consumption	1.35	-0.15	1.52
Corrected speed	0.30	-0.10	0.13
Compressor pressure ratio	0.38	-0.86	0.25
Compressor temperature ratio	0.24	-0.17	0.40
Turbine efficiency	1.00	-0.65	0.90
Combustor temperature ratio	0.12	+0.18	0.49
Combustor pressure ratio	0.31	+0.72	0.35
Engine temperature ratio	0.64	+0.39	0.40
Engine pressure ratio	0.49	-0.43	0.12
Corrected torque	1.03	+0.63	1.41

repeatability determined during the rebuild study. This would suggest that the TiN compressor coating did not have any significant effect on the engine performance. Close examination of the performance shifts indicated that certain performance parameters shifted in a fashion which contradicted the expected changes resulting from rebuild tolerance measurements of the compressor tip clearances after the TiN coating had been applied. At the time, it was speculated that a build-up of coating material on the leading and trailing edges of the blades could account for the slight performance changes. However, there is no direct evidence to support this claim.

The results of the engine testing with coated compressor blades indicated that for the engine user, the effects of the coating on the performance on the engine are less than, or equal to the effects of rebuilding the compressor alone. For the users of coated engine parts, it is unlikely that the aerothermodynamic effects of the TiN coating would be detected during field use.

## CONCLUSIONS

Erosion resistant titanium nitride coatings applied to compressor airfoils should enhance their useful life, as predicted from a computer simulation using appropriate erosion models. The life enhancement increases significantly with the thickness of the applied coatings up to about 20  $\mu\text{m}$ . At this thickness, the expected life extension is three fold. Above 20  $\mu\text{m}$  thickness, the rate of improvement decreases as the location of major material loss is shifted from the trailing to the leading edge exclusively.

Laboratory tests and engine qualification tests carried out on a test bed engine confirmed that titanium nitride coatings can be successfully applied to existing compressor designs, without adversely affecting their mechanical properties or aerodynamic characteristics. The comparatively thin coatings do not alter the natural frequency of the blades and if properly applied, should not reduce their fatigue resistance.

The Reactive Ion Coating process has demonstrated its unique ability to produce hard, adherent, erosion resistant coatings on actual engine hardware. The equipment and tooling was scaled to coat all the blades and vanes of the T56 axial compressor with acceptable results. Engine testing confirmed that the aerodynamic effects of the initial coating on new engine performance are insignificant and are unlikely to be detected during field use.

## ACKNOWLEDGEMENT

This project was conducted under a joint Collaborative Research Agreement between Liburdi Engineering and the Institute for Aerospace Research of the National Research Council of Canada under financial assistance from NRC's, Industrial Research Assistance Programme and from the Department of National Defence.

The authors express their grateful thanks to J. Chander, Senior Project Manager, IRAP, for his interest and support in this work, to J. Liburdi for his continued support and involvement, and to G.P.D'Alessio for his erosion model calculations.

## REFERENCES

1. Tuitt, D.A., Proc. 4th Internat. Conf. on Rain Erosion and Associated Phenomena, edited by Fyall, A.A., King, R.B., Meersburg, Germany, 1974.
2. Abdelrazik, A., Cheney, P., "Compressor Cleaning Effectiveness for Marine Gas Turbines", Canadian Gas Assoc. Symp. on Industrial Appl. of Gas Turbines, Banff, Alberta, 1991.
3. Kleinert, G., "Turbofan Engine Maintenance for Fuel and Hardware Conservation", Sermatech Review, No. 33, (1990) pp2-3.
4. Bammert, K., Sandstede, H., "Influences of Manufacturing Tolerances and Surface Roughness of Blades on the Performance of Turbines", J. of Engineering for Power, 98, (1976) pp29-36.
5. Tabakoff, W., Lakshminarasimha, A.N., Pasin, M., "Simulation of Compressor Performance Deterioration Due to Erosion", ASME J. of Turbomachinery, 122, (1990) pp78-83.
6. Finnie, I., "Erosion of Surfaces By Solid Particles", Wear, 3, (1960) pp87-103.
7. Wiederhorn, S.M., Hockey, B.J., "Effect of Material Parameters on the Erosion Resistance of Brittle Materials", J. Mater. Sci., 18, (1983) pp766-780.
8. Evans, A.G., Gulden, M.E., Rosenblatt, M.E., Proc. of the Royal Society, (London), A 361 (1978) pp343.
9. Hockey, B.J., Wiederhorn, S.M., Johnson, H., "Erosion of Brittle Materials by Solid Particle Impact," Institute for Materials Research, National Bureau of Standards, Washington, D.C. 20234.
10. Sue, J.A., Troue, H.H. "High Temperature Erosion Behaviour of Titanium Nitride and Zirconium Nitride Coatings," International Conference on Metallurgical Coatings and Thin Films, San Diego, California, 22-26 April 1991.
11. Parameswaran, V.R., Nagy, D.R., Immariageon, J-P., Chow, D., Morphy, D., "Erosion Resistant Coatings for Compressor Applications", International Symposium on Advances in Gas Turbine Engine Materials, Ottawa, Canada, 1991.
12. D'Alessio, G.P., Nagy, D.R., "Performance of Erosion Resistant Coatings for Compressor Airfoils", Journal of the Canadian Ceramic Society, 63, (1994) pp59-63.



13. Sulonen, M.S., Korhonen, A.S., "TiN coatings Deposited by Triode Ion Plating on Tools and Dies," *Annals of the CIRP*, 35, (1986) pp133-136.

14. Fleischer, W., Schulze, D., Wilberg, R., Lunk, A., Schrade, F., "Reactive Ion Plating With Auxiliary Discharge and the Influence of the Deposition Conditions on the Formation and Properties of TiN Films", *Thin Solid Films*, 63, (1979) pp347-356.

15. Håkansson, G., Hultman, L., Sundgren, J-E., Greene, J.E., Münz, W-D., "Microstructure of TiN films grown by various PVD techniques", *Surface and Coatings Technology*, 48, (1991) pp51-67.

16. Molarius, J.M., Korhonen, A.S., Harju, E., Lappalainen, R., "Comparison of Cutting Performance of Ion-Plated NbN, ZrN, TiN and (Ti,Al)N Coatings," *Surface and Coatings Technology*, 33, (1987) pp117-132.

17. TiN powder courtesy of Tioxide Inc., Mississauga, Ontario, Canada.

18. Standard Test Method for Microhardness of Materials, ASTM E382.

19. MacLeod, J.D., LaFlamme, J.C.G., "Compressor Coating Effects on Gas Turbine Engine Performance", *ASME Journal of Engineering for Gas Turbines and Power*, 113, (1991) pp530-534.

20. Knotek, O., Elsing, R., Kramer, G., Jungblut, F., "On the Origin of Compressive Stress in PVD Coatings - an Explicative Model", *Surface and Coatings Technology*, 46, (1991) pp265-274.

21. Rickerby, D.S., Bull, S.J., Jones, A.M., Cullen, F.L., Bellamy, B.A., "High Temperature X-Ray Diffraction Studies of PVD Titanium Nitride," *Surface Coatings and Technology*, 39/40, (1989) pp397-408.

## QUESTIONS

### **DARRELL MANN (UK)**

- Q. Your erosion tests were carried out at impact velocities markedly lower than those seen in actual turbomachinery. How, therefore, do you justify the life improvement claims for your costing?  
You also commented that protection of blade leading edges was difficult. Bearing in mind that the tendency on modern, high-work compressors is likely to be towards less trailing edge and greater leading edge erosion, how do you anticipate coatings technology will progress to tackle the problem?
- A. The erosion life model I have presented is intended to illustrate the key concepts behind the protection of a compressor blade with a ceramic coating. Actual engineering testing, including some by Professor Tabakoff's group, has also been performed but is proprietary to the engine companies involved. The actual engine performance is such a very complex issue that I doubt that any erosion test could predict it fully.  
For your second question: you are correct, the engines we are presently testing are relatively old. Nevertheless, they are by no means no longer useful. But maybe because they are older, they primarily suffer trailing edge erosion. I would suggest that leading-edge erosion may require re-optimization of the coating to increase its toughness and possibly thickness. The advantage of the Reactive Ion Coating process is its ability to do just that by independently controlling the coating ion species, their density and energy levels.

### **HENK KOLKMAN (NLR)**

- Q. TiN is considerably more noble than the 17 - 4 PH base metal. This gives rise to the following two questions:
- i) In one of your slides, this coating was applied to the tips of the blades only. I would expect severe corrosion of the base metal near the boundary of coated and uncoated material, if the base metal were 17 - 4 PH steel. Hence my question: Are the blades in the Allison T56 application coated entirely, or on the tips only.
  - ii) TiN coatings usually contain defects through which the aggressive environment can reach the base metal, resulting in pitting corrosion. Please comment.
- A.
- i) For the Allison T56 engine application, the whole airfoil was coated, including the platform.
  - ii) For the T-56 application in the C-130 transport, over 3,000 aircraft have been sold and they fly all over the world. But if you look at the engines at overhaul, it is clear that some operators are in corrosive environments (such as yourself). Others (such as the Middle-East operators) are in erosion dominated environments. Our application testing will take place in an erosive environment with the participation of Allison Engine Company.

## New Trends in Coatings Developments for turbine blades : Materials Processing and Repair

S. Alperine<sup>†</sup>, R. Martinou<sup>†</sup>, R. Mévrel<sup>‡</sup> and J.P. Huchin<sup>\*</sup>

<sup>†</sup> SNECMA, Materials and Process Department  
BP 81, 91003 EVRY Cedex, France

<sup>‡</sup> ONERA Materials Science Department  
BP 72, 92322 Châtillon, France

<sup>\*</sup> SOCHATA ZI Nord, rue Maryse Bastié  
BP 129, 86101 Châtelleraut Cedex, France

### ABSTRACT

Turbine engines for aeronautic applications now have to face strenuous requirements concerning not only operating performances but also reliability and reparability. This evolution of the specifications induces important consequences regarding the choice and the design of turbine blades protective coatings. This paper presents several key features concerning the deposition techniques and the real-life behavior of such coatings :

- Complex aluminides well suited to the protection against high temperature oxidation and hot corrosion of directionally solidified nickel-base superalloy turbine blades,
- Ceramic coatings used as thermal barriers; they have to exhibit both high resistance to thermomechanical fatigue and adequate smoothness,
- Processing techniques for thermal barriers, including plasma spraying, electron beam physical vapor deposition and plasma enhanced chemical vapor deposition,
- Blades and coatings repair techniques.

## 1. INTRODUCTION

Aeronautic turbine engines are submitted to strenuous requirements concerning their overall performances. Not only technical goals must be met; the reliability and cost of the processes also are of utmost importance. Thus, for turbine blades, the technology has moved to an increase of the turbine inlet temperatures, associated with more and more ambitious targets concerning lifetime and maintainability. The progression of these specifications is directly dependant on the progresses made on materials properties and processing routes.

The goal of this presentation is to point out, in the more specific domain of turbine blades protective coatings, how the achievements, whether in coatings composition or application, have provided some useful answers to the evolution of components requirements. To illustrate this point, several examples are being presented,

dealing with aluminide coatings, overlays, thermal barrier coatings (TBC) as well as some specific repair techniques.

## 2. COMPLEX ALUMINIDE COATINGS

### 2.1 "Simple" aluminides and their limitations

Simple aluminides are, even today, the very most widespread protective coatings for turbine blades [1,2]. The most probable reason for this industrial success can be found in the conjunction of interesting operational properties of these coatings and a deposition process well suited for industrial needs. Thermal deposition processes are indeed non directionnal (which allows to coat with a great homogeneity oddly shaped components such as nozzle guide vanes multi-blades sectors), but also very flexible. It is possible to adapt the temperature of the deposition process so as to be compatible with most alloys thermal treatments, since

aluminizing can be carried out at temperatures as low as 750°C and as high as 1175°C. This possibility to perform simultaneously the coating process and one of the alloy thermal treatment, that offered by CVD processes to coat components in large batches, and the easy control of production quality, by introducing test samples inside the deposition retort, all lead to an attractive low fabrication cost for these coatings.

The main limitation for the use of simple aluminides for the protection of hot components in gas turbines, resides in the lack of performances they sometimes confer to nickel base superalloys, when facing hot corrosion with fused salt deposits [3]. The lack of chromium in the coatings leaves the protective alumina scale grown at their surface during exposure to high temperature, highly sensitive to basic fluxing in fused sodium sulfate, in a temperature range between 750 and 950°C (this phenomenon is known as type I hot corrosion). After a certain incubation time, which can be very short (between 100 and 300 hours), pitting corrosion appears, leading to rapid sulfidizing of the substrate (some tens hours).

In the higher temperature range, where only oxygen from the air is active in corrosion mechanisms (between 1000 and 1100°C), the protective alumina scale formed on NiAl is not extremely adherent. Its repeated cracking and spalling during thermal cycles progressively exhausts the aluminum reservoir available throughout the coating thickness. Simple aluminide coatings then perish after the appearance of non protective external oxides (NiO, spinels), that come just before an accelerated internal oxidation of the coating, then of the substrate.

## 2.2 Chromium modified aluminides

The alloys used for rotating turbine blades are nickel-based superalloys with low chromium content (< 13 wt. %), and relatively high aluminum and titanium contents ( $[Ti] + [Al] \approx 10\%$ ). Their high temperature creep resistance is mainly provided by the precipitation of an ordered  $\gamma'$  phase ( $Ni_3Al, Ti$ ), highly coherent with the  $\gamma$  matrix. The low chromium content of these alloys renders them highly sensitive to type I hot corrosion.

As mentioned above, a simple aluminide coating cannot provide satisfactory enough a protection against this type of sollicitation. If one can enrich in chromium the surface of the superalloy, in association with a regular aluminizing treatment, it is possible to significantly enhance the hot corrosion resistance of the component (see fig. 3). Several processes have been studied, aiming at simultaneously depositing aluminum and chromium on superalloy substrates. On the industrial scale, however, the most widespread process

achieves this goal in two consecutive steps, using thermochemical deposition methods : a chromizing, then an aluminizing treatment.

The chromium modified aluminide coating used at SNECMA, named C1A [4], is for instance applied on single crystal AM1 blades. Indeed, if one considers the high lifetime potential of this alloy regarding creep, it is necessary to use a protective coating capable of efficiently facing different kind of environmental aggressions. One of the difficulties encountered, while tailoring the C1A process to AM1, was the obligation to maintain the alloy's good mechanical properties. The duplex thermochemical treatment thus had to meet strenuous demands regarding the choice of such

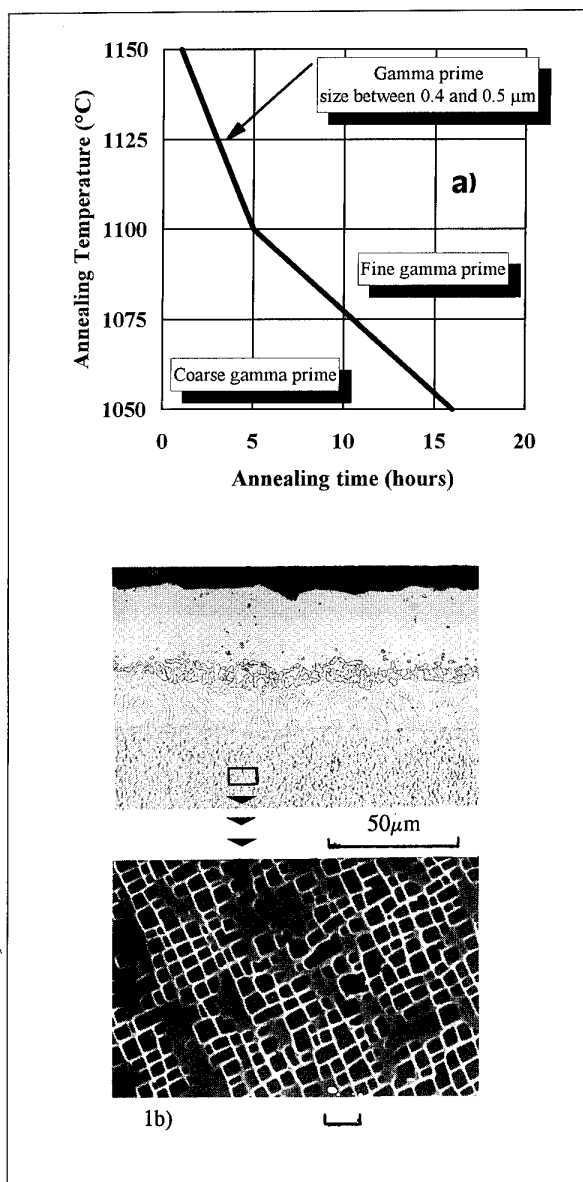


Figure 1 : Chromium modified C1A aluminide applied on AM1 single crystal superalloy ; a) Size of  $\gamma'$  precipitates as a function of thermal treatments b) Coating and  $\gamma'$  microstructure

parameters as duration, temperature and cooling rate, lest it would alter the size and microstructure of the strengthening  $\gamma'$  phase (figure 1a). The vapor phase thermochemical processes, avoiding any contact between the parts and the cement, meet this demand. The selected operating parameters (chromizing treatment during 5 hours at 1050°C plus aluminizing treatment 10 hours at 1050°C) do not alter significantly the mechanical properties of the alloy and lead to a coating (figure 1b) currently applied at the industrial stage. It is satisfactorily resistant to high temperature oxidation ( $T > 950^\circ\text{C}$ ) and to fused salt induced hot corrosion ( $750^\circ\text{C} < T < 950^\circ\text{C}$ ). This coating is a good example of the tailoring of an already known and relatively low-cost process to suit a new alloy the high mechanical properties of which had to be preserved.

### 2.3 Noble metal modified aluminides

Contrarily to the case of chromium modified aluminides, the modifying metal, in the case of noble metal modified aluminides, is provided by a plating process and not by a thermochemical one. Two different families of noble metal aluminide coatings have been developed.

#### *Platinum modified aluminides* [5,6]

The first platinum modified aluminides appeared more than twenty years ago [5]. In most cases, these coatings are processed by applying on the superalloy to be coated an electrolytic platinum plate about 8  $\mu\text{m}$  thick; partial interdiffusion between the substrate and the predeposit is then achieved through a vacuum annealing treatment, to ensure a good adherence of the predeposit. At last, the superalloy thus coated is aluminized by a pack or a vapor phase process. The fact that the solubility limit of platinum in the  $\beta$ -NiAl phase is very low at the temperature of the aluminizing treatment, leads in most cases to the formation of a complex two-phase coating, containing the intermetallic  $\text{PtAl}_2$ . It is easy to understand that according to the relative magnitude of the nickel and aluminum diffusion fluxes from each side of the initial predeposit, different repartition of these two phases can be obtained. An important consequence of this fact is that the coating structure, and in some instances its effectiveness, may significantly vary according to the aluminizing conditions, but also to the nature of the superalloy substrate.

Thus, in the process known as LDC2, the coating is composed in its external part of a continuous layer of  $\text{PtAl}_2$  intermetallic. Conversely, in the coating developed by Chromalloy under the denomination RT22, the external part is a mixture of  $\text{PtAl}_2$  in a NiAl

matrix saturated with platinum (several weight percents). The internal part of the coating is composed of a single phase. A typical micrograph of this type of coating is reproduced on figure 2a.

The main advantage of platinum, as a modifying metal, is to provide nickel aluminides with increased high temperature environmental resistance, especially in hot corrosion solicitations (figure 3). Although the mechanisms leading to such an improvement have not been entirely clarified, it is generally proposed that platinum has a marked effect on aluminum activity in the coating, but also on the resistance of the grown protective alumina scales to basic dissolution in sodium sulfate melts. It is also thought that this element enhances alumina scale adherence.

The main limitations of this family of coatings come from their structure on the one hand, and on their processing route on the other. Several authors suggest that the presence of  $\text{PtAl}_2$  intermetallic in the external part of the coating may embrittle it, which would in some instances limit its life expectation, when facing themomechanical solicitations, especially below 700°C. Besides, platinum electroplating technique is rather uneasy when complex shaped components such as turbine vanes are to be coated. It is to be mentioned that individual components like blades cannot be barrel-plated using this technique, which may have a negative incidence on the plating costs.

However, coatings such as RT22 are used in the industry on a relatively large scale, for instance for Rolls Royce engine blades (HP turbine blades of the RB211-524 engine).

#### *Palladium modified aluminides*

The design of this family of coatings is far more recent than that of platinum modified aluminides. It was initially motivated by the lower price of the latter modifying noble metal. The first attempts to design such coatings were made in the United States; they were not successful. The coatings obtained were porous and insufficiently resistant to hot corrosion [9]. More recent studies have indicated that the structural defects formerly observed were mainly due to coating hydrogen embrittlement during the aluminizing treatment [10]. It was shown that it was possible to completely avoid the formation of such defects, if the pure palladium deposit was replaced by a predeposit of Pd X wt.% Ni alloy (typically  $10 < X < 30$ ). A duplex predeposit could also be used, consisting of a pure palladium undercoat, topped by a thin layer of chromium, nickel or cobalt (only a few micrometers thick), which would act as a diffusion barrier towards hydrogen [11].

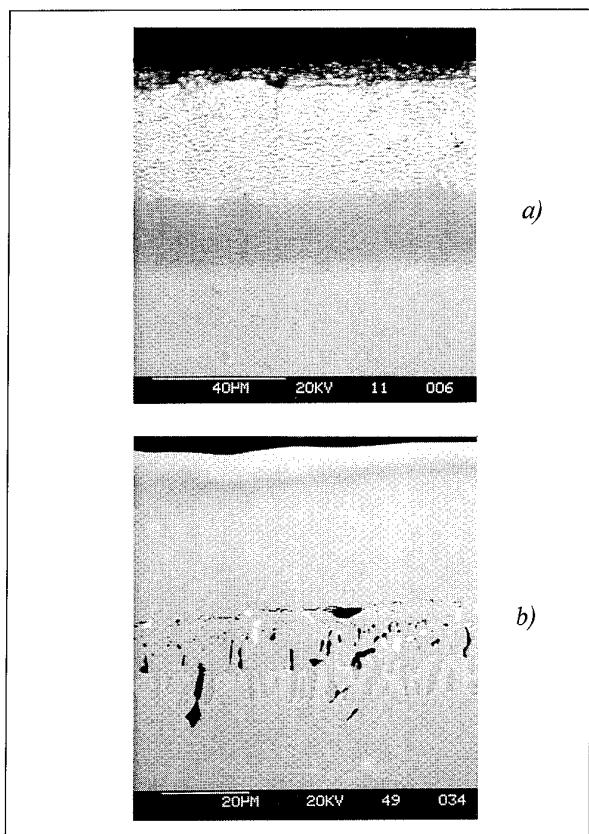


Figure 2 : Precious metal modified aluminides ; a) platinum modified aluminide RT22 on C1023 substrate b) palladium modified vapor phase aluminide on IN100 sustrate

The metallurgical structure of palladium modified aluminides significantly differs from that of their platinum counterpart. The main reason is the high solubility of Pd in the  $\beta$ -NiAl phase. Recent studies have thus shown that PdAl and NiAl were mutually soluble up to the obtention of  $(\text{Pd}_{0.7}\text{Ni}_{0.3})\text{Al}$  alloy (ie 35 mole % of Pd in NiAl). A practical consequence of this result is that all palladium modified aluminide coatings are composed of a single  $\beta$  (Ni,Pd)Al phase with a negative palladium concentration gradient from the coatings surface to the substrate (see fig. 2b). The equivalence of the crystallographic structures of simple and palladium modified aluminides is important on more than one ground. It leads to a coating structure which barely varies when the nature of the substrate superalloy or the aluminizing conditions are being varied [13] (which was not the case for platinum modified aluminides). It is thus possible to build protective coatings with very similar properties on equiax or single crystal superalloys, using pack, vapor phase or slurry type aluminizing treatments. This equivalence of structures also allows to avoid the structural problems associated with the presence of the brittle  $\text{PtAl}_2$  phase in platinum modified aluminide coatings.

The resistance of palladium modified aluminides to cyclic oxidation and hot corrosion is generally speaking very satisfactory, equivalent to that of platinum modified aluminides (see figure 3). It is thought that palladium as a solute in the  $\beta$  phase significantly increases aluminum activity as well as its diffusion coefficient in the  $\beta$  phase. It seems necessary however to determine in a more fondamental way, the role played by palladium on alumina scale growth mechanisms, but also on the resistance of those scales to basic fluxing (hot corrosion).

As far as industrial developments are concerned, palladium modified aluminides provide specific advantages. Pd-Ni alloy electrodeposits have a throwing power superior to that of platinum electroplating baths, which allows to coat homogeneously, with the appropriate set of anodes, even very complex shaped components. This type of predeposit can also be easily barrel plated (batch treatments of turbine blades). Last but not least, Pd-Ni can be selectively « brush plated » with important industrial consequences for components coatings local repair.

First industrial developments of these protective coatings have been recently performed in France, on engines components suffering from particularly severe corrosive environments. Turboméca is for instance using a slurry type palladium modified Sermaloy J coating for the second stage guide vanes of its MAKILA and ARRIEL engines ; Sochata is considering this family of coatings for the repair of APVS or C1A coatings on blades and vanes.

### 3. OVERLAY COATINGS [14]

Despite all the advantages mentionned above, diffusion coatings bear limitations essentially related to their microstructure and composition. An « ideal » protective coating may have a composition or structure impossible to achieve through diffusion treatments. To overcome this difficulty, overlay coatings of the MCrAlY type (M= Ni, Co, Fe or a combination of the above elements) could be designed, thanks to the evolution of coatings deposition processes.

The first technique used to achieve this goal, which is still widely used in the USA, is the electron beam physical vapor deposition (EBPVD). In the early eighties, controlled atmosphere plasma spraying appeared (primary vacuum or protective argon shroud). With such processes, it is possible to freely tailor a coating which would be chemically and mechanically compatible with the superalloy substrate and also resistant to the environment.

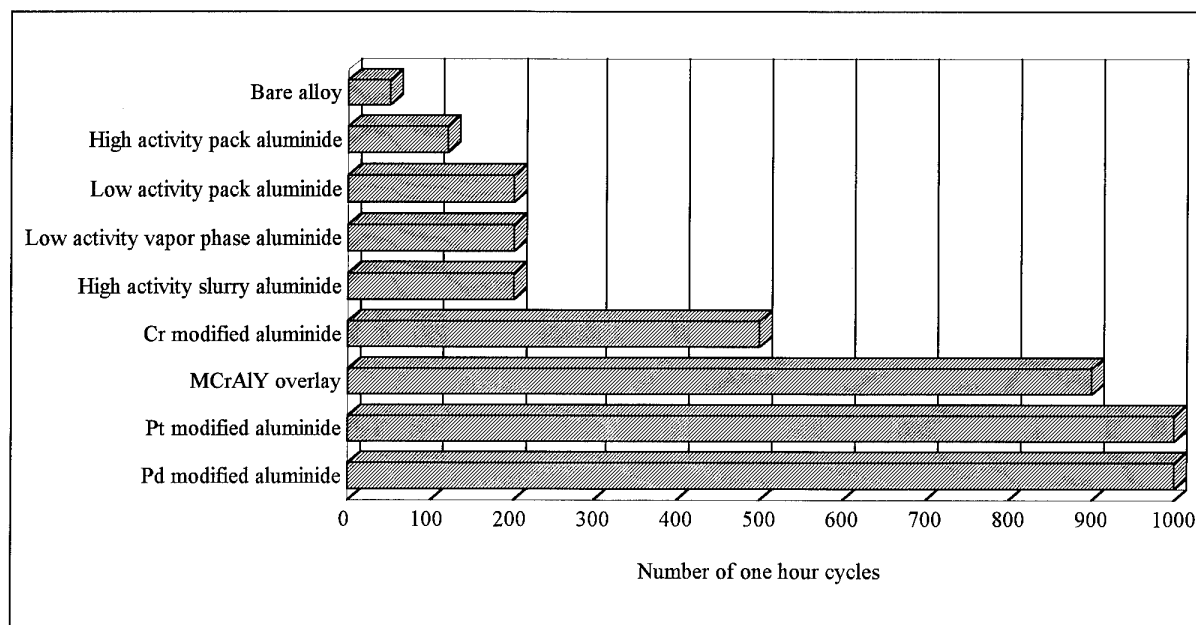


Figure 3 : Hot corrosion resistance of several protective coatings on IN100 superalloy substrate; number of one hour cycles to failure ; burner rig testing at 850°C in air + sodium sulfate

As an example, a typical MCrAlY coating is composed of nickel (base), 20 wt% Cobalt (used to avoid the deleterious  $\gamma$  Ni +  $\beta$  NiAl  $\rightarrow$   $\gamma'$  Ni<sub>3</sub>Al +  $\alpha$  Cr transformation around 1000°C), 20 to 25 % chromium (hot corrosion resistance), 6-8 % Al (to ensure alumina scale formation) and 0.5 % yttrium, the latter element being known to enhance oxide scale adhesion. According to the conditions of use, an element can be added, or its concentration modified. Thus, it can be useful, in the case of type II vanadium enhanced hot corrosion to increase chromium concentration up to 30 wt. %. Numerous MCrAlY compositions are commercially available. Some disadvantages of these coatings should however be mentioned: they are more costly than diffusion built coatings; evaporation or spraying processes are line-of-sight and coating complex shaped components can be a serious problem.

At last, it should be noted that other processes have been proposed for the obtention of MCrAlY coatings : co-electroplating, electrophoresis followed by an aluminizing consolidation treatment, triod sputtering. Although those processes are on technical, and sometimes economical grounds interesting, none has been presently industrially developed, to our knowledge; a probable explanation could be found in the difficulty to substitute to already industrially proven processes.

## 4. THERMAL BARRIERS

### 4.1. The concept

Part of the enhancement of turboengines efficiency is obtained through an increase of the gas temperatures at the turbine inlet. Such an increase has been obtained through constant enhancement of metallic materials properties but also through the design of more and more sophisticated cooling systems, for hollow blades. It should be kept in mind, indeed, that metallic turbine blades, the melting point of which is usually under 1400°C, are able to work in an environment of combustion gases at a temperature sometimes above 1600°C. A concept meant to lower the metal temperature, which has been used for more than twenty years in combustion chambers, consists of coating the components with a relatively thin thermal insulating layer (<300  $\mu$ m) that induces on the metallic surface of internally cooled blades, in steady state conditions, a temperature decrease of about 100°C (figure 4). Moreover, such a thermal barrier also provides, in transient regime, less steep temperature changes, which is a good thing for the resistance of the coated components to thermal fatigue solicitations (changes in the engines regime). The multiple interests associated with this concept are easily conceivable:

- The metallic parts may work at lower temperatures - everything being otherwise equal - with a correlative increase in creep-limited lifetimes;
- it is possible to increase the TIT (turbine inlet temperature) and thus the efficiency of the engine, keeping the same working temperature for the metallic parts;

- the air cooling rates can be decreased, or the cooling passages geometry simplified, gaining in engine efficiency and/or design and fabrication cost.

We will see that although such coatings are presently applied, at the industrial stage, on turbine vanes only, they are now seriously envisaged on rotating blades. They allow theoretically, as far as engines' thermal physics is concerned, to make a forward leap as dramatic as the one allowed by the substitution of single crystal to equiaxed superalloys. Thus, it is easily understandable that thermal barriers are presently the scope of intense research and development work in the laboratories of most engine manufacturers. The main efforts are presently focused on coatings reliability, aerothermal behavior, as well as problems dealing with costs and necessary investments.

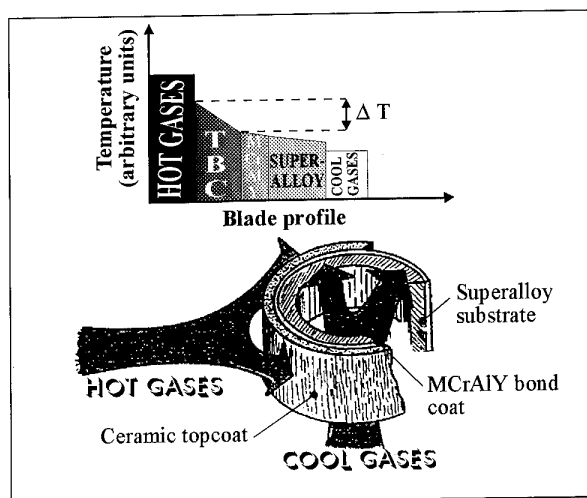


Figure 4 : Thermal barrier coating, the concept

#### 4.2 Ceramic composition, microstructure and properties

The use of thermal barriers on components sollicitated at extreme temperatures, i.e. such that the uncoated metallic components would have an extremely low potential, requires the obtention of coatings the very first quality of which is **reliability**. This reliability requires high bond coat's environmental resistance, as well as its ability to accomodate differential thermal expansion strains in the ceramic topcoat. The highest possible toughness for the ceramic part of the coating must also be aimed, since one of the most common degradation mode of thermal barrier coatings is macrocrack propagation into the ceramic [15]. The chemical nature of the ceramic layer, at last, will strongly influence its intrinsic resistance at high temperature in the presence of fused salt deposits [15]. The only systems presently envisaged for turboengines hot parts are based on partially stabilized zirconia [15]. It has been shown that among the known stabilizing agents of the zirconia cubic variety, yttrium oxide was the one that provided the highest refractarity; it is thus

the most widely used for high temperature applications. Stecura et al. [17] have first pointed out that intermediate stabilizer contents, with the formation of a variety of zirconia known as « partially stabilized », provided coating markedly more resistant to thermal fatigue (see fig.5). It has been shown since by several authors, that these good properties were closely linked to the appearance during the coating building process (especially during plasma spraying) of a non-equilibrium, non-transformable, high toughness tetragonal phase [18]. More recently, Lelait and al. [19] have proposed that the remarkably high tenacity of this  $t'$  phase could be associated with fine microstructures, linked to some mechanism blocking its return to equilibrium. The appearance during annealing treatments in the usage domain for these coatings (between 1100 and 1200°C), of fine, stable precipitates acting as crack deviators, has been described (figure 6). It can thus be said that for the choice of a ceramic system able to play the role of a thermal barrier, the possibility of obtaining non-equilibrium quenched phases is a key issue influencing coating toughness.

It has been shown that if the initial adhesion of the ceramic coating to the bondcoat is rather low, it is rapidly increased during high temperature annealing in oxidizing atmosphere, by the growth between MCrAlY and zirconia of a very adherent alumina layer. The adherence of this layer to the MCrAlY is insured by the well-known yttrium active element effect [14]. It has been shown otherwise [20], that the adherence of this alumina scale to zirconia is largely based upon an interfacial chemical reaction (zirconia reduction by aluminum cations).

The fact that thermal barrier coatings are, as built, microcracked is also a key factor explaining their good resistance to thermal shocks. The presence of this microcracks network allows the coating to accomodate more easily the compressive stresses it has to sustain during the cooling down of the superalloy + bondcoat + topcoat assembly. The topology of this network is strongly influenced by the coatings building process (intra and inter droplet space in plasma spraying, inter columnar spacing for PVD coatings), and for a given process, by various deposition parameters.

Special requirements associated with certain applications, such as the presence in burned kerosene of more or less important quantities of vanadium, sodium chloride in the ingested air, or engine use at intermediate regimes (with components skin temperatures between 700 and 950°C), have lead to examining possible interactions between the ceramic coating and fused salt media such as sulfates or vanadates. The general conclusion is that yttrium oxide is stable enough towards basic dissolution phenomena



that it can be used in type I corrosion domain (no vanadates,  $850^{\circ}\text{C} < T < 950^{\circ}\text{C}$ ) [21]. However, in more acidic fused salt environments (sulfate and vanadate induced type II hot corrosion), destabilization of zirconia by selective dissolution of  $\text{Y}_2\text{O}_3$  has been observed [22]. Stabilizing agents such as  $\text{CeO}_2$ ,  $\text{Yb}_2\text{O}_3$  or  $\text{Sc}_2\text{O}_3$  can therefore be used. A deleterious physical interaction between the fused salt and the ceramic coating has also been described [16]. It consists in crack obturation by solidified salt upon cooling, with a correlative increase of the thermal mismatch stresses applied to the ceramic.

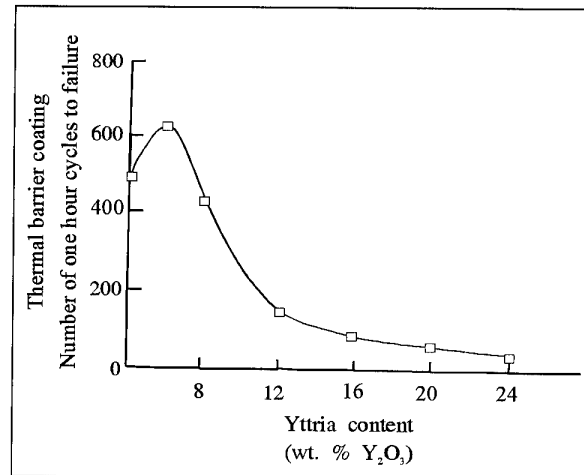


Figure 5 : life duration of zirconia thermal barrier coatings as a function of yttria content ; thermal cycling at  $1100^{\circ}\text{C}$ , from [17]

#### 4.3 Deposition processes

Thermal barriers have been deposited in combustion chambers by air plasma spraying for more than twenty years and, more recently, on turbine rings. In the latter cases, ceramic thicknesses are more important (1.5 to 2 mm). For the most performing systems the MCrAlY bondcoat is deposited by low pressure or controlled atmosphere plasma spraying. As far as thermal barriers on turbine blades are concerned, hence for more severe applications and more critical use, the EBPVD and plasma spraying processes are in competition.

Several engine manufacturers already apply thermal barriers on turbine vanes:

- Pratt & Whitney [23] on vane platforms for JT9D-7R4 engine and for all PW2000, PW4000 and V2500 engines, as well as on fixed blades airfoils (first and second stages) of PW4000.
- Rolls-Royce [24] on guide vane platforms in high pressure stages of several engines, including RB211 535-E4, equipping Boeing 747 aircrafts.

In the plasma spraying process, the material to be deposited is introduced as prealloyed powder in a plasma jet; powder grains are heated to the liquid state and accelerated towards the substrate where they splash, solidify and eventually pile up. Coating deposition rates are high. For a metallic coating such as a MCrAlY, one has to operate under a controlled atmosphere (argon shroud or primary vacuum), to avoid selective oxidation of alloying elements such as yttrium, aluminum or chromium. The coatings obtained are dense and adherent if the surface preparation is appropriate.

In the case of a ceramic coating such as yttria stabilized zirconia, the thermal stresses during individual cooling of the droplets provoke microcracking of the splats, with the formation of a characteristic lamellar structure (figure 7a), which certainly plays a useful role in the thermomechanical behavior of the thermal barrier. A surface treatment, usually tribofinishing, is required after plasma spraying to reduce coatings roughness. This step can be difficult to control, especially on thin walls.

In the EBPVD process, the material to be deposited is evaporated under the action of an electron beam, the kinetic energy of which is transformed into thermal energy. Several advantages have been claimed to the EBPVD process for thermal barrier deposition, as compared to plasma spraying : better thermal cycling resistance attributed to the columnar structure of the deposit illustrated on figure 7b, lower surface roughness compatible with the demands of aerodynamicists (this low level of roughness is also maintained in service life), better erosion resistance. This technique has essentially been developed in the USA and requires very heavy investments as well as

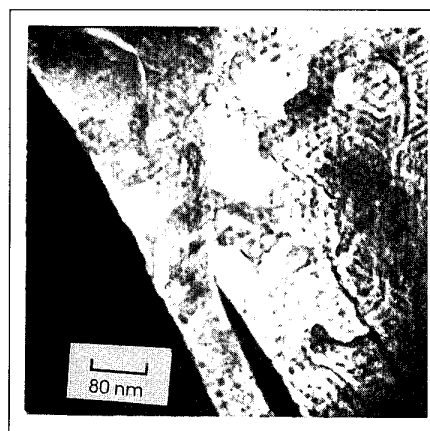


Figure 6 : Microstructure of a plasma sprayed  $\text{ZrO}_2$ -8wt.%  $\text{Y}_2\text{O}_3$  TBC annealed 100h at  $1200^{\circ}\text{C}$ ; transmission electron microscopy, dark field imaging of stable nanometric cubic precipitates in a  $t'$  matrix, acting as crack deviators.

rather high production costs. Recent information indicate that EBPVD technique would be present at a significant industrial development stage in several countries of the CEI, most particularly in Russia and Ukraine. The presence of around ten industrial operating units has been mentioned.

It should be noticed that both EBPVD and plasma spraying processes are line-of-sight. This can prevent efficient coating of some complex shape components, such as multiblades. Recently, a new process [25] has been developed at ONERA, in collaboration with the University of Paris-Sud Orsay, to build the ceramic topcoat. It consists of a CVD (Chemical Vapor Deposition) process, assisted with a microwave plasma. This process leads to oxide layers having a columnar microstructure well suited to adapt thermomechanical solicitations, with relatively high deposition rates (150  $\mu\text{m/h}$ ). It should be applicable to complex shaped components.

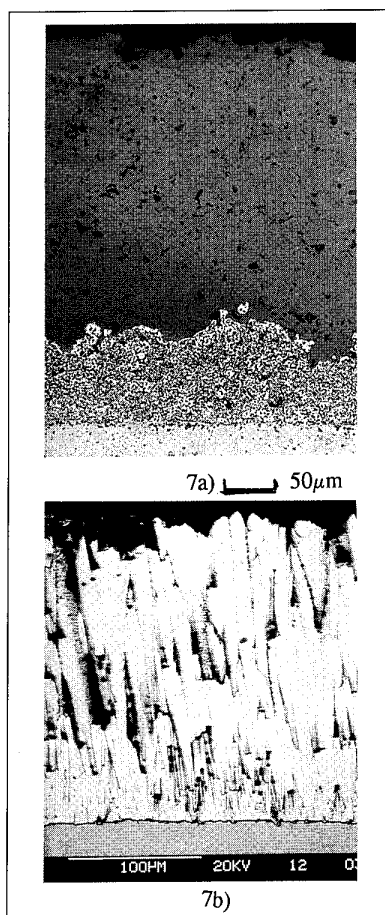


Figure 7: Examples of thermal barrier coatings, polished cross sections, scanning electron micrographs ; a) plasma spraying b) EBPVD process

#### 4.4 Modelling

An important effort on the life prediction modelling of thermal barriers has been carried out in the United States [26]. These models are generally based upon a phenomenologic approach and more work would be needed to better describe several problems, particularly the effect of geometry (roughness of the oxide/metal interface, radius of curvature of this interface), ceramic mechanical behavior, and the effect of bondcoat oxidation.

### 5 REPAIR PROCESSES

#### 5.1 Volume repair

The concept of repairing the surface of a coated component is issued from an economical consideration: that of preserving the potential of components exhibiting extended but not generalized oxido-corrosion attacks, before they have reached the life duration imposed by mechanical degradations (critical creep deformation rate, extended crack growth). Repairing the component then mainly consists of chemically stripping the corroded coating parts and applying a new protective coating. This set of operations can lead to an excessive decrease of components dimensions. On turbine vanes which may also present thermomechanical fatigue cracks, it is accepted that one can simultaneously fill up the fatigue cracks and « reconstruct » the volume depleted during the coatings stripping process. For this, after having cleaned the surface thoroughly (with processes such as high temperature fluoride treatments), one has to use reloading + diffusion brazing techniques, based on the application of alloyed powders containing eutectic former elements such as boron and/or silicon. One of the recent techniques currently applied at *Sochata Chatellerault* uses melt-spun 50 to 100  $\mu\text{m}$  thick, microcrystallized ribbons, containing low melting point elements. The thickness of the ribbons is adapted to the volume of metallic alloy to be restored and, after electric discharge welding, diffusion brazing is carried out in the 1150-1200°C temperature range, in a vacuum or controlled atmosphere furnace. Melt depressing elements diffuse into the substrate and the final product is a restored surface with a composition close to that of the substrate to be repaired, on the top of which a new protective coating can be safely built.

#### 5.2 Local surface repair

It is not always necessary to apply a total rebuilt of the surface to be repaired. In certain instances, it is advisable, for technical or economical reasons, to locally regenerate a protective coating, particularly on new components which have been incidentally scratched or impacted.

Only few industrial solutions are currently used for local repair of protective coatings. It is possible to locally aluminize components by masking or slurry techniques, but simple aluminides are in principle not good enough to provide an important new potential to the repaired parts (cf. § 2.1). One of the solutions applied in the case of components initially coated with simple aluminides, consists of chemically stripping the coating and then applying a chromium modified aluminide complete coating schedule; one then has to face the limitations quoted in the previous section.

An advantageous solution would be to apply locally, on the corroded parts, a noble metal deposit and then realuminize the whole component. The complexity of the platinum electroplating baths makes this operation in practice very difficult to perform. However, the flexibility and simplicity of palladium-nickel baths operation, make it possible to apply locally such a deposit using the « brush-plating » technique. It is then possible to realuminize part of or the whole component.

Attempts to locally repair components have shown that this simple technique could be applied with great efficiency on most of the existing metallic coatings : simple pack, slurry or vapor phase aluminides, aluminides modified by Cr, Pt and Pd, MCrAlY overlay coatings [27]. It is foreseen that this local repair technique will experience a rapid industrial development, since it fills a « technological gap » and implies only minor alterations of the surface treatment schedules presently applied on superalloy components.

## 6 CONCLUSION

The protection of turbine blades requires the use of a whole batch of processes that have been apparently well established for a number of years, but have in fact experienced a constant evolution. The major trends of this evolution rely on surface treatment specialists efforts to adapt their processes to more and more demanding requirements. These requirements are technical (temperature and lifetime increases) and economical; reliability and repairability are also important points.

The answer to this demand finds important support in the evolution of the coatings deposition processes, but also sometimes in their combination. Most of the time, all the different actors concerned by the coatings technologies (designers, production engineers, maintenance and repair people) have to work in close interaction to meet this challenge.

## REFERENCES

- [1] R. MÉVREL, C. DURET, R. PICHOT : « Pack cementation processes », Materials Science and Technology, Vol. 2 pp. 201-206 (1986).
- [2] G. GAUGÉ, R. MORBIOLI in « High temperature protective coatings », (ed. S.C. Singhal), pp. 13-26 (1983), Warrendale, Pa, The Metallurgical Society of AIME.
- [3] F. P. TALBOOM & J.A. PETRUSHA : « Superalloy coatings for components of gas turbine engine applications », AFML-TR-66-15, 1966, USA; Air Force Materials Laboratory, Wright-Patterson, Ohio.
- [4] Y. HONNORAT; R. MORBIOLI : « Corrosion and oxidation protections in aeronautical engines by vapor phase process »; Proc. Of 1st NATO advanced workshop on coatings for heat engines (Acqua fredda di Maratea, Italy), April 1-6 1984, pp.179-191.
- [5] G. LEHNERT & H.W. MEINHARDT, Electrodeposition and Surface treatments, Vol.1 (1972), pp.195-198.
- [6] R. STREIFF & D. H. BOONE, Reactivity of solids, Elsevier Ed. Amsterdam (1972), pp.195-198.
- [7] K. SCHNEIDER, H. VON ARNIM & H. W. GRÜNLING, Thin Solid films, Vol. 84 (1981) p. 29.
- [8] S. ALPÉRINE, P. STEINMETZ, A. FRIANT & P. JOSSO, Surf. Coatings Tech. Vol. 43/44 (1990), pp. 347-358.
- [9] A. MAC MINN, R. VISWANATHAN & C.L. KNAUF, Trans. ASME, Vol. 110 (1988), p. 142.
- [10] S. ALPÉRINE, P. STEINMETZ, P. JOSSO & A. COSTANTINI, Mat. Sci. & Engin., Vol. A121 (1989), pp.367-372.
- [11] S. ALPÉRINE, P. JOSSO, French Patent n° 88 - 13991 (1988).
- [12] P. STEINMETZ, S. ALPÉRINE, P. JOSSO & J.M. CLAUDE : «Effect of palladium based undercoat on the formation, structure and properties of diffusion aluminide coatings », Proc. 3rd International Conf. on high temperature Corrosion and Protection, Les Embiez, France 25-29 May 1992.

- [13]S. ALPÉRINE, P. STEINMETZ, A. FRIANT & P. JOSSO, *Surf. Coatings Techn.*, Vol. 43/44 (1990), pp. 347-358.
- [14]R. MÉVREL & R. MORBIOLI: « MCrAlY coatings », *Proc. 1st Int. Congr. On High-Tech Materials & finishing* (Berlin, 12-14 March 1989), pp. 204-216.
- [15]D. LEVINE & R. A. MILLER: « Thermal barrier coatings for utility gas turbine », EPRI AP-2618, Palo-Alto USA, 1982.
- [16]S. ALPÉRINE: « Molten salt induced degradation of thermal barrier coatings » AGARD CP N°461 « High temperature surface interactions » (1989), pp. 6.1-6.18.
- [17]S. STECURA, NASA Technical Memo 86905 (1985).
- [18]V. LANTERI, R. CHAIM and A. H. HEUER, *J. Am. Ceram. Soc.*, Vol. A121 (1986), pp. 258-261.
- [19]L. LELAIT & S. ALPÉRINE, *Scripta Metallurgica et Materialia*, Vol. 25 (1991), pp. 1815-1820
- [20]L. LELAIT, S. ALPÉRINE & R. MEVREL, *J. Mat. Sci.*, Vol. 27 (1992) pp.5-12.
- [21]D.W. Mc KEE & W. A. SIEMERS, *Thin Solid Films*, Vol. 73 (1980), pp. 439-445.
- [22]A. S. NAGELBERG, *J. Electrochem. Soc.*, Vol. 132 n°10 (1985), pp. 2502-2507.
- [23]S. M. MEIER, D. K. GUPTA, K. D. SCHEFFLER, *Jornal of Metals* (1991), pp. 50-53.
- [24]F. C. TORIZ, A.B. THAKKER & S. K. GUPTA, *Surf. Coat. Tech.*, Vol. 39/40 (1989) pp. 161-172.
- [25]G. SEIBERRAS, M. BEJET, C. INDRIGO, R. MEVREL, LE PENNEC, Ph. LEPRINCE, French Patent Application n° 92 11391 (1992).
- [26]R. A. MILLER, NASA TM 100283 (1988)
- [27]P. JOSSO, S. ALPÉRINE, unpublished results (1992).

## BRAZE REPAIR POSSIBILITIES FOR HOT SECTION GAS TURBINE PARTS

by  
**G. Marijnissen,**  
Interturbine Holding B.V.  
Lomm, the Netherlands

and  
**R. van Gestel,**  
Elbar B.V.  
P.O. Box 4339  
the Netherlands  
5944 ZG Arcen

### 1. SUMMARY

Overlay braze repair is a good technique for restoring aircraft vanes and industrial blades and vanes.

The negative effects of the intermetallic phase, formed during the overlay braze process, can be reduced in such a way that the mechanical properties - creep rupture, strength and ductility - can be achieved close to the properties of the base materials.

The elimination of the negative effects can be achieved by a combination of careful selection of the chemistries of the repair materials and the application of the correct procedures for cleaning and heat cycle.

### 2. INTRODUCTION

The repair of hot section turbine parts is in many cases more economical than replacement with new parts, assuming that the properties of the repaired parts are close to those of the new parts. Furthermore from a strategic point of view it is clear that certain materials are becoming more scarce, and from an ecological point of view repair processes produce less pollution than manufacturing new parts.

The damage which occurs to turbine parts, can be divided in two main areas:

- a. internal damage, caused by microstructural degeneration processes, creep, fatigue etc. As this kind of damage is repairable, it must be done by special heat treatment;
- b. external damage, caused by low cycle fatigue, foreign object damage, corrosion, erosion and/or wear.

External damage can be repaired either by welding or by brazing techniques. Welding has its limitations, not only because of the tendency of superalloys to crack in the heat affected zone, but also because of the properties of the available weld filler materials <sup>1-2</sup>).

Braze mix repairs, which use a nickel based braze alloy to restore the surface of a superalloy, have been employed for over ten years <sup>3-4-5</sup>).

Although good results are obtained and this overlay braze technique is acceptable for repairing aircraft vanes and industrial blades and vanes, the process has some disadvantages, in particular:

- special cleaning processes are required prior to brazing <sup>6</sup>);
- the melting point depressing elements present in the braze alloys result in the formation of brittle

intermetallics, which influence the properties of the added material.

Although, in general, the mechanical strength of a braze repair mix is better than that of a weld repair, it does not match the mechanical strength of the original substrate material. Work was carried out into the development of "Powder metallurgy repair" <sup>7</sup>) and into the development of high strength high ductility braze mix materials <sup>8</sup>).

### 3. BRAZE MIX REPAIR

For surface restoration of eroded and/or corroded areas, mixtures of nickel based braze alloys - mostly from the boron family - and superalloy powders are brazed onto the surface. The braze mixture (powders + organic binder) may be applied as a paste, as a tape, or as sintered preforms.

After application of the mixture onto the surface, the part will be heated up to the brazing temperature.

In figure 1 the different steps of the process are indicated.

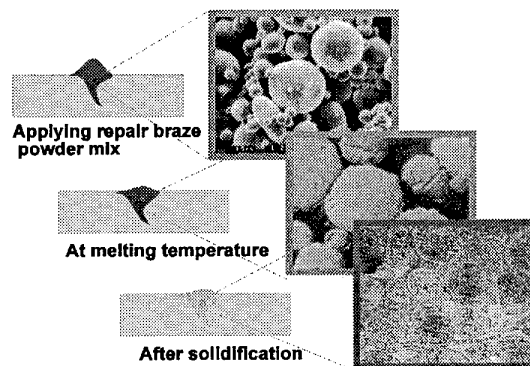


Fig. 1 - Schematic view of the principle of overlay braze repair

During the brazing process, the braze alloy powder in the mixture will melt. The liquid alloy will flow in between the superalloy particles filling up all gaps by the capillary forces in the narrow areas between the metal powder particles. Elements of the braze alloy powder will diffuse into the superalloy particles as well as into the base material, resulting in surface melting.

During cooling, the molten material in the braze mix will solidify. This results in the formation of brittle intermetallics, figure 1c.

After the brazing cycle a diffusion cycle is often performed. During this cycle the boron, which is used as a melting point depressant, is further diffused into the superalloy particles and into the base material. By this treatment, the amount of brittle borides in the system will be reduced and better distributed. The boron will dissolve partially in the matrix of the substrate material.

It is evident that the chemistry of the braze mix will strongly influence the phase formation and, as a consequence, the properties of the repaired parts. It is also clear that an effective cleaning procedure prior to brazing is essential to achieve good results. It is however much less realized that the braze mix preparation and the brazing cycle can have a dramatic influence on the final results.

### 3.1 Cleaning prior to brazing

In all repair and coating processes cleanliness of the part is very important. In particular braze mix repair surfaces and cracks must be completely free of oxides and other contaminations.

After vapor degreasing and grit blasting, the parts are examined to determine whether stripping of coating, machining or hand grinding is necessary. Mechanical cleaning is used for removing large quantities of oxides and other contaminants from the surface; thermo-chemical processes have been developed to remove oxides and sulfides.

A hydrogen-reducing atmosphere is used for removing sulfides and oxides from the surfaces of stainless steels and most cobalt base alloys.

For nickel based superalloys containing aluminum and titanium, which form oxides at the surface which cannot be reduced by hydrogen or vacuum, special techniques must be used.

Fluor based processes, such as the Fluor Carbon Process FCP<sup>6)</sup> can reduce oxides and remove sulfides, although only in smaller quantities.

The FCP process reduces not only oxides and sulfides from the surface but also from the inside of cracks. Combining FCP with high temperature brazing is called Fluor Activate Bonding, FAB; this gives a joint that has similar properties to those of the base material.

The FCP process takes place in a retort with a hydrogen atmosphere. In the retort some solid PTFE is necessary for the cleaning actions.

During the fluor carbon cleaning process the following reactions take place:

- \* At about 500-650°C PTFE reduces to ethylene fluoride, which forms HF by a reaction with hydrogen. At this temperature the HF reacts with all oxides (and sulfides) and form carbon monoxide and metal fluoride.
- \* At about 650-800°C reactive elements such as aluminum and titanium present in the base material, react with hydrogen fluoride and formed gaseous metal fluoride; the surface will thus be depleted of these elements.
- \* At about 800°C hydrogen reacts with chromium difluoride and chromium and hydrogen fluoride are formed.

An additional peening and heat treatment completes the cleaning process. Figure 2 shows a structure of the superalloy IN738 after the cleaning process.

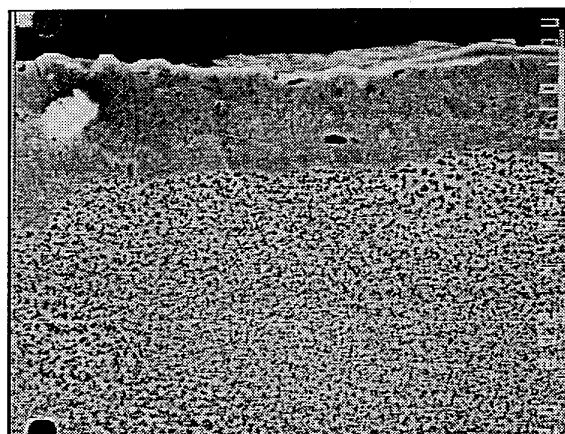


Fig. 2 - Cross section of IN738 after the FCP process. All oxides are removed and the surface is depleted of active elements like aluminum and titanium.

### 3.2 Braze preparation

The materials employed for surface build up can be applied in different ways. The most usual method is a paste, applied to the surface with a brush, a spray gun or a syringe. For this method the braze repair powder has to be mixed with a binder and solvent. The binder and solvents have to decompose and evaporate during the heating up part of the brazing cycle in a vacuum furnace.

Depending on the type and amount of binder during the decomposition, carbon may form which can cause carbide formation in the braze. If this occurs in an uncontrolled way, the repaired material can suffer from serious embrittlement.

Other ways of adding repair material to the surface are by the use of tapes and sintered preforms.

Tapes also contain binders, but can be controlled more easily. Sintered preforms can be produced with and without binders. In general the use of sintered preforms will minimize the problems. During the braze preparation, the areas may not be contaminated with braze material, should be protected by masking materials. These materials prevent flowing of the braze because they contain oxides which are not wettable. Masking materials are available in paint, putty and tape form.

### 3.3 Braze repair materials

As stated, braze material is a mixture of a superalloy powder and a nickel based braze powder. The braze powder is a nickel alloy containing melting point depressing elements like boron and/or silicon. In most cases only boron is used. The mixture contains a large number of different elements, each of which has a special task in the alloy. Table 1 gives a summary of the effect of the major elements on the properties of the alloy.

The melting point depressing elements form intermetallic phases with nickel, chromium, and the refractory elements in the super alloy. In general these phases have a negative influence on the properties of the material; ductility in particular can be influenced dramatically.

Figure 3 shows the boride formation of various refractory elements.



Fig. 3a - Tantalum borides

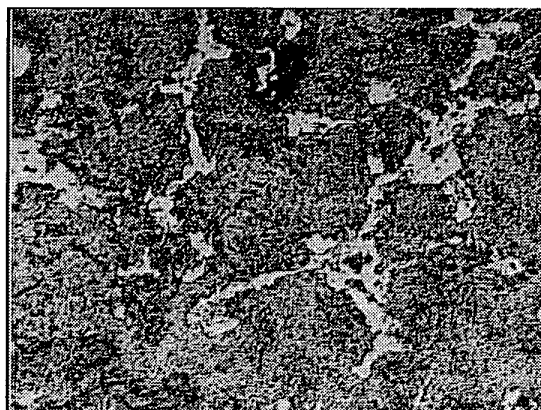


Fig. 3c - Chromium borides

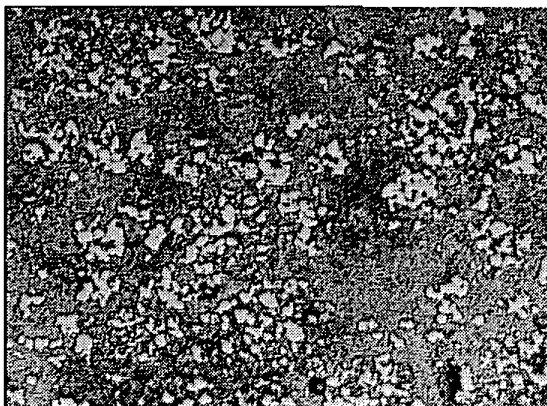


Fig. 3b - Tungsten borides



Fig. 3d - Molybdenum borides

Fig. 3 - Boride formation, the types of borides are strongly dependent on the chemistry

Fig. 3 shows that tantalum tends to form needle-like borides, whilst the chromium borides have dogbone shapes and tungsten forms cubic borides.

Table 1 - Elements used in advanced repair braze material

Element	Effect
Cr, Al	corrosion resistance
W, Mo, Ta, Nb	strengthening
Pt group	strengthening
Y, Hf, La	influencing phase formation
B	melting point reduction
Al, Ti	gamma prime strengthening
Fe	ductility

There is a strong correlation between phase formation and properties. Brittle intermetallics all along the grain boundaries will cause embrittlement. Also needle-like phase formation is very negative for the ductility.

This means, that the chemical composition of braze and superalloy powders have to be chosen in such a way that a good compromise is found between alloying elements and boride formation, in order to achieve optimal thermo-mechanical properties. In general the creep and tensile strengths of the braze materials are close to those of the nickel base super alloy IN738 (Fig.4).

However, the ductility however of the first generation of repair brazes was low. The main developments were to increase this ductility. Figure 5 shows the increase in ductility for the different generations of braze repair materials.

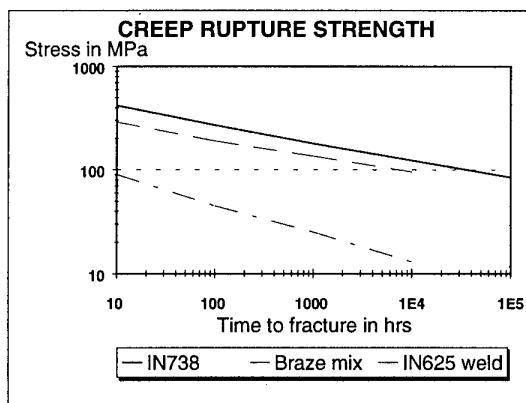


Fig. 4 - Creep rupture strength of overlay braze repair materials compared to IN738 and weld repair with IN625

Another important property is the thermal cycling resistance.

All braze materials passed a test of 100 cycles between 100 and 1000°C, with heating and cooling speeds more than 300°C/min. without any cracking.

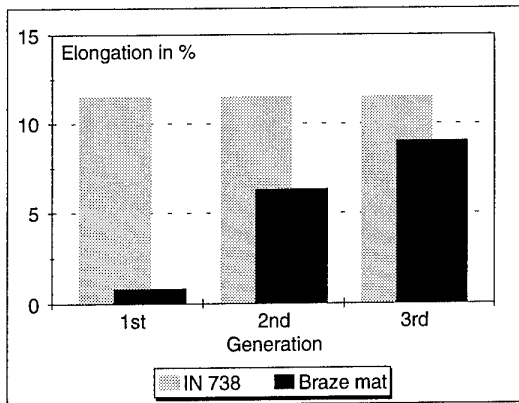


Fig. 5 - Development of the ductility of overlay braze materials; elongations measured during creep rupture at 870°C.

### 3.4 Compatibility to base material

During the brazing boron will not only diffuse into the metal powder particles present in the braze mix, but also into the base material, where it reacts and forms intermetallics. The shape of the intermetallics will be dependent on the chemical composition of the base material, and is comparable to those in the braze as shown in Figure 3. This means that the properties of the base material in the diffusion zone can be influenced. Table 2 gives the most likely boride formations in the diffusion zone of the most common materials when brazed with brazes which contain only boron as a melting point depressant.

Table 2 - Typical boride formation in the diffusion zone of superalloys, brazed with materials containing only boron as melting point depressant.

Molybdenum borides (eutect like, along grain boundaries)	U500, U520, U700, IN617, IN625, Nim 105 René 41
Tungsten borides (cubic)	PD21, MM002, René 80, SRR99, IN6000MA, PWA 1422, CSMX 3, MM247
Tantalum borides (needles)	PWA 1480
Chromium borides (eutectic type)	Nim 75, Nim 80A, Nim 90, IN100
Mixed	IN738, IN939, IN792, U710, U720, C1023

### 3.5 Braze cycle

The actual brazing takes place in a vacuum furnace. During the first part of the heat cycle a number of processes occur, which can lead to various problems:

- The decomposition of the binder causes porosity or even flaking of the braze material from the surface before reaching the melting point. By carefully controlling the ramp rate and the vacuum level, these detrimental effects can be avoided.
- Binders are organic in origin. During decomposition in a vacuum most binders tend to carbon formation. This carbon will react with elements from the repair braze material. Carbon formation is not always detrimental since it can improve the wetting of the

braze.

In general a slow ramp rate is needed to solve the problems of binder decomposition. To achieve a uniform brazing temperature, a hold just below the solidus temperature of the braze material is advisable.

All these considerations are in contradiction to the fact that nickel based super alloys, which contain aluminum and titanium, will slowly oxidize in technical vacuum systems, and therefore the time at temperature before melting has to be reduced as much as possible. Therefore in practice the heating up is always a compromise.

At temperature the braze component of the repair mixture is molten. To obtain the required diffusion into the superalloy particles of the repair mix, a certain time is required. On the other hand, the time and temperature must be limited in order to limit the interaction with the base material. Most braze repair materials are sensitive to the brazing temperature. A too high temperature will cause flowing away of the braze to areas where not wanted, and a too low temperature causes inadequate bonding and porosity. In order to minimize the amount of boron, which forms the brittle intermetallic phases, the brazing temperature is relatively high. In a number of cases this is very close to the temperature where incipient melting of the base material can occur. If this happens the parts will be completely destroyed. The temperature must therefore be very carefully controlled.

During cooling down the braze material will solidify, causing shrinkage. During building up of thick layers this can cause the so called "crocodile skin" effect. This effect can be minimized by controlling the cooling rate during solidification.

Figure 6 shows a typical example of a braze repaired nozzle guide vane segment.

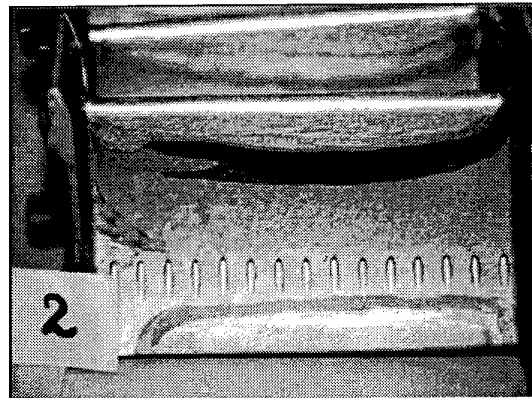


Fig. 6 - A typical example of a braze repaired vane segment.

### 3.6 Post treatments

An additional heat treatment will diffuse the boron somewhat more, and gives in general a less detrimental boride formation. For the braze materials which are especially developed for optimal intermetallic formation, this additional diffusion heat treatment is not required for the braze material. However, the base material must undergo a heat treatment to restore the original mechanical properties.



#### 4. DISCUSSION AND CONCLUSIONS

Overlay braze mix techniques have been successfully applied to the repair of aircraft nozzles and industrial blades and vanes for over 10 years. The brazing developments discussed in this paper have changed the function of braze repair from cosmetic to real stress bearing. This means that the improved overlay braze repair can be used for high stressed areas with sufficient impact strength. An additional problem is the adhesion of the braze to the substrate material. This is mostly influenced by the

cleanliness of the surface prior to brazing. In order to obtain optimal results, special cleaning techniques like FCP are required for nickel base superalloys.

Most of the overlay braze mixes are mixtures of nickel base superalloys and high temperature nickel base brazes with boron as a melting point depressant element. These mixtures always form brittle intermetallic borides. Controlling the size, shape and amount of these borides makes it possible to produce repair materials with high strength and high ductility. Controlling the boride formation is not only a question of chemical composition of the materials; pre-treatments, heat cycle and post-treatments are also important.

The underlining conclusion is that overlay braze repair techniques will produce high quality repairs, assuming that all conditions are optimized.

#### REFERENCES

1. J.H.G. Mattheij, "Onderzoek naar de lasbaarheid van nikkelbasis superlegering IN738", Graduation Report,

University of Technology, Eindhoven, August 1979.

2. G. Marijnissen, "Repair of Gas Turbine Components", Proc. 17th CIMAC, Warsaw, June 1987.

3. H. van Esch and G. Marijnissen, "The Role of Brazing in the Repair of Hot Gas Turbine Components", Turbomachinery, Sept./Oct. 1986.

4. J.H.G. Mattheij, "Role of Brazing in the Repair of Superalloy Components - Advantages and Limitations", Materials Science and Technology, Aug. 1985, vol.1, pp 608-612.

5. P. Branny, M. Hammerschmidt and M. Malik, "Repair of Air Cooled Turbine Vanes of High Performance Aircraft Engines", Materials Science and Technology, Aug. 1985, vol. 1, pp 719-727.

6. J.W. Chasteen, "Method for Cleaning Metal Parts", U.S.patent 4.405.379, 20 September 1983.

7. K.A.Ellison, P.Lowden and J.Liburdi, "Powder Metallurgy Repair of Turbine Components", ASME paper 92-GT-312, presented Köln, June 1992.

8. G. Marijnissen, R. van Gestel, B. Verhappen en P. van Neerven, "High Strength High Ductility Braze Mixes for Turbine Component Repair", Proc. 3rd International Conference on High Temperature Brazing, Aachen, Nov. 1992.

## Gas Turbine Compressor Corrosion and Erosion in Western Europe

H.J. Kolkman

National Aerospace Laboratory NLR

P.O. Box 90502

1006 BM Amsterdam

The Netherlands

### SUMMARY

It is shown that for gas turbines in the West European environment:

- \* during operation hygroscopic salts - notably ammonium sulphate (originating from manure) and sodium and magnesium chloride (from sea salt) - are deposited on compressor components.
- \* during shutdowns these wet deposits acidify owing to the absorption of the air pollutants  $\text{NO}_2$  and  $\text{SO}_2$ .

The response of the compressor metals can be broadly categorized as follows:

- a) Different steels show different degrees of corrosion. Especially pitting corrosion can lead to component rejection and compressor disintegration.

This necessitates frequent washing and/or corrosion resistant coatings. Modern cleaners are environmentally friendly and contain a corrosion inhibitor. The performance of cleaners and coatings is discussed.

- b) Nickel-base superalloys and titanium alloys are not prone to corrosion in compressor applications. In order to avoid problems these materials should be used even for secondary components. This is exemplified by a crash due to stress corrosion of a component costing only a few dollars.

Compressor erosion as such is not a major problem in Western Europe. However, corrosion resistant coatings usually have a poor erosion resistance. Moreover, engine manufacturers and users prefer a general compressor coating for use in both corrosive and erosive environments. Developments with respect to compressor cleaners and coatings are discussed.

### 1. CORROSION

#### 1.1 Environmental conditions in The Netherlands

A number of case studies of corrosion problems are illustrated in Figs. 1 - 3. It is seen that *pitting corrosion* can result in rejection of compressor components or even compressor disintegration. This is especially true for gas turbines that are relatively infrequently operated, such as jet engines in military aircraft and industrial gas turbines used for peak demands. The reason is that pitting corrosion is an electrochemical corrosion process that requires the presence of an electrolyte. For the later stages of a compressor an electrolyte can be present only during *shutdown* periods, since during operation the temperature and pressure exclude the presence of liquids [1].

The presence of an electrolyte during shutdowns is caused by *deposition* of *hygroscopic* salts collected during *operation*, notably  $\text{NaCl}$ ,  $\text{MgCl}_2$  and  $(\text{NH}_4)_2\text{SO}_4$  [1-3]. The former two salts are constituents of *sea salt* and can be found in marine and coastal areas.  $(\text{NH}_4)_2\text{SO}_4$  is the result of a chemical

reaction between  $\text{NH}_3$  (originating from *manure* produced by intensive stock farming of especially pigs) and the *air pollutant*  $\text{SO}_2$ . Hence this salt is especially deposited during operation in/over rural areas. This is reflected by the striking difference in ammonium(sulphate) content in Table 1. In addition, other compounds can be found that are specific for operation in a particular environment, e.g. phosphates for operation near a fertilizer plant.

Table 1 Composition of water-soluble deposits (in weight %) for two gas turbine types operated in The Netherlands

Application		Fighter jet engine	Helicopter engine
Operation area		Mainly over land	Over land
No. of analyses		5	13
I O N  T Y P E	$\text{Cl}^-$	4.6 - 8.3	2.9 - 11.2
	$\text{SO}_4^{=}$	57.1 - 66.8	50.2 - 60.5
	$\text{NO}_3^-$	0 - 2.9	<1 - 13.0
	$\text{NH}_4^+$	0.01 - 0.1	5.0 - 20.0
	$\text{Na}^+$	16 - 21.9	9.1 - 29.4
	$\text{K}^+$	1.4 - 2.6	not analyzed
	$\text{Ca}^{++}$	3.5 - 7.2	2.1 - 4.7
	$\text{Mg}^{++}$	2.0 - 2.9	0.3 - 1.6

$(\text{NH}_4)_2\text{SO}_4$  and  $\text{NaCl}$  absorb moisture from the air at critical relative humidities exceeding 78% and 81% respectively. These values depend only slightly on the temperature. In view of the *high relative humidity* in the Netherlands (Fig. 4) this means that the deposits are *mostly wet*, so that electrochemical corrosion can occur.  $\text{MgCl}_2$  is always wet in view of its critical relative humidity of 32%. The presence of this salt in the helicopter engines mentioned in Figs. 1c and 3 has been established [2].

The salt droplets on the compressor components are *acidified* by absorption of the *air pollutants*  $\text{SO}_2$  and  $\text{NO}_2$  [2]: pH values as low as 3.3 were found in water collected after the rinsing of helicopter engines [2]. In view of the strong dilution, the actual pH of the salt solution on the compressor components must have been in fact much lower. In this acid electrolyte pitting corrosion is promoted by the *chloride* ions in the aforementioned salts  $\text{NaCl}$  and  $\text{MgCl}_2$ .

- (a) Base material : AISI **403** steel  
 Component : Blades  
 Application : Industrial gas turbine (peak demand)  
 Coating : None (coating eroded away)  
 Cleaning : Nut shells; later on steam cleaning during shut-downs

Pitting : Yes  
 ↓  
 Fatigue crack initiation and propagation  
 ↓  
 Blade failure after 18.000 h (15 years) (see figure 2)  
 ↓  
**Compressor disintegration**

- (b) Base material : AISI **410** steel  
 Component : Disks  
 Application : Marine patrol aircraft  
 Coating : NiCd  
 Cleaning : Washing monthly, later weekly

Pitting : Yes  
 ↓  
**Rejection** of many disks within 3.000 h

- (c) Base material : **17 - 4 PH** steel  
 Component(s) : Blisks and vanes  
 Application : Helicopter engine  
 Coating : None (coating erodes away)  
 Cleaning : Rinsing + washing

	monthly	weekly
	weekly	daily

Pitting : Yes : Hardly  
 ↓  
 Fatigue crack initiation and propagation  
 ↓  
 Blade failure within 800 h (3 years)  
 ↓  
**Compressor disintegration** (see figure 3)

- (d) Base material(s) : **Titanium alloys:**  
 Ti 6-4; Ti 6-2-4-6; Ti 8-1-1  
**Nickel-base superalloys:**  
 Astroloy; Waspaloy; IN 100;  
 Inconel 718; Incoloy 901; Inco X-750  
 Component(s) : Blades, vanes and disks  
 Application : Fighter engine  
 Coating : None  
 Cleaning : No rinsing, no washing  
 shop cleaning only  
 Pitting : **None**

Fig. 1 Examples of pitting corrosion problems in compressors of gas turbines operated in The Netherlands

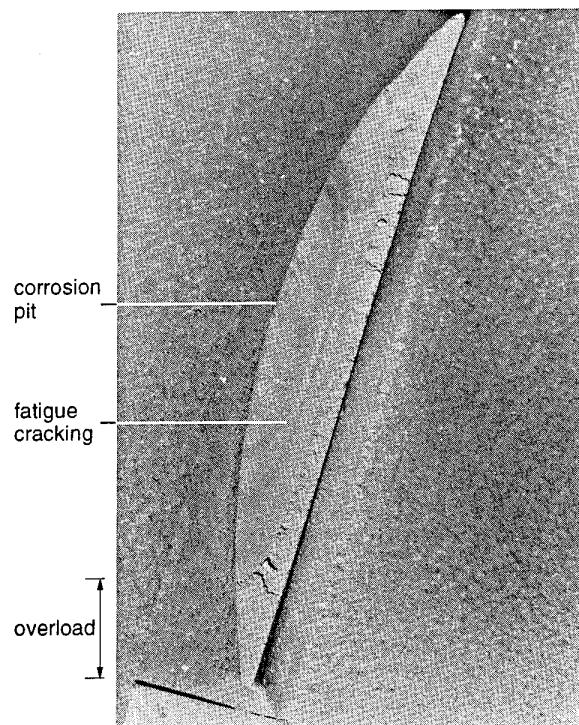


Fig. 2 Compressor blade failure in an industrial gas turbine compressor (see figure 1a): blade material 403 steel

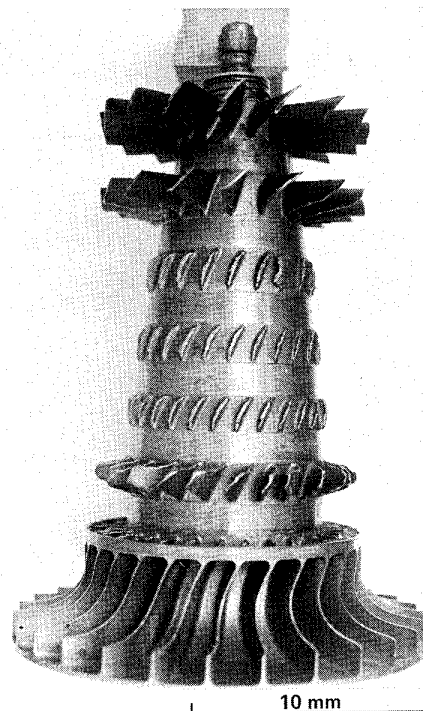


Fig. 3 Compressor rotor of helicopter engine after service failure caused by pitting corrosion (see figure 1c): rotor material 17 - 4 PH steel

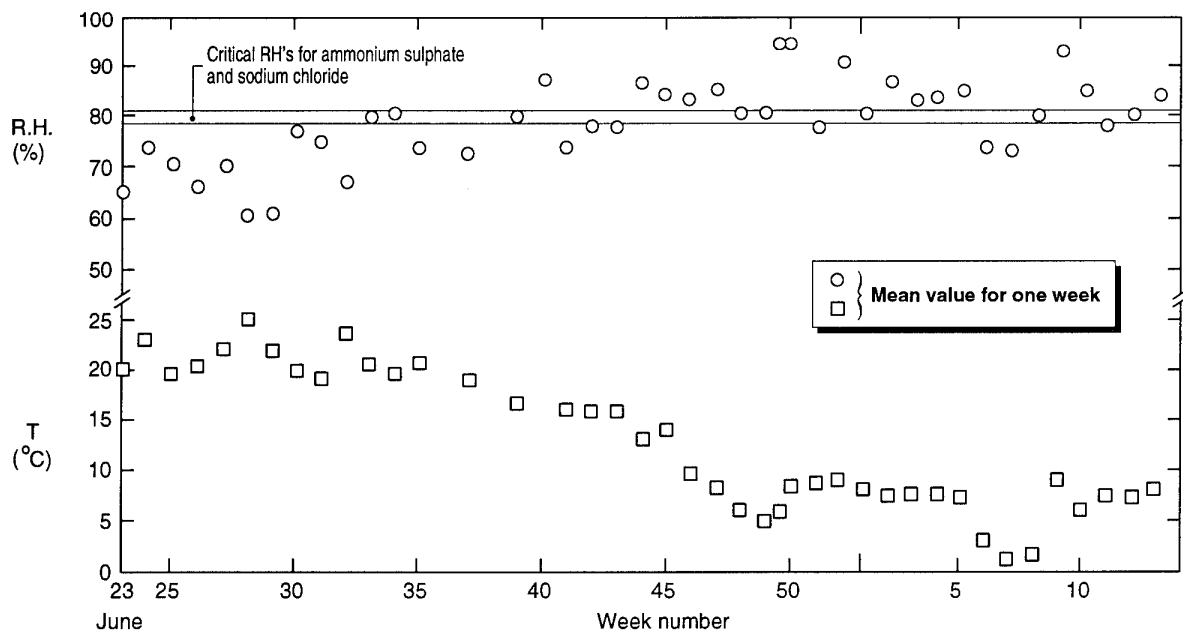


Fig. 4 Measurements of the environment in a shelter in The Netherlands [Ref. 4]

### 1.2 Base metals

Both from practice (exemplified in Fig. 1) and tests under simulated (West European) service conditions it follows that common compressor materials can be broadly categorized into two groups:

1 On the one hand *steels* (such as AM 355, 403, 410, Custom 450 and 17-4 PH) exhibit *pitting corrosion*. Of course there are differences in this group. For instance, a wet,  $\text{SO}_2$  containing atmosphere introduces pitting in 410, but not in 17-4 PH (left-hand side of Fig. 5, i.e. "Not soaked").

However, the presence of NaCl (introduced by soaking in a very dilute solution; see the solid curves in Fig. 5) promotes pitting in both materials and under this circumstance the difference vanishes.

2 On the other hand *titanium alloys and nickel-base superalloys* do not exhibit pitting corrosion (e.g. see Fig. 1d). However, it should be realized that even when primary components (blades, vanes, disks) are made of these corrosion resistant materials severe corrosion problems can arise because *secondary components* are made of less

	Soaking in:	Simulates:
x	not soaked	washing with rinsing and drying
●—●	200 ppm NaCl	washing without rinsing and drying
○ ○	200 ppm NaCl + cleaner	washing with cleaner without rinsing and drying
□ □	cleaner	idem, less severe circumstances

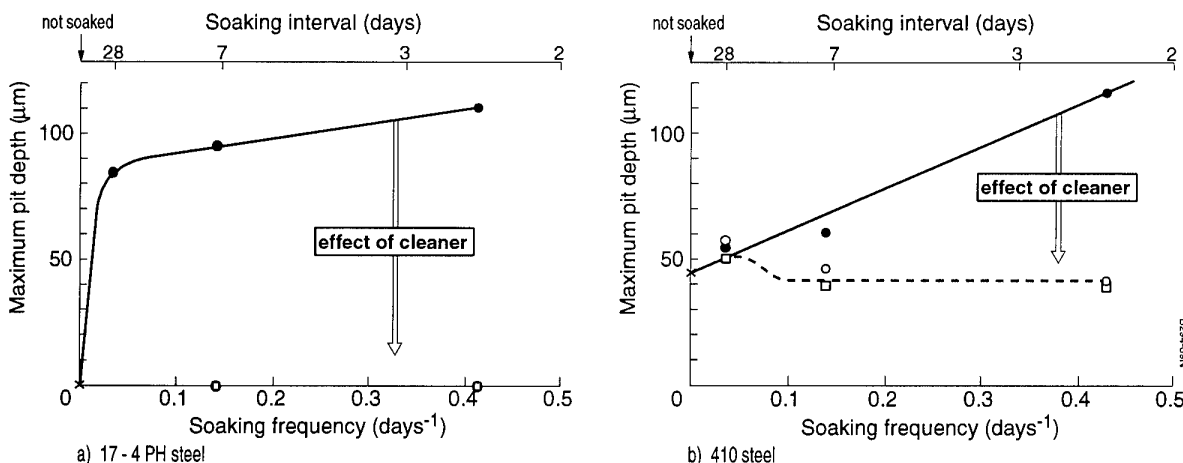


Fig. 5 Maximum pit depth in  $60 \times 30 \text{ mm}^2$  coupons after 28 days in a special climate room ( $3 \text{ ppm SO}_2$ , 95% RH,  $20^\circ \text{C}$ ) interchanged with soaking in different solutions [Ref. 3]

Table 2 Relationship between the presence of external salt and the occurrence of SCC in the Pins of the levers of a compressor variable vane stage

		pins with		Total
		SCC	no SCC	
arms with	salt	8	10	18
	no salt	0	72	72
Total		8	82	90

corrosion resistant materials. In the Netherlands an aircraft crash was caused by failure of a pin of a lever of the variable vane system of the engine referred to in Fig. 1d [5]. It turned out that the failure mode was *Stress Corrosion Cracking* (SCC) and that a number of pins in other engines of the same type suffered from SCC. There was a close relationship between the presence of NaCl on these levers (Fig. 6) and the occurrence of SCC (Table 2). Engines operated in the USA showed the same phenomena after about ten times the service hours. This illustrates the *aggressive corrosive conditions in Western Europe*. The solution has been to replace the pin material - Nitronic 60 steel - by the nickel-base alloy Inconel 625.

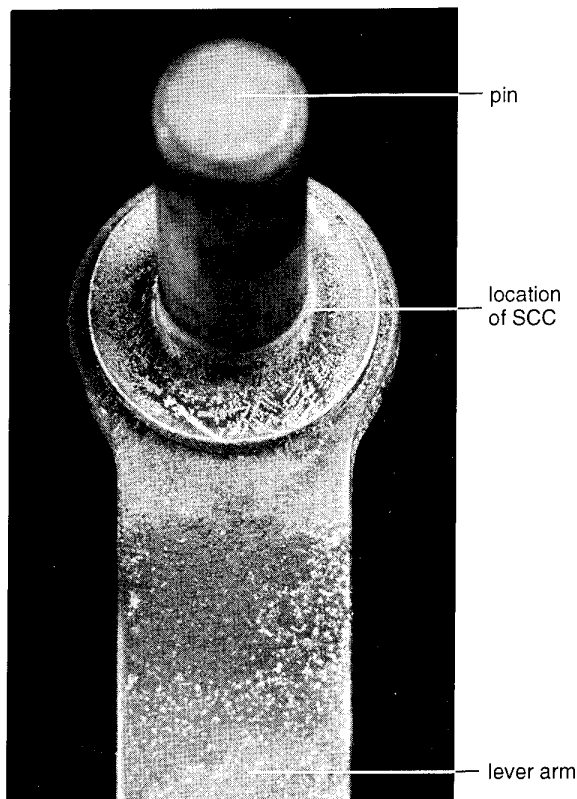


Fig. 6 Extreme example of salt deposits on a pin-lever arm assembly for a compressor variable vane: pin material Nitronic 60 steel

### 1.3 Countermeasures

The use of steels requires measures to combat corrosion such as washing to remove the corrosive deposits and application of corrosion resistant coatings.

*Water washing* or rinsing and *washing with a cleaner* (detergent) can be very *effective*. For instance, the pitting problem illustrated in Figs. 1c and 3 was almost completely eliminated by increasing the rinsing and washing frequencies. This can be understood as follows: Fig. 5 illustrates that the blade and vane material (17-4 PH) does not exhibit pitting in the absence of chloride. Fig. 7 shows that - as expected - the chloride quantity decreases with increased washing frequency. The variation is large because of the different mission types involved, but the tendency is clear.

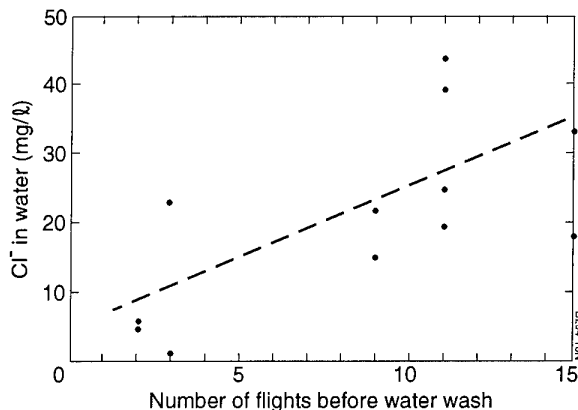


Fig. 7 Relationship between the chloride concentration of water collected after water washing of a helicopter engine (figure 1c) and the number of flights preceding that water wash

*Coatings* require testing. The standard neutral salt spray test (ASTM B-117) does not simulate the (acid) service conditions. There is a modification (ASTM B-287) in which the salt solution to be sprayed is acidified with acetic acid. This cannot be regarded as being realistic for atmospheric corrosion. The NLR developed a special test rig to simulate compressor service conditions [1]. Alternatives to test large quantities of coupons are the method mentioned in Fig. 5 and salt spraying with a salt solution acidified with nitric and sulphuric acid to pH = 3. An example for AISI 410 steel is given in Fig. 8. A coupon was regularly taken out to measure the pit depth. For uncoated 410 the maximum pit depth turned out to be a linear function of the square root of the salt spraying time. A NiCd coating protected the base metal unless the top layer was removed (to simulate erosion, wear, etc.) and the remaining coating was locally removed in the form of a "corrosion cross". The aluminium-pigmented coating Sermatech 2241 protected the base metal under all conditions (with and without "corrosion cross"; with and without the top layer removed).

Comparing the results for bare 410 steel it is seen that the test method applied in Fig. 8 (acid salt spraying) is more aggressive than the test method in Fig. 5. (exposure in a humid SO<sub>2</sub> atmosphere with or without some NaCl). It also follows from Fig. 8 that *conventional compressor coatings* can offer satisfactory protection against corrosion.

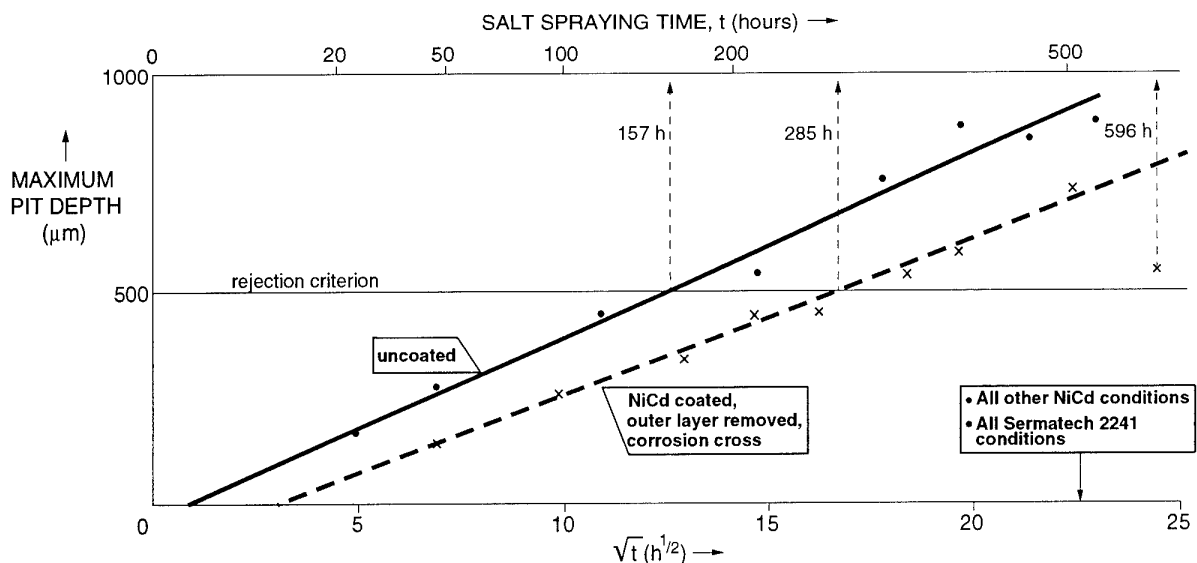


Fig. 8 Results of salt spray testing of 410 steel coupons with a salt solution acidified with nitric and sulphuric acid

However, the NiCd/410 coating/base metal combination referred to in Fig. 8 gave rise to the pitting problems in practice addressed in Fig. 1b, especially in the slots in the disk. This can be attributed to *wear* of the coating in these slots. The NiCd coating consists of a NiCd outer layer and a pure nickel interlayer. The latter is more noble than the base metal. Hence the base metal will be preferentially attacked if the NiCd coating is removed by wear and the nickel layer is locally damaged (as established by tests: see the dashed curve in Fig. 8).

In addition to wear, *conventional compressor coatings are prone to erosion*, as will be discussed in subsections 2.1 and 2.3.

## 2. FOD AND EROSION

### 2.1 Environmental conditions in The Netherlands

Bird hits especially occur near airports in coastal areas. This applies - for instance - both to Schiphol Airport near Amsterdam in The Netherlands and the Narita Airport near Tokyo in Japan.

The West European environment is not very erosive. Some exceptions are related to the subject of corrosion: most corrosion resistant compressor coatings erode away quickly. This follows both from practice (Fig. 9) and tests (to be discussed in subsection 2.3). Moreover, in order to remove the corrosive deposits, "dry" cleaning methods are sometimes applied that involve the deliberate injection of erodents (such as rice, walnut shells, etc.) in the intake air.

### 2.2 Base metals

With respect to common compressor base metals it follows from the literature - e.g. [6-8] - that the erosion resistance increases in the sequence: aluminium alloys - titanium alloys - nickel-base superalloys and steels. The differences between these groups of alloys are relatively small, however.

### 2.3 Coatings

There is a need for erosion resistant coatings especially for application to engines that are partly operated in more erosive parts of the world than Western Europe. In addition, corrosion protection of compressor steels also requires an

erosion resistant coating. For example, the coating seen in Fig. 9 was applied to combat the corrosion problem addressed in Figs. 1c and 3, but eroded away quickly. It



Fig. 9 The same blades as shown in figures 1c and 3 after 200 h service with an aluminium pigmented coating

should be emphasized that the base metal - 17-4 PH steel - did not suffer markedly from erosion under identical conditions. This illustrates the general statement that *conventional compressor coatings have a poor erosion resistance* as compared with the common base metals. This holds for NiCd, aluminium diffusion coatings (such as SA 12) and aluminium pigmented coatings (such as the Sermatel/Sermatech coatings) and follows from tests, e.g. in [9,10].

Hence there is a need for a universal compressor coating, i.e. a coating that offers both corrosion and erosion resistance. Titanium nitride (TiN) is a candidate. It should be emphasized that *the term TiN does not unambiguously identify the coating*, since the properties depend on the (PVD) processing conditions during coating application. This is illustrated in Fig. 10. Here the erosion (expressed as coating volume loss per weight unit of erodent) is plotted as function of the angle of incidence of the erodent. It is seen that the erosion resistances of different TiN coatings differ by an order of magnitude, see also [11].

It is also seen in Fig. 10 that even the best TiN coating protects the base metal (410 in this example) only for glancing incidence. *Maximum erosion loss occurs at and near perpendicular impact*, i.e. near the *leading edge*. Fortunately the erosion resistance of the base metal is high for perpendicular impact. Another drawback is that TiN is more noble than steel. Hence *preferential corrosive attack of the base metal* is found near coating imperfections (Fig. 11), at least when the base metal is steel. The application of TiN on titanium alloys might be more satisfactory in this respect, but there is a *penalty in the fatigue life of the base metal* [12]. This effect is probably related to residual tensile stresses in

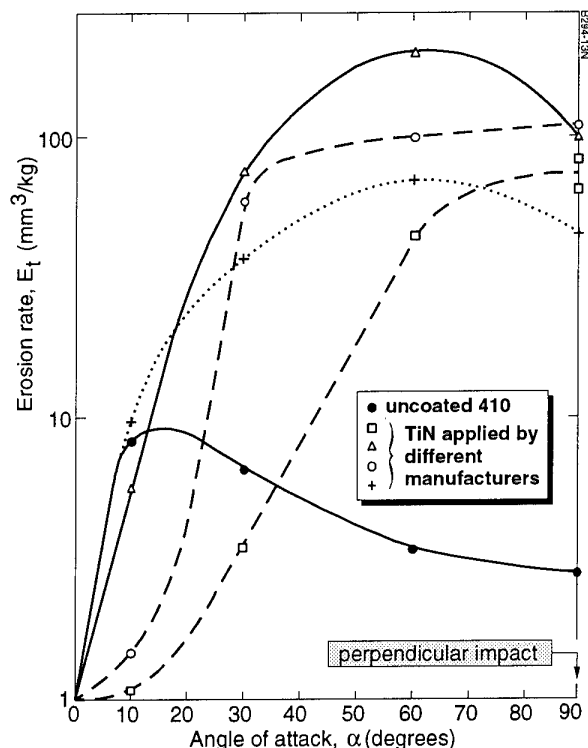


Fig. 10 Erosion rates of different TiN coatings applied to 410 steel

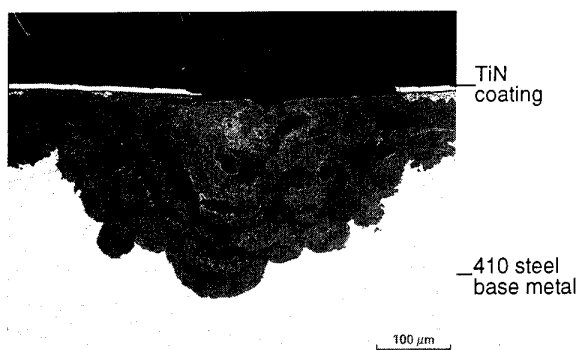


Fig. 11 Representative cross-section of a corrosion tested TiN coated coupon of 410 steel

the base metal that have to compensate the compressive stresses in the coating, and is therefore expected to increase with increasing coating thickness. Accordingly, the effect was not found in 6 - 10  $\mu\text{m}$  coatings [11], but it was observed for a more realistic thickness of 50  $\mu\text{m}$  (Fig. 12).

With the exception of the first stages, in practice most erosion takes place near the blade tips (Fig. 9) since the erodent is centrifuged outwards. On the other hand, the aforementioned possible fatigue problems (which occur because of initiation at corrosion pits and/or decreased fatigue resistance of the base metal) apply to the highly stressed blade roots. Therefore it is not uncommon to apply an erosion resistant coating to the blade tips only. It will be clear that this solution cannot be applied if the coating has to offer corrosion resistance in addition to erosion resistance.

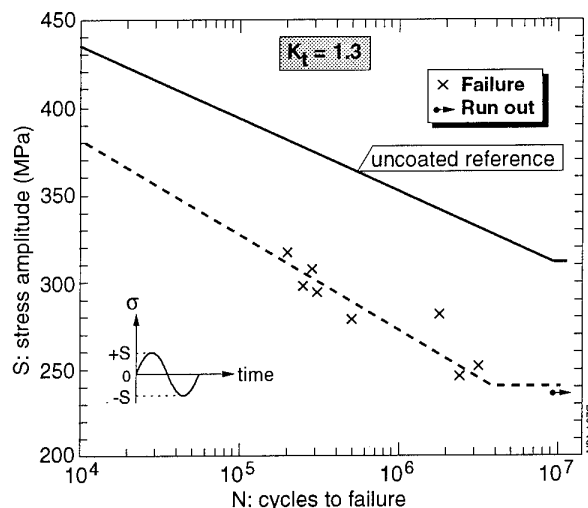


Fig. 12 S - N curve for titanium alloy Ti-6Al-4V coated with 50  $\mu\text{m}$  thick TiN

### 3. RECENT AND FUTURE DEVELOPMENTS

Since steel compressors remain in use in Western Europe, there will be a further need for corrosion protection by coating and washing. It should be noted here that the severity of the air pollution in Western Europe is decreasing (e.g. in terms of  $\text{SO}_2$  and acidity of rain water). The effect on

compressor corrosion is difficult to evaluate, however. For instance, the absorption of  $\text{SO}_2$  by the electrolyte has two opposite effects. On the one hand, the resulting acidification of the electrolyte promotes pitting corrosion. On the other hand, the  $\text{SO}_2$  molecules are transformed into sulphate ions that act as inhibitors for pitting corrosion [12]. Hence the effect of a decreased  $\text{SO}_2$  concentration on compressor corrosion is difficult to predict.

In order to remove water-insoluble compounds water washing or rinsing is usually interchanged with washing with a compressor cleaner (detergent). Because of safety and environmental issues many *ecologically friendly* compressor cleaners have been developed recently. These cleaners have a lower cleaning efficiency than the old cleaners [3]. They are meant to keep a clean compressor clean and not to clean a dirty compressor.

In addition, many modern cleaners contain a *corrosion inhibitor*. Apparently these inhibitors effectively eliminate the influence of chloride ions (Fig. 5).

Finally, *multilayer coatings* are being developed [11,13]. This is driven by the wish to have good erosion resistance for all angles of incidence and all normal erodent particle sizes. However, the corrosion resistance (e.g. of TiN on steel) is also expected to improve, since multilayer coatings contain less through-thickness defects.

#### 4. REFERENCES

- [1] Kolkman, H.J. and Mom, A.J.A., "Corrosion and Corrosion Control in Gas Turbines, Part I: The Compressor Section", ASME Paper 84-GT-225,
- [2] Kolkman, H.J., "Coatings for Gas Turbine Compressors", pp. 224 - 230 in "Materials Development in Turbo-Machinery Design", edited by Taplin, D.M.R., Knott, J.F. and Lewis, M.H., The Institute of Metals, London, Book 456, 1989.
- [3] Kolkman, H.J., "Performance of Gas Turbine Compressor Cleaners", ASME Paper 92-GT-360, presented at the 37th Int. Gas Turbine Conference and Exhibit, Cologne, Germany, June 3-4, 1992.
- [4] Hart, W.G.J. 't, "Influence of Atmospheric Corrosion on Stress Corrosion and Fatigue Properties of High Strength Aluminium Aircraft Materials", NLR TR 78133, National Aerospace Laboratory NLR, Amsterdam, November 1978.
- [5] Kolkman, H.J., Kool, G.A. and Wanhill, R.J.H., "Aircraft Crash caused by Stress Corrosion Cracking", to be presented at the 39th Int. Gas Turbine Conference and Exhibit, to be held in The Hague, The Netherlands, June 13-16, 1994.
- [6] Restall, J.E., pp. 269 - 273 in "The Development of Gas Turbine Materials", edited by Meetham, G.W., Applied Science Publishers Ltd, London, 1981.
- [7] Wakeman, T. and Tabakoff, W., J. Aircraft **16** (1979) 828 - 833.
- [8] Goodwin, J.E., Sage, W. and Tilly, G.P., Proc. Instn. Mech. Engrs. **184** (1969 - 1970), pp. 279 - 292.
- [9] Kolkman, H.J., "Erosion of Corrosion Resistant Coatings for Jet Engine Compressors", paper 45 of the 6th Int. Conf. on Erosion by Liquid and Solid Impact, Cambridge (UK), 1983.
- [10] Kolkman, H.J., "New Erosion Resistant Compressor Coatings", ASME Paper 88-GT-186, presented at the 33th Int. Gas Turbine Conference and Exhibit, Amsterdam, The Netherlands, June 6-9, 1988.
- [11] Parameswaran, V.R., Immarigeon, J.-P. and Nagy, D., Surface and Coatings Technology **52** (1992) 251 - 260.
- [12] Szklarska-Smialowska, Z., "Pitting Corrosion of Metals", NACE, 1986.
- [13] Brite Euram Programme 3339, "The Development of Advanced Erosion Resistant Coatings for Gas Turbine Compressor Applications", 1990-1993.

#### QUESTIONS

##### A. ROSSMANN (Ge)

- Q. a) Why did you not consider the possibility of coating the IN 100 blade material?
- b) What is the physical background of the better performance of the single crystal blades in your test rig (as compared with IN 100)?
- A. a) At the time, SR 99 had already been chosen as the new blade material, due to its improved creep life.
- b) SR 99 apparently has better oxidation resistance than IN 100 because of its chemical composition. Another possible advantage is the absence of grain boundaries which would be sensitive to sulfidation.



## Revêtements anti-érosion multicouches

P. Monge-Cadet - F. Pellerin  
C. Farges\* - D. Rickerby\*\* - E. Quesnel\*\*\*

TURBOMECA - 64511 BORDES - FRANCE  
\* ETCA/DGA - 94114 ARCUEIL - FRANCE  
\*\* ROLLS ROYCE - DERBY DE2 8BJ - UNITED KINGDOM  
\*\*\* CENG/CEREM - 38041 GRENOBLE - FRANCE

### ABSTRACT

Gas turbine for helicopters are prone to high degradations by abrasive particle ingestion when taking off, landing or during low altitude flights.

Multilayer coatings have been developed to protect critical compressor components. After a presentation of the relevant parameters for conception and achievement of erosion resistant coatings, the most promising systems will be described. They are based on stacking arrangement of ductile layers (tungstène) and hard layers (solid solution of carbon or nitrogen into tungstène, titanium diboride). These multilayer coatings exhibit an erosion resistance improved by more than two orders of magnitude compared with that of uncoated Ti6Al4V alloy.

### RESUME

Les turbines à gaz pour hélicoptères subissent des dégradations importantes dues à l'ingestion de particules abrasives au cours des phases de décollage, d'atterrissage ainsi que lors de vols effectués à basse altitude.

Des revêtements multicouches ont été développés pour protéger les pièces du compresseur les plus exposées. Après une présentation des paramètres pertinents pour la conception et la réalisation de revêtements anti-érosion, les solutions les plus prometteuses sont présentées. Elles sont basées sur une alternance de couches ductiles (tungstène) et de couches de haute dureté (solution solide de carbone ou d'azote dans le tungstène, diborure de titane). Ces multicouches présentent une résistance à l'érosion améliorée de deux ordres de grandeurs par rapport à l'alliage TA6V non revêtu.

### INTRODUCTION

Un moteur d'hélicoptère est conçu pour aspirer une grande quantité d'air au travers des différents étages de compression. De ce fait, toute particule en suspension dans l'air sera aspirée, accélérée et viendra impacter et éroder les différentes pièces de la veine gazeuse. Le phénomène est activé par l'effet du rotor de l'hélicoptère qui crée de véritables nuages de poussière lors des phases de décollage ou d'atterrissage et lors de manœuvres à basse altitude dans des atmosphères sablonneuses. Les dégradations résultant de ce phénomène sont

particulièrement critiques au niveau des premiers étages de compresseur puisqu'elles peuvent représenter 60 à 70 % des causes de rebut (compresseur axial 1er étage).

Il existe toutefois plusieurs façons de lutter contre l'érosion :

- Utilisation de systèmes de filtration ou de séparation de particules en amont du compresseur : ceux-ci ont pour effet d'alourdir l'hélicoptère et de faire chuter ses performances.
- Utilisation de matériaux plus performants vis-à-vis de l'érosion : le gain est limité (coefficient compris entre 1,5 et 2 en remplaçant un alliage de titane par un acier) et s'accompagne automatiquement d'une augmentation de la masse.
- Utilisation de revêtements anti-érosion.

Nous nous proposons ici de faire la synthèse des activités menées par TURBOMECA dans ce domaine lors des cinq dernières années et dans le cadre des actions suivantes :

- Programme BRITE BE 3339 - Contrat n° BREU-0122 [1],
- Soutien STPA/Ma pour le développement de revêtements multicouches à base de tungstène [2] [3].

### TECHNIQUES EXPERIMENTALES

#### Elaboration des revêtements

Les revêtements monocouches W et TiB<sub>2</sub> ou multicouches W/W-C, W/W-N, W/TiB<sub>2</sub> et NiCr/TiB<sub>2</sub> ont été déposés par pulvérisation cathodique magnétron courant continu, à partir de cibles planes en W, TiB<sub>2</sub> ou en NiCr (80/20). Les substrats étaient des parallélépipèdes en alliage de titane TA6V de dimensions 50 x 50 x 3 mm. Préalablement au dépôt, l'enceinte de pulvérisation a été pompée jusqu'à une pression résiduelle d'environ 5 x 10<sup>-4</sup> Pa et les échantillons nettoyés par bombardement ionique en atmosphère d'argon pur.

La distance cible-substrat était de 70 mm pour le multicouche W/W-C et de 90 mm pour tous les autres revêtements. Les couches W-C et W-N ont été synthétisées respectivement dans des mélanges Ar + CH<sub>4</sub> et Ar + N<sub>2</sub>. Les couches de TiB<sub>2</sub>, W et NiCr ont été déposées en atmosphère d'argon pur. Les débits d'argon, de méthane et d'azote ont été contrôlés au moyen de débitmètres massiques. La température des substrats a été déterminée par thermocouple chromel-alumel implanté dans le porte-substrat.

La dureté Vickers des monocouches a été mesurée au moyen d'un appareil de micro-indentation sous une charge de 1N. La nature cristallographique des couches TiB<sub>2</sub>, W-N et W-C a été déterminée par diffraction des rayons X en utilisant respectivement une anticathode de Cu et de Co. La concentration en carbone des couches W-C a été déterminée par analyse de réactions nucléaires en utilisant la réaction nucléaire <sup>12</sup>C(d,p)<sup>13</sup>C avec un faisceau de deutons d'énergie 1,05 MeV. La composition des couches TiB<sub>2</sub> a été déterminée par analyse en microsonde électronique. Le profil de composition des couches W-N a été analysé par spectroscopie de lampe à décharge lumineuse.

Les revêtements TiN et Ti/TiN ont été élaborés par la technique d'évaporation par arc dans une installation Interatom 32" Ion Bond<sup>TM</sup>, à partir de sources en titane. La structure multicouche Ti/TiN a été obtenue en opérant alternativement en atmosphère d'argon ou d'azote.

#### Erosion : conditions d'essais

Les performances en érosion des matériaux et revêtements ont été évaluées sur un banc d'essai dont le principe et les caractéristiques sont détaillés respectivement en Figure 1 et Tableau 1.

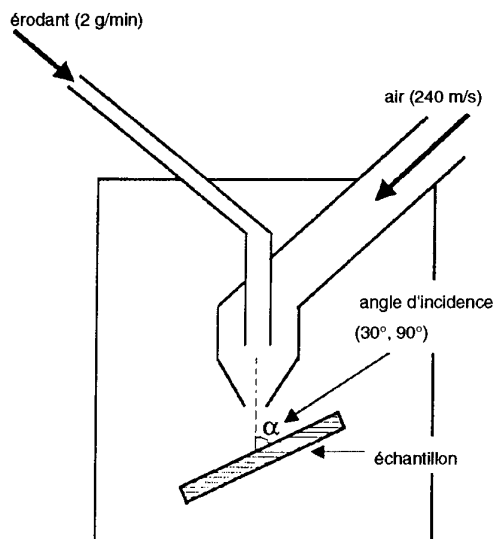


Figure 1 : schéma de principe de banc érosion

Tableau 1  
Conditions de l'essai d'érosion.

PARAMETRES FIXES	
nature érodant	quartz angulaire
vitesse air	240 m/s
débit érodant	2 g/min
diamètre buse	6 mm
distance buse/échantillon	25 mm
température	ambiante

PARAMETRES VARIABLES	
angle d'incidence	30° - 90°
diamètre moyen des particules érodantes	80 µm - 600 µm
durée essai	25 min maximum (l'essai est interrompu dès que le revêtement est totalement érodé)

Le comportement en érosion dépend de nombreux paramètres tels que la nature, la taille, la vitesse, l'angle d'incidence des particules érodantes ou les propriétés du matériau. Il est par exemple bien connu (Figure 2) que le taux d'érosion est maximal sous faible incidence pour un métal (matériau de type ductile), et sous incidence normale pour une céramique (matériau de type fragile).

En ce qui concerne la nature et la taille des particules, les normes faisant référence (MIL - E- 5007 C, BS 1701 C, AC COARSE), spécifient des particules de quartz dont le diamètre peut varier de quelques microns à 1 mm. Afin d'étudier l'influence de la taille des particules, deux types d'érodant présentant une distribution beaucoup plus resserrée et un diamètre moyen de 80 et 600 µm ont été choisis.

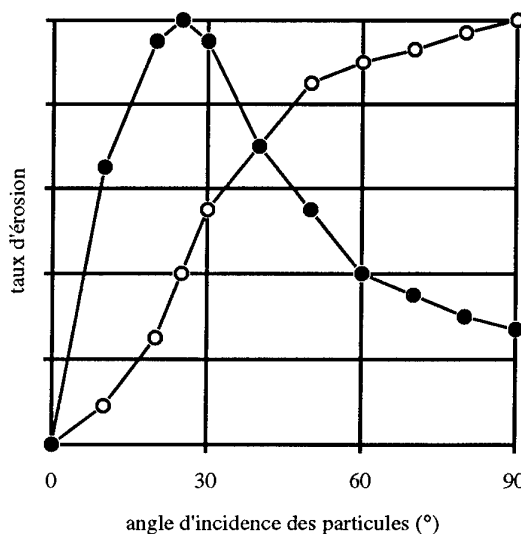


Figure 2 : influence de l'angle d'incidence des particules érodantes sur le comportement en érosion des matériaux métalliques et céramique.

Leurs caractéristiques sont comparées en Figure 3 à celles des érodants normalisés. L'essentiel des essais a cependant été réalisé avec l'érodant de forte granulométrie, ce qui correspond aux conditions les plus sévères.

Les performances des différents revêtements sont mesurées en faisant un suivi de la perte de masse de chacun des échantillons en fonction du temps. Le taux d'érosion E (mg/kg), représente alors la perte de masse exprimée en mg et rapportée à 1 kg d'érodant.

Les résultats sont présentés en normalisant ce taux d'érosion à celui du substrat TA6V, systématiquement utilisé, et en tenant compte des densités relatives.

Il en résulte le facteur d'amélioration suivant :

$$FA = \frac{E_{TA6V}}{E_{revêtement}} \cdot \frac{\rho_{revêtement}}{\rho_{TA6V}}$$

avec :

$E$  = taux d'érosion

$\rho$  = densité

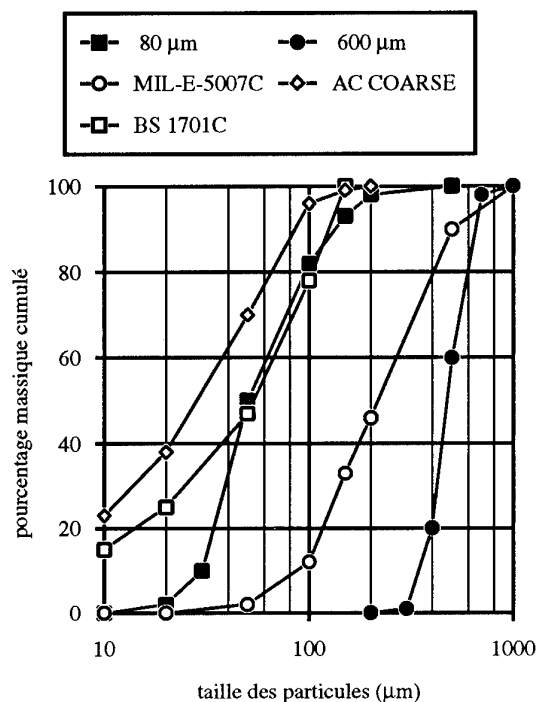


Figure 3 : distribution granulométrique des différents érodants.

## RESULTATS

### Analyse des monocouches

Les profils de composition enregistrés par spectroscopie de lampe à décharge lumineuse révèlent que l'intensité de la raie d'émission spectrale de l'azote est constante sur toute l'épaisseur des couches W-N et proportionnelle au débit d'azote. La Figure 4 montre l'évolution des spectres de diffraction des rayons X des couches W et W-N pour quatre valeurs du débit d'azote.

Quel que soit le débit d'azote, compris entre 0 et 50 cm<sup>3</sup>.standard min<sup>-1</sup> (sccm), seule la phase  $\alpha$ -W de structure cubique centrée (Fd3m) est identifiée. La couche de tungstène a un paramètre de maille de 0,3184 nm et présente une texture (110) de type monocristalline. Les couches de solution solide d'azote dans le tungstène, W-N, ont une orientation préférentielle (111) qui

décroît avec la concentration en azote. Le paramètre de maille, indépendant de la concentration en azote dans la limite du domaine exploré, est égal à 0,319 nm Figure 4.

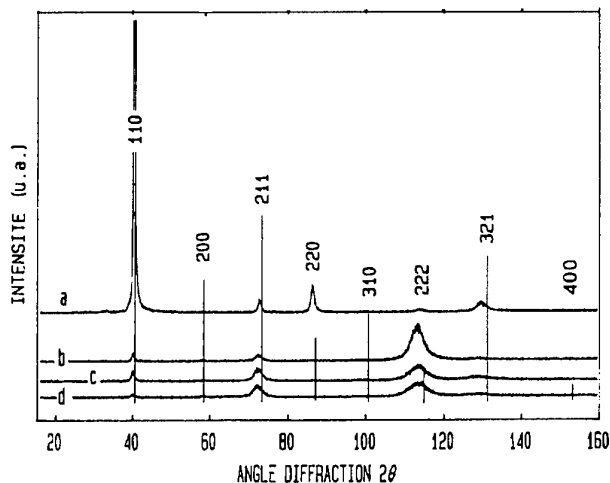


Figure 4 : spectres de diffraction des couches W et W-N pour différents débits d'azote, (a) 0 sccm, (b) 10 sccm, (c) 30 sccm et (d) 50 sccm.

La dureté  $HV_{0,1}$  augmente avec le débit d'azote depuis la valeur du tungstène pur 13,5 GPa, pour atteindre 33 GPa pour un débit d'azote de 50 sccm. L'augmentation de dureté avec le débit d'azote (Fig. 5a) correspond à une variation de la largeur à mi-hauteur des raies de diffraction ( $B_{hkl}$ ). A titre d'exemple,  $B_{222}$  augmente de 2,1 à 3,8 puis 5,2 lorsque le débit d'azote augmente de 0 à 10, puis 50 sccm.

Les résultats de la caractérisation des couches W-C ayant été publiés en détail par ailleurs [4, 5], seules les principales caractéristiques nécessaires à la compréhension de leur comportement aux essais d'érosion sont rappelées ici. Pour une concentration en carbone comprise entre 0 et 22,5 % at., toutes les couches présentent une structure  $\alpha$ -W. Le diagramme de variation de la dureté Vickers en fonction de la concentration en carbone présenté en Figure 5b, montre que la dureté des couches W-C passe par un maximum de 26 GPa pour une concentration en carbone de 14 % at. La variation de la dureté peut être expliquée par la dilatation du réseau de la structure  $\alpha$ -W avec la concentration en carbone. Dans l'intervalle 0 à 14 % at. C, la dilatation du réseau est progressive et isotrope dans les trois directions principales du cristal. Au-delà de 14 % at., une anisotropie de dilatation apparaît dans une des directions principales. Ce phénomène qui s'accompagne d'un élargissement des raies de diffraction correspond à une diminution de la dureté des couches.

Les couches élaborées à partir d'une cible en TiB<sub>2</sub> ont une concentration en bore de 71 ± 1 % at. (TiB<sub>2,5</sub>). Quels que soient les paramètres de dépôt utilisés, elles présentent une forte texture de fibre (001). Leur dureté  $HV_{0,1}$  est égale à 43 ± 6 GPa.

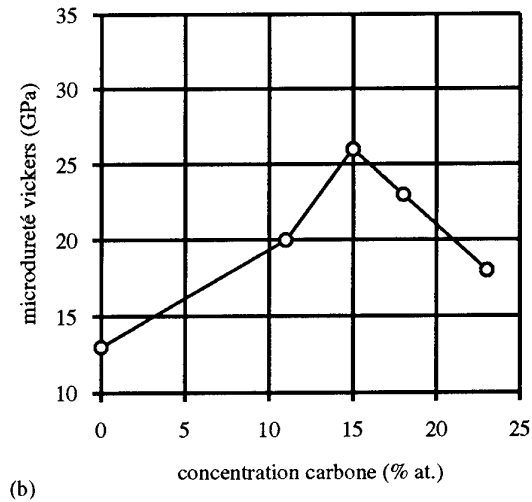
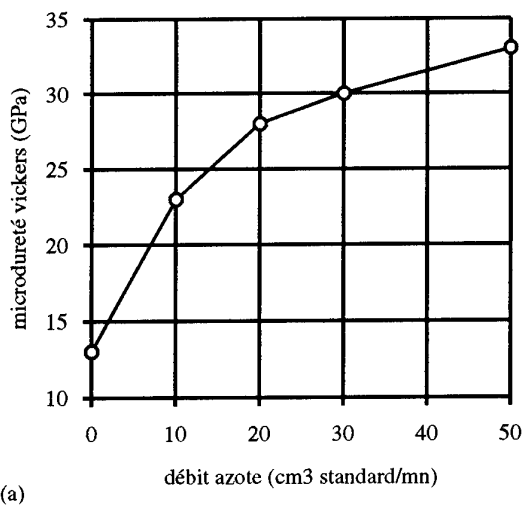


Figure 5 : variation de la microdureté Vickers, (a) des couches W-N (mesurée sous 100g) en fonction du débit d'azote, (b) des couches W-C (mesurée sous 50g) en fonction de la concentration en carbone.

### Caractérisation des revêtements en érosion

La liste et les caractéristiques des revêtements évalués en érosion sont présentées dans le tableau 2, mais avant de détailler les résultats obtenus, quelques remarques s'imposent pour bien comprendre le cheminement suivi.

Quand on s'intéresse à l'angle d'incidence des particules lors de l'impact sur les aubes d'un compresseur, on s'aperçoit que dans une région située en intrados bord d'attaque, cet angle varie très rapidement (en quelques millimètres) d'une incidence normale à une incidence rasante [6]. Dans ces conditions, si l'on se reporte à la Figure 2, un revêtement ou un matériau pour être performant doit pouvoir allier à la fois un comportement de type ductile et de type fragile.

Le matériau constitutif des aubes, l'alliage de titane TA6V, étant un matériau ductile, la première démarche pour résoudre le problème d'érosion a consisté à étudier des revêtements durs de type fragile.

#### Revêtements monocouches

Compte tenu des conditions d'érosion imposées, il est rapidement apparu qu'une épaisseur de revêtement de 50 à 60  $\mu\text{m}$  était nécessaire, épaisseur acceptable d'un point de vue aérodynamique, et qui correspond à une limite technologique eu égard aux matériaux et aux procédés de dépôt choisis.

Dans ces conditions, un revêtement monocouche de TiN ou de TiB<sub>2</sub> se révèle performant sous faible incidence d'impact comme le montre les résultats de la Figure 6 : les facteurs d'amélioration sont respectivement de 243 et de 101. Ces résultats s'expliquent par le fait que seule une faible partie de l'énergie des particules est absorbée lors de l'impact (angle faible), si bien que les revêtements restent dans le domaine élastique compte tenu de leur haut module et de leur grande dureté.

Sous incidence normale, ces revêtements peuvent rester protecteurs pour des érodants de faible granulométrie comme illustré en Figure 7, mais il existe une énergie critique au dessus de laquelle apparaît leur caractère fragile qui conduit rapidement à une fissuration et à un écaillage du dépôt. Avec un érodant de forte granulométrie (600  $\mu\text{m}$ ), la Figure 6 montre les faibles performances du TiN et du TiB<sub>2</sub> puisque les facteurs d'amélioration sont respectivement de 0,2 et de 0,4.

#### Erodant : 600 $\mu\text{m}$

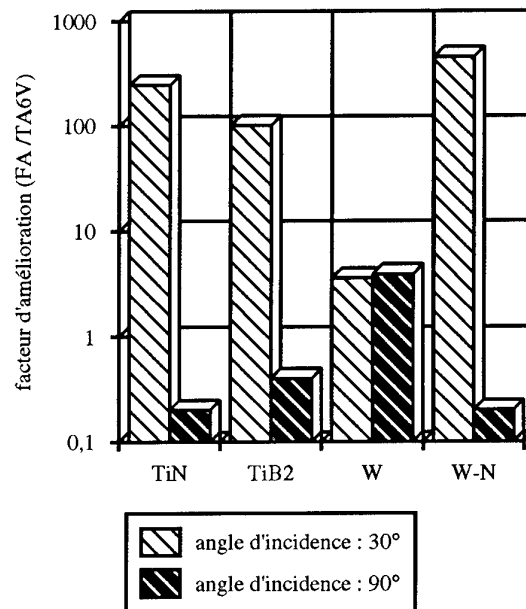


Figure 6 : comportement en érosion des revêtements monocouches.

**Tableau 2**  
**Caractéristiques des revêtements testés en érosion**

Revêtement	Type d'empilement	Epaisseur (μm)	Nombre de couches	Dureté de surface sous 1 Kg (GPa)	Résultats d'érosion (FA) érodant 600μm	
					30°	90°
TiN	-	50	1	18,6	243	0,2
TiB <sub>2</sub>	-	50	1	26,7	101	0,4
W	-	35	1	10,8	3,6	3,9
WN	-	50	1	24,8	449	0,2
Ti/TiN (0,3/0,3)	0,3/0,3	50	150	8,5	2,8	0,5
Ti/TiN (1/1)	1/1	50	50	7,3	3	1,2
Ti/TiN (1/10)	1/10	55	10	16,7	24	0,3
Ti/TiN (10/10)	10/10	50	5	7,6	0,7	0,1
Ti/TiB <sub>2</sub>	1/1	50	50	9,3	1	0,5
NiCr/TiN	0,3/0,3	50	50	9,1	0,2	0,1
NiCr/TiB <sub>2</sub>	1/1	50	50	15,7	17,5	1,2
W/TiB <sub>2</sub>	1/1	50	50	21,6	526	460
W/WN	1/1	50	50	21,2	382	334
W/WC	5/5	61	12	21,9	509	668

A ce stade, il est intéressant d'analyser le comportement d'une monocouche de tungstène. Ce matériau présente l'inconvénient d'une densité élevée mais a des atouts très intéressants vis-à-vis de l'érosion. C'est d'abord un matériau métallique, donc de type ductile, mais qui possède un très haut module d'élasticité (406 GPa) et une grande dureté (13 GPa). Dans les conditions d'érosion de la Figure 6, le tungstène devient alors protecteur quel que soit l'angle d'incidence, mais avec toutefois un facteur d'amélioration relativement faible notamment sous incidence rasante si l'on se réfère au TiN.

L'augmentation de la dureté de la couche de tungstène par l'ajout de carbone ou d'azote, permet de retrouver une protection équivalente à celle du TiN sous un angle d'incidence de 30°. Mais bien que la solution solide ainsi obtenue soit moins fragile [4], le facteur d'amélioration chute sous incidence normale (FA = 0,10). En fait, un revêtement monocouche ne peut pas résoudre notre problème d'érosion.

#### *Revêtements multicouches*

Afin de bénéficier des avantages des matériaux fragiles (incidence rasante) et ductiles (incidence normale), des revêtements multicouches constitués d'une alternance de couches élémentaires de chacun des deux types ont été étudiés. Pour des raisons de compatibilité de matériaux, mais également de simplicité de dépôt, les premiers multicouches évalués ont été les revêtements Ti/TiN.

La première phase du programme BRITE BE 3339 [1] a consisté à étudier l'influence de l'épaisseur des couches élémentaires (à épaisseur de revêtement équivalente) sur le comportement en érosion. Les résultats présentés en Figure 8 mettent en évidence des phénomènes distincts en fonction de l'angle d'incidence des particules érodantes.

Dans les conditions les plus sévères, c'est-à-dire avec un érodant de forte granulométrie (600 μm) et sous incidence normale, on note une amélioration du comportement à l'érosion lorsque les couches métalliques et céramiques sont de même épaisseur et lorsque cette épaisseur est faible : Ti/TiN (1/1) et (0,3/0,3). En fait ce type d'empilement conduit à des revêtements de type ductile présentant des performances médiocres sous incidence rasante. Dans ces conditions d'essai, le multicouche le plus performant est celui pour lequel le taux de céramique est le plus important : Ti/TiN (1/10). Le remplacement du matériau céramique, TiB<sub>2</sub> à la place du TiN, n'a aucun effet bénéfique sur le résultat final. En revanche, la modification de la couche métallique, notamment en augmentant son module d'élasticité, permet de réduire le caractère ductile de ces multicouches comme le montrent également les résultats de la Figure 8. Le fait de doubler le module, remplacement du Ti (116 GPa) par du NiCr (207 GPa) n'a pas d'effet quand cette couche métallique est associée à du TiN, mais se traduit par une nette amélioration sous incidence rasante avec du TiB<sub>2</sub> : le multicouche NiCr/TiB<sub>2</sub> présente un facteur d'amélioration de 17,5 sous 30° et 1,2 sous 90°. L'utilisation du tungstène dont le module est de 406 GPa, permet d'augmenter à nouveau cet effet, et le multicouche W/TiB<sub>2</sub> présente alors des performances remarquables, avec un facteur d'amélioration supérieur à 450 quel que soit l'angle d'incidence.

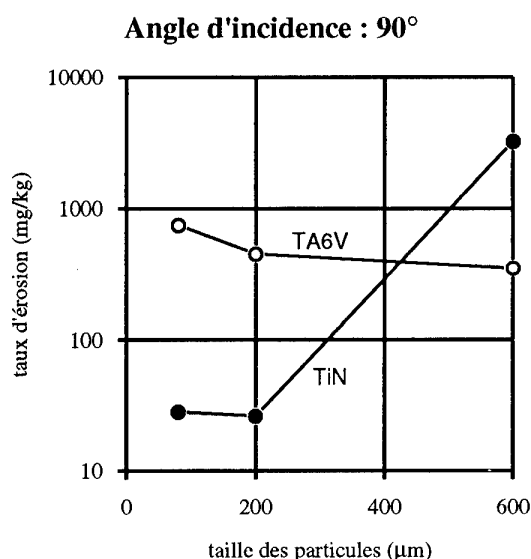


Figure 7 : influence de la taille des particules érodantes sur le comportement en érosion.

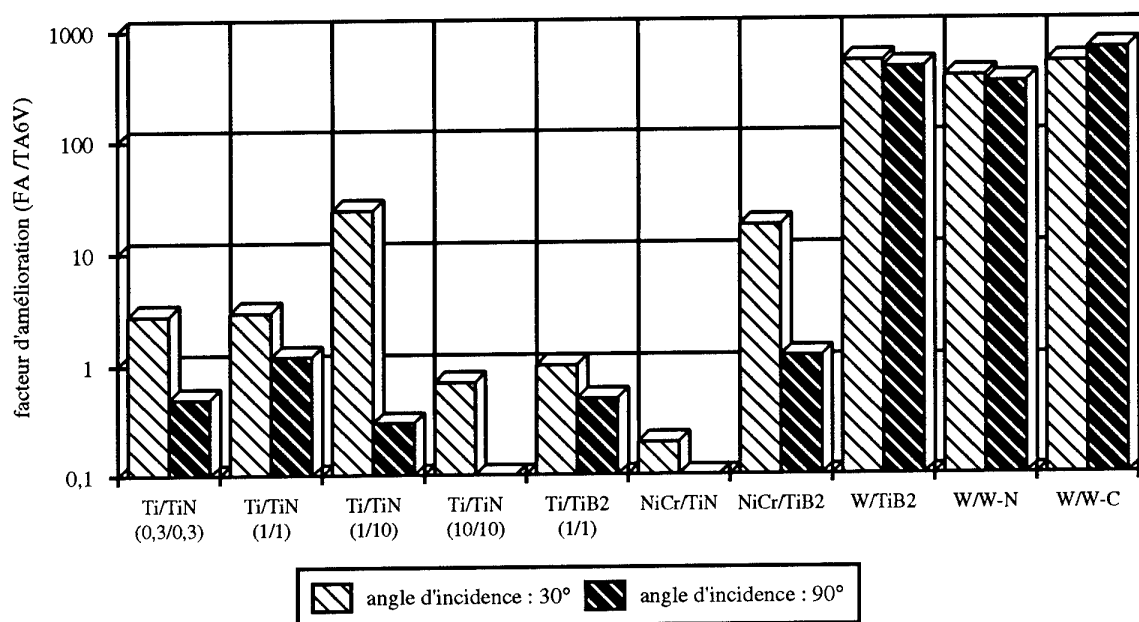
Erodant : 600  $\mu\text{m}$ 

Figure 8 : comportement en érosion des revêtements multicouches.

Des résultats équivalents sont obtenus avec des multicouches W/W-C et W/W-N où W-C et W-N sont respectivement des solutions solides de carbone et d'azote dans du tungstène. Les structures et les morphologies types de ces deux revêtements sont illustrées en Figures 9 et 10. On peut noter en particulier la différence d'épaisseur des couches élémentaires (5  $\mu\text{m}$  pour W-C et 1  $\mu\text{m}$  pour W-N) et l'absence de structure colonnaire dans les couches W-C.

Il est intéressant d'analyser le comportement de ces 3 revêtements. Sous faible incidence d'impact, les facteurs d'amélioration élevés s'expliquent par une dureté de surface (Tableau 2) supérieure à 20 GPa et tout à fait comparable à celle d'une monocouche de TiN ou de TiB<sub>2</sub>. Les trois revêtements ont alors un comportement de type fragile.

En revanche, sous incidence normale, on ne retrouve absolument pas ce comportement, puisque les fissures qui apparaissent dans les couches dures sont déviées et/ou stoppées [5] lorsqu'elles atteignent les interfaces et les couches de tungstène, comme illustré en Figure 10 sur un multicouche W/W-C. La morphologie de la zone érodée d'un revêtement W/TiB<sub>2</sub> présentée en Figure 11, met en évidence ce phénomène, mais montre également les déformations plastiques (au voisinage de la zone érodée) que peut supporter ce type de revêtement.

## DISCUSSION

Jusqu'à présent, les matériaux ou revêtements pouvaient être classés en deux catégories vis à vis de l'érosion : matériaux de type ductile et matériaux de type fragile.

Avec les revêtements à base de tungstène, un nouveau type de comportement apparaît. Ce comportement, illustré en Figure 12 peut se résumer et s'expliquer de la façon suivante :

- sous incidence d'impact rasante (Fig 12 a) : le comportement est identique à celui d'un revêtement de type fragile. En fait, sous l'impact, le revêtement reste dans le domaine élastique compte tenu d'une part que la dureté de surface du multicouche est très élevée (> 20 GPa) et d'autre part que les couches de métal et de céramique présentent des modules non seulement élevés mais également voisins (respectivement 406 GPa et 550 GPa pour le W et le TiB<sub>2</sub> par exemple).

- sous incidence d'impact normale (Fig 12 b) : il apparaît une période d'incubation au cours de laquelle la totalité de l'énergie d'impact des particules est absorbée sans qu'apparaisse la moindre dégradation. Ce phénomène est à corrélérer à un mécanisme de sollicitation et de dégradation du type fatigue, pendant lequel il y a accumulation de "défauts" sans propagation. Il peut s'expliquer par une absorption, aux interfaces, de l'énergie des fissures, et se traduit par une déviation voire un arrêt de la propagation dans les couches ductiles de tungstène.

A cet égard, la ténacité interfaciale est un paramètre primordial et de ce point de vue, la "cohérence" du réseau cristallographique entre le tungstène et les solutions solides est favorable. Dans ces conditions, le haut module du tungstène joue également un autre rôle puisqu'il permet de limiter la déformation du revêtement et donc la fissuration qui en résulte.

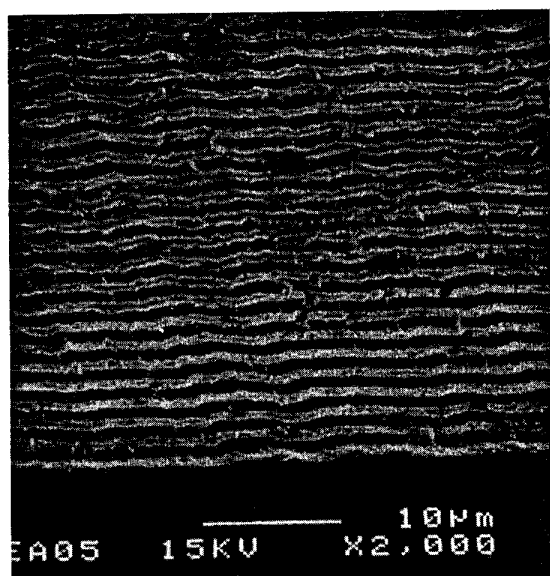


Figure 9 : Coupe métallographique (MEB) du revêtement W/W-N (vue partielle)

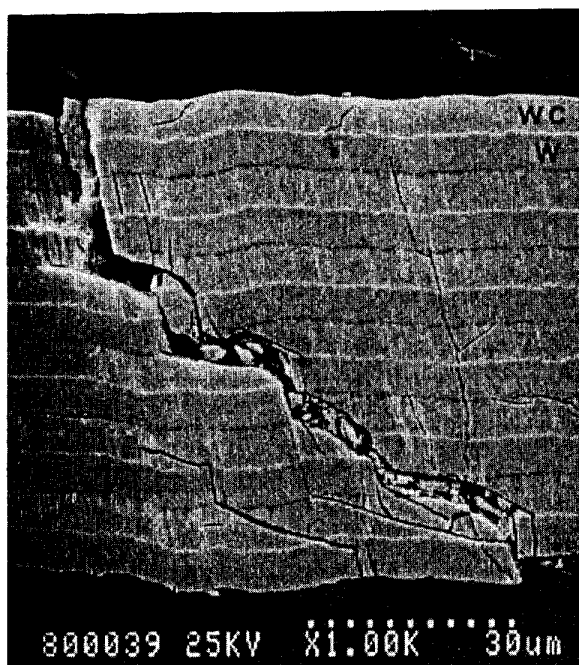


Figure 10 : Coupe métallographique (MEB) du revêtement W/W-C après un essai d'érosion de 35 min (durée exceptionnelle) sous incidence normale



Figure 11 : Fractographie (MEB) du revêtement W/TiB<sub>2</sub> après un essai d'érosion de 25 min sous incidence normale.

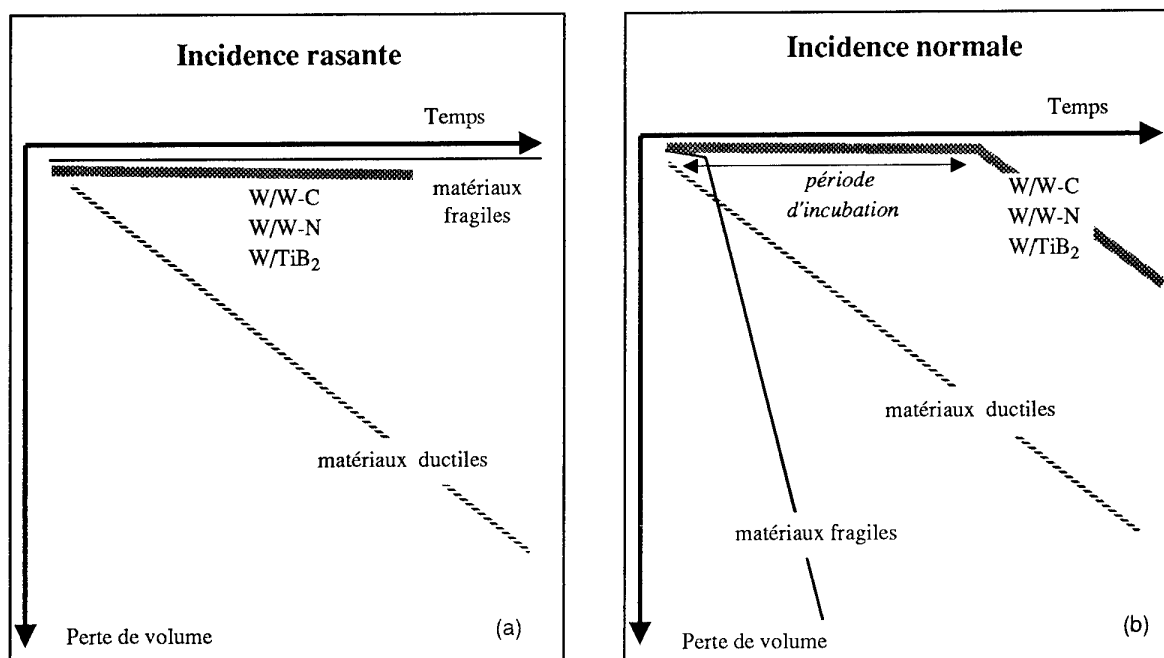


Figure 12 : mécanismes de dégradation des différentes familles de matériaux en fonction de l'angle d'incidence des particules érodantes.

## CONCLUSION

Les revêtements multicouches à base de tungstène W/W-C, W/W-N et W/TiB<sub>2</sub> constituent une nouvelle génération de revêtements anti-érosion dans la mesure où leurs mécanismes de dégradations font appel à des lois nouvelles par rapport aux comportements de type ductile ou fragile connus jusqu'alors. Les résultats obtenus dans nos conditions d'essais laboratoire font apparaître des gains spectaculaires de plus de deux ordres de grandeurs qui permettent d'envisager une issue favorable à nos problèmes d'érosion. Il reste cependant à résoudre un certain nombre de points notamment au niveau des contraintes résiduelles (fortes contraintes de compression), de la faisabilité de ces revêtements sur pièce réelle et de la validation de ces solutions dans des essais moteurs normalisés.

## REMERCIEMENTS

Les travaux concernant les revêtements à base de TiN et de TiB<sub>2</sub> ont été réalisés dans le cadre d'un programme BRITE [1]. Les auteurs remercient l'ensemble des partenaires dont la liste est donnée en référence [1], et tout particulièrement P. HATTO de la société ASET qui a réalisé tous les revêtements à base de TiN. Ce programme a donné lieu à un dépôt de brevet.

Les études concernant les revêtements W/W-C, effectuées conjointement par TURBOMECA et le Centre d'Etude Nucléaire de Grenoble, ont été soutenues par le Ministère Français de la Défense (Service Technique des Programmes Aéronautiques Matériaux) et ont fait l'objet d'un brevet français [7].

Les travaux concernant les revêtements W/W-N, réalisés par l'ETCA (Etablissement Technique Centrale de l'Armement), ont également fait l'objet d'un brevet français [8].

Ces deux brevets ont fusionné lors du dépôt à l'étranger [9].

## REFERENCES

- [1] Programme BRITE n° BE - 3339 - contrat BREU - 0122. "Development of advanced erosion resistant coatings for gas turbine compressor applications". Partenaires : Rolls-Royce Plc (UK) leader, Turboméca (France), Cranfield Institute of Technology (UK), ASET (UK), MIRTEC (Greece), ETCA et IMP/CNRS (France), BC&C (UK), NLR (Holland), AEA Technology (UK) replacing SGM (Holland).
- [2] Marché STPA/Ma n°88-96010 BC 12 - lot B - rapport interne TURBOMECA NT 4616.
- [3] Marché STPA/Ma n°90-96027 BC 10 - lot A - rapport interne TURBOMECA NT 5008.
- [4] Y. PAULEAU, Ph. GOUY-PAILLER and S. PAIDASSI, Surf-Coat. Technol., 54-55 (1992) 324.
- [5] E. QUESNEL, Y. PAULEAU, P. MONGE-CADET, M. BRUN, "Tungsten and tungsten-carbon PVD multilayered structures as erosion-resistant coatings." Surfaces and Coatings Technology 62 (1993) 474-479.
- [6] G.C.HORTON, H. VIGNAU, G. LEROY, "simulation de l'érosion dans les compresseurs de turbine à gaz", AGARD PEP, Rotterdam, 15, avril 1994.
- [7] Brevet Français n°91 12616.
- [8] Brevet Français n°92 08500.
- [9] Brevet PCT/FR92100969.



# HIGH VELOCITY OXYGEN FUEL SPRAYING OF EROSION AND WEAR RESISTANT COATINGS ON JET ENGINE PARTS.

A.T.J. Verbeek, Turbine Support Europa b.v.,  
Siriusstraat 55, 5015 BT Tilburg, the Netherlands

## 0 ABSTRACT

High Velocity Oxygen Fuel (HVOF) spraying is the most recent development in the field of thermal spraying. The importance of this technique for the repair and new part manufacturing of jet engine parts is rapidly increasing.

The HVOF uses a supersonic oxygen-fuel flame to heat and accelerate the powder particles that form the coating.

The high particle velocity results in a high density and a low porosity, a high bond strength and a high macro and micro hardness of the coating. The high quality of the HVOF coatings makes it possible to use these coatings on high loaded, rotating parts in jet engines.

This paper will highlight the use of HVOF processes to apply erosion resistant cermet coatings to high pressure compressor blades. These blades are exposed to severe erosion. Next to the D-gun process, HVOF spraying is the only non proprietary technique that can be used to apply these high performance coatings.

Also the use of the HVOF process to apply wear resistant coatings and superalloys to jet engine parts will be discussed. The difference between HVOF coatings and plasma sprayed coatings will be highlighted.

During HVOF spraying, the parts are exposed to a high heat flow. Solutions to avoid overheating and especially of titanium parts will be presented.

## 1. INTRODUCTION

Thermal spraying is widely used to apply protective coatings to jet engine parts. Until now, plasma spraying and flame spraying were the most used processes. The last years, however, high velocity oxygen fuel (HVOF) spraying has become more and more important. HVOF coatings distinguish themselves through their high bond strength, high wear resistance, low porosity and high hardness. For many applications that will be discussed further on, HVOF coatings offer advantages compared to plasma or flame sprayed coatings.

HVOF coatings are dense, have a high bond strength and are harder and more wear resistant than plasma sprayed or flame sprayed coatings. These characteristics make HVOF coatings suitable for application on highly loaded jet engine parts. The coatings can have two functions: to restore the dimensions of worn parts or to protect a surface against wear, erosion or corrosion. Because of the fact that HVOF makes it possible to spray dense (porosity < 1%) super alloy coatings with a low oxide content (< 1%) and a high bondstrength (>10,000 PSI), the process is used to restore the dimensions of highly loaded rotating parts, made of these superalloys.

Due to their high hardness (>1200 Hv0.3), HVOF coatings of WC-Co and Cr<sub>3</sub>C<sub>2</sub>-NiCr, are used to protect jet engine parts against erosion and wear.

This paper describes the principles of HVOF spraying. It gives some coating applications of HVOF coatings and gives a comparison of plasma sprayed coatings and HVOF coatings.

## 2 HVOF SPRAYING, PRINCIPLES.

HVOF spraying is not a new technique. It was developed by Linde as the Detonation-gun (D-gun) technique. The D-gun operates on an intermittent basis. A fuel oxygen mixture is led into a combustion chamber through a valve and subsequently ignited by a spark plug. The combustion gasses travel with supersonic speed through a long barrel. Powder that is injected in the barrel is heated up and accelerated. The molten powder particles collide on a surface where a dense and well adhering coating is build up. The Detonation gun operates on a frequency of approximately 8 Hz.

The new HVOF systems, on the contrary, operate with continuous combustion. A HVOF system consists of a fuel and oxygen supply, a gun to generate the supersonic flame and a powder feed system. The whole system can be integrated in a robotic system to manipulate the gun and the part the coating has to be applied to.

The fuel and oxygen are fed into a combustion chamber where they are mixed and ignited. The hot gasses expand through a "Laval" nozzle. Due to the special shape of the nozzle, the

flame reaches a supersonic velocity. The velocity of the flame can range from 1400 to 2200 m/s. Characteristic for an supersonic flame is the presence of shock diamonds. Figure 1 gives the principle of HVOF spraying.

The maximum temperature of the flame varies from 3000 to 3300 °C. The particle temperature varies from 1400 °C to 2500 °C and the velocity ranges from 400 to 1100 m/s. (Depending on particle size)

There exist several types of commercially available HVOF guns. They all operate and conform to the same principle but the fuel they use and the way they are cooled may differ. The fuel can be liquid or gaseous. Propylene, hydrogen, propane and acetylene are used as fuel gases, whereas kerosene is used as a liquid fuel. Both water cooling and air cooling are applied to cool the gun. Powder injection can be radial or axial. Radial powder injection makes more powder ports possible, resulting in a higher deposition rate, but may lead to clogging of coating material in the nozzle. Axial injection has the advantage that the powder is injected in the centre of the flame and that the danger of clogging is diminished. The spray rate, however, is lower than when using radial injection. See figure 1 for the injection principles.

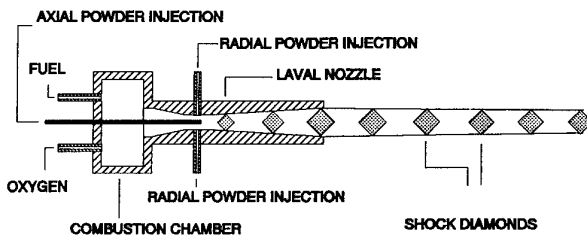


Figure 1 Schematic view of a HVOF gun. The shock diamonds in the flame and the laval nozzle are characteristic for the HVOF process.

### 3 HVOF SPRAYING, CHARACTERISTICS

This paragraph describes the main characteristics of the HVOF process. It describes the advantages and disadvantages of the HVOF spraying technique and compares

#### 3.1 Limitations and possibilities of materials to be sprayed with HVOF

HVOF spraying is a flame spray process. This implies that the flame temperature is limited to approximately 3580 K. Compared to plasma spraying, where flame temperatures of 20,000 K can be reached, this is rather low. The lower flame temperature combined with the high flame velocity (1400 – 2200 m/s) makes HVOF spraying less suitable for the application of ceramic coatings. The dwell time [1], that is the time a particle stays in the flame, is too short to obtain a well heated particle. As a result, ceramic particles, which have a

high melting point and a low thermal conductivity, will not be fully melted during HVOF spraying. The adhesion of these particles will be bad and they will not flatten during impact on the substrate because of the fact that their cores are still solid. On the other hand, HVOF spraying is ideal for spraying metallic and cermet materials without the risk of overheating the particles. Overheating the particles may lead to excessive oxidation in metallic coatings or phase changes in cermet materials.

#### 3.2 Limitation of part temperatures during HVOF spraying.

One of the limitations of HVOF spraying is the high heat input in the part. When using plasma spraying, the highest heat input is caused by the solidifying particles [2]. When using HVOF spraying, the highest heat input is caused by the flame. This is not only due to the extended flame (Plasma 50 mm, HVOF 200mm) but this is also caused by the mass flow of the combustion gasses. The mass flow of HVOF spraying can be 5 to 10 times as high as that of plasma spraying.

Because of the high heat input in the part, a cooling system is required to avoid overheating of the part. Mostly air coolers are used for this. A new development is the use of carbon dioxide to cool the part. [10] The carbon dioxide is sprayed on the part as 'snow'. During sublimation, the CO<sub>2</sub> takes away the heat of the part. If due to the shape of the part, or the material the part is made of, air or CO<sub>2</sub> cooling alone is not sufficient, a cooling time has to be introduced between each spray cycle or a fixed amount of cycles to let the part cool down.

This principle can be optimized by the use of a temperature control system that checks the temperature of the part. The temperature of the part is measured by a thermocouple. The voltage of this thermocouple is transferred to a receiver and a controller that are coupled to the manipulator or the robot that handle the gun. If a specific threshold temperature of the part is exceeded, the HVOF gun is moved away from the part and the part can cool down. After the part temperature has dropped below a specific temperature, the spraying process continues. This temperature control system is used at Turbine Support Europa and makes the use of a robot system or an advanced manipulator system necessary. For critical parts made of titanium alloys, such a system is necessary. Titanium alloys are very sensitive to hydrogen embrittlement and oxidation. So the temperature of these parts may not exceed 148 °C.

A new development to reduce the part's temperature is a flame stopper that is mounted on the HVOF gun. The flame stopper consists of a water cooled block with a hole that is centred to the axis of the flame and the particle jet. Only the center of the particle jet and the flame can pass the hole. In this way, heating of the part can be reduced. [13]

### 3.3 Advantages of HVOF spraying

In general it can be said that HVOF is less suitable for spraying ceramic coatings. For cermet and metallic coatings, however, the process has a number of advantages. Thorpe [5] mentions the following advantages of HVOF spraying:

Advantage	Cause
Higher density	High impact energy
Improved corrosion barrier	Less through porosity
Higher hardness	Less carbide degradation
	Better bond
Better wear resistance	Harder and tougher coating
Higher bondstrength	Improved particle bonding
Higher adhesive strength	Improved particle bonding
Fewer unmelted particle content	Better particle heating
Thicker coatings	Less residual stress
Greater chemistry/phase retention	Reduced time at temperature
Smoother surface	Higher impact energy.

To this list some extra advantages can be added that were found during investigations at TSE. Usually, a surface to be coated is grit blasted before application of the coating. This grit blasting is performed to clean the surface and increase its surface energy by plastic deformation [12], resulting in a higher bond strength. If for both plasma spraying and HVOF spraying the same grit blasting process is used, the coating/substrate interface of the HVOF coating will show a lower grit content than the plasma coating. The grit particles that are embedded in the substrate after grit blasting are removed by the HVOF flame. The upper layer of the surface is heated up strongly and expands locally. The grit particles are then pressed out of the surface and are blown away by the fast moving flame. This phenomena can be observed during preheating of the surface. The removed grit particles can be seen as sparks in the flame. Figure 2 shows this principle.

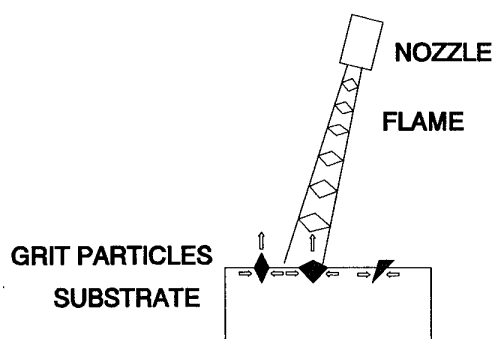


**Figure 2** Removal of grit particles that are embedded in the substrate. The surface of the substrate is heated up by the HVOF flame and expands. The grit particles are pressed out and blown away by the fast moving flame.

HVOF coatings have proven to possess a high bond strength, even on non grit blasted surfaces. Figure 3 shows the comparison of the bond strength of a WC-12% Co HVOF

coating on a grit blasted and a non grit blasted surface. It can be seen that the coating, sprayed on the non grit blasted substrate still has a high average bond strength of 9557 PSI. The grit blasted testpieces had a bondstrength of 10,900 PSI.

The possibility to apply greater coating thicknesses with HVOF spraying makes repairs possible that could not be performed with plasma spraying. In general, the thickness of plasma sprayed layers is limited to 0.5 mm. A coating of 1 mm is already regarded as very thick. These coating thicknesses, however, can be applied with HVOF spraying without danger of spalling or peeling of the layer.

Another advantage of HVOF spraying is the fact that HVOF is a non proprietary process, unlike the D-gun coating application. This makes operators more independent in their choice of coatings.

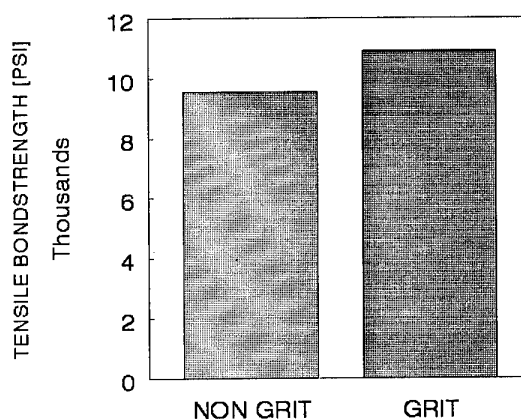


**Figure 3** Bondstrength of a WC-Co HVOF coating on a gritblasted and a non gritblasted Ti-6Al-4V substrate. Grit blast conditions: pressure 40 PSI, grit distance 200 mm, grit angle 30 °, grit size 60 Mesh, Alumina grit.

### 4. HVOF SPRAYING, APPLICATIONS

Compared to plasma sprayed coatings, HVOF coatings have a higher erosion resistance and a better wear resistance. Also the corrosion resistance of HVOF coatings is higher due to the low porosity of the coating. This makes HVOF coatings suitable for application on high loaded jet engine parts.

As will be discussed in the following paragraphs, HVOF spraying is suitable for the application of cermet and metallic coatings. Cermets are ceramic-metal coatings, consisting of a metal matrix containing hard ceramic particles. These ceramic particles give the coatings the high wear and erosion resistance. The most used cermet coatings are WC-Co [4] and  $\text{Cr}_3\text{C}_2$ -NiCr [8].

Furthermore, the HVOF process is used for stainless steel coatings as AISI 316 and AISI 321 [9] and superalloys as Triballoy 800 and Inconel 718.

The amounts and types of parts that are coated by HVOF are rapidly increasing. The following list will provide you with some examples of the application of HVOF coatings on jet engine parts of General Electric and CFMI jet engines. The list gives also the specific function of the coating.

Engine	part	coating	function
CF6-80C	HPT shroud I	CoNiCrAlY	Corrosion
CFM 56-5A	HPT shroud I	CoNiCrAlY	Corrosion
CF6-50	Fan Blade	WC-Co	Wear
CF6-80A/C2	Fan blade	WC-Co	Wear
CF6-6	Fan Midshaft	WC-Co	Wear
CF6-50	Fan Midshaft	WC-Co	Wear
CF6-80A/C2	Fan Midshaft	WC-Co	Wear
CFM 56-2/3	HPT shroud supp	Trib 800	Wear
CFM 56-2/3	HPT shroud supp	Inconel 718	Wear
CF6-6	Comp Rear Frame	Inconel 718	Wear
CF6-80 A	Comp rear frame	Inconel 718	Wear
CFM 56-2/3	HPC blades	WC-Co	Erosion
CFM 56-2/3	HPC blades	Cr <sub>3</sub> C <sub>2</sub> -NiCr	Erosion

## 5 EXAMPLES OF COATING APPLICATIONS

The following paragraphs give some examples of HVOF coatings that are applied on Jet engine parts. Whenever possible, the coatings are compared to plasma sprayed coatings of the same material and the advantages, or disadvantages of HVOF spraying are mentioned.

### 5.1. WC-Co coatings

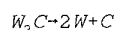
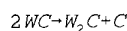
WC-Co coatings are widely used as wear and erosion resistant coatings. They consist of WC-particles in a matrix of Co. The most used powders contain 12 or 17 % cobalt.

WC-Co coatings are applied as erosion resistant coatings on the tips of compressor blades, as wear coatings on bearing journals and as protection against sliding wear or hammer wear on midspan stiffeners of fanblades.

To obtain a WC-Co coating with a high hardness and low porosity, the coating must be applied by high energy plasma spraying (HEP) HVOF spraying or Detonation gun spraying.

#### 5.1.1 Chemical stability of WC-Co

Due to the high heat input during spraying, the WC-particles may transform to W<sub>2</sub>C and finally decompose to W and C. This transformation is driven by time and temperature. [4]. The reactions can be described by the following equations:



Finally, the free carbon can react with oxygen to form carbon mono-oxide, resulting in decarburization of the coating.



Although W<sub>2</sub>C is harder than WC, it is more brittle and hence less suitable to be used in wear and erosion resistant coatings. If W<sub>2</sub>C decomposes in W and C, the coating will lose its hard particles, and the coating is no longer capable of fulfilling its function. To avoid the reactions as described above, the time the particle stays in the flame and the flame temperature has to be limited. Because of these requirements, HVOF spraying is ideal to spray this coating material. The dwell time of the particles is limited by the high particle velocity (400 – 1100 m/s) and the restricted heat input (Maximum flame temperature of 3300 °C).

The amount of primary WC that is retained after spraying of the powder can be determined by X-ray diffraction. Figure 4 shows the diffraction patterns of WC-Co coatings that have been sprayed by HVOF and by HEP. [4] It can be seen that the HVOF coating contains more WC than the HEP coating and that the HEP coating contains a higher amount of W<sub>2</sub>C than the HVOF coating.

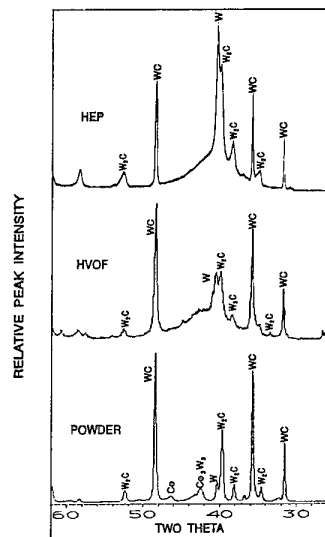


Figure 4 X-ray diffraction of WC-Co powder, the HVOF sprayed coating and the HEP sprayed coating. It can be seen that the HEP coating contains more W<sub>2</sub>C than the HVOF coating [4].

#### 5.1.2 Plasma sprayed and HVOF sprayed WC-17Co.

Because of the higher primary carbide content and the lower porosity, the HVOF coating has a higher hardness than the HEP coating. In figure 5 the hardness of a WC-17Co HVOF and the same material sprayed by HEP are given. Figure 6 shows the bond strengths of a HVOF and a HEP WC-17Co coating on a Ti-6Al-4V substrate. These coatings are applied on bearing journals and midspan stiffeners of fan blades.

The cross sections of these coatings as given in figure 7 A and 7 B, show that the HVOF coating is denser and shows a higher primary WC content. The interface of the HVOF coating is less contaminated than that of the HEP coating.

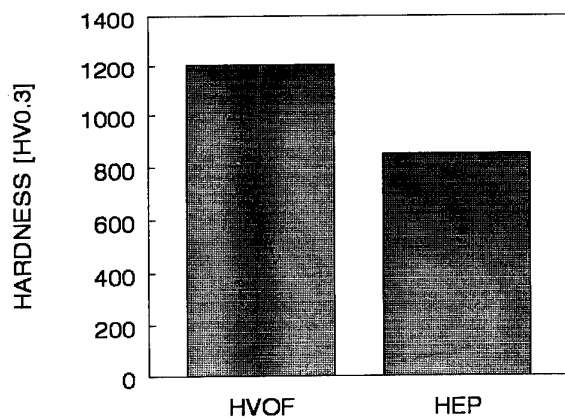


Figure 5 Microhardness of a HVOF and a HEP WC-17Co coating. The hardness of the HVOF coating is remarkably higher than the hardness of the HEP coating.

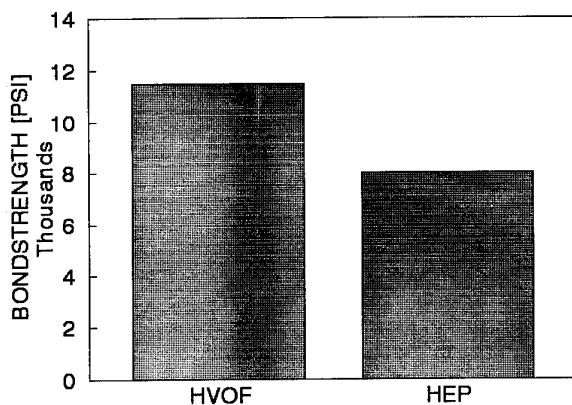


Figure 6 Bondstrength of a HVOF WC-17Co coating and a WC-17Co HEP coating.

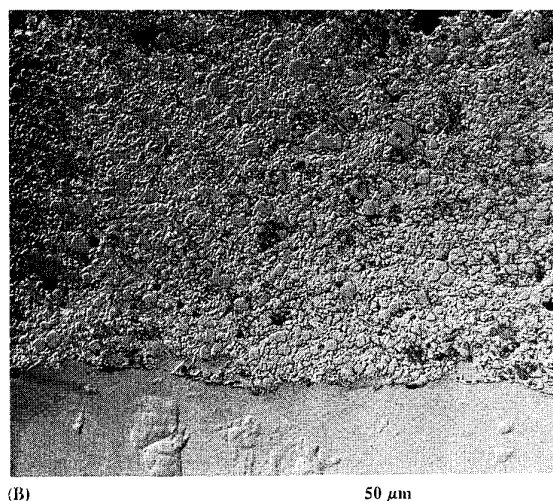
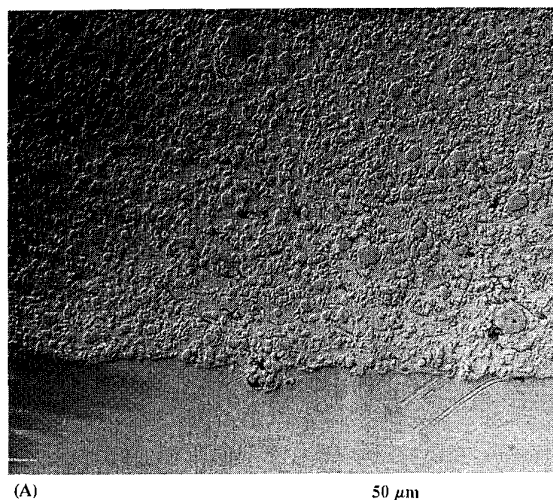


Figure 7 Cross sections of the HVOF (A) and the HEP (B) WC-17Co coating. The HVOF coating has a higher primary carbide content and a higher hardness. The porosity of the HVOF coating is less than 1 %. The HEP coating has a porosity of 3-4 %.

### 5.1.3 HVOF WC-12Co as erosion resistant coating on compressor blades.

A jet engine consists of a compressor part and a turbine part. The air that is needed for the combustion of the kerosene in the combustor is compressed in a multi stage compressor that is driven by the turbine.

Usually an engine has a low pressure compressor (LPC) that is driven by the low pressure turbine (LPT) and a high pressure compressor (HPC) that is driven by the high pressure turbine (HPT).

The High Pressure Compressor of a CFM 56-3 engine, compresses the intake air in 9 stages from 2.2 to 24.3 bars. The HPC is operating at a rotation speed of approximately 10,000 RPM. This results in a blade tip speed of approximately 260 m/s. The speed of the air in the HP compressor ranges from 158 to 173 m/s (Engine at a fixed point). At these velocities, the blades of the HP compressor are exposed to erosion.

Especially when the intake air contains abrasive particles like sand, the erosion rate increases rapidly. To protect the blade tips against this erosion, they are coated with a thin (max 0.1 mm) erosion resistant coating. This coating is applied to the concave side of the blade only. Until now, this coating is applied with the detonation gun technique. HVOF spraying, however, offers a comparable coating quality and can be used as an alternative to the Detonation gun coating.

The first 5 stages of the blades will be coated with a WC-12%Co HVOF coating, whereas stage 6 to 9 will be coated with a  $\text{Cr}_3\text{C}_2$ -NiCr coating.

Figure 8 shows a stage 2 HPC blade. The shaded area is the area to be coated with HVOF WC-12Co.

The requirements on this HVOF coating with a thickness between 0.05 and 0.1 mm are high. The coating must resist

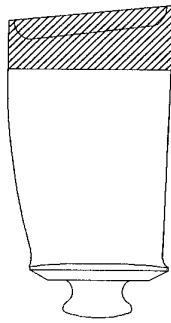


**Figure 8** Second stage high pressure compressor blade of the CFM 56-3 engine. The shaded area is coated with a WC-12Co HVOF coating to protect the blade against blade tip erosion.

erosion tests at elevated temperatures at a particle speed of 300 m/s. The hardness must be higher than 1200  $H_{V0.3}$  and the porosity must be lower than 1 %. Figure 9 shows a cross section of this coating on a Ti-6Al-4V testpiece. It can be seen that this coating consists of a dense metallic matrix with finely dispersed WC particles. The particles give the coating its high hardness and erosion resistance.

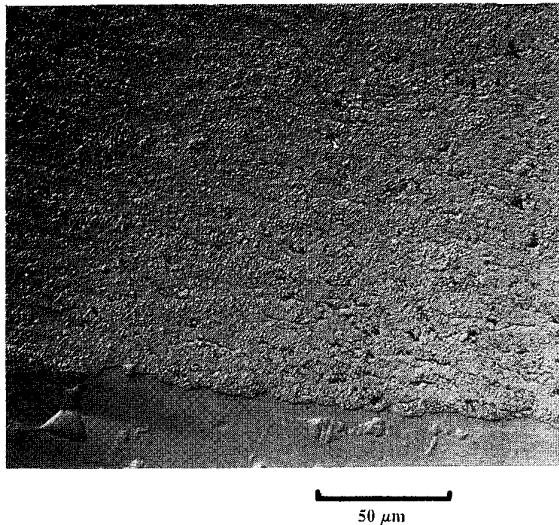


**Figure 9** Cross section of a WC-12Co HVOF coating for application to HPC blades. The coating applied on a non-gritblasted substrate of Ti-6Al-4V. The bondstrength of the coating is greater than 10,000 PSI. The microhardness is 1300  $H_{V0.3}$

The stage 1 through 3 HPC blades are made of titanium alloys. Because of this, the substrate temperature has to be limited to 148 °C during spraying. Because of the fact that the thickness of the airfoil of the HPC blades can be less than 1 mm, the danger of overheating the parts is seriously present. This means that the titanium blades have to be cooled intensively during spraying. When no cooling was applied, temperatures above 350 °C were measured at the thin airfoils.

## 5.2 Inconel 718

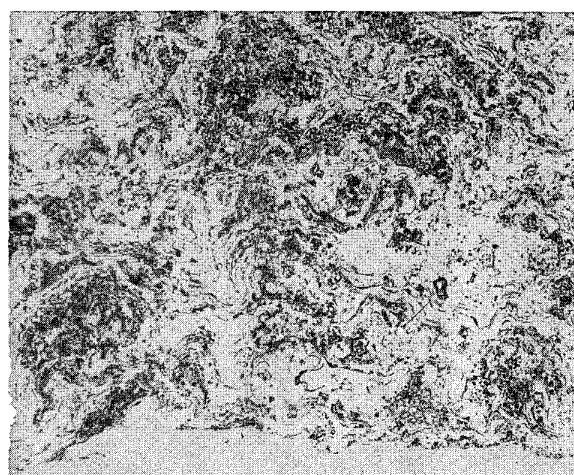
Coatings of inconel 718 are widely used and produced on a large scale by plasma spraying. The use of HVOF spraying for the application of this coating type may have two reasons: the required coating thickness is higher than the maximum allowed coating thickness to be applied by plasma spraying, or the coating quality (density, hardness, bond strength, oxide content) of the plasma sprayed coating is not sufficient. The first application of plasma sprayed coating mainly concerns stationary parts (support etc), whereas the second one mainly concerns rotating parts or turbine parts.

HVOF coatings of Inconel 718 have a low porosity (<1%) and a bondstrength over 10,000 PSI. The oxide content may vary strongly, depending on the function of the coating. When the coating has to be very hard and must have a high compressive strength, a high oxide content is desired. In the case the coating has to serve as corrosion or oxidation barrier a low oxide content and a low porosity are required. This brings us to another advantage of HVOF spraying. By varying the amount of oxygen in the flame, resulting in a fuel rich or a lean flame, the oxide content of the coating can be varied strongly. Oxide contents of less than 1% can be reached, whereas oxide contents of more than 20 % are also possible and can be reproduced consistently.

Knight and Smith [3] state in their article that a surplus of oxygen in the flame results in a lower oxide content of the coating. As a reason for this he states that a flame with a surplus of oxygen has a lower temperature than a lean flame. The higher flame temperature, and hence the higher particle temperature, may lead to a stronger oxidation of the particles. The results of Smith are the opposite of what was found at TSE. Here it was found that a higher oxygen flow resulted in a higher oxide content of the coating. This difference may be caused by different standoff distances of the gun and different ways of cooling the substrate. Figure 10 A and 10 B show HVOF Inconel 718 coatings, sprayed with hydrogen with different oxygen flows. The oxide content in the coatings differs strongly. The hardness of the coating with the high oxide content was 85 HR 15 N whereas the hardness of the low oxide coating was 81 HR 15 N.

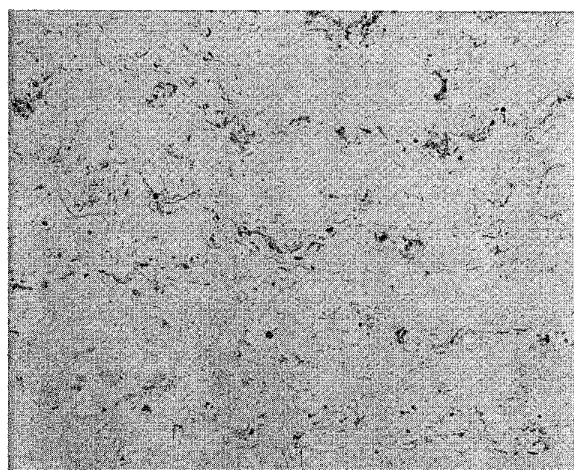
A high oxide content of the Inconel 718 coating results in a hard coating with a high compressive strength. These characteristics are required when the coating is subjected to high compressive stresses. A typical example of this is the high pressure turbine rotor (HPTR) pressure tube/coupling nut of the CF6-80A/C2 engine. This part is subjected to wear and becomes shorter during service. To restore it to its original dimensions, a HVOF Inconel 718 coating is used. From experiments at GE it was learned, that the coating must have a high compressive strength. Tests had shown that almost oxide free coatings were deformed plastically when they were loaded.

An Inconel 718 coating with a high oxide content, on the contrary, showed no plastic deformation. [6]



(A)

50 μm



(B)

50 μm

**Figure 10** Cross section of a high oxide (A) coating and a low oxide (B) Inconel 718 HVOF coating. The hardness of the high oxide coating is 85 HR 15 N and of the low oxide coating is 81 HR 15 N. Coating A was sprayed with a surplus of oxygen whereas coating B was sprayed with an almost stoichiometric flame.

## 6 NEW DEVELOPMENTS IN HVOF SPRAYING

In this paragraph, recent and future developments in HVOF spraying will be discussed briefly.

The HVOF spraying of MCrAlY coatings like NiCoCrAlY or NiCrAlY is subject of investigation now. The coating is sprayed with a low oxide content and a high amount of unmelted particles. The spraying process is followed by a diffusion heat treatment.

Expectations are that these HVOF MCrAlY coatings have the same high quality as vacuum plasma sprayed MCrAlY coatings and can be used in high temperature corrosive conditions. [11]

If the particle velocity with HVOF spraying is further increased, the kinetic energy of the particles can be used to melt them when they collide on the surface. This principle is called Hyper Velocity Impact Fusion [5]. It is no longer necessary to heat the particles beyond their melting points. As a result, the oxidation of the particles is restricted. HVIF will result in dense and almost oxide free coatings.

As stated in the foregoing paragraphs, HVOF spraying is limited to metallic and cermet coatings. New developments in HVOF guns, however, make it possible to spray ceramics like  $Al_2O_3$  and  $ZrO_2$  [13]. By using extended nozzles, up to several hundreds of mm's, the dwell time of the particles is increased, resulting in well molten ceramic particles. Long nozzles, however, limit the versatility of the use of the HVOF guns. The application of coatings to internal diameters will be more difficult.

## References

- [1] Houben J.M. Remarks Concerning a Rational Plasma for Thermal Spraying. Proceedings 9th thermal Spraying Conference, The Hague, The Netherlands. 1980
- [2] Verbeek A.T.J. Plasma Sprayed Thermal Barrier Coatings: Production, Characterization and Testing. Doctor's Thesis. Eindhoven University of Technology, 1992.
- [3] Knight R., Smith R.W. HVOF Sprayed 80/20 NiCr Coatings. Proceedings International Thermal Spray Conference 1992. Orlando Florida. Editor C. Berndt. pp 159-164. ASM International, Ohio, 1992.
- [4] Nerz J., Kushner B., Rotolico A. Microstructural Evaluation of WC-Co coatings. Journal of Thermal Spray Technology. Vol 1, no 2 pp 147-152.
- [5] Thorpe M.L., Richter H.J. A pragmatic Analysis and Comparison of HVOF Processes. Journal of Thermal Spray Technology, vol 1, no2. pp 161-170.
- [6] Grossklaus W. General Electric REDO. Private communication. 1993
- [7] Browning J.B. And Now Hypersonic Velocity Impact Fusion. Proceedings International Thermal Spray Conference 1992. Orlando Florida. Editor C. Berndt. pp 123-125. ASM International, Ohio, 1992.

[8] Takeuchi J., Nakahira A., Barbezat G.  $\text{Cr}_3\text{C}_2$ -NiCr Cermet Coatings Using Some HVOF, APS and VPS Processes. pp 11-14. Proceedings Thermal Spraying Conference, Aachen Germany, 1993. DVS Verlag. Düsseldorf, 1993.

[9] Dorfman M.R., Kushner B.A., Rotolico A.J. DeBarro J.A. Development and Applications of Corrosion Resistant Thermal Sprayed Coatings. pp 171-174. Proceedings Thermal Spraying Conference, Aachen Germany, 1993. DVS Verlag. Düsseldorf, 1993.

[10] Werner S., Heinrich P., Schmidtke W., Schüfer R. Practical Experience with the Cooling Process During Thermal Spraying. pp 45-46. Proceedings Thermal Spraying Conference, Aachen Germany, 1993. DVS Verlag. Düsseldorf, 1993.

[11] Thorpe R., Zwetsloot M. Lecture at ASM thermal spray meeting, Apeldoorn, the Netherlands, 1993.

[12] Strompen N., Plasmagespritzte Metalloxid und Oxid Schichten. Doctor's Thesis, Aachen University of Technology. 1986

[13] Schwarz E., Hühne E., Grasme D., Kröschel R., Recent Advances in HVOF-spraying using acetylene and other gases. pp 47-52. Proceedings Thermal Spraying Conference, Aachen Germany, 1993. DVS Verlag. Düsseldorf, 1993



## QUESTIONS

### **DOUG NAGY (Ca)**

Q. As you mentioned that your coatings are smoother than plasma spray, how smooth are they as deposited on compressor blade tips and do they need to be further polished? How thick are they?

A. The roughness of HVOF coatings is lower than the roughness of plasma sprayed coatings. This is caused by the higher impact velocity of the particles resulting in a better flattening of the particles. Furthermore, the particle size of HVOF powder is smaller than the particle size of plasma spray powder. This also contributes to a smoother coating.

The coating that is deposited on the compressor blades requires no further polishing. The maximum roughness is about 80 AA. The thickness ranges from 0.05 to 0.1mm.

### **M. ZWAAN (Ne)**

Q. HVOF coatings are superior in relation to normal plasma coatings. What techniques must be used to remove dense coatings like HVOF coatings?

A. HVOF coatings can be removed by grinding, turning or milling. Some coatings can also be stripped chemically.

According to Pratt and Whitney, it is possible to strip cermets as WC-Co and  $\text{Cr}_3\text{C}_2$ -NiCr and a superalloy as Triballoy 800 by water jet stripping.

### **F. AYDINMAKINE (Tu)**

Q. On your explanation, we have understood that there is a wider use on commercial airlines. You had no applications for the military. How do you interpret this?

a) You have not gone to the military.

b) They don't want to understand you.

c) They have too much bureaucracy.

d) As military engines (like F110 of GE) have much lower flight hours, it is too early for the repair procedures to be authorized.

A. a) Turbine Support Europa (TSE) does not use HVOF for military repair applications because of the fact that the shop manuals of the military

engines that are repaired at TSE do not specify HVOF repairs.

- b) HVOF is a rather new technique and will be understood also by military, but it will take some time before this technique is implemented in military repairs. The introduction of HVOF for the civil market is also very recent.
- c) In my opinion, it is not a matter of bureaucracy. Airforces are even more free than commercial airlines because the airforce can develop and certify new repairs by their own. Approval by the FAA is not required.
- d) Military engines have less flight hours than commercial engines. But if the wear on a military part exceeds the thickness that can be repaired by conventional thermal spray methods, I can imagine that HVOF repairs will be developed for these parts.

# THERMAL TESTING OF HIGH PERFORMANCE THERMAL BARRIER COATINGS FOR TURBINE BLADES.

**L. Bertamini \***

**A. Di Gianfrancesco \*\***

\* Centro Sviluppo Materiali, 38057 Ciré di Pergine, Trento, Italy -

\*\*Centro Sviluppo Materiali, via di Castel Romano 100-102, 00129 Roma, Italy

## SUMMARY

A 350  $\mu\text{m}$  thick 7wt.%  $\text{Y}_2\text{O}_3\text{-ZrO}_2$  (7YSZ) ceramic Thermal Barrier Coating (TBC) was manufactured in an argon atmosphere and with a strictly controlled substrate temperature on flat IN 600 samples and on IN 100 aircraft turbine blades. This new Atmosphere and Temperature Controlled Spraying (ATCS) allows the reduction of the residual stresses and an improvement in the microstructure and in the mechanical properties of the coating.

The good performance of these new TBC's was assessed in Thermal Fatigue and in Thermal Shock Tests carried out in air at 1100°C and at 1280°C respectively. The oxidation rate of the metal - ceramic interface was measured at 1100°C.

Failure of the TBC's was induced only by the deterioration (like oxidation, cracking, ...) of the uncoated parts of the samples, as testing temperature was too severe for the base metals. Spalling was thereafter driven by compressive stresses near the aluminium oxide layer at the metal-ceramic interface.

The results of these tests underline the good quality of the ceramic coating manufactured by the new ATCS technology.

## 1. INTRODUCTION

Manufacturing of Thermal Barrier Coatings (TBC's) by plasma spraying for the insulation and the protection of heat engines has been investigated since a long time (1,2,3). The beneficial effects of using TBC's in aero engines are the increase of turbine gas inlet temperature and the decrease of cooling air and of metal temperature, thus increasing both engine efficiency, performance and component reliability and life (4).

As a matter of fact spallation makes ceramic coatings still unreliable. Actually the behaviour of TBC's produced with the Air Plasma Sprayed (APS) technology are markedly influenced by thermomechanic stresses, by corrosion and erosion processes and by the oxidation of the bond coat (4,5,6). The development of high performance TBC's requires thus great improvements in the microstructure of the coating.

Porosity and large cracks are usually necessary inside the coating to achieve a high strain-tolerance, which is fundamental to withstand thermal and mechanical strains without spallation. On the other hand, the reduction of the density of the ceramic coating decreases drastically its cohesion and increases the bond coat oxidation rate (7,8,9). Some investigations (10)

demonstrated that also the corrosion resistance of the TBC is improved by a factor of four when a higher density is produced, thanks to the reduction of the flooding of aggressive gases through big pores and large macrocracks. Sealing by laser the upper surface of the coating has been tried (11) and cavitation erosion resistance is also improved by eliminating surface porosity (12). The advantages of a dense but microcracked microstructure (where vertical microcracks enables the coating to be strain-tolerant) were thus foreseen (2), but not realised with the Plasma Spray technology.

The effects of some of the process parameters on the microstructure and on the lifetime of the TBC's have been investigated (7). In particular the effect of cooling during deposition has been recognised to be a key parameter in the production of advanced TBC's (13,14). Previous works (15) demonstrated that a strong cooling of the coating being deposited provides a superior microcracking pattern. A low deposition temperature keeps residual stresses (16,17,18) under control, but on the other side can also reduce the adhesion and the cohesion values of the coating (19,20), due to various wetting phenomena (21), and thus the life of the TBC.

A new Plasma Spray method has been now developed for the manufacturing of high performance TBC's. This Atmosphere and Temperature Controlled Spraying (ATCS) technology consists in the deposition of the ceramic coating inside an argon filled chamber, while keeping the substrate and the coating temperature low with a cryogenic argon fog (22).

The cooling lay-out and the cooling parameters were first modified and improved by CSM (15), in order to control the liquid argon flow and to prevent both the plasma and the sprayed particles from being cooled by the cryogenic fog. The effects of the cryogenic cooling and of the inert atmosphere were thereafter explained and the main features of the new coating underlined (18).

As deposition temperature can be closely controlled, virtually no residual stresses are present in the coating manufactured at room temperature. The argon atmosphere produces a longer plasma jet, that protect the melted particles before splashing, clean and preheat the surface up

to 2000 K (but not the whole substrate) only during the deposition of each ceramic layer(23). Therefore, in spite of the low substrate temperature, high values of adhesion and cohesion are obtained, while a very homogeneous microstructure is produced, free of big porosity or large cracks (23). The strong cooling induces a vertical microsegmentation in these denser ceramic layers being deposited, leading to the improved strain tolerant microstructure, claimed for high-performance TBC's (2).

In this paper this improved TBC's, manufactured with the new ATCS technology (which is currently Patent Pending), are tested at high temperatures. The Oxidation Rate of the metal-ceramic interface is measured at 1100°C. Thermal Fatigue and Thermal Shock Tests are carried out in air at 1100°C and at 1260°C, 1280°C and 1300°C respectively. A failure analysis, mainly by means of metallographic methods, is finally proposed to discuss the experimental observations.

## 2. EXPERIMENTAL

### 2.1 Sample preparation

TBC's were manufactured on four flat Inconel 600 samples (size 10 x 80 x 5 mm) and on seven Inconel 100 aircraft turbine blades. After mechanical and ultrasonic cleaning of the surface, a 130-180  $\mu\text{m}$  thick Co32Ni21Cr8Al0.5Y bonding layer was prepared by the Vacuum Plasma Spray (VPS) technology. No thermal treatments were performed to improve the quality and the adhesion of the metallic layer.

A 7%Y2O3-ZrO2 (7YSZ) ceramic layer was sprayed with the ATCS technology. This coating was 300  $\mu\text{m}$  thick on bars, while the average thickness on turbine blades was 350  $\mu\text{m}$ , with a minimum values of 300  $\mu\text{m}$  on both airfoils edges.

During the deposition of the ceramic layer on a turbine blade, surface temperature was controlled by means of a low-temperature pyrometer. A k-type thermo-couple, placed either in a 4 mm depth hole (flat samples), or in the largest cooling hole corked on the other side with a steel wire (blades), was used to measure the metal temperature. The substrate was preheated to increase coatings adhesion. The ceramic coatings were than

manufactured at 120°C on Inconel 600 substrates, while four different deposition temperatures (30°, 60, 110° and 150°C) were employed on turbine blades.

Fig.1 presents typical time vs. temperature curves, for both substrate and surface. The cryogenic cooling enables the deposition of the ceramic layer at very low temperatures. On the other side no thermal gradients forms as the TBC is deposited, thanks to the efficient front cooling, that limits the heat flow towards the substrate.

The microstructure of the as-sprayed TBC's was evaluated on a cross-section of both type of substrates.

## 2.2. Oxidation and Thermal Fatigue Tests

The Oxidation Rate of the metal-ceramic interface and the Thermal Fatigue Resistance of the ATCS-TBC's were tested on the flat samples in air.

a) Two samples were isothermal heat treated at 1100°C. Heat up rate was 10°C/min and slow furnace cooling was also used to minimise thermal shock effects. Cross-sections were made after 100 h and after 300 h heat treatment to analyse and to measure the oxide layer thickness at the metal-ceramic interface. One sample was also thermally cycled (20 min heating at 1100°C and 20 min cooling in still air).

b) One bar was tested at 1100°C after 100 hours isothermal heat treatment at the same temperature. Following Thermal Fatigue cycles were randomly applied:

20 min heating and 20 min cooling;  
5 min heating and 5 min cooling;  
15 min heating and 8 min cooling.

Heating was made in air, while cooling was performed in still air at room temperature.

The samples were visually inspected every 4 hours. Spalling was defined as the first visible damage of the ceramic coating. Finally, after failure of the ceramic layer, a cross-section was made near the spalled area for metallographical analysis.

## 2.3. Thermal Shock Tests on turbine blades

Thermal Shock Tests were carried out on coated aircraft turbine blades. Four of them (deposition temperature: 30°, 60°, 110°, 150°C) were tested with a furnace temperature of 1280°C. Two other blades (deposition temperature: 60°C) were tested at a temperature of 1260°C and of 1300°C respectively. During testing temperature variations were less than  $\pm 15^\circ\text{C}$ . A thermal gradient was present inside the furnace, with the top of the blade 10°-15°C hotter than its basement.

Thermal shock tests were performed with 67 s heating and 60 s compressed air cooling (gas pressure: 6 bar). No cooling air was blown inside the cooling holes to keep substrate temperature lower during testing. The blades were visually inspected every 50 cycles to check the failure of the coating. The presence of macrocracks or internal decohesions was easily detected, as dark areas appeared on the uniform colour of the coating, when the blade was incandescent.

The Thermal Shock Cycle, when furnace temperature was 1280°C, was measured placing a k-type thermocouple inside the largest cooling hole, corked on the other side with a steel wire, of both a coated and an uncoated blade. The surface temperature was also checked in a 0,5 mm depth hole drilled on the surface of an uncoated blade. All the measurements were performed in the central zone of the blade.

## 3. RESULTS

### 3.1. As sprayed coatings

The metallographic analysis carried out on flat samples and on turbine blades evidences that, in spite of the low deposition temperature (30°C), the microstructure of the 7%YSZ coating manufactured with the improved ATCS system is very homogeneous as demonstrated in Fig.2a. A dense microstructure is formed and neither macrocracks, nor large porosity, nor wide decohesions can be found inside the ceramic coating. At higher magnifications the vertical microcracking network can be better appreciated (see Fig.2b). Normally microcracks do not exceed one or two layers, so that the ceramic coating is microsegmented, without generating dangerous segmentation macrocracks.

### 3.2. Oxidation Test results

The effect of 100 h and of 300 h isothermal heat-treatment in air on the evolution of the metal-ceramic interface were well evidenced using the Scanning Electronic Microscopy (SEM). A new layer is formed, recognised to be Aluminium Oxide, according to a qualitative Energy Dispersed Spectroscopy (EDS) analysis. This well agrees with more accurately investigations reported in the literature (24,25). No oxidation was recognised beyond the reaction layer, inside the bond-coat.

Tab.1 reports the results of the visual inspections after hot oxidation tests. As the morphology of the oxide layer is quite complex, together with the average thickness, also maximum and minimum values are given.

Basically the oxide growth follows a parabolic law (25). The  $Al_2O_3$  layer grows mainly during the first 100 h of air-heat treatment and acts thereafter as diffusion barrier for the Oxygen towards the metallic layer. No significant increase in the oxide thickness were found after 200 cycles on the samples heat-treated for 300 h, as Tab.1 indicates.

The data presented in Tab.1 agree very well with other measurements performed on the same Co32Ni21Cr8Al0.5Y - 8YSZ system (25).

### 3.3. Thermal Fatigue Test results

Testing of the TBC on the flat Inconel 600 samples was stopped after the following cycles:

isothermal heat-treatment : 100 h;  
 20 min heating and 20 min cooling : n.200 cycles;  
 5 min heating and 5 min cooling : n.2100 cycles;  
 15 min heating and 8 min cooling : n.500 cycles.

The failure of the top coating was preceded by the spallation of many small ceramic fragments along the border of the sample. A cross-section near the edge of the sample is presented in Fig.3. Big oxide scales are present on the side face of the In 600 bar. From Fig.3 it can be suggested that the uncoated parts of the Inconel 600 substrate were heavily oxidised. In fact its wide was reduced by

more than 1 mm. Fig.3 demonstrates also that the oxidation induced the bending of the border of the sample. Cracks developed than inside the top-layer near the bonding layer. In Fig.3 also the formation of porosity under the bonding layer, due to interdiffusion phenomena, is evidenced.

Tab.1 reports the measured values of thickness (average, minimum and maximum) of the reaction layer grewed at the metal-ceramic interface, as measured by means of SEM investigations on a cross-section.

No cracking in the microstructure of the coating can be otherwise found.

### 3.4. Thermal Shock Test results

The evolution of the temperature inside and outside the turbine blade during the Thermal Shock Cycle, when furnace temperature is 1280°C, is plotted in Fig.4. Maximum surface temperature (curve *a*) is 1220°C, while metal (curve *c*) reaches only 1050°C inside the blade. These results underline that the presence of a TBC decreases the blade temperature of about 120°C, with respect to the uncoated blade (curve *b*). Furthermore it can be suggested (27) that an internal cooling (curves *d*) will reduce the blade temperature of about 150°-250°C (grey area), making base metal safe at such a high temperatures (1280°C) or permitting an increase of the gas temperature. Actually this is the reason why TBC's are so interesting for such an application.

From Fig.4 also the transient stresses during thermal shock tests can be better understood. A very simple model was developed to evaluate in a qualitative way these stresses.

The thermal dilatation of the substrate metal and of the free surface ceramic layers can be predicted respectively as:

$$\begin{aligned} L_{\text{met}} &= L_c (1 + \alpha_{\text{met}}(T_{\text{met}} - T_{\text{dep}})) \\ L_{\text{cer}} &= L_c (1 + \alpha_{\text{cer}}(T_{\text{cer}} - T_{\text{dep}})) \end{aligned} ;$$

where:

$L_c$  is the starting length at the deposition temperature ( $T_{\text{dep}}$ )

$$\alpha_{\text{met}} = (12.7 - 6.61E-4 T + 4.94E-6 T^2) E-6 \text{ 1/K}$$

(T in the range 0 - 1100°C)

$$\alpha_{\text{cer}} = 10.6 \text{ E-6 } 1/\text{K}$$

(T in the range 0 - 1200°C)

are the Thermal Expansion Coefficients (TEC) of the two materials (23). The metal and the ceramic temperatures  $T_{\text{met}}$  and  $T_{\text{cer}}$  are described by the curves 'c' and 'a' in Fig.4 respectively.

Under the hypothesis that the substrate is much thicker than the TBC, the difference of expansion

$$(L_{\text{cer}} - L_{\text{met}})/L_c$$

can be considered to be nearly proportional to the thermally induced strains inside the external layer of the ceramic coating (where temperature evolution was evaluated). The results of this simple model are reported in Fig.5. Positive values correspond to compressive strains inside the ceramic layer. On the contrary negative values have indicates tensile strains.

It should be noted that these strains values can not be directly converted into stresses values, because some accommodations will occur inside the TBC. Moreover this model do not takes into account stress-concentration effects, phase transformations, cracking or sintering in the ceramic layer and the oxidation of the metal-ceramic interface or the creep of the bonding layer. Anyway it can give a good indication of the stresses evolution inside the TBC during the Thermal Shock Test. The difference of the TEC and of the temperatures between the ceramic surface and the base metal (600°C after 20 seconds heating and 500°C after 15 seconds cooling) leads to high compressive stresses inside the surface of the TBC, that are additional to the residual stresses. At high temperature and during the cooling phase, on the contrary, tensile stresses appears inside the ceramic, with a maximum peak after about 12 seconds.

No difference was found in the resistance of the coatings manufactured at different deposition temperatures and tested at 1280°C. Thermal Shock Tests at 1260°, 1280°C and 1300°C were stopped after 2500, 1500, 900 cycles respectively, due to failure of the top of the blade. No ceramic cracking or spalling was evidenced in the central area of the blade (where the thermal cycle was calibrated), but only near the top area.

It was not possible to define the number of Thermal Shock Cycles before spallation of the TBC. In fact small fragments of the ceramic coating started to spall after 350 - 600 cycles from the border of the coating near the top of the blade, on both leading and trailing edges and than the failure of the ceramic layer walked slowly down along the sample.

Fig.6 compares the coated blades after 2500 cycles testing with a furnace temperature of 1260°C (blade *a*), with one just after spraying (blade *b*). From Fig.6 the effect of the Thermal Shock on the TBC's can be well appreciated. The ceramic layer is spalled only near the top of the turbine blade. It has to be noted, that in this area also the base metal is deformed and cracked. The uncoated zones of the blade were always to heavily oxidised. Cracks formed in the base metal and ran towards and under the ceramic layer.

Metallographic analysis on a cross-section made near the spalled area (see Fig.7) demonstrated that spalling started near both edges. The ceramic coating was than pushed away from the substrate. This type of failure is typically induced by a concentration of compressive stresses. The spallation was than driven by a 5 µm thick oxide layer grown at the metal-ceramic interface.

More accurate SEM analysis indicated some sintering inside the ceramic layer, but again no macrocracks were evidenced. Porosity formed during testing inside the bonding layer and interdiffusion phenomena with the substrate changed its chemical composition (e.g. titanium diffused in the first 50 µm). EDS analysis indicated the presence of wide aluminium and chromium depleted zones.

## 5. DISCUSSION

The metallographic investigations indicates that the ATCS technology guarantees the production of a dense homogeneous ceramic coating, free of segmentation cracks, decohesions, large porosity, even when it is manufactured at a low deposition temperature. It can be suggested that this is especially important for the protection of the TBC from the corrosion and from the erosion during service.

The dense vertical microcracking pattern, caused by the strong cooling conditions adopted, keeps the coating compliance (that is its ability to withstand thermal strains) high, as Elastic Modulus measurements confirmed (23), even when porosity is reduced or segmentation crack are not present.

Finally the efficient cooling allow the controls of the substrate and of the ceramic temperature during its deposition. This allows a control of the detrimental residual stresses that forms inside the TBC as a consequence of the plasma spray process.

To understand the failure of the TBC during the Thermal Shock Tests the presence of uncoated areas on the top and on the bottom of the blade have to be considered. Moreover no internal cooling was used during testing. The heat can flow under the TBC and makes the substrate hotter. The temperature becomes too high for the superalloy. The spalling of small fragments of the ceramic layer is induced by the metal deformations (due to oxidation, cracking and perhaps volume changes from  $\gamma'$  dissolution) near the thermally unprotected zone. A new area becomes unprotected and spalling can proceed along the blade.

All these experimental observations demonstrate that the Thermal Shock Cycle was too severe for the base material. As ATCS-TBC's were still in good conditions in the central part of the blade (where the thermal shock cycle was measured and away from the unprotected zones) it is possible to infer that its resistance to 67 seconds furnace heating and 60 seconds compressed air cooling is higher than 1500 cycles at 1280°C and higher than 2500 cycles at 1260°C. A even higher Thermal Shock resistance can be suggested if an internal cooling is used to protect the blades from excessive heat.

The results of the Thermal Fatigue Tests are similar to the above discussion: spalling was induced by substrate oxidation.

In both Fatigue and Shock tests only a limited modification or deterioration of the ATCS ceramic layer was underlined by the metallographic investigations. On the other side these confirmed the importance of the alumina

layer growth at the metal - ceramic interface in the failure of TBCs. For this reason further research is currently carried out by CSM to improve the resistance of the TBC against interface oxidation.

## 6. CONCLUSIONS

The severe furnace Thermal Shock Tests demonstrate the good quality of the ATCS - 7YSZ coatings, as failure occurred as a consequence of the deterioration of the substrate. This can be correlated to the good microstructure of the ceramic coating, obtained with this new plasma spray technology. It can be suggested that this good quality will be maintained for service conditions, as such a microstructure should also reduce the erosion of the coating and improve the corrosion resistance of the TBC, by limiting the flooding of the corrosive gases.

The experimental results underline also the importance of the presence of a Thermal Barrier Coating to the reduction of metal temperature and to the protection of aircraft turbine blades.

The oxidation of the metal-ceramic interface has to be considered as one of the main reasons for the failure of the TBC and improvements in this field are required to achieve reliable TBC's.

## REFERENCES

1. Lackey, W.J., Stinton, D.P., Cerny, G.A., Fehrenbacher, L.L. and Schaffhauser, A.C., "Ceramic coatings for heat engine materials - Status and future trends", ORNL/TM-8959, December 1984.
2. Anderson, N.P. and Sheffler, K.D., "Development of strain-tolerant thermal barrier coating system", NASA-CR-168251, December 1983.
3. Holtman, R.L., Layne, J.L. and Schechter, B., "An investigation of enhanced capability thermal barrier coating system for diesel engine components", DOE/NASA/0326-1, NASA CR-174820, August 1984.
4. Rhys-Jones, T.N. and Toriz, F.C., "Thermal barrier coatings for turbine applications in aero engines", High Temperature Technology, 7, 1989, pp 73-81.
5. Miller, R.A. and Lowell, C.E., "Failure mechanisms of thermal barrier coatings exposed



- to elevated temperatures", NASA Technical Memorandum 82905.
6. Wu, B.C., Chang, E., Chang, S. and Tu, D., "Degradation mechanisms of ZrO<sub>2</sub>-8%Y<sub>2</sub>O<sub>3</sub>/Ni-22Cr-10Al-1Y thermal barrier coatings", J. Am. Ceram. Soc., 72, 1989, pp 212 - 218.
  7. Stecura, S., "Effects of plasma spray parameters on two-layer thermal barrier coating system live", NASA, Technical Memo TM81724, March 1981.
  8. Johner, G. and Schweitzer, K.K., "Thermal Barrier Coatings (TBC) for jet engine improvement", Int. Conf. on Metallurgical Coatings, 9-13 April 1984, San Diego, California, USA.
  9. Prater, J.T. and Courtright, E.L., "Ceramic thermal barrier coatings with improved corrosion resistance", Surface and Coatings Technology, 32, 1987, pp 389-397.
  10. Andersson, C.A., Lau, S.K., Bratton, R.J., Lee, S.Y., Rieke, K.L., Allen, J. and Munson, K.E., NASA CR-165619, 1982.
  11. Sivakumar, R. and Mordike, B.L., "Laser melting of plasma sprayed ceramic coatings", Surf. Eng., 1988, pp 127-140.
  12. Adamski, A. and Mc Pherson, R., "Laser processing of thermally sprayed coatings", 11th Int. Therm. Spray Conf. 1986, pp 555-562.
  13. Duvall, D.S. and Ruckle, D.L., "Ceramic thermal barrier coatings for turbine engine components", Gas Turbine Conference and Exhibition, 19-22 April 1982, pp 19-22, Pap.n. 82-GT-322.
  14. Levine, S.R., Miller, R.A. and Gedwill, M.A., "Thermal barrier coatings research at NASA Lewis", Proc. 2nd Conf Adv Mater for alt fuel-capable heat engines, 24-28 August 198, Monterey, CA, USA.
  15. Beber, P., Bertamini, L., Pawlowski, L. and Sturlese, S., "New plasma spray coatings for heat engines", EUROMAT '92, 22-24 September 1992, pp.1247-1255.
  16. Takeuchi, S., Ito, M. and Takeda, K., "Modelling of residual stress in plasma sprayed coatings: effect of substrate temperature", Surface and Coatings Technology, 43/44, 1990, pp 426-435.
  17. Gill, S.C. and Clyne, T.W., "Stress distributions and material response in thermal spraying of metallic and ceramic deposits", Metallurgical Transactions B, 21B, 1990, pp 377-385.
  18. Bertamini, L., Sturlese, S. and Beber, P., "Atmosphere and Temperature Controlled Spraying (ATCS) of thermal barrier coatings on aluminium alloys", Proc. 26th ISATA Conference, Aachen, Germany, 13-17 September 93, pp 477-485.
  19. Houben, J.M., "Relation of the adhesion of plasma sprayed coatings to the process parameters size, velocity and heat content of the spray particles", Ph.D. Thesis, Thechnical University of Eindhoven, 1988.
  20. Dallaire, S., "Influence of temperature on the bonding mechanism of plasma sprayed coatings", Thin Solid Films, 95, 1982, pp.237-244.
  21. Steffens, H.D., Wielage and B., Drozak, J., "Interface phenomena and bonding mechanism of thermally-sprayed metals and ceramic composites", Surface and Coating Technology, 43/44, 1991, pp 299-308.
  22. Boncoeur, B. and Hans, B., French Patents 8309889, June 1983, and 8403750, March 1984.
  23. Commission of the European Communities BRITE Programme, Project BE-4212-90, Modelling and characterisation of the manufacturing process of ceramic thermal barrier coatings, 18 Months Report.
  24. Lelait, L., Alperine, S. and Mévrel, R., "Alumina scale growth at zirconia-MCrAlY interface: a microstructural study", J. Mat. Sci., 27, 1992, pp 5-12.
  25. Brindley, W.J. and Miller, R.A., "Thermal barrier coating live and isothermal oxidation of low-pressure plasma-sprayed bond coat alloys", Surf. and Coat, Techn., 43/44, 1990, pp 446-457.
  26. Kojima, Y., Onaka, N. and Iizuka, N., "Hot oxidation and hot corrosion resistance of thermal barrier coating by low-pressure plasma sprayed coating system", proc ATTAC '88 Conference, Osaka, Japan, May 1988, 1, pp 277-281.
  27. Schneidenbanger, S., MTU-Germany, private communication.

Tab.1- Effect of isothermal heat treatments and of thermal cycles on the thickness of the reaction layer at the metal-ceramic interface.

Sample (hours of Heat Treatment)	average oxide thickness ( $\mu\text{m}$ )	minimum oxide thickness ( $\mu\text{m}$ )	maximum oxide thickness ( $\mu\text{m}$ )
flat (as sprayed)	0	0	0
flat (100 h)	4,5	3	10
flat (300 h)	7,5	5	18
flat (300h and 200 cycles)	8	5	20
flat / Thermal Fatigue Test	8	5	20
blades / Thermal Shock Test	5	3	13

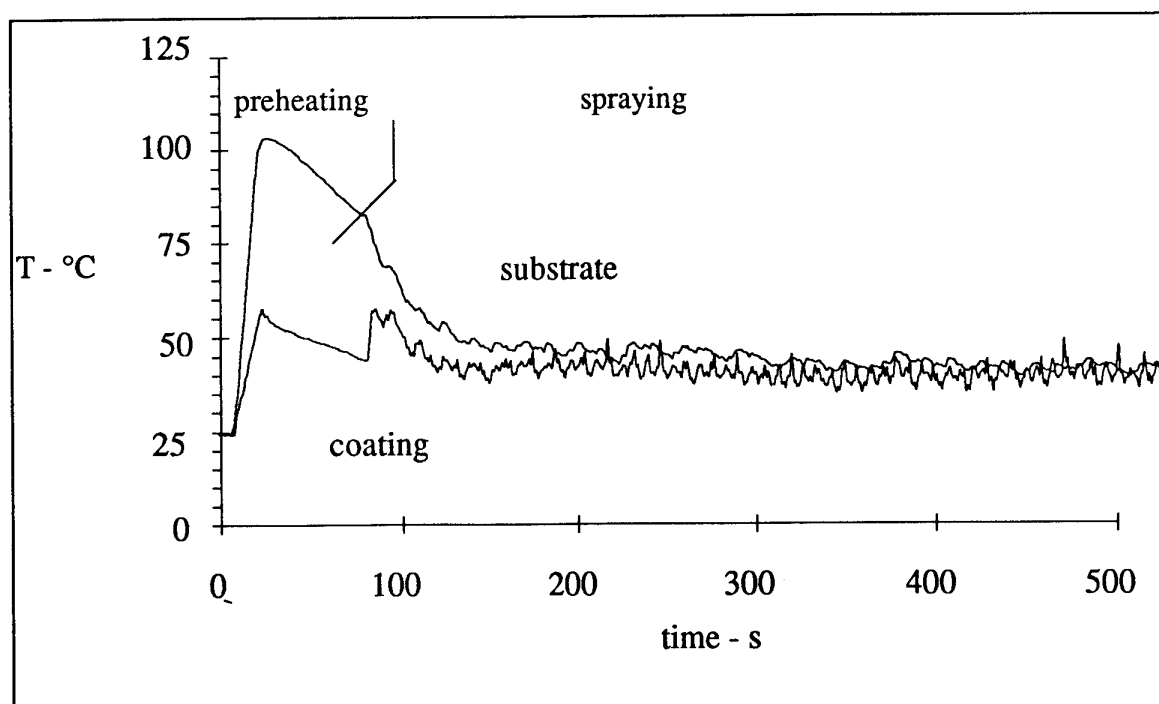


Fig.1 - Time vs. temperature curve during deposition of a ceramic TBC on a turbine blade. Both substrate and surface temperature are reported. The line indicates the start of spraying.

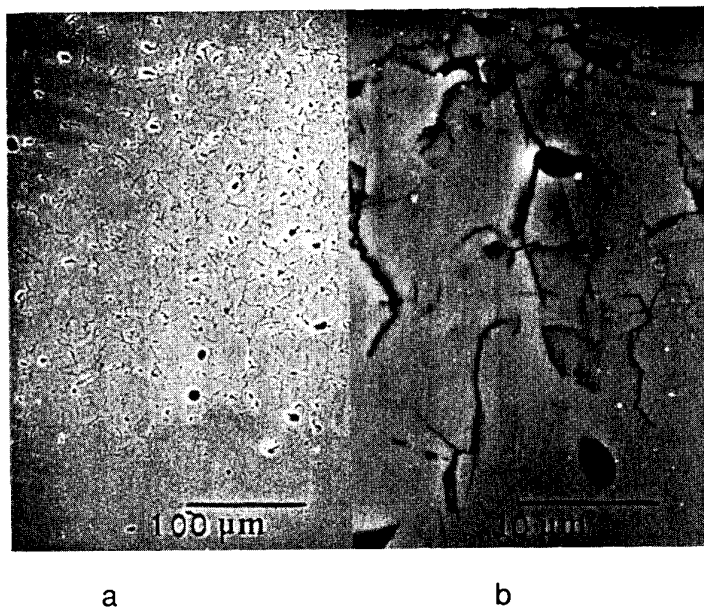


Fig.2 - The microstructure of an ATCS-7YSZ coating:

- a) at low magnifications (200x) the good homogeneity can be appreciated; There are only few big porosity and no large cracks;
- b) at high magnifications (2000x) the microcracking network becomes clear.

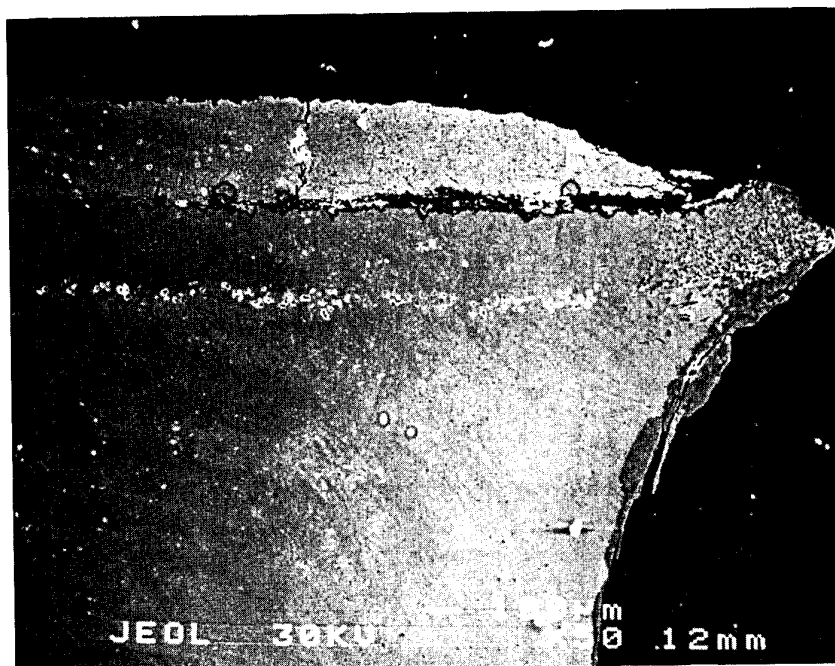


Fig.3 - Cross-section of the flat sample after Thermal Fatigue Test at low magnification (50x) the effect of the oxidation of the uncoated surface is outlined.

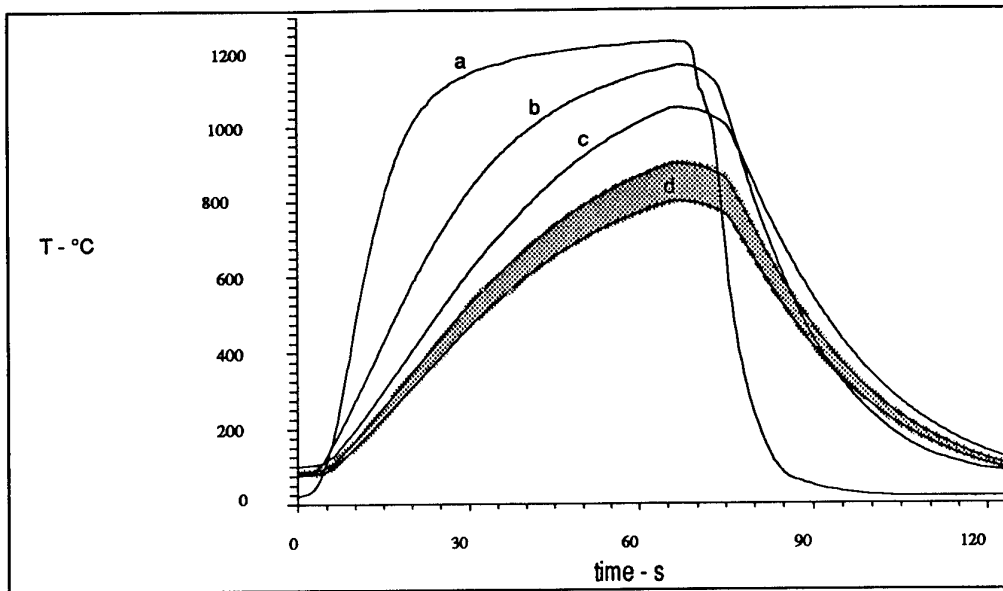


Fig.4 - Thermal shock cycles on turbine blades coated with the TBC when furnace temperature is 1280°C: (a) surface temperature of an uncoated blade; (b) inside temperature without the TBC; (c) inside temperature with the TBC; (d) suggested blade temperature with the TBC and an air cooling trough the cooling holes.

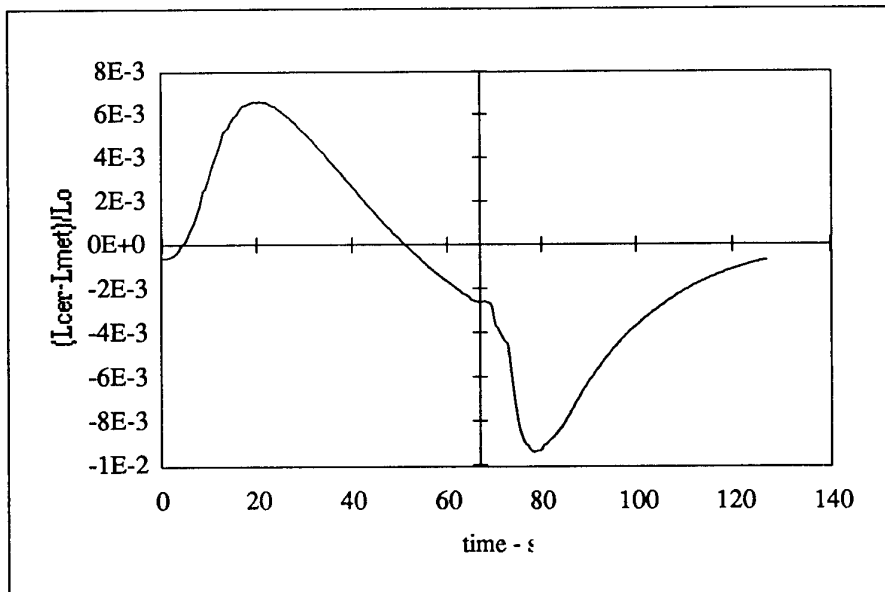


Fig.5 - Results of calculations about the difference in thermal strains between the surface layers of the ceramic coating and the metal inside the blade. Positive values correspond to compressive stresses inside the ceramic layer.

**Centro Sviluppo  
Materiali**

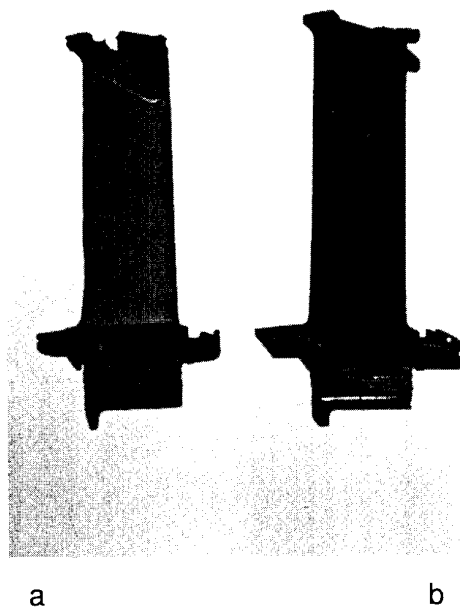


Fig.6 - Appearance of the blades after 900 cycles Thermal Shock Tests at 1280°C. Comparison of the TBC after 2500 cycles (blade a) and just after spraying (blade b).

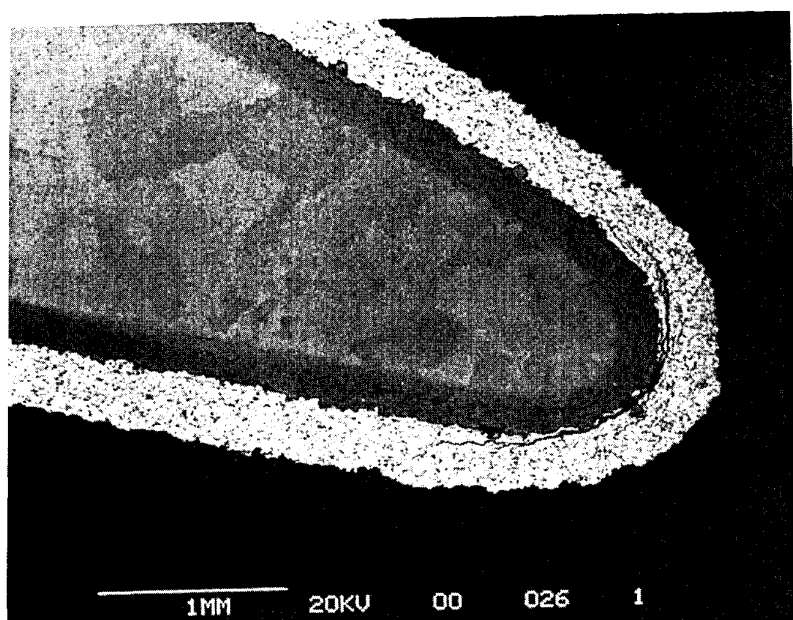


Fig.7 - Cross-section of the tested blade, near the spalled area on the trailing edge.

# X-ray Absorption Spectroscopy in High Temperature Oxidation of Metals and Alloys

Daniele Gozzi

Dipartimento di Chimica, Università 'La Sapienza', P.le Aldo Moro 5, 00185 Roma, Italy

Massimo Tomellini

Dipartimento di Scienze e Tecnologie Chimiche, Università 'Tor Vergata', Via della Ricerca Scientifica, 00133 Roma, Italy

## 1. SUMMARY

An experimental technique is described that allows for the joint study of the kinetics and of the oxide structure during the high temperature oxidation of metal surfaces. Oxygen is supplied at the metal through an electrochemical oxygen pump and the oxygen pressure, at the metal surface, is measured during oxidation by a YSZ (Yttria Stabilized Zirconia) oxygen sensor. XAS (X-ray Absorption Spectroscopy) is performed in fluorescence mode at the cation K edge and after each oxidation step. An appropriate analysis of the XAS spectra could provide information on both the oxidation kinetics and oxide structure. Experimental data on the high temperature oxidation of Nickel, Cobalt and of Fe(64%)Ni(36%) alloy, at low oxygen pressure, are reported and analysed according to the proposed data reduction. These results indicate the presented technique to be particularly suitable for studying the hot corrosion of oxide film too thick for common surface spectroscopy (AUGER, ESCA) and too thin for conventional thermogravimetric technique.

## 2. INTRODUCTION

The knowledge of the kinetics of oxidation of metals and alloys is a basic topic of the Materials Science and it has a prominent position in the modern technology. In particular, the development of devices and/or processes working at the high temperatures require to know the fundamental aspects of the thermodynamics and kinetics of the oxide growth. A spread literature was especially dedicated to this subject and a large number of data can be found, for instance, on the oxidation kinetics at high temperatures of metals in air or in pure oxygen. The scenario changes considerably in literature when one looks for data at low oxygen partial pressures. Also for the common machinable metals such as nickel, copper, iron, cobalt, etc. it is

difficult to find a sufficient number of data in those experimental conditions. There are a growing number of applications where the behaviour of metallic materials versus the oxidation in reduced oxygen pressures has to be studied, as for example in the jet turbines, in order to increase the efficiency by increasing the working temperature.

The aim of the present paper is to show an overview on one of the techniques developed by the authors in the frame of a project to study the kinetics of oxidation of metals and alloys at high temperatures and low oxygen partial pressure<sup>(1)</sup>. It is based on the XAS (X-ray Absorption Spectroscopy) and its major potentialities are to follow: *i.* selectively the oxide growth of a certain metal present in a heterogeneous matrix or in a solid solution; *ii.* the structure changes of the growing oxide.

## 3. EXPERIMENTAL

The experimental set-up is shown in Fig. 1. It

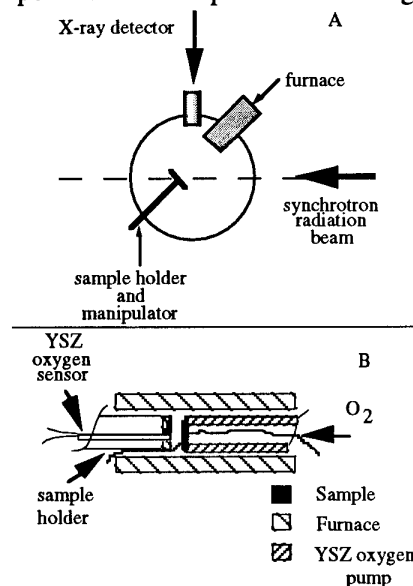


**Fig. 1** (A) Schematic view of the experimental apparatus for the *in situ* high temperature oxidation of metal surfaces. (B) Details of the microfurnace and sample holder

consists of a high vacuum multiport chamber positioned in one of the beam lines of the Adone<sup>1</sup>, the synchrotron ring of the National Laboratories of Frascati operating at 1.5 GeV and 50 mA. Several ancillary devices are connected to the chamber to allow its functionality. We consider only those ones characterizing our measurements. They are a feedthrough manipulator, a small furnace and a X-ray detector. A solid state electrochemical oxygen pump is coaxially mounted in the furnace positioned with its flat end in the isothermal zone. The manipulator allows to move inside and outside the furnace (up to the centre of the chamber) the sample holder in which a solid state oxygen sensor is encased just close to the sample. When the sample is positioned in the centre of the chamber it intercepts the synchrotron radiation beam and the X-ray spectrum in fluorescence mode can be performed. An Si (111) channel-cut monocrystal is used as monochromator with an energy resolution of 0.5 eV. The data acquisition is computer-assisted. The oxidation of the sample occurs inside the furnace (up to 1100 °C) being exposed to the oxygen flux generated electrochemically by a ceramic electrolyte cell. This oxygen pump is constituted by a flat end YSZ (Yttria Stabilized Zirconia) tube having Pt porous electrodes. As it is well-known, since the SZs are ionic conductors in a wide range of temperature and oxygen partial pressure,  $P_{O_2}$ ,

$$J_{O_2} = \frac{t_i I}{4FA}, \text{ if a current, } I, \text{ is imposed at the}$$

interfaces a flux of oxygen,  $J_{O_2}$ , can be set from an interface to the other one according to the current direction. In the present experiment the inner part of the tube is fluxed with pure oxygen at 1 bar and a constant current (galvanostatic mode) is applied in such a way to transfer oxygen just over the sample (the positive electrode is outside the YSZ tube). In

this condition  $J_{O_2} = \frac{t_i I}{4FA}$  where  $t_i$ ,  $F$  and  $A$  are, respectively, the ionic transport number, the Faraday's constant and surface area of the oxygen pump.  $t_i$  is, in our working conditions, very close to 1. The oxygen partial pressure is measured by a YSZ oxygen sensor in contact with the sample and the measured emf is a function of the actual  $P_{O_2}$  under which the oxide is growing. The oxygen sensor

constituted by a small close at one end and round tube made of YSZ with Pt-porous electrodes has an inner reference of the oxygen chemical potential based on a 1:1 weight mixture of Fe and  $Fe_{1-x}O$  (wüstite). At fixed temperature, the oxygen chemical potential in equilibrium with the condensed phase can be calculated according to the thermodynamic data.

The oxygen pump and sensor are homemade devices which were described elsewhere<sup>(2)</sup>.

## 4. RESULTS AND DISCUSSION

### 4.1 XAS measurements

Because of the geometrical arrangement of the experimental apparatus, the spectroscopic measurements have to be collected in reflection geometry. The cross section of the absorption process is therefore measured indirectly through the measurements of the fluorescence radiation emitted by the solid. In particular, the synchrotron radiation that strikes the metal/oxide surface induces a photon absorption process that leaves core holes in the K- edge of metal atoms. The successive recombination process between electrons and core holes gives rise to the emission of fluorescence light. The intensity of the fluorescence radiation is therefore proportional to the cross section for photon absorption at the metal K-edge. It is important to point out that fluorescence intensity is used to measure the X-ray Absorption cross section under some restriction on the sample thickness or specimens concentration in the sample. In fact the fluorescence intensity emitted under the solid angle  $\Omega$  by a sample layer of thickness  $dx$  located at a distance  $x$  from the surface is<sup>(4)</sup>:

$$dI(x) = I_0(x)\mu_i(E)\epsilon\left[\frac{\Omega}{4\pi}\right]dx \quad (1)$$

where  $\mu_i$  is the absorption coefficient of species  $i$  at photon energy  $E$ ,  $\epsilon$  is the radiative probability (for the fluorescence process) and  $I_0(x)$  is the intensity of the incoming radiation at depth  $x$  from the surface. Furthermore, the incoming and emitted intensities to and from  $x$  are related with the corresponding values at  $x=0$ , i.e. just above the surface, through the relationships:

$$I_0(x) = I_0 e^{-(\mu_t(E)x)} \quad (2)$$

<sup>1</sup>Dismantled on December 1993.

$$dI = dI(x)e^{-(\mu_t(E_f)x)} \quad (3)$$

where  $I_0(0)=I_0$  is the intensity of the synchrotron radiation at  $x=0$ ,  $\mu_t$  is the total absorption coefficient and  $E_f$  is the energy of the fluorescence photon. Using eqns.2 and 3 in eqn.1 the fluorescence intensity emitted by the sample is finally obtained in the form:

$$I = \int_0^L dI = I_0 \mu_i(E) \epsilon \left[ \frac{\Omega}{4\pi} \right] \frac{\{1 - \exp[-(\mu_t(E) + \mu_t(E_f))L]\}}{(\mu_t(E) + \mu_t(E_f))} \quad (4)$$

where  $L$  is the sample thickness. Two important cases may be considered: i) thin concentrated sample for which  $(\mu_t(E) + \mu_t(E_f))L \ll 1$  and ii) thick dilute samples for which  $(\mu_t(E) + \mu_t(E_f))L \gg 1$ . Under these constraints eqn.4 reduces, respectively, to the following expressions (4):

$$i) I = I_0 \mu_i(E) \epsilon \left[ \frac{\Omega}{4\pi} \right] L \quad (5)$$

$$ii) I = I_0 \mu_i(E) \epsilon \left[ \frac{\Omega}{4\pi} \right] \frac{1}{(\mu_t(E) + \mu_t(E_f))} \quad (6)$$

The fluorescence yield can be reasonably identified with the absorption coefficient in these two limiting cases. With reference to the proposed technique, the oxidation of a *one component* system implies eqn.5 to be fulfilled and the use of thin specimens is therefore required. The same considerations hold in the case of the oxidation of non dilute two component system, namely metal alloys. The requirement of thin films, whose thickness is of the order of magnitude of a few microns, represents the main limitation of this technique. However, this problem could be overcome through the measurement of the absorption coefficient at the oxygen K-edge rather than at the metal one. In fact, for low values of the oxide thickness grown over the metal surface, the *metal-oxide* sample can be regarded as a dilute solution of oxygen ions in a metal matrix.

## 4.2 Kinetics and spectral analysis

As reported in the experimental section, the spectroscopic measurement have been carried out at the metal K-edge. This is due to the fact that soft X-ray radiation was not available from the beam line dedicated to this research. Since the oxide grows on the parent metal, the fluorescence intensity is representative of both cations in the metal and in the oxide structures. The measured spectra is the superposition of these two contributions. An appropriate data reduction is therefore needed to separate the fluorescence spectrum associated to the own cations of the oxide layer to the one related to the unoxidized metal sites.

The procedure for the data analysis, that is mainly based on the use of eqn.5, has been described elsewhere (3). The total fluorescence signal representative of the cation sites recorded after  $j$  galvanostatic steps,  $S_j$ , is given according to:

$$S_j = \sum_r \left[ \frac{n_{r-1,r}}{N_0} \right] S_{r-1,r}(\text{MO}) + \left[ 1 - \sum_r \frac{n_{r-1,r}}{N_0} \right] S(\text{M}) \quad (7)$$

where the subscript  $i-1,i$  denotes a quantity (intensity, site number, oxidation time) related to the  $i$ -th oxide layer, grown after  $i$ -th oxidation steps. In eqn.7  $n$  is the number of cation sites in the oxidized state,  $N_0$  the whole number of sites,  $S(\text{MO})$  and  $S(\text{M})$  the intensities of the oxide and pure metal spectra, respectively. It is possible to show that for metal oxidation during film growth:

$$\frac{n}{N_0} = \left\{ \frac{\rho_{\text{ox}}}{\rho_{\text{me}}} \right\} \frac{\ell}{X_0} \propto \ell \quad (8)$$

where  $\rho_{\text{ox}}$  and  $\rho_{\text{me}}$  are, respectively, the cation densities in the oxide and metal phases,  $\ell$  is the oxide thickness and  $X_0$  the initial thickness of the metal film. From eqns.7, 8 the  $S_j - S_{j-1} = \Delta S_j$  term can be so evaluated:

$$\Delta S_j = (x_j - x_{j-1})(S_{j-1,j} - S_M) = x_{j-1,j} \Delta S_{j-1,j} \quad (9)$$



where  $x = \left\{ \frac{\rho_{ox}}{\rho_{me}} \right\} \frac{\ell}{X_0}$  and

$\Delta S_{j-1,j} = (S_{j-1,j} - S_M)$ . Under the assumption the oxide structure does not change during the growth process, and considering the sample oxidation completed after  $n$  steps, the relation holds:

$$\Delta S_{j-1,j} = \Delta S = S_n - S_M \quad (10)$$

and eqn.9 gives to:

$$x_{j-1,j} = \frac{\Delta S_j}{\Delta S} \quad (11)$$

This equation can be used to study the oxidation kinetics through the knowledge of the time elapsed during the  $j$ -th step:  $t_{j-1,j}$ . In the simple case of a single oxidation step eqn.7 reads:

$$S_1 = \beta S_1(MO) + (1 - \beta) S_M \quad (12)$$

where  $\beta = \frac{n_1}{N_0}$ . Therefore a linear

superposition of the separate reference spectra of the oxide and metal should reproduce the measured intensity. We observe that eqn. 12 can be also used to describe the experimental data in a *restricted energy region* of the spectra. Moreover, when a part of the spectra, in a restricted energy region, is not expected to differ from the one of a *reference* oxide, then the  $S(MO)$  spectra can be reconstructed. The  $\beta$  factor can be determined applying eqn.12 to this limited energy interval <sup>(3)</sup>. In this way the  $S_1$  unknown spectra can be extracted, in the *whole energy region*, through the inversion of eqn.12.

### 4.3 Oxidation of one component systems

To test the proposed technique, preliminary experiments on the oxidation of Ni and Co at high temperature have been carried out on metal microfoils ( $X_0=6\mu m$ ) <sup>(3)</sup>. Oxygen was produced electrochemically through potentiostatic steps, and the faradic current simultaneously recorded. It was in the range 50-100mA for an applied voltage of 1V. Ni oxidation was performed at 665 and 720°C by five galvanostatic steps of 5, 15, 40, 42 (T=665°C, I=50mA) and 30 min (T=720°C, I=100mA). Cobalt was oxidized at T=720,

780°C by three steps of 5, 30 (T=720°C, I=100mA) and 50 min (T=780°C, I=100 mA). The steady state value of the oxygen pressure measured close to the sample surface was about  $10^2$  Pa, compared with a blank value of  $10^{-3}$  Pa. The calculated oxygen flux at I=50mA was of the order of  $10^{-6}$  moles  $cm^{-2} s^{-1}$ . Spectroscopic measurements at the Ni and Co K-edges were recorded after each of the oxidation steps, when the sample temperature was fallen below 250°C. However, we did not observe any substantial change in the fluorescence spectrum up to sample temperature of about 500°C.

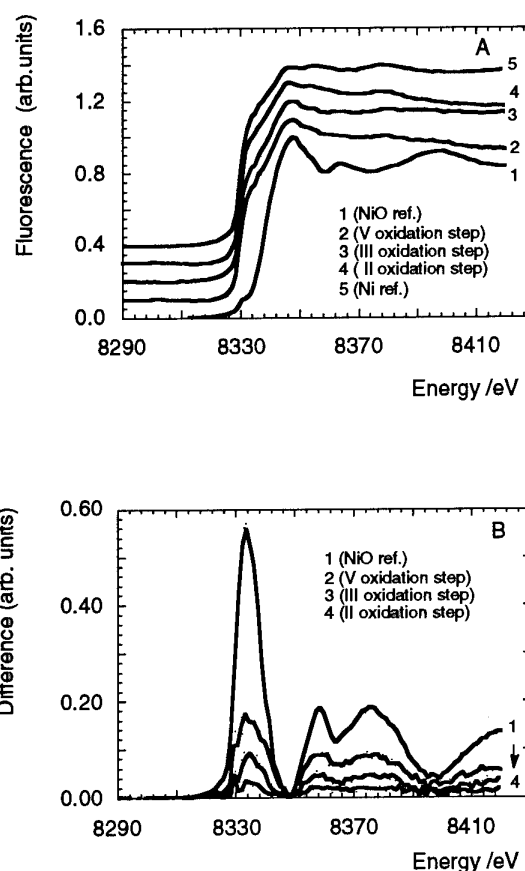


**Fig. 2** Ni K-edge spectra measured in fluorescence mode after several oxidation steps (A): in panel B is shown the spectrum difference between pure metal and oxidized metal.

As an example in fig.2 are reported the fluorescence spectra of the Ni K-edges recorded after the second, the third and the fifth oxidation steps, jointly to the spectrum of the pure metal foil. In the same figure is also shown the fluorescence yield of the reference

specimen, namely NiO powder with a content of metal impurities lower than 20 ppm. In panel B the differences between the spectrum of the unoxidized surface and the measured spectra after the oxidation steps, have also been reported. Similar spectra have been collected for the Co K-edge during the oxidation of the Co microfoil, where a high purity CoO powder was used as reference oxide. The measured spectra of both Co and Ni specimens were also found to be in agreement with previous measurements (5).

The oxidation kinetics is extracted from the spectroscopic data on the basis of the data reduction reported in section 4.2. In particular, eqn. 1 is applied by assuming that the oxide structure does not change during the growth process. The relation holds:

$$S(M) - S_k = \beta_k [S(M) - S_k(MO)] \quad (13)$$

that indicates that each spectral difference reported in fig.2B is proportional to the difference between the spectrum of the metal and of the oxide layer. It is quite reasonable to assume the fluorescence yield, in the energy region *close to the absorption edge*, to be entirely related to the  $Co^{2+}$  or  $Ni^{2+}$  ions, regardless of the oxide defectivity. This point has been addressed in ref. 3 and allows to evaluate the  $\beta$  term according to:

$$\beta_k = \frac{\delta I_k}{\delta I_{ref}} \quad (14a)$$

$\delta I_k$  and  $\delta I_{ref}$  being - with reference to fig.2B - the area of the peaks at *c.a.* 8330eV in the spectral difference of growing and reference oxides, respectively. Once the  $\beta_k$  value is known, the oxide thickness is determined through eqn.8:

$$\beta_k = \frac{\rho_{ox}}{\rho_{me}} \frac{\ell}{X_0} \quad (14b)$$

On the other side the  $\beta$  value provides for the oxide spectrum to be reconstructed by inversion of eqn.13:

$$S_k(MO) = S(M) - [S(M) - S_k] \frac{1}{\beta_k} \quad (15)$$

Therefore, it is possible to extract information on the oxidation kinetics and oxide structure,

jointly. The oxidation kinetics are reported in fig.3 and compared with experimental data reported in the literature and obtained using conventional techniques (6,7).

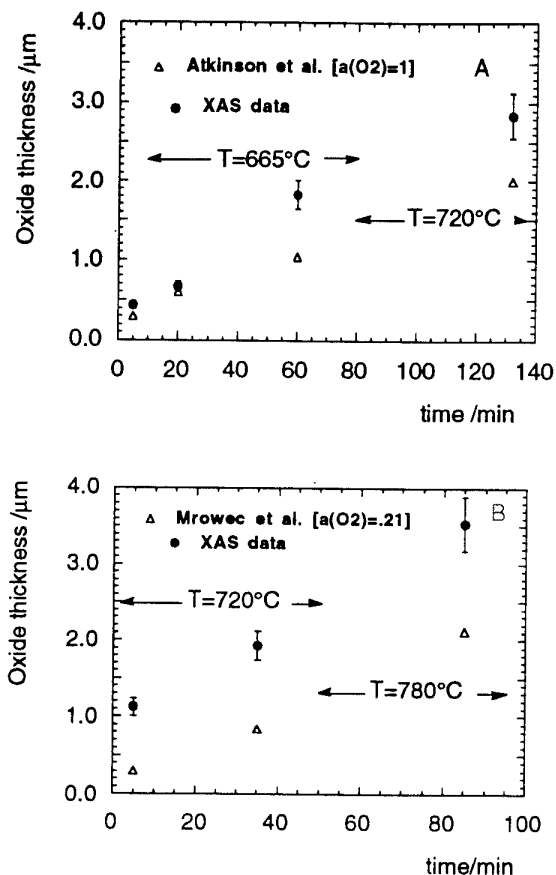


**Fig.3** The oxidation kinetics of (A) Ni and (B) Co, as obtained by the present technique, are compared with kinetic data reported in the literature.  $a(O_2)$  stands for the oxygen activity.

This comparison indicates that there is agreement between the order of magnitude of the reaction rates and oxide thicknesses. In fig.4 the kinetic data are shown in a more detailed way for the first oxidation step of the Ni foil. In particular, in panel A is reported the EMF recorded by the sensor and in panel B the oxygen partial pressure normalized to the background value,  $P(0)$ . In panel C the time evolution of the oxide thickness,  $x(t)$ , is also reported. It has been evaluated by assuming a parabolic growth law for the oxide scale and a time dependence of the oxygen pressure given by fig.4B.

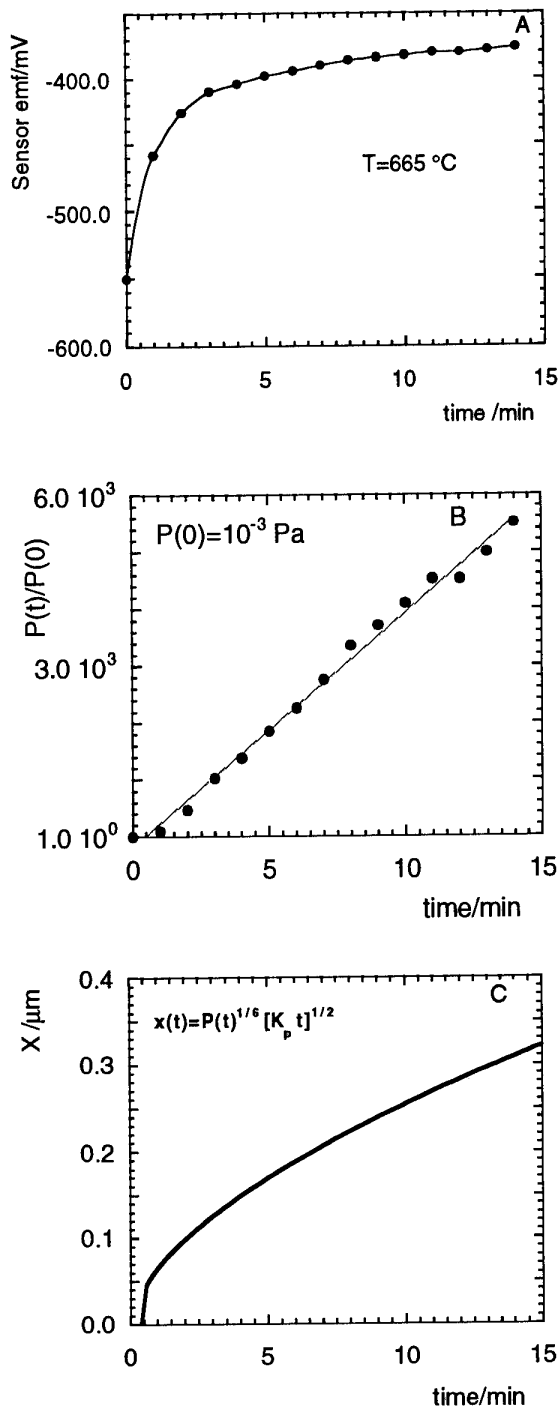


**Fig.4** (A) Sensor EMF; (B)  $P_{\text{O}_2}$  normalized to the  $P(0)$  blank value; (C) the oxidation kinetics evaluated on the basis of the parabolic law

The oxygen pressure is evaluated on the basis of the EMF value by the equation

$$P(t) = P_{\text{ref}} \exp \left[ -\frac{4FE}{RT} \right] \quad (16)$$

where  $P_{\text{ref}}$  is the oxygen partial pressure in equilibrium at temperature  $T$  in the Fe-wüstite mixture,  $E$  is the EMF value,  $F$  and  $R$  are, respectively, Faraday's constant and the gas constant. Assuming a parabolic growth law, the rate constant of the oxidation process (first oxidation step) is evaluated on the basis of the  $P(t)$  function and from the  $x(t)$  values obtained by the analysis of the fluorescence spectra. The calculation gives  $K_p=10^{-10}\text{ cm}^2\text{ s}^{-1}$  (fig.4C).

Spectra were also *reconstructed*, in the whole energy range, according to the procedure above reported. No substantial change has been observed between the spectra of the oxide layers and of the reference oxide.

#### 4.4 Oxidation of two component systems

The oxidation of an iron-nickel alloy was also studied with the present technique.

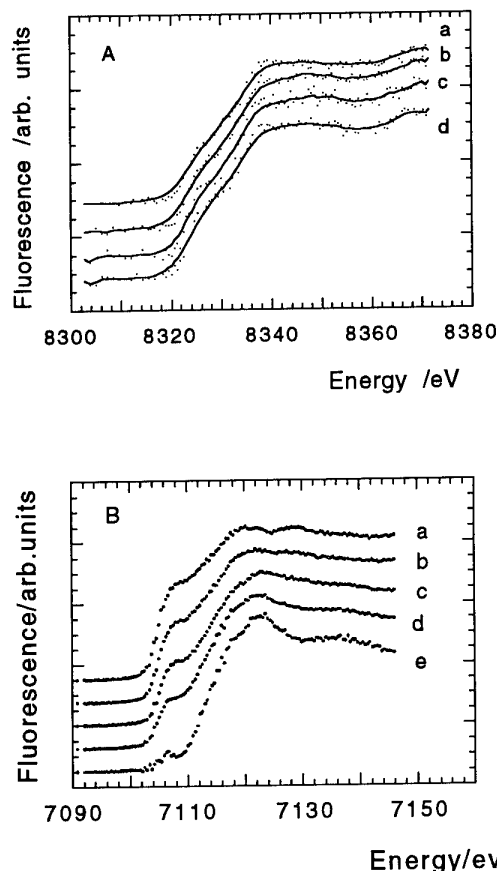


**Fig.5** XAS spectra of unoxidized (a) and oxidized (a-->d) alloy collected at the Ni (panel A) and Fe (panel B) K-edges.

The specimen was a polycrystalline alloy containing 64% of Fe and 36% of Ni,

oxidation was performed through three successive oxidation steps at the constant temperature of 660°C and at an oxygen partial pressure of about 0.3Pa. The selectivity of the XAS spectroscopy towards the atomic species, indicates this technique to be particularly suitable for studying the oxidation of Ni and Fe, separately. This is due to the fact that the Ni and the Fe K-absorption edges are well separated in energy.

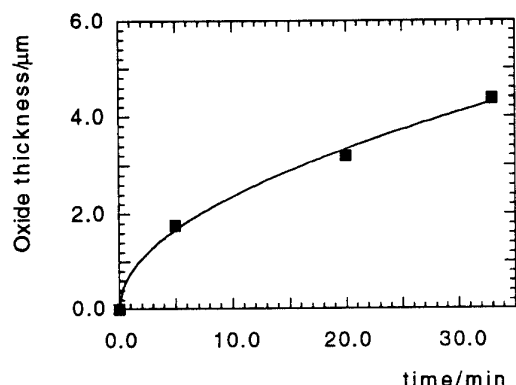


**Fig.6** Oxidation kinetics of iron oxide over Fe(64%)Ni(36%) alloy at  $T=660^{\circ}\text{C}$  and  $P_{\text{O}_2}=0.3\text{Pa}$ .

In figure 5 the fluorescence yields at the Ni (A) and Fe (B) K-edges are shown for the oxidized (b-->d spectra) and unoxidized (a spectra) alloy. As it appears by the XAS measurements, changes at the Fe K-edges are detected, whereas no appreciable modifications are observed in the Ni K-edge spectra. Therefore, under present conditions, the Fe-Ni alloy oxidation gives rise to iron oxidation, only. The kinetics of the Fe oxidation has been evaluated according to the data treatment reported in section 4.2 and is shown in fig.6. This analysis was carried out under the assumption that  $\text{Fe}^{2+}$  was the ionic state of iron in the oxide layer. The formation of the FeO phase has been established on the basis of the reconstructed spectrum and energy position of the absorption edge. In fact the energy shift between the adsorption edge of iron in  $\text{Fe}_2\text{O}_3$  and FeO is about 3eV, a value that can be well resolved by the XAS spectroscopy. Moreover, the oxidation kinetics is found to be in agreement with a parabolic growth law with a rate constant of  $4.5 \cdot 10^{-11} \text{ cm}^2 \text{ s}^{-1}$  (fig.6)(8).

#### 4.5 Detection limit

An important quantity that is required to be known in order to assess the minimum value detectable by a given technique is the so called *detection limit*. In this case, it represents the lowest oxide thickness that can be detected by the XAS performed in fluorescence mode. To extract this information

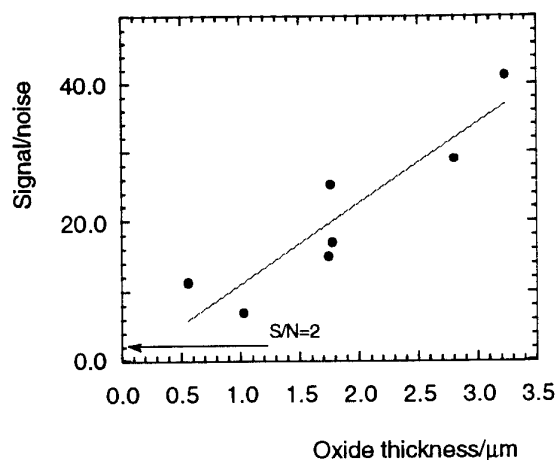


**Fig.7** Signal to noise ratio obtained by measuring Ni and Co K-edges.

from the experimental data, we reported the signal to noise ratio (S/N) obtained from the Ni and Co K-edges as a function of the oxide thickness. The results are shown in fig.7 and provides a thickness value of about  $0.2\mu\text{m}$  when, as usual, a S/N ratio equal two is considered. Therefore, a detection limit of  $0.2\mu\text{m}$  seems to be appropriate for the present technique.

#### 5. CONCLUSIONS

In this paper we presented an experimental technique that should be suitable for the joint study of the oxidation kinetics and oxide structure of an oxide layer grown on parent metal at high temperature. XAS results on the oxidations of one component systems were analysed according to the *spectra subtraction method* presented in section 4.2. Accordingly, both the oxidation kinetics and the reconstructed spectra are accessible from the experimental data. This technique seems to be particularly promising for studying the oxidation of multi component systems. In fact, our preliminary results show that the selectivity of the spectroscopy, toward the atomic species, allows for the oxidation of each component to be *observed*, separately.

selectivity of the spectroscopy, toward the atomic species, allows for the oxidation of each component to be *observed*, separately. Finally, the analysis of the S/N ratio indicates a detection limit, of  $0.2\mu\text{m}$  a value that is too low and too high for thermogravimetric and ESCA analysis, respectively.

## 6. ACKNOWLEDGEMENTS

The authors wish to thank the CSM (Centro Sviluppo Materiali, Roma) and PULS-INFN LNF (Laboratori Nazionali di Frascati) for the joint financial support given to realize the high temperature system on the *hard X-ray* beam line facility.

## 7. REFERENCES

- 1) D. Gozzi and M. Tomellini in High Temperature Corrosion Research in Progress, EPRI EAR-7433, Project 2426-10, Special Report, August 1991, p. 418-421
- 2) D. Gozzi, P.L. Cignini, G. Carnevale L. Petrucci and M. Tomellini, High Temperatures & High Pressures, 1988, **20**, 385-396; J. Materials Science, 1990, **25**, 4562-4566
- 3) M. Tomellini, D. Gozzi, I. Davoli, J. Mater. Chem. 1992, **2**(7), 745
- 4) J. Jaklevic, J.A. Kirby, M.P. Klein, A.S. Robertson, G.S. Brown, P. Eisenberger, S. State Comm. 1977, **23**, 679
- 5) L. A. Grunes, Phys. Rev. 1983, **27**, 2111
- 6) A. Atkinson, Rev. Modern Phys. 1985, **57**, 437
- 7) S. Mrowec, K. Przybylski, Oxid. Met. 1977, **11**, 365
- 8) Per Kofstad, High Temperature Corrosion, Elsevier Applied Science, London (1988)

## RESISTANCE OF SILICON NITRIDE TURBINE COMPONENTS TO EROSION AND HOT CORROSION/OXIDATION ATTACK

Thomas E. Strangman  
AlliedSignal Engines  
Phoenix, Arizona, USA

Dennis S. Fox  
NASA Lewis Research Center  
Cleveland, Ohio, USA

### 1 SUMMARY

Silicon nitride turbine components are under intensive development by AlliedSignal to enable a new generation of higher power density auxiliary power systems. In order to be viable in the intended applications, silicon nitride turbine airfoils must be designed for survival in aggressive oxidizing combustion gas environments. Erosive and corrosive damage to ceramic airfoils from ingested sand and sea salt must be avoided.

Recent engine test experience demonstrated that NT154 silicon nitride turbine vanes have exceptional resistance to sand erosion, relative to superalloys used in production engines. Similarly, NT154 silicon nitride has excellent resistance to oxidation in the temperature range of interest - up to 1400C.

Hot corrosion attack of superalloy gas turbine components is well documented. While hot corrosion from ingested sea salt will attack silicon nitride substantially less than the superalloys being replaced in initial engine applications, this degradation has the potential to limit component lives in advanced engine applications. Hot corrosion adversely affects the strength of silicon nitride in the 850 to 1300C range.

Since unacceptable reductions in strength must be rapidly identified and avoided, AlliedSignal and the NASA Lewis Research Center have pioneered the development of an environmental life prediction model for silicon nitride turbine components. Strength retention in flexure specimens following 1 to 3300 hour exposures to high temperature oxidation and hot corrosion has been measured and used to calibrate the life prediction model. Predicted component life is dependent upon engine de-

sign (stress, temperature, pressure, fuel/air ratio, gas velocity, and inlet air filtration), mission usage (fuel sulfur content, location [salt in air], and times at duty cycle power points), and material parameters.

Preliminary analyses indicate that the hot corrosion resistance of NT154 silicon nitride is adequate for AlliedSignal's initial engine applications. Protective coatings and/or inlet air filtration may be required to achieve required ceramic component lives in more aggressive environments.

### 2 Introduction

Silicon nitride ceramics are under intensive development for advanced gas turbine applications. In order to be viable, silicon nitride turbine airfoils must be designed for survival in aggressive erosive, oxidizing combustion gas environments. This paper reviews the stability of silicon nitride in aggressive environments and describes the status of environmental life prediction for gas turbine applications.

### 3 Experimental Procedure

The NT154 silicon nitride used for this study was manufactured by Norton Advanced Ceramics (Northboro, MA). This commercially available hot isostatically pressed (HIPped) silicon nitride material contains 4 weight percent yttria added as the densification aid.

Billets for flexure specimens were cold isostatically pressed from the powder and then HIPped to full density. Turbine vanes used in the erosion tests were produced by slip casting the vane to near-net-shape and HIPping to

full density. A high-temperature heat treatment was used to crystallize most of the grain boundary phases. Flexure specimens and turbine vanes were diamond ground from the billets and castings. Following machining, the specimens were given a lower temperature heat treatment to improve the surface strength of the material. (Process HIP and heat treatment conditions are proprietary to Norton Advanced Ceramics.)

Machined flexure specimens were used to assess the effects of environmental (furnace oxidation and burner rig hot corrosion) exposure conditions on room temperature strength. Three specimens geometries were used. Oxidation effects were evaluated with 3 x 4 x 50 mm specimens, which had the tensile surface machined in the transverse (lowest strength) direction. Thick (6.35 x 12.7 x 101.6 mm), specimens machined in the longitudinal (highest strength) direction were used for 1 atmosphere burner rig hot corrosion tests. Thin, longitudinally machined specimens (2.4 x 4.8 x 26.4 mm) were used in the 5 atmosphere burner rig.

### 3.1 Furnace Oxidation

A matrix of 180 transverse machined NT154 specimens (shown in Figure 1) was exposed in an electric furnace in air for logarithmically distributed times (1 to 1000 hours) and temperatures in the range of 982 to 1400C. This distribution of specimens permitted effects of oxidation on strength to be analyzed as a function of exposure time and temperature.

### 3.2 One Atmosphere Burner Rig Hot Corrosion Test

NT154 flexure specimens were exposed to the series of cyclic burner rig hot corrosion environments indicated in Table 1 for logarithmically distributed times up to about 3287 hours.

The following nominal conditions were used for each test:

Fuel: Jet A (0.035% sulfur [nominal])

Air: 5ppm synthetic sea salt (ASTM specification D1141-52)

Fuel/air weight ratio: 0.0606

Combustion gas velocity: 267 meters/second

Operation of the burner rig was controlled with the aid of a personal computer. Combustion products from the burner were ducted through a rotating (800 rpm) carousel that contained eight vertically mounted specimens. One of the specimens contained a thermocouple embedded below the surface in the 3 cm long hot zone test section. This thermocouple was monitored continuously by computer during the test. Due to the thickness of the specimens used in the 1 atmosphere burner rig tests, interior temperatures lagged surface temperatures by several seconds. In order to avoid overtemperature of the surface during rapid heating, an optical pyrometer continuously measured surface temperature. Optical surface temperatures were used to facilitate computer adjustments to the burner's fuel flow during heating. Testing was periodically interrupted for removal and replacement of individual specimens (to achieve a logarithmic distribution of exposure times) and for daily visual inspection. Following test interruptions, a steady state thermocouple measurement of hot zone temperature was obtained and used to calibrate the pyrometer's emissivity.

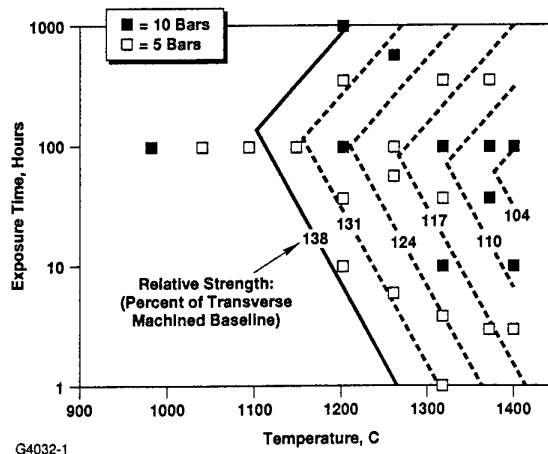


**Figure 1. Air Furnace Oxidation Exposures Initially Improved Strength of Transverse Machined NT154 Silicon Nitride Flexure Specimens.**

Table 1. Atmospheric Burner Rig Cyclic Hot Corrosion Environments.

Test	Cycle	Test Duration
1	860C/27 minutes + air cool/3 minutes	3287 hours
2	890C/27 minutes + air cool/3 minutes	600 hours
3	954C/27 minutes + air cool/3 minutes	600 hours
4	982C/27 minutes + air cool/3 minutes	400 hours
5	1052C/27 minutes + air cool/3 minutes	300 hours
6	1121C/27 minutes + air cool/3 minutes	300 hours
7	1218C/27 minutes + air cool/3 minutes	300 hours
8	968C/3min + 1218C/24min + air cool/3min	600 hours
9	968C/3min + 1288C/24min + air cool/3min	300 hours

ASTM synthetic sea salt was added to the combustion air at a concentration of 5ppm (weight) by injecting an air atomized salt spray solution through a hole in the combustor's liner. Chemical analysis of the ASTM sea salt is provided in Table 2.

Table 2. Composition of Synthetic Sea Salt Used in Burner Rig Hot Corrosion Tests.

Salt Constituent	Weight %
NaCl	58.49
MgCl <sub>2</sub> -6H <sub>2</sub> O	26.46
Na <sub>2</sub> SO <sub>4</sub>	9.75
CaCl <sub>2</sub>	2.765
KCl	1.45
NaHCO <sub>2</sub>	0.477
KBr	0.238
H <sub>3</sub> BO <sub>3</sub>	0.071
SrCl <sub>2</sub> -6H <sub>2</sub> O	0.095
NaF	0.007

Following exposure to the above environments, flexure specimens were water washed to remove any unreacted salt and photographed to document the extent of corrosion as a function of exposure time in the test.

### 3.3 Five atmosphere burner rig test

Gas turbine engines operate at internal pressures greater than one atmosphere. For this reason, a NASA Lewis Research Center burner rig that can be pressurized up to five atmospheres was also used in this study. Hot corrosion occurs in a temperature range between the melting point of the salt and the dew point.[1] An increase in the rig pressure increases the dew point, thereby widening the temperature range in which corrosion will occur. The 5-atmosphere burner rig has been used previously to study the sodium sulfate hot corrosion of silicon nitride and silicon carbide.[2-4] In those studies, which were focused on identification of corrosion

mechanisms and effect of corrosion on strength, the four experimental variables (exposure time, exposure temperature, rig pressure, and salt concentration) were fixed.

The current study is different in that another salt (ASTM D1141-52 synthetic sea salt) is used, and measured effects of pressure (1, 3 and 5 atmospheres), salt concentration in the combustion air (2, 5 and 10 ppm), and exposure time are obtained to facilitate development and validation of a life prediction model. A series of short (2 hour) 5 atmosphere burner rig tests was conducted at higher temperatures with 5 ppm sea salt to experimentally establish the dew point for salt deposition.

The NASA rig consists of a standard Mach 0.3 burner [2] with the samples enclosed in a flame tunnel. Pressure is increased by closing an exhaust control valve.[3] Groups of specimens were exposed for up to 75 hours in a 980C five-atmosphere burner rig (and subsequently flexure tested at room temperature). In the 5 atmosphere tests Jet A fuel was burned at a fuel/air weight ratio of 0.025, and the combustion gas velocity was 53 m/sec. A total of eight samples were tested at each of the five exposure times. Sample size was 2.64 x 0.48 x 0.24 cm. The samples (four per run) were positioned horizontally with their thicknesses facing the flow. The sample ends were held in aluminosilicate (grade A lava) holders. The temperature was monitored with two type R thermocouples positioned between the specimens in the gas stream.[3] The salt was added by aspirating a salt water solution into the flame.

### 3.4 Flexure test

Exposed specimens were broken at room temperature in four-point flexure to quantify the effect of the environment on the surface strength of the NT154 silicon nitride. To facilitate testing of specimens exposed to hot corrosion conditions, silicate reaction products were re-



moved from the loading pin locations. Specimens exposed for long times in the one-atmosphere burner rig required a combination of abrasive grinding (240 grit) and dilute HF acid etching. Cleaning of the tensile surface of the specimens was limited to water washing. Loading pin locations on specimens exposed in the five-atmosphere burner rig were cleaned by abrasive grinding with 180 grit. Specimens exposed in a furnace air oxidation environment received no post-exposure cleaning prior to testing.

Specimen geometries and room-temperature four-point bend flexure test conditions used to characterize effects of prior oxidation and hot corrosion environments are provided in Table 3.

### 3.5 Erosion test

Sand erosion tests were conducted using a GTCP85 auxiliary power unit. The test was conducted with a hybrid turbine nozzle consisting of 17 silicon nitride vanes and 6 superalloy vanes. The test was conducted for 9 hours at the maximum power setting. During this 9 hour period, AC coarse silica sand (0 to 200  $\mu\text{m}$  particle diameter) was injected into the combustor at a rate of 0.34 kilograms/hour.

### 3.6 Post-test analysis

All flexure specimens were examined visually at a minimum 10X magnification in order to identify the fracture origin. Selected specimens were also examined under the SEM to further characterize the fracture origin and oxidation/hot corrosion microstructures. EDX and WDX spectroscopy were used during the SEM analyses to characterize elements present in the corrosion products.

Engine tested vanes were examined visually and with fluorescent penetrant for evidence of erosion and cracking.

## 4 Results and Discussion

### 4.1 Oxidation

#### Effect of oxidation on flexure strength

Following exposure in the static air furnace, the specimens were tested in four-point bending at room temperature. Test results are shown as lines of relative strength in Figure 1. Test data and failure origin locations for individual specimens are documented in Reference 5.

Unexpectedly, exposure to the oxidation environment increased strength, relative to as-received specimens, which had the standard Norton pre-oxidation heat treatment. Exposures in the 980 to 1200C range provided the largest improvement (up to a 38% increase) in strength. For longer exposure times (up to 100 hours) in the 1100C to 1400C temperature range, specimen strength decreased, but still remained above as-received values.

Figure 1 also illustrates unusual behavior for exposures longer than 100 hours in the 1100 to 1400C temperature range; the average specimen strength increased with additional exposure time. This behavior was unexpected since it was not observed in an earlier evaluation of NT154 specimens oxidized in a cyclic 1260C Mach 0.3 burner rig environment.[6] Following exposure to this cyclic burner rig test environment, which more closely simulates conditions within gas turbines, measured room temperature flexure strength continued to decline for exposures up to 1000 hours. The rate of strength reduction during 1000 hours in the burner rig environment was consistent with that of furnace exposed specimens for times up to 100 hours.

**Table 3. Four-Point Flexure Tests Were Used to Quantify the Effects of Environment on the Surface Strength of NT154 Silicon Nitride.**

Type of Test	Specimen Geometry	Flexure Test Parameters	
		Inner/outer Spans	Crosshead Speed
Oxidation	3 x 4 x 50mm	20/40 mm	0.5 mm/minute
1 atm burner rig	6.35x12.7x101.6mm	19/38 mm	0.25 mm/minute
5 atm burner rig	2.4 x 4.8x 26.4mm	9.5/19 mm	0.5 mm/minute

Post-exposure room temperature flexure strength was modeled as a function of exposure time and temperature, using data with exposures less than or equal to 100 hours. In this time range, constant strength lines in Figure 1 have constant values of  $T + 33.33 \ln[t]$ , where T is the temperature in degrees C and t is the time in hours. Strengths for the 145 specimens with exposure times up to 100 hours was described with the following equation:

$$\text{average flexure strength} = 1690 - 0.614 \cdot (T + 33.33 \cdot \ln[t]) > 925 \text{ MPa}$$

G4700-74

Fractures in the as-received specimens, which were pre-oxidation heat treated by Norton, typically initiated in the chamfered edge of the specimen. Only seven percent of the as-received transverse machined specimens failed on the tensile surface. This result implies that machining damage was more severe on the chamfer than on the transverse machined surface.

Exposure to the high-temperature oxidizing environment reduced the severity of chamfer damage; i.e., over eighty percent of the environmentally exposed specimens failed on the tensile surface. When specimens associated with chamfer failure are eliminated from the database, scatter in the data is reduced, as shown in Figure 2.

#### Oxidation Affected Surface Layer

Although specimen weights were measured before and after exposure to the furnace air environment, weight changes were trivial -- within measurement error. Therefore, fracture surfaces were examined on the SEM to determine the thickness of the oxidation-affected layer. In this analysis, it was found that growth of the oxidation-affected layer of these specimens appeared to follow logarithmic instead of expected parabolic growth behavior. Wavelength dispersive X-ray (WDX) maps from fracture surfaces indicated that an oxygen gradient

existed in the surface layer of the silicon nitride. WDX analysis also indicated that the concentration of nitrogen in the oxygen-affected zone remained high -- almost to the level present below the oxygen-affected zone.

Applicability of logarithmic or parabolic growth kinetics in NT154 is the subject of an on-going investigation. At this time the kinetics remain ambiguous in a 1300C air environment. Parabolic growth was documented in a 1300C oxygen environment.

#### Discussion

Oxidation at temperatures below 1400C strengthened the surface of NT154 and reduced the severity of machining induced surface flaws. It is speculated that the increase in flexure strength is a consequence of oxidation induced compressive stresses. Examination of fracture surfaces indicated that oxidation in this temperature range did not occur as a plane front process; i.e., an oxygen gradient exists below the surface, which is thought to imply preferential oxidation within grain boundaries (and machining microcracks). Compressive stresses are expected when the volume expansion associ-

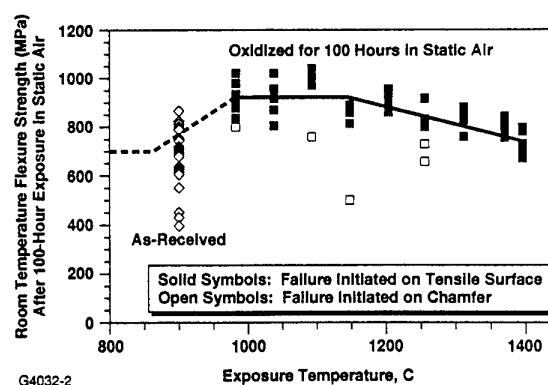


**Figure 2. Oxidation Increased Flexure Strength of Transverse Machined Specimens and Reduced Incidence of Chamfer Initiated Failures.**

ated with oxidation (conversion of silicon nitride to silicon oxynitride) in grain boundaries and microcracks is constrained by unoxidized silicon nitride grains. Maximum strength is anticipated when oxidation induced stresses aren't relaxed by deformation in the oxynitride grain boundary phase. At higher temperatures, stress relaxation in the oxynitride grain boundaries (e.g., by extrusion of grain boundary material to the free surface) may be responsible for the decreasing benefit of oxidation at temperatures in the 1200 to 1400C range. (Following exposure to 1371C oxidation, yttrium disilicate crystals were observed on specimen surfaces. Yttrium in these crystals was initially present in the grain boundaries.) At this time the above explanation for strengthening remains speculative; i.e., compressive surface stresses in oxidized specimens has not been confirmed.

## 4.2 Hot Corrosion

In contrast with oxidation behavior, reaction between salt deposits and NT154 resulted in significant reduction in room temperature flexure strength. For tests conducted at 893C and above, the most severe loss in strength occurred during the initial hour(s) of exposure (Figure 3). The rate of strength loss then slowed significantly as exposure time increased.

During exposure to 860C burner rig combustion environment, salt deposited on the specimen, but remained virtually unmelted. EDX examination of salt deposits removed from specimens indicated that Na, K, Mg, Ca, and S were present. With the exception of isolated areas, salt deposits were easily removed by water washing. Visual examination confirmed that surface reaction with salt deposits was minimal. In contrast with other tests discussed below, strength reduction was minimal following exposure to the 860C hot corrosion.

Room temperature flexure strength data obtained following exposure of specimens to a range of 982C burner rig environments are illustrated in Figure 4. This figure shows that the surface strength is reduced by 30 to 40 percent during the first few hours of exposure to the hot corrosion environment. Following the initial 50 hours of exposure, room temperature strength decreased gradually -- even though the surface became roughened. Reducing the concentration of salt ingested into the burner results in a predictable increase in strength retention. Similar strength retention was predicted and ob-

served for tests conducted at 1, 3 and 5 atmospheres; this result occurred because the product of salt deposition (increased by pressure) times salt basicity (reduced by pressure) remained constant.

The initial reduction in strength coincides with the initial formation of a glassy silicate layer by reaction between deposited salt and the silicon nitride. Glassy silicate reaction products on several specimens were qualitatively analyzed using the EDX and WDX spectroscopy capabilities of the SEM; results of these analyses indicated that the glassy silicates on the surface contain Na, K, Mg, Ca, Si, Y, O and N. Co, Ni, and Fe were also present in small concentrations in some spectrographs; these elements are present in the burner rig system.

It is speculated that the initial rapid reduction in strength may be attributed to relaxation of pre-oxidation strengthening (e.g., by elimination of compressive pre-oxidation stresses). Although the average depth of reaction during the initial hour(s) of exposure is minimal (less than 1 micron), reaction with the salt can transform the refractory yttrium silicon oxynitride grain boundary phases at the surface to a viscous (Na, K, Mg, Ca, Y, Si, O, N) glass.

Longer exposures result in surface roughening, which is associated with small variations in the corrosion rate of the NT154 silicon nitride and large variations in the distribution of the viscous silicate scale, which flows under the influence of impinging high-velocity combustion gases. Flow induced roughening of the surface of specimens exposed at 982C is shown in Figure 5. Despite the size and thickness of the silicate deposits, there was no obvious correlation between deposit thickness and the fracture origin. This result is attributable to the high level of gas porosity within the silicate scale, which reduces its strength and effectiveness as a stress raiser.

Surface recession was minimal (less than 25 microns) during exposure to 1 atmosphere burner rig hot corrosion at or below 982C. Above this temperature, surface recession was more rapid and may be life limiting. Surface recession (thickness loss) rates were approximately linear with time. Recession rate as a function of temperature are illustrated in Figure 6. Corrosion penetration is sufficiently rapid above 1000C to be life limiting for thin-walled (e.g., 625 microns [0.025 inch] thick) components.

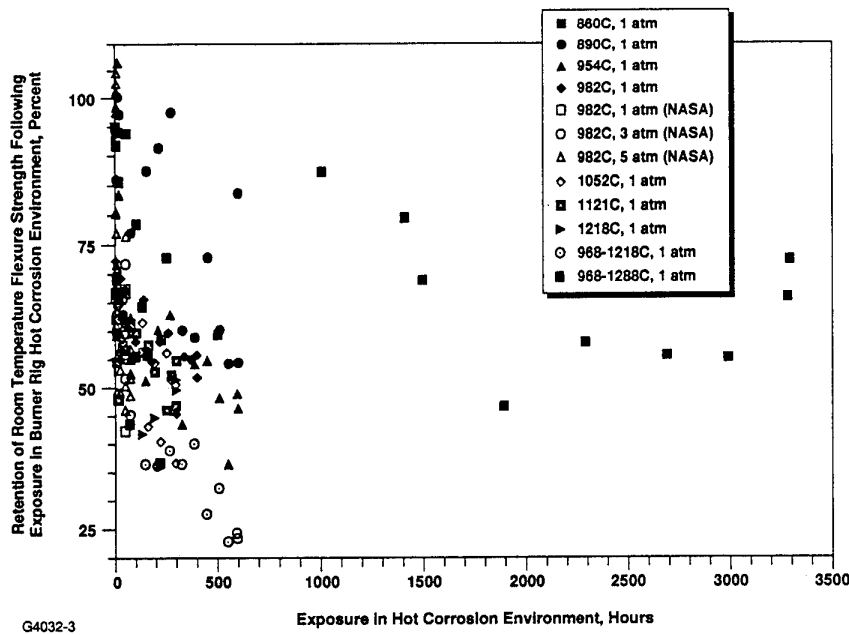


**Figure 3. Exposure to a Hot Corrosion Environment Reduced the Surface Strength of NT154 Silicon Nitride.**

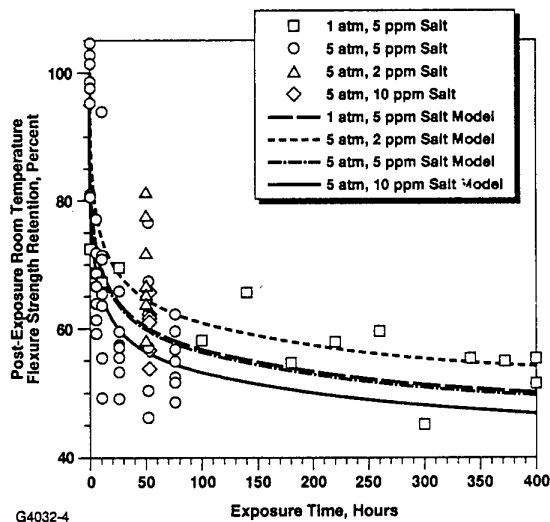
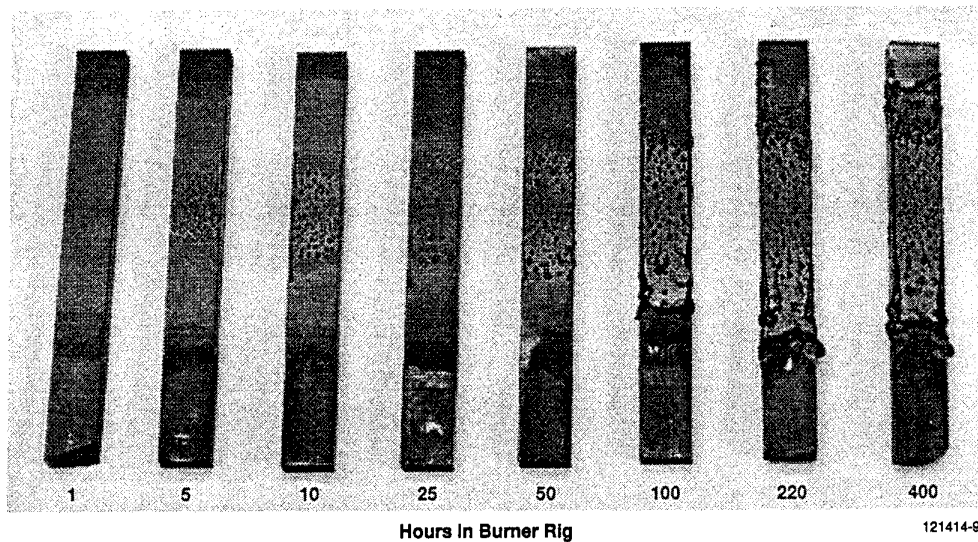


**Figure 4. Surface Strength Reduction is Sensitive to Exposure Time and the Severity of the Corrosive 982C Burner Rig Environment.**

Calculated dew points for the evaporation of sodium sulfate are approximately 950 and 1030C, respectively, for the 1 and 5 atmosphere test conditions used in this investigation. Consequently, a narrow temperature range for hot corrosion was initially expected. However, corrosive sodium rich silicate scales were unexpectedly present in the hot zones of specimens exposed 1050 and 1121C in the 1 atmosphere burner rig. Inspection of the specimens exposed in the 1218C test indicated that the actual dew point for a sodium-free surface was near 1200C at 1 atmosphere. In a series of short (2 hour) 5 atmosphere burner rig tests conducted with 5 ppm sea salt, the dew point was near 1290C. Reasons for the unexpectedly high dew point for sodium deposits are under investigation.

Multi-temperature 1 atmosphere hot corrosion exposure conditions (tests 8 and 9 in Table 1) more closely simulate idle and max power conditions anticipated for advanced gas turbines. In the multi-temperature tests, salt deposition occurred when the specimen was held at 968C for 3 minutes. Glassy silicates and severe surface recession were observed in the test with a 1218C maximum temperature. In contrast, exposure in the cycle



- 982C (1800F) Mach 0.3, 1 atm Burner Rig
- 5 ppm Sea Salt in Combustion Air
- Jet A Fuel
- Cycle: 27 min Hot + min Forced Air Cool

G4032-5

**Figure 5. Glassy Silicate Layer Roughened the Surface of NT154 Specimens During Exposure to 982C Burner Rig Hot Corrosion Environment.**

with a higher maximum temperature (1288C) promoted sodium-salt evaporation and inhibited formation of sodium silicate.

Surface recession ceased when the maximum test temperature inhibited sodium-salt deposition. A thin layer rich in magnesia, calcia, and silica was present on the hot zone surface of specimens exposed in tests 7 and 9 (Table 1). Reaction between the silica rich surface of NT154 and deposited Ca and Mg oxides roughened the interface. Small pits (about 25 microns deep), which containing trace amounts of sodium oxide, were observed on the fracture surfaces of a few specimens.

#### 4.3 Erosion

Engine tested NT154 silicon nitride exhibited superior resistance to sand erosion. As illustrated in Figure 7, ceramic vanes exhibited negligible damage in this erosion test. In contrast, all of the nickel-base superalloy vanes exhibited severe erosion of trailing edges. Based on these test results, particulate erosion will not be a significant damage mode for silicon nitride airfoils.

### 5 Life Prediction

While oxidation and hot corrosion from ingested sea salt attack silicon nitride substantially less than the superalloys being replaced in initial engine applications, this mode of degradation has the potential to limit component lives in advanced engine applications. Hot corrosion adversely affects the strength of silicon nitride in the 850 to 1300C range. Since unacceptable reductions in strength must be rapidly identified and avoided, we have pursued the development of an environmental life prediction model for silicon nitride turbine components. The following paragraphs provide a summary of model development.

The approach to modeling is similar to that used for predicting environmental lives of turbine airfoil coatings [7]. Overall, the rate of environmental (hot corrosion) degradation is modeled as the product of the severity of the environment (salt deposition times salt corrosiveness [basicity]) times stress dependent degradation mechanism (surface strength reduction and thickness loss in-

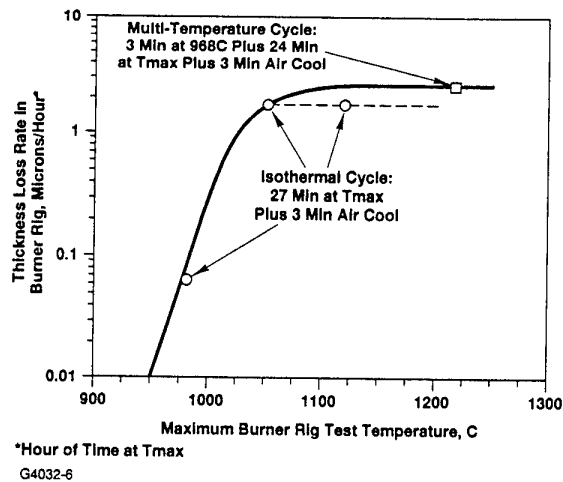
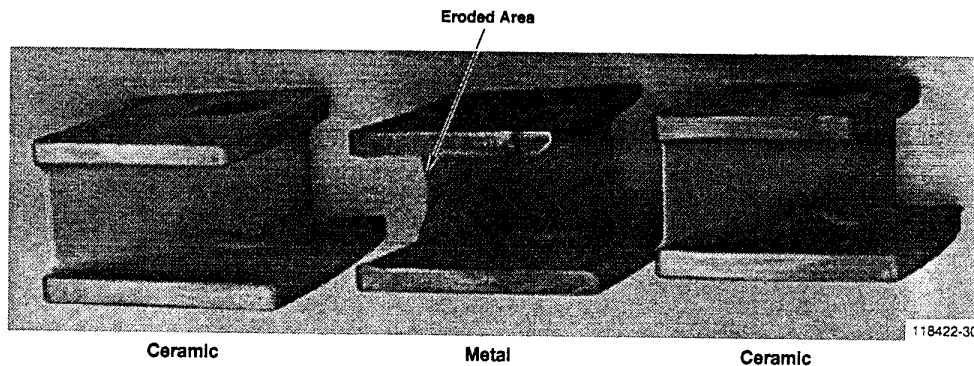


**Figure 6. Surface Recession Rates Were High in NT154 Flexure Specimens Exposed to Hot Corrosion at Temperatures Above 982C.**



- 6 Metal Nozzles and 17 Ceramic Nozzles
- 9 Hours at Maximum Power
- 0.34 kg/hr AC Coarse Silica Injected into Combustor
- No Power Loss
- All Ceramic Nozzles Showed No Wear
- All Metal Nozzles Showed Wear

G4032-7

**Figure 7. Erosion Testing Demonstrated Superior Ceramic Capability.**

duced rupture) functions. Operative temperature ranges for the degradation modes are illustrated in Figure 8.

In order to be a useful design tool, the environmental life prediction model has been formulated to utilize parameters recognized by those designing and operating the engine. Therefore, the model predicts the time for

surface strength retention as functions of engine design (stress, temperature, pressure, fuel/air ratio, gas velocity, and inlet air filtration), mission usage (fuel sulfur content, location [salt in air], and times at duty cycle power points), and material parameters. Effects of design stress and inlet air filtration on the predicted life of NT154 silicon nitride components in a 10 atmosphere turbine

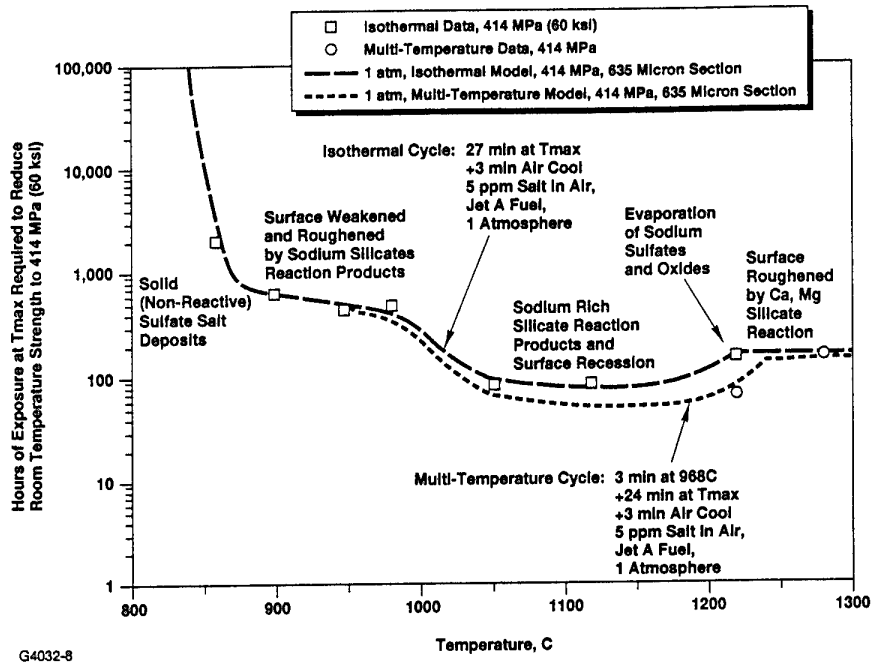


**Figure 8. A Mechanistic Model Predicts the Environmental (Strength Retention) Life of NT154 Silicon Nitride.**

operating at a coastal location are indicated in Figure 9 and Figure 10 illustrate the current capabilities of the model. These preliminary results indicate a need for protective (salt resistant) coatings to facilitate use of silicon nitride turbine components in high temperature, corrosive combustion environments.

#### **Conclusions**

- Silicon nitride has superior resistance to sand erosion in a gas turbine environment.
- Oxidation of NT154 in the 1000 to 1400C range is very slow and significantly increases room temperature flexure strength.
- Hot corrosion attack significantly reduces the strength of NT154 silicon nitride in the 850 to 1300C range.
- A mechanistic model was developed to predict the strength retention life of silicon nitride turbine components.
- The predicted environmental life of a component is dependent on engine design (stress, temperature, pressure, fuel/air ratio, gas velocity, air filtration efficiency), mission usage (fuel[sulfur content], location[salt in air], time at duty cycle power points), and material system parameters.

Pressure at Max Power: 10 atm  
 Time at Max Power: 90%  
 Pressure at Idle: 5 atm  
 Time at Idle: 10%  
 Idle Temp = Max Power Temp <900C  
 Idle Temp = 900C for Max Power Temp >900C

Fuel: Jet A (0.035% S)  
 Fuel/Air: 0.02  
 Gas Velocity: 850 ft/sec  
 Location: Coast  
 Altitude: Sea Level  
 Air Filtration: None

Section Thickness: 0.025 Inch

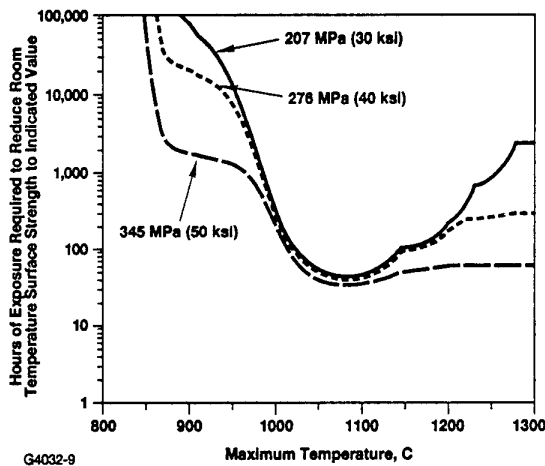


**Figure 9. Predicted Environmental Lives of NT154 Silicon Nitride Components are Dependent on Design Stress and Temperature.**

Pressure at Max Power: 10 atm  
 Time at Max Power: 90%  
 Pressure at Idle: 5 atm  
 Time at Idle: 10%  
 Idle Temp = Max Power Temp <900C  
 Idle Temp = 900C for Max Power Temp >900C

Fuel: Jet A (0.035% S)  
 Fuel/Air: 0.02  
 Gas Velocity: 850 ft/sec  
 Location: Coast  
 Altitude: Sea Level

Section Thickness: 0.025 Inch

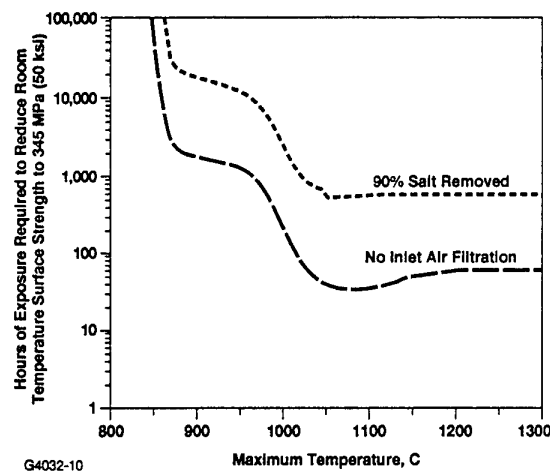


**Figure 10. Air Filtration Increases Predicted Environmental Lives of NT154 Silicon Nitride Components.**

## REFERENCES

- Jacobson, N.S., "Sodium sulfate: deposition and dissolution of silica," *Oxidation of Metals*, 31 [1-2] 91-103 (1989).
- Jacobson, N.S., "Corrosion of silicon-based ceramics in combustion environments," *J. Am. ceram. Soc.*, 76 [1] 3-28 (1993).
- Fox, D.S. and Smialek, J.L., "Burner rig hot corrosion of silicon carbide and silicon nitride," *J. Am. Ceram. Soc.*, 73 [2] 303-11 (1990).
- Jacobson, N.S., Stearns, C.A., and Smialek, J.L., "Burner rig hot corrosion of SiC at 1000C," *Adv. Ceramic Materials*, 1 [2] 154-161 (1986).
- Cuccio, J.S., et al., "Life Prediction Methodology for Ceramic Components of Advanced Heat Engines - Final Report," Department of Energy Contract 86X-SC674C, submitted for publication in 1993.
- Lindberg, L.J., "Cyclic oxidation of advanced silicon nitrides," pp. 79-86 in *Proceedings of the Annual Automotive Technology Development Contractors' Coordination Meeting* (Dearborn, Michigan), published by Society of Automotive Engineers, Warrendale, PA, 1991.
- Strangman, T.E., "Turbine coating life prediction model," pp. II-35 to II-43 in *Proceedings of the 1990 Coatings for Advanced Heat Engines Workshop* (Castine, Maine), U.S. Department of Energy Publication CONF-9008151, 1990.



## TESTING CONSIDERATIONS FOR MILITARY AIRCRAFT ENGINES IN CORROSIVE ENVIRONMENTS (A NAVY PERSPECTIVE)

Frank T. Carroll and Deborah R. Parish  
Naval Air Warfare Center Aircraft Division  
P.O. Box 7176  
Trenton, New Jersey 08628-0176  
USA

### ABSTRACT

This paper describes the considerations given to the testing of aircraft engines intended for use by the United States military (primarily the Navy) in potentially corrosive environments. The origins and intent of the Navy's full-scale corrosion susceptibility test are explored, and the evolution of the test from its early form to the present 1,200-hour program is described in detail. Sample results illustrating the effectiveness of the current test procedure are presented. Also noted are the activities currently underway to improve the test's effectiveness in the face of advancing engine and test equipment technologies.

### INTRODUCTION

The maritime environment in which the U.S. Navy operates its aircraft exposes these machines to some of the harshest corrosive conditions possible. Because of this extreme operational environment, the Navy subjects each of its new aircraft engine types to a rigorous test program intended to evaluate the engine's resistance to corrosion. Throughout its use the Navy's full-scale corrosion susceptibility test has been successful in identifying engine hardware which is not adequately protected against the corrosive effects of a maritime environment.

The corrosion susceptibility test has been utilized for over thirty years and has undergone a number of evolutionary changes throughout this period. Although the test has remained in its present form since the mid-1970's, it is currently being modified to reflect changes both in engine technology and in the manner in which contemporary engines are operated. These changes include longer engine service lives, new engine materials such as carbon composites, and mission profiles which subject modern engines to unprecedented operating temperatures and pressures.

### CAUSES AND EFFECTS OF CORROSION

Several forms of corrosion can be experienced by a gas turbine engine operating in a maritime environment. The major forms are cold corrosion, hot-salt stress corrosion cracking, and hot corrosion, or, more specifically, sulfidation. Cold corrosion attack takes the form of fretting or pitting. This corrosion occurs at lower temperatures (less than 550°F

(290°C)) so it is typically seen in areas such as the inlet or the gearbox housing. During maritime operations, water droplets containing sea salts impinge and deposit on these relatively cool engine surfaces. Once deposited, the chlorides within the salt react in the presence of oxygen to generate corrosion.

Hot-salt stress corrosion cracking (SCC) is the result of a combination of stress and temperature within an environment containing high levels of chloride salts. It is characterized by the formation of small intergranular cracks, which may be self limiting, and little material loss or general corrosion. Titanium parts are particularly prone to this form of corrosion which occurs at a minimum temperature of 550°F to 600°F (290°C to 315°C) (ref 1).

The third important type of corrosion is sulfidation, commonly called hot corrosion. Sulfidation can occur in the combustor and turbine where sulfur-laden combustion products have entered the airstream. The sulfur products of the fuel in combination with the sodium from the salt air form a corrosive ash of sodium sulfate. The sulfur then may react with the powerplant materials to form a sulfide scale. These sulfide scales are typically more likely to crack and spall than oxide scales, making sulfidation a particularly destructive form of corrosion (ref 1). Sulfidation is temperature dependent and most readily occurs at temperatures of 1300°F to 1700°F (705°C to 925°C) (ref 2).

Without adequate protection from the noted types of corrosion, a gas turbine engine can be adversely affected in a number of ways. The most potentially serious corrosion-related problem is the structural degradation of corroded engine hardware. Such hardware can fail catastrophically from mechanisms such as stress corrosion fractures and structural fatigue induced by corrosion pitting. The ensuing engine damage can, in the worst case, result in the loss of the aircraft and aircrew.

Corrosion can also decrease engine performance, and therefore mission capability by increasing the roughness of compressor airfoils, altering the shape of turbine blades, and degrading flow-path seals and coatings. Additionally, corrosion can adversely affect engine maintainability by causing difficulties in the disassembly process, and by necessitating the premature replacement of engine hardware due to corrosion or disassembly damage.

In order to prevent corrosion damage, various forms of protection are used on Navy engines. Base materials may be chosen for their corrosion resistance. In addition, protective coatings are used on many components. Some of these coatings contain aluminum and/or chromium. Others are ceramic thermal barrier coatings. A third method of minimizing corrosion potential is the use of an inlet particle separator (IPS), used in turboshaft configurations. The IPS serves to extract particles, including sea spray, from the air entering the engine. While the IPS cannot totally eliminate the salts entering the engine, it does help reduce the levels during low altitude hovers over the ocean. No matter how corrosion protection is achieved, each new system must be tested in conditions similar to those that will be seen in fleet service in order to demonstrate effective marinization.

## BACKGROUND OF CORROSION SUSCEPTIBILITY TESTING

The U.S. Navy initiated corrosion susceptibility testing in the mid-1960's. This action was taken in response to the adverse impact which corrosion was having on the service lives of gas turbine aircraft engines operated by the fleet. Rather than remaining operable to the life limit, fleet engines were being retired prematurely due to the effects of corrosion. Additionally, the Navy was expending millions of labor-hours annually on aircraft corrosion control during this period.

The initial specification corrosion susceptibility test was relatively simple. Salt was sprayed into an engine motoring at 300 to 500 RPM. Once the engine interior was thoroughly wetted (as evidenced by the appearance of salt mist out of the tailpipe), the engine was stopped and its inlet and exhaust pipe were plugged. The engine was allowed to sit in this condition for one week, after which it was started and accelerated to intermediate power. The entire process was then repeated. Following the second week of testing, the engine was disassembled and any signs of corrosion were noted.

While the original test was useful in revealing engine hardware susceptible to cold corrosion, potential hot corrosion was completely ignored. At the time the program was being developed, engine operating temperatures were rising into the regime where sulfidation in the turbine section was becoming an increasingly significant factor. Because the original test contained no engine operation, the effects of high temperatures, high pressures, and the presence of combustion products were not accounted for. This led to the modification of the original program into a full-scale test containing significant periods of engine operation. This transition occurred in the late 1960's and early 1970's.

## INITIATION OF FULL-SCALE TESTING

From its initial inception to the present, the objective of the full-scale corrosion susceptibility test has been to expose the test article to a humid environment containing a significant concentration of airborne salt. This objective was initially accomplished by exposing the first test articles (T64 and T58 turboshaft engines) to a natural maritime environment. Specifically, these engines were each operated for 150 hours

on open-air test rigs located adjacent to the ocean at Key West Naval Air Station, Florida.

Although each test article exhibited corrosion at the end of the Key West programs, the extent of the corrosion was far less than that normally occurring after the engine types' normal service lives. Additionally, the open-air test methodology did not allow any direct control of the environmental factors which influence the rate and severity of corrosion (i.e., airborne salt concentration and ambient temperature and humidity). This flaw was the most evident in the wide range of ambient airborne salt concentration levels measured throughout the three open-air programs (1.6 to 27.5 parts per billion (ppb)) (ref 3).

At the time the open-air tests were being conducted, the Navy was also pursuing a means of performing corrosion testing indoors under controlled conditions. The goal of this exercise was to develop a program which would expose the test article to a consistent, predetermined set of environmental conditions representative of a lifetime exposure to a maritime environment. The resulting program would subsequently serve as a means of assigning the engine manufacturer accountability for providing a product with sufficient corrosion resistance for use in the Navy's operational environment.

In developing the full-scale corrosion susceptibility test, considerable effort was expended in defining the key factors which drive the rate of corrosion within a gas turbine engine.

These factors consist of the operating environment (i.e., airborne salt concentration, humidity, and temperature), the time of exposure, and the engine operating cycle.

The Navy's initial attempt at conducting a full-scale corrosion susceptibility test under controlled indoor conditions took place in 1972 using a J79 turbojet engine. The process used in defining the specific test conditions and methodologies for the test program is noteworthy since the current version of the test is based heavily on this benchmark effort.

The issue of the airborne salt concentration level in a maritime environment was explored extensively throughout the 1950's and 1960's. Studies conducted during this period indicate that the airborne salt concentration above the ocean varies greatly with the weather condition, sea state, altitude above the water, and geographic location. A summary of the salt concentration levels reported by these studies is contained in Table I.

The Navy chose to use the results of a 1966 study by the Navy's Aeronautical Engine Division (NAWC AD, Trenton's predecessor) as the guideline in establishing the salt concentration levels for the initial J79 test. This exercise reported an airborne salt concentration level of 200 ppb twenty feet above the Atlantic Ocean as measured from a hovering UH-1A helicopter. The study also noted a concentration of 27 ppb at ground level under calm conditions adjacent to the ocean at Key West, Florida.

The intent of the initial J79 effort was to expose the engine to both a worst-case salt concentration level (i.e., that of a helicopter hovering over the ocean at low altitude) as well as a lower level more representative of the exposure which the

Location	Type of Study	Salt Concentration	Remarks
Key West, Florida	AED during engine test	10 ppb average 27 ppb maximum	protected, no surf beach
Atlantic City, New Jersey	NAVSEC study	70 ppb	over ocean (?) 100 yards from surf
Guantanamo Bay, Cuba	NAVSEC study on USS America	70 ppb	50 feet above water
Mediterranean Sea	NAVSEC study on USS Davis	120-780 ppb	
Cape Horn, South America	NAVSEC study on USS Glennon	500 ppb	
New Jersey coast	AED using a UH-1A helicopter	200 ppb	hover 20 feet above ocean surface
Patuxent River, Maryland (Chesapeake Bay)		400 ppb	2-7 feet above water

**Table I**  
**Atmospheric Salt Concentration Levels**

engine would experience over the majority of its service life. Therefore, twenty-five percent of the initial test was conducted using an airborne salt concentration of 200 ppb, with the remainder being completed at a lower concentration of 27 ppb. The exposure was accomplished by injecting atomized salt-water solution into the engine inlet airstream while the engine was operating. The salt-water solution was a man-made product prepared using the existing American Society for Testing and Materials specification for substitute ocean water (ASTM D1141-52) as a guideline.

The engine run cycle (throttle sequence) and the length of the initial J79 test were taken directly from the Navy's 150-hour mission qualification test (MQT) for turbojet engines (the precursor to today's mission endurance tests). The existing MQT cycle was initially employed rather than creating a new cycle unique to the corrosion test for several reasons. First, the cycle subjected the engine to a relatively high number of throttle transients. Such transients are necessary to ensure that the engine stall margin remains satisfactory as the test progresses. Additionally, the MQT cycle incorporated enough high-temperature operation to uncover potential hot-section sulfidation, and was of sufficient duration to permit an evaluation of the long-term effects of salt deposits within the engine. Another advantage of employing the MQT cycle was that it permitted a direct comparison of engine performance with and without the effects of salt-laden air, since the MQT test was conducted as part of the normal engine qualification process.

In addition to the 150 hours of engine operation, the initial J79 test subjected the engine to approximately 75 total hours of exposure to a salt-laden airstream while the engine was not being operated. The intent of this phase of the program, designated the dynamic soak, was to expose the engine's exterior surfaces and forward internal flow-path to an environment conducive to cold corrosion. Since the mechanisms of cold corrosion are always active in a maritime environment (even while the aircraft is parked on the ground),

the ambient ground-level salt concentration of 27 ppb was utilized for this phase of testing.

At the conclusion of the test, the engine exhibited significantly less corrosion than high-time J79 engines from the fleet (ref 4). Since the intent of the program was to simulate an equivalent lifetime exposure to a maritime environment, the test conditions and procedures were modified to increase the severity of the exposure. The test was then repeated. The major departure from the initial effort was the use of the worst-case airborne salt concentration level of 200 ppb throughout the entire engine operating and dynamic soak phases. Additionally, the total duration of the dynamic soak period was increased to provide a one-to-one ratio with the total engine operating phase interval.

Another departure from the first effort was the addition of an eight-hour static soak following each six hours of engine operation and dynamic soak. The static soak functioned as an incubation period allowing the salt deposited during the previous phases to act as an accelerated corrosive mechanism in the presence of high ambient temperature and humidity (110°F (43°C) and 95 percent).

At the conclusion of the second test, the condition of the test article was comparable to that of a high-time (1150-hour) J79 engine in terms of corrosive attack (ref 4). These results were of great significance in demonstrating the need to expose the test article to an artificially harsh set of conditions in order to simulate a lifetime of exposure to a maritime environment over a relatively short period of testing.

Using the J79 program as a guideline, additional full-scale corrosion susceptibility tests were conducted on T58, T400, and T700 turboshaft engines. The results of these efforts also correlated well with high-time fleet engines. As experience with the test was gained, the program eventually became accepted as the benchmark by which the Navy judged the

corrosion resistance of each new engine type.

## EVOLUTION OF THE CORROSION SUSCEPTIBILITY TEST

As noted previously, the full-scale corrosion susceptibility test has undergone a series of evolutionary changes throughout its use. One significant modification was the imposition of minimum humidity and temperature levels (73 percent and 50°F (10°C)) during the engine operating and dynamic soak phases. These minimums were enacted to prevent recrystallization of the salt particles suspended within the water droplets in the inlet airstream. Such recrystallization is undesirable since the dry crystals will not adhere to the cool surfaces of the engine, thereby reducing the salt exposure of the engine cold section.

Another significant milestone in the test's evolution was the eventual increase of the dynamic and static soak durations to accommodate the relatively slow propagation rate of cold corrosion. The ratio of the total dynamic soak to engine operating phase exposure was increased to 7:3, while the ratio of total static soak to engine operating phase time was increased to 4:1. Since the primary intent of the two soaks is to induce cold corrosion, this modification represented an effective increase in the ratio of cold corrosion to hot corrosion test time.

As the full-scale test was refined based on the results of each subsequent program, further changes were introduced to improve the test's effectiveness. The engine cycle was modified to include a two-hour shutdown halfway through each six-hour period of engine operation. This change served to increase the number of engine starts and shutdowns throughout the program. The interruption also functioned as a prescribed interval for the normal daily maintenance of the test cell and engine. A further increase in the number of engine starts and shutdowns was eventually achieved by halving the duration of each test phase while keeping the total duration of the program constant (i.e., by doubling the number of individual cycles while halving their durations).

The engine throttle sequence was further modified by replacing the intervals of engine operation at lower power settings with a prolonged dwell at ninety percent of intermediate power. This modification ensured sufficient operational time at the high turbine section temperatures conducive to hot corrosion. Additionally, a ten-minute interval was added at the conclusion of every second engine operating phase to allow evaluation of the engine's relative performance level without the necessity of a separate calibration.

## THE CURRENT TEST PROGRAM

Each of the previously noted evolutionary changes are reflected in the contemporary version of the full-scale corrosion susceptibility test. The test is currently performed as a series of twenty-five cycles, each 48 hours in duration. The first half of the cycle (24 hours) consists of the following four phases:

- Phase 1: 3 hr. engine operation (with salt flow)
- Phase 2: 2 hr. ambient static soak (no salt flow)
- Phase 3: 7 hr. dynamic soak (with salt flow)
- Phase 4: 12 hr. hot/humid static soak (no salt flow)

This sequence is repeated in phases five through eight of the subsequent half-cycle. The two half-cycles are identical with the exception of the engine operating phases.

Figures 1 and 2 detail the throttle sequences utilized for the two engine operating phases. The differences which exist between the phases are related to the origin of the throttle sequence (i.e., the six-hour MQT cycle). As previously noted, the original six-hour MQT engine run was halved in order to expose the test article to an extra shut-down and start sequence. Phase one therefore reflects the first half of the MQT cycle, and phase five the following portion.

The current program's total test hours equate to 1,200, with the following breakdown among the individual phases:

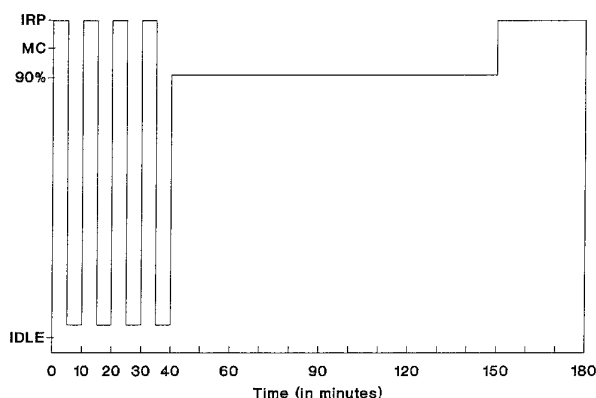


Figure 1  
Throttle Sequence for Phase 1

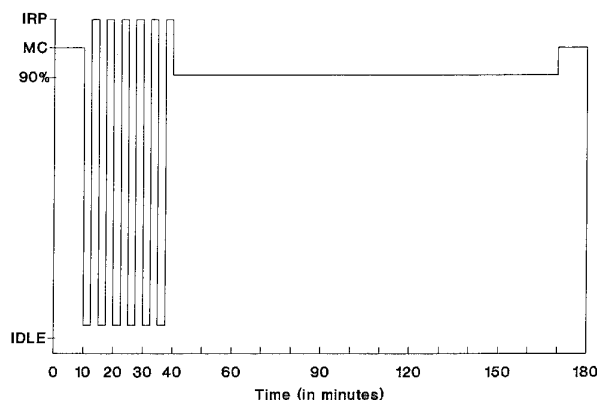


Figure 2  
Throttle Sequence for Phase 5

Engine operating phase	150 hr.
Ambient static soak	100 hr.
Dynamic soak	350 hr.
Hot/humid static soak	600 hr.

Throughout the engine operating and dynamic soak phases, the airborne salt concentration level in the inlet airflow is maintained at 200 ppb. The minimum humidity and temperature of the inlet air are maintained at the 73 percent and 50°F (10°C) levels noted previously. The total pressure of the inlet air and the test cell environment remains at ambient levels (i.e., approximately sea-level) throughout the entire test cycle.

During the static soaks, no air is directed into or out of the test cell, and no additional salt is introduced into the test environment. In conducting the twelve-hour static soak, the ambient temperature and humidity are maintained at the 110°F (43°C) and 90 percent levels also noted previously. No environmental conditioning whatsoever is performed during the ambient soak (i.e., maintenance period).

Table II contains a listing of the atmospheric conditions of the current corrosion susceptibility test.

## SUCCESS CRITERIA

Prior to first corrosion cycle, a performance calibration is conducted at sea-level static, standard-day conditions to establish the baseline engine performance level. A post-test calibration is also performed at these conditions upon completion of the twenty-fifth cycle. Successful completion of the test requires that the non-recoverable loss in shaft horsepower (turbohaft engines) or thrust (turbojet/turbofan engines) not exceed five percent relative to the baseline level. A maximum deterioration allowance of five percent is also placed on specific fuel consumption relative to the baseline level. Additionally, the test article must retain its ability to operate transiently in accordance with the requirements of its respective model specification.

Successful completion of the test is also subject to the engine's physical appearance at the conclusion of the program. According to the Navy's general engine specification, all internal parts exposed to gas-path air shall exhibit no impairment in their function due to corrosion.

Minor corrosive attack is acceptable only when the part design criteria (e.g., fatigue resistance) are not affected. Corrosion-protected parts shall not exhibit any effects of corrosion upon cleaning and stripping of the protective scheme. The recoating of parts designed for recoating shall restore the parts to an as-new condition. All other parts shall exhibit no corrosion which affects component integrity or prescribed maintenance procedures. Compliance with these criteria are judged by Navy personnel during both dirty and clean layouts of the test article following post-test disassembly.

## TEST HARDWARE AND PROCEDURES

NAWC AD, Trenton has been the U.S. Navy's sole facility for conducting the full-scale corrosion susceptibility test from its inception. Much of the hardware used for the test is unique to a corrosion test installation. The installation includes an environmental housing, a steam heater, a dehumidifier, and a corrosion rig.

The corrosion susceptibility test is conducted as a free-stream installation (i.e., the engine inlet bellmouth is not connected directly to the facility inlet duct). This configuration allows the inlet airflow supplied during the dynamic soaks to exit the inlet duct and flow freely around the exterior of the engine. During the engine operating phases, sufficient facility airflow is directed at the engine inlet to ensure that the engine ingests conditioned inlet air only rather than ambient air entrained from the test cell environment.

Since the program is conducted under sea-level atmospheric conditions, one of the facility's two sea-level ram test cells is generally utilized in conducting the program. Each of these cells is connected to the facility blower wing, allowing the use of the Trenton's full inlet-air conditioning capability throughout the test. When conducting the test in the sea-level cells, an aluminum housing is utilized around the engine to confine the test environment to the immediate vicinity of the engine (figure 3). This feature is utilized to reduce the total test cell volume which must be maintained at the required environmental conditions. The housing also protects the test cell from the corrosive effects of the test environment.

Smaller engines may also be tested in one of Trenton's small engine altitude cells, which provide a better "fit" for these

<u>Phase</u>	<u>Duration</u>	<u>Engine Condition</u>	<u>Salt Concentration</u>	<u>Ambient Temperature</u>	<u>Ambient Humidity</u>
1 & 5 (engine run)	3 hours	operating	200 ppb	50°F min	73% min
2 & 6 (maintenance)	2 hours	not operating	0	atmospheric	atmospheric
3 & 7 (dynamic soak)	7 hours	not operating no rotation permitted	200 ppb	50°F min	73% min
4 & 8 (static soak)	12 hours	not operating	0	110 ± 10°F	90% min

Table II  
Atmospheric Requirements for the U.S. Navy Corrosion Test

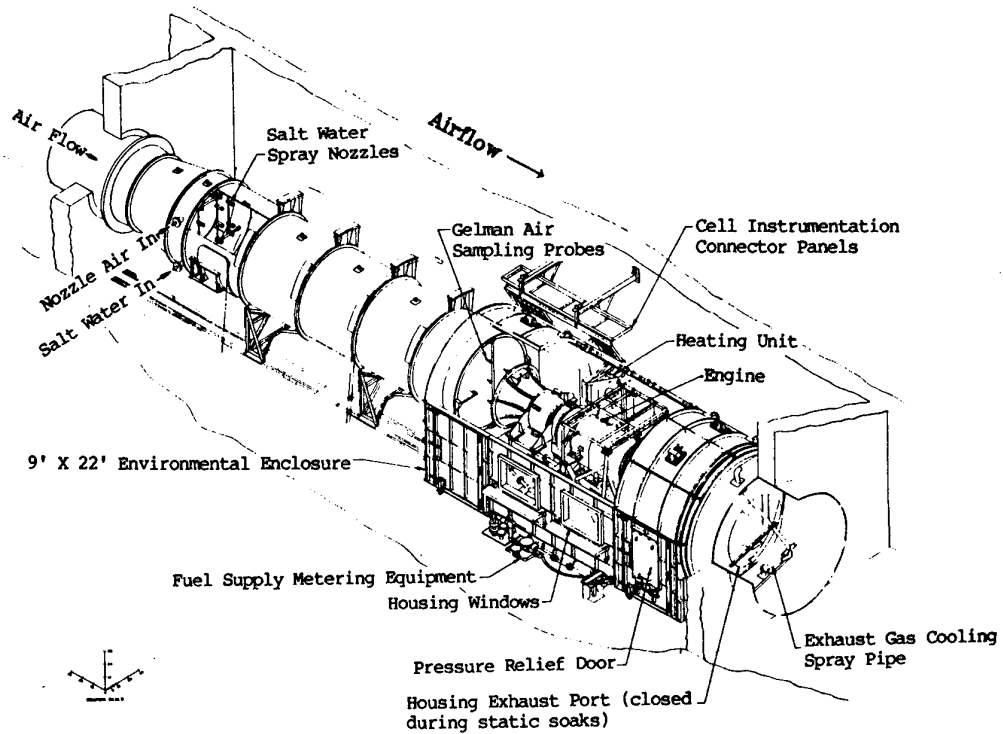


Figure 3  
Environmental Housing Installed in Test Cell

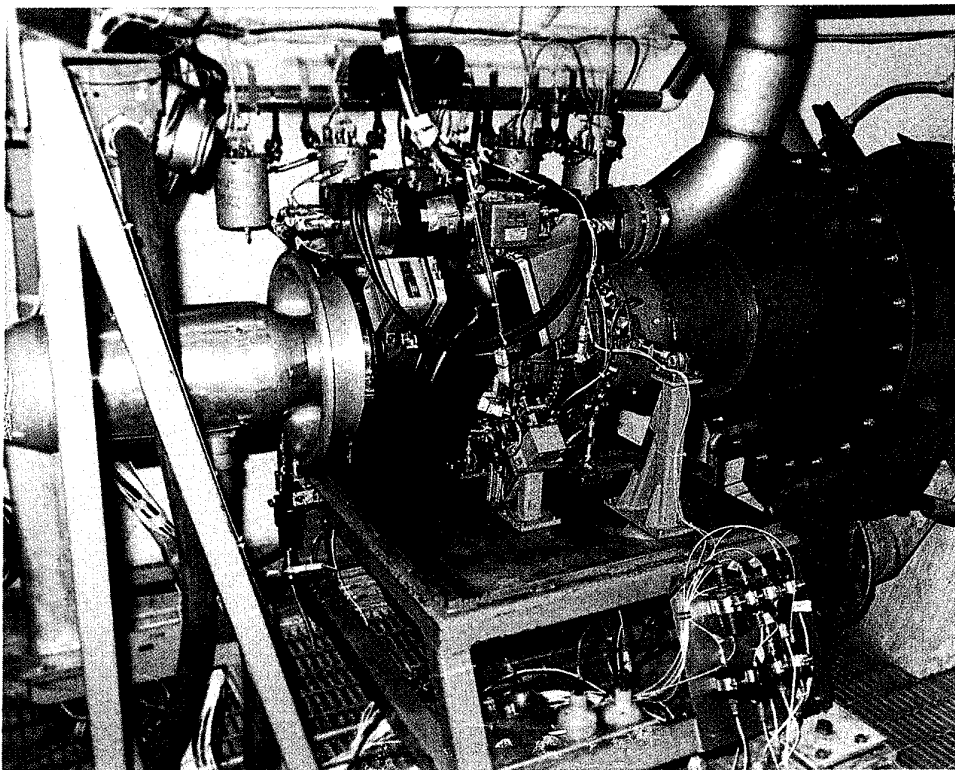


Figure 4  
Small Altitude Cell Installation

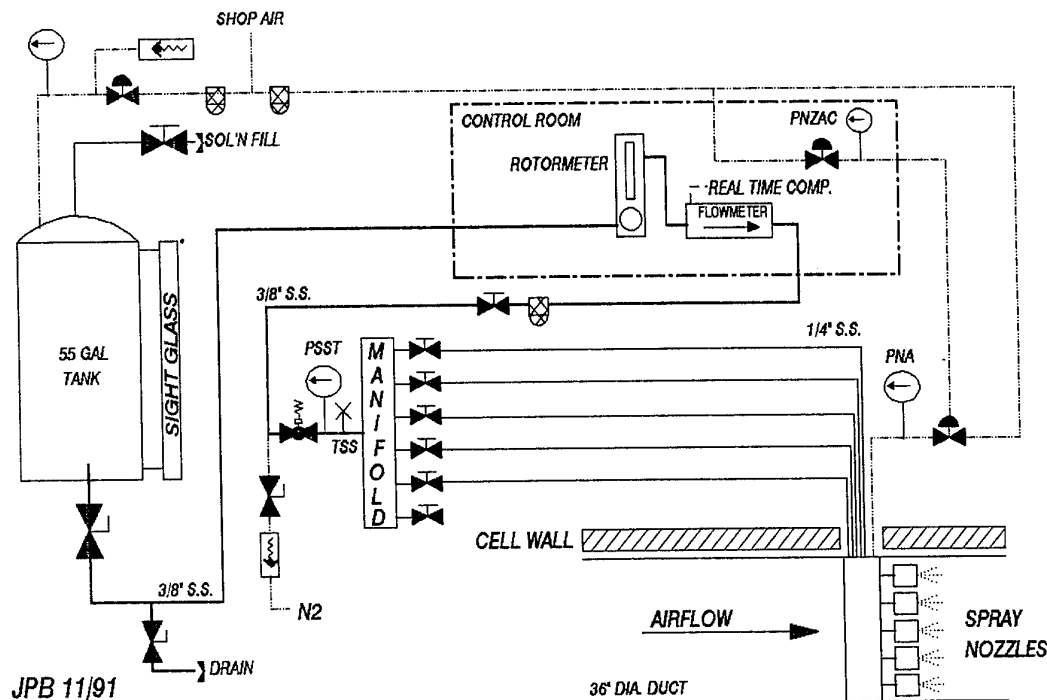


Figure 5  
Salt Spray System (As Installed in 4W Altitude Cell)

engines than the relatively large environmental housing (although care must be taken to ensure that any resulting corrosive damage to the cell is repaired following the test). Such an installation is illustrated in figure 4.

A steam heater is mounted inside the environmental housing (or the small engine altitude test cell) to maintain the cell temperature at the required level during the twelve-hour static soaks. Steam generated by the facility is routed directly into the environmental housing during these soaks to maintain the specified humidity level. A dew-point sensor installed within the enclosure is utilized to monitor the humidity level throughout the soak. Covers are installed over the cell inlet and exhaust throughout this period to further confine the soak environment to the immediate vicinity of the engine. The engine inlet and exhaust remain open throughout the entire test.

A dehumidifier is employed to minimize the effects of interruptions in the test cycle (e.g., normal weekend shut-downs). The unit removes moisture from the test cell and thereby inhibits corrosion during non-cycle time. Additionally, an engine wash is generally conducted prior to such interruptions to further discourage corrosion.

The Trenton corrosion rig contains the hardware necessary to introduce salt into the inlet airstream in the required amounts. The rig hardware includes spray nozzles, Gelman impactors, pressurized holding tanks for the synthetic sea water solution, and the tubing and manifolds necessary to route the solution between the holding tank and the spray nozzles. The system also includes a section of six-foot diameter inlet ducting containing accommodations for the spray nozzle manifolds. A schematic illustration of the salt spray system is presented

as figure 5.

Salt is introduced into the inlet airstream via atomizing spray nozzles located in the facility inlet duct (figure 6). Synthetic sea-water solution and high-pressure air are routed separately to each nozzle and ejected together to form atomized salt water droplets. The total number of nozzles utilized in a particular installation is proportional to the airflow rates established during the engine operating and dynamic soak phases of the program. As few as three nozzles may be utilized during the testing of small turboshaft engines, while larger turbofan engine installations can require the use of up to ten nozzles. Each nozzle is equipped with a remotely

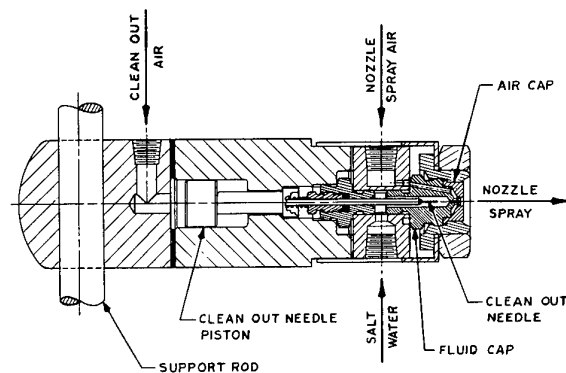
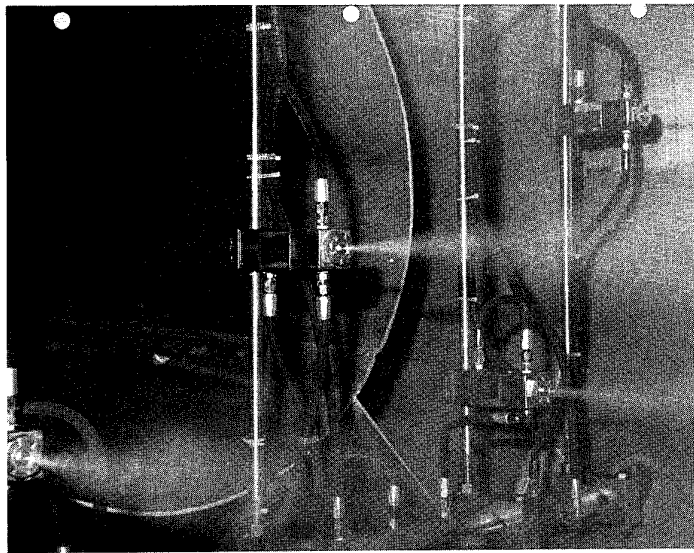


Figure 6  
Atomizing Spray Nozzle



**Figure 7**  
**Spray Nozzle Installation**

operated clean-out needle to remove salt deposits from the nozzle's internal passages during testing.

The spray nozzles are mounted on aluminum support bars arranged vertically within the inlet duct (figure 7). The bars are supported by an upper and a lower manifold mounted horizontally across the duct. High-pressure air is routed through the lower manifold, while synthetic salt water is directed through the lower unit. The air and water are routed individually from the manifolds to each nozzle via rubber tubing. Water flow-rate is set and monitored from the test cell control room using a rotameter, a variable-area flow meter.

Gelman impactors are utilized to measure the airborne salt concentration level directly upstream of the engine inlet. An

illustration of one of these units is contained in figure 8. Salt concentration measurement is accomplished by collecting salt from the airstream on a filter located within the impactor. Following the sampling period, the quantity of captured salt is measured using an atomic absorption spectrophotometer. The measured quantity is then correlated with an airborne salt concentration level based the impactor's capture area, the length of the sampling period, and the inlet air velocity.

Salt concentration levels are measured throughout the entire facility calibration process. During the actual test program, concentration measurements are acquired at the beginning of each dynamic soak to ensure that the calibration remains valid and the corrosion rig is operated in the proper manner and configuration. Salt concentration measurements are not acquired during the engine operating phase due to the non-feasibility of interrupting the engine run to retrieve the impactors after the relatively short sampling period. Additionally, the impactors would impose a foreign object damage (FOD) hazard on an operating engine, as well as create undesired distortion of the inlet airflow.

Prior to the installation of the test article, the corrosion rig is subjected to a calibration process which ensures that the engine is exposed to the required salt concentration level during the engine operating and dynamic soak phases. In conducting the calibration, several key factors are varied singly or in combination until the required airborne salt concentration level is produced uniformly across the engine inlet plane. These factors include the overall flow-rate of synthetic sea water to the nozzle spray rig, the individual water flow-rate to each nozzle, the concentration of the sea-water solution, the nozzle locations, and the total number of nozzles.

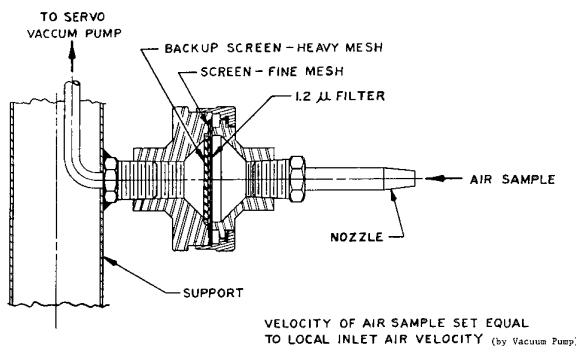


**Figure 8**  
**Schematic of a Gelman Impactor**



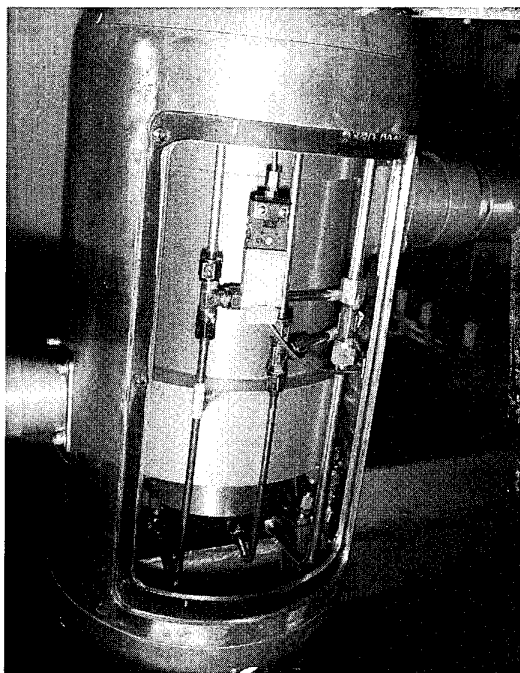


**Figure 9**  
**Waterbrake Installed in Protective Housing**

The installation of the engine and instrumentation for a corrosion test also requires some special consideration. Turboshaft engine installations require the use of a power absorber to dissipate the shaft power generated by the test article. Waterbrakes are generally utilized at Trenton for power absorption. Because of the harsh environment, a cover is used to protect the waterbrake while still providing access for maintenance. Figure 9 shows a waterbrake with its cover.

Engine and facility instrumentation is positioned away from the corrosive test environment, if possible. Instrumentation which must be installed in the cell requires some means of protection from the harsh environment. Such protection is generally accomplished by placing the instrumentation within a protective enclosure, if feasible. Electrical connectors are particularly susceptible to the effects of the corrosive test environment, and are generally protected by heavy amounts of sealant applied prior to the test.

#### **SAMPLE TEST RESULTS**

The full-scale corrosion susceptibility test has proven to be a very effective vehicle for identifying engine hardware with insufficient corrosion resistance for use in a maritime environment. As an example, the F110-GE-400 Corrosion Susceptibility Test (1986) uncovered several corrosion-prone areas which were subsequently modified prior to full-scale engine production (ref 5). Because these potential problems were identified relatively early, the time and cost penalties associated with modifying production hardware and retrofitting existing fleet engines were avoided. Additionally, the detection of these discrepancies prior to service introduction eliminated the risks posed by a potential engine failure to the fleet aircraft and aircrew.

Corrosion-prone hardware identified as a result of the F110

test included the blade-tip rub seals employed in the first three stages of the high-pressure compressor. Corrosion within the bond coating of the seals resulted in widespread delamination of the seals partway through the program (figure 10). The resulting loss of the seal material decreased engine performance by more than five percent and produced impact damage to over one hundred compressor airfoils. As a consequence of this finding, more corrosion resistant materials were employed in the manufacture of the seals and bond coating for production engines.

The F404-GE-400 Corrosion Susceptibility Test (1980) also demonstrated its effectiveness in identifying engine hardware with insufficient corrosion resistance for use in the Navy's operational environment (ref 6). Like the F110-GE-400, the test article experienced widespread corrosion-induced delamination of the compressor rub seals which resulted in unacceptable performance losses. Additionally, the engine's fan speed transmitter failed during testing due to corrosion on the sensing surface (figure 11). Several exterior surface areas susceptible to cold corrosion were also identified as a result of the program (e.g., fan inlet guide vanes, fan inlet centerbody).

The most recent corrosion tests have been on turboshaft engines. In 1987, the T700-GE-401C was tested as part of its qualification prior to a multi-service buy. The test followed the test plan as defined in the Navy specification. The engine passed the test marginally on performance (4.9 percent degradation in horsepower) and the test did reveal some potential corrosion problems in the turbine section (ref 2). The hot section corrosion problem is being addressed through the use of coatings, with the optimal one currently being defined.

In 1992, the T800-LHT-800 was tested for the U.S. Army. This test was the Army's first attempt at defining a corrosion



Figure 10  
F110-GE-400 Blade-tip Rub Seals

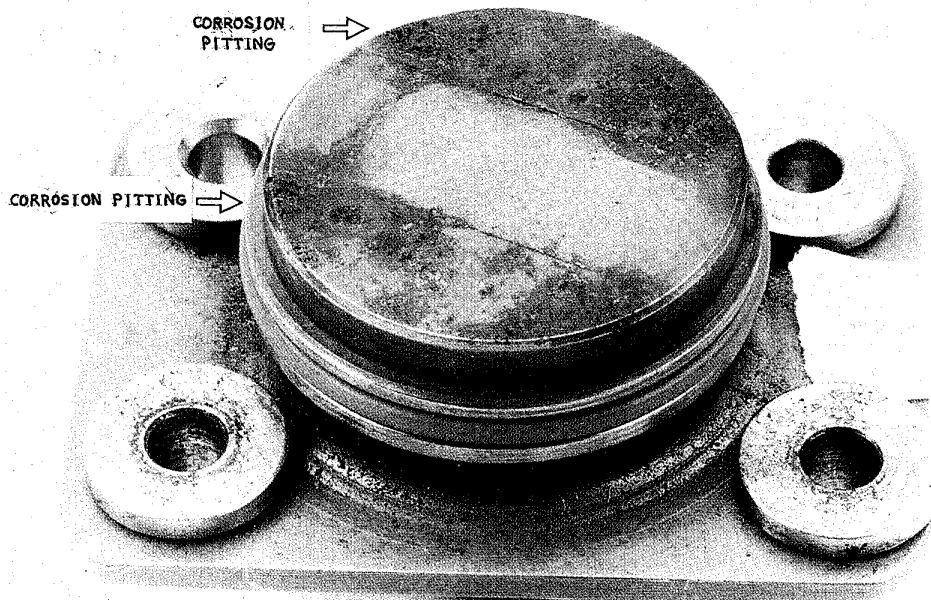


Figure 11  
F404-GE-400 Fan Speed Transmitter

Engine	Test Date	Test Length	Perf. Loss	Report	Remarks
J79-GE-8	Nov 68-Mar 69	150 hrs	9.5%	NAPTC LTR AEP22: MJD:fcf 13720 SerNo 513 of 11 MAR 69	MQT cycle. 27 and 200 ppb salt concentration.
J79-GE-8	Aug 69-Nov 69	102 hrs	6.1%	NAPTC-PE-5 of Feb 73	MQT cycle. Addition of 8 hr soaks.
T58-GE-10	Aug 70-Nov 70	150 hrs	5%	NAPTC-AED-1961 of Feb 72	
T58-GE-10	Apr 71-Jun 71	146.5 hrs	2%	NAPTC-AED-1976 of Sep 72	Engine failed at 146.5 hrs.
T400-CP-400	Jun 74-Nov 74	150 hrs	20%	NAPTC-PE-63 of Aug 75	Test results correlated with 2000 hour operation within 20 miles of sea.
YT700-GE-700	Apr 75-Jun 75	150 hrs	10%	NAPTC-PE-70 of Dec 75	
T400-CP-400/402	Nov 76-Feb 77	150 hrs	4.7%	NAPC-PE-5 of Dec 78	
T700-GE-401	Mar 79-Jun 79	108 hrs	9.5%		Test terminated because of high non-recoverable performance loss. Heavy corrosion in compressor diffuser.
F404-GE-400	Mar 80-Jun 80	150 hrs	8.0%	NAPC-PE-49 of Mar 81	
T700-GE-401	1982				
F110-GE-400	Mar 86-Nov 86	84 hrs	>5%	GE R87AEB409 of Jun 87	Test terminated due to non-corrosion related failure
T700-GE-401C	Oct 87-Feb 88	150 hrs	4.9%	NAPC-PE-192 of Apr 89	
T56-A-427	Apr 88-Aug 88			not published	Hot section test - no planned static soaks
T800-LHT-800	Apr 92-Jun 92	50 hrs - salt 100 hrs - no salt	2.0%	NAVAIRWARCEN ACDIVTRN-PE-254 of May 93	Army test cycle: Ten 57-hour cycles with only 50 hrs of engine operations in salt spray.

**Table III**  
**Summary of Trenton Corrosion Tests**

test that would more closely simulate their usage of an engine. The test contained a two-hour sand run prior to the beginning of corrosion testing. The salt portion of the test contained ten 57-hour cycles. This reduced the total test time to 570 hours versus the 1200 hours of the Navy test. A breakdown of the test time shows 50 hours of engine operation in a salt spray, 100 hours of "non-salt" engine operation, 40 hours of ambient soak, 140 hours of dynamic soak, and 240 hours of static soak, significantly less than the Navy test.

Over this duration, the engine showed little performance degradation (2.0 percent). However, there was severe corrosion on the output shaft retaining nut which precluded successful removal of the power turbine (ref 7). This problem is being corrected through a redesign.

A summary of the engine corrosion susceptibility tests conducted at NAWC AD, Trenton is shown in Table III.

## FUTURE TESTING CONSIDERATIONS

The evolution of the full-scale corrosion susceptibility test continues today in response to current advances in gas turbine engine technology. The next generation full-scale corrosion susceptibility test will be introduced this year in the new tri-service engine specification being released jointly by the U.S. Navy, Air Force, and Army.

A significant advancement in the next generation test is the use of a "missionized stair-step" throttle sequence. As noted previously, the current throttle sequence is based on the MQT cycle of the 1960's and represented a satisfactory starting point given the limited understanding of mission cycle modeling at the time.

The effects which different types of engine mission duty cycles impose on engine hardware are much better understood today than in the 1960's. Throttle cycles have been defined which can realistically subject an engine to the operational characteristics of its service environment given its projected application (e.g., fighter, low-level attack, search and rescue, etc.). These advancements have led to the incorporation of a missionized throttle cycle into the corrosion susceptibility test. The intent of the modification is to enhance the effectiveness of the program by more accurately simulating the projected operational environment of the test article during the engine operating phase.

A stair-step progression (a series of relatively short dwells at incrementally increasing or decreasing power settings) has also been added to the throttle sequence to reflect increases in the hot-section temperatures of contemporary engines. As noted earlier, the full-scale test was developed during the period in which turbine operating temperatures were reaching the minimum level conducive to sulfidation. Turbine operating temperatures within contemporary engines have exceeded this minimum level, and in most cases span the entire range in which sulfidation may occur. Additionally, operating temperatures have increased to the extent that potentially sulfidizing conditions may now exist in the cooler sections of most turbines at certain operating conditions. The stair-step progression has thus been incorporated into the throttle sequence to ensure that the turbine section is subjected to its entire range of operating temperatures during the test program.

The first application of a missionized throttle sequence will occur during the upcoming F119-PW-100 Corrosion Susceptibility Test. This program will also mark the first full-scale testing of a U.S. Air Force engine for corrosion susceptibility. The Air Force is initiating this testing in response to corrosion-related field problems with engines operated in maritime locations such as Okinawa, Japan.

The mission duty cycle of the U.S. Air Force's F-22 aircraft will subject the F119 engine to relatively high inlet temperatures. Because of this operational requirement, the F119 Corrosion Susceptibility Test will be conducted utilizing elevated inlet air temperatures during the engine operating phase of the program. Specifically, twenty to thirty percent of the test cycles will be conducted using each of the following inlet air temperatures: 60°, 90°, 120°, and 160°F (16°C, 32°C, 49°C, and 71°C). One particular engine

characteristic which has strongly driven this testing requirement is the utilization of carbon composites and high-strength titanium alloys in the F119. These materials are being used in high-temperature applications within the engine, and their behavior in a high-temperature, salt-laden operating environment has not yet been evaluated.

Salt measurement is the other facet of the test which will see refinement in the next ten years. The current process of using Gelman impactors to collect salt samples for off-line analysis has some major drawbacks. First, because it is an obtrusive system (ie, the Gelmans are installed in front of the engine inlet), samples are not taken during an engine run. The samples are only collected during the first portion of a dynamic soak. It is time consuming to install and remove the Gelmans and creates a disruption in the test cycle. It is also time consuming to conduct the atomic absorption spectrography. This results in delays in making any necessary adjustments to the salt concentration.

The uncertainty in the analysis is the other major drawback. Extreme care must be taken to avoid introducing any extraneous salt into the process. And, all measurements during the process must be precise. Because the process has so many sources for error, the uncertainty is high - currently quoted at  $\pm 20$  percent.

In order to eliminate the problems with the Gelmans, a new salt measurement system which employs laser technology is being developed under contract. This system should provide the ability to measure not only droplet salt concentration but also droplet size and velocity in-situ. The system is non-intrusive, so real time analysis of the airstream can be obtained during the engine runs as well as the dynamic soaks. And, because the system is self-contained, most of the sources of gross error in the salt analysis process are eliminated.

## SUMMARY

Since its introduction in response to widespread corrosion throughout the Navy's aircraft fleet, the full-scale corrosion susceptibility test has evolved from a simple period of oceanside engine operation into a sophisticated scientific exercise conducted under rigorously controlled conditions. The effectiveness of the program is reflected in the vast improvement in the corrosion resistance of contemporary fleet engines relative to their earlier counterparts. The test is currently being refined to accommodate advances in engine and test equipment technology, ensuring that the program will keep pace with the Navy's testing needs well into the next century.

## REFERENCES

1. Brasunas, A. de S. (editor), "Corrosion Basics An Introduction", Houston, Texas, USA, National Association of Corrosion Engineers, 1984 (ISBN 0-915567-02-4), p 118.
2. Parish, D. R., "T700-GE-401C Corrosion Susceptibility Test", NAPC-PE-192, April 1989.

3. Lynch,R.J., "Study of Sea Salt Concentration Requirement for MIL-E-5007D/8593A Corrosion Susceptibility Test (4.6.4.3)",NAPC:PE3:RJL:vmd ltr number 13700, August 1979.
4. Newhart,J.E. and Wagner,W.W., "Full Scale Corrosion Test of the J79-GE-8 Engine",NAPTC-PE-5, February 1973.
5. Dugas,P.E., "Corrosion Qualification Test for the F110-GE-400",GE R87AEB409, June 1987.
6. Cifone,A.J., "F404-GE-400 Engine Official Corrosion Susceptibility Test",NAPC-PE-49, March 1981.
7. Parish,D.R., "Corrosion Susceptibility Qualification Test for the T800-LHT-800 Engine",NAWCADTRN-PE-254, May 1993.

## REPORT DOCUMENTATION PAGE

<b>1. Recipient's Reference</b>	<b>2. Originator's Reference</b> AGARD-CP-558	<b>3. Further Reference</b> ISBN 92-836-0005-3	<b>4. Security Classification of Document</b> UNCLASSIFIED														
<b>5. Originator</b>	Advisory Group for Aerospace Research and Development North Atlantic Treaty Organization 7 rue Ancelle, 92200 Neuilly-sur-Seine, France																
<b>6. Title</b>	Erosion, Corrosion and Foreign Object Damage Effects in Gas Turbines																
<b>7. Presented at</b>	The Propulsion and Energetics Panel (PEP) Symposium held in Rotterdam, The Netherlands, 25-28 April 1994.																
<b>8. Author(s)/Editor(s)</b> Multiple	<b>9. Date</b> November 1994																
<b>10. Author's/Editor's Address</b> Multiple	<b>11. Pages</b> 354																
<b>12. Distribution Statement</b>	There are no restrictions on the distribution of this document. Information about the availability of this and other AGARD unclassified publications is given on the back cover.																
<b>13. Keywords/Descriptors</b>	<table><tr><td>Aircraft engines</td><td>Birds</td></tr><tr><td>Gas turbine engines</td><td>Dust</td></tr><tr><td>Aircraft maintenance</td><td>Ice</td></tr><tr><td>Damage</td><td>Sand</td></tr><tr><td>Corrosion</td><td>Coatings</td></tr><tr><td>Erosion</td><td>Repair</td></tr><tr><td>Foreign bodies</td><td>Deposition</td></tr></table>			Aircraft engines	Birds	Gas turbine engines	Dust	Aircraft maintenance	Ice	Damage	Sand	Corrosion	Coatings	Erosion	Repair	Foreign bodies	Deposition
Aircraft engines	Birds																
Gas turbine engines	Dust																
Aircraft maintenance	Ice																
Damage	Sand																
Corrosion	Coatings																
Erosion	Repair																
Foreign bodies	Deposition																
<b>14. Abstract</b>	<p>The Conference Proceedings contains 31 papers presented at the Propulsion and Energetics Panel Symposium on Erosion, Corrosion and Foreign Object Damage Effects in Gas Turbines which was held from 25-28th April 1994, in Rotterdam, The Netherlands. The Technical Evaluation Report and the Keynote Address are included at the beginning and discussions follow most papers.</p> <p>The Symposium was arranged in the following Sessions: Operational Experience and Requirements (7); Deposition and Erosion (7); Foreign Object Damage (5); Coatings, Repair and Materials Aspects — 1 (4); Coatings, Repair and Materials Aspects — 2 (7); Testing and Certification Procedures (1).</p>																

<p>AGARD-CP-558 Advisory Group for Aerospace Research and Development North Atlantic Treaty Organization EROSION, CORROSION AND FOREIGN OBJECT DAMAGE EFFECTS IN GAS TURBINES Published November 1994 354 pages</p> <p>The Conference Proceedings contains 31 papers presented at the Propulsion and Energetics Panel Symposium on Erosion, Corrosion and Foreign Object Damage Effects in Gas Turbines which was held from 25-28th April 1994, in Rotterdam, The Netherlands. The Technical Evaluation Report and the Keynote Address are included at the beginning and discussions follow most papers.</p>	<p>AGARD-CP-558</p> <p>Aircraft engines Gas turbine engines Aircraft maintenance Damage Corrosion Erosion Foreign bodies Birds Dust Ice Sand Coatings Repair Deposition</p>	<p>AGARD-CP-558 Advisory Group for Aerospace Research and Development North Atlantic Treaty Organization EROSION, CORROSION AND FOREIGN OBJECT DAMAGE EFFECTS IN GAS TURBINES Published November 1994 354 pages</p> <p>The Conference Proceedings contains 31 papers presented at the Propulsion and Energetics Panel Symposium on Erosion, Corrosion and Foreign Object Damage Effects in Gas Turbines which was held from 25-28th April 1994, in Rotterdam, The Netherlands. The Technical Evaluation Report and the Keynote Address are included at the beginning and discussions follow most papers.</p>	<p>AGARD-CP-558</p> <p>Aircraft engines Gas turbine engines Aircraft maintenance Damage Corrosion Erosion Foreign bodies Birds Dust Ice Sand Coatings Repair Deposition</p>
<p>AGARD-CP-558 Advisory Group for Aerospace Research and Development North Atlantic Treaty Organization EROSION, CORROSION AND FOREIGN OBJECT DAMAGE EFFECTS IN GAS TURBINES Published November 1994 354 pages</p> <p>The Conference Proceedings contains 31 papers presented at the Propulsion and Energetics Panel Symposium on Erosion, Corrosion and Foreign Object Damage Effects in Gas Turbines which was held from 25-28th April 1994, in Rotterdam, The Netherlands. The Technical Evaluation Report and the Keynote Address are included at the beginning and discussions follow most papers.</p>	<p>AGARD-CP-558</p> <p>Aircraft engines Gas turbine engines Aircraft maintenance Damage Corrosion Erosion Foreign bodies Birds Dust Ice Sand Coatings Repair Deposition</p>	<p>AGARD-CP-558 Advisory Group for Aerospace Research and Development North Atlantic Treaty Organization EROSION, CORROSION AND FOREIGN OBJECT DAMAGE EFFECTS IN GAS TURBINES Published November 1994 354 pages</p> <p>The Conference Proceedings contains 31 papers presented at the Propulsion and Energetics Panel Symposium on Erosion, Corrosion and Foreign Object Damage Effects in Gas Turbines which was held from 25-28th April 1994, in Rotterdam, The Netherlands. The Technical Evaluation Report and the Keynote Address are included at the beginning and discussions follow most papers.</p>	<p>AGARD-CP-558</p> <p>Aircraft engines Gas turbine engines Aircraft maintenance Damage Corrosion Erosion Foreign bodies Birds Dust Ice Sand Coatings Repair Deposition</p>

<p>The Symposium was arranged in the following Sessions: Operational Experience and Requirements (7); Deposition and Erosion (7); Foreign Object Damage (5); Coatings, Repair and Materials Aspects — 1 (4); Coatings, Repair and Materials Aspects — 2 (7); Testing and Certification Procedures (1).</p> <p>ISBN 92-836-0005-3</p>	<p>The Symposium was arranged in the following Sessions: Operational Experience and Requirements (7); Deposition and Erosion (7); Foreign Object Damage (5); Coatings, Repair and Materials Aspects — 1 (4); Coatings, Repair and Materials Aspects — 2 (7); Testing and Certification Procedures (1).</p> <p>ISBN 92-836-0005-3</p>
<p>The Symposium was arranged in the following Sessions: Operational Experience and Requirements (7); Deposition and Erosion (7); Foreign Object Damage (5); Coatings, Repair and Materials Aspects — 1 (4); Coatings, Repair and Materials Aspects — 2 (7); Testing and Certification Procedures (1).</p> <p>ISBN 92-836-0005-3</p>	<p>The Symposium was arranged in the following Sessions: Operational Experience and Requirements (7); Deposition and Erosion (7); Foreign Object Damage (5); Coatings, Repair and Materials Aspects — 1 (4); Coatings, Repair and Materials Aspects — 2 (7); Testing and Certification Procedures (1).</p> <p>ISBN 92-836-0005-3</p>



Aucun stock de publications n'a existé à AGARD. A partir de 1993, AGARD détiendra un stock limité des publications associées aux cycles de conférences et cours spéciaux ainsi que les AGARDographies et les rapports des groupes de travail, organisés et publiés à partir de 1993 inclus. Les demandes de renseignements doivent être adressées à AGARD par lettre ou par fax à l'adresse indiquée ci-dessus. *Veuillez ne pas téléphoner.* La diffusion initiale de toutes les publications de l'AGARD est effectuée auprès des pays membres de l'OTAN par l'intermédiaire des centres de distribution nationaux indiqués ci-dessous. Des exemplaires supplémentaires peuvent parfois être obtenus auprès de ces centres (à l'exception des Etats-Unis). Si vous souhaitez recevoir toutes les publications de l'AGARD, ou simplement celles qui concernent certains Panels, vous pouvez demander à être inclu sur la liste d'envoi de l'un de ces centres. Les publications de l'AGARD sont en vente auprès des agences indiquées ci-dessous, sous forme de photocopie ou de microfiche.

CENTRES DE DIFFUSION NATIONAUX

## ALLEMAGNE

Fachinformationszentrum,  
Karlsruhe  
D-76344 Eggenstein-Leopoldshafen 2

## BELGIQUE

Coordonnateur AGARD-VSL  
Etat-major de la Force aérienne  
Quartier Reine Elisabeth  
Rue d'Evere, 1140 Bruxelles

## CANADA

Directeur, Services d'information scientifique  
Ministère de la Défense nationale  
Ottawa, Ontario K1A 0K2

## DANEMARK

Danish Defence Research Establishment  
Ryvangs Allé 1  
P.O. Box 2715  
DK-2100 Copenhagen Ø

## ESPAGNE

INTA (AGARD Publications)  
Pintor Rosales 34  
28008 Madrid

## ETATS-UNIS

NASA Headquarters  
Code JOB-1  
Washington, D.C. 20546

## FRANCE

O.N.E.R.A. (Direction)  
29, Avenue de la Division Leclerc  
92322 Châtillon Cedex

## GRECE

Hellenic Air Force  
Air War College  
Scientific and Technical Library  
Dekelia Air Force Base  
Dekelia, Athens TGA 1010

## ISLANDE

Director of Aviation  
c/o Flugrad  
Reykjavik

## ITALIE

Aeronautica Militare  
Ufficio del Delegato Nazionale all'AGARD  
Aeroporto Pratica di Mare  
00040 Pomezia (Roma)

## LUXEMBOURG

Voir Belgique

## NORVEGE

Norwegian Defence Research Establishment  
Attn: Biblioteket  
P.O. Box 25  
N-2007 Kjeller

## PAYS-BAS

Netherlands Delegation to AGARD  
National Aerospace Laboratory NLR  
P.O. Box 90502  
1006 BM Amsterdam

## PORTUGAL

Força Aérea Portuguesa  
Centro de Documentação e Informação  
Alfragide  
2700 Amadora

## ROYAUME-UNI

Defence Research Information Centre  
Kentigern House  
65 Brown Street  
Glasgow G2 8EX

## TURQUIE

Millî Savunma Başkanlığı (MSB)  
ARGE Dairesi Başkanlığı (MSB)  
06650 Bakanlıklar-Ankara

**Le centre de distribution national des Etats-Unis ne détient PAS de stocks des publications de l'AGARD.**

D'éventuelles demandes de photocopies doivent être formulées directement auprès du NASA Center for Aerospace Information (CASI) à l'adresse ci-dessous. Toute notification de changement d'adresse doit être fait également auprès de CASI.

AGENCES DE VENTE

NASA Center for  
AeroSpace Information (CASI)  
800 Elkridge Landing Road  
Linthicum Heights, MD 21090-2934  
Etats-Unis

ESA/Information Retrieval Service  
European Space Agency  
10, rue Mario Nikis  
75015 Paris  
France

The British Library  
Document Supply Division  
Boston Spa, Wetherby  
West Yorkshire LS23 7BQ  
Royaume-Uni

Les demandes de microfiches ou de photocopies de documents AGARD (y compris les demandes faites auprès du CASI) doivent comporter la dénomination AGARD, ainsi que le numéro de série d'AGARD (par exemple AGARD-AG-315). Des informations analogues, telles que le titre et la date de publication sont souhaitables. Veuillez noter qu'il y a lieu de spécifier AGARD-R-nnn et AGARD-AR-nnn lors de la commande des rapports AGARD et des rapports consultatifs AGARD respectivement. Des références bibliographiques complètes ainsi que des résumés des publications AGARD figurent dans les journaux suivants:

Scientific and Technical Aerospace Reports (STAR)  
publié par la NASA Scientific and Technical  
Information Division  
NASA Headquarters (JTT)  
Washington D.C. 20546  
Etats-Unis

Government Reports Announcements and Index (GRA&I)  
publié par le National Technical Information Service  
Springfield  
Virginia 22161  
Etats-Unis  
(accessible également en mode interactif dans la base de  
données bibliographiques en ligne du NTIS, et sur CD-ROM)



AGARD holds limited quantities of the publications that accompanied Lecture Series and Special Courses held in 1993 or later, and of AGARDographs and Working Group reports published from 1993 onward. For details, write or send a telefax to the address given above. *Please do not telephone.*

AGARD does not hold stocks of publications that accompanied earlier Lecture Series or Courses or of any other publications. Initial distribution of all AGARD publications is made to NATO nations through the National Distribution Centres listed below. Further copies are sometimes available from these centres (except in the United States). If you have a need to receive all AGARD publications, or just those relating to one or more specific AGARD Panels, they may be willing to include you (or your organisation) on their distribution list. AGARD publications may be purchased from the Sales Agencies listed below, in photocopy or microfiche form.

NATIONAL DISTRIBUTION CENTRES

## BELGIUM

Coordonnateur AGARD — VSL  
Etat-major de la Force aérienne  
Quartier Reine Elisabeth  
Rue d'Evere, 1140 Bruxelles

## CANADA

Director Scientific Information Services  
Dept of National Defence  
Ottawa, Ontario K1A 0K2

## DENMARK

Danish Defence Research Establishment  
Ryvangs Allé 1  
P.O. Box 2715  
DK-2100 Copenhagen Ø

## FRANCE

O.N.E.R.A. (Direction)  
29 Avenue de la Division Leclerc  
92322 Châtillon Cedex

## GERMANY

Fachinformationszentrum  
Karlsruhe  
D-76344 Eggenstein-Leopoldshafen 2

## GREECE

Hellenic Air Force  
Air War College  
Scientific and Technical Library  
Dekelia Air Force Base  
Dekelia, Athens TGA 1010

## ICELAND

Director of Aviation  
c/o Flugrad  
Reykjavik

## ITALY

Aeronautica Militare  
Ufficio del Delegato Nazionale all'AGARD  
Aeroporto Pratica di Mare  
00040 Pomezia (Roma)

## LUXEMBOURG

See Belgium

## NETHERLANDS

Netherlands Delegation to AGARD  
National Aerospace Laboratory, NLR  
P.O. Box 90502  
1006 BM Amsterdam

## NORWAY

Norwegian Defence Research Establishment  
Attn: Biblioteket  
P.O. Box 25  
N-2007 Kjeller

## PORTUGAL

Força Aérea Portuguesa  
Centro de Documentação e Informação  
Alfragide  
2700 Amadora

## SPAIN

INTA (AGARD Publications)  
Pintor Rosales 34  
28008 Madrid

## TURKEY

Millî Savunma Başkanlığı (MSB)  
ARGE Dairesi Başkanlığı (MSB)  
06650 Bakanlıklar-Ankara

## UNITED KINGDOM

Defence Research Information Centre  
Kentigern House  
65 Brown Street  
Glasgow G2 8EX

## UNITED STATES

NASA Headquarters  
Code JOB-1  
Washington, D.C. 20546

**The United States National Distribution Centre does NOT hold stocks of AGARD publications.**

Applications for copies should be made direct to the NASA Center for AeroSpace Information (CASI) at the address below.

Change of address requests should also go to CASI.

SALES AGENCIES

## NASA Center for

AeroSpace Information (CASI)  
800 Elkridge Landing Road  
Linthicum Heights, MD 21090-2934  
United States

ESA/Information Retrieval Service  
European Space Agency  
10, rue Mario Nikis  
75015 Paris  
France

The British Library  
Document Supply Centre  
Boston Spa, Wetherby  
West Yorkshire LS23 7BQ  
United Kingdom

Requests for microfiches or photocopies of AGARD documents (including requests to CASI) should include the word 'AGARD' and the AGARD serial number (for example AGARD-AG-315). Collateral information such as title and publication date is desirable. Note that AGARD Reports and Advisory Reports should be specified as AGARD-R-nnn and AGARD-AR-nnn, respectively. Full bibliographical references and abstracts of AGARD publications are given in the following journals:

Scientific and Technical Aerospace Reports (STAR)  
published by NASA Scientific and Technical  
Information Division  
NASA Headquarters (JTT)  
Washington D.C. 20546  
United States

Government Reports Announcements and Index (GRA&I)  
published by the National Technical Information Service  
Springfield  
Virginia 22161  
United States  
(also available online in the NTIS Bibliographic  
Database or on CD-ROM)

